Environmental Chemistry for a Sustainable World 36

Saravanan Rajendran
Mu. Naushad
Lorena Cornejo Ponce
Eric Lichtfouse *Editors*

Green Photocatalysts for Energy and Environmental Process

Springer

Environmental Chemistry for a Sustainable World

Volume 36

Series Editors
Eric Lichtfouse, Aix-Marseille University, CEREGE, CNRS, IRD, INRA, Coll France, Aix-en-Provence, France
Jan Schwarzbauer, RWTH Aachen University, Aachen, Germany
Didier Robert, CNRS, European Laboratory for Catalysis and Surface Sciences, Saint-Avold, France

Other Publications by the Editors

Books
Environmental Chemistry
http://www.springer.com/978-3-540-22860-8

Organic Contaminants in Riverine and Groundwater Systems
http://www.springer.com/978-3-540-31169-0

Sustainable Agriculture
Volume 1: http://www.springer.com/978-90-481-2665-1
Volume 2: http://www.springer.com/978-94-007-0393-3

Book series
Environmental Chemistry for a Sustainable World
http://www.springer.com/series/11480

Sustainable Agriculture Reviews
http://www.springer.com/series/8380

Journals
Environmental Chemistry Letters
http://www.springer.com/10311

Agronomy for Sustainable Development
http://www.springer.com/13593

More information about this series at http://www.springer.com/series/11480

Saravanan Rajendran • Mu. Naushad
Lorena Cornejo Ponce • Eric Lichtfouse
Editors

Green Photocatalysts for Energy and Environmental Process

Springer

Editors
Saravanan Rajendran
Faculty of Engineering, Mechanical
Department
University of Tarapacá
Arica, Chile

Lorena Cornejo Ponce
Faculty of Engineering, Department
of Mechanical Engineering
University of Tarapacá
Arica, Chile

Mu. Naushad
Department of Chemistry, College of Science
King Saud University
Riyadh, Saudi Arabia

Eric Lichtfouse
CNRS, IRD, INRA, Coll France, CEREGE
Aix Marseille University
Aix-en-Provence, France

ISSN 2213-7114 ISSN 2213-7122 (electronic)
Environmental Chemistry for a Sustainable World
ISBN 978-3-030-17637-2 ISBN 978-3-030-17638-9 (eBook)
https://doi.org/10.1007/978-3-030-17638-9

© Springer Nature Switzerland AG 2020
This work is subject to copyright. All rights are reserved by the Publisher, whether the whole or part of the material is concerned, specifically the rights of translation, reprinting, reuse of illustrations, recitation, broadcasting, reproduction on microfilms or in any other physical way, and transmission or information storage and retrieval, electronic adaptation, computer software, or by similar or dissimilar methodology now known or hereafter developed.
The use of general descriptive names, registered names, trademarks, service marks, etc. in this publication does not imply, even in the absence of a specific statement, that such names are exempt from the relevant protective laws and regulations and therefore free for general use.
The publisher, the authors, and the editors are safe to assume that the advice and information in this book are believed to be true and accurate at the date of publication. Neither the publisher nor the authors or the editors give a warranty, express or implied, with respect to the material contained herein or for any errors or omissions that may have been made. The publisher remains neutral with regard to jurisdictional claims in published maps and institutional affiliations.

This Springer imprint is published by the registered company Springer Nature Switzerland AG.
The registered company address is: Gewerbestrasse 11, 6330 Cham, Switzerland

Preface

Photocatalysis is a unique, gifted method which was invented by Fujishima and Honda in the year 1972. Photocatalysis is one of the most promising technologies for the decomposition of organic and air pollutants. Many photocatalysts have been used over the last decades for the decomposition of various types of pollutants. This book describes the photocatalyst and its diverse applications in the environmental and energy fields. Especially, removal of air and water pollutants, generation of hydrogen, photo fuel cell, electrophotocatalyst, solar energy conversion, and green biophotocatalyst are defined in more depth. Moreover, the role of catalysts along with their chemical reactions, challenges, past developments, and directions for further research on photocatalyst are also discussed here. This book presents necessary knowledge and visualization of the fundamental differences that exist between photocatalytic and photoelectrocatalytic fuel cells to the new researchers in this field, as well as serves as a handy manual to the experienced researchers. The book also deals with the recent developments of quantum dots (QDs) and photocatalytic applications of QDs such as carbon materials like carbon and graphene-based QDs, metal, metal sulfide, and metal oxide-based QDs. It also includes a detailed review on various types of templates used for the preparation of porous g-C_3N_4 and its applications with special reference to dye degradation, reduction of hexavalent Cr, and reduction of CO_2 and for the evolution of H_2 photocatalytically. This book offers an intriguing and useful guide for a broad readership in various fields of catalysis, material sciences, environment, and energy.

Arica, Chile — Saravanan Rajendran
Riyadh, Saudi Arabia — Mu. Naushad
Arica, Chile — Lorena Cornejo Ponce
Aix-en-Provence, France — Eric Lichtfouse

Acknowledgements

First of all, we would like to thank Almighty God for giving us strength and ability to complete this book. We are highly grateful to all the authors for their valuable contributions to this book. Our sincere thanks to the series editor and advisory board members for accepting our book as a part of the series entitled Environmental Chemistry for a Sustainable World. We are also very grateful to the reviewers for their appropriate and constructive suggestions/comments to improve the quality of this book. We would like to express our sincere thanks to the researchers and publisher for permitting us the copyright to use their figures and tables. We would, at the outset, like to offer our apologies to any copyright holder if unknowingly their right is being infringed.

Saravanan Rajendran would like to thank Prof. Francisco Gracia (DIQBT, University of Chile) and Prof. Rodrigo Palma (Director, SERC) for their constant support, encouragement and valuable suggestions to complete the task. Furthermore, he is grateful to the Government of Chile (CONICYT-FONDECYT-Project No.: 11170414) and SERC-Chile (CONICYT/FONDAP/15110019) for financial support. Finally, He expresses his sincere thanks to the Faculty of Engineering in the Department of Mechanical Engineering at the University of Tarapacá, Arica, Chile.

Lorena Cornejo Ponce likes to express her sincere thanks to the Faculty of Engineering in the Department of Mechanical Engineering at the University of Tarapacá, Arica. She extends her thanks for the financial support from Ayllu Solar and SERC-CHILE (CONICYT/FONDAP/15110019).

Dr. Mu. Naushad extends his appreciation to the Deanship of Scientific Research at King Saud University, Saudi Arabia for financial support.

Arica, Chile Saravanan Rajendran
Riyadh, Saudi Arabia Mu. Naushad
Arica, Chile Lorena Cornejo Ponce
Aix-en-Provence, France Eric Lichtfouse

Contents

1 Green Photocatalyst for Diverge Applications . . . 1
D. Durgalakshmi, R. Ajay Rakkesh, Saravanan Rajendran, and Mu. Naushad

2 Photocatalysts and Photoelectrocatalysts in Fuel Cells and Photofuel Cells . . . 19
Prasenjit Bhunia and Kingshuk Dutta

3 Titania-Based Heterojunctions for Hydrogen Generation by Water Photolysis . . . 57
L. K. Preethi, Rajini P. Antony, and Tom Mathews

4 Quantum Dots in Green Photocatalytic Applications for Degradation of Environmental Pollutants and Hydrogen Evolution . . . 87
Selvaraj Devi and Vairaperumal Tharmaraj

5 Evolution of ZnO-Based Photocatalyst for the Degradation of Pollutants . . . 109
S. Kaviya

6 Designing Metal-Organic Frameworks Based Photocatalyst for Specific Photocatalytic Reactions: A Crystal Engineering Approach . . . 141
Partha Pratim Bag and Pathik Sahoo

7 Photobiocatalysis: At the Interface of Photocatalysis and Biocatalysts . . . 187
Madan L. Verma, Sarita Devi, and Motilal Mathesh

8 Photo-/Electro-catalytic Applications of Visible Light-Responsive Porous Graphitic Carbon Nitride Toward Environmental Remediation and Solar Energy Conversion 211
Sulagna Patnaik, Gayatri Swain, and K. M. Parida

9 Photocatalysts for Indoor Air Pollution: A Brief Review 247
Shanmuga Sundar Dhanabalan, Sivanantha Raja Avaninathan, Saravanan Rajendran, and Marcos Flores Carrasco

10 Two Dimensional-Based Materials for Photocatalysis Applications 275
Gnanaseelan Natarajan, Felipe Caballero-Briones, and Sathish-Kumar Kamaraj

11 Synthesis and Characterization of Single-Phased $BiFeO_3$ Nanostructures for Photocatalytic Applications: Hydrothermal Approach 295
Muniyandi Muneeswaran, Radhalayam Dhanalakshmi, and Ali Akbari-Fakhrabadi

Index 317

About the Editors and Contributors

Editors

Saravanan Rajendran received his PhD in Physics–Material Science in 2013 from the Department of Nuclear Physics, University of Madras, Chennai, India. He was awarded the University Research Fellowship (URF) during the years 2009–2011 by the University of Madras. After working as an Assistant Professor in Dhanalakshmi College of Engineering, Chennai, India, during the year 2013–2014, he was awarded SERC and CONICYT-FONDECYT postdoctoral fellowship, University of Chile, Santiago, in the years 2014–2017. He has worked (2017–2018) in the research group of Professor John Irvine, School of Chemistry, University of St Andrews, UK, as a postdoctoral research fellow within the framework of an EPSRC-Global Challenges Research Fund for the removal of Blue-Green Algae and their toxins. Currently, he is working as a research scientist in the Faculty of Engineering, Department of Mechanical Engineering, University of Tarapacá, Arica, Chile, and is Research Associate in SERC, University of Chile, Santiago, Chile. He is Associate Editor of the *International Journal of Environmental Science and Technology* (Springer). His research interests focus on the area of nanostructured functional materials, photophysics, surface chemistry and nanocatalysts for renewable energy and waste water purification. He has published several international peer-reviewed journals, five book chapters, and three books published by renowned international publishers.

Mu. Naushad is presently Associate Professor in the Department of Chemistry, College of Science, King Saud University (KSU), Riyadh, Kingdom of Saudi Arabia. He obtained his MSc and PhD in Analytical Chemistry from Aligarh Muslim University, Aligarh, India, in 2002 and 2007, respectively. He has a vast research experience in the fields of Materials Chemistry and Environmental Science. He holds several US patents, over 250 publications in international journals of repute, 20 book chapters and several books published by renowned international publishers. He has more than 6000 citations with a Google Scholar H-Index of more than 47. He has successfully run several research projects funded by National Plan for Science, Technology and Innovation (NPST) and King Abdulaziz City for Science and Technology (KACST), Kingdom of Saudi Arabia. He is the editor/editorial member of several reputed journals like *Scientific Report* (Nature); *Process Safety & Environmental Protection* (Elsevier); *Journal of Water Process Engineering* (Elsevier), and *International Journal of Environmental Research & Public Health* (MDPI). He is also the associate editor for *Environmental Chemistry Letters* (Springer) and *Desalination & Water Treatment* (Taylor & Francis). He has been awarded the Scientist of the Year Award – 2015 from National Environmental Science Academy, Delhi, India, and Almarai Award – 2017, Saudi Arabia.

Lorena Cornejo Ponce is currently working as a professor in the Faculty of Engineering in the Department of Mechanical Engineering at University of Tarapacá, Arica, Chile. She obtained her Master's degree in Chemistry (Analytical Chemistry) and PhD (Science-Chemistry) at the State University of Campinas, Campinas-Brazil, in the years 1988–1995. Further, she continued her postdoctorate in the same university in the year 1998. She is interested in the field of spectroscopic analysis, environmental issues and novel catalysts, developing new technology in the area of decontamination, water disinfection, and solar water treatment. She has published several articles in ISI publications, book chapters, and conference proceedings. She has handled successfully several national and international research projects financed by different government and private funding agents such as FONDECYT, FONDAP, FIC, CONICYT, OAS, and CYTED. She obtained international recognition awards – 2 MERCOSUR (Science and Technology – integration category) in 2006 and 2011. Also, she is Coordinator in the Laboratory of Environmental Research of Arid Zones, LIMZA. In addition, she holds the position of Principal Investigator and Coordinator of Line No. 1: Solar Water Treatment of SERC-CHILE. She also participates in the AYLLU SOLAR Project, Solar Energy: Sustainable Development for Arica and Parinacota as a member of the Steering Committee and as the Coordinator of the 'Solar Water Treatment' area.

Eric Lichtfouse (PhD), born in 1960, is an environmental chemist working at the University of Aix-Marseille, France. He has invented carbon-13 dating, a method that allows measuring of the relative age and turnover of molecular organic compounds occurring in different temporal pools of any complex media. He is teaching scientific writing and communication, and has published the book *Scientific Writing for Impact Factors*, which includes a new tool – the Micro-Article – to identify the novelty of research results. He is the founder and chief editor of scientific journals and series in environmental chemistry and agriculture. He received the Analytical Chemistry Prize by the French Chemical Society, the Grand Prize of the Universities of Nancy and Metz, and a Journal Citation Award by the Essential Indicators.

Contributors

R. Ajay Rakkesh Centre for Advanced Study in Crystallography and Biophysics, University of Madras, Chennai, India

Ali Akbari-Fakhrabadi Advanced Materials Laboratory, Department of Mechanical Engineering, University of Chile, Santiago, Chile

Rajini P. Antony Water and Steam Chemistry Division, BARC – F, Kalpakkam, Tamil Nadu, India

Partha Pratim Bag Department of Basic Science and Humanitics, Dumka Engineering College, Dumka, Jharkhand, India

Prasenjit Bhunia Department of Chemical Engineering, Indian Institute of Technology, Kharagpur, India

Felipe Caballero-Briones Instituto Politécnico Nacional, Materiales para Energía, Salud y Medio Ambiente (GESMAT), CICATA Altamira, Altamira, México

Marcos Flores Carrasco Department of Physics, Universidad de Chile, Santiago, Chile

Sarita Devi Department of Patents and Designs, BoudhikSampada Bhawan, Dwarka, New Delhi, India

Selvaraj Devi Department of Inorganic Chemistry, University of Madras, Chennai, India

Radhalayam Dhanalakshmi Department of Chemical Engineering, Indian Institute of Technology Madras, Chennai, Tamil Nadu, India

D. Durgalakshmi Department of Medical Physics, Anna University, Chennai, India

Kingshuk Dutta Department of Materials Science and Engineering, Cornell University, Ithaca, NY, USA
Advanced Research School for Technology and Product Simulation (ARSTPS), School for Advanced Research in Polymers (SARP), Central Institute of Plastics Engineering and Technology (CIPET), Chennai, India

Sathish-Kumar Kamaraj Instituto Tecnológico El Llano (ITEL)/Tecnológico Nacional de México (TecNM), Laboratorio de Cultivo de Tejidos Vegetales, Aguascalientes, México

S. Kaviya Department of Chemical Engineering, Indian Institute of Science (IISC), Bangalore, India

Eric Lichtfouse Aix Marseille University, CNRS, IRD, INRA, Coll France, CEREGE, Aix-en-Provence, France

Motilal Mathesh Institute of Molecules and Materials, Radboud University, Nijmegen, The Netherlands

Tom Mathews Thin Films and Coatings Section, Surface and Nanoscience Division, Materials Science Group, Indira Gandhi Centre for Atomic Research, Kalpakkam, Tamil Nadu, India

Muniyandi Muneeswaran Advanced Materials Laboratory, Department of Mechanical Engineering, University of Chile, Santiago, Chile

Gnanaseelan Natarajan Instituto Politécnico Nacional, Materiales para Energía, Salud y Medio Ambiente (GESMAT), CICATA Altamira, Altamira, México

Mu. Naushad Department of Chemistry, College of Science, King Saud University, Riyadh, Saudi Arabia

K. M. Parida Centre for Nano Science and Nanotechnology, Siksha O Anusandhan (Deemed to be University), Bhubaneswar, Odisha, India

Sulagna Patnaik Centre for Nano Science and Nanotechnology, Siksha O Anusandhan (Deemed to be University), Bhubaneswar, Odisha, India

Lorena Cornejo Ponce Faculty of Engineering, Department of Mechanical Engineering, University of Tarapacá, Arica, Chile

L. K. Preethi Centre for Nanoscience and Nanotechnology, International Research Centre, Sathyabama Institute of Science and Technology, Chennai, Tamil Nadu, India

Saravanan Rajendran Faculty of Engineering, Mechanical Department, University of Tarapacá, Arica, Chile

Pathik Sahoo Soft Chemistry Group, International Center for Materials Nanoarchitectonics, National Institute for Materials Science (NIMS), Tsukuba, Ibaraki, Japan

Shanmuga Sundar Dhanabalan Department of Physics, Universidad de Chile, Santiago, Chile

Sivanantha Raja Avaninathan Department of ECE, Alagappa Chettiar Government College of Engineering & Technology, Karaikudi, Tamil Nadu, India

Gayatri Swain Centre for Nano Science and Nanotechnology, Siksha O Anusandhan (Deemed to be University), Bhubaneswar, Odisha, India

Vairaperumal Tharmaraj Department of Analytical Chemistry, National Chung-Hsing University, Taichung, Taiwan

Madan L. Verma Center for Chemistry and Biotechnology, Deakin University, Geelong, VIC, Australia
Department of Biotechnology, Dr. YS Parmar University of Horticulture and Forestry, Hamirpur, Himachal Pradesh, India

Chapter 1
Green Photocatalyst for Diverge Applications

D. Durgalakshmi, R. Ajay Rakkesh, Saravanan Rajendran, and Mu. Naushad

Contents

1.1 Introduction . . . 2
1.2 Need for Green Materials . . . 5
1.3 Green Photocatalysis . . . 6
  1.3.1 Metal Oxide-Based Photocatalyst . . . 6
1.4 Green Materials in Fuel Cells . . . 8
1.5 Green Photocatalytic Disinfection of Water . . . 9
1.6 Bio-Based Materials . . . 10
1.7 Simultaneous Removal of Organic and Inorganic Pollutants Using Activated Carbon . . 12
1.8 Conclusion . . . 12
References . . . 14

Abstract The demand for sustainable materials in the area of energy and environment has been going forth among researchers over the past several years. This is imputable to the increasing demand globally in the field of energy and environmental sectors to conserve the materials for future needs, either in the form of reuse or reprocessing the materials by environmentally friendly style. The advancement in the green photoactive nanostructure materials for energy- and environmental-related applications has been increased gradually, and sophisticated progress has also been developed and carried out innovatively. Various synthesis approaches have been demonstrated to synthesize materials using environmentally benign chemicals.

D. Durgalakshmi (✉)
Department of Medical Physics, Anna University, Chennai, India

R. Ajay Rakkesh
Centre for Advanced Study in Crystallography and Biophysics, University of Madras, Chennai, India

S. Rajendran
Faculty of Engineering, Mechanical Department, University of Tarapacá, Arica, Chile

M. Naushad
Department of Chemistry, College of Science, King Saud University, Riyadh, Saudi Arabia

S. Rajendran et al. (eds.), *Green Photocatalysts for Energy and Environmental Process*, Environmental Chemistry for a Sustainable World 36,
https://doi.org/10.1007/978-3-030-17638-9_1

There are several green chemicals available in our ecosystem, including biomass, recycling chemical waste and carbon dioxide, etc. On the whole, the incorporation of green chemistry is an essential role to maintain vast technological development and the economic competitiveness of advanced social club as easily as for future generations.

Keywords Green photocatalyst · Nanomaterials · Energy · Environment · Bio-based materials · Solar disinfection

1.1 Introduction

Manufacturing green and sustainable materials has received global recognition in recent decades. The US Department of Commerce defined the term “sustainable manufacturing” as “the creating of manufactured products that use processes that are non-polluting, conserve energy and natural resources, and are economically sound and safe for employees, communities, and consumers” (Moldavska and Welo 2017). These sustainable materials are mainly focused on the energy conservation and expensive resources in the form of recycling, recovery, and reuse of the industrial waste virtually in the entire sector, but not constrained to agriculture, infrastructure development, transportation, aerospace, powerhouse, and many others.

The estimated production of electrical energy can rise by an average of 2.4% per year (Company 2018). Currently, the combustion of fossil fuel generates of about 65% in the world’s electric power (Covert et al. 2016). But severe demands have been forced by international governing bodies, and government agreements are approaching carbon dioxide-free energies. The global energy generation development since 2003 is given in Fig. 1.1 (Ren21 2016). The chart shows the increase in the percentage of solar, geothermal, biomass, and wind energy sources in recent years. Figure 1.2 illustrates the emission of carbon dioxide during the consumption of electrical energy from various sources (Goldemberg 2007; Ramesh et al. 2010). As of now, lowest carbon dioxide emission can be obtained by the use of wind, nuclear, and hydroelectric energies. For the reason that hazardous waste can be produced in the power generation, they can be named as “green and clean” power generation. With these power generation sources, it is possible to increase cycling efficiencies, reduce the cost of installation, and reduce carbon dioxide emission. These developments are naturally connected to the performance of the material.

Apart from the power generation and green sources, many naturally available materials are currently applicable for disinfection of toxic pollutants, pathogens, and harmful chemical wastes in the drinking water (Naushad et al. 2017; Alqadami et al. 2017; Ghasemi et al. 2014). For urban development, eco-friendly and catalyst-supported materials are widely used for the replacement of asbestos, toxic chemicals, and dyes in the building constructions (Milani 2005, Singh et al. 2015a). Natural biological macromolecules are abundant resources in our ecosystem. They possess very good biodegradable activity as well as biological capability. By applying heat

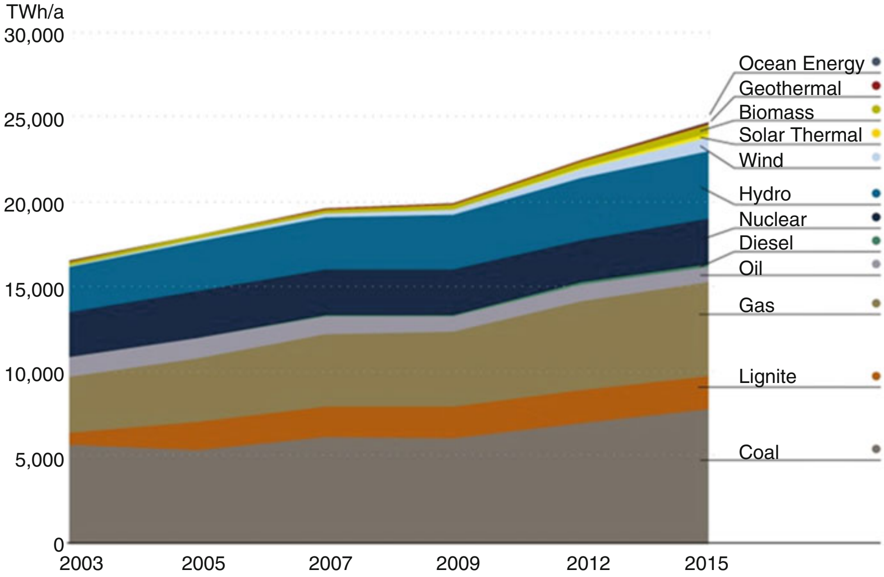

Fig. 1.1 Global power generation development since 2002. (Source: International Energy Agency, Paris, France; Ren21 2016)

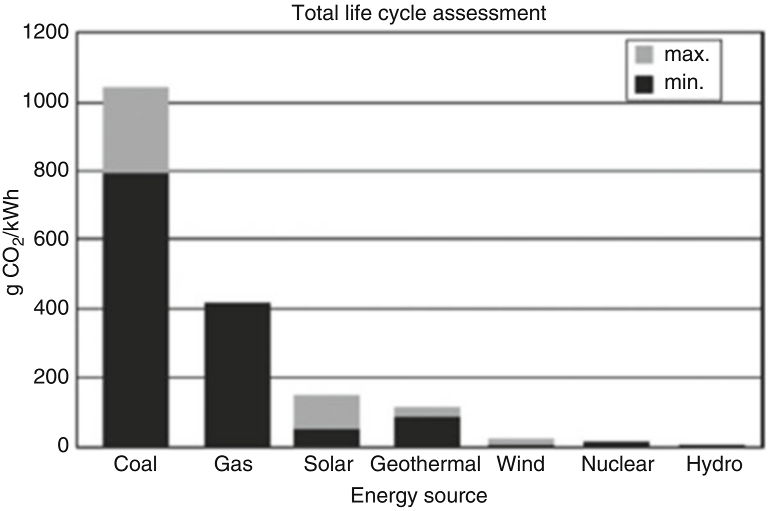

Fig. 1.2 The comparison chart illustrates the carbon dioxide emission vs. various energy sources during the production of electrical energy. (Ramesh et al. 2010)

treatment and carbonization of naturally available wood and bamboo biomasses at the desired temperature, natural biological macromolecules are formed (Yahya et al. 2015). These methods of preparing natural materials show higher efficiency than the chemically prepared one, and recycling capability with the natural resources is highly favorable and reproducible.

The usual conception and leadership of eco-material management and the materials, which are used for environmental engineering, are not only to induce the decontamination function but also to organize the ecosystem to safeguard the environment. Moreover, extensive researches have been carried out in recent days on the field of environmental engineering-based materials to hold up the idea of environmental purification, pollution control and prevention, and recycling of the waste (Salvato et al. 2003; Saha and Darnton 2005; Sharma et al. 2017). Some of the major contaminations of envrionmental materials includes, asbestos may contain a diverse fire-retarding capability and plastics like highly flammable, noise prevention, dust and smoke filter material, UV absorb material and more. The effect of electromagnetic/radioactive waves to the humans increases every year and causes serious health issues to mankind (Zhi et al. 2017; Aldrich and Easterly 1987). In order to reduce radioactive contamination, scientists are looking for the perfect design of shielding materials (Heusser 1995). The purpose of the electromagnetic shielding material is to protect mankind from the exposure of electromagnetic radiations generated by electronics devices (Varadan et al. 1994; Gupta et al. 2014; Wen et al. 2014).

Photocatalysis is a new technology for the control of environmental pollutions (Schultz and Yoon 2014; Spasiano et al. 2015); however, the practical usage of this technology has been constrained owing to poor efficacy and insufficient light-absorbing capability and can stimulate the photocatalytic activity only under the UV light. To resolve these limitations, various technologies have been adopted and demonstrated to discover some fruitful findings (Moniz et al. 2015; Dong et al. 2015; Fagan et al. 2016; Lang et al. 2014). Recently, researchers have developed TiO_2 nanostructures with various metal and nonmetal ions doping to engineer the native properties of the TiO_2. This kind of modulation in the materialistic perspective could effectively improve the photocatalytic performances of the TiO_2 nanostructures (Jaiswal et al. 2015; Etacheri et al. 2015).

The process of synthesizing materials without the use of toxic or hazardous chemical precursors is known as green synthesis or green processing technique. This processing route avoids the chemical waste by creating pollutants within the material processing and also an economically viable route for synthesizing several types of nanostructures (Lancaster 2016). Using this green chemistry route, metal oxides, noble metals and carbon nanostructures are bring produced at very cost by using biomass and low toxic chemical precursors. It requires very low power, low pollution, less wastage, and economically viable route to construct the materials from atomic level for photocatalytic applications (Sheldon 2016; Lancaster 2016; Yaremenko et al. 2016).

1.2 Need for Green Materials

Synthesis of materials from natural, renewable, and biological resources should be maintained to increase the significance in the near future. Materials like semiconductors, noble metals, and ceramics are prepared from the abovementioned natural resources, which involve minimal energy for the fabrication process and fewer by-products for removal (Prusty et al. 2016). For example, materials like carbon-based nanostructures are fabricated from renewable resources such as sugarcane bagasse, coconut coir, peanuts, bamboo wood, groundnut shell, and coal (Al-Othman et al. 2012). It requires less energy to produce carbon-based nanostructures by calcination and filtration of mentioned naturally available resources.

Comparing the conventional method of producing carbon nanostructure requires sophisticated fabrication methods like chemical vapor deposition and molecular beam epitaxy and thermal exfoliation techniques. Those techniques consume very high energy, involve toxic chemicals and release of harmful gases, and have very high cost of production (Ramírez-Rico et al. 2017; Singh et al. 2015b). In the vision of green technology, more products can be manufactured through an eco-friendly way without being harmful to our society and the ecosystem. The consumption of energy and the release of toxic emission are comparably less in the green chemistry route. The existing technologies for the energy distribution throughout the world are wind energy, nuclear energy, and hydroelectric energy, which produced in a greener way from fossil fuels (Bilgili et al. 2015; Abas et al. 2015). To balance the total need of energy for the world population, alternate energy production techniques should be implemented in a greener way.

Materials are a basic boon for the recent technology, and their performance and varieties of properties establish the product reliability and effectiveness. Moreover, current advancement in the creation of new materials can be directly used for energy- and environmental-related applications. The new materials can be processed by the advanced technology, which is capable of making the relationship between the protocol creator, material maker, designer, and developer. This is a comprehensive way to identify a sustainable material for environmental processes. In another few years, there will be a huge global need in the advanced materials for energy and environmental fields. It is the only way to avoid high carbon emission and high power consumption materials for energy production (Ali et al. 2017; Schandl et al. 2016). The current goal is to develop a sustainable material for energy- and environmental-related fields, and awareness should be created in the form of education or governmental programs for the new generation about the usage of sustainable materials in the near future (Priedulena and Hogeforster 2016).

1.3 Green Photocatalysis

The process of splitting of water into hydrogen and oxygen with the help of metal oxide photocatalysts under the illumination of UV light was first reported by Fujishima and Honda in the year 1972. Further, the work has been extended in a fruitful manner and obtained significant results in terms of efficiency (Kumar et al. 2019). Since 1972, the field has received great interest among the researchers due to the excellent potential in the field of energy- and environmental-related issues. For the past few decades, metal oxide semiconductors play a vital role in the field of photocatalysis due to high reactivity, great stability, and being chemically inert and low cost. Certain metal oxide semiconductors like TiO_2, ZnO, MoO_3, Fe_3O_4, and so on are the suitable materials for water remediation, hydrogen fuel production, removal of toxic wastes in the water bodies, and pharmaceutical waste removal applications (Lee et al. 2016; Chan et al. 2011; Daghrir et al. 2013; Wu et al. 2011; Naushad et al. 2015). Those materials show excellent physiochemical, electronic, and structural properties, which helps to perform better in the mentioned applications. The term photocatalysis is the process of converting solar or light energy into chemical energy. The word photo means light, and the word catalysis means to speed up or break apart or degrade the chemical reaction. On the whole, the photocatalysis facilitates to degrade the toxic pollutants present in the aqueous solution by breaking it with the help of light energy and to activate the chemical reactions effectively (Lin et al. 2018).

Photocatalysts are classified into several types; mainly three types are majorly focused on recent research reports, namely, semiconductor photocatalyst, plasmonic photocatalyst, and heterogeneous photocatalyst. The detailed survey on each type has been discussed in the following sections. In general, green photocatalysis is a process of synthesizing route, which helps to prepare different photocatalysts with the use of natural resources, biomasses, and biological extract (Fox and Dulay 1993). Those precursors (resource materials) are eco-friendly, green sources, and economically viable route for the conversion of light energy to chemical energy over the semiconducting materials, for instance, the removal of pollutants in the water bodies, the reduction of toxic molecules, and the production of hydrogen fuels (Fox and Dulay 1993; Herrmann 2005; Herrmann 1999).

1.3.1 Metal Oxide-Based Photocatalyst

Metal oxide-based semiconducting nanomaterials have been used for the photocatalytic technology for treating environmental pollutions because of its unusual physiochemical properties, high thermal and chemical stability, and excellent charge transport capability. It plays a major role in the generation of fossil fuels (hydrogen) by the photo-electrochemical splitting of water into hydrogen and oxygen and also degradation of toxic pollutants in water (Ni et al. 2007; Ahmad et al. 2015). The creation of radical reactive species at the surface of the

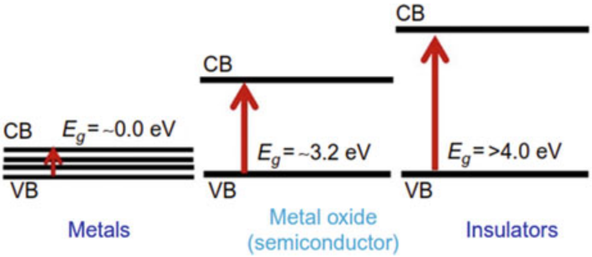

Fig. 1.3 Pictorial representation of energy gap for metals, semiconductors, and insulators

photocatalyst plays a significant role in the photocatalytic performance, which can be controlled or influenced by the native defect or vacancies in the lattice of the crystal system.

When a light source interacts with the surface of the semiconducting materials like TiO_2, ZnO, MoO_3, Fe_3O_4, and so on and absorbs the light energy at the appropriate wavelength, electron-hole pairs are generated in the conduction and valence band, respectively (Clavero 2014; Djurišić et al. 2014). The residing electrons in the valence band of the semiconductor excited to the conduction band when irradiated by light, leaving the holes in the VB. The positively charged holes and negatively charged electrons are created. The gap between the valence and conduction band is called bandgap of a material. Figure 1.3 illustrates the energy structure of metals, semiconductors, and insulators (Khan 2018).

Apart from different types of metal oxide semiconductors, TiO_2 has gained wider interest among the researchers due to their wider bandgap, unusual physiochemical properties, chemically inert, low cost, biocompatibility, high stability, and non-toxicity (Diebold 2003; Gaya and Abdullah 2008). A considerable variety of photocatalytic nanomaterials, especially metal oxide photocatalyst, plasmonic photocatalytic, and metal chalcogenides, have been demonstrated for the effective degradation of toxic pollutants. Recently, some other metal oxide-based photocatalysts like ZnO, SnO_2, MoO_3, Fe_2O_3, and V_2O_5 have been demonstrated widely and also improve the photocatalytic performances by engineering the structural, chemical, and electronic properties of the host material by doping methodologies (Candal and Martínez-de la Cruz 2015).

However, low bandgap materials have also been used in the field of photocatalyst by engineering in a better way to absorb a wide range of light intensity, fast-charge separation, and transfer processes and thus possess a significant material for photocatalyst. To date, considerable literature is reported on the fabrication of excellent photocatalytic material with wider light-capturing capacity and also superior photocatalytic efficiency (Cao and Yu 2014; Chen et al. 2010; Yang et al. 2013). In this way, favorable results have been collected with the use of several approaches by engineering the material architecture to get the enhanced optical and physiochemical properties of different types of semiconductors, including noble metal incorporation, doping, substitution, dye sensitization, and composite formation. But, most of the photocatalysts can be applicable to treat air contamination, water purification, environmental disinfection, and fuel generations that are in the laboratory-scale level.

1.4 Green Materials in Fuel Cells

The production of fuels from green processes or chemistry is a vital source for the current generation. The major dependency on the existing fuels like petroleum products creates more pollution and high cost due to lower availability in our environment. It is necessary to identify an alternate source for energy materials, which is environmentally friendly, low cost, and easily available in nature. The green photocatalyst is the method of creating fossil fuels with light energy and natural resources. For example, hydrogen fuels and biodiesel can be obtained from the biomasses (Demirbas 2008, 2011). Hydrogen fuel is one of the zero-carbon emission transportation fuels, which can be derived from the biomass, but it is limited for the large production process (Demirbas 2011).

This kind of fuels produced from the natural resources can reduce the emission of greenhouse gases to our environment and improves the quality of the atmospheric air. Nanotechnology is the best tool for making this happen into the real world (Clavero 2014; Gupta et al. 2014; Iavicoli et al. 2014). This signifies an excellent platform for the research groups to bring out the new renewable energy materials with the aid of nanotechnology. The current studies listed out different areas where nanotechnology plays a vital role in the alternative energy production: Li-ion batteries, flow batteries, supercapacitors, fuel cells, solar cells, and fire and heat retardant insulation applications.

Nanotechnology presents a better way for the production of solar cell technology. Essentially, the process of fabrication is purely based on the absorption of light and transportation of charge carriers, readily accessible and low cost of production (Berardi et al. 2014; Zhou et al. 2010). Coloring agents extracted from plants are used for the sensitization purpose in the dye-sensitized solar cells (DSSCs). The coloring agents help to absorb wide light radiation, which increases the solar cell efficiency.

Figure 1.4 illustrates the comparison of biomass-derived battery electric and hydrogen fuels for vehicular transportation. Hydrogen fuels are produced by the

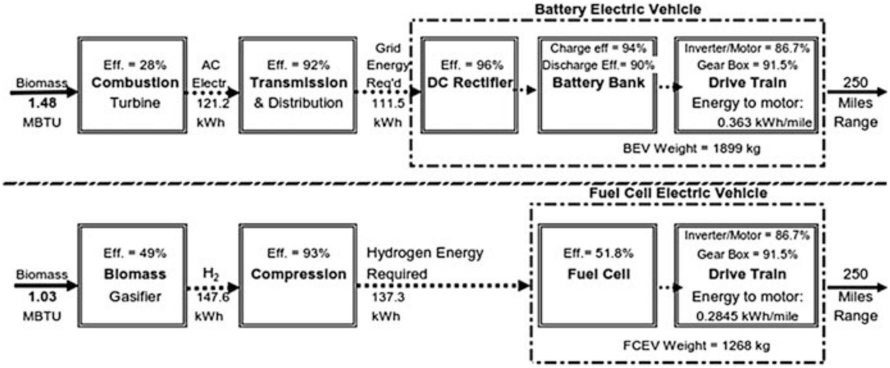

Fig. 1.4 Block diagram represents the comparison of converting biomass into a battery electric vehicle and a fuel cell electric vehicle. (Thomas 2009)

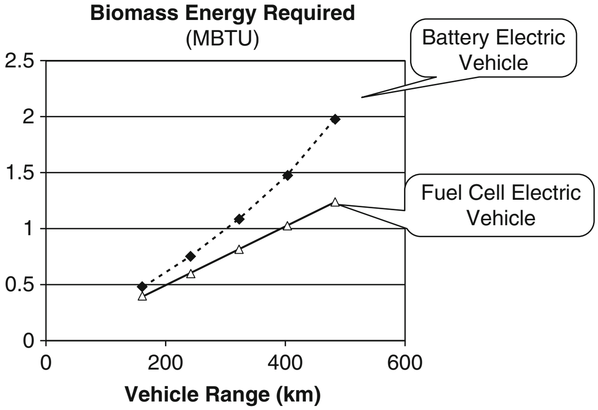

Fig. 1.5 The efficiency plot as a function of biomass energy required vs. vehicle range (km) for battery electric vehicle and the fuel cell electric vehicle. (Thomas 2009)

conversion of biomass, which consumes 35% less energy than the electricity produced to travel 400 km by a battery electric vehicle. Figure 1.5 shows the advantages of the use of natural gas for fuel cell electric vehicle decreases if both vehicle ranges are reduced to about 160 km.

1.5 Green Photocatalytic Disinfection of Water

Water is an essential need for human life. The existence of fresh and clean water in our ecosystem is very limited (Gnanasekaran et al. 2018; Albadarin et al. 2017). Most of the water bodies got polluted due to industrialization and modernization of urban areas. Some of the industries like textiles, tanneries, and pharmaceuticals are releasing their waste or by-products in the water bodies. Sunlight is an abundant natural source, which can be available freely on Earth surface, and the collective radiation of sunlight light energy can destroy the pathogenic present in the water bodies. Evidently, some of the process parameters can directly hinder the photocatalytic efficiency of the solar disinfection (SODIS) process, such as the light intensity, temperature of the incoming light, and nature of the pathogens (McGuigan et al. 2012). The most viable approach to kill the pathogens effectively is the use of heterogeneous photocatalysis.

Clasen et al. reported the prevention of diarrhea with the household-based cost-effective method (Clasen et al. 2008). They concluded that, the household-based water purification system is the most cost-effective and excellent solar disinfection efficacy. Even though it stands slightly higher cost than the chlorination, it possesses overall higher disinfection effectiveness than the solar disinfection process (SODIS) (Fig. 1.6).

The water purification process can be conducted in an aqueous solution by immobilizing the photocatalyst under the irradiation of sunlight (Kumar et al. 2017). Before and after the light exposure at a certain interval, the aqueous solution should be tested for the disinfection level. Water disinfection efficiency of TiO_2

Fig. 1.6 A simple household-based water purification system for solar disinfection of water SODIS process. (McGuigan et al. 2012)

photocatalysts shows better performance than the UVA treatment alone. Alrousan et al. demonstrated the solar light-induced photocatalytic (SPC-DIS) and solar disinfection (SODIS) of *E. coli*-polluted water using two different configurations with and without photocatalyst (TiO_2) (Alrousan et al. 2012). According to the recent scientific reports, doping of metal ion incorporation in the host material is the most promising approach to achieve the effective catalytic activity under the irradiation of visible light (Islam et al. 2017; Gupta et al. 2018). However, the researches in the disinfection of microorganism are limited, and the reported publications are also minimal compared with the publication available for photocatalytic disinfection of organic contaminants.

1.6 Bio-Based Materials

Plant-based materials which are renewable at the short time are of high interest in the market. These materials are also encouraged and utilized in sustainable buildings by various governmental sectors (Bischel 2015). Other than these, a lot of bio-based products are being incorporated in building utilities and related products for sustainable and eco-friendly living. To specify on this, polymers such as polylactic acid, polyolefins, polyethylene terephthalate, and polyurethane which are used traditionally for so long have been replaced completely or partially by bio-based material feedstocks. Notably, bio-based chemicals can also be suggested to replace some of the commercial petrochemical products extracted from castor beans, soy, corn, and sugarcane (Omrani et al. 2015). In addition to the field of construction and petrochemical products, the end uses for these bio-based materials also spread effectively in food package and automobile industries. There is a larger growth in the research related to identifying new natural fibers that could be used in the automobile industry. The application of latex is also recently interested in automobile industries and also for medicinal uses as an alternative to petrochemical-based materials (Mooibroek and Cornish 2000). The Centre for Automotive Research in their 2012 report emphasized the advantages of bio-based materials in the automobile-related products such as cotton fibers in car interior soundproofing systems; flax fibers in brakes; abaca fibers in lower body panels; reinforced fibers made from wheat, flax, sisal, and hemp in dashboards and headliners; and storage bins (Tracy et al. 2018). These fibers from bio-based feedstock are utilized in nonstructural components as a replacement of glass fiber reinforcement. However, larger research is also focused on intending these bio-based fibers for structural components (Tracy et al. 2018; Mohanty et al. 2002). Other than plant-based bio-based materials, sheep's wool is also considered as an insulating material in building construction.

In addition to polymers, ceramics and glasses can also be contenders bio-based materials. Recently, a pyrolyzing process to extract the mineral components from food wastes has been patented by the researchers at the Colorado School of Mines (Cornejo et al. 2015). Some of the notable similar ceramic extraction from plant base bio-wastes are, (i) silica from rice husks; (ii) potassium oxide, magnesium oxide and calcium oxide from peanut shells; and (iii) aluminium oxide from tea. Similar to ceramics, soda-lime silicate glasses (window glass) were also made with 100% bio-based materials obtained from food stock wastes. In most of the glasses, silica is the major source. For this, some other researchers also investigated the procedure of incorporating silica from rice husks instead of another chemical precursor of silica (Bondioli et al. 2010). Even though much interest has been made by a lot of researcher in this field of developing bio-based materials as desirable products, which will be used by many end users, there are also certain issues that need to be addressed in the composition of the end products with complete bio-based content alone to show it as a sustainable product. The durability of this partial composition or the content-based bio-based materials also does not consider or compare with the non-bio-based product. In the automobile industry, the comparison on contented bio-based materials and non-bio-based products prominent area of consideration. In most of the cases, the bio-based products are often compared with petroleum-based products with respect to its lifetime. Even though the lifetime of petroleum-based product lasts for 15 years compared to the bio-based product, which lasts only for 5 years, the need for environmentally friendly products is highly considered. In the present decade, deciding the overall environmental preferability on considering contented bio-based materials in many industries may not provide at present with the available information. Hence, an alarm has been set in the development of a 100% bio-based product, which is to be replaced twice to achieve the same overall lifetime.

1.7 Simultaneous Removal of Organic and Inorganic Pollutants Using Activated Carbon

The extensive usage of pharmaceutical products and its disposable wastes and the high concentrations of heavy metals are also released from industries, which find their way to water bodies and polluted drastically. Adsorption is a popular approach that has been taken to resolve this issue, which has proven to be an efficient method on many varieties of contaminants, both organic and inorganic (Kongjao et al. 2008). The most common way to adsorption pollutants is the usage of porous carbon materials, which is also called activated carbon (AC). Depending on the treatment of starting material, thermal, chemical, or physical, the AC is suitable for a variety of things. For adsorption of pollutants from agricultural sources, AC is a good method since the materials are used in high amounts (Dias et al. 2007). However, the activation process of carbon is expensive; thus, a cheaper alternative has been examined. Thermal treatment, in low-oxygen concentration conditions, of biomass, creates a carbon-rich compound called biochar (Lehmann and Joseph 2015). This has been found to be effective as an adsorbent of different pollutants in the air, soil, and aquatic environments. Depending on the technique, temperature, and duration of the formation process of the biochar, as well as the starting material, it contains different functional groups; hence, it adsorbs different contaminants (Liu et al. 2015). Biochars have been observed as an efficient adsorbent for some heavy metals, such as arsenic (As) (Agrafioti et al. 2014). Other heavy metals, such as copper, have been observed to be in a less available state when biochar is present (Inyang et al. 2016). The efficiency of biochars as an adsorbent of heavy metals has been found to be pH dependent; for example, at low pH, the mobility of copper is decreased. Furthermore, the concentration of the inorganic contaminant in solution affects the absorbance efficiency since the surface becomes saturated; thus, at high concentrations, the mobility of the contaminants increases. One of the most common inorganic pollutants found in aquatic environments is mercury (Hg), which is highly toxic since it causes damage to the central nervous system (Clarkson 1997). It has been observed that adsorption of nonpolar hydrophobic or negatively charged contaminants, such as diclofenac, is temperature and pH dependent. An illustration demonstrating system for energy production and the role of renewable energy along with other production options are given in Fig. 1.7, which depicts a systemic approach is needed to conduct lifecycle assessments.

1.8 Conclusion

In-depth research is extremely essential to determine the efficient material for photocatalytic applications, which is capable of capturing visible light intensity and also disinfecting the pollutant at a very short period of time. Advancement in

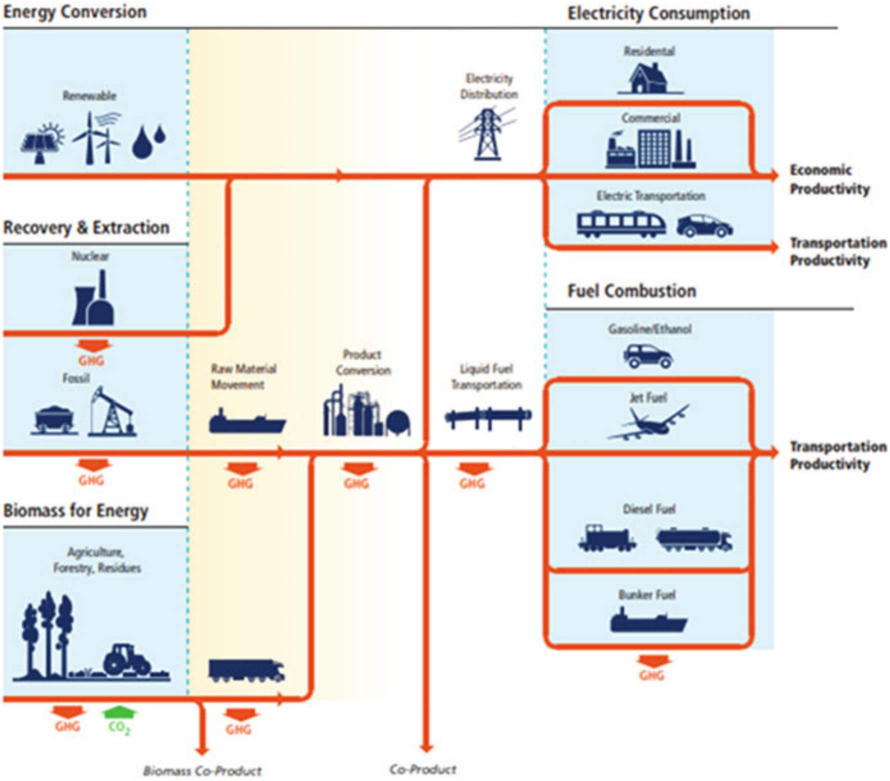

Fig. 1.7 Pictorial representation illustrates the energy production and the role of renewable energy with other production options. (Edenhofer et al. 2011)

the design and construction of the photocatalytic reactor can build this technology more viable at very low cost for the degradation of toxic pollutants in the water bodies. The photo-electrochemical water splitting using a heterogeneous photocatalyst under visible light was considered a "dream reaction." Now, new strategies are able to achieve the separation of electrons and holes in an efficient way and can be experimented in the powdered semiconductor photocatalysts. Such an achievement will help to solve the global energy and environmental problems toward the realization of a sustainable society.

Acknowledgment One of the authors D. Durgalakshmi gratefully acknowledges DST-INSPIRE Faculty Fellowship under the sanction DST/INSPIRE/04/2016/000845 for their funding. R. Saravanan gratefully acknowledges financial support from the SERC (CONICYT/FONDAP/15110019), FONDECYT, Government of Chile (Project No.: 11170414), and School of Mechanical Engineering (EUDIM), Universidad de Tarapacá, Arica, Chile.

References

Abas N, Kalair A, Khan N (2015) Review of fossil fuels and future energy technologies. Futures 69:31–49

Agrafioti E, Kalderis D, Diamadopoulos E (2014) Arsenic and chromium removal from water using biochars derived from rice husk, organic solid wastes and sewage sludge. J Environ Manag 133:309–314

Ahmad H, Kamarudin S, Minggu L, Kassim M (2015) Hydrogen from photo-catalytic water splitting process: a review. Renew Sust Energ Rev 43:599–610

Al-Othman ZA, Ali R, Naushad M (2012) Hexavalent chromium removal from aqueous medium by activated carbon prepared from peanut shell: adsorption kinetics, equilibrium and thermodynamic studies. Chem Eng J 184:238–247. https://doi.org/10.1016/j.cej.2012.01.048

Albadarin AB, Charara M, Abu Tarboush BJ et al (2017) Mechanism analysis of tartrazine biosorption onto masau stones; a low cost by-product from semi-arid regions. J Mol Liq 242:478. https://doi.org/10.1016/j.molliq.2017.07.045

Aldrich TE, Easterly CE (1987) Electromagnetic fields and public health. Environ Health Perspect 75:159–171

Ali SH, Giurco D, Arndt N, Nickless E, Brown G, Demetriades A, Durrheim R, Enriquez MA, Kinnaird J, Littleboy A (2017) Mineral supply for sustainable development requires resource governance. Nature 543(7645):367

Alqadami AA, Naushad M, Alothman ZA, Ghfar AA (2017) Novel metal-organic framework (MOF) based composite material for the sequestration of U(VI) and Th(IV) metal ions from aqueous environment. ACS Appl Mater Interfaces 9(41):36026–36037. https://doi.org/10.1021/acsami.7b10768

Alrousan D, Polo-López M, Dunlop P, Fernández-Ibáñez P, Byrne J (2012) Solar photocatalytic disinfection of water with immobilised titanium dioxide in re-circulating flow CPC reactors. Appl Catal B Environ 128:126–134

Berardi S, Drouet S, Francas L, Gimbert-Suriñach C, Guttentag M, Richmond C, Stoll T, Llobet A (2014) Molecular artificial photosynthesis. Chem Soc Rev 43(22):7501–7519

Bilgili M, Ozbek A, Sahin B, Kahraman A (2015) An overview of renewable electric power capacity and progress in new technologies in the world. Renew Sust Energ Rev 49:323–334

Bischel MS (2015) Moving beyond single attributes to holistically assess the sustainability of materials. In: Green and sustainable manufacturing of advanced material. Elsevier, Amsterdam, pp 11–29

Bondioli F, Barbieri L, Ferrari AM, Manfredini T (2010) Characterization of rice husk ash and its recycling as quartz substitute for the production of ceramic glazes. J Am Ceram Soc 93 (1):121–126

Candal R, Martínez-de la Cruz A (2015) New visible-light active semiconductors. In: Photocatalytic semiconductors. Springer, Cham, pp 41–67

Cao S, Yu J (2014) g-C3N4-based photocatalysts for hydrogen generation. The J Phys Chem Lett 5 (12):2101–2107

Chan SHS, Yeong Wu T, Juan JC, Teh CY (2011) Recent developments of metal oxide semiconductors as photocatalysts in advanced oxidation processes (AOPs) for treatment of dye waste-water. J Chem Technol Biotechnol 86(9):1130–1158

Chen X, Shen S, Guo L, Mao SS (2010) Semiconductor-based photocatalytic hydrogen generation. Chem Rev 110(11):6503–6570

Clarkson TW (1997) The toxicology of mercury. Crit Rev Clin Lab Sci 34(4):369–403

Clasen T, McLaughlin C, Nayaar N, Boisson S, Gupta R, Desai D, Shah N (2008) Microbiological effectiveness and cost of disinfecting water by boiling in semi-urban India. Am J Trop Med Hyg 79(3):407–413

Clavero C (2014) Plasmon-induced hot-electron generation at nanoparticle/metal-oxide interfaces for photovoltaic and photocatalytic devices. Nat Photonics 8(2):95

Company BP (2018) BP statistical review of world energy. British Petroleum Company, London

Cornejo IA, Reimanis IE, Ramalingam S (2015) Methods of making glass from organic waste food streams. Google Patents

Covert T, Greenstone M, Knittel CR (2016) Will we ever stop using fossil fuels? J Econ Perspect 30 (1):117–138

Daghrir R, Drogui P, Robert D (2013) Modified TiO2 for environmental photocatalytic applications: a review. Ind Eng Chem Res 52(10):3581–3599

Demirbas A (2008) Biofuels sources, biofuel policy, biofuel economy and global biofuel projections. Energy Convers Manag 49(8):2106–2116

Demirbas A (2011) Competitive liquid biofuels from biomass. Appl Energy 88(1):17–28

Dias JM, Alvim-Ferraz MC, Almeida MF, Rivera-Utrilla J, Sánchez-Polo M (2007) Waste materials for activated carbon preparation and its use in aqueous-phase treatment: a review. J Environ Manag 85(4):833–846

Diebold U (2003) The surface science of titanium dioxide. Surf Sci Rep 48(5–8):53–229

Djurišić AB, Leung YH, Ng AMC (2014) Strategies for improving the efficiency of semiconductor metal oxide photocatalysis. Mater Horiz 1(4):400–410

Dong S, Feng J, Fan M, Pi Y, Hu L, Han X, Liu M, Sun J, Sun J (2015) Recent developments in heterogeneous photocatalytic water treatment using visible light-responsive photocatalysts: a review. RSC Adv 5(19):14610–14630

Edenhofer O, Pichs-Madruga R, Sokona Y, Seyboth K, Kadner S, Zwickel T, Eickemeier P, Hansen G, Schlömer S, von Stechow C (2011) Renewable energy sources and climate change mitigation: special report of the intergovernmental panel on climate change. Cambridge University Press, Cambridge

Etacheri V, Di Valentin C, Schneider J, Bahnemann D, Pillai SC (2015) Visible-light activation of TiO2 photocatalysts: advances in theory and experiments. J Photochem Photobiol C: Photochem Rev 25:1–29

Fagan R, McCormack DE, Dionysiou DD, Pillai SC (2016) A review of solar and visible light active TiO2 photocatalysis for treating bacteria, cyanotoxins and contaminants of emerging concern. Mater Sci Semicond Process 42:2–14

Fox MA, Dulay MT (1993) Heterogeneous photocatalysis. Chem Rev 93(1):341–357

Gaya UI, Abdullah AH (2008) Heterogeneous photocatalytic degradation of organic contaminants over titanium dioxide: a review of fundamentals, progress and problems. J Photochem Photobiol C: Photochem Rev 9(1):1–12

Ghasemi M, Naushad M, Ghasemi N, Khosravi-fard Y (2014) Adsorption of Pb(II) from aqueous solution using new adsorbents prepared from agricultural waste: adsorption isotherm and kinetic studies. J Ind Eng Chem 20:2193–2199. https://doi.org/10.1016/j.jiec.2013.09.050

Gnanasekaran L, Hemamalini R, Naushad M (2018) Efficient photocatalytic degradation of toxic dyes using nanostructured TiO2/polyaniline nanocomposite. Desalin Water Treat 108:322–328. https://doi.org/10.5004/dwt.2018.21967

Goldemberg J (2007) Ethanol for a sustainable energy future. Science 315(5813):808–810

Gupta TK, Singh BP, Mathur RB, Dhakate SR (2014) Multi-walled carbon nanotube–graphene–polyaniline multiphase nanocomposite with superior electromagnetic shielding effectiveness. Nanoscale 6(2):842–851

Gupta PK, Khan ZH, Solanki PR (2018) Effect of nitrogen doping on structural and electrochemical properties of zirconia nanoparticles. Adv Sci Lett 24(2):867–872

Herrmann J-M (1999) Heterogeneous photocatalysis: fundamentals and applications to the removal of various types of aqueous pollutants. Catal Today 53(1):115–129

Herrmann J-M (2005) Heterogeneous photocatalysis: state of the art and present applications in honor of Pr. RL Burwell Jr (1912–2003), former Head of Ipatieff Laboratories, Northwestern University, Evanston (Ill). Top Catal 34(1–4):49–65

Heusser G (1995) Low-radioactivity background techniques. Annu Rev Nucl Part Sci 45 (1):543–590

Iavicoli I, Leso V, Ricciardi W, Hodson LL, Hoover MD (2014) Opportunities and challenges of nanotechnology in the green economy. Environ Health 13(1):78

Inyang MI, Gao B, Yao Y, Xue Y, Zimmerman A, Mosa A, Pullammanappallil P, Ok YS, Cao X (2016) A review of biochar as a low-cost adsorbent for aqueous heavy metal removal. Crit Rev Environ Sci Technol 46(4):406–433

Islam S, Nagpure S, Kim D, Rankin S (2017) Synthesis and catalytic applications of non-metal doped mesoporous titania. Inorganics 5(1):15

Jaiswal R, Bharambe J, Patel N, Dashora A, Kothari D, Miotello A (2015) Copper and nitrogen co-doped TiO2 photocatalyst with enhanced optical absorption and catalytic activity. Appl Catal B Environ 168:333–341

Khan MM (2018) 2 – Metal oxide powder photocatalysts. In: Lin Z, Ye M, Wang M (eds) Multifunctional photocatalytic materials for energy. Woodhead Publishing, Cambridge, pp 5–18. https://doi.org/10.1016/B978-0-08-101977-1.00002-8

Kongjao S, Damronglerd S, Hunsom M (2008) Simultaneous removal of organic and inorganic pollutants in tannery wastewater using electrocoagulation technique. Korean J Chem Eng 25 (4):703

Kumar A, Naushad M, Rana A et al (2017) ZnSe-WO3 nano-hetero-assembly stacked on Gum ghatti for photo-degradative removal of Bisphenol A: Symbiose of adsorption and photocatalysis. Int J Biol Macromol 104:1172–1184. https://doi.org/10.1016/j.ijbiomac.2017.06.116

Kumar S, Terashima C, Fujishima A, Krishnan V, Pitchaimuthu S (2019) Photocatalytic degradation of organic pollutants in water using graphene oxide composite. In: A new generation material graphene: applications in water technology. Springer, Cham, pp 413–438

Lancaster M (2016) Green chemistry 3rd edition: an introductory text. Royal Society of Chemistry, Cambridge

Lang X, Chen X, Zhao J (2014) Heterogeneous visible light photocatalysis for selective organic transformations. Chem Soc Rev 43(1):473–486

Lee KM, Lai CW, Ngai KS, Juan JC (2016) Recent developments of zinc oxide based photocatalyst in water treatment technology: a review. Water Res 88:428–448

Lehmann J, Joseph S (2015) Biochar for environmental management: science, technology and implementation. Routledge, London

Lin Z, Ye M, Wang M (2018) Multifunctional photocatalytic materials for energy. Woodhead Publishing, Cambridge

Liu W-J, Jiang H, Yu H-Q (2015) Development of biochar-based functional materials: toward a sustainable platform carbon material. Chem Rev 115(22):12251–12285

McGuigan KG, Conroy RM, Mosler H-J, du Preez M, Ubomba-Jaswa E, Fernandez-Ibañez P (2012) Solar water disinfection (SODIS): a review from bench-top to roof-top. J Hazard Mater 235:29–46

Milani B (2005) Building materials in a green economy: community-based strategies for dematerialization. University of Toronto, Toronto

Mohanty AK, Misra M, Drzal L (2002) Sustainable bio-composites from renewable resources: opportunities and challenges in the green materials world. J Polym Environ 10(1–2):19–26

Moldavska A, Welo T (2017) The concept of sustainable manufacturing and its definitions: a content-analysis based literature review. J Clea Prod 166:744–755. https://doi.org/10.1016/j.jclepro.2017.08.006

Moniz SJ, Shevlin SA, Martin DJ, Guo Z-X, Tang J (2015) Visible-light driven heterojunction photocatalysts for water splitting – a critical review. Energy Environ Sci 8(3):731–759

Mooibroek H, Cornish K (2000) Alternative sources of natural rubber. Appl Microbiol Biotechnol 53(4):355–365

Naushad M, Mittal A, Rathore M, Gupta V (2015) Ion-exchange kinetic studies for Cd(II), Co(II), Cu(II), and Pb(II) metal ions over a composite cation exchanger. Desalin Water Treat 54:2883–2890. https://doi.org/10.1080/19443994.2014.904823

Naushad M, Ahamad T, Al-Maswari BM et al (2017) Nickel ferrite bearing nitrogen-doped mesoporous carbon as efficient adsorbent for the removal of highly toxic metal ion from aqueous medium. Chem Eng J 330:1351. https://doi.org/10.1016/j.cej.2017.08.079

Ni M, Leung MK, Leung DY, Sumathy K (2007) A review and recent developments in photocatalytic water-splitting using TiO2 for hydrogen production. Renew Sust Energ Rev 11 (3):401–425

Omrani E, Barari B, Moghadam AD, Rohatgi PK, Pillai KM (2015) Mechanical and tribological properties of self-lubricating bio-based carbon-fabric epoxy composites made using liquid composite molding. Tribol Int 92:222–232

Priedulena E, Hogeforster M (2016) Improvement of skills in the green economy through the advanced training programs on cradle to cradle. BoD–Books on Demand, Norderstedt

Prusty JK, Patro SK, Basarkar S (2016) Concrete using agro-waste as fine aggregate for sustainable built environment – a review. Int J Sustain Built Environ 5(2):312–333

Ramesh T, Prakash R, Shukla K (2010) Life cycle energy analysis of buildings: an overview. Energ Buildings 42(10):1592–1600

Ramírez-Rico J, Martínez-Fernandez J, Singh M (2017) Biomorphic ceramics from wood-derived precursors. Int Mater Rev 62(8):465–485

Ren21 R (2016) Global status report. REN21 Secretariat, Paris

Saha M, Darnton G (2005) Green companies or green companies: are companies really green, or are they pretending to be? Bus Soc Rev 110(2):117–157

Salvato JA, Nemerow NL, Agardy FJ (2003) Environmental engineering. Wiley, New York

Schandl H, Hatfield-Dodds S, Wiedmann T, Geschke A, Cai Y, West J, Newth D, Baynes T, Lenzen M, Owen A (2016) Decoupling global environmental pressure and economic growth: scenarios for energy use, materials use and carbon emissions. J Clean Prod 132:45–56

Schultz DM, Yoon TP (2014) Solar synthesis: prospects in visible light photocatalysis. Science 343 (6174):1239176

Sharma G, Naushad M, Kumar A et al (2017) Efficient removal of coomassie brilliant blue R-250 dye using starch/poly(alginic acid-cl-acrylamide) nanohydrogel. Process Saf Environ Prot 109:301–310. https://doi.org/10.1016/j.psep.2017.04.011

Sheldon RA (2016) Green chemistry and resource efficiency: towards a green economy. Green Chem 18(11):3180–3183

Singh M, Ohji T, Asthana R (2015a) Green and sustainable manufacturing of advanced material. Elsevier, Amsterdam

Singh M, Ohji T, Asthana R (2015b) Green and sustainable manufacturing of advanced materials—progress and prospects. In: Green and sustainable manufacturing of advanced material. Elsevier, Amsterdam, pp 3–10

Spasiano D, Marotta R, Malato S, Fernandez-Ibanez P, Di Somma I (2015) Solar photocatalysis: materials, reactors, some commercial, and pre-industrialized applications. A comprehensive approach. Appl Catal B Environ 170:90–123

Thomas CE (2009) Fuel cell and battery electric vehicles compared. Int J Hydrogen Energy 34 (15):6005–6020. https://doi.org/10.1016/j.ijhydene.2009.06.003

Tracy AA, Bhatia SK, Ramadurai KW (2018) Bio-based materials as applicable, accessible, and affordable healthcare solutions. Springer, Cham

Varadan VK, Varadan VV, Williams NR, Cresko JW (1994) Electromagnetic shielding materials. Google Patents

Wen B, Cao M, Lu M, Cao W, Shi H, Liu J, Wang X, Jin H, Fang X, Wang W (2014) Reduced graphene oxides: light-weight and high-efficiency electromagnetic interference shielding at elevated temperatures. Adv Mater 26(21):3484–3489

Wu W, Zhang S, Ren F, Xiao X, Zhou J, Jiang C (2011) Controlled synthesis of magnetic iron oxides@ SnO 2 quasi-hollow core–shell heterostructures: formation mechanism, and enhanced photocatalytic activity. Nanoscale 3(11):4676–4684

Yahya MA, Al-Qodah Z, Ngah CZ (2015) Agricultural bio-waste materials as potential sustainable precursors used for activated carbon production: a review. Renew Sust Energ Rev 46:218–235

Yang X, Cui H, Li Y, Qin J, Zhang R, Tang H (2013) Fabrication of Ag3PO4-graphene composites with highly efficient and stable visible light photocatalytic performance. ACS Catal 3 (3):363–369

Yaremenko IA, Vil VA, Demchuk DV, Terent'ev AO (2016) Rearrangements of organic peroxides and related processes. Beilstein J Org Chem 12(1):1647–1748

Zhi W-J, Wang L-F, Hu X-J (2017) Recent advances in the effects of microwave radiation on brains. Mil Med Res 4(1):29

Zhou H, Li X, Fan T, Osterloh FE, Ding J, Sabio EM, Zhang D, Guo Q (2010) Artificial inorganic leafs for efficient photochemical hydrogen production inspired by natural photosynthesis. Adv Mater 22(9):951–956

Chapter 2
Photocatalysts and Photoelectrocatalysts in Fuel Cells and Photofuel Cells

Prasenjit Bhunia and Kingshuk Dutta

Contents

2.1 Introduction 20
2.2 Basic Principles of PC and PFCs 22
  2.2.1 Mechanism of PFC Operation 25
  2.2.2 Advancement of PFC cells 30
2.3 Basic Principles of PEC Cells 33
  2.3.1 Types of PEC Cells 34
  2.3.2 Basic Configuration/Structure of a PEC Cell 36
  2.3.3 Semiconductors for Photoanodes 38
  2.3.4 Semiconductors for Cathodes/Photocathodes 41
  2.3.5 Advancement of PEC Cells 42
2.4 Concluding Remarks and Future Perspectives 44
References 45

Abstract The present concern in the energy sector is the very high rate of decrease of the reserves of fossil fuel of our planet. Therefore, the continuously increasing need for reliable energy supply has led to a boost in research and development of alternative energy sources. These alternative energy sources should essentially exhibit ready availability, renewability, sustainability, and environmental friendliness. Two prime examples of such green energy sources are solar energy and energy from readily available fuels (such as waste matter and biomass). This has led to the development of photofuel cells (PFCs), which combine the unique properties of solar cells and fuel cells. In addition, the use of photocatalysts and

---

P. Bhunia
Department of Chemical Engineering, Indian Institute of Technology, Kharagpur, India

K. Dutta (✉)
Department of Materials Science and Engineering, Cornell University, Ithaca, NY, USA

Advanced Research School for Technology and Product Simulation (ARSTPS), School for Advanced Research in Polymers (SARP), Central Institute of Plastics Engineering and Technology (CIPET), Chennai, India
e-mail: kd426@cornell.edu

S. Rajendran et al. (eds.), *Green Photocatalysts for Energy and Environmental Process*, Environmental Chemistry for a Sustainable World 36,
https://doi.org/10.1007/978-3-030-17638-9_2

photoelectrocatalysts in normal fuel cells serves the purpose of trapping solar energy to cause oxidation of the fuel in fuel cells, which in turn results in generation of electrical energy.

This chapter has mainly dealt with fundamental differences between photocatalytic fuel cells (a type of photoelectrochemical cells) and other photoelectrochemical cells. The fundamental aspects and configurations of photocatalytic fuel cells, the mechanism of their operation, and the often employed photocatalysts for the fabrication of photoanodes and photocathodes have been systematically and elaborately discussed. The photocatalytic fuel cells, also called PFCs, photocatalytically degrade organic substances or biomass or water-soluble wastes to produce electricity in spontaneous mode, i.e., $\Delta G < 0$ in the electrolyte. In photoelectrochemical fuel cell, electrical energy gets converted from photon energy without changing the composition of the reduction-oxidation electrolyte or the counter or semiconductor electrode. The major effort of this chapter is to offer necessary knowledge and visualization of the fundamental differences that exist between photocatalytic and photoelectrocatalytic fuel cells to the new researchers in this field, as well as a handy manual to the experienced researchers.

Keywords Photocatalysts · Photoelectrocatalysts · Photofuel cells · Fuel cells · Photoelectrochemical cells · Solar energy · Photocathode · Photoanode · Clean energy · Renewable energy

2.1 Introduction

In the twenty-first century, the most important challenge facing humanity is energy. At present, the major global energy requirements are fulfilled from the energy derived from the fossil fuels that are essentially nonrenewable. This, in turn, will surely adversely influence the sustainable development of mankind (Liu et al. 2014; Dutta et al. 2015a, 2017). Until now, the energy market has been dominated by fossil fuels, which account for about 87% of the total energy consumption in the global scale (Tollefson and Monastersky 2012). However, the study on renewable energy sources attained "explosive" dimension with the decrease of reserves of fossil fuel and increasing concerns on environmental issues (Rühl et al. 2012; Dutta et al. 2015a, 2017; Dutta 2017; Das et al. 2015). It is very important to develop other ways to convert, harvest, and store energy in order to address this challenge (Kundu and Dutta 2016; Dutta et al. 2014; Kumar et al. 2014a, b; Banerjee and Dutta 2017; Kundu and Dutta 2018). Among the alternative ways, electrical energy transformed directly from sunlight and harvesting of the energy stored in chemical bonds are regarded as the most important strategies (Latibari and Sadrameli 2018; Das et al. 2015, 2016; Dutta and Kundu 2014; Dutta et al. 2015b), considering their abundance and renewable nature. Therefore, two important sources of sustainable energy are solar energy and waste materials/biomass energy (Sahoo 2016; Kundu and Dutta 2018; Nandy et al. 2015; Das et al. 2018; Dutta and Kundu 2018), which can be technically converted to electricity with the help of suitable photocatalysts or photoelectrocatalysts (Potočnik 2007).

The overall process of photocatalysis (PC) principally consists of two major steps: (a) absorption of photon to produce excited charge carriers of electron holes and (b) use of these carriers, after photoexcitation, to catalytically trigger redox reactions. More precisely, PC is involved in the use of natural light from the sun for the purpose of remediation of the environment (e.g., degradation of environmental pollutants), transformations via chemical means (e.g., photoreduction of CO_2), and production of clean energy (e.g., production of hydrogen) (Kumar et al. 2018; Zhang et al. 2012, 2010). However, factors such as low use of visible light, lack of stability of the photocatalysts, and low quantum efficacy reduce the improvement of heterogeneous PC. Based on the principle of PC, the photocatalytic fuel cells (also known as photofuel cells) (PFCs) that degrade organic substances, biomasses, or water-soluble wastes photocatalytically to produce electricity with non-zero free energy change in the electrolyte were first time proposed by Kaneko et al. (2006). Although PFCs are a part of photoelectrochemical (PEC) cell, they have been discussed here separately in order to bring out their clear distinction from other PEC cells. In these categories of cells, the photon's energy and the chemical energy stored within organic substances, biomasses, or water-soluble wastes, i.e., "fuel," get transformed into electrical energy and/or preserved as useful chemical energy (e.g., hydrogen energy). Owing to this, PEC cells that operate by fuel consumption are termed PFCs.

Besides the rapid development in heterogeneous PC, the potentials of photoelectrocatalysis based on semiconductors have also witnessed enormous attraction for harvesting of solar energy and its storage. It should be mentioned here that the photocatalytic activity was found to be significantly influenced by the applied potential, more accurately the photocatalytic activity enhanced manifold with application of external bias (Liu et al. 2000; Khan et al. 2002). The semiconductors that are photocatalytically inactive, however, can deliver photoelectrocatalytic activity (Sun and Chou 1998; Sun and Chou 2000; Luo and Hepel 2001), which signifies that the photoinduced activity is dependent in a strong way on the properties of the materials employed, as well as on the absence/presence of the potential applied. The PEC cell is a promising device having dual advantages in terms of environmental aspect, i.e., (a) consumption of wastes and (b) transformation of sunlight into useful energy forms through decomposition of organic wastes photocatalytically (Sharma et al. 2017; Dhiman et al. 2017). This generation of electricity from sun's energy and waste materials/biomasses shall decrease the need for fossil fuels (Kundu and Dutta 2018). The functionality of PEC cells is entirely dependent on the nature of the semiconductor/electrolyte interface. Inspired by the pioneering work of Fujishima and Honda (1972), based on illuminated TiO_2 electrodes for splitting of water molecules (Fujishima and Honda 1972), the study on PEC cells received a large emerging interest. Thereafter, a large volume of literature has been published in this field. The interest has later somehow diminished after the original excitement (Borman 1991). However, the broad experience accumulated in the last 40 years of research on decomposition of organic matter photocatalytically (Kawai and Sakata 1980; Borganello et al. 1982; Herrmann et al. 1984; Licht et al. 1987;

Hoffmann et al. 1995; Karakitsou and Verykios 1993; Fox and Dulay 1993; Linsebigler et al. 1995; Vinodgopal et al. 1996; Ohtani et al. 1997; Wu et al. 1998; Sclafani and Herrmann 1998; Negishi et al. 1998; Fujishima et al. 2000, 2008; Vulliet et al. 2002; Di Paola et al. 2002; Guillard et al. 2002; Arabatzis et al. 2003; Nakade et al. 2003; Coronado et al. 2003; Mrowetz et al. 2004; Konstantinou and Albanis 2004; Yang and Dionysiou 2004; Zhu et al. 2006; Patsoura et al. 2006; Bahnemann et al. 2007; Pelentridou et al. 2009), coupled with the developments of new nanostructured photocatalysts (Lianos 2011), such as graphene (Nouri et al. 2016; Ning et al. 2016; Xu et al. 2016; Li et al. 2016a) and carbon nanotube (Wang et al. 2005a, b, 2008; Gao et al. 2008, 2009; Xia et al. 2007), along with the method optimization of deposition of materials, and, in general, the noteworthy advances in the field of materials in conjunction to the enhanced awareness on environmental health have led to the creation of new enthusiasm in this field.

This chapter will not focus on covering the entire literature published but will concentrate on certain important works and progress made in order to enable the readers to get an easily penetrable integral knowledge of this area of research. Simultaneously, this chapter will also aim at demonstrating the recent progress in PFC and PEC fuel cells.

2.2 Basic Principles of PC and PFCs

The semiconductor's optical band gap is an essential factor in realizing its ability to absorb light. In this process, a pair of electron hole gets formed within the semiconductor when it absorbs photoenergy ($h\nu$) that is higher compared to the energy of the band gap (E_g) [ν = frequency and $h\nu > E_g$]. Therefore, when a semiconductor gets irradiated with light that possess energy higher compared to the band gap, the electron-hole pairs that get photogenerated in situ can get transferred to surface-adsorbed species as a result of gas or solution phase contact (Nosaka and Fox 1988). If this transfer of charge is exothermic and continuous, and the semiconductor remains unchanged, the process is designated as "heterogeneous photocatalysis" (Linsebigler et al. 1995). The generation of charge carriers "electron hole" on a semiconductor under irradiation of light is the initial stage of heterogeneous PC (Scheme 2.1). The excitation of electrons takes place to the conduction band (CB) from the valence band (VB) of the semiconductors under irradiated light, having energy greater than the energy of the band gap (Scheme 2.1). Of course, there are several readily available pathways of de-excitation of the holes and electrons that get photogenerated. These carriers of charge get transferred either to the species adsorbed on the surface of the semiconductor or to the solvent directly. To note, this process of transfer of electron demonstrate more efficiency when the species get pre-adsorbed on the semiconductor surface compared to the hole transfer process (Matthews 1988). The excited electrons of the semiconductor are able to reduce a surface-adsorbed electron acceptor (pathway C), and the holes move to the surface in order to combine with the holes present in the surface, therefore causing

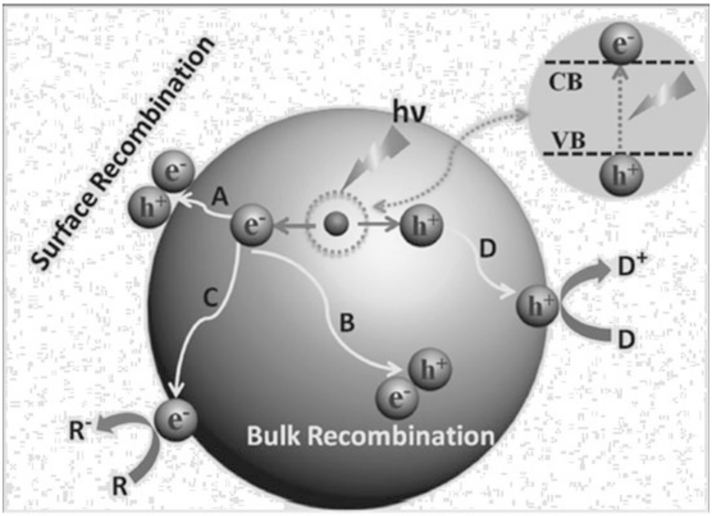

Scheme 2.1 A schematic depiction of the process of excitation and the possible reactions that took place on the surface and in the bulk of the semiconductor under irradiation. (Reproduced after modification from Linsebigler et al. 1995, with permission from the American Chemical Society)

oxidation of the donor (pathway D). It is to be noted that the positions of the energy level of the VB and CB, and the levels of the redox potential of the species adsorbed, determines the charge transfer rate. In addition to the surface reduction/oxidation process, the process of recombination can be realized simultaneously during the phenomenon of photocatalysis that undergoes competition with the transfer of charge of the holes and electrons generated upon irradiation of photons. The recombination process may take place either by pathway A (i.e., on the surface) or by pathway B (i.e., within the bulk phase). The process of back-donation from the species adsorbed on the surface of the semiconductor may also serve as the other possibility of charge recombination. It is clear from the aforementioned analysis that the reinforcement of the process of separation of the hole and electron generated upon photo irradiation is crucial for enhancing the semiconductor's photocatalytic efficiency. In the solar PEC cell, the electron-hole pairs generated by photo irradiation are efficiently driven in opposite directions by an electric field that exists at the semiconductor/electrolyte solution interface. Again, the photocatalytic efficiency can be greatly enhanced upon employment of a positive bias potential across the electrodes through effective charge carriers (photogenerated) separation (Kim and Anderson 1994). The same process can take place on a single particle of semiconductor; however, the electric field in this case may be extremely small in magnitude (O'Regan et al. 1990). Therefore, the separation of carriers should be done by diffusion, having nanoscale sinks and sources. In systems where particles of semiconductor remain suspended in a solution of liquid, the semiconductor excitation can result in redox processes in the region interfacial between each particle. The biomass or organic waste, i.e., the "fuel," present in the electrolyte photoelectrocatalytically oxidized to produce electricity or storable chemical energy in PFCs. Although the

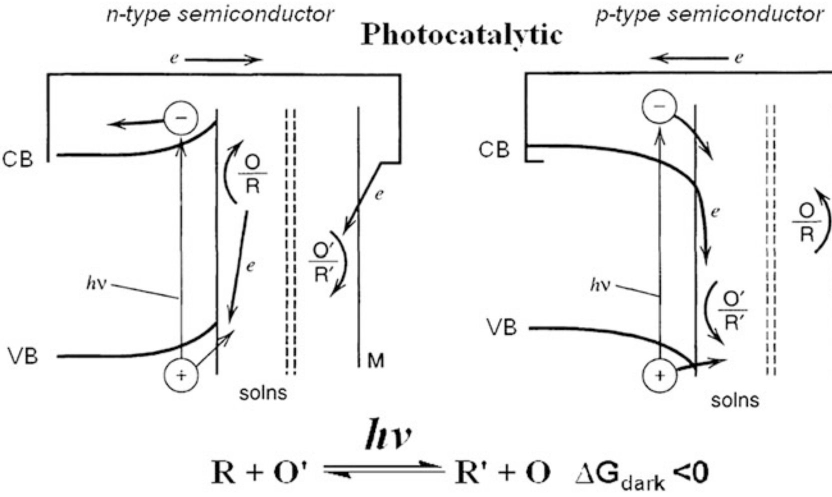

Fig. 2.1 Illustration of basic principle photocatalytic energy conversion device for *p*-type and *n*-type semiconductors. (Reproduced after modification from Bard and Faulkner 2001, with permission from Wiley)

PFCs are a part of the PECs, this chapter will lay a special focus on distinguishing between the PFCs and the PECs.

In this type of energy conversion device, unlike photovoltaic and photoelectrosynthetic devices, the initial excitation by photons does not take place in the semiconductor but instead in a light-absorbing visible dye (Fig. 2.1). Subsequent introduction of an electron into the CB of the semiconductor from the photoexcited dye leads to the current flow though the external circuit. The regeneration of the reduced dye through a reversible redox couple facilitates the sustainable conversion of light energy (O'Regan and Grätzel 1991). However, many instances are there that involve photooxidation of organic matter, where light merely accelerates the rate of the reaction. More precisely, aqueous suspensions that comprise of irradiated particles of semiconductor can be regarded as an assembly of short-circuited microelectrochemical cells. Thus, these cells are said to be operated in the photocatalytic mode. The relative locations of the potentials of the oxidation/reduction (O/R and O′/R′) couples get changed in photocatalytic cells (Fig. 2.1). In this case the reaction is forwarded in the spontaneous direction ($\Delta G < 0$). The process would be normally very slow in the dark; therefore, here the energy of light is used to overcome the process's activation energy.

Photoexcitation generates an electron delocalized in the CB and leaves behind a hole delocalized in the VB—a phenomenon called band-to-band transition, which generates pairs of electron hole. The positively charges holes (h^+) serve as powerful oxidants and decompose the organic substrates present within the system. The electrons generated upon photo irradiation are channeled to the cathode via an external circuit, and simultaneously, the protons (H^+) that get produced upon photooxidation diffuse through the electrolyte solution and transport toward the negative electrode. The hydrogen ions either get reduced to molecular hydrogen by external electrons under anaerobic conditions or form water after interaction with oxygen under aerobic conditions. However, in either of these two cases, electricity flows between the positive and the negative electrodes. In this type of device, the fuel gets photocatalytically degraded and consumed at the photoanode producing electricity or chemical energy, hence the name "photoactivated" or "photocatalytic" fuel cells. Instead of external power supply, the PFC is used to provide a bias to achieve effective removal of biomass or organic waste. Photocatalytic oxidation functions not only with pure chemical substances but also with their mixtures. Therefore, materials which are considered water-soluble wastes or pollutants may be used as fuel in PFCs. In essence, this situation offers the dual environmental benefits of production of renewable energy as well as remediation of environment through waste material consumption. Most efficient organic fuels are those having composition $C_xH_yO_z$, e.g., alcohols, diols, organic acids, and carbohydrates, which may be the products of biomass. Therefore, a large family of fuels used in PFCs may derive from biomass products (Dou et al. 2014), which otherwise are too expensive to process by other methods.

2.2.1 Mechanism of PFC Operation

The PFC may be operated either to produce electricity or to store energy in chemical bonds with expense of photon energy (which generates electron-hole charge carriers). Based on the nature and composition of the photocatalyst, a substantial percentage of these charge carriers recombine to dissipate their energy; whereas, those charge carriers escaping from recombination take active part in oxidation and reduction reactions. Mostly, the electrons get transported via an externally present circuit to the counter electrode, participating in reduction processes. In the counter electrode, they produce molecular hydrogen under anaerobic condition according to the following Reactions 2.1 and 2.2 either through reduction of protons or water. In the latter case, the protons are consumed by hydroxyl (OH^-) ions producing water at high pH; therefore, reduction of water molecules leads to the formation of molecular hydrogen. Other reactions may prevail or may both occur simultaneously, depending on the pH and the availability of protons:

$$2H^+ + 2e^- \rightarrow H_2(\text{at } 0.00\text{ V and pH} = 0) \qquad \text{(Reaction 2.1)}$$

$$2H_2O + 2e^- \rightarrow H_2 + 2OH^-(\text{at} - 0.77\text{ V and pH} = 13) \qquad \text{(Reaction 2.2)}$$

The dependency of the redox potential on pH can be realized according to the following standard rule:

$$\Delta V(\text{Volts}) = -0.059 \times \Delta pH \tag{2.1}$$

where ΔV is the variation of the potential with the variation of pH (equal to ΔpH). Thus, the potential is close to 0.0 V vs NHE at very low pH (i.e., strong acidic pH); whereas, at pH 13, the potential is −0.77 V vs NHE.

Both hydrogen and water can take part in reduction reactions at low as well as high pH under aerobic condition according to Reactions 2.3 and 2.4:

$$2H^+ + ½O_2 + 2e^- \rightarrow H_2O \text{ (at + 1.23 V and pH = 0)} \qquad \text{(Reaction 2.3)}$$

$$H_2O + ½\,O_2 + 2e^- \rightarrow 2OH^- \text{(at + 0.46 V and pH = 13)} \qquad \text{(Reaction 2.4)}$$

The reaction can occur within the range of potential between +1.23 V and + 0.46 V vs NHE following Eq. 2.2:

$$V(\text{Volts}) = +1.23 - 0.059 \times pH(\text{presence of } O_2) \tag{2.2}$$

The reduction reactions are not automated and require the presence of an electrocatalyst to reduce the overpotential established between the electrode and the liquid electrolyte. More accurately, the electrocatalyst accelerates the exchange of electron with the liquid electrolyte phase, thus eliminating the overpotential; and the potential of operation of the counter electrode may be considered to be the same as the electrochemical potential of the corresponding reduction reactions. Obviously, the electrocatalyst is a thin mesoporous film whose standard composition is for, e.g., carbon nanoparticles mixed with platinum (Pt) nanoparticles (Antoniadou and Lianos 2010). However, there is an intense effort going on toward finding suitable alternative materials, since Pt is rare and expensive (Sfaelou et al. 2015; Kumagai et al. 2015; Lin et al. 2014; Kibsgaard and Jaramillo 2014; Antoniadou et al. 2014a). On the other hand, the positive holes participate in the oxidation processes that occur at the photoanode. The hole is eliminated through donation of electrons in presence of attached sacrificial agent on the surface of the photocatalyst. However, it is well established that in most of the cases involving organic sacrificial agents, oxidation is carried in solution through the intermediately formed hydroxyl radicals (•OH), created upon the interaction of OH⁻ with holes according to Reaction 2.5:

$$OH^- + h^+ \rightarrow \bullet OH \text{ (high pH)} \qquad \text{(Reaction 2.5)}$$

The electrochemical potential of hole scavenging by OH^- is +2.02 vs NHE (at pH = 0), which again varies with pH according to Eq. 2.1. Thus, it may be concluded that the oxidation level (VB, where the photogenerated holes reside) of the photocatalyst semiconductor or the combined photocatalyst/co-catalyst (sensitizer) must be more positive compared to that of the $\bullet OH/OH^-$ couple in order to produce •OH as well as for the oxidation of the organic fuel. Therefore, only some selected metal oxide semiconductors have this capability; whereas, most of them are

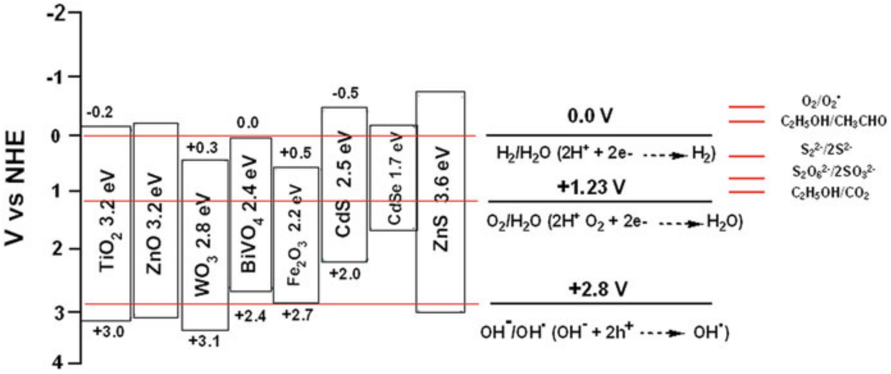

Fig. 2.2 Some frequently used metal oxide semiconductors photocatalysts along with their energy states and band gap. The reduction level (vs NHE) in anaerobic and aerobic conditions at pH zero, are displayed

incapable. For instance, few widely used semiconductor photocatalysts with their redox levels are enlisted in Fig. 2.2.

However, the holes are introduced into the sensitizer's VB when a semiconductor photocatalyst is combined with a sensitizer; and in that case their oxidation level may decrease, losing its capability of producing •OH (Sfaelou et al. 2014). The reactions which occur at lower potentials are frequently used for the production of hydrogen (e.g., in the case of sulfide/sulfite electrolytes, according to the oxidation Reactions 2.6 and 2.7) (Buehler et al. 1984). At zero pH, these values correspond to +0.58 V and + 0.31 V. All semiconductors enlisted in Fig. 2.2 are then capable of oxidizing sulfide and sulfite species. The E^0 values were calculated from Eq. 2.3, where n represents the number of electron moles participating in the oxidation, F represents the Faraday constant (i.e., 96.486 kC mol^{-1}), and standard free energy change ΔG^0 is in kJ mol^{-1}:

$$2SO_3{}^{2-} + 2h^+ \rightarrow S_2O_6{}^{2-}(-0.25\ \mathrm{V}\ vs\,\mathrm{NHE\ at\ pH\ 14}) \qquad \text{(Reaction 2.6)}$$

$$2S^{2-} + 2h^+ \rightarrow S_2{}^{2-}(-0.52\ \mathrm{V}\ vs\,\mathrm{NHE\ at\ pH\ 14}) \qquad \text{(Reaction 2.7)}$$

$$E^0 = \Delta G^0 / -nF \qquad (2.3)$$

It is well established that water oxidation level lies at +1.23 V vs NHE at zero pH. As a result, several semiconductor photocatalysts can oxidize pure water that results in the generation of molecular oxygen. However, emission of oxygen is hardly detected when the sacrificial agents are present.

The final products of the oxidation reactions at the photoanode depend on the pH of the solution as well as on the absence/presence of oxygen. The production of H$^+$ gets mediated by holes according to the overall Reaction 2.8 under anaerobic condition and at low pH:

$$C_2H_5OH + 3H_2O + 12h^+ \rightarrow 2CO_2 + 12H^+(\text{low pH}) \qquad \text{(Reaction 2.8)}$$

In practice, the reaction proceeds in a series of steps. For instance, in the case of ethanol, the scheme—ethanol → acetaldehyde → acetic acid → CO_2 + H_2O—takes place (Lianos 2011). Although majority of such intermediately occurring reactions are by nature endothermic and the ΔG^0 is positive (for Reaction 2.8), the overall balance is by nature endergonic and gets assisted through holes generated upon photo irradiation. Similar interpretation holds for other reactions for chemical substances having $C_xH_yO_z$ as the general composition and can be presented by Reaction 2.9 (Lianos 2011; Sfaelou and Lianos 2016):

$$\begin{aligned} &C_xH_yO_z + (2x - z)H_2O + (4x + y - 2z)h^+ \\ &\quad \rightarrow xCO_2 + (4x + y - 2z)H^+ \end{aligned} \qquad \text{(Reaction 2.9)}$$

A large number of hydroxyl radicals get produced upon interaction of holes with hydroxyl ions through Reaction 2.5. As a result, the process of decomposition via photocatalysis must be realized through their participation at higher pH. In practice, photodegradation of ethanol follows the same path of ethanol → acetaldehyde → acetic acid → CO_2 + H_2O through intermediate acetaldehyde formation (Panagiotopoulou et al. 2010). However, as the number of H^+ ions at high pH are limited or absent depending on the extent of neutralized with OH^-, therefore, the degradation of ethanol via photocatalysis at high pH can be more realistically represented by Reaction 2.10a and 2.10b, while a more general scheme can be written by Reaction 2.11:

$$OH^- + h^+ \rightarrow OH\bullet(\text{high pH}) \qquad \text{(Reaction 2.10a)}$$

$$C_2H_5OH + 12\bullet OH \rightarrow 2CO_2 + 9H_2O \qquad \text{(Reaction 2.10b)}$$

$$C_xH_yO_z + (4x + y - 2z)\bullet OH \rightarrow xCO_2 + (4x + y - z)H_2O \qquad \text{(Reaction 2.11)}$$

A different set of photocatalytic degradation steps may be presumed, when oxygen is present, through the generation of molecular hydrogen. In aerated condition, it was noticed that oxygen causes acceleration of ethanol mineralization, thus reducing the flow of current through the external circuit (Panagiotopoulou et al. 2010). In this case, one-hole interactions are significant according to Reaction 2.12a and 2.12b, leading to ethanol radical formation:

$$C_2H_5OH + h^+ \rightarrow C_2H_5O\bullet + H^+ \qquad \text{(Reaction 2.12a)}$$

$$C_2H_5OH + OH\bullet \rightarrow C_2H_5O\bullet + H_2O \qquad \text{(Reaction 2.12b)}$$

As these radicals are highly unstable, they release their energy through introduction of electrons into the photocatalyst's CB, resulting in an effect called "current doubling" (Maeda et al. 1981; Kalamaras and Lianos 2015). In this case, the count of electrons that flows via the external circuit is higher compared to the count of photons absorbed (Antoniadou et al. 2012a). Therefore, under anaerobic condition, electricity as well as hydrogen get produced; whereas, only electricity gets produced under aerobic condition according to the following overall Reactions 2.13 and 2.14.

Absence of oxygen/anaerobic, ethanol reforming

$$C_2H_5OH + 3H_2O \rightarrow 2CO_2 + 6H_2 \qquad \text{(Reaction 2.13)}$$

Presence of oxygen/aerobic, ethanol mineralization

$$C_2H_5OH + 3O_2 \rightarrow 2CO_2 + 3H_2O \qquad \text{(Reaction 2.14)}$$

Additionally, the corresponding reactions for substances with general formula $C_xH_yO_z$ (Michal et al. 2014) can be represented by Reaction 2.15 under anaerobic condition (photocatalytic reforming) and Reaction 2.16 under aerobic condition (photocatalytic degradation):

$$C_xH_yO_z + (2x - z)H_2O \rightarrow xCO_2 + (2x + y/2 - z)H_2 \qquad \text{(Reaction 2.15)}$$

$$C_xH_yO_z + (x + y/4 - z/2)O_2 \rightarrow xCO_2 + y/2H_2O \qquad \text{(Reaction 2.16)}$$

In PFC, the driving force for operation in either of the aforementioned conditions is owing to the established difference of potential between the photoanode and the counter electrode. Although the electrode materials by themselves are able to introduce some bias, these are significantly low in practice. As already mentioned, the counter electrode's potential is mainly due to the reduction reaction, which is influenced by the solution pH and the environment (i.e., aerobic or anaerobic). It is well established that the position of the CB of the photocatalyst semiconductor and its Fermi level decide the potential of the photoanode. Mostly, the conduction band level of *n*-type nanocrystalline semiconductors is deployed as a handy index of the photoanode potential for practical purposes. The CB of semiconductor becomes more negative after excitation and when a sacrificial agent is present, which is attributed to consumption of holes and liberation of electrons. The potential difference between photoanode and counter electrode is dependent upon the open circuit potential (V_{oc}) of PFC. In dark, the V_{oc} is low and increases under illumination and becomes even higher when a sacrificial agent is present. For instance, it was observed that for a standard PFC functioning with aerated counter electrode and a photoanode consisting of nanocrystalline titania photocatalyst (nc-TiO_2), the V_{oc} was found to be +0.35 V in the dark, +0.75 V under illumination and increased further to about +1.1 V in the presence of ethanol (Sfaelou and Lianos 2016). The CB of nc-TiO_2 is located approximately at −0.2 V vs NHE and oxygen reduction at +1.23 V vs NHE (at pH = 0). This large difference of +1.43 V cannot be reached owing to the inevitable losses and justifies the actual experimental voltage.

When the counter electrode is placed in an inert environment, hydrogen gets generated through reduction of protons or water at 0.0 V vs NHE under a pH value of 0. In such case, the potential difference between the photoanode and the counter electrode is too small to provide enough driving force to run the system. Therefore, an external bias is mandatory to run the system and has been demonstrated in several reports. There are examples of some photocatalysts that have high enough CB to produce hydrogen without bias photoelectrocatalytically (in principle); however, in practice, such reports are not scarce. On the contrary, the vast majority of works involve the application of a forward bias, which may also be of chemical nature. A theoretically calculated forward bias is required (determined from Eq. 2.1) if the cell is composed of two compartments, in which the anode compartment consisted of an electrolyte that is alkaline, while the cathode compartment is filled with an electrolyte that is acidic. It can be concluded from the above discussion that a PFC can be smoothly operated both when fuel is present and absent, just by illuminating light of appropriate wavelength on the photoanode to excite the photocatalyst.

2.2.2 *Advancement of PFC cells*

From the in-depth analysis of the mechanism of PFC operation in the above section, it is clear that the PFCs generate electricity from an organic material (treated as "fuel") through oxidation at the photoanode and oxygen's reduction at the counter electrode. A brief literature survey comparing different types of photocatalysts, sacrificial reagents, and electrolytes concerning PFC operation has been summarized in Table 2.1 (Antoniadou and Lianos 2010; Sfaelou et al. 2014; Bai et al. 2016; Xia et al. 2016a, b; Lee et al. 2017, 2016; Khalik et al. 2016; Ying et al. 2016; Liu et al. 2016; Hu et al. 2015; Wang et al. 2017; Tantis et al. 2015; Sui et al. 2015; Yang et al. 2014). From the survey, it can be realized that titania (TiO_2) is the conventional material for fabricating the photoanodes. Titania nanotube (TNT) is also a favorable choice as a photoanode material. Titania sensitized by cadmium sulfide (CdS) exhibits the highest values of current under visible light. In addition, some metal sulfide quantum dots (QDs) may be used as sensitizers of TiO_2 due to their higher oxidative power as combined photocatalyst-sensitizer system (Sfaelou et al. 2014). Only few metal sulfide sensitizers, such as CdS, zinc selenide (ZnSe), and some CdS-zinc sulfide (ZnS) combinations, exhibit this property (Antoniadou et al. 2014b, 2012a, 2011); however, it should be noted that ZnS independently cannot absorb visible light owing to its large band gap. Although various electrolyte can be employed in PFCs, neutral electrolytes like Na_2SO_4 have been mostly used. However, it should be noted that alkaline media produced higher current densities as it facilitates reduction of oxygen. As the PFCs are designed for production of energy through degradation of wastes and pollutants, several dyes have been used as the model fuel. However, oxygenated organic compounds of the general formula $C_xH_yO_z$ are considered to be the best performing fuel, since they yield the highest values of electric power. Even after a large development, unfortunately, no work has been performed to analyze their suitability in PFC application.

Table 2.1 Literature survey of various types of photocatalysts used in PFCs along with their performance data. Reproduced from Lianos 2017, with permission from Elsevier

Sacrificial agent	Photocatalyst	Electrolyte	J_{sc} ($mAcm^{-2}$)	V_{oc} (V)	Maximum power density ($mWcm^{-2}$)	References
Ethanol	TiO_2	NaOH	0.79	1.2	–	Antoniadou and Lianos (2010)
Ethanol	CdS/TiO_2	NaOH	6.9	1.2	–	Sfaelou et al. (2014)
Glucose	$BiVO_4/TiO_2$	Na_2SO_4	–	–	0.116	Bai et al. (2016)
	ZnO/CuO					
Tetracycline	$BiVO_4/WO_3$	KH_2PO_4	0.26	0.78	0.2	Xia et al. (2016a)
Methanol	TiO_2	KOH	0.66	1.2	–	Xia et al. (2016b)
Reactive Green 19	ZnO	Water	0.0427	–	0.0102	Lee et al. (2017)
Methylene blue	ZnO	Water	–	–	0.0032	Lee et al. (2016)
Reactive Black 5	ZnO	Na_2SO_4	1.3	0.908	0.335	Khalik et al. (2016)
Reactive Black 5	ZnO	MgSO4	1.2	0.628	0.256	Khalik et al. (2016)
Reactive Black 5	ZnO	NaCl	1.05	0.523	0.245	Khalik et al. (2016)
Glucose	TNT	Na_2SO_4	0.15	0.70	–	Ying et al. (2016)
Rhodamine B	Ag/AgCl/GO	Na_2SO_4	0.5	–	–	Liu et al. (2016)
	$ZnIn_2S_4$					
Triethanolamine	TNT	Na_2SO_4	0.37	0.09	0.09	Hu et al. (2015)
Methanol	TNT	Na_2SO_4	0.20	0.96	0.03	Hu et al. (2015)
Glucose	TNT	Na_2SO_4	0.17	1.07	0.04	Hu et al. (2015)
Methanol	WO_3 nanotubes	Na_2SO_4	0.06	0.52	0.004	Hu et al. (2015)
Methanol	Nb_2O_5 nanotubes	Na_2SO_4	0.02	0.96	0.004	Hu et al. (2015)
Organic polymer + metal ions	TiO_2	KOH	0.23	0.63	0.084	Wang et al. (2017)
Acid orange 7	TiO_2	NaCl	0.4	0.75	–	Tantis et al. (2015)

(continued)

Table 2.1 (continued)

Sacrificial agent	Photocatalyst	Electrolyte	J_{sc} (mAcm^{-2})	V_{oc} (V)	Maximum power density (mWcm^{-2})	References
Rhodamine B	TNT	NaCl	0.25	0.45	0.032	Sui et al. (2015)
Rhodamine B	WO_3/TNT	Na_2SO_4	0.05	0.18	–	Yang et al. (2014)
	CuO/TNT					

2.3 Basic Principles of PEC Cells

The PEC cell is one of the simplest systems for transformation of solar energy into electrical energy and chemical energy. Thorough realization of the principle of a PEC cell shows that the photogenerated holes get transported to the interface of the photoelectrode/electrolyte to produce oxygen; whereas, the photogenerated electrons get moved to the counter electrode to yield hydrogen. More precisely, the entire process consists of three major steps: (a) absorption of light, (b) separation and subsequent transportation of charge carrier, and (c) chemical reactions occurring at the surface (Lin et al. 2011). In PEC water splitting cell, the holes and electrons, generated upon photo irradiation, are involved to produce oxygen and hydrogen evolution (i.e., splitting of water molecules), respectively, at the photoelectrode and the counter electrode. The simplest configuration of a PEC cell can be visualized as a cell comprising of a metallic counter electrode and a photoactive semiconductor *p*- or *n*-type electrode, immersed in an electrolyte.

As in PFCs, upon illuminating the semiconductor/electrolyte interface with a higher energy light (compared to the energy of the semiconductor's band gap), separation of the generated electron-hole pairs occur in the space charge region. Subsequently, the minority carriers, i.e., holes in case of *n*-type or electrons in case of *p*-type, reach the semiconductor/electrolyte interface and get accumulated on the non-illuminated side of the semiconductor that is not in contact with the electrolyte. The photogenerated minority carriers get moved to the counter electrode through a load via the connecting wire. These subsequently react electrochemically with the redox electrolyte, causing reduction of the electrolyte with *n*-type and oxidation with *p*-type semiconductors.

On the other hand, the minority carriers that are generated at the semiconductor interface perform the opposite reaction and, thus, consume the carriers. Because of these two opposite processes, no net change occurs in the electrolyte and production of electrical power takes place in the load. Therefore, in a regenerative PEC, conversion to electrical energy from energy of the photons occurs without hampering the composition of the electrolyte or the electrodes.

The mathematical expressions for determination of the cumulative influences of absorption of light, migration of charge and chemical reactions occurring on the surface are discussed in-depth by Linsebigler et al. (1995). The fundamental operation of a PEC system for water splitting appears to be simple; however, a thorough realization of its complex underlying principles does not exist at the level of the molecules, particularly at the semiconductor/electrolyte interface, which significantly affects the regulation and optimization of the efficiency of the PEC cell. The semiconductor/electrolyte interface contains three well defined layers: a Gouy layer, a Helmholtz layer, and a space charge layer (Hagfeldt and Gratzel 1995; Salvdor 1984). Notably, the thickness of the Helmholtz layer is around 0.3 nm to 0.5 nm, which is independent of the photoelectrode (Li et al. 2013). On the other hand, the thickness of the Gouy layer and the space charge layer get reduced with increasing concentration of the charge carrier present within the photoelectrode/

electrolyte interface. Again, an *n*-type semiconductor's space charge layer is further classified into (a) the accumulation layer containing accumulated mobile electrons, (b) the depletion layer where reduction of the mobile electrons from uncompensated ions and compensation of excess space charges by acceptors take place, and (c) the inversion layer containing the accumulated mobile holes. The space charge layer's thickness has been estimated by Linsebigler et al. (1995). The photoinduced charges diffuse and leave the depletion layer. The minority carrier diffusion length (*Lp*) is the distance that a hole can diffuse prior to recombining and is represented according to Eqs. 2.4 and 2.5 (Lin et al. 2011):

$$L_p = (D\tau)^{1/2} = [(\mu k_b T/q)\tau f]^{1/2} \tag{2.4}$$

$$\mu = q\tau/m^* \tag{2.5}$$

where D represents the coefficient of diffusion of the minority carrier and τ represents the lifetime. The coefficient of diffusion is related to the mobility of the minority carrier μ ($\mathrm{m^2\ V^{-1}\ s^{-1}}$) that can be realized by Eq. 2.5, where m^* represents the effective mass of the minority carrier. It can be concluded from these equations that a reduction in m^* is helpful for an enhancement in L_p. It should be clarified here that all the conditions mentioned above are applicable for an *n*-type semiconductor PEC cell.

However, all the processes occurring under illuminated conditions are comparable except the fact that for a *p*-type semiconductor, the dopants (ionized) are negatively charged and the solution in vicinity of the photoelectrode is charged positively. Thus, the electrons flow into the acceptor species (positively charged) that are adsorbed at the interface of the semiconductor and the electrolyte (Zhou et al. 2013).

2.3.1 Types of PEC Cells

There are mainly two categories of PEC cells for conversion of solar energy, as illustrated in Scheme 2.2, viz., photovoltaic and photoelectrosynthetic cells.

2.3.1.1 Regenerative or Photovoltaic Cell

In the first kind, the optical energy gets transformed into energy of electricity with zero change in the free energy ($\Delta G = 0$) of the reduction-oxidation electrolyte (Scheme 2.2). Here, the electrochemical reduction undergoing at the counter electrode surface is reverse to the photooxidation occurring at the *n*-type electrode (Fig. 2.3a). Thus, the energy from light gets transformed into energy of electricity, unaltering the solution composition or electrode material and operated in regenerative mode. When the counter electrode reaction occurs in the dark (Fig. 2.3a), instead

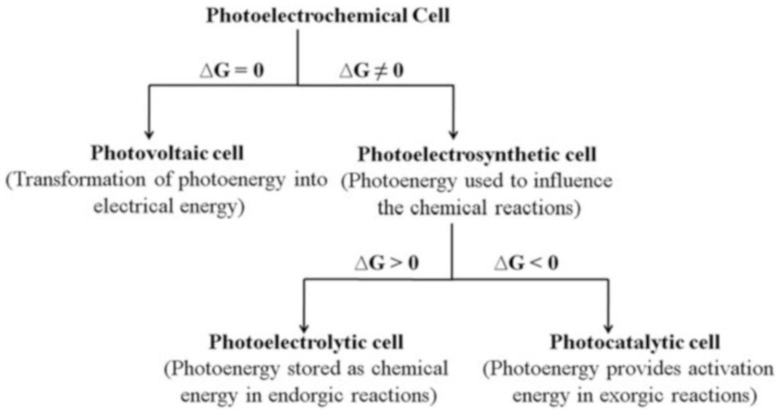

Scheme 2.2 Classification of PEC cells. (Reproduced after modification from Sharon 2007, with permission from Wiley)

of an electrocatalytic electrode (Hodes et al. 1977; Hodes et al. 1980), a *p*-type photocathode can also be employed in a tandem regenerative cell. In these instances, the operation of the cells occurs in the photovoltaic mode where the input energy of the photons gets converted into electrical energy.

2.3.1.2 Photoelectrosynthetic Cell

In the second kind, namely, a photoelectrosynthetic cell (Fig. 2.3b), optical energy gets transformed into chemical energy, suffering non-zero change of free energy in the electrolyte. In photoelectrosynthetic cells, the reaction at the counter electrode differs from that at the semiconductor (so that a separator might be necessary in the cell to keep the products apart). This category of cell may be further categorized as photocatalytic cell ($\Delta G < 0$) and photoelectrolytic cell ($\Delta G > 0$) (already elaborated in Sect. 2.2) (Scheme 2.2), which depends on the relative location of the values of potential of the two reduction-oxidation couples (i.e., O′/R′ and O/R).

In the photoelectrolytic cell, a net change of the chemical composition takes place upon illumination. More accurately, the cell reaction gets forwarded in the contra-thermodynamic direction (i.e., $\Delta G > 0$) by light in the photoelectrolytic mode (Fig. 2.3b). On the other hand, in the latter category of conversion of energy device, the cathodic and the anodic compartments must remain separated in order to hinder the mixing of the two reduction-oxidation couples. The initial excitation by photons does not take place in the semiconductor (contrary to that occurring in the device counterparts presented in Fig. 2.3) but instead take place in organic compounds or dyes that absorb visible light (where light accelerates the rate of the reaction) (Fig. 2.1). Subsequent introduction of an electron from the compound or dye (excited by photons) into the CB of the semiconductor leads to the transport of an electrical charge in the external circuit. In essence, aqueous suspensions containing

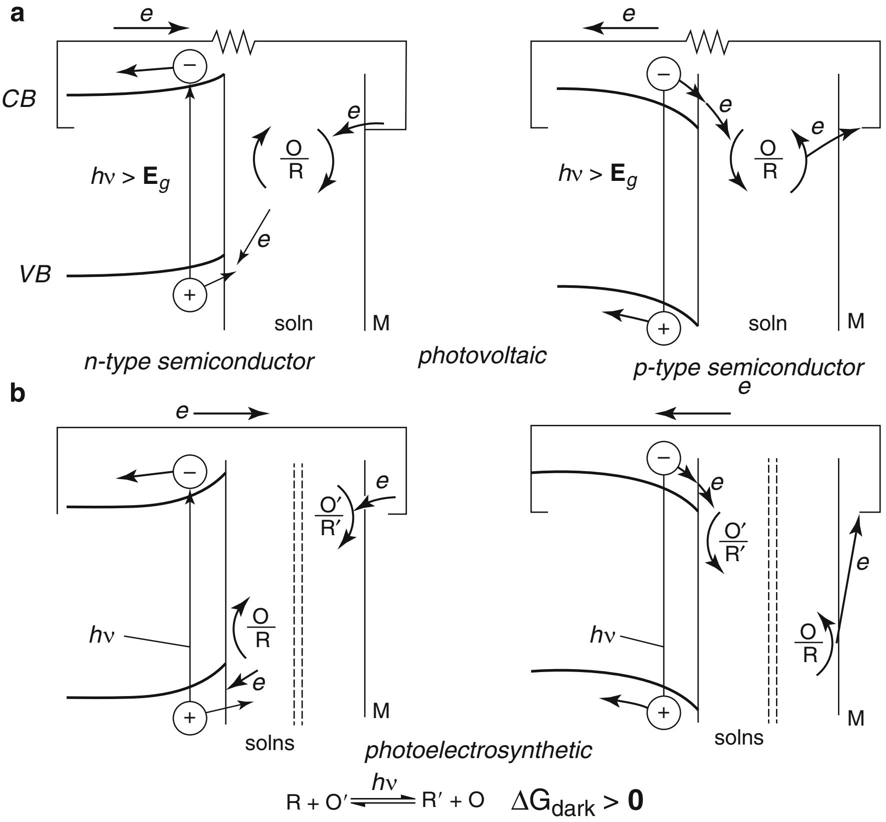

Fig. 2.3 Photoelectrochemical devices for conversion of solar energy in presence of *p*-type and *n*-type semiconductor photocatalyst: (**a**) regenerative or photovoltaic cell and (**b**) photoelectrolytic cell. (Reproduced after modification from Bard and Faulkner 2001, with permission from Wiley)

irradiated particles of semiconductor can be realized as an assembly of short-circuited microelectrochemical cells that functions in the photocatalytic mode.

2.3.2 Basic Configuration/Structure of a PEC Cell

From the survey of several publications listed here, it can be realized that the fundamental configuration of a PEC cell as well as a PFC cell has not evolved a lot over the years (Kaneko et al. 2006; Fujishima and Honda 1972; Borman 1991; Chojnowski et al. 1981; Getoff 1990; Bak et al. 2002; Park et al. 2006; Tode et al. 2010; Antoniadou et al. 2010; Kaneko et al. 2009a, b; Canterino et al. 2009; Nowotny et al. 2005; Kamat 2007). The cell typically comprises of a photoanode that carries a photocatalyst semiconductor, an electrolyte, and a cathode (counter electrode) carrying a reduction photocatalyst/electrocatalyst. The cathode and the anode remain connected through an external load. Usually, an *n*-type photocatalyst semiconductor serves as the photoanode (negative electrode), whereas the noble metal electrocatalysts (mostly Pt) or p-type semiconductor photocatalyst serves as the photocathode (positive electrode); thus, the electrons get transported to the negative electrode from the positive electrode. Naturally, electrode potential of each electrode regulates the direction of the external current. The potential of the anode is dependent on the Fermi level of the photocatalyst semiconductor. In widely used titania, the conduction band, that at zero pH has slightly positive potential, becomes slightly negative upon excitation (Bak et al. 2002). On the contrary, at zero pH the potential of the cathode in contact with an aqueous electrolyte is dependent on the absence (anaerobic) or presence (aerobic) of O_2. Under anaerobic conditions, the cathode plays the role of a hydrogen electrode (zero potential); whereas, the cathode plays the role of an oxygen electrode in presence of oxygen. Its potential value can be determined by Reactions 2.17 and 2.18, and its magnitude varies between +0.68 V and + 1.23 V (Ueno et al. 2009):

$$O_2 + 4H^+ + 4e^- \rightarrow 2H_2O(+1.23\ \text{V}) \qquad \text{(Reaction 2.17)}$$

$$O_2 + 2H^+ + 2e^- \rightarrow H_2O_2(+0.68\text{V}) \qquad \text{(Reaction 2.18)}$$

In the absence of oxygen, this difference of potential is too low to cause spontaneous operation of the cell due to some unavoidable losses. Therefore, an external bias is required between the electrodes for enhancing the electromotive force that drives the electrons to the negative electrode from the positive electrode (Getoff 1990). In most of the instances, this additional bias is supplied by the renewable energy devices (Bak et al. 2002; Kim et al. 2009; Brillet et al. 2010; Miller et al. 2003). Under aerobic conditions, bias is not required, as the difference of potential is large enough between two electrodes (Antoniadou and Lianos 2010). Thus, the PEC cells can function spontaneously under oxygen environment.

In the anode compartment of PEC cells, an organic or an inorganic substance, dissolved within the electrolyte of the anode compartment, acts as the feed fuel, which is photocatalytically degraded and consumed at the photoanode producing electricity or chemical energy. However, not only with pure organic and inorganic substances or water itself, photocatalytic oxidation can also take place with their mixtures. Therefore, materials which are considered water-soluble wastes or pollutants may be used as fuel in a PEC cell. It has been observed that the most efficient organic fuels are those having $C_xH_yO_z$ composition, i.e., alcohols (methanol, ethanol, and propanol), polyols (lactose, fructose, glucose, sorbito, xylitol, and glycerol), organic pollutants (triton X-100, ammonia, urea, sodiumdodecyl sulfate, cetyltrimethylammonium bromide), and carbohydrates, which may be the products of biomass.

Depending on the nature of applications, the PFCs may be configured as either one compartment or two compartments. Both of them are applicable for production of electricity. It should be mentioned here that the elimination of the separator membrane will bring the fuel in contact with the counter electrode and the electrocatalyst, inducing electrocatalytic oxidation of the fuel and creating a reverse flow of current indicated from the decreased value of the V_{oc} of the cell (Antoniadou et al. 2014b, 2013). At the same time, removal of the membrane will decrease the internal resistance leading to higher current generation. Therefore, one-compartment cells are able to generate higher current but lower voltage compared to two-compartment cells (Antoniadou et al. 2014b). Of course, a chemical bias may be applied through incorporation of different electrolytes in the two compartments in a two-compartment cell, which is not required in one-compartment cells. The applied chemical bias further enhances the V_{oc} and, thereby, provides additional drive to operate the cell. In two compartment cells, the produced hydrogen will remain separated from the oxidation reaction, thus avoiding the losses of hydrogen during photoelectrocatalytic hydrogen production. Introduction of an electrolyte, which is acidic, within the cathode compartment acts like a proton sink and enhances the hydrogen production (Horiuchi et al. 2013; Antoniadou and Lianos 2009; Monfort et al. 2016; Selli et al. 2007). The separation membrane may then be a proton transfer membrane, the functionality of which is preserved in contact with the acidic electrolyte. In addition, an alkaline electrolyte may be introduced in the photoanode compartment introducing a chemical bias, which facilitates the oxidation of fuel in an alkaline environment (Monfort et al. 2016; Selli et al. 2007). Therefore, the choice of the electrolytes for generation of chemical bias should be a matter of optimization (Selli et al. 2007). When water is used as a fuel, a two-chambered cell is necessary to keep the produced oxygen and the hydrogen separated. However, hydrogen production can be performed in one-compartment cell if the oxidation product from the fuel interfere less with the produced hydrogen.

2.3.3 Semiconductors for Photoanodes

An electrode deposited with a nanocrystalline semiconductor film is typically employed as a photoanode. Mesoporous nanocrystalline anatase titania is widely used for the fabrication of photoanodes, both for PFCs and various types of PEC cells. Various procedures have been employed to produce mesoporous 1-D TiO_2 nanostructures, such as nanowires, nanotubes, nanorods, etc. The vast choices of low dimensional nanostructures are due to less possibility of the recombination of electron-hole pairs and high specific surface area (SSA) (Lianos 2017). TNTs, synthesized by employing the electrochemical anodization method on a web of microfibers of Ti, can directly be used as a photoanode (Stoll et al. 2016). In the case of nanoparticulate titania film, it is necessary to get them deposited with very high SSA and crystallinity. For instance, fabrication of photoanodes from titania synthesized by flame-spray-pyrolysis with SSA 249 $m^2\ g^{-1}$ generates double photocurrent compared to that obtained upon using titania P-25 (SSA 50 $m^2\ g^{-1}$) (Tantis et al. 2016). It should be mentioned here that TiO_2 has reasonably high charge transport capability compared to other common oxide-based semiconductors. Even after having very high hole diffusion length (order of ~10^4 nm) compared to that of tungsten trioxide (WO_3) and hematite (Liu et al. 2012), titania often suffers from extensive recombination of electron-hole pairs. In order to overcome this drawback, two-dimensional graphene, which is known to create electron "highway" facilitating electron-hole separation, is introduced into the titania nanostructure (Nouri et al. 2016). In addition, incorporation of graphene or reduced form of graphene oxide (RGO) enhances the active surface area as well as the active sites of the photocatalysis (Ning et al. 2016).

It is well established that as two different species having difference in band level is brought into contact, the charge carriers (generated upon photo irradiation) present in the first species will get introduced into the second species owing to favorability in the position of the states of energy. Based on this principle, some foreign nanoparticulate semiconductor or metallic co-catalysts have been employed as an alternative solution, assisting the electron-hole separation. For instance, a combined titania and WO_3 possesses higher efficiency as a photocatalyst compared to the individual semiconductors (Dozzi et al. 2016). The photocatalytic hydrogen production can be carried out by the combination of titania with noble metal nanoparticles. Similar combinations have also been employed for photoelectrocatalysis (Zhang et al. 2015; Antoniadou et al. 2012b).

Even after having lots of advantages, the most critical drawback of TiO_2 is its complete excitation in the ultraviolet region. As a solution, numerous reports have been made on titania sensitization using different sensitizers that absorb visible light, which mostly applies to dye sensitized solar cells (DSSCs) as well as solid-state and liquid electrolyte solar cells. On the other hand, the sensitization process in aqueous environment has to go through many hurdles, such as instability. QDs of metal sulfides are well known to be the most effective titania sensitizers, due to easy incorporation into mesoporous titania structure through simple chemical techniques (e.g., Successive Ionic Layer Adsorption and Reaction, SILAR method) (Nicolau 1985). Metal sulfides, such as CdS and cadmium selenide (CdSe), possess *n*-type characteristics, which can suffer self-oxidation by holes present in VB. As a result, the stability of these semiconductors is dependent on fast rate of scavenging of holes generated upon photo irradiation by suitable donors of electrons. This principle has also been effectively applied in water splitting when inorganic sulfur-containing sacrificial agents are present (Lianos 2017). Apart from metal sulfides sensitization, graphene QDs have also been applied as a sensitizer of titania in photoelectrochemical water splitting (Sudhagar et al. 2016). Although dye sensitizers are not known for their stability in aqueous environment, there are reports on dye sensitization (Li et al. 2016b).

Besides titania, WO_3 photoanodes has been widely used owing to its band gap of 2.5–2.8 eV, absorbing visible light up to 500 nm. It can be classified as an *n*-type indirect semiconductor, which is reasonably stable at low pH (Gan et al. 2014). In PEC water splitting, it has been extensively used as the photoanode material (Liu et al. 2012; Lianos 2017; Gan et al. 2014). However, when a sacrificial agent is present, such as organic substances and wastes, the photocurrent gets substantially enhanced by WO_3 photoanodes (Sfaelou et al. 2016). The disadvantages of TiO_2 are lower stability and favorability in electrolytes that are acidic in nature only, while the films of tungsten trioxide possess lower specific surface areas compared to majority of TiO_2 films.

Another medium band gap semiconductor photocatalyst, excited in visible light for water splitting applications, is bismuth vanadate ($BiVO_4$) (Gan et al. 2014). The active and common $BiVO_4$ polymorph possesses a monoclinic crystalline scheelite-like morphology, having 2.4 eV band gap. Sayama et al. (2003) have reported an incident photon-to-current efficiency (IPCE) at 420 nm of 29% for decomposition of water by photoelectrochemical means and upon application of +1.9 V bias vs RHE. However, Jia Reproduced from Lianos et al. (2012) obtained a higher value (73%) of IPCE for +1 V bias vs Ag/AgCl. It follows that to obtain a substantial photocurrent by using $BiVO_4$ photoanodes a bias is mandatory, since recombination of electron-hole pairs is critical in BiVO4. In this regard, a comprehensive review enlisting the photocurrents achieved when different biases are applied and different structures of $BiVO_4$ are employed has recently been published (Li et al. 2013).

However, due to extensive recombination of electron-hole pairs and low mobility of charges, the actual efficiencies of pure $BiVO_4$ are unsatisfactory (Monfort et al. 2016). Thus, bismuth vanadate is analyzed when metal dopants are present, so that the efficiency of water splitting gets improved (Ye et al. 2010; Monfort et al. 2017; Quiñonero et al. 2016; Antony et al. 2016). Presence of metallic dopants results in modification of the electronic properties and the band structure of the materials and causes enhancement of the photocurrent. Here “dopant” stands for donor impurity. For instance, upon introduction of Nb(V), the density of current in a water splitting device got increased by threefold (Monfort et al. 2017).

Application of oxygen evaluation catalyst is an alternative process to improve the performance of bismuth vanadate photoanode. O_2 evolution catalysts, such as cobalt phosphate, FeOOH, or NiOOH, have been employed on bismuth vanadate, hampering the recombination on surface and decreasing the overpotential of evolution of oxygen. Therefore, introduction of FeOOH/NiOOH catalyst leads to significant enhancement of the photocurrent (Kim and Choi 2014).

Hematite (α-Fe_2O_3), excited in the visible region, is another popular photocatalyst (Sivula et al. 2011; Shi et al. 2015a; Mishra and Chun 2015; Warren et al. 2013). Having a 2.0 eV band gap, hematite possesses the ability to absorb light beyond 600 nm; thus, it demonstrates a theoretical value of >15% of solar-to-hydrogen efficiency (SHE) (Li et al. 2013) when the anticipated density of current can become 14 $mAcm^{-2}$ (Li et al. 2013; Warren et al. 2013). Even after having lots of advantages, there are some deficiencies. For instance, hematite demonstrates fast rates of recombination and low values of conductivity owing to its charge carriers’ large effective mass. For this reason, for allowing charge carriers to get to the electrode, it is essential to be applied on thin film electrodes. The photoanode made from hematite is undoubtedly a good candidate for oxidation of water; however, for reduction of water, the presence of a bias is essential as it does not have enough potential for water redox (0.00 V to +1.23 V vs SHE).

As for $BiVO_4$, the hematite photoanode performance can be improved through introduction of metal dopants (i.e., impurities) such as Pt (Rahman and Joo 2013), Zn, and Ti (Kalamaras et al. 2016; Mirbagheri et al. 2014). Doping repairs defects and, therefore, reduces the recombination of electron-hole pairs. Electrodeposition-based doping by metal is typically followed by annealing at high temperatures. This process influences grain boundaries and sizes, leading to affecting the overall performance of the photocatalyst (Phuan et al. 2015). For instance, the photocurrent increased more than double upon the introduction of Ti^{4+} impurities (Kalamaras et al. 2016). In addition, betterment of the performance of the photoanode made from hematite may also be achieved by introducing catalysts for oxygen evolution, as for bismuth vanadate (Zheng et al. 2015).

2.3.4 Semiconductors for Cathodes/Photocathodes

The materials for the cathode of PFCs are limited compared to the multiple choices available in case of the photoanodes. In most of the cases, a Pt foil or wire or black (cast or sprayed or hot pressed) is employed (Kaneko et al. 2006). Besides platinum cathodes, platinum foils that are platinized or non-platinized, nanoparticles of metal deposited on TiO_2/stannic oxide (SnO_2) with fluorine doping and platinized stannic oxide with fluorine are fabricated into electrodes, e.g. $Ni/TiO_2/SnO_2$, $Ag/TiO_2/SnO_2$, $Au/TiO_2/SnO_2$, $Pd/TiO_2/SnO_2$ and $Pt/TiO_2/SnO_2$. A cloth of carbon loaded with Pt has also been utilized as a material for cathode. The reported current, voltage, and efficiency of the platinized SnO_2 with fluorine electrode are 1.15 $mAcm^{-2}$, 1340 mV, and 12.3%, respectively, which are much better than that obtained with other materials. The cloth of carbon loaded with Pt demonstrated the highest value of efficiency (32.3%) (Ren and Gan 2012).

The photocathode must possess *p*-type characteristics, having a negatively positioned edge of CB for reduction of water. In addition, the photocathode's Fermi level must be higher compared to the photoanode. This is the sole mean to produce interior bias in order to circulate the photoanode's electrons via the external circuit for the purpose of combining with the photocathode's holes. The photoanode's holes and the photocathode's electrons can then be made available for decomposition of organic matter and reduction of water. Therefore, the less availability of *p*-type photocatalysts compared to *n*-type photocatalysts restricts the availability of the photocathodes. This is because the *p*-type semiconductors suffer from instability when placed in an electrolyte's contact. As a result, they should be provided protection to retain their functionality, which is a difficult task. One example of *p*-type photocatalysts is cuprous oxide (Cu_2O) for its convenient synthetic procedure, for example, by electrodeposition (Paracchino et al. 2011). The positions of its energy levels are at +1.3 V and − 0.7 V vs SHE for the VB and the CB, respectively. Of course, there are possibilities of self-photoreduction of Cu_2O like self-photooxidation of some *n*-type semiconductors. Thus, protection needs to be provided for Cu_2O. By atomic layer deposition (ALD) of TiO_2 and ZnO thin layers on Cu_2O, the photocurrent was observed to be enhanced by threefold with substantially longer lifetime of the photocathode (Paracchino et al. 2011). The various protective layers reported in recent literatures are SnO_2 (Azevedo et al. 2016), Ga_2O_3 (Li et al. 2016c), carbon (Shi et al. 2015b), Cu_2S (Minguez-Bacho et al. 2015), etc. The main function of the photocathode is to cause electron exchange with the electrolyte. However, the overpotential produced between the phases restricts this exchange. For overcoming this overpotential, along with the layer of protection, co-catalysts such as Pt, RuO_2 (Azevedo et al. 2016), and NiO_x (Lim et al. 2014) must also be employed.

Besides copper-based chalcogenide semiconductors, a second class of *p*-type photocatalysts has also been exclusively used as photocathodes (Chen et al. 2016). The most characteristic semiconductors of this family are Cu_2ZnSnS_4 (CZTS) and Cu(In,Ga)Se_2 (CIGS), which have been successfully deployed as photocathodes for splitting of water (Chen et al. 2016). The band gap in CIGS photocathodes can be tuned in the range 1.0 eV to 1.7 eV upon modification of their composition (Chen et al. 2016). These chalcopyrites consist of Ga and In that are rare and costly. Recently, the focus has been on copper chalcogenides of the type Cu_2ZnSnS_4, consisting of more available and nontoxic Se to resolve the situation (Wang et al. 2016).

2.3.5 Advancement of PEC Cells

The related published literatures are sufficient to draw solid conclusion that oxidation of organic sacrificial agents photoelectrocatalytically generated higher values of photocurrents compared to oxidation of water, leading to higher rates of production of hydrogen. The data found in recent literatures on utilization of different photocatalysts, such as Ti-Fe_2O_3, WO_3, TiO_2 nanotubes, TiO_2 nanoparticles, etc., are enlisted in Table 2.2 (Zhang et al. 2015; Sfaelou et al. 2016; Kalamaras et al. 2016; Iwu et al. 2013; Seger et al. 2012; Bashiri et al. 2016; Liang et al. 2016). The organic wastes employed for photoelectrolytic hydrogen generation are derivatives of biomass, such as oxygenates, organic acids, and alcohols, as they demonstrate higher rates of production of hydrogen. Due to substantial absorption in the visible region, Ti- and WO_3-modified Fe_2O_3 are photocatalysts with very high efficiency. In these instances, hydrogen gets generated under applied bias or in an array in which the necessary bias is offered by a solar cell.

Inorganic sacrificial agents, e.g., sulfide/sulfite salt mixtures which are irreversibly oxidized, are enable to generate hydrogen following the oxidation Reactions 2.6 and 2.7. The oxidation of other inorganic agents, namely, water and ammonia, which does not evolve hydrogen, differ from organic materials and inorganic sacrificial agents. Their sole role is to scavenge holes during production of hydrogen upon reduction of water. Therefore, splitting of pure water by oxidation is often confused with production of hydrogen when sulfide/sulfite reagents are present. A comprehensive survey result on production of hydrogen in their presence is enlisted in recent literature (Lianos 2017). The most familiar selection of photoanode for production of hydrogen, when mixtures of sulfite/sulfide are present, is mesoporous

Table 2.2 Survey on production of hydrogen photoelectrocatalytically through organic sacrificial agents' oxidation using various photocatalysts along with their performances. Reproduced from Lianos 2017, with permission from Elsevier

Sacrificial agent	Photocatalyst	Electrolyte	Current density (mAcm^{-2})	Bias (V vs Ag/AgCl)	H_2 evolution rate (μmolmin^{-1})	References
Water	WO_3	$NaClO_4$	3.0	1.6	2.0	Sfaelou et al. (2016)
Ethanol	WO_3	$NaClO_4$	6.0	1.6	7.3	Sfaelou et al. (2016)
Water	WO_3	H_2SO_4	0.8	–	–	Esposito et al. (2012)
Glucose	WO_3	H_2SO_4	1.4	–	–	Esposito et al. (2012)
Water	Ti-Fe_2O_3	NaOH	2.2	0.7	1.2	Kalamaras et al. (2016)
Ethanol	Ti-Fe_2O_3	NaOH	3.2	0.7	2.0	Kalamaras et al. (2016)
Ar + H_2O	TiO_2	Nafion	0.015	–	–	Iwu et al. (2013)
Formic acid	TiO_2	H_2SO_4	0.15	–	0.045	Seger et al. (2012)
Glycerol	Cu-Ni/TiO_2	KOH	–	–	1.58	Bashiri et al. (2016)
Ascorbate + glucose	CdS	Na_2SO_4	0.167	–	0.71	Liang et al. (2016)
Water	Pd/TNT	KOH	0.6	–	–	Zhang et al. (2015)
Glucose	Pd/TNT	KOH	1.1	–	0.47	Zhang et al. (2015)

TiO_2 fabricated with QDs of CdSe and/or CdS. The sulfide salt heals the QDs' self-photooxidation, while the potential of oxidation of these salts is similar to the combined photocatalyst's level of oxidation. In addition, metal sulfides nanostructures are also frequently utilized as electrocatalysts for evolution of hydrogen in sulfite/sulfide electrolytes. It has been observed that the maximum current density, larger than 15 $mAcm^{-2}$, was obtained for $CdSe/CdS/TiO_2$ photoanode. A significant volume of literature is concerned with photoelectrocatalytic splitting of pure water, generating H_2 at the cathode and O_2 at the anode (Lianos 2017).

2.4 Concluding Remarks and Future Perspectives

This chapter has been concerned with clear distinction of photocatalytic and photoelectrocatalytic fuel cells and their most essential fundamental aspects. In spite of the fact that photocatalytic fuel cells are capable of producing higher energy yield compared to water splitting, less attention has been paid on them. Photocatalytic fuel cells are easily constructible devices by which electrical energy can be produced through consumption of organic wastes (i.e., fuels) upon irradiation of the photoanode with appropriate light's wavelength. The focus of the related works is limited to titania photoanodes, and few of them are aimed on visible-light-absorbing photoanodes based on photocatalysts, namely, Fe_2O_3, $BiVO_4$, and WO_3. Thus, photoanodes' low level of functionality imposed a lack of interest in research on counter electrodes as well. However, the extent of counter electrode's functionality toward reduction of oxygen is equally important as photoanode for photocatalytic fuel cell efficiency. In-depth knowledge on photocatalytic fuel cells is essential for the fabrication of O_2 reducing electrocatalysts that do not contain Pt. More precisely, the selection of cathodic electrocatalysts or photocatalysts is limited, leaving enough space for further research. Similarly, the in-depth mechanism for fuels (that are photodegradable) for photocatalytic fuel cell is mostly studied for ethanol and methanol, with lesser focus on glycerol. Whereas, the effects observed upon using higher polyols and sugars are not clear even after lot of interests.

The oxidation of an inorganic or organic sacrificial agent, such as H_2O, as well as the reduction of O_2, H^+, or H_2O, determines the efficiency of a photoelectrocatalytic cell. The main components of photoelectrocatalytic fuel cells, including electrolytes, counter electrodes, photocathodes, and photoanodes, have been discussed thoroughly. A photoelectrolytic cell can be operated with a cathode when O_2 is absent, producing H_2. Under appropriate conditions, the by-products formed in the process of photodegradation may contain other fuels. Thus, simultaneous production of electricity and fuel can occur in a photoelectrolytic cell. It has been realized that hydrogen production efficiency is higher in a photocatalytic fuel cell compared to the photoelectrocatalytic operation. Therefore, photocatalytic fuel cell is more effective to produce only electricity. The photoelectrocatalytic fuel cell technology is a relatively mature technology irrespective of the prevailing drawbacks. Now, it is the prime time to undertake necessary research and developmental works on cell design and to address upscaling issues.

Acknowledgments KD would like to thank the Science and Engineering Research Board (SERB) [Department of Science and Technology (DST), Govt. of India] and the Indo-US Science and Technology Forum (IUSSTF) for the Indo-US Postdoctoral Fellowship (Award No. 2017/8-Kingshuk Dutta).

References

Antoniadou M, Lianos P (2009) Near ultraviolet and visible light photoelectrochemical degradation of organic substances producing electricity and hydrogen. J Photochem Photobiol A Chem 204:69–74. https://doi.org/10.1016/j.jphotochem.2009.02.001

Antoniadou M, Lianos P (2010) Production of electricity by photoelectrochemical oxidation of ethanol in a photofuel cell. Appl Catal B Environ 99:307–313. https://doi.org/10.1016/j.apcatb.2010.06.037

Antoniadou M, Kondarides DI, Labou D, Neophytides S, Lianos P (2010) An efficient photoelectrochemical cell functioning in the presence of organic wastes. Sol Energy Mater Sol Cells 94:592–597. https://doi.org/10.1016/j.solmat.2009.12.004

Antoniadou M, Daskalaki VM, Balis N, Kondarides DI, Kordulis C, Lianos P (2011) Photocatalysis and photoelectrocatalysis using (CdS-ZnS)/TiO_2 combined photocatalysts. Appl Catal B Environ 107:188–196. https://doi.org/10.1016/j.apcatb.2011.07.013

Antoniadou M, Kondarides DI, Dionysiou DD, Lianos P (2012a) Quantum dot sensitized titania applicable as photoanode in photoactivated fuel cells. J Phys Chem C 116:16901–16909. https://doi.org/10.1021/jp305098m

Antoniadou M, Panagiotopoulou P, Kondarides DI, Lianos P (2012b) Photocatalysis and photoelectrocatalysis using nanocrystalline titania alone or combined with Pt, RuO_2 or NiO co-catalysts. J Appl Electrochem 42:737–743. https://doi.org/10.1007/s10800-012-0408-2

Antoniadou M, Han C, Sfaelou S, Michailidi M, Dionysiou D, Lianos P (2013) Solar energy conversion using photo-fuel-cells. Sci Adv Mater 5:1756–1763. https://doi.org/10.1166/sam.2013.1628

Antoniadou M, Sfaelou S, Dracopoulos V, Lianos P (2014a) Platinum-free photoelectrochemical water splitting. Catal Commun 43:72–74. https://doi.org/10.1016/j.catcom.2013.09.010

Antoniadou M, Sfaelou S, Lianos P (2014b) Quantum dot sensitized titania for photo-fuel-cell and for water splitting operation in the presence of sacrificial agents. Chem Eng J 254:245–251. https://doi.org/10.1016/j.cej.2014.05.106

Antony RP, Bassi PS, Abdi FF, Chiam SY, Ren Y, Barber J, Loo JSC, Wong LH (2016) Electrospun Mo-$BiVO_4$ for efficient photoelectrochemical water oxidation: Direct evidence of improved hole diffusion length and charge separation. Electrochim Acta 211:173–182. https://doi.org/10.1016/j.electacta.2016.06.008

Arabatzis IM, Stergiopoulos T, Andreeva D, Kitova S, Neophytides SG, Falaras P (2003) Characterization and photocatalytic activity of Au/TiO_2 thin films for azo-dye degradation. J Catal 220:127–135. https://doi.org/10.1016/S0021-9517(03)00241-0

Azevedo J, Tilley SD, Schreier M, Stefik M, Sousa C, Araújo JP, Mendes A, Grätzel M, Mayer MT (2016) Tin oxide as stable protective layer for composite cuprous oxide water-splitting photocathodes. Nano Energy 24:10–16. https://doi.org/10.1016/j.nanoen.2016.03.022

Bahnemann W, Muneer M, Haque MM (2007) Titanium dioxide-mediated photocatalysed degradation of few selected organic pollutants in aqueous suspensions. Catal Today 124:133–148. https://doi.org/10.1016/j.cattod.2007.03.031

Bai J, Wang R, Li Y, Tang Y, Zeng Q, Xia L, Li X, Li J, Li C, Zhou B (2016) A solar light driven dual photoelectrode photocatalytic fuel cell (PFC) for simultaneous wastewater treatment and electricity generation. J Hazard Mater 311:51–62. https://doi.org/10.1016/j.jhazmat.2016.02.052

Bak T, Nowotny J, Rekas M, Sorrell CC (2002) Photo-electrochemical hydrogen generation from water using solar energy. Materials-related aspects. Int J Hydrog Energy 27:991–1022. https://doi.org/10.1016/S0360-3199(02)00022-8

Banerjee J, Dutta K (2017) Materials for electrodes of Li-ion batteries: issues related to stress development. Crit Rev Solid State Mater Sci 42:218–238. https://doi.org/10.1080/10408436.2016.1173011

Bard AJ, Faulkner LR (2001) Electrochemical methods: fundamentals and applications, 2nd edn. Wiley, New York

Bashiri R, Mohamed NM, Kait CF, Sufian S, Kakooei S, Khatani M, Gholami Z (2016) Optimization hydrogen production over visible light-driven titania-supported bimetallic photocatalyst from water photosplitting in tandem photoelectrochemical cell. Renew Energy 99:960–970. https://doi.org/10.1016/j.renene.2016.07.079

Borganello E, Kiwi J, Gratzel M, Pelizzetti E, Visca M (1982) Visible light induced water cleavage in colloidal solutions of chromium-doped titanium dioxide particles. J Am Chem Soc 104:2996–3002. https://doi.org/10.1021/ja00375a010

Borman S (1991) Photoelectrochemical cells: energy source for the future? Chem Eng News 69:17–25. https://doi.org/10.1021/cen-v069n029.p017

Brillet J, Cornuz M, Le Formal F, Yum J-H, Grätzel M, Sivula K (2010) Examining architectures of photoanode-photovoltaic tandem cells for solar water splitting. J Mater Res 25:17–24. https://doi.org/10.1557/JMR.2010.0009

Buehler N, Meier K, Reber JF (1984) Photochemical hydrogen production with cadmium sulfide suspensions. J Phys Chem 88:3261–3268. https://doi.org/10.1021/j150659a025

Canterino M, Di Somma I, Marotta R, Andreozzi R, Caprio V (2009) Energy recovery in wastewater decontamination: simultaneous photocatalytic oxidation of an organic substrate and electricity generation. Water Res 43:2710–2716. https://doi.org/10.1016/j.watres.2009.03.012

Chen Y, Feng X, Liu M, Su J, Shen S (2016) Towards efficient solar-to-hydrogen conversion: fundamentals and recent progress in copper-based chalcogenide photocathodes. Nano 5:524–547. https://doi.org/10.1515/nanoph-2016-0027

Chojnowski F, Clechet P, Martin J-R, Herrmann J-M, Pichat P (1981) Hydrogen production by water photoelectrolysis with a powder semiconductor anode. Chem Phys Lett 84:555–559. https://doi.org/10.1016/0009-2614(81)80407-1

Coronado JM, Zorn ME, Tejedor-Tejedor I, Anderson MA (2003) Photocatalytic oxidation of ketones in the gas phase over TiO_2 thin films: a kinetic study on the influence of water vapor. Appl Catal B Environ 43:329–344. https://doi.org/10.1016/S0926-3373(03)00022-5

Das S, Dutta K, Shul YG, Kundu PP (2015) Progress in developments of inorganic nanocatalysts for application in direct methanol fuel cells. Crit Rev Solid State Mater Sci 40:316–357. https://doi.org/10.1080/10408436.2015.1030493

Das S, Dutta K, Kundu PP (2016) Sulfonated polypyrrole matrix induced enhanced efficiency of Ni nanocatalyst for application as an anode material for DMFCs. Mater Chem Phys 176:143–151. https://doi.org/10.1016/j.matchemphys.2016.03.046

Das S, Dutta K, Rana D (2018) Polymer electrolyte membranes for microbial fuel cells: a review. Polym Rev. 58:610–629. https://doi.org/10.1080/15583724.2017.1418377

Dhiman P, Naushad M, Batoo KM et al (2017) Nano FexZn1−xO as a tuneable and efficient photocatalyst for solar powered degradation of bisphenol A from aqueous environment. J Clean Prod 165:1542–1556. https://doi.org/10.1016/j.jclepro.2017.07.245

Di Paola A, Marci G, Palmisano L, Sciavello M, Uosaki K, Ikeda S, Ohtani B (2002) Preparation of polycrystalline TiO_2 photocatalysts impregnated with various transition metal ions:

characterization and photocatalytic activity for the degradation of 4-nitrophenol. J Phys Chem B 106:637–645. https://doi.org/10.1021/jp013074l

Dou B, Song Y, Wang C, Chen H, Xu Y (2014) Hydrogen production from catalytic steam reforming of biodiesel byproduct glycerol: issues and challenges. Renew Sust Energ Rev 30:950–960. https://doi.org/10.1016/j.rser.2013.11.029

Dozzi MV, Marzorati S, Longhi M, Coduri M, Artiglia L, Selli E (2016) Photocatalytic activity of TiO_2-WO_3 mixed oxides in relation to electron transfer efficiency. Appl Catal B Environ 186:157–165. https://doi.org/10.1016/j.apcatb.2016.01.004

Dutta K (2017) Polymer-inorganic nanocomposites for polymer electrolyte membrane fuel cells. In: Lin Z, Yang Y, Zhang A (eds) Polymer-engineered nanostructures for advanced energy applications, Ch. 15. Springer, Cham, pp 577–606. https://doi.org/10.1007/978-3-319-57003-7_15

Dutta K, Kundu PP (2014) A review on aromatic conducting polymers-based catalyst supporting matrices for application in microbial fuel cells. Polym Rev 54:401–435. https://doi.org/10.1080/15583724.2014.881372

Dutta K, Kundu PP (2018) Introduction to microbial fuel cells. In: Kundu PP, Dutta K (eds) Progress and recent trends in microbial fuel cells, Ch. 1. Elsevier, Amsterdam, pp 1–6. https://doi.org/10.1016/B978-0-444-64017-8.00001-4

Dutta K, Kundu PP, Kundu A (2014) Fuel cells – exploratory fuel cells | micro-fuel cells. In: Reedijk J (ed) Reference module in chemistry, molecular sciences and chemical engineering. Elsevier, Amsterdam. https://doi.org/10.1016/B978-0-12-409547-2.10975-8

Dutta K, Das S, Kundu PP (2015a) Synthesis, preparation, and performance of blends and composites of π-conjugated polymers and their copolymers in DMFCs. Polym Rev 55:630–677. https://doi.org/10.1080/15583724.2015.1028631

Dutta K, Das S, Rana D, Kundu PP (2015b) Enhancements of catalyst distribution and functioning upon utilization of conducting polymers as supporting matrices in DMFCs: A review. Polym Rev 55:1–56. https://doi.org/10.1080/15583724.2014.958771

Dutta K, Rana D, Han HS, Kundu PP (2017) Unitized regenerative fuel cells: a review on developed catalyst systems and bipolar plates. Fuel Cells 17:736–751. https://doi.org/10.1002/fuce.201700018

Esposito DV, Forest RV, Chang Y, Gaillard N, McCandless BE, Hou S, Lee KH, Birkmire RW, Chen JG (2012) Photoelectrochemical reforming of glucose for hydrogen production using a WO_3-based tandem cell device. Energy Environ Sci 5:9091–9099. https://doi.org/10.1039/C2EE22560C

Fox MA, Dulay MT (1993) Heterogeneous photocatalysis. Chem Rev 93:341–357. https://doi.org/10.1021/cr00017a016

Fujishima A, Honda K (1972) Electrochemical photolysis of water at a semiconductor electrode. Nature 238:37–38. https://doi.org/10.1038/238037a0

Fujishima A, Rao TN, Tryk DA (2000) Titanium dioxide photocatalysis. J Photochem Photobiol C: Photochem Rev 1:1–21. https://doi.org/10.1016/S1389-5567(00)00002-2

Fujishima A, Zhang X, Tryk DA (2008) TiO_2 photocatalysis and related surface phenomena. Surf Sci Rep 63:515–582. https://doi.org/10.1016/j.surfrep.2008.10.001

Gan J, Lu X, Tong Y (2014) Towards highly efficient photoanodes: boosting sunlight-driven semiconductor nanomaterials for water oxidation. Nanoscale 6:7142–7164. https://doi.org/10.1039/C4NR01181C

Gao B, Peng C, Chen GZ, Puma GL (2008) Photo-electro-catalysis enhancement on carbon nanotubes/titanium dioxide (CNTs/TiO_2) composite prepared by a novel surfactant wrapping sol-gel method. Appl Catal B Environ 85:17–23. https://doi.org/10.1016/j.apcatb.2008.06.027

Gao B, Chen GZ, Puma GL (2009) Carbon nanotubes/titanium oxide (CNTs/TiO_2) nanocomposites prepared by conventional and novel surfactant wrapping sol-gel methods exhibiting enhanced photocatalytic activity. Appl Catal B Environ 89:503–509. https://doi.org/10.1016/j.apcatb.2009.01.009

Getoff N (1990) Photoelectrochemical and photocatalytic methods of hydrogen production: a short review. Int J Hydrog Energy 15:407–417. https://doi.org/10.1016/0360-3199(90)90198-8

Guillard C, Beaugiraud B, Dutriez C, Herrmann J-M, Jaffrezic H, Jaffrezic-Renault N, Lacroix M (2002) Physicochemical properties and photocatalytic activities of TiO_2-films prepared by sol-gel methods. Appl Catal B Environ 39:331–342. https://doi.org/10.1016/S0926-3373(02)00120-0

Hagfeldt A, Graetzel M (1995) Light-induced redox reactions in nanocrystalline systems. Chem Rev 95:49–68. https://doi.org/10.1021/cr00033a003

Herrmann J-M, Disdier J, Pichat P (1984) Effect of chromium doping on the electrical and catalytic properties of powder titania under UV and visible illumination. Chem Phys Lett 108:618–622. https://doi.org/10.1016/0009-2614(84)85067-8

Hodes G, Manassen J, Cahen D (1977) Photo-electrochemical energy conversion: electrocatalytic sulphur electrodes. J Appl Electrochem 7:181–182. https://doi.org/10.1007/BF00611041

Hodes G, Manassen J, Cahen D (1980) Electrocatalytic electrodes for the polysulfide redox system. J Electrochem Soc 127:544–549. https://doi.org/10.1149/1.2129709

Hoffmann MR, Martin ST, Choi W, Bahnemann DW (1995) Environmental applications of semiconductor photocatalysis. Chem Rev 95:69–96. https://doi.org/10.1021/cr00033a004

Horiuchi Y, Toyao T, Takeuchi M, Matsuoka M, Anpo M (2013) Recent advances in visible-light-responsive photocatalysts for hydrogen production and solar energy conversion – from semiconducting TiO_2 to MOF/PCP photocatalysts. Phys Chem Chem Phys 15:13243–13253. https://doi.org/10.1039/C3CP51427G

Hu C, Kelm D, Schreiner M, Wollborn T, Mädler L, Teoh WY (2015) Designing photoelectrodes for photocatalytic fuel cells and elucidating the effects of organic substrates. ChemSusChem 8:4005–4015. https://doi.org/10.1002/cssc.201500793

Iwu KO, Galeckas A, Kuznetsov AY, Norby T (2013) Solid-state photoelectrochemical H_2 generation with gaseous reactants. Electrochim Acta 97:320–325. https://doi.org/10.1016/j.electacta.2013.03.013

Jia Q, Iwashina K, Kudo A (2012) Facile fabrication of an efficient $BiVO_4$ thin film electrode for water splitting under visible light irradiation. Proc Natl Acad Sci U S A 109:11564–11569. https://doi.org/10.1073/pnas.1204623109

Kalamaras E, Lianos P (2015) Current doubling effect revisited: current multiplication in a photofuelcell. J Electroanal Chem 751:37–42. https://doi.org/10.1016/j.jelechem.2015.05.029

Kalamaras E, Dracopoulos V, Sygellou L, Lianos P (2016) Electrodeposited Ti-doped hematite photoanodes and their employment for photoelectrocatalytic hydrogen production in the presence of ethanol. Chem Eng J 295:288–294. https://doi.org/10.1016/j.cej.2016.03.062

Kamat PV (2007) Meeting the clean energy demand: nanostructure architectures for solar energy conversion. J Phys Chem C 111:2834–2860. https://doi.org/10.1021/jp066952u

Kaneko M, Nemoto J, Ueno H, Gokan N, Ohnuki K, Horikawa M, Saito R, Shibata T (2006) Photoelectrochemical reaction of biomass and bio-related compounds with nanoporous TiO_2 film photoanode and O_2-reducing cathode. Electrochem Commun 8:336–340. https://doi.org/10.1016/j.elecom.2005.12.004

Kaneko M, Ueno H, Saito R, Nemoto J (2009a) Highly efficient photoelectrocatalytic decomposition of biomass compounds using a nanoporous semiconductor photoanode and an O_2-reducing cathode with quantum efficiency over 100. Catal Lett 131:184–188. https://doi.org/10.1007/s10562-009-0011-2

Kaneko M, Ueno H, Saito R, Suzuki S, Nemoto J, Fujii Y (2009b) Biophotochemical cell (BPCC) to photodecompose biomass and bio-related compounds by UV irradiation with simultaneous electrical power generation. J Photochem Photobiol A Chem 205:168–172. https://doi.org/10.1016/j.jphotochem.2009.04.024

Karakitsou KE, Verykios XE (1993) Effects of altervalent cation doping of titania on its performance as a photocatalyst for water cleavage. J Phys Chem 97:1184–1189. https://doi.org/10.1021/j100108a014

Kawai T, Sakata T (1980) Photocatalytic decomposition of gaseous water over TiO_2 and TiO_2-RuO_2 surfaces. Chem Phys Lett 72:87–89. https://doi.org/10.1016/0009-2614(80)80247-8

Khalik WF, Ong S-A, Ho L-N, Wong Y-S, Voon C-H, Yusuf SY, Yusoff NA, Lee S-L (2016) Influence of supporting electrolyte in electricity generation and degradation of organic pollutants in photocatalytic fuel cell. Environ Sci Pollut Res 23:16716–16721. https://doi.org/10.1007/s11356-016-6840-9

Khan SUM, Al-Shahry M, Ingler WB Jr (2002) Efficient photochemical water splitting by a chemically modified n-TiO_2. Science 297:2243–2245. https://doi.org/10.1126/science.1075035

Kibsgaard J, Jaramillo TF (2014) Molybdenum phosphosulfide: an active, acid-stable, earth-abundant catalyst for the hydrogen evolution reaction. Angew Chem Int Ed 53:14433–14437. https://doi.org/10.1002/anie.201408222

Kim DH, Anderson MA (1994) Photoelectrocatalytic degradation of formic acid using a porous titanium dioxide thin-film electrode. Environ Sci Technol 28:479–483. https://doi.org/10.1021/es00052a021

Kim TW, Choi K-S (2014) Nanoporous $BiVO_4$ photoanodes with dual-layer oxygen evolution catalysts for solar water splitting. Science 343:990–994. https://doi.org/10.1126/science.1246913

Kim T-H, Saito M, Matsuoka M, Tsukada S, Wada K, Anpo M (2009) Photocatalytic oxidation of ethanethiol on a photoelectrochemical circuit system consisting of a rod-type TiO_2 electrode and a silicon solar cell. Res Chem Intermed 35:633–642. https://doi.org/10.1007/s11164-009-0060-6

Konstantinou IK, Albanis TA (2004) TiO_2-assisted photocatalytic degradation of azo dyes in aqueous solution: Kinetic and mechanistic investigations: a review. Appl Catal B Environ 49:1–14. https://doi.org/10.1016/j.apcatb.2003.11.010

Kumagai H, Minegishi T, Sato N, Yamada T, Kubota J, Domen K (2015) Efficient solar hydrogen production from neutral electrolytes using surface-modified Cu(In,Ga)Se_2 photocathodes. J Mater Chem A 3:8300–8307. https://doi.org/10.1039/C5TA01058F

Kumar P, Dutta K, Kundu PP (2014a) Enhanced performance of direct methanol fuel cells: a study on the combined effect of various supporting electrolytes, flow channel designs and operating temperatures. Int J Energy Res 38:41–50. https://doi.org/10.1002/er.3034

Kumar P, Dutta K, Das S, Kundu PP (2014b) An overview of unsolved deficiencies of direct methanol fuel cell technology: factors and parameters affecting its widespread use. Int J Energy Res 38:1367–1390. https://doi.org/10.1002/er.3163

Kumar A, Kumar A, Sharma G et al (2018) Biochar-templated g-C3N4/Bi2O2CO3/CoFe2O4 nano-assembly for visible and solar assisted photo-degradation of paraquat, nitrophenol reduction and CO2 conversion. Chem Eng J 339:393–410. https://doi.org/10.1016/j.cej.2018.01.105

Kundu PP, Dutta K (2016) Hydrogen fuel cells for portable applications. In: Ball M, Basile A, Veziroglu TN (eds) Compendium of hydrogen energy, Vol. 4. Hydrogen use, safety and the hydrogen economy, Woodhead Publishing Series in Energy # 86, Ch. 6. Elsevier, Amsterdam, pp 111–131. https://doi.org/10.1016/B978-1-78242-364-5.00006-3

Kundu PP, Dutta K (2018) Progress and recent trends in microbial fuel cells, 1st edn. Elsevier, Dordrecht. https://doi.org/10.1016/C2016-0-04695-8

Latibari ST, Sadrameli SM (2018) Carbon based material included-shaped stabilized phase change materials for sunlight-driven energy conversion and storage: an extensive review. Sol Energy 170:1130–1161. https://doi.org/10.1016/j.solener.2018.05.007

Lee S-L, Ho L-N, Ong S-A, Lee G-M, Wong Y-S, Voon C-H, Khalik WF, Yusoff NA, Nordin N (2016) Comparative study of photocatalytic fuel cell for degradation of methylene blue under sunlight and ultra-violet light irradiation. Water Air Soil Pollut 227(1–8):445. https://doi.org/10.1007/s11270-016-3148-9

Lee S-L, Ho L-N, Ong S-A, Wong Y-S, Voon C-H, Khalik WF, Yusoff NA, Nordin N (2017) A highly efficient immobilized ZnO/Zn photoanode for degradation of azo dye reactive green 19 in a photocatalytic fuel cell. Chemosphere 166:118–125. https://doi.org/10.1016/j.chemosphere.2016.09.082

Li Z, Luo W, Zhang M, Feng J, Zou Z (2013) Photoelectrochemical cells for solar hydrogen production: current state of promising photoelectrodes, methods to improve their properties, and outlook. Energy Environ Sci 6:347–370. https://doi.org/10.1039/C2EE22618A

Li X, Wang G, Jing L, Ni W, Yan H, Chen C, Yan Y-M (2016a) A photoelectrochemical methanol fuel cell based on aligned TiO_2 nanorods decorated graphene photoanode. Chem Commun 52:2533–2536. https://doi.org/10.1039/C5CC09929C

Li H, Li F, Wang Y, Bai L, Yu F, Sun L (2016b) Visible-light-driven water oxidation on a photoanode by supramolecular assembly of photosensitizer and catalyst. ChemPlusChem 81:1056–1059. https://doi.org/10.1002/cplu.201500539

Li C, Hisatomi T, Watanabe O, Nakabayashi M, Shibata N, Domen K, Delaunay J-J (2016c) Simultaneous enhancement of photovoltage and charge transfer in Cu_2O-based photocathode using buffer and protective layers. Appl Phys Lett 109(1–5):033902. https://doi.org/10.1063/1.4959098

Liang X, Liu J, Zeng D, Li C, Chen S, Li H (2016) Hydrogen generation promoted by photocatalytic oxidation of ascorbate and glucose at a cadmium sulfide electrode. Electrochim Acta 198:40–48. https://doi.org/10.1016/j.electacta.2016.03.023

Lianos P (2011) Production of electricity and hydrogen by photocatalytic degradation of organic wastes in a photoelectrochemical cell: the concept of the photofuelcell: a review of a re-emerging research field. J Hazard Mater 185:575–590. https://doi.org/10.1016/j.jhazmat.2010.10.083

Lianos P (2017) Review of recent trends in photoelectrocatalytic conversion of solar energy to electricity and hydrogen. Appl Catal B Environ 210:235–254. https://doi.org/10.1016/j.apcatb.2017.03.067

Licht S, Hodes G, Tenne R, Manassen J (1987) A light-variation insensitive high efficiency solar cell. Nature 326:863–864. https://doi.org/10.1038/326863a0

Lim Y-F, Chua CS, Lee CJJ, Chi D (2014) Sol-gel deposited Cu_2O and CuO thin films for photocatalytic water splitting. Phys Chem Chem Phys 16:25928–25934. https://doi.org/10.1039/C4CP03241A

Lin Y, Yuan G, Liu R, Zhou S, Sheehan SW, Wang D (2011) Semiconductor nanostructure-based photoelectrochemical water splitting: a brief review. Chem Phys Lett 507:209–215. https://doi.org/10.1016/j.cplett.2011.03.074

Lin C-Y, Mersch D, Jefferson DA, Reisner E (2014) Cobalt sulphide microtube array as cathode in photoelectrochemical water splitting with photoanodes. Chem Sci 5:4906–4913. https://doi.org/10.1039/C4SC01811G

Linsebigler AL, Lu G, Yates JT (1995) Photocatalysis on TiO_2 surfaces: principles, mechanisms, and selected results. Chem Rev 95:735–758. https://doi.org/10.1021/cr00035a013

Liu H, Cheng S, Wu M, Wu H, Zhang J, Li W, Cao C (2000) Photoelectrocatalytic degradation of sulfosalicylic acid and its electrochemical impedance spectroscopy investigation. J Phys Chem A 104:7016–7020. https://doi.org/10.1021/jp000171q

Liu X, Wang F, Wang Q (2012) Nanostructure-based WO_3 photoanodes for photoelectrochemical water splitting. Phys Chem Chem Phys 14:7894–7911. https://doi.org/10.1039/C2CP40976C

Liu C, Dasgupta NP, Yang P (2014) Semiconductor nanowires for artificial photosynthesis. Chem Mater 26:415–422. https://doi.org/10.1021/cm4023198

Liu Y, Liu L, Yang F (2016) Energy-efficient degradation of rhodamine B in a LED illuminated photocatalytic fuel cell with anodic Ag/AgCl/GO and cathodic $ZnIn_2S_4$ catalysts. RSC Adv 6:12068–12075. https://doi.org/10.1039/C5RA25557K

Luo J, Hepel M (2001) Photoelectrochemical degradation of naphthol blue black diazo dye on WO_3 film electrode. Electrochim Acta 46:2913–2922. https://doi.org/10.1016/S0013-4686(01)00503-5

Maeda Y, Fujishima A, Honda K (1981) The investigation of current doubling reactions on semiconductor photoelectrodes by temperature change measurements. J Electrochem Soc 128:1731–1734. https://doi.org/10.1149/1.2127720

Matthews RW (1988) An adsorption water purifier with *in situ* photocatalytic regeneration. J Catal 113:549–555. https://doi.org/10.1016/0021-9517(88)90283-7

Michal R, Sfaelou S, Lianos P (2014) Photocatalysis for renewable energy production using photofuelcells. Molecules 19:19732–19750. https://doi.org/10.3390/molecules191219732

Miller EL, Rocheleau RE, Deng XM (2003) Design considerations for a hybrid amorphous silicon/photoelectrochemical multijunction cell for hydrogen production. Int J Hydrog Energy 28:615–623. https://doi.org/10.1016/S0360-3199(02)00144-1

Minguez-Bacho I, Courté M, Fan HJ, Fichou D (2015) Conformal Cu_2S-coated Cu_2O nanostructures grown by ion exchange reaction and their photoelectrochemical properties. Nanotechnology 26(1–10):185401. https://doi.org/10.1088/0957-4484/26/18/185401

Mirbagheri N, Wang D, Peng C, Wang J, Huang Q, Fan C, Ferapontova EE (2014) Visible light driven photoelectrochemical water oxidation by Zn- and Ti-doped hematite nanostructures. ACS Catal 4:2006–2015. https://doi.org/10.1021/cs500372v

Mishra M, Chun D-M (2015) α-Fe_2O_3 as a photocatalytic material: a review. Appl Catal A: General 498:126–141. https://doi.org/10.1016/j.apcata.2015.03.023

Monfort O, Pop L-C, Sfaelou S, Plecenik T, Roch T, Dracopoulos V, Stathatos E, Plesch G, Lianos P (2016) Photoelectrocatalytic hydrogen production by water splitting using $BiVO_4$ photoanodes. Chem Eng J 286:91–97. https://doi.org/10.1016/j.cej.2015.10.043

Monfort O, Sfaelou S, Satrapinskyy L, Plecenik T, Roch T, Plesch G, Lianos P (2017) Comparative study between pristine and Nb-modified $BiVO_4$ films employed for photoelectrocatalytic production of H_2 by water splitting and for photocatalytic degradation of organic pollutants under simulated solar light. Catal Today 280:51–57. https://doi.org/10.1016/j.cattod.2016.07.006

Mrowetz M, Balcerski W, Colussi AJ, Hoffmann MR (2004) Oxidative Power of nitrogen-doped TiO_2 photocatalysts under visible illumination. J Phys Chem B 108:17269–17273. https://doi.org/10.1021/jp0467090

Nakade S, Saito Y, Kubo W, Kanzaki T, Kitamura T, Wada Y, Yanagida S (2003) Enhancement of electron transport in nano-porous TiO_2 electrodes by dye adsorption. Electrochem Commun 5:804–808. https://doi.org/10.1016/j.elecom.2003.07.008

Nandy A, Kumar V, Mondal S, Dutta K, Salah M, Kundu PP (2015) Performance evaluation of microbial fuel cells: effect of varying electrode configuration and presence of a membrane electrode assembly. New Biotechnol 32:272–281. https://doi.org/10.1016/j.nbt.2014.11.003

Negishi N, Takeuchi K, Ibusuki T (1998) Surface structure of the TiO_2 thin film photocatalyst. J Mater Sci 33:5789–5794. https://doi.org/10.1023/A:1004441829285

Nicolau YF (1985) Solution deposition of thin solid compound films by successive ionic-layer adsorption and reaction process. Appl Surf Sci 22-23:1061–1074. https://doi.org/10.1016/0378-5963(85)90241-7

Ning F, Shao M, Xu S, Fu Y, Zhang R, Wei M, Evans DG, Duan X (2016) TiO_2/graphene/NiFe-layered double hydroxide nanorod array photoanodes for efficient photoelectrochemical water splitting. Energy Environ Sci 9:2633–2643. https://doi.org/10.1039/C6EE01092J

Nosaka Y, Fox MA (1988) Kinetics for electron transfer from laser-pulse irradiated colloidal semiconductors to adsorbed methylviologen: dependence of the quantum yield on incident pulse width. J Phys Chem 92:1893–1897. https://doi.org/10.1021/j100318a039

Nouri E, Mohammadi MR, Lianos P (2016) Impact of preparation method of TiO_2-RGO nanocomposite photoanodes on the performance of dye-sensitized solar cells. Electrochim Acta 219:38–48. https://doi.org/10.1016/j.electacta.2016.09.150

Nowotny J, Sorrell CC, Sheppard LR, Bak T (2005) Solar-hydrogen: environmentally safe fuel for the future. Int J Hydrog Energy 30:521–544. https://doi.org/10.1016/j.ijhydene.2004.06.012

O'Regan B, Grätzel M (1991) A low-cost, high-efficiency solar cell based on dye-sensitized colloidal TiO_2 films. Nature 353:737–740. https://doi.org/10.1038/353737a0

O'Regan B, Moser J, Anderson M, Graetzel M (1990) Vectorial electron injection into transparent semiconductor membranes and electric field effects on the dynamics of light-induced charge separation. J Phys Chem 94:8720–8726. https://doi.org/10.1021/j100387a017

Ohtani B, Iwai K, Nishimoto S-i, Sato S (1997) Role of platinum deposits on titanium(IV) oxide particles: structural and kinetic analyses of photocatalytic reaction in aqueous alcohol and amino acid solutions. J Phys Chem B 101:3349–3359. https://doi.org/10.1021/jp962060q

Panagiotopoulou P, Antoniadou M, Kondarides DI, Lianos P (2010) Aldol condensation products during photocatalytic oxidation of ethanol in a photoelectrochemical cell. Appl Catal B Environ 100:124–132. https://doi.org/10.1016/j.apcatb.2010.07.021

Paracchino A, Laporte V, Sivula K, Grätzel M, Thimsen E (2011) Highly active oxide photocathode for photoelectrochemical water reduction. Nat Mater 10:456–461. https://doi.org/10.1038/nmat3017

Park JH, Kim S, Bard AJ (2006) Novel carbon-doped TiO_2 nanotube arrays with high aspect ratios for efficient solar water splitting. Nano Lett 6:24–28. https://doi.org/10.1021/nl051807y

Patsoura A, Kondarides DI, Verykios XE (2006) Enhancement of photoinduced hydrogen production from irradiated Pt/TiO_2 suspensions with simultaneous degradation of azo-dyes. Appl Catal B Environ 64:171–179. https://doi.org/10.1016/j.apcatb.2005.11.015

Pelentridou K, Stathatos E, Karasali H, Lianos P (2009) Photodegradation of the herbicide azimsulfuron using nanocrystalline titania films as photocatalyst and low intensity black light radiation or simulated solar radiation as excitation source. J Hazard Mater 163:756–760. https://doi.org/10.1016/j.jhazmat.2008.07.023

Phuan YW, Chong MN, Zhu T, Yong S-T, Chan ES (2015) Effects of annealing temperature on the physicochemical, optical and photoelectrochemical properties of nanostructured hematite thin films prepared via electrodeposition method. Mater Res Bull 69:71–77. https://doi.org/10.1016/j.materresbull.2014.12.059

Potočnik J (2007) Renewable energy sources and the realities of setting an energy agenda. Science 315:810–811. https://doi.org/10.1126/science.1139086

Quiñonero J, Lana-Villarreal T, Gómez R (2016) Improving the photoactivity of bismuth vanadate thin film photoanodes through doping and surface modification strategies. Appl Catal B Environ 194:141–149. https://doi.org/10.1016/j.apcatb.2016.04.057

Rahman G, Joo O-S (2013) Electrodeposited nanostructured α-Fe_2O_3 thin films for solar water splitting: Influence of Pt doping on photoelectrochemical performance. Mater Chem Phys 140:316–322. https://doi.org/10.1016/j.matchemphys.2013.03.042

Ren K, Gan YX (2012) In: Lallart M (ed) Advances in photoelectrochemical fuel cell research in small-scale energy harvesting. Intech Open, London, pp 3–26. https://doi.org/10.5772/50799

Rühl C, Appleby P, Fennema J, Naumov A, Schaffer M (2012) Economic development and the demand for energy: a historical perspective on the next 20 years. Energy Policy 50:109–116. https://doi.org/10.1016/j.enpol.2012.07.039

Sahoo SK (2016) Renewable and sustainable energy reviews solar photovoltaic energy progress in India: a review. Renew Sust Energy Rev 59:927–939. https://doi.org/10.1016/j.rser.2016.01.049

Salvdor P (1984) Hole diffusion length in *n*-TiO_2 single crystals and sintered electrodes: photoelectrochemical determination and comparative analysis. J Appl Phys 55:2977–2985. https://doi.org/10.1063/1.333358

Sayama K, Nomura A, Zou Z, Abe R, Abe Y, Arakawa H (2003) Photoelectrochemical decomposition of water on nanocrystalline $BiVO_4$ film electrodes under visible light. Chem Commun:2908–2909. https://doi.org/10.1039/B310428A

Sclafani A, Herrmann J-M (1998) Influence of metallic silver and of platinum-silver bimetallic deposits on the photocatalytic activity of titania (anatase and rutile) in organic and aqueous media. J Photochem Photobiol A Chem 113:181–188. https://doi.org/10.1016/S1010-6030(97)00319-5

Seger B, Lu GQ, Wang L (2012) Electrical power and hydrogen production from a photo-fuel cell using formic acid and other single-carbon organics. J Mater Chem 22:10709–10715. https://doi.org/10.1039/C2JM16635F

Selli E, Chiarello GL, Quartarone E, Mustarelli P, Rossetti I, Forni L (2007) A photocatalytic water splitting device for separate hydrogen and oxygen evolution. Chem Commun:5022–5024. https://doi.org/10.1039/B711747G

Sfaelou S, Lianos P (2016) Photoactivated fuel cells (photofuel cells). An alternative source of renewable energy with environmental benefits. AIMS Mater Sci 3:270–288. https://doi.org/10.3934/matersci.2016.1.270

Sfaelou S, Sygellou L, Dracopoulos V, Travlos A, Lianos P (2014) Effect of the nature of cadmium salts on the effectiveness of CdS SILAR deposition and its consequences on the performance of sensitized solar cells. J Phys Chem C 118:22873–22880. https://doi.org/10.1021/jp505787z

Sfaelou S, Zhuang X, Feng X, Lianos P (2015) Sulfur-doped porous carbon nanosheets as high performance electrocatalysts for photofuel cells. RSC Adv 5:27953–27963. https://doi.org/10.1039/C5RA02027A

Sfaelou S, Pop L-C, Monfort O, Dracopoulos V, Lianos P (2016) Mesoporous WO_3 photoanodes for hydrogen production by water splitting and photofuel cell operation. Int J Hydrog Energy 41:5902–5907. https://doi.org/10.1016/j.ijhydene.2016.02.063

Sharma G, Bhogal S, Naushad M et al (2017) Microwave assisted fabrication of La/Cu/Zr/carbon dots trimetallic nanocomposites with their adsorptional vs photocatalytic efficiency for remediation of persistent organic pollutants. J Photochem Photobiol A Chem 347:235–243. https://doi.org/10.1016/j.jphotochem.2017.07.001

Sharon M (2007) In: Licht S (ed) The photoelectrochemistry of semiconductor/electrolyte solar cells in encyclopedia of electrochemistry: Vol. 6 Semiconductor electrodes and photoelectrochemistry. Wiley, New York, pp 287–316

Shi Z, Wen X, Guan Z, Cao D, Luo W, Zou Z (2015a) Recent progress in photoelectrochemical water splitting for solar hydrogen production. Ann Phys 358:236–247. https://doi.org/10.1016/j.aop.2015.04.005

Shi W, Zhang X, Li S, Zhang B, Wang M, Shen Y (2015b) Carbon coated Cu_2O nanowires for photo-electrochemical water splitting with enhanced activity. Appl Surf Sci 358:404–411. https://doi.org/10.1016/j.apsusc.2015.08.223

Sivula K, Le Formal F, Grätzel M (2011) Solar water splitting: progress using hematite (α-Fe_2O_3) photoelectrodes. ChemSusChem 4:432–439. https://doi.org/10.1002/cssc.201000416

Stoll T, Zafeiropoulos G, Tsampas MN (2016) Solar fuel production in a novel polymeric electrolyte membrane photoelectrochemical (PEM-PEC) cell with a web of titania nanotube arrays as photoanode and gaseous reactants. Int J Hydrog Energy 41:17807–17817. https://doi.org/10.1016/j.ijhydene.2016.07.230

Sudhagar P, Herraiz-Cardona I, Park H, Song T, Noh SH, Gimenez S, Sero IM, Fabregat-Santiago-F, Bisquert J, Terashima C, Paik U, Kang YS, Fujishima A, Han TH (2016) Exploring graphene quantum dots/TiO_2 interface in photoelectrochemical reactions: solar to fuel conversion. Electrochim Acta 187:249–255. https://doi.org/10.1016/j.electacta.2015.11.048

Sui M, Dong Y, You H (2015) Enhanced photocatalytic activity for the degradation of rhodamine B by integrating salinity gradient power into a photocatalytic fuel cell. RSC Adv 5:94184–94190. https://doi.org/10.1039/C5RA20093H

Sun C-C, Chou T-C (1998) Kinetics and mechanism of photoelectrochemical oxidation of nitrite ion by using the rutile form of a TiO_2/Ti photoelectrode with high electric field enhancement. Ind Eng Chem Res 37:4207–4214. https://doi.org/10.1021/ie980222u

Sun C-C, Chou T-C (2000) Electrochemically promoted photocatalytic oxidation of nitrite ion by using rutile form of TiO_2/Ti electrode. J Mol Catal A Chem 151:133–145. https://doi.org/10.1016/S1381-1169(99)00260-5

Tantis I, Stathatos E, Mantzavinos D, Lianos P (2015) Photoelectrocatalytic degradation of potential water pollutants in the presence of NaCl using nanocrystalline titania films. J Chem Technol Biotechnol 90:1338–1344. https://doi.org/10.1002/jctb.4549

Tantis I, Dozzi MV, Bettini LG, Chiarello GL, Dracopoulos V, Selli E, Lianos P (2016) Highly functional titania nanoparticles produced by flame spray pyrolysis. Photoelectrochemical and solar cell applications. Appl Catal B Environ 182:369–374. https://doi.org/10.1016/j.apcatb.2015.09.040

Tode R, Ebrahimi A, Fukumoto S, Iyatani K, Takeuchi M, Matsuoka M, Lee CH, Jiang C-S, Anpo M (2010) Photocatalytic decomposition of water on double-layered visible light-responsive TiO_2 thin films prepared by a magnetron sputtering deposition method. Catal Lett 135:10–15. https://doi.org/10.1007/s10562-010-0262-y

Tollefson J, Monastersky R (2012) The global energy challenge: Awash with carbon. Nature 491:654–655. https://doi.org/10.1038/491654a

Ueno H, Nemoto J, Ohnuki K, Horikawa M, Hoshino M, Kaneko M (2009) Photoelectrochemical reaction of biomass-related compounds in a biophotochemical cell comprising a nanoporous TiO_2 film photoanode and an O_2-reducing cathode. J Appl Electrochem 39:1897–1905. https://doi.org/10.1007/s10800-009-9897-z

Vinodgopal K, Wynkoop DE, Kamat PV (1996) Environmental photochemistry on semiconductor surfaces: Photosensitized degradation of a textile azo dye, acid orange 7, on TiO_2 particles using visible light. Environ Sci Technol 30:1660–1666. https://doi.org/10.1021/es950655d

Vulliet E, Emmelin C, Chovelon J-M, Guillard C, Herrmann J-M (2002) Photocatalytic degradation of sulfonylurea herbicides in aqueous TiO_2. Appl Catal B Environ 38:127–137. https://doi.org/10.1016/S0926-3373(02)00035-8

Wang W, Serp P, Kalck P, Faria JL (2005a) Photocatalytic degradation of phenol on MWNT and titania composite catalysts prepared by a modified sol-gel method. Appl Catal B Environ 56:305–312. https://doi.org/10.1016/j.apcatb.2004.09.018

Wang W, Serp P, Kalck P, Faria JL (2005b) Visible light photodegradation of phenol on MWNT-TiO_2 composite catalysts prepared by a modified sol-gel method. J Mol Catal A Chem 235:194–199. https://doi.org/10.1016/j.molcata.2005.02.027

Wang W, Serp P, Kalck P, Silva CG, Faria JL (2008) Preparation and characterization of nanostructured MWCNT-TiO_2 composite materials for photocatalytic water treatment applications. Mater Res Bull 43:958–967. https://doi.org/10.1016/j.materresbull.2007.04.032

Wang J, Yu N, Zhang Y, Zhu Y, Fu L, Zhang P, Gao L, Wu Y (2016) Synthesis and performance of Cu_2ZnSnS_4 semiconductor as photocathode for solar water splitting. J Alloys Compd 688:923–932. https://doi.org/10.1016/j.jallcom.2016.07.012

Wang D, Li Y, Puma GL, Lianos P, Wang C, Wang P (2017) Photoelectrochemical cell for simultaneous electricity generation and heavy metals recovery from wastewater. J Hazard Mater 323:681–689. https://doi.org/10.1016/j.jhazmat.2016.10.037

Warren SC, Voïtchovsky K, Dotan H, Leroy CM, Cornuz M, Stellacci F, Hébert C, Rothschild A, Grätzel M (2013) Identifying champion nanostructures for solar water-splitting. Nat Mater 12:842–849. https://doi.org/10.1038/nmat3684

Wu T, Liu G, Zhao J, Hidaka H, Serpone N (1998) Photoassisted degradation of dye pollutants. V. self-photosensitized oxidative transformation of *Rhodamine B* under visible light irradiation in aqueous TiO_2 dispersions. J Phys Chem B 102:5845–5851. https://doi.org/10.1021/jp980922c

Xia X-H, Jia Z-J, Yu Y, Liang Y, Wang Z, Ma L-L (2007) Preparation of multi-walled carbon nanotube supported TiO_2 and its photocatalytic activity in the reduction of CO_2 with H_2O. Carbon 45:717–721. https://doi.org/10.1016/j.carbon.2006.11.028

Xia L, Bai J, Li J, Zeng Q, Li X, Zhou B (2016a) A highly efficient $BiVO_4/WO_3/W$ heterojunction photoanode for visible-light responsive dual photoelectrode photocatalytic fuel cell. Appl Catal B Environ 183:224–230. https://doi.org/10.1016/j.apcatb.2015.10.050

Xia M, Chen R, Zhu X, Liao Q, An L, Wang Z, He X, Jiao L (2016b) A micro photocatalytic fuel cell with an air-breathing, membraneless and monolithic design. Sci Bull 61:1699–1710. https://doi.org/10.1007/s11434-016-1178-8

Xu X, Feng B, Zhou G, Bao Z, Hu J (2016) Efficient photon harvesting and charge collection in 3D porous RGO-TiO_2 photoanode for solar water splitting. Mater Des 101:95–101. https://doi.org/10.1016/j.matdes.2016.03.132

Yang Q, Dionysiou DD (2004) Photolytic degradation of chlorinated phenols in room temperature ionic liquids. J Photochem Photobiol A Chem 165:229–240. https://doi.org/10.1016/j.jphotochem.2004.03.022

Yang J, Liao W, Liu Y, Murugananthan M, Zhang Y (2014) Degradation of rhodamine B using a visible-light driven photocatalytic fuel cell. Electrochim Acta 144:7–15. https://doi.org/10.1016/j.electacta.2014.08.036

Ye H, Lee J, Jang JS, Bard AJ (2010) Rapid screening of $BiVO_4$-based photocatalysts by scanning electrochemical microscopy (SECM) and studies of their photoelectrochemical properties. J Phys Chem C 114:13322–13328. https://doi.org/10.1021/jp104343b

Ying D, Cao R, Li C, Tang T, Li K, Wang H, Wang Y, Jia J (2016) Study of the photocurrent in a photocatalytic fuel cell for wastewater treatment and the effects of TiO_2 surface morphology to the apportionment of the photocurrent. Electrochim Acta 192:319–327. https://doi.org/10.1016/j.electacta.2016.01.210

Zhang Y, Tang Z-R, Fu X, Xu Y-J (2010) TiO_2-graphene nanocomposites for gas-phase photocatalytic degradation of volatile aromatic pollutant: is TiO_2-graphene truly different from other TiO_2-carbon composite materials? ACS Nano 4:7303–7314. https://doi.org/10.1021/nn1024219

Zhang Y, Zhang N, Tang Z-R, Xu Y-J (2012) Transforming CdS into an efficient visible light photocatalyst for selective oxidation of saturated primary C-H bonds under ambient conditions. Chem Sci 3:2812–2822. https://doi.org/10.1039/C2SC20603J

Zhang Y, Zhao G, Shi H, Y-n Z, Huang W, Huang X, Wu Z (2015) Photoelectrocatalytic glucose oxidation to promote hydrogen production over periodically ordered TiO_2 nanotube arrays assembled of Pd quantum dots. Electrochim Acta 174:93–101. https://doi.org/10.1016/j.electacta.2015.05.094

Zheng JY, Son SI, Van TK, Kang YS (2015) Preparation of α-Fe_2O_3 films by electrodeposition and photodeposition of Co-Pi on them to enhance their photoelectrochemical properties. RSC Adv 5:36307–36314. https://doi.org/10.1039/C5RA03029C

Zhou M, Lou XW, Xie Y (2013) Two-dimensional nanosheets for photoelectrochemical water splitting: possibilities and opportunities. Nano Today 8:598–618. https://doi.org/10.1016/j.nantod.2013.12.002

Zhu J, Chen F, Zhang J, Chen H, Anpo M (2006) Fe^{3+}-TiO_2 photocatalysts prepared by combining sol-gel method with hydrothermal treatment and their characterization. J Photochem Photobiol A Chem 180:196–204. https://doi.org/10.1016/j.jphotochem.2005.10.017

Chapter 3
Titania-Based Heterojunctions for Hydrogen Generation by Water Photolysis

L. K. Preethi, Rajini P. Antony, and Tom Mathews

Contents

3.1 Introduction 58
3.2 Heterojunctions: An Overview 59
3.3 Synthesis Strategies for TiO_2-Based Heterojunctions 62
  3.3.1 Synthesis of Type 2 Heterojunction 62
  3.3.2 Synthesis of Schottky Heterojunction 65
  3.3.3 Synthesis of TiO_2-Based p-n Heterojunction 67
  3.3.4 Synthesis of TiO_2-Based Z-Scheme Heterojunction 68
  3.3.5 Synthesis of Mixed-Type Heterojunctions 69
3.4 Photolytic Hydrogen Generation 71
3.5 Probing Heterojunctions 73
  3.5.1 Time-Resolved Spectroscopy 76
  3.5.2 Kelvin Probe Force Microscopy and Photovoltage Spectroscopy 78
  3.5.3 Impedance Spectroscopy, Mott-Schottky Analysis, and Photocurrent Measurements 79
  3.5.4 Other Techniques/Methods 81
3.6 Conclusions and Future Perspectives 82
References 83

Abstract The depleting fossil fuels and their serious environmental impact have heightened the need for an alternative renewable energy resource. The hydrogen obtained from sunlight-assisted water splitting is found to be a promising alternate to

---

L. K. Preethi
Centre for Nanoscience and Nanotechnology, International Research Centre, Sathyabama Institute of Science and Technology, Chennai, Tamil Nadu, India

R. P. Antony
Water and Steam Chemistry Division, BARC – F, Kalpakkam, Tamil Nadu, India
e-mail: rajiniantony@igcar.gov.in

T. Mathews (✉)
Thin Films and Coatings Section, Surface and Nanoscience Division, Materials Science Group, Indira Gandhi Centre for Atomic Research, Kalpakkam, Tamil Nadu, India
e-mail: tom@igcar.gov.in

S. Rajendran et al. (eds.), *Green Photocatalysts for Energy and Environmental Process*, Environmental Chemistry for a Sustainable World 36,
https://doi.org/10.1007/978-3-030-17638-9_3

the fossil fuel. The proposal of generating hydrogen from solar water splitting has a great potential to solve the energy and environmental issues and introduce an energy revolution in sustainable and cleaner way. A variety of photocatalysts ranging from organic to inorganic materials have been studied, but their overall efficiency is limited due to varied reasons. The prevalent reason is the poor control over the recombination of photoexcited charge carriers. It has been investigated that integrating different materials in the form of heterojunction can improve the photocatalyst's efficiency in multiple folds. These heterojunctions would enhance the charge carrier mobility and lifetime, absorption coefficient, stability, etc. which leads to improved charge separation at the heterointerface and hence their efficiency in H_2 generation by photo-assisted water splitting.

In view of this, the present chapter mainly focuses on reviewing TiO_2-based heterojunctions, a widely studied material for photocatalytic hydrogen generation. The basic working principle of different heterojunctions of TiO_2, their concerned drawbacks, and the recent impressive progress in developing other forms of TiO_2 heterojunctions are presented. In addition, the overviews of synthesis strategies of various TiO_2-based heterojunction materials are reviewed. The performance and stability of any heterojunction photocatalyst are dependent on the synergistic functioning of the interfaces between the individual materials forming heterojunction. The study of light matter interaction in these heterointerfaces is expected to provide crucial information helpful for exploiting the potential of these photocatalysts for commercial viability. Therefore, the present chapter also demonstrates the existing methodologies to probe these heterojunctions under light irradiation for charge carrier dynamic analysis. Finally, the chapter is concluded with the ups and downs of TiO_2-based heterojunction research and the future perspectives.

Keywords Hydrogen generation · Photocatalysis · Titania · Heterojunction · Charge transfer dynamics · Light matter interaction · Time-resolved spectroscopy · Kelvin probe spectroscopy · Electrochemical impedance spectroscopy · Schottky heterojunction · p-n heterojunction · Type 2 heterojunction · Z-scheme

3.1 Introduction

Titanium, the ninth most abundant element in the earth's crust, is thermally stable, chemically inert, biocompatible, nonflammable, and nonhazardous. Titania has been investigated for over several years due to their photoelectric and photocatalytic properties. After the discovery of Fujishima and Honda (Fujishima and Honda 1972), the concept of light-assisted water splitting for hydrogen generation has been a rife in the research community. This stimulated extensive research on water splitting by using different phases of TiO_2, and their photochemistry are being reported till date (Anandan and Yoon 2003; Chen and Mao 2007; Hoffmann et al. 1995; Mills et al. 1993; Preethi et al. 2017b). This includes the study of different TiO_2 structures ranging from small particles in the form of powders, clusters, and colloids to large crystals that support oxidative and reductive reactions of various organic and inorganic adsorbates.

This is followed by studies on the effect of various phases, morphologies, pore sizes, and synthesis methods on their photocatalytic activities. It is observed that an optimized combination of the physicochemical properties of TiO_2 is necessary to produce an efficient photocatalyst for enhanced water splitting. Though the maximum theoretical solar-to-hydrogen (STH) conversion efficiency of TiO_2 is only ~1%, the titania is most studied due to its relatively strong reducing capability of the excited CB electrons and hole oxidizing power as a result of their suitably straddling energy levels with respect to water redox potential. High stability of titania in basic and acidic medium and their availability makes it an attractive material for photocatalytic water splitting (Bärtsch and Niederberger 2017).

The poor visible light absorption (band gap in the UV range ~3.2 eV) and high charge pair recombination are the major hindrances toward water splitting. Due to the high recombination rate, only a small fraction of the excited charge carriers (5%) can participate in redox processes at the interface. These problems hinder the commercialization possibility of TiO_2 as a solar water splitting material. Band gap engineering of TiO_2 is a strategy widely investigated to address these challenges. The commonly applied techniques are cation/anion doping, co-catalyst loading, dye sensitization, coupling with other semiconductors, addition of electron donors (hole scavengers), etc. Among them, heterojunction introduced between two different semiconducting materials of suitable band energy offsets is considered to be an effective method to facilitate the interparticle charge transfer, thereby overcoming the charge pair recombination (Licht 2001). The chemical potential difference between two semiconductors leads band bending at the interface. This induces a built-in field which drives the photogenerated charge carriers (electrons and holes) to move in opposite directions, leading to their spatial separation across the heterojunction (Uddin et al. 2017) (Haring et al. 2014; Scanlon et al. 2013). The present chapter gives an overview of widely studied TiO_2-based heterojunctions and the way to probe them for efficient hydrogen generation.

3.2 Heterojunctions: An Overview

The inefficiency of single-phase pristine TiO_2 to satisfy the desired requirements of efficient solar-to-hydrogen conversion by water splitting bottlenecks the material's performance, and it is difficult to systematically improve such limitations. Therefore, the material interface with another suitable material to enhance the efficiency is highly desirable. The interface between two phases of unequal band structure is termed as heterojunction. Depending on the band edge positions and the type of materials that forms interfaces, the heterojunctions are classified as follows:

- *Type 1 or straddling heterojunction:* The heterojunction that is formed when band gap of semiconductor B is completely contained in the band gap of semiconductor A as represented in Fig. 3.1a.

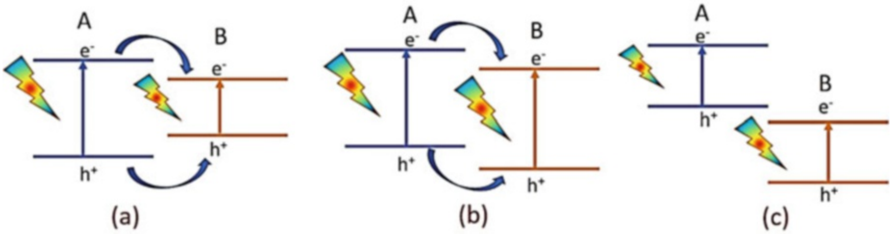

Fig. 3.1 (**a**) Type 1 or straddling heterojunctions, (**b**) type 2 or staggered heterojunction, and (**c**) type 3 or broken heterojunction. A and B represent two different semiconductors

- *Type 2 or staggered heterojunction:* The heterojunction formed when the band edges of semiconductor A (conduction band edge (CBE) and the valence band edge (VBE)) are higher than the corresponding band edges of the semiconductor B (Fig. 3.1b) giving rise to electron confinement in CBE of one material and that of holes in VBE of other material.
- *Type 3 or broken heterojunction:* The heterojunction that is formed when the band edges of two materials do not overlap at all, as represented in Fig. 3.1c. The carrier transfer is similar to that in type 2 heterojunction, just more pronounced.

Appropriate band alignment at the interface is a key requirement to obtain efficient photogenerated charge separation. It is observed that the band alignments, such as type 1 (straddling gap) and type 3 (broken gap), impede the charge separation processes. Thus, the interfaces between the phases need to be energetically tuned for efficient charge collection. In addition, they can also act as blocking contact for the other type of carriers (Dasgupta et al. 2017; Kim et al. 2015). Type 2 heterojunction offers such convenience, and therefore it is prevalently studied in case of TiO_2 heterojunctions (Preethi et al. 2017a; Saha et al. 2017; Zhang et al. 2017). However, there are numerous problems that restrict the practical applications of type 2 heterojunction photocatalysts. One of them is that their reduction and oxidation reactions occur for semiconductor B having a lower reduction potential and semiconductor A with a lower oxidation potential, respectively (Sun 2015; Xiao et al. 2015). Thus, the redox capability of type 2 heterojunction photocatalysts will be decreased (Low et al. 2017; Kumar et al. 2017). In addition, the electrostatic repulsion of like charges makes it tough for photogenerated electrons in semiconductor A and photogenerated holes in semiconductor B to migrate to the electron-rich CB of semiconductor B and the hole-rich VB of semiconductor A, respectively. Thus, it is highly desired to fabricate alternate heterostructured photocatalysts to surmount these issues.

Other Heterojunctions

Another type of heterojunction called Z-Scheme photocatalyst is found to be an effective route for efficient separation and transfer of photogenerated charge carriers. The concept was inspired from natural photosynthesis occurring in green plants. In

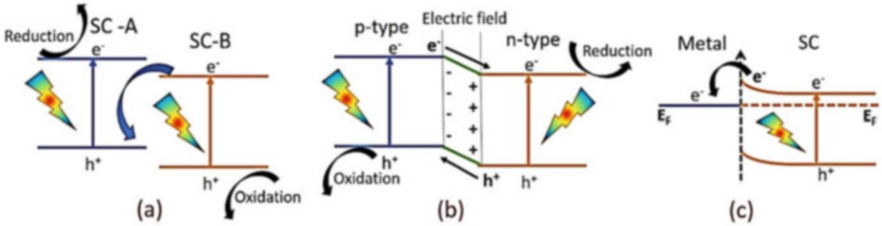

Fig. 3.2 Schematic showing the band straddling of (**a**) Z-scheme, (**b**) p-n heterojunction, and (**c**) Schottky heterojunction

this type of heterojunction (Fig. 3.2a), the electrons in CB of semiconductor B (SC-B) transfer to the VB of semiconductor A (SC-A) leading to electron-hole recombination. Meanwhile the electrons in CB of A reduce water into hydrogen, and the holes in CB of B oxidize water leading to the evolution of oxygen gas.

The p-n junction is similar to “type 2 heterojunction” system with the materials having “p”- and “n”-type semiconductor-based photocatalysts. The junction formed by “n” and “p” materials facilitates the accumulation of photogenerated electrons near n-type interface and the holes near p-type. This effect is mainly due to the different electronic structures of p- and n-type semiconductors. This leads to a potential gradient at the interface which facilitates the photoexcited charge carrier’s transportation with efficient charge separation (Fig. 3.2b), thereby increasing the overall efficiency of photocatalytic reaction. Schottky heterojunction is another category of heterojunction, where electrons flow from the photocatalyst to the co-catalyst across their interface (from a higher Fermi level to the lower) in order to equilibrate the Fermi levels as represented in Fig. 3.2c. A space charge layer is generated as a result of excess negative charge generated on the co-catalyst and excess positive charges on the semiconductor closer to the interface. An upward bending of CB and VB of the semiconductor is thus developed near to the interface thereby forming a Schottky junction between the semiconductor and co-catalyst resulting in electron trap at the Schottky junction. The electron trap thus formed can efficiently capture the photoinduced electrons and boost the photocatalytic activity (Fig. 3.2c). In all the cases, “the band offset” or “potential discontinuity” plays a vital role in photocatalytic activity as it is this discontinuity which causes the quantum behavior of the structures. As soon as a heterojunction is made, the charge carriers flow across the junction, building space charges until the Fermi energy is the same everywhere in the materials. Far away from the interface, everything is unchanged. Titania has been interfaced with many materials to obtain all the above alternate heterojunctions for efficient photocatalytic water splitting (Enzhou et al. 2018; Hao et al. 2018; Niu et al. 2014; Piyush et al. 2018; Ren et al. 2018; Xu et al. 2018; Yan et al. 2016; Yang et al. 2015; Zhao et al. 2017).

3.3 Synthesis Strategies for TiO_2-Based Heterojunctions

Choosing synthesis route of heterojunctions is one way to minimize the cost of the H_2 production technology, and hence one should design the fabrication in a cost-effective manner both in terms of technique and the materials employed. Moreover, strategy adopted should enable to have an efficient interface between TiO_2 and the desired material for an easy electron transport and charge separation leading to improved solar-to-hydrogen conversion efficiency. The present section discusses the different fabrication techniques taken up for different types of heterojunctions used for H_2 generation demonstration experiments.

3.3.1 Synthesis of Type 2 Heterojunction

Vertically aligned core-shell $PbTiO_3$@TiO_2 heterojunction nanotube array is an interesting type 2 heterojunction which showed good photoelectrochemical and photocatalytic performance with sunlight illumination (Jang et al. 2017). As shown in schematic of Fig. 3.3a, initially Ti film was coated on FTO glass by electron beam vapor deposition method followed by electrochemical anodization in fluoride ion-containing glycerol medium. Thereafter known concentration of $Pb(C_2H_3O_2)_2{\cdot}3H_2O$ solution was spin coated onto the annealed TiO_2 nanotube arrays. The dried $Pb(C_2H_3O_2)_2{\cdot}3H_2O$-coated TiO_2 nanotube arrays were annealed at desired temperature to form core-shell-type $PbTiO_3$@TiO_2 heterojunction and evaluated for its photocatalytic activity. The synthesis strategy was helpful in having better contact between TiO_2 and FTO glass for efficient electron transport, and the heterojunction formed between $PbTiO_3$ and TiO_2 enabled favorable staggering band alignment (type 2) for efficient visible light absorption followed by photogenerated carrier separation leading to improved solar conversion efficiency.

Visible light-absorbing porous Bi_2WO_6/TiO_2 thin films are another class of metal oxide-based heterojunction which showed enhanced photocatalytic and photoelectrochemical properties due to the favorable valence band interactions between the semiconductor films (Xu et al. 2011). Heterojunctions were made through a hydrophilicity-assisted dip coating process. To fabricate Bi_2WO_6 thin films, a known quantity of diethylene triaminepenta acetic acid and ammonia is added to hot deionized water for dissolution. Thereafter Bi_2O_3 and 5 $(NH_4)_2O.12WO_3.5H_2O$ were added in stoichiometric ratio, and the whole system was kept at 80 °C under stirring in oil bath. For the fabrication of Bi_2WO_6 under layer, the FTO glass was first subjected to alcohol cleaning followed by annealing at 500 °C for 30 min thereafter allowing for natural cooling. This enables the FTO surface to obtain hydrophilic nature. These hydrophilic FTO glasses were then dipped in Bi_2WO_6 solution for 1 min and withdrawn in a controlled fashion which are then dried under vacuum for removal of organic species. The thin films were then subjected to annealing to obtain Bi_2WO_6 under layer. For the fabrication of Bi_2WO_6/

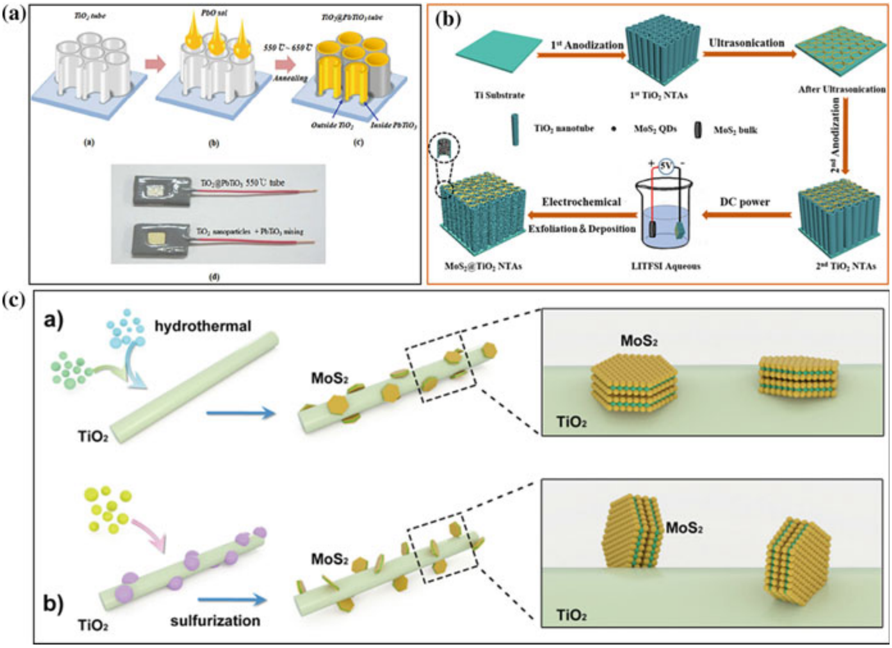

Fig. 3.3 (**a**) Synthesis of $PbTiO_3@TiO_2$ heterojunction nanotubes. Photographs of photoanodes prepared by $PbTiO_3@TiO_2$ nanotube and a physical mixture of $PbTiO_3$ and TiO_2 powders are shown below. (Reprinted with permission from (Jang et al. 2017) copyright (2017) American Chemical Society). (**b**) The illustration of the preparation of the hierarchical $MoS_2@TiO_2$ NTAs and (**c**) schematic preparing of TiO_2/MoS_2 composite. (Reprinted with permission from (Dong et al. 2018) copyright (2018) Elsevier). (a) Synthesis routes on wet chemical method for the fabrication of TiO_2/MoO_2/(B) composite, in which MoS_2 nanoplates are in contact with titania surface along basal planes (B); (b) in the CVD strategy employed to prepare TiO_2/MoS_2(E) composite, MoS_2 nanoplates are in contact with TiO_2 surface along highly conductive planes (E). (Reprinted with permission from (He et al. 2016) copyright (2016) Wiley)

TiO_2 heterojunctions, TiO_2 sol was prepared by a sol-gel-assisted route, where titanium isopropoxide was used as the Ti precursor. The heterojunctions were fabricated by the similar dip coating route in TiO_2 sol followed by calcination process to get Bi_2WO_6/TiO_2 heterojunction films.

A facet-dependent engineering of TiO_2-graphene interface was done by Liu et al. (Liu et al. 2014). TiO_2 nanocrystal with (TiO_2-101-G), (TiO_2-100-G), and (TiO_2-001-G) facets was anchored on graphene by a hydrothermal route where the direction of growth is controlled by different capping anions. For the preparation of TiO_2-101-G and TiO_2-100-G, $TiCl_4$ was used as the precursor, and in both the cases, Ti$(OH)_4$-graphene was formed by adding $TiCl_4$ in aqueous HCl thereafter mixing with GO in desired amount. The solution pH was maintained at 6 by adding ammonia to it. Thereafter $Ti(OH)_4$-graphene was stirred in water-isopropanol mixture for aging and then autoclaved for 24 h at 180 °C which leads to the formation of TiO_2-101-G. For the preparation of TiO_2-100-G, ammonium sulfate was added to the mixture and subjected to autoclaving. To synthesize TiO_2-001-G, GO-dispersed ethanolic solution of $Ti(OC_4H_9)_4$ was used as precursor. Autoclaving was done for HF-containing precursor solution under the same conditions used for other systems. Thus, when no capping agents were employed, the preferential orientation of TiO_2 is {101} (Anandan and Yoon), and when sulfate anions were used as the capping agent, the preferential orientation turned out to be {100}, and finally F^- when used as the capping agent, the {001} planes were the preferred one.

Tan and co-workers suggested and validated an easy single-step method to realize the g-C_3N_4 nanostructuring and its combination with commercial P25 TiO_2. A vapor deposition methodology was adopted for this, and the as-obtained nanostructured g-C_3N_4/TiO_2 showed higher H_2 generation efficiency compared to bulk g-C_3N_4 in visible light (10.8 times). The vapor deposition setup consists of a covered crucible with a cylinder inside in which commercial TiO_2 was kept on the top of the cylinder. C_3N_4 precursor (melamine) was loaded on the bottom of the cylinder. This system was further subjected to annealing (520 C for 4 h) leading to the development of nanostructured g-C_3N_4/TiO_2 (Tan et al. 2018).

Elbanna et al. formulated g-C_3N_4 nanosheets/TiO_2 mesocrystals represented as g-C_3N_4 NS/TMC which is a metal-free composite, where combining g-C_3N_4 with TiO_2 increases the charge separation (Elbanna et al. 2017). Melamine was chosen as the precursor for formation of bulk C_3N_4 which was heated at 550 °C for 3 h under airflow. Further the exfoliation was carried out by ultrasonication of the bulk C_3N_4 in isopropanol for 10 h. The residual was got rid of by centrifugation at 3000 rpm, and the resultant supernatant was further centrifuged at 10000 rpm for 5 min to obtain exfoliated g-C_3N_4. To fabricate TMC, the precursor solution of titanium tetrafluoride, ammonium nitrate, ammonium fluoride, water, and NH_4F (molar ratio = 1:6.6:4:117) was placed on a silicon wafer to form a thin layer and further annealed at 500 °C for 2 h and thereafter annealed in O_2 flow for 8 h to remove the impurities. Finally, the TMC and g-C_3N_4 NS were added in appropriate quantities in methanol to obtain a uniform solution through ultrasonication for ~30 min. The suspension was then stirred for 12 h and centrifuged to obtain preferred catalysts. The performance improvement was ~7% for the TMC/g-C_3N_4 NS compared to P25/g-C_3N_4 catalyst. Kalanur and co-workers reported an efficient CdS-TiO_2 heterojunction system toward photoelectrochemical (PEC) water oxidation ((Kalanur et al. 2013). For this, commercial anatase TiO_2 was coated onto FTO substrate by drop-casting route and calcined at desired temperature for crystallinity. These substrates were subjected to solvothermal treatment in cadmium acetate-containing ethanolic solution for varying time intervals at 120 °C. The improvement in the current density was due to the improvement in the interfacial contact between the CdS and TiO_2.

Cheng et al. demonstrated the water splitting efficiency of commercial P25 TiO_2-graphene hybrid (Cheng et al. 2012), where graphene oxide (GO) was fabricated by modified Hummer's route (Park and Ruoff 2009). A solvothermal route was adopted to fabricate the heterojunction where appropriate amount of GO and P25 was added to ethanol and dispersed ultrasonically for few hours. The homogenous solution was then moved to a hydrothermal reactor and kept at 180 °C for 8 h. This strategy helped for the further reduction of GO leading to graphene and to obtain a better interface between TiO_2 and graphene.

It was proposed by Zhong et al. that impedance in charge transfer process can be overcome by fabricating well-defined nanosheet-nanosheet (ns) (2D-2D) heterojunctions, which provide large area for efficient migration of charge carriers at the interface (Zhong et al. 2018). A one-pot solvothermal route was adopted to fabricate these composites where TiO_2 ns were grown in situ on oxidized C_3N_4 ns in a Teflon liner at 150 °C for 20 h.

Electrochemical fabrication of heterojunction using MoS_2 quantum dots on titania nanotube arrays (TNTA) was carried out by Dong et al. and demonstrated an improvement in the photoelectrochemical and electrocatalytic hydrogen evolution (Dong et al. 2018). A convenient, two step anodization strategy was adopted to fabricate TNTA-MoS_2 quantum dots that were synthesized by electrochemical-assisted exfoliation route from the bulk MoS_2 powder. To perfrom this, pelletized MoS_2 (0.5 g 15 MPa for 60 s) was used as an anode in the electrochemical cell, and TNTA was employed as the cathode in 0.1 wt% lithium bis(sulfonamide) salt as the electrolyte. The distances between the electrodes were 1 cm and the applied voltage was 5 V. The fabrication steps are pictorially shown in Fig. 3.3b. A twofold improvement in the PEC activity for MoS_2-TNTA was obtained compared to pristine TNTA along with the improved electrocatalytic hydrogen evolution of 73 mV dec^{-1}. The results showed that the current synthesis route enabled to obtain a better interface between MoS_2 and TNTA for efficient charge separation and catalytic reaction. He and co-workers constructed edge-on junctions using MoS_2 and TiO_2 for an improved electronic contact and enhanced electron transport pathway. For this, initially both TiO_2 and MoO_2 nanoparticles were synthesized by hydrothermal route (He et al. 2016). A two-step synthesis strategy was adopted to synthesis edge MoS_2-TiO_2 where in the first step MoO_2 particles were decorated on TiO_2 surface by dispersing both in DI water and stirring for 12 h. Thereafter the as-prepared MoO_2-TiO_2 was sulfurized by annealing at 400 ° C for 1 h under vacuum using sulfur powder in the upstream. It is observed that with 3% of MoS_2 loading, the H_2 generation rate was enhanced 36 times (4300 μmol h^{-1} g^{-1}) with respect to pristine TiO_2 and the performance is due to the improved charge transport pathway. Formation of edge on MoS_2-TiO_2 heterojunction is shown in Fig. 3.3c.

3.3.2 Synthesis of Schottky Heterojunction

TiO_2-based Schottky heterojunctions are basically a metal-TiO_2 system where the metal nanoparticles are generally deposited on TiO_2 by reduction of metal ions by different means. This section discusses synthesis of various types of Schottky heterojunction used for reactions involving hydrogen generation and water splitting.

Lian et al. have fabricated Pt-loaded TiO_2 by an in situ ionothermal route which was found to facilitate an easy charge transfer from bulk to surface states for hydrogen production (Lian et al. 2017). In a typical synthesis procedure (Li et al. 2015), known quantities of DMF, lithium acetate, and glacial acetic acid were mixed in glass vessel and stirred well till we get a clear solution. Into this solution, cleaned Ti foil and ionic liquid (1-methyl-imidazolium tetrafluoroborate) were incorporated and transferred to autoclave and maintained under 200 °C for ~24 h. The powder obtained was washed thoroughly and dried under vacuum for 12 h. For Pt doping, a different amount of chloroplatinic acid was incorporated into the above system and kept for autoclaving under similar conditions mentioned above to form Pt-loaded Ti^{3+}-TiO_2.

Recently Montoya and Gillan investigated the hydrogen generation efficiency of transition metal-loaded commercial P25 TiO_2 (Montoya and Gillan 2018). The metal loading was carried out using UV solution photodeposition route employed by photoreduction of metal ions in sacrificial methanol oxidant. In the typical synthesis process, commercial P25 TiO_2 was dispersed in metal chloride dissolved in 1:1 methanol-water mixture followed by UV exposure (450 W Hg lamp, Ace Hanovia) under argon blanket for 90 min. The resultant solids were then isolated by centrifugation followed by drying at vacuum conditions. Schottky junctions using Cu, Pt, and CuPt nanoparticles (NPs) on square-shaped TiO_2 nanotube arrays (STNTAs) were fabricated by Karthik and co-workers where Cu-STNTA showed 80% higher photocurrent values toward solar water oxidation reaction (Piyush et al. 2018) with a plasmonic behavior at 550 nm (Fig. 3.4). The obtained improvement in the activity was due the combined plasmonic and photocatalytic activity of the heterojunctions. STNTA in their studies was fabricated by conventional electrochemical anodization using fluoride-containing organic electrolyte (ethylene glycol) in two-electrode mode with an applied potential of 30 V. A flame annealing was carried out for calcination using a propane torch at 450 °C for 30 min. Further a photochemical approach was done to load the metal nanoparticles with metal acetylacetonate precursor in methanol using a solar simulator with AM 1.5 filter (1 sun illumination). The schematic of the synthesis process is shown in Fig. 3.4.

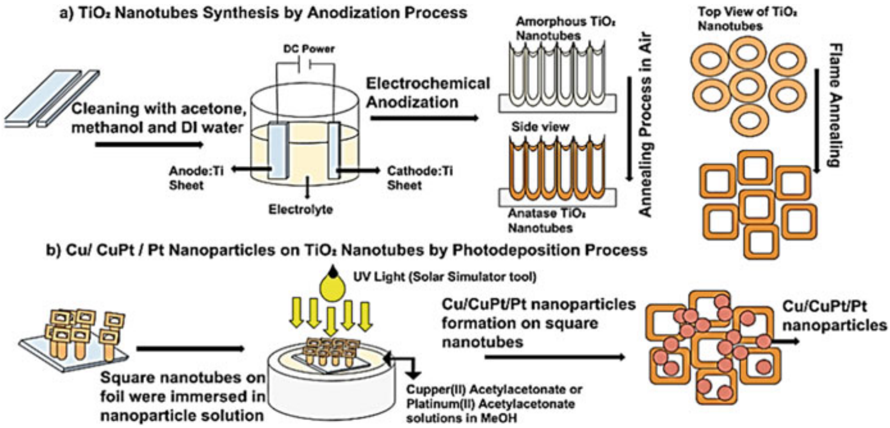

Fig. 3.4 Schematic of the process flow for the development of square-shaped TiO_2 nanotube arrays (STNTAs) and deposition process of Cu, CuPt, and Pt nanoparticles (NPs) on STNTAs. (Reprinted with permission from (Piyush et al. 2018) copyright (2018) IOP publishers)

In a similar way, a Schottky heterojunction was made by loading Ag nanoparticles on CdSe-TNTA by Liu et al. in 2018 (Enzhou et al. 2018). In their study, a two-step anodization route was adopted to fabricate the TNTAs. The calcined TNTAs were then subjected to Ag loading by a microwave-assisted chemical reduction route, and thereafter an in situ sensitization route was adopted to fabricate CdSe-Ag-TNTA. The resultant system was showing a hydrogen generation efficiency of 413.99 μmol cm^{-2} which was four times higher compared to pristine TNTA.

3.3.3 Synthesis of TiO_2-Based p-n Heterojunction

The present section focusses on the fabrication routes of TiO_2-based p-n-type heterojunctions which were demonstrated for H_2 generation by water splitting. In 2003, Withala and co-workers developed Cu_2O-TiO_2 heterojunction-based photoelectrode, where the favorable band structure alignment of n-TiO_2 and p-Cu_2O was utilized along with chemical stability of TiO_2 and photon absorption ability of Cu_2O, respectively (Siripala et al. 2003). In their work Cu_2O was electrodeposited on Ti foils in a three-electrode mode under potentiostatic condition at −0.2 V vs Ag/AgCl. An electron beam evaporation of TiO_2 was done thereafter on electrodeposited Cu_2O thin film under high vacuum conditions (10^{-6} torr). The heterojunction developed by this route has successfully overcome the limitations of photo-corrosion of Cu_2O and the UV-visible activity of TiO_2. Introducing Schottky and p-n heterojunctions in a single system is an effective way of charge separation for efficient water splitting reaction.

Nanostructured TiO_2@Ag_2O p-n heterojunction arrays, which was another class of p-n junctions developed recently by Hao and co-workers, showed ~1.6 mAcm^{-2} photocurrent density and was twice to that of pristine one (Fig. 3.5b) (Hao et al. 2018). A hydrothermal route was adopted to fabricate the TiO_2 nanowire array on FTO glass where titanium-n-butoxide was used as the Ti precursor in HCl-containing DI water for hydrolysis. The solution containing vertically stranded FTO glass is subjected to autoclaving at 150 °C for ~20 h followed by calcination to form crystalline TiO_2 nanowire arrays over FTO substrate. Ag_2O deposition was further done by a chemical bath deposition route, where in the first stage, a known quantity of NaOH was added to a beaker containing DI water and TiO_2 nanowire-coated FTO glass was vertically placed inside the beaker. Ag precursor solution was then added drop by drop into the beaker and kept for aging at 50 °C for ~8 h. Finally, the Ag_2O-loaded TiO_2 nanowire arrays were washed with DI water and dried at 60 °C. The pictorial illustration of the synthesis technique is shown in Fig. 3.5a.

Yang et al. explored the photoanode performance of n-Fe_2O_3 to N + -TiO_2 heterojunction where a combination of heavily doped TiO_2 (N+) and lightly doped hematite (n-) constitutes the heterojunction (Yang et al. 2015). In their study, disjoined (DNS) and continuous (CNS) TiO_2 nanostructures were fabricated where the former consists of separated nanorods and nanoparticles, whereas the later

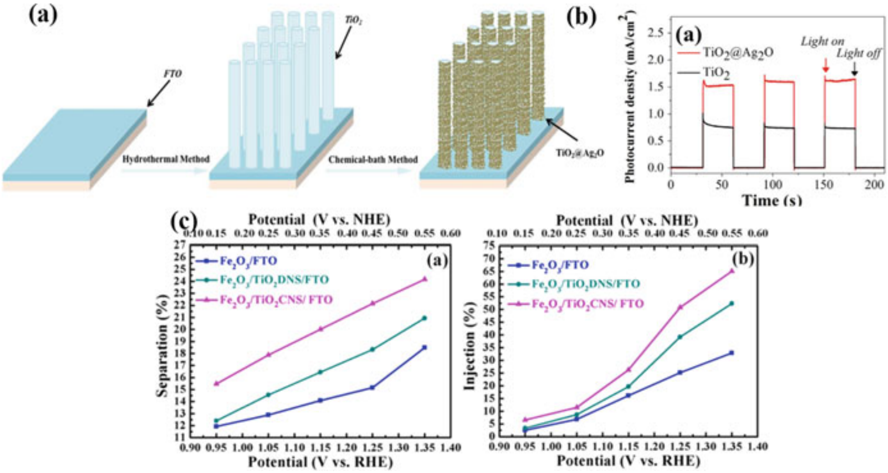

Fig. 3.5 (**a**) Schematic representation of two-step fabrication steps for the $TiO_2@Ag_2O$ nanowire arrays by hydrothermal-chemical bath methods. (**b**) Transient photocurrent density plots under illumination at a bias of 1.23 V vs RHE (0.5 M Na_2SO_4 electrolyte). (Reprinted with permission from (Hao et al. 2018) copyright (2018) Elsevier). (**c**) Charge separation and charge injection efficiency plots estimated for hematite/FTO, hematite/TiO_2-DNS/FTO, and hematite/TiO_2-CNS/FTO photoanodes. (Reprinted with permission from (Yang et al. 2015) copyright (2015) American Chemical Society)

possess continuous nanoparticle layer. The DNS structure was initially fabricated by a hydrothermal route using HCl (8 M) and titanium tert-butoxide (0.5 ml) at 150 °C for 3.5 h. From this DNS TiO_2, a chemical bath deposition route was adopted to fabricate CNS TiO_2 film in a mixture of HCl (0.25 M) and of titanium tetra isopropoxide (1 ml) at 95 °C for 4 h. Thereafter, a CVD route was adapted to deposition hematite thin films, and the deposition conditions are N_2/O_2 flow (500 ccm) with a temperature of 550 °C and pressure of 3 Torr. A considerable improvement in the charge separation and injection efficiencies was obtained for these interesting heterojunctions whose improvement in the separation and injection efficiencies is shown in Fig. 3.5c.

3.3.4 Synthesis of TiO_2-Based Z-Scheme Heterojunction

For the Z-scheme-based photocatalysis, where both oxidation and reduction of water take place, appropriate synthesis methodology must be chosen for the desired efficiency. Present section gives selected results on development of TiO_2-based Z-scheme photocatalysts. A simple electrospinning technique was adopted by Gao et al. to fabricate Z-scheme one-dimensional photocatalyst system for water splitting where WO_3 was chosen as the hole collector in combination with TiO_2 (Gao et al. 2017a). Pt was used as the reaction site for hydrogen production, and the resultant photocatalyst was known as $WO_3/TiO_2/Pt$ heterojunction. Tert-butyl titanate, ammonium tungstate, and chloroplatinic acid were chosen as the precursor for this. In the typical synthesis process, desirable amounts of all the above mentioned precursors were taken in ethanol-acetic acid mixture with polyvinylpyrrolidone (PVP) as the sacrificial polymer. The viscous solution thus prepared was used for electrospinning at an applied bias of 15 kV between the collector and the needle kept 15 cm apart. Finally, the as-obtained electrospun nanofibers were annealed at 520 °C with a heating rate of 5 °C per min for 30 min. The H_2 production rate was reached to 27.73 $molg^{-1}$ h^{-1} for the Z-scheme photocatalyst prepared from an undetectable regime for pristine TiO_2 nanofibers. Another interesting approach to fabricate Z-scheme photocatalysts is to design core-shell hybrid nanofibers where TiO_2 forms the skeleton and few layers of NiS form the outer layer (Xu et al. 2018).

A 14.6-fold improvement in the hydrogen production (655 μmol h^{-1} g^{-1}) was obtained for this catalyst. Like the previous synthesis, TiO_2 nanofibers were synthesized by electrospinning route using tert-butyl titanate and PVP in ethanol-acetic acid solution. A nickel precursor ($NiCl_2$.6 H_2O) was then mixed in a solution of hexamethylenetetramine and trisodium citrate to form a clear solution. Known amount of TiO_2 nanofibers fabricated was suspended in this solution and heated at 90 °C in an oil bath; the resultant product is then dried overnight at 80 °C. Further sulfidation process was done by immersing the sample in $NaHS_xH_2O$ under magnetic stirring and keeping for 5 h at room temperature. The as-obtained solid powder was dried to get TiO_2/NiS heterojunction. The schematic illustration of the synthesis of TiO_2/NiS heterojunction is shown in Fig. 3.6a.

Yan and co-workers adopted one-step hydrothermal route to develop C_3N_4-based Z-scheme photocatalysts (C_3N_4-TiO_2) with (001) facet exposed facet of TiO_2 (Yan et al. 2016). For this g-C_3N_4 was synthesized by thermal condensation of urea at 550 °C for 4 h, and appropriate quantity of C_3N_4 was added to the aqueous solution of $TiCl_4$ and autoclaved at 150 °C for 24 h. When $TiCl_4$ was dissolved in water, Ti $(OH)^{-}x$ adsorb onto the reaction sites of bulk C_3N_4. Under high-temperature and high-pressure condition, the $Ti(OH)^{-}x$ nucleates to form TiO_2, and the bulk C_3N_4 converts to layered g-C_3N_4. The formation of (001) facet was explained as the restriction effect of 2D layered structure which otherwise normally forms in presence of fluorine. Figure 3.6b shows the schematic of the formation of (001) exposed TiO_2 facets by the self-restriction effect of g-C_3N_4.

3.3.5 Synthesis of Mixed-Type Heterojunctions

Ren and group achieved an SPN (Schottky and p-n) junction by Ni intercalation into NiO-TiO_2 heterojunction (Ren et al. 2018). For this, to prepare TiO_2 nanotubes, first a hydrothermal route was adopted, and the fabricated nanotubes were added to aqueous solution of Ni precursor. $NaBH_4$ (reducing agent) was added to the ice-cold solution to form Ni-TiO_2. The resultant solution was washed well to remove excess $NaBH_4$ and dried overnight. A controlled oxidation procedure was adopted to

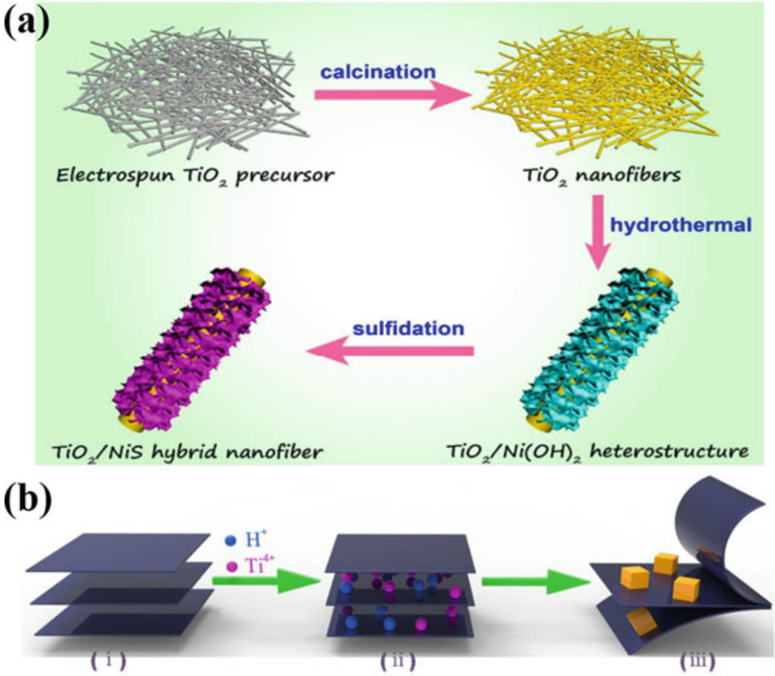

Fig. 3.6 (**a**) Visual representation for the fabrication of core-shell TiO_2/NiS hybrid nanofibers. (Reprinted with permission from (Xu et al. 2018) copyright (2018) American Chemical Society). (**b**) Pictorial illustration of the bulk g-C_3N_4-induced (001) facet exposed anatase TiO_2 formation and heterojunction formation. (i) and (ii) Ti^{4+} reacts with H_2O molecules to form $Ti(OH)^{x-}$ and incorporated into layers of g-C_3N_4 framework, thereafter adsorbed onto the reaction sites; (ii) to (iii) the $Ti(OH)^{x-}$ adsorbed undergoes heterogeneous nucleation on the C_3N_4 layers; due to the restriction and template effect of layers and (001) exposed anatase, TiO_2 is formed in situ. At the same time, the bulk g-C_3N_4 forms thin layer due to self-exfoliation effect. (Reprinted with permission from (Yan et al. 2016) copyright (2016) Elsevier)

fabricate NiO-Ni-TiO_2 where the system was treated with air initially for 2 h at room temperature and thereafter stored in an argon-saturated glove box. 4653 μmol h^{-1} g^{-1} of H_2 was generated using NiO-Ni-TiO_2 SPN system which was ~ 10 times higher compared to pristine TiO_2.

Another report by Boppella and co-workers explains the fabrication of plasmon-sensitized graphene/TiO_2 inverse opal nanostructures where the heterostructures boosted the efficiency for charge collection in solar water splitting (Boppella et al. 2017). TiO_2 inverse opal structures were fabricated by spin coating Ti precursor in HCl-containing ethanol solution which was then calcined at 500 °C for 30 min. Polystyrene (PS) beads were then drop casted on to TiO_2-coated FTO substrate and dried overnight. Tightening of the neighboring PS beads was done for structural stability by heating the film at 70 °C for 1 h. In the next stage, PS-coated film was then dipped vertically into a solution containing Ti precursor for 1 min, and resultant

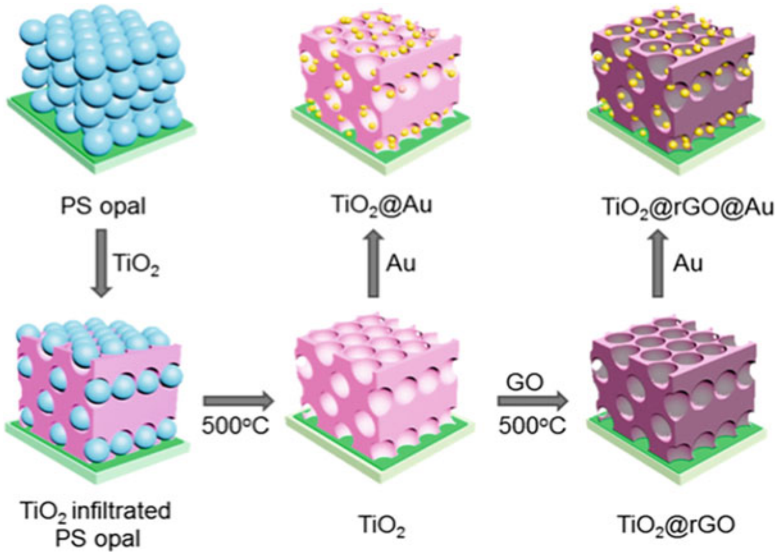

Fig. 3.7 Pictorial representation for the synthesis steps of inverse opal-nanostructured TiO_2 loaded with rGO and AuNPs in organized configurations. (Reprinted with permission from (Boppella et al. 2017) copyright (2017) Journal of American Chemical Society)

film was then annealed at 550 °C for 3 h. For plasmon sensitization, Au nanoparticles were employed, and for graphene loading, GO was fabricated by modified Hummer's route as discussed elsewhere (Park and Ruoff 2009). To load Au nanoparticles, the inverse opal-structured TiO_2 films were dipped into the citrate-capped Au nanoparticle colloid solution and dried at 100 °C for 1 h to form Au@TiO_2 films. A two-step sequential deposition technique was applied for GO incorporation where TiO_2 films were first dipped in polyallylamine hydrochloride (PAH) solution for 2 h followed by water washing to remove excess PAH. This was to facilitate the interaction and incorporation of negatively charged GO on to TiO_2 inverse opal voids by positively charged NH_2 functional moieties. The resultant films were then dipped in GO suspension for 5 h followed by calcinations at 500 °C under Ar flow condition for 3 h. The schematic of the fabrication route is shown in Fig. 3.7a.

3.4 Photolytic Hydrogen Generation

The photo-assisted water splitting using heterojunction photocatalysts can be performed under two different configurations. They are: (i) photoelectrochemical systems in which two electrodes, with one having the photocatalyst on its surface, in aqueous electrolyte perform oxidation and reduction reactions, respectively, and (ii) particulate photocatalytic systems (or direct water splitting) where the powder

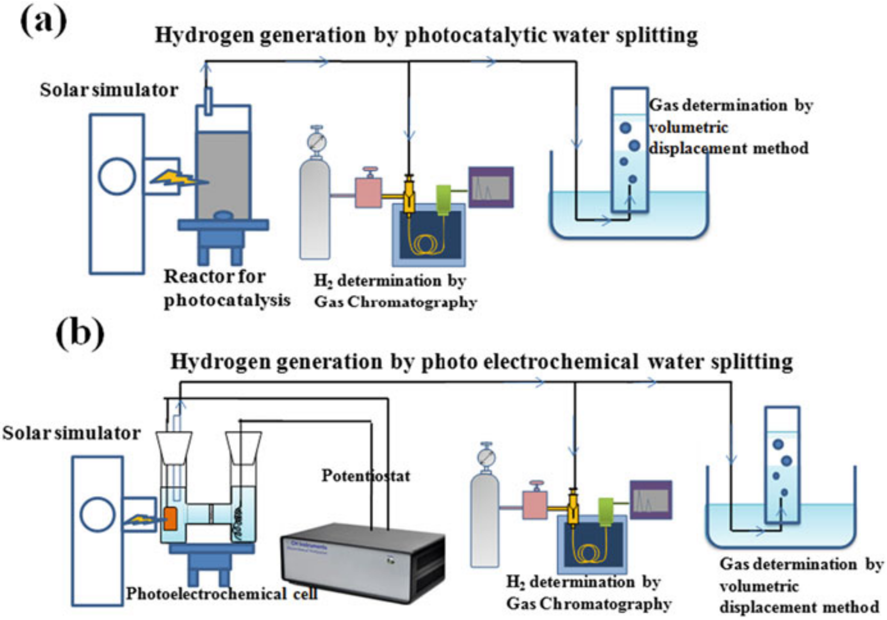

Fig. 3.8 Pictorial illustration of experimental setup used for hydrogen generation measurement by (**a**) photocatalytic and (**b**) photoelectrochemical route

photocatalysts are suspended in aqueous solution and redox reactions take place at its surface. Comparing the two configurations, particulate photocatalysis is advantageous as it is simple and cost-effective and does not require expensive transparent electrodes and electrical energy. However, it faces difficulty in separation of generated hydrogen and oxygen due to the possibility of reverse reaction (Navarro Yerga et al. 2009; Saravanan et al. 2018), which are suppressed by introducing alcohols, aldehydes, etc. (Melvin et al. 2015; Preethi et al. 2016).

Figure 3.8 shows the pictorial illustration of the experimental setups used for photocatalytic (Fig. 3.8a) and photoelectrochemical (Fig. 3.8b) hydrogen generation. In photocatalysis, the hydrogen generation ability of the samples is assessed in hole scavenger-water mixture (commonly used hole scavengers are methanol or ethanol at different v/v ratio with water) under light irradiation (usually a solar simulator with 1 sun intensity). In a typical procedure, a known quantity of catalyst can vary from 10 to 100 mg per 100 ml of 20% (v/v) alcohol-water in a quartz reactor connected to a gas chromatography. The air inside the reactor is removed by argon purging, followed by the light illumination for few hours (typically done for 4 h). The hydrogen generated in the headspace of the reactor is carried by a continuous Ar flow and analyzed using gas chromatography (Fig. 3.8a). To analyze the performance stability of the sample, the sample was centrifuged, dried, and tested for hydrogen generation. The stability of the samples can also be tested by storing the solution under dark conditions and repeating the hydrogen generation experiment as a second run. In the case of photoelectrochemical water splitting, an extra bias is applied in addition to the light illumination, and the increase in the current density under light conditions is the indication of water oxidation process. The H_2 evolved corresponding to the photocurrent can be measured using gas chromatography and water displacement route (Fig. 3.8b).

The hydrogen generation efficiency of different photocatalysts is quantified with the term called solar-to-hydrogen (STH) generation efficiency. The STH of powder photocatalyst for particulate water splitting at AM 1.5G illumination is measured using the formula (Liao et al. 2012):

$$\mathrm{STH} = \frac{\left(\mathrm{mmol}\ H_2/_s\right) * \left(\frac{237\ kJ}{\mathrm{mol}}\right)}{P_{\mathrm{total}}\left(\frac{mW}{\mathrm{cm}^2}\right) * \mathrm{Area}\ (\mathrm{cm}^2)} \tag{3.1}$$

where the $P_{\mathrm{total}} * Area$ represents the total power of incident simulative sunlight (AM 1.5G) on a given area and the numerator is the product of the H_2 evolution rate and the Gibbs free energy for generating 1 mole of H_2 from water. Similarly, the STH of photoelectrochemical solar cells for water splitting at AM 1.5G illumination is defined as (Chen et al. 2011)

$$\mathrm{STH} = \frac{\left|J_{\mathrm{sc}}\left(\frac{mA}{\mathrm{cm}^2}\right)\right| * 1.23\ (V) * \eta_{\mathrm{F}}}{P\left(\frac{mW}{\mathrm{cm}^2}\right)} \tag{3.2}$$

where J_{sc} is the photocurrent density, η_{F} is the faradaic efficiency, and P is the incident illumination power intensity (Chen et al. 2011).

The hydrogen generation values of different heterojunction photocatalysts based on titania are listed in Table 3.1. Although a summary of hydrogen generation volume obtained from different TiO_2-based heterojunctions is given in the table, we will make no attempt at presenting a complete survey of hydrogen generation obtained by TiO_2-based photocatalysts.

3.5 Probing Heterojunctions

The insight on the band alignment, light matter interaction-induced charge transfer dynamics, and the resultant photocatalytic efficiency are essential for fine-tuning the physical and chemical aspects of TiO_2-based heterojunctions which can show higher efficiency for energy conversion. So far, most of the studies on various TiO_2-based heterojunctions for photocatalytic hydrogen generation have been limited to the exploration of synthesis techniques and screening of different materials. Investigations of the charge carrier dynamics across TiO_2-based heterojunctions are limited. The detailed examination of charge carrier dynamics in heterostructures allows us to uncover the hydrogen production process which in turn provides insightful guidance to design highly efficient TiO_2 photocatalysts. This requires accurate characterizations of the material for band offset studies and their light matter interaction properties, apart from the basic characterization techniques such as X-ray diffraction,

Table 3.1 Photocatalytic hydrogen generation values of selected TiO_2-based heterojunctions obtained from recent reports

Photocatalyst	Type of heterojunction	Light source	Quantity of photocatalyst and the medium	Hydrogen generation
Hydrogenated MoS_2 QD-TiO_2 (Saha et al. 2017)	Type 2	1 sun Solar simulator (AM 1.5G)	0.2 mg/mL of 1:5 methanol-water	3.1 mmol g^{-1} h-1
Graphitic carbon nitride nanosheets/(TiO_2) nanoparticle heterostructures (Zhang et al. 2017)	Type 2	Xe lamp (300 W) cutoff filter (vis, $\geq$ 420 nm)	0.5 mg/mL of 1:10 TEOA/water	40 mmol h^{-1}
Anatase-rutile-brookite TiO_2 nanotubes	Type 2	Xe lamp (300 W) with AM 1.5 cutoff filter)	10 mg in ethanol-aqueous solution (1:4 ratio)	161.2 μmol g^{-1} h^{-1}
CdSe/Ag/TiO_2 nanotubes (Enzhou et al. 2018)	Mixed	Xe lamp (340 mW/cm^2)	Photocatalyst film (0.785 cm^2) in 100 mL electrolyte (0.35 M Na_2S and 0.25 M Na_2SO_3)	165.5 μmol cm^{-2} h^{-1}
NiO-Ni-TiO_2 (Ren et al. 2018)	Mixed Schottky and p-n	Xe lamp (300 W)	1 mg/mL in water: Methanol mixture (4:1) (Pt nanoparticles as co-catalyst)	4653 μmol g^{-1} h-^{1}
TiO_2/NiS core-shell nanohybrid (Xu et al. 2018)	Z-scheme	Xe lamp (350 W)	50 mg/80 mL in water: Methanol mixture (4:1)	655 μmol h^{-1} g^{-1}
TiO_2/C_3N_4 (Yan et al. 2016)	Z-scheme	Xe lamp (150 W) (λ = 200–2500 nm)	1 mg/mL in 1:10 (v/v) triethanolamine: Water	10.23 μmol h^{-1}
TiO_2-graphene nanocomposites (Liu et al. 2014)	Type 2	Hg lamp (300 W) λ = 365 nm	1 mg/mL in 4:1 H_2O and CH_3OH (20 mL)	193 mmol h^{-1}
g-C_3N_4/TiO_2 (Tan et al. 2018)	Type 2	Xe lamp (300 W) with a cutoff filter ($\lambda > 420$ nm)	1 mg/mL in 1:10 triethanolamine-water mixture	513 μmol g^{-1} h^{-1}
g-C_3N_4 nanosheets/TiO_2 mesocrystals (Elbanna et al. 2017)	Type 2	200 mW cm^{-2} with 420 nm cutoff filter	3 mg/5 mL in 5:1 water-methanol mixture	3.6 μmol h^{-1}
TiO_2-graphene (Cheng et al. 2012)	Type 2	Xe lamp (300 W)	3.3 mg/ml in 4:1 H_2O-methanol mixture with 0.5 wt% Pt as co-catalyst	668 mmol/h

2D/2D O-g-C_3N_4/TiO_2 (Zhong et al. 2018)	Type 2	Xe lamp (300 W) with a UV cutoff filter ($\lambda > 400$ nm)	1 mg/ml in 5:1 water-TEOA, with 3 wt% Pt co-catalyst	587.1 μmol h^{-1} g^{-1}
Cu-TiO_2 (Montoya and Gillan 2018)	Schottky	UV lamp (photon flux of 4.0×10^{17} photon s^{-1})	1 mg/ml in 2:1 water-methanol solution	8500 μmol h^{-1} g^{-1}
TiO_2/WO_3 nanofibers (Gao et al. 2017a)	Z-scheme	Xe lamp (300 W)	0.05 g in 45 ml deionized water and 25 ml methyl alcohol	128.66 mol g^{-1} h^{-1}

transmission electron microscopy, high-resolution TEM, scanning electron microscopy, UV-visible absorption spectroscopy, X-ray photoelectron spectroscopy, photoluminescence (PL), etc. There are several advanced characterization techniques available for the heterojunction studies. Among them, time-resolved (TR) spectroscopic techniques such as time-resolved photoluminescence (TRPL), time-resolved infrared spectroscopy, time-resolved transient absorption spectroscopy (TAS), and time-resolved diffuse reflectance spectroscopy; Kelvin probe force microscopy (KPFM) and surface photovoltage (SPV) studies; and electrochemical impedance spectroscopy (EIS) and Mott-Schottky (MS) analysis are widely used. This section primarily focuses on how these techniques have been used to study various TiO_2-based heterojunctions for photocatalytic hydrogen generation.

3.5.1 Time-Resolved Spectroscopy

Although various advanced techniques have been utilized to characterize TiO_2-based heterojunctions for their physical, chemical, and optical properties, it is still challenging to investigate the fast or ultrafast charge separation/recombination and charge transfer processes using the conventional characterization tools. Time-resolved spectroscopic studies are the best solution for all these problems as they aid in studying the charge carrier dynamics.

TAS is a spectroscopic tool to study the dynamic processes that occur in the materials during light irradiation. The spectroscopic measurements are performed on the material using pump-probe technique. Among the TiO_2-based heterojunctions in photocatalysis, heterojunctions formed by their polymorphs mainly anatase-rutile interphase are the most widely studied. Despite much collected evidence, the band energy alignment of anatase-rutile heterojunctions and the direction of charge transfer for charge separation and catalytic reactions are still under debate. Thus far, the time-resolved methods used to investigate this system have focus both on the nature of photogenerated electrons and holes (Kafizas et al. 2016; Shen et al. 2014; Wang et al. 2015). For instance, Kafizas et al. (2016) employed TAS to investigate the hole transfer across anatase-rutile heterojunction-based thin films as a function of phase composition. They tracked the photogenerated holes which transferred from rutile to anatase on submicrosecond timescales by exploiting differences in the photoinduced absorption of trapped charges in anatase and rutile. They demonstrated the significance of trap-state energetics in deducing the direction of photogenerated charge pair separation across anatase-rutile heterojunctions using TAS (Fig. 3.9a).

On the other report, Chen et al. (Yubin et al. 2017) studied the charge carrier transfer properties of bare CdSe quantum dots (QDs) and CdSe QDs/TiO_2 structures, obtained by chemical route synthesis, using femtosecond TAS. They found that the presence of TiO_2 decreases the average exciton lifetime of CdSe QDs, owing to the transfer of electron photoexcited CdSe QDs to TiO_2. The band alignment analysis using XPS valence band spectra and the UV-visible absorption spectroscopy revealed that CdSe/TiO_2 acquired type 2 heterostructure. This result emphasizes

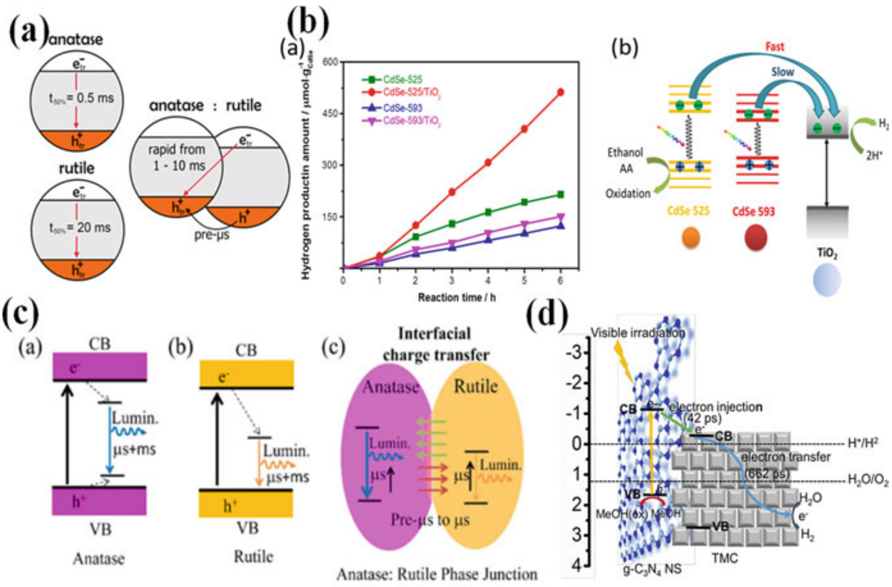

Fig. 3.9 (**a**) Graphical representation of hole transfer pathway in anatase-rutile heterojunction obtained from TAS analysis (Kafizas et al. 2016). (**b**) Photocatalytic hydrogen generation on CdSe-525, CdSe-593, CdSe-525/TiO_2, and CdSe-593/TiO_2 and the proposed photocatalytic process on CdSe/TiO_2 heterostructure (Reprinted with permission from (Yubin et al. 2017) copyright (2017) IOP publishers). CdSe QDs with the reaction time of 12 and 40 min, respectively, exhibited the first exciton absorption peaks at 525 and 593 nm, which were thus denoted as CdSe-525 and CdSe-593. (**c**) Pictorial illustration of charge transfer and recombination pathways at anatase-rutile heterojunction (Reprinted with permission from (Wang et al. 2016) copyright (2016) Elsevier publishers). (**d**) Schematic showing electron transfer in g-C_3N_4 NS (31 wt %)/TMC during visible light irradiation. (Reprinted with permission from (Elbanna et al. 2017) copyright (2017) Journal of American Chemical Society)

the inevitable role of electron transfer between CdSe and TiO_2 in enhancing the photocatalytic hydrogen generation of CdSe QDs/TiO_2 structures compared to CdSe QDs (Fig. 3.9b).

Similarly, Zhang et al. demonstrated the 3D architectures of TiO_2 mesocrystals (TMC) uniformly packed with a chemically exfoliated MoS_2 shell (MoS_2 – TMC) (Zhang et al. 2015) exhibit promising H_2 evolution efficiency (with HER rate of 0.55 mmol h^{-1} g^{-1}) and good reusability (over 25 h) in HER under UV irradiation. The charge carrier dynamics of this heterojunction was monitored by TAS. They observed that the fast decay of electron was within tens of picoseconds, indicating the efficient electron transfer at the electrode-electrolyte interface.

On the other hand, Wang et al. (Wang et al. 2016) explored TRPL technique to study the charge transfer process at an anatase-rutile TiO_2 phase junction for mechanically mixed anatase-rutile sample (Fig. 3.9c). It was demonstrated that the major charge transfer pathway of anatase-rutile heterojunction was from rutile to anatase. They also observed an increase in concentration of the charge carriers on a timescale of microsecond. This was due to the charge separation at the anatase-rutile heterojunction, thus accounting to the high photocatalytic efficiency.

Similarly, Elbanna et al. (Elbanna et al. 2017) studied the charge separation processes in the heterojunction formed by g-C_3N_4 nanosheets (NS) and TiO_2 mesocrystal (TMC) to boost the HER activity. The photocatalytic H_2 evolution rate of g-C_3N_4 NS/TMC (3.6 μmol h^{-1}) was higher than that of g-C_3N_4 NS and g-C_3N_4 NS/P25 composite (~20 times and ~7 times, respectively), under visible light irradiation, without any co-catalyst. To realize the reason behind the difference in activities, fundamental photo-physicochemical processes involved in bulk g-C_3N_4 and composites such as g-C_3N_4 NS and g-C_3N_4/TMC were studied by femtosecond time-resolved diffuse reflectance (fs-TDR) spectroscopy. The results demonstrate that titania mesocrystal acts as an electron transfer channel, promoting charge pair separation in g-C_3N_4/TMC (Fig. 3.9d) which resulted in increase in lifetime of electrons and holes.

A TRPL imaging studies were performed on $PbTiO_3$@TiO_2 heterostructured nanotubes and nitrogen-doped TiO_2 nanoparticles by Jang et al. (Jang et al. 2017), to understand the charge carrier dynamics. The obtained TRPL images revealed that both of these samples possess extremely variant PL lifetimes, where the average lifetime of $PbTiO_3$@TiO_2 heterojunction nanotubes was found to be much higher than that of N-doped TiO_2 nanoparticles, revealing a slow recombination process due to efficient charge separation. These results were well corroborated with their PEC activities.

3.5.2 Kelvin Probe Force Microscopy and Photovoltage Spectroscopy

KPFM is another effective approach to study the charge carrier dynamics and the energy band alignment of a heterojunction. Introducing phase junction in a material is proved to be an effective strategy to obtain enhanced charge separation in photocatalytic water splitting. The charge transfer dynamics across such phase junctions are investigated by KPVM. For instance, Gao et al. (Gao et al. 2017b) investigated the surface potential profile of anatase-rutile TiO_2 phase junction by direct measurement. They observed a built-in electric field up to 1 kV/cm from rutile to anatase nanoparticle using KPFM. In addition, studies using homebuilt spatially resolved surface photovoltage spectroscopy (SRSPS) revealed the vectoral photogenerated electron transfer from rutile to anatase as represented in Fig. 3.10a.

Xie et al. (Xie et al. 2014) fabricated different molar ratios of TiO_2/$BiVO_4$ nanocomposites by chemical and thermal treatments. The photogenerated charge carriers in this composite possessed considerably longer lifetime (up to milliseconds) leaving to efficient charge separation as analyzed from the steady-state and transient-state SPV responses. This results in an unexpected activity of photocatalytic hydrogen generation. They suggested that the unusual spatial transfer of visible light-excited high-energy electrons of $BiVO_4$ to TiO_2 was responsible for the long lifetime

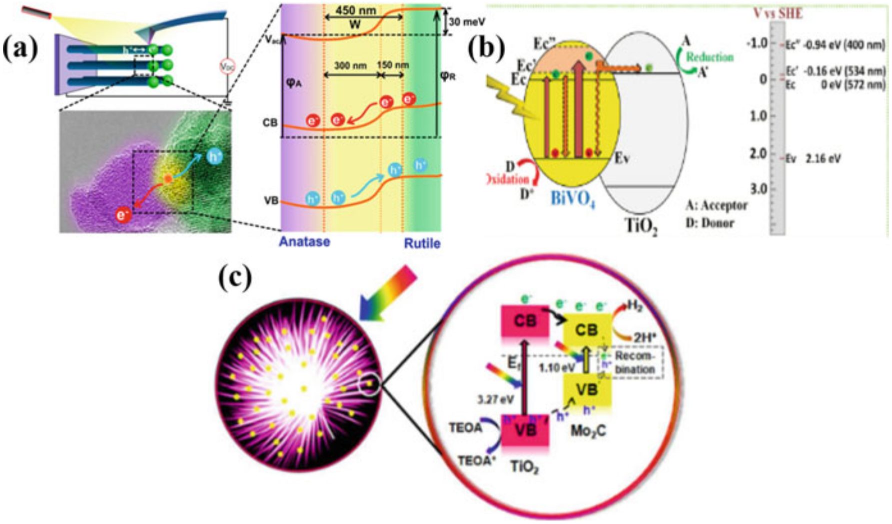

Fig. 3.10 Schematic of (**a**) band energy alignment of a rutile/anatase phase heterojunction and the photogenerated charge transfer direction at the TiO_2 phase junction interface studied using cross-section KPFM. (Reprinted with permission from (Gao et al. 2017b) copyright (2017) Elsevier). (**b**) Photogenerated high-energy electron transfer and separation of $TiO_2/BiVO_4$ system under visible illumination. (Reprinted with permission from (Xie et al. 2014) copyright (2017) Journal of American Chemical Society). (**c**) Schematic illustrating the mechanism for photocatalytic activity of MO_2C/TiO_2 hetero-nanostructures. (Reprinted with permission from (Yue et al. 2017) copyright (2017) RSC publishers)

and enhanced photoexcited charge separation in $TiO_2/BiVO_4$ nanocomposite and is schematically shown in Fig. 3.10b.

Xinzheng et al. (Yue et al. 2017) developed Mo_2C nanoparticles (NP)/3D TiO_2 hetero-nanostructure by well-controlled synthesis strategy for photocatalytic hydrogen production. This heterostructure showed excellent photocatalytic activity (H_2 evolution rate of 39.4 mmol h-^{1} g^{-1}) and was 25 times higher than that of pristine TiO_2 and possessed long-term durability (>20 h). The charge carrier dynamics of this heterostructure were analyzed using PL, TRPL, SPV, and open circuit potential (OCP) decay studies, and the results demonstrated an efficient charge pair separation at Mo_2C/TiO_2 interface. The band alignment of Mo_2C/TiO_2 and the charge transfer were drawn with the aid of Mott-Schottky analysis and UV-visible absorption spectroscopy (Fig. 3.10c).

3.5.3 Impedance Spectroscopy, Mott-Schottky Analysis, and Photocurrent Measurements

The basic step in studying the heterojunction is first to confirm the efficient charge pair separation qualitatively before proceeding to the above characterization techniques to probe the heterojunction. The interfacial charge transfer properties in TiO_2-based heterojunctions can be easily confirmed using electrochemical impedance spectroscopic (EIS) analysis. The Mott-Schottky analysis and I–V measurements provide backup support for the efficient charge pair separation by providing, respectively, the charge density and the current-voltage values. There are numerous studies reported based on these techniques. Few are summed up here.

Lian et al. (Lian et al. 2017) synthesized Pt-Ti^{3+}/TiO_2 where Pt was doped in mesoporous self-doped TiO_2 containing Ti^{3+} using an ionothermal route and obtained a significantly higher hydrogen evolution compared to that of Pt-loaded TiO_2 and commercial P25. The photogenerated electron transfer from bulk to surface of TiO_2 was facilitated by Pt-O bond bridges formed by the presence of various valence states of Pt. This was confirmed using EIS analysis where they observed a smaller semicircle at a high frequency region in the Nyquist plot for Pt-Ti^{3+}/TiO_2. The diameter of the semicircle in the Nyquist plot is in general proportional to the charge transfer resistance. Further, the photocurrent measurements and MS analysis supports the above charge transfer efficiency by providing higher photovoltage and enhanced charge density values, for Pt-Ti^{3+}/TiO_2 compared to Pt-TiO_2 and P25 samples. Thus, a lower resistance of charge transfer across the interface favored the photocatalytic efficiency.

The same methodology was followed by Boppella et al. (Boppella et al. 2017), to study the charge transfer mechanism of gold (Au) and reduced graphene oxide (rGO)-incorporated TiO_2 inverse opals and compared with pristine TiO_2. The plasmonic effects of Au nanoparticles along with the efficient conductivity and effective electron-capturing nature of rGO were directing toward the enhanced charge pair separation in TiO_2@Au@rGO and thereby increasing PEC activity. This was confirmed by their decreased charge transfer resistance in EIS analysis. The increased charge carrier density also boosted photocurrent performance as confirmed from the respective MS plots. The mechanism involved in the charge transfer process in TiO_2@Au@rGO under photo-illumination is illustrated in Fig. 3.11.

In other report by Liu et al. (Liu et al. 2014), the EIS analysis was used in addition to TRPL analysis to study the charge transfer properties of TiO_2-graphene composite (Fig. 3.12). They observed a longer half-life of PL signals from TiO_2 (different

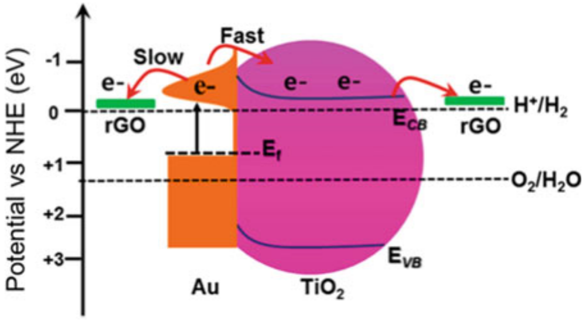

Fig. 3.11 Graphical illustration of the mechanism proposed for the charge separation and transfer in the TiO_2@rGO@Au photoelectrode under illumination conditions. (Reprinted with permission from (Boppella et al. 2017) copyright (2017) Journal of American Chemical Society)

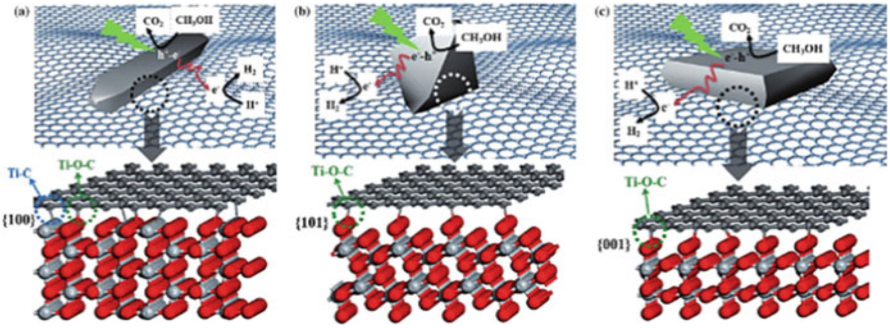

Fig. 3.12 Schematic illustration of atomic structures of interfaces between graphene and different TiO_2 crystal facets and the photocatalytic process by TiO_2-graphene nanocomposites (Liu et al. 2014)

facets)-graphene composites than those of pristine TiO_2 nanocrystals, thus indicating the suppression of photogenerated charge pairs. Similarly, the EIS analysis of TiO_2-graphene composite resulted in a small semicircle showing low resistance of charge transfer across the solid-liquid interface corroborating with their high photocatalytic hydrogen evolution rate.

3.5.4 Other Techniques/Methods

There are many other techniques proposed to study the charge carrier mobility in TiO_2-based heterojunctions. For instance, Scanlon et al. (2013), with the aid of state-of-the-art material simulation techniques and X-ray photoemission experiments, demonstrated that anatase-rutile heterojunction possesses a type 2 staggered band alignment of ~0.4 eV with anatase possessing the higher electron affinity. This indicated that the direction of flow of photogenerated conduction electrons was from rutile to anatase. Their results aid in explaining the instant separation of photoexcited charge carriers between the two phases and highlight a route to efficient photocatalysts. The proposed band alignment of anatase-rutile heterojunction is illustrated in Fig. 3.13a.

Preethi et al. (Preethi et al. 2017b) reported the electrochemical synthesis of triphase TiO_2 nanotubes (anatase-rutile-brookite (ARB) forming heterojunction in a single nanotube). ARB nanotubes showed a hydrogen evolution rate which was nearly twice and 1.6 times that of anatase and anatase-rutile TiO_2 nanotubes, respectively, which are also obtained from the same synthesis technique. They have constructed a band diagram for triphase TiO_2 system and extracted their photoexcited charge transfer pathway from deconvolution analysis of PL spectra and synchrotron radiation-assisted valence band edge analysis. It was demonstrated that the photoexcited charge transfer pathway of triphase TiO_2 was from rutile to anatase to brookite as shown in Fig. 3.13b.

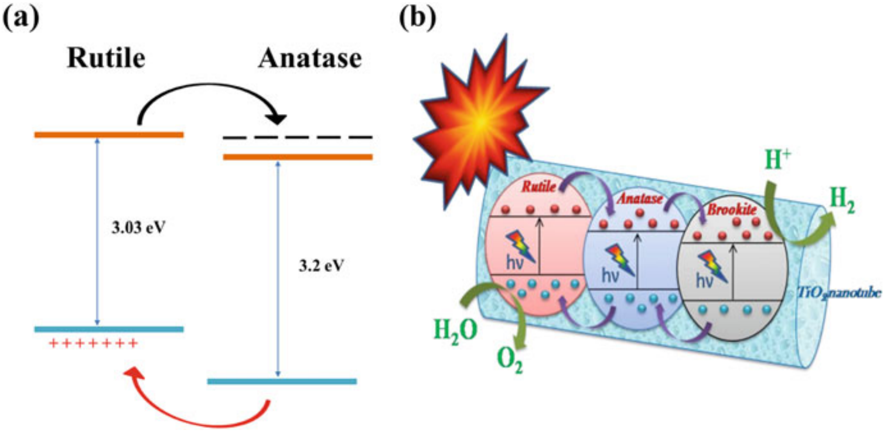

Fig. 3.13 (**a**) Proposed valence and conduction band alignment of the anatase-rutile interface. (Black and red arrows demonstrate the electrons and holes transfer in the conduction and valence band, respectively). Negative and positive signs represent electrons and holes, respectively. (**b**) Graphical abstract representing the charge transfer pathway of triphase TiO_2 nanotubes for photocatalytic hydrogen generation. (Reprinted with permission from (Preethi et al. 2017b) copyright (2017) Elsevier)

Kang et al. (Kang et al. 2012) calculated the band alignment of rutile/anatase TiO_2 heterostructure using passivated quantum dots computationally. They found that the VB maxima of anatase and rutile are nearer to each other, whereas the CB minimum of anatase was about 0.2 eV higher than that of rutile, in agreement with the experimental evidences. They also tested the reliability of this method on several other semiconductors, and they claim to obtain reasonable results.

3.6 Conclusions and Future Perspectives

In the past few years, numerous studies have been carried out for the preparation of TiO_2-based heterojunction photocatalysts for water splitting. In this chapter, we presented a concise appraisal of the TiO_2-based heterojunctions studied recently, their synthesis strategies, and probing mechanisms to understand the light matter interaction-induced charge carrier dynamics. Though the reported heterojunctions of TiO_2 are found to be efficient in photocatalytic hydrogen generation compared to their counterparts, their practical applications and commercialization require further substantial growth in the engineering of TiO_2-based heterojunctions.

Future research directions for the study of TiO_2-based heterojunctions:

(i) It is observed that the detailed reports on TiO_2-based heterojunctions for photocatalytic water splitting are limited. Therefore, to understand a TiO_2 heterojunction in depth, the future studies should have a focus on gaining control over the morphology, contact interface, crystallization, and hierarchical assembly of the heterojunction. In addition, the importance should be given to charge carrier dynamic study during light matter interaction and the formation mechanism of heterojunctions. These studies provide an insight which helps in engineering the material for high-efficiency practical applications.

(ii) The charge transfer pathway of photogenerated charge carriers in TiO_2 heterojunctions requires further systematic and in-depth studies. Most of the studies reveal the evidence for the spatial separation of photogenerated negative- and positive-charge carriers; however, there are only few direct evidences of the actual migration direction of electron-hole pairs across the heterojunction interface. The light matter interaction-induced charge transfer studies are crucial to understand a photocatalyst for any solar conversion application. Therefore, more powerful advanced characterization tools should be used to investigate the TiO_2-based heterojunctions.

(iii) Studies on theoretical calculations and modeling for TiO_2 heterojunctions are limited, and therefore, this area should gain more attention. Experimental evidence of compatibility of materials and their charge carrier dynamics with the theoretical support is highly desirable for obtaining a true knowledge of the photocatalyst behavior in hydrogen generation by water splitting.

(iv) The development of functional new hybrids of photocatalyst materials for heterojunctions to obtain a stable efficient photocatalyst with less investment is one of the primary research goals to be focused on. The materials such as two-dimensional organic and inorganic photocatalysts, perovskite materials in different dimensions, etc. are currently been focused for TiO_2 heterojunction studies.

References

Anandan S, Yoon M (2003) Photocatalytic activities of the nano-sized TiO_2-supported Y-zeolites. J Photochem Photobiol C: Photochem Rev 4:5–18. https://doi.org/10.1016/S1389-5567(03)00002-9

Bärtsch M, Niederberger M (2017) The role of interfaces in heterostructures. ChemPlusChem 82:42–59. https://doi.org/10.1002/cplu.201600519

Boppella R, Kochuveedu ST, Kim H, Jeong MJ, Marques Mota F, Park JH, Kim DH (2017) Plasmon-sensitized graphene/TiO_2 inverse opal nanostructures with enhanced charge collection efficiency for water splitting. ACS Appl Mater Interfaces 9:7075–7083. https://doi.org/10.1021/acsami.6b14618

Chen X, Mao SS (2007) Titanium dioxide nanomaterials: synthesis, properties, modifications, and applications. Chem Rev 107:2891–2959. https://doi.org/10.1021/cr0500535

Chen Z et al (2011) Accelerating materials development for photoelectrochemical hydrogen production: standards for methods, definitions, and reporting protocols. J Mater Res 25:3–16. https://doi.org/10.1557/JMR.2010.0020

Cheng P, Yang Z, Wang H, Cheng W, Chen M, Shangguan W, Ding G (2012) TiO_2–graphene nanocomposites for photocatalytic hydrogen production from splitting water. Int J Hydrog Energy 37:2224–2230. https://doi.org/10.1016/j.ijhydene.2011.11.004

Dasgupta U, Bera A, Pal AJ (2017) Band diagram of heterojunction solar cells through scanning tunneling spectroscopy. ACS Energy Lett 2:582–591. https://doi.org/10.1021/acsenergylett.6b00635

Dong J et al (2018) Boosting heterojunction interaction in electrochemical construction of MoS_2 quantum dots@TiO_2 nanotube arrays for highly effective photoelectrochemical performance and electrocatalytic hydrogen evolution. Electrochem Commun 93:152–157. https://doi.org/10.1016/j.elecom.2018.07.008

Elbanna O, Fujitsuka M, Majima T (2017) g-C_3N_4/TiO_2 Mesocrystals composite for H_2 evolution under visible-light irradiation and its charge carrier dynamics. ACS Appl Mater Interfaces 9:34844–34854. https://doi.org/10.1021/acsami.7b08548

Enzhou L, Peng X, Jia J, Xiaozhuo Z, Zhen J, Jun F, Xiaoyun H (2018) CdSe modified TiO_2 nanotube arrays with Ag nanoparticles as electron transfer channel and plasmonic photosensitizer for enhanced photoelectrochemical water splitting. J Phys D Appl Phys 51:305106

Fujishima A, Honda K (1972) Electrochemical photolysis of water at a semiconductor electrode. Nature 238:37. https://doi.org/10.1038/238037a0

Gao H, Zhang P, Hu J, Pan J, Fan J, Shao G (2017a) One-dimensional Z-scheme TiO_2/WO_3/Pt heterostructures for enhanced hydrogen generation. Appl Surf Sci 391:211–217. https://doi.org/10.1016/j.apsusc.2016.06.170

Gao Y et al (2017b) Directly probing charge separation at Interface of TiO_2 phase junction. J Phys Chem Lett 8:1419–1423. https://doi.org/10.1021/acs.jpclett.7b00285

Hao C, Wang W, Zhang R, Zou B, Shi H (2018) Enhanced photoelectrochemical water splitting with TiO_2@Ag_2O nanowire arrays via p-n heterojunction formation. Sol Energy Mater Sol Cells 174:132–139. https://doi.org/10.1016/j.solmat.2017.08.033

Haring AJ, Ahrenholtz SR, Morris AJ (2014) Rethinking band bending at the P3HT–TiO_2 Interface. ACS Appl Mater Interfaces 6:4394–4401. https://doi.org/10.1021/am500101u

He H et al (2016) MoS_2/TiO_2 edge-on Heterostructure for efficient photocatalytic hydrogen evolution. Adv Energy Mater 6:1600464. https://doi.org/10.1002/aenm.201600464

Hoffmann MR, Martin ST, Choi W, Bahnemann DW (1995) Environmental applications of semiconductor photocatalysis. Chem Rev 95:69–96. https://doi.org/10.1021/cr00033a004

Jang JS et al (2017) Vertically aligned core–shell $PbTiO_3$@TiO_2 heterojunction nanotube array for photoelectrochemical and photocatalytic applications. J Phys Chem C 121:15063–15070. https://doi.org/10.1021/acs.jpcc.7b03081

Kafizas A et al (2016) Where do photogenerated holes go in anatase: rutile TiO_2? A transient absorption spectroscopy study of charge transfer and lifetime. Chem A Eur J 120:715–723. https://doi.org/10.1021/acs.jpca.5b11567

Kalanur SS, Hwang YJ, Joo O-S (2013) Construction of efficient CdS–TiO_2 heterojunction for enhanced photocurrent, photostability, and photoelectron lifetimes. J Colloid Interface Sci 402:94–99. https://doi.org/10.1016/j.jcis.2013.03.049

Kang J, Wu F, Li S-S, Xia J-B, Li J (2012) Calculating band alignment between materials with different structures: the case of anatase and rutile titanium dioxide. J Phys Chem C 116:20765–20768. https://doi.org/10.1021/jp3067525

Kim G-H et al (2015) High-efficiency colloidal quantum dot photovoltaics via robust self-assembled monolayers. Nano Lett 15:7691–7696. https://doi.org/10.1021/acs.nanolett.5b03677

Kumar A, Shalini SG et al (2017) Facile hetero-assembly of superparamagnetic Fe3O4/BiVO4 stacked on biochar for solar photo-degradation of methyl paraben and pesticide removal from soil. J Photochem Photobiol A Chem 337:118–131. https://doi.org/10.1016/j.jphotochem.2017.01.010

Li G et al (2015) Ionothermal synthesis of black Ti^{3+}-doped single-crystal TiO_2 as an active photocatalyst for pollutant degradation and H_2 generation. J Mater Chem A 3:3748–3756. https://doi.org/10.1039/C4TA02873B

Lian Z, Wang W, Li G, Tian F, Schanze KS, Li H (2017) Pt-enhanced mesoporous Ti^{3+}/TiO_2 with rapid bulk to surface Electron transfer for photocatalytic hydrogen evolution. ACS Appl Mater Interfaces 9:16959–16966. https://doi.org/10.1021/acsami.6b11494

Liao C-H, Huang C-W, Wu JCS (2012) Hydrogen production from semiconductor-based Photocatalysis via water splitting. Catalysts 2:490

Licht S (2001) Multiple band gap semiconductor/electrolyte solar energy conversion. J Phys Chem B 105:6281–6294. https://doi.org/10.1021/jp010552j

Liu L, Liu Z, Liu A, Gu X, Ge C, Gao F, Dong L (2014) Engineering the TiO_2–graphene Interface to enhance photocatalytic H_2 production. ChemSusChem 7:618–626. https://doi.org/10.1002/cssc.201300941

Low J, Jiang C, Cheng B, Wageh S, Al-Ghamdi AA, Yu J (2017) A review of direct Z-scheme Photocatalysts. Small Methods 1:1700080. https://doi.org/10.1002/smtd.201700080

Melvin AA, Illath K, Das T, Raja T, Bhattacharyya S, Gopinath CS (2015) M-Au/TiO_2 (M = Ag, Pd, and Pt) nanophotocatalyst for overall solar water splitting: role of interfaces. Nanoscale 7:13477–13488. https://doi.org/10.1039/c5nr03735b

Mills A, Davies RH, Worsley D (1993) Water purification by semiconductor photocatalysis. Chem Soc Rev 22:417–425. https://doi.org/10.1039/cs9932200417

Montoya AT, Gillan EG (2018) Enhanced photocatalytic hydrogen evolution from transition-metal surface-modified TiO_2. ACS Omega 3:2947–2955. https://doi.org/10.1021/acsomega.7b02021

Navarro Yerga RM, Álvarez Galván MC, del Valle F, Villoria de la Mano JA, Fierro JLG (2009) Water splitting on semiconductor catalysts under visible-light irradiation. ChemSusChem 2:471–485. https://doi.org/10.1002/cssc.200900018

Niu M, Cheng D, Cao D (2014) SiH/TiO_2 and GeH/TiO_2 heterojunctions: promising TiO_2-based Photocatalysts under visible light. Sci Rep 4:4810. https://doi.org/10.1038/srep04810

Park S, Ruoff RS (2009) Chemical methods for the production of graphenes. Nat Nanotechnol 4:217. https://doi.org/10.1038/nnano.2009.58

Piyush K, Yun Z, Najia M, Ujwal KT, Benjamin DW, Ryan K, Karthik S (2018) Heterojunctions of mixed phase TiO_2 nanotubes with Cu, CuPt, and Pt nanoparticles: interfacial band alignment and visible light photoelectrochemical activity. Nanotechnology 29:014002

Preethi LK, Antony RP, Mathews T, Loo SCJ, Wong LH, Dash S, Tyagi AK (2016) Nitrogen doped anatase-rutile heterostructured nanotubes for enhanced photocatalytic hydrogen production: promising structure for sustainable fuel production. Int J Hydrog Energy 41:5865–5877. https://doi.org/10.1016/j.ijhydene.2016.02.125

Preethi LK, Antony RP, Mathews T, Walczak L, Gopinath CS (2017a) A study on doped heterojunctions in TiO_2 nanotubes: an efficient Photocatalyst for solar water splitting. Sci Rep 7:14314. https://doi.org/10.1038/s41598-017-14463-0

Preethi LK, Mathews T, Nand M, Jha SN, Gopinath CS, Dash S (2017b) Band alignment and charge transfer pathway in three phase anatase-rutile-brookite TiO_2 nanotubes: an efficient photocatalyst for water splitting. Appl Catal B Environ 218:9–19. https://doi.org/10.1016/j.apcatb.2017.06.033

Ren X et al (2018) NiO/Ni/TiO_2 nanocables with Schottky/p-n heterojunctions and the improved photocatalytic performance in water splitting under visible light. J Colloid Interface Sci 530:1–8. https://doi.org/10.1016/j.jcis.2018.06.071

Saha A, Sinhamahapatra A, Kang T-H, Ghosh SC, Yu J-S, Panda AB (2017) Hydrogenated MoS_2 QD-TiO_2 heterojunction mediated efficient solar hydrogen production. Nanoscale 9:17029–17036. https://doi.org/10.1039/C7NR06526D

Saravanan R, Manoj D, Qin J, Naushad M, Gracia F, Lee AF, Khan MM, Gracia-Pinilla MA (2018) Mechanothermal synthesis of Ag/TiO_2 for photocatalytic methyl orange degradation and hydrogen production. Process Saf Environ Prot 120:339–347. https://doi.org/10.1016/j.psep.2018.09.015

Scanlon DO et al (2013) Band alignment of rutile and anatase TiO_2. Nat Mater 12:798–801. https://doi.org/10.1038/nmat3697

Shen S, Wang X, Chen T, Feng Z, Li C (2014) Transfer of Photoinduced electrons in anatase–rutile TiO_2 determined by time-resolved mid-infrared spectroscopy. J Phys Chem C 118:12661–12668. https://doi.org/10.1021/jp502912u

Siripala W, Ivanovskaya A, Jaramillo TF, Baeck S-H, McFarland EW (2003) A Cu_2O/TiO_2 heterojunction thin film cathode for photoelectrocatalysis. Sol Energy Mater Sol Cells 77:229–237. https://doi.org/10.1016/S0927-0248(02)00343-4

Sun S (2015) Recent advances in hybrid Cu_2O-based heterogeneous nanostructures. Nanoscale 7:10850–10882. https://doi.org/10.1039/C5NR02178B

Tan Y, Shu Z, Zhou J, Li T, Wang W, Zhao Z (2018) One-step synthesis of nanostructured g-C_3N_4/TiO_2 composite for highly enhanced visible-light photocatalytic H_2 evolution. Appl Catal B Environ 230:260–268. https://doi.org/10.1016/j.apcatb.2018.02.056

Uddin MT, Nicolas Y, Olivier C, Jaegermann W, Rockstroh N, Junge H, Toupance T (2017) Band alignment investigations of heterostructure NiO/TiO_2 nanomaterials used as efficient heterojunction earth-abundant metal oxide photocatalysts for hydrogen production. Phys Chem Chem Phys 19:19279–19288. https://doi.org/10.1039/C7CP01300K

Wang X et al (2015) Transient absorption spectroscopy of Anatase and rutile: the impact of morphology and phase on photocatalytic activity. J Phys Chem C 119:10439–10447. https://doi.org/10.1021/acs.jpcc.5b01858

Wang X, Shen S, Feng Z, Li C (2016) Time-resolved photoluminescence of anatase/rutile TiO_2 phase junction revealing charge separation dynamics. Chin J Catal 37:2059–2068. https://doi.org/10.1016/S1872-2067(16)62574-3

Xiao J, Xie Y, Cao H (2015) Organic pollutants removal in wastewater by heterogeneous photocatalytic ozonation. Chemosphere 121:1–17. https://doi.org/10.1016/j.chemosphere.2014.10.072

Xie M, Fu X, Jing L, Luan P, Feng Y, Fu H (2014) Long-lived, visible-light-excited charge carriers of TiO_2/$BiVO_4$ nanocomposites and their unexpected photoactivity for water splitting. Adv Energy Mater 4:1300995. https://doi.org/10.1002/aenm.201300995

Xu QC, Wellia DV, Ng YH, Amal R, Tan TTY (2011) Synthesis of porous and visible-light absorbing Bi_2WO_6/TiO_2 heterojunction films with improved photoelectrochemical and photocatalytic performances. J Phys Chem C 115:7419–7428. https://doi.org/10.1021/jp1090137

Xu F, Zhang L, Cheng B, Yu J (2018) Direct Z-scheme TiO_2/NiS Core–Shell hybrid nanofibers with enhanced photocatalytic H_2-production activity. ACS Sustain Chem Eng 6:12291–12298. https://doi.org/10.1021/acssuschemeng.8b02710

Yan J, Wu H, Chen H, Zhang Y, Zhang F, Liu SF (2016) Fabrication of TiO_2/C_3N_4 heterostructure for enhanced photocatalytic Z-scheme overall water splitting. Appl Catal B Environ 191:130–137. https://doi.org/10.1016/j.apcatb.2016.03.026

Yang J-S, Lin W-H, Lin C-Y, Wang B-S, Wu J-J (2015) n-Fe_2O_3 to N^+-TiO_2 heterojunction Photoanode for photoelectrochemical water oxidation. ACS Appl Mater Interfaces 7:13314–13321. https://doi.org/10.1021/acsami.5b01489

Yubin C, Chi-Hung C, Zhixiao Q, Shaohua S, Tennyson D, Clemens B (2017) Electron-transfer dependent photocatalytic hydrogen generation over cross-linked CdSe/TiO_2 type-II heterostructure. Nanotechnology 28:084002

Yue X, Yi S, Wang R, Zhang Z, Qiu S (2017) A novel architecture of dandelion-like Mo_2C/TiO_2 heterojunction photocatalysts towards high-performance photocatalytic hydrogen production from water splitting. J Mater Chem A 5:10591–10598. https://doi.org/10.1039/C7TA02655B

Zhang P, Tachikawa T, Fujitsuka M, Majima T (2015) Efficient charge separation on 3D architectures of TiO_2 mesocrystals packed with a chemically exfoliated MoS_2 shell in synergetic hydrogen evolution. Chem Commun 51:7187–7190. https://doi.org/10.1039/C5CC01753J

Zhang H, Liu F, Wu H, Cao X, Sun J, Lei W (2017) In situ synthesis of g-C_3N_4/TiO_2 heterostructures with enhanced photocatalytic hydrogen evolution under visible light. RSC Adv 7:40327–40333. https://doi.org/10.1039/C7RA06786K

Zhao Z-J et al (2017) Three-dimensional plasmonic Ag/TiO_2 nanocomposite architectures on flexible substrates for visible-light photocatalytic activity. Sci Rep 7:8915. https://doi.org/10.1038/s41598-017-09401-z

Zhong R, Zhang Z, Yi H, Zeng L, Tang C, Huang L, Gu M (2018) Covalently bonded 2D/2D O-g-C_3N_4/TiO_2 heterojunction for enhanced visible-light photocatalytic hydrogen evolution. Appl Catal B Environ 237:1130–1138. https://doi.org/10.1016/j.apcatb.2017.12.066

Chapter 4
Quantum Dots in Green Photocatalytic Applications for Degradation of Environmental Pollutants and Hydrogen Evolution

Selvaraj Devi and Vairaperumal Tharmaraj

Contents

4.1 Introduction 88
4.2 Metal-Based Quantum Dots for Hydrogen Evolution and Pollutant Degradation 89
  4.2.1 Metal Sulfide Quantum Dots 89
  4.2.2 Metal Oxide Quantum Dots 93
  4.2.3 Metal Quantum Dots 94
4.3 Metal-Free Quantum Dots for Hydrogen Evolution and Pollutant Degradation 97
  4.3.1 Carbon Quantum Dot (C QD)-Based Photocatalyst 98
  4.3.2 Graphene Quantum Dot-Based Photocatalyst 101
4.4 Conclusions 103
References 104

Abstract In recent years, environmental pollutions and energy issues have attracted much attention for the sustainable development of human life. It is of great challenge for the researcher to find a clean, biocompatible, nontoxic, and environment-friendly method for solving the problems associated with the environment. Photocatalysis is one of the effective strategies for mitigating the energy crisis and environmental pollutions. Several photocatalysts were developed for the efficient degradation of environmental pollutants into useful products. Mainly, quantum dot (QD)-based photocatalysts have attracted the researchers due to their attractive properties such as quantum confinement effect, large surface area, and high catalytic activity that makes its promising applications in the field of photocatalysis, sensing, light-emitting diodes, energy storage devices, bioimaging, and solar cell.

S. Devi
Department of Inorganic Chemistry, University of Madras, Chennai, India

V. Tharmaraj (✉)
Department of Analytical Chemistry, National Chung-Hsing University, Taichung, Taiwan

S. Rajendran et al. (eds.), *Green Photocatalysts for Energy and Environmental Process*, Environmental Chemistry for a Sustainable World 36,
https://doi.org/10.1007/978-3-030-17638-9_4

This chapter deals with the recent developments of QDs, (a) overview of quantum dots such as carbon, graphene, cadmium sulfide, zinc oxide, cadmium selenium, core-shell quantum dots and (b) photocatalytic applications of QDs such as carbon materials like carbon- and graphene-based QDs and metal-, metal sulfide-, and metal oxide-based QDs. The detailed discussions are made on the efficiency of photocatalytic behaviors of QDs, surface-modified QDs with different functionalities, and the doping of QDs with other elements like S, N, B, Si, etc. and also provided the reaction mechanisms of QDs in photocatalysis.

Keywords Green photocatalyst · Photocatalysis · Quantum dots · Environmental pollutants · Photodegradation · Carbon quantum dots · Graphene quantum dots

4.1 Introduction

Currently, growth of population and industries and large consumption of nonrenewable fossil fuels such as coal and natural gas lead to environmental pollution and energy shortage that restricts the progress of human life and their survival in the world (Alqadami et al. 2017). Hence, it is necessary to develop a technology for solving environmental problems and energy crisis by eliminating pollutants and producing renewable energy sources like hydrogen (H_2), respectively. Various techniques such as flocculation, coagulation, adsorption, and membrane-based technologies have been used for the decomposition of organic/inorganic pollutants present in water (Naushad et al. 2018; Kumar et al. 2017). However, these technologies lead to the production of harmful substances at the end of decomposition that limits its practical applications. Recently, photocatalytic technique offers a "green" approach for the complete elimination of environmental pollutants and the production of hydrogen from water splitting that tackles the current environmental and energy issues (Hoffmann et al. 1995).

In general, photocatalysts are metal oxide semiconductors. They are inexpensive, stable, and earth-abundant photocatalysts. Initially titanium dioxide (TiO_2) and zinc oxide (ZnO) have been used to bleach the dyes. Afterward, Fujishima and Honda have reported the production of H_2 on TiO_2 photoelectrode (1972). Nevertheless, some limitations such as low utilization of solar light (4%) and fast electron-hole recombination hamper the practical applications of TiO_2 and ZnO (Chen and Mao 2007). The photocatalytic efficiency can be improved by developing visible light-driven (VLD) heterogeneous photocatalysts with suitable band energy level for utilizing the solar energy effectively (Kudo and Miseki 2009). Since, researchers have been focusing on the development of cheap novel QD-based greener photocatalysts with high efficiency to harvest light absorption in the whole solar spectrum region.

A variety of VLD photocatalysts with heterojunction such as m-$BiVO_4$/t-$BiVO_4$, Ag_2O/Ag_2CO_3, and BiOI/BiOBr were developed for H_2 production and degradation of organic pollutants. Unfortunately, these photocatalysts could suffer high recombination rate and limited nonlocalized conductivity and absorb visible light with wavelength shorter than 450 nm and low surface area that leads to poor photocatalytic activity (Lopes et al. 2016; Cao et al. 2011; Moniz et al. 2015; Zhang et al. 2009). To overcome these problems, the photocatalytic materials were modified with quantum dots to increase the surface area which absorb the light in whole solar region and thereby increase their photocatalytic performance.

Quantum dots, also called as colloidal semiconductor, are zero-dimensional nanostructures. QDs have the nanoscale dimension smaller than 20 nm in diameter with composing an inorganic core surrounded by an organic layer in outside. Quantum dots have attracted tremendous research interest due to their excellent photocatalytic properties and their applications in photocatalysis, sensing, light-emitting diodes, energy storage devices, bioimaging, and solar cell. The properties of QDs can be tuned by doping or modification of surface with different functionalities. The advantages of QDs in photocatalysis are as follows.

1. It generates multiple charge carriers in a single photon.
2. Due to the quantum size effect, (a) the exciton properties are affected due to the large surface area, leading to large access of electrons and holes to the surface; thereby oxidation and reduction processes occurred efficiently; (b) the bandgap width is increased with fast diffusion of photogenerated charges to the surface of QDs.
3. There is a high area of interface that can be constructed between the two semiconductors, resulting in enhanced separation of photoinduced electrons and holes.

Herein, we highlighted the photocatalytic applications of various QD-based materials.

4.2 Metal-Based Quantum Dots for Hydrogen Evolution and Pollutant Degradation

4.2.1 Metal Sulfide Quantum Dots

In the past few decades, many photocatalysts with wide bandgap have been developed for the production of H_2 by splitting of water and H_2S, although they are not highly efficient for H_2 production under visible light irradiation. Hence, researches have been focusing on metal sulfides with narrow bandgap-based visible light-driven photocatalysts.

Among II–VI semiconductor, CdS, an n-type semiconductor with narrow bandgap of 2.4 eV, is an attractive material as sensitizer in photocatalysis due to its extraordinary properties such as adjustable bandgaps, tunable morphology, and highly light absorption capability. However, the low separation efficiency between photoinduced electrons and holes reduces the photocatalytic activity of bulk CdS. The charge separation can be promoted by decreasing the size of bulk CdS in nanometer scale. Among different-shaped CdS, CdS quantum dots act as efficient photocatalysts due to their large surface area, more visible light absorption, and quantum confinement effect. However, the corrosion of CdS QD caused by the photoinduced holes created during photocatalytic reaction and rapid charge recombination restricts its application. The incorporation of CdS QD on certain supporting materials such as carbon materials and carbon nitride and formation of composite with other semiconducting materials like TiO_2 or core/shell nanostructure enhanced the stability, charge separation, and photocatalytic efficiency of CdS QD. The pure CdS QD or composites can be synthesized by various methods including impregnation, sol-gel, and coprecipitation.

For instance, CdS QD was deposited on magnetized powder activated carbon (MPAC) through impregnation techniques. The QDs have been synthesized using cadmium chloride and thiourea as starting precursors and thioglycolic acid as capping agent. The photocatalytic property of CdS QD deposited on MPAC was examined by the degradation of methylene blue (MB), crystal violet (CV), and ethyl green (EG) under two different solar irradiation sources, namely, fluorescent lamp and natural sunlight (Samadi-Maybodi and Hajar Farzinia 2018). The photocatalytic efficiency for degradation of organic pollutants was influenced by the effect of pH, irradiation time, agitation rate, and amount of catalyst (Thakur et al. 2017). As compared with fluorescence lamp, the photocatalytic efficiency of CdS QD deposited on MPAC under sunlight irradiation was higher. The same group has also synthesized amino acid-stabilized CdS QD for degradation of alizarin under visible light (Samadi-Maybodi et al. 2014).

The photocatalytic activity and photostability of CdS QD can also be improved by its coupling with different nanostructures of TiO_2 in appropriate amount. CdS QD was deposited on TiO_2 nanotube by ionic layer adsorption reaction method for hydrogen production and degradation of RhB under visible light irradiation (Zhu et al. 2015). The photocatalytic activity of CdS QD/TNT was higher than that of pure CdS or TNT due to the improvement in light harvesting property and charge separation between electron and holes. However, the amount of QD deposited on TNT will determine the photocatalytic performance of QD. The photocatalytic activity was decreased if more number of CdS deposited on TNT due to the aggregation of CdS particles. This material can be reused with good stability after recovering from the photocatalytic reaction. As similar, CdS combined with TiO_2 nanowires, carbon nitride coupled with CdS-TiO_2 nanodot, and polymeric g-C_3N_4 coupled with CdS QDs have been used for hydrogen production under visible light (Wu et al. 2012; Jiang et al. 2017; Ge et al. 2012). Li et al. have also used CdS composites for degradation of organic pollutants and oxidation of NO under visible light (2009). Recently, Zhang et al. (2018) have achieved degradation of ethylene using TNT/CdS/reduced graphene oxide. Other than TiO_2, indium- and gallium oxide-supported CdS QDs have also been used for the production of H_2 by splitting of water under visible light (Pan et al. 2014). Herein, platinum was used as a cocatalyst. The photocatalytic activity of CdS QD can be improved by varying the defects present on the surface of metal oxides.

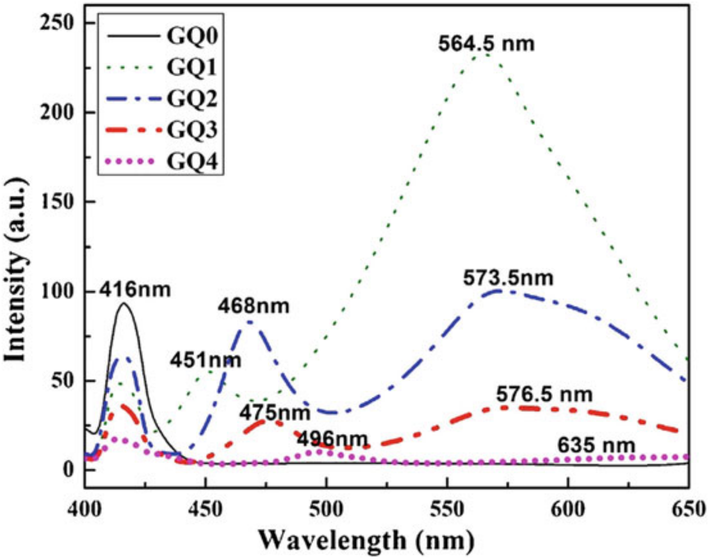

Fig. 4.1 Photoluminescence spectra of CdS QD on glass samples

Wang et al. (2014) have prepared hybrid CdS QD containing nickel and mercaptopropionic acid for hydrogen production from glycerol and water under visible light irradiation. The hybrid CdS QD showed higher photocatalytic activity than that of MPA/CdS QD. Zou et al. (2018) have fabricated a new type of heterostructure catalytic materials as tungsten sulfide (WS_2)/graphitic carbon nitride (CN) nanosheet and CdS quantum dot (QD) using impregnation method for production of H_2. The TEM studies have shown the deposition of QD on CN nanosheet. UV-visible spectroscopy studies revealed that the QD with WS_2 or CN showed poor absorption ability in the visible range that decreased the photocatalytic efficiency of QDs/WS_2 or QDs/CN. The evolution rate of H_2 under visible light irradiation was higher than that of pure CN nanosheet.

Janbandhu et al. (2018) have reduced the photocorrosion property of CdS QD by its growth on borosilicate glass system (SiO_2-B_2O_3-Na_2O-ZnO) through conventional melt quenching method. The growth of CdS QD on glass samples was monitored by photoluminescence (PL) studies. The PL spectra showed that the emission peak was shifted to longer wavelength with decrease in the intensity (Fig. 4.1). This is due to the increased size and decreased electron-hole recombination of QD. Powder XRD pattern was confirmed the amorphous nature of glass and hexagonal nature of QD. Moreover, the color of the glass has also been changed. The photocatalytic study was carried out on degradation of methylene blue (MB) under sunlight irradiation. The decrease in the absorption peak at 663 nm indicated the degradation of MB.

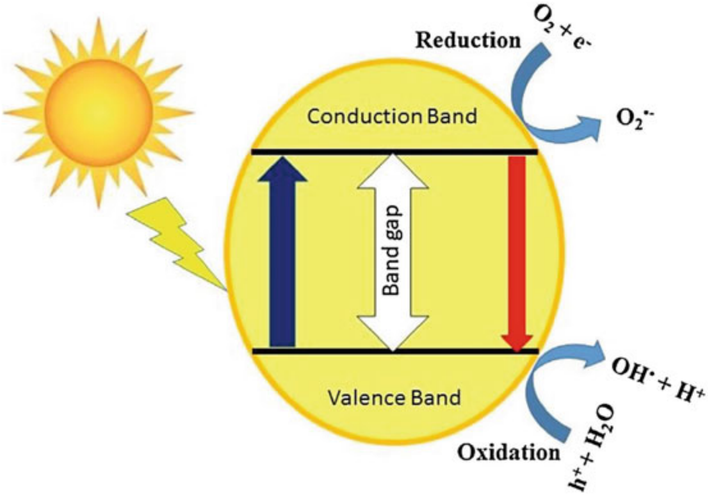

Scheme 4.1 Proposed mechanism for degradation of MB using CdS QDs on glass matrix

Scheme 4.1 shows the possible mechanism for degradation of MB using CdS QD on glass matrix. At first, the holes are created in the valence band (VB) by jumping the electrons to the conduction band (CB) when the suspension irradiated under sunlight. The redox reactions occurred on catalyst by using electron (e^-)-hole (h^+) pairs. During the redox reaction, the catalyst accepts electrons into its VB and donates the excited electron to CB. Furthermore, the reaction between water, photogenerated holes, electrons, and dissolved oxygen produced free radicals such as OH, superoxide, hydroperoxyl, and hydroxyl radicals followed by MB oxidation into CO_2 and H_2O. Similarly, H_2 was produced from copious waste H_2S under solar light irradiation using stable and efficient orthorhombic CdS QDs-GeO_2 glass as photocatalyst (Apte et al. 2012). Lead sulfide QD nanocomposite can also be used for degradation of organic pollutants like glyphosate under visible light irradiation (Lv et al. 2018). Due to the toxic nature of Cd and Pb, other metal sulfides such as MoS_2, ZnS, and SnS_2 QDs have been used in photocatalytic applications.

Recently, SnS_2 QD-supported graphene oxide was used for the photocatalytic reduction of Cr(VI) under visible light irradiation (Yuan et al. 2017). MoS_2-decorated g-C_3N_4/Ag heterostructured photocatalyst was synthesized via a two-step process, namely, in situ microemulsion-assisted reduction and wetness impregnation method (Fu et al. 2018). The photocatalytic activity of the material was evaluated using methyl orange under visible light irradiation. The enhanced photocatalytic activity of MoS_2 QD-decorated g-C_3N_4/Ag hybrid photocatalysts can be attributed to the efficient separation of photogenerated charge carriers, enhanced visible light absorption, large surface area, and unique defect-rich structure.

Zinc (Zn)-based nanomaterials have also attracted great attention in photocatalysis. Zinc sulfide (ZnS) QD was used in the field of medical and environmental applications because of its high surface area that enhanced the absorption of photon at the nanointerfaces and also increased the bandgap energy. Mansur et al. (2014) have prepared ZnS QDs with biocompatible capping ligand such as chitosan by chemical precipitation method using zinc chloride and sodium sulfide as a starting precursors. The photocatalytic activity was investigated by the degradation of methyl blue (MB) and methyl orange (MO). Kaur et al. (2017) have synthesized ZnS QDs using dodecyl sulfate as a stabilizing agent through coprecipitation method using zinc acetate dihydrate and sodium sulfide as a precursor for QDs. The catalytic activity was tested under solar light for degradation of brilliant green dye.

4.2.2 Metal Oxide Quantum Dots

Metal oxide semiconductors like TiO_2, ZnO, and SnO_2 QDs have been used as photocatalyst for water treatment. Among them, TiO_2 QDs were widely used in photocatalytic reactions due to their unique properties such as thermal stability and nontoxicity. However, the drawbacks such as agglomeration and poor recovery of TiO_2 QDs hindered their applications in photocatalysis. To overcome the drawbacks, recently Pan et al. (2018) have formed TiO_2 QDs in the porous of SiO_2 foams through in situ hydrolysis of Ti-alkoxide for H_2 evolution. The aggregation of TiO_2 QDs and their phase transformation from anatase to rutile can be prohibited through the anchoring effect of QDs in the pore wall of SiO_2 foams. The XRD pattern confirmed the anatase phase of TiO_2 QDs. The enhanced H_2 evolution rate on TiO_2 QDs/SiO_2 foams was due to the high anatase crystalline phase that enhanced light-driven activity and shorter electron transfer distance.

ZnO has also received great attention among metal oxide semiconductors owing to their easy synthesis for the formation of different nanostructures such as nanoribbons, nanowires, nanorods, nanobelts, etc. It has excellent physicochemical properties such as chemical stability, large exciton binding energy, and high optical activity. Several methods such as hydrothermal synthesis, spray pyrolysis, thermal evaporation, ion beam-assisted deposition, chemical vapor deposition, sputter deposition, template-assisted growth, and laser ablation are available for synthesizing ZnO nanostructured materials. The suitable bandgap (~3.37 eV) of ZnO allows the degradation of organic pollutants in photocatalytic applications.

Wahab et al. (2013) have used ZnO QDs for the removal of indoor volatile organic compounds like acetaldehyde under UV irradiation. White color ZnO QDs were synthesized through refluxing zinc nitrate hexahydrate, n-propylamine, and sodium dodecyl sulfate (SDS) in methanol. TEM images showed the formation of aggregated spherical ZnO QDs (Fig. 4.2a), and the lattice constant obtained from the distance between adjacent lattice planes confirmed the wurtzite hexagonal phase of ZnO (Fig. 4.2b).

The synthesized ZnO QDs were highly pure with no structural defects. Photocatalytic reaction was also carried out under light irradiation for the conversion of acetaldehyde into acetic acid. The higher photocatalytic activity of ZnO QD was due to their high surface area that allowed the adsorption of more number of

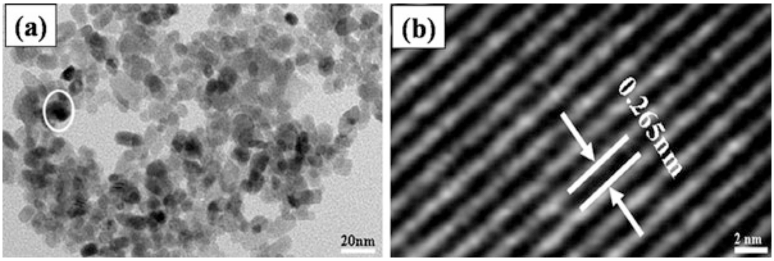

Fig. 4.2 HR-TEM images of ZnO QDs at different magnifications (**a** and **b**)

CH_3CHO. The pure ZnO QDs absorb only UV region of solar light with the fast recombination rate of electron-hole pairs, resulting in decreased photocatalytic activity. The photocatalytic activity of ZnO QD can be improved by changing the bandgap of ZnO that absorbs visible region of solar light.

Recently, the bandgap of ZnO QDs can be changed by the deposition of QD on GO through simple chemical method. The formation of strong chemical bond between ZnO QDs and GO, resulting in increased light harvesting ability. The photocorrosion property of ZnO can be reduced by adding a certain amount of GO with ZnO QD. The photocatalytic efficiency was studied from the degradation of MO (Tayyebi et al. 2016). The enhanced photocatalytic activity of hybrid can be attributed to the inhibition of electron-hole recombination, the extended absorption of visible light, and the adsorption of more number of MO on high surface area of GO. Due to the narrow spectral response for sunlight and high recombination rate of photogenerated carriers, other metal oxide semiconductors such as SnO_2, WO_3, etc. have been employed as photocatalyst for the degradation of organic pollutants and H_2 evolution. Recently, Zhao et al. (2018) have improved the catalytic performance of GO/Mg-doped ZnO by modification with WO_3QDs (GOMZ) via a coprecipitation method. The photocatalytic degradation of composite was tested using RhB degradation under sunlight irradiation.

4.2.3 Metal Quantum Dots

Noble metal QDs such as Ag and Pt have been employed as photocatalyst. Bi et al. (2016) have used Pt with $Bi_{12}O_{17}Cl_2$ for the degradation of methyl orange and phenol. Similarly, Di et al. (2016) have used Ag quantum dot (Ag QD)-modified BiOBr ultrathin nanosheets for the degradation of antibiotic agent such as tetracycline hydrochloride (TC) and ciprofloxacin (CIP) and CO_2 reduction under visible light irradiation. Visible light irradiation on modified Ag QDs activates the molecular oxygen through hot electron reduction, and also they act as charge separation, adsorption, and photocatalytic reaction centers. Instead of expensive and less availability of noble metals, Bi QDs were used for CO_2 reduction (Yang et al. 2018).

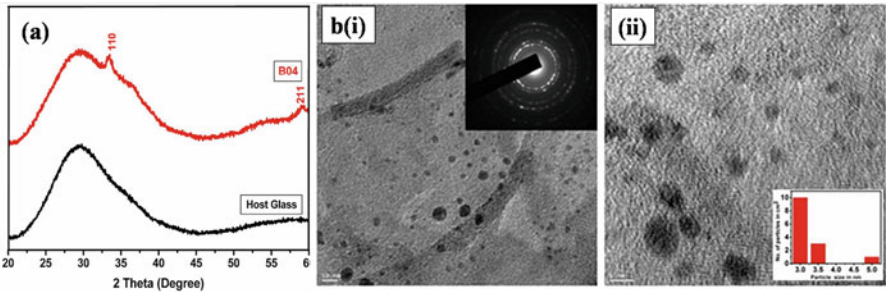

Fig. 4.3 (**a**) XRD pattern of glass and Bi QDs/glass matrix. (**b**) TEM images of Bi QDs/glass matrix

Bismuth, a semimetal having rhombohedral structure, has attracted much attention for studying quantum size effects due to their unique electronic band structure. They were used as a promising material in the application of optical devices, thermoelectricity, and magnetoresistance. Bismuth QDs without cocatalyst can be used for hydrogen evolution from poisonous H_2S under solar light. However, their unstability in air limits their applications. To improve the stability of pure Bi QDs, it was grown on germanate glass through auto-thermo-reduction route (Apte et al. 2013). The formation of Bi QDs on glass matrix was confirmed from XRD pattern, indicating the amorphous nature and cubic phase of Bi QDs (Fig. 4.3a). The broadening of peak indicated the formation of bismuth along with bismuth ions in glass matrix. TEM images showed the formation of spherical-shaped Bi QDs with homogenous distribution as seen in Fig. 4.3b. The hydrogen evolution rate on Bi QDs was higher than that of metal sulfide and metal oxide semiconductors. The energy required for the photo splitting of hydrogen sulfide (H_2S) was less compared to that of H_2O.

Xiao et al. (2017) have deposited Bi QDs on TiO_2 NPs via thermal process for the reduction of bromate under visible light irradiation without using any sacrificial agent. Sacrificial agent is the material needed to deplete photogenerated holes that increased complexity and expensive operation. The photocatalytic efficiency of Bi QDs/TiO_2 was increased toward bromate reduction due to the lowering of charge carrier recombination.

QDs containing two metals have been also considered as attractive materials in photocatalytic reaction. As well known, cadmium selenide (CdSe) quantum dots were employed as efficient photocatalyst in photooxidation due to their size-tunable bandgap that allowed the absorption of UV-visible region of solar light. However, due to the toxic nature of bare Cd-based nanomaterials, the materials were coated with other chemicals to prevent the leaching of Cd^{2+} in water. Hemmateenejad et al. (2015) have prepared biocompatible polysaccharide like starch that stabilized CdSe QDs for degradation of methyl green and malachite green.

Recently, Thirugnanam et al. (2017) have synthesized CdSe QDs on graphene oxide (GO) as photocatalyst via chemical precipitation method using cadmium acetate and selenium as precursor. The catalytic efficiency was tested toward the

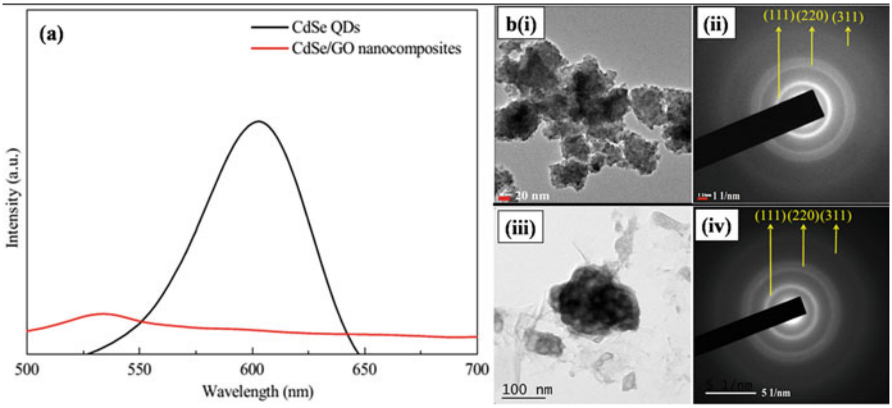

Fig. 4.4 (**a**) PL spectra of CdSe QDs and CdSe/GO nanocomposite. (**b**) TEM images of CdSe (*i* and *ii*) and CdSe/GO nanocomposite (*iii* and *iv*)

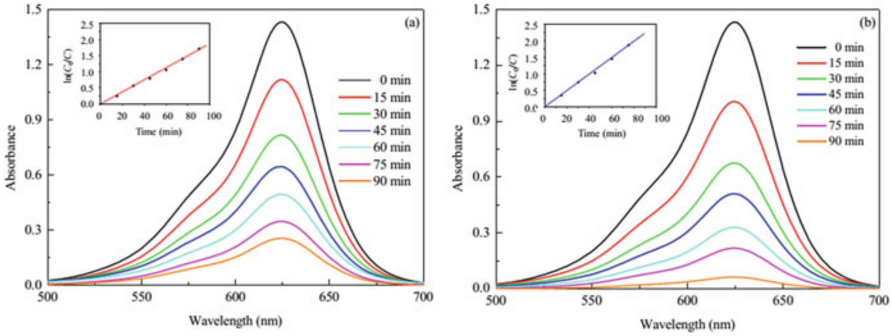

Fig. 4.5 UV-Vis absorption spectra of brilliant green dye over (**a**) CdSe QDs; (**b**) CdSe QDs/GO nanocomposite. Inset shows linear plot between ln(C_0/C) and time interval

degradation of brilliant green under sunlight. The PL spectra of CdSe/GO and CdSe QDs showed the decrease in the intensity of CdSe/GO as compared with CdSe QDs that attributed to the inhibition of electron-hole pair recombination, resulting in increased photocatalytic activity (Fig. 4.4a). The blueshift of emission peak in composite was due to the electrostatic interaction between GO and CdSe and also van der Waals interaction between GO layers. TEM images showed the spherical shape of CdSe QDs (Fig. 4.4b). After decoration with GO, CdSe are agglomerated on GO surface as seen in Fig. 4.4b(*iv*). The SAED pattern showed the zinc blende cubic phase of CdSe (Fig. 4.4b (*ii*) and (*iv*)).

UV-visible spectra for degradation of brilliant green (BG) dye were monitored from the peak intensity at 624 nm. The absorption intensity was decreased with increased reaction time as seen in Fig. 4.5. Faster dye degradation was observed on CdSe/GO nanocomposite due to the increased surface area and reduced electron-hole pair recombination by the presence of GO, while, in the case of pure CdSe, the degradation of brilliant green (BG) dye was slower than that of CdSe/GO composites under same irradiation time. GO acted as good electron acceptor under irradiation of sunlight on CdSe/GO nanocomposite. The proposed mechanisms for the degradation of BG on CdSe/GO composite are as follows: the electrons were transferred from GO to CB of CdSe, and also CdSe itself create electrons and holes. The electrons and holes participated in photocatalytic reaction to form free radicals such as oxygen peroxide and hydroxyl radicals. These radicals degraded BG into CO_2, H_2O, and other products. Similarly CdTe quantum dots (QDs) were used as photocatalyst with extended absorbance region for utilization of solar energy. Cadmium tellurium (CdTe) QD-$KTaO_3$ composite was used for degradation of toluene in gas phase with improved photocatalytic performance (Bajorowicz et al. 2017).

The photocatalytic activity and photostability of CdX (X = S, Se, Te) QDs can be further improved by the formation of core-shell structure with sulfurated layered double hydroxide (LDH). Yue et al. (2017) have reported the synthesis of FeNiS/CdTe/CdS. The electron transfer between FeNiS nanoparticles and CdTe/CdS QDs could be facilitated by the interaction between S of FeNiS nanoparticles and Cd^{2+} of CdTe/CdS QDs that enhanced the photocatalytic hydrogen evolution. Similar group has also reported the synthesis of CdTe/CdS core/shell with sulfur-tolerant catalysts of the $[Mo_3S^{13}]^{2-}$ nanocluster for enhanced visible light-driven hydrogen evolution (Yue et al. 2016).

Other than metal QDs, nonmetal QDs can also be used for water splitting. Zhou et al. (2017) have synthesized phosphorus QDs (P QDs) for water splitting. P QDs have exploited in the field of gas sensing, nonlinear optics, and flexible memory devices due to their peculiar optical and electronic properties. Two types of phosphorus, namely, black and blue P QDs, were prepared with zigzag and armchair structure, respectively, for hydrogen evolution under the same irradiation condition. The photocatalytic applications of metal-based QDs are listed in Table 4.1.

4.3 Metal-Free Quantum Dots for Hydrogen Evolution and Pollutant Degradation

Even though the metal-containing QDs have attracted significant attention, their expensiveness, less availability, and toxic nature limit their applications as photocatalysts. In the last few years, the use of metal-free carbon materials such as graphene and carbon nanotube (CNT) composites has increased great attention in photocatalysis (Woan et al. 2009). The enhanced photocatalytic activity of composites was due to the superior charge transport properties of carbon materials that reduced the recombination rate of photogenerated electron-holes and also the large surface area of composites. However, the drawbacks such as zero bandgap of graphene and the wide absorption of light impeded its application in photocatalysis. Recently, the research have been focused on the development of carbon-based quantum dots as photocatalyst.

Table 4.1 Photocatalytic applications of various metal sulfide, metal oxide, and metal QDs

Photocatalysts	Method of synthesis	Starting precursor of QDs	Applications	References
CdS QDs/MWCNT	Solvothermal	Cadmium acetate and thioacetamide	Malachite green degradation	Fang et al. (2016)
MoS_2 QDs@TNT	Electrodeposition	Ammonium molybdate and tetrahydrate dibenzyl disulfides	Hydrogen production	Wang et al. (2018a, b, c)
CuS QDs	Ball milling	Pure powders of Cu and S	Rhodamine B degradation	Li et al. (2016)
Ag_2S QDs/SnS_2	In situ hydrothermal ion exchange method	$AgNO_3$ and SnS_2	MO and Cr (VI)	Liu et al. (2017)
Bi_2WO_6 QDs/montmorillonite	Hydrothermal	Bismuth nitrate and $Na_2WO_4{\cdot}2H_2O$	NH_3 degradation	Sun et al. (2014)
SnO_2 QDs	Microwave	$SnCl_2.2H_2O$ and amino acids	Eosin Y, humic acid	Bhattacharjee and Ahmaruzzaman (2015) and Begum et al. (2016)
$AgVO_3$ QDs/g-C_3N_4	Ultrasonication	$AgNO_3$ and NH_4VO_3	Bacteria *Salmonella*	Wang et al. (2017)
CdSe QDs	Reflux	Cadmium acetate and Se	H_2 evolution	Sawaguchi-Sato et al. (2017)
ZnSe QDs	Coprecipitation	Zinc nitrate and Se	Methylene blue	Yousefi et al. (2018)

4.3.1 Carbon Quantum Dot (C QD)-Based Photocatalyst

Carbon quantum dots like carbon nanotube, graphene, and fullerene, a new member of carbon family, have considered great attention due to their interesting properties such as wide light assimilation, ease of surface functionalization, low biological toxicity, water solubility, and tunable photoluminescence with upconverted photoluminescence, making them a promising candidate in the field of medicine, energy storage devices, sensor, photocatalysis, and optoelectronics. At first, it was accidentally obtained in 2004 during the electrophoretic separation of single-walled carbon nanotubes. The structure of C QDs can be amorphous or crystalline cores in which the carbon is in SP^2 hybridization state fused with SP^3 carbon, and also it terminated with oxygen moieties that provided easy functionalization on C QDs. C QDs can be synthesized via two approaches: (a) bottom-up approaches produce C

QDs from molecular carbon precursors through chemical reactions including hydrothermal/solvothermal, microwave-assisted synthesis, combustion, and pyrolysis method and (b) top-down approaches involved the breakdown of macroscopic carbon materials into small one through various physical and chemical processes including laser ablation, chemical ablation, electrochemical carbonization, ultrasonic synthesis, and arc discharge. In photocatalysis, the role of C QDs was similar to other conventional semiconductors. The main factor in determining the photocatalytic activity of C QDs was the ability to trap and transfer electrons. Thus C QDs acted as both photoinduced electron acceptors and donors. Even though they have excellent light absorption properties, the insignificant electrons transfer inside the structure of C QDs, hindering their utilization in photocatalyst. The photocatalytic performance can be improved by changing the structure of C QDs via doping or modification of composite with other materials that controlled their intrinsic properties such as surface structure, charge carriers, electronic property, and chemical states (Wang et al. 2017).

Recently, C QDs and N-doped C QDs have been synthesized using *pomelo or Citrus grandis* juice as a starting precursor via a facile one-step hydrothermal process (Ramar et al. 2018). Amorphous C QDs are obtained as a dark brown product with average particle size of 3 nm, while NC QDs have amorphous structure with average particle size of 70 nm. The presence of aromatic and amide functional group was confirmed from UV-Vis and FT-IR spectral studies. The synthesized materials have better photocatalytic activity for the degradation of methylene blue (MB) under direct sunlight radiation than that of white light. NC QDs have little bit higher tendency to degrade MB as compared with that of undoped C QDs. The dye degradation follows pseudo-first-order kinetics according to the Langmuir-Hinshelwood model.

Scheme 4.2 showed the proposed catalytic mechanism involved in the reaction of MB on NC QDs. Herein, C QDs acted as both catalyst and light absorber. The VB electrons of C QDs get excited to CB of C QDs in the presence of sunlight that resulted in creating a hole in VB. The participation of electrons and holes in photocatalysis produced superoxide radical, hydrogen peroxide (H_2O_2), and OH radical. These radicals were further involved in the degradation of MB. Similarly, Aghamali et al. (2018) have prepared NC QDs by hydrothermal process using diethylenetriamine as surface passivation agent and citric acid as carbon source for degradation of MB under sunlight. The increased photocatalytic activity was observed for doped C QDs than that of undoped C QDs. This could be attributed to the doping of C QDs with N, inducing charge delocalization that promoted efficient electron transfer ability for QDs.

Bamboo was used as green carbon source for synthesizing C QDs through hydrothermal process (Wang et al. 2018a, b, c). The prepared QDs were modified with $Bi_3Ti_4O_{12}$ nanosheets for enhancing the photocatalytic activity toward ciprofloxacin. The enhanced photocatalytic activity was due to the increased distance between electron-hole pairs and the upconverted PL property of C QDs that resulted in the full utilization of sunlight.

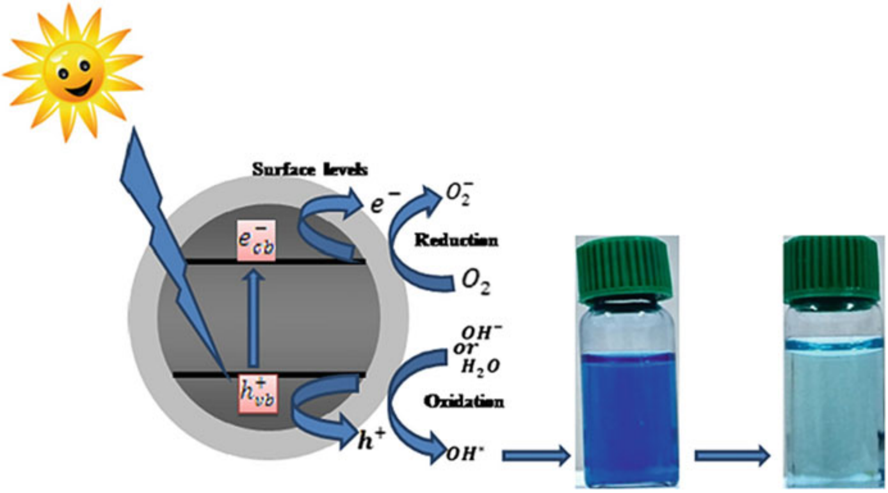

Scheme 4.2 Proposed mechanism for the degradation of MB dye on nitrogen-doped C QDs

Moreover, some C QD-based composites acted as green photocatalyst in terms of formation of useful products at the end of degradation of organic pollutants or evaluate hydrogen under visible light. For instance, copper nanoparticle/C QDs hybrid was used as a photocatalyst under visible light for the oxidation of cyclohexane using tert-butyl hydroperoxide as oxidant at low temperature (Zhang et al. 2017a, b). C QDs were synthesized using electrochemical ablation of graphite, resulting in the formation of C QDs as dark yellow solution. After the addition of C QDs into Cu, the solution color was changed to gray blue color. The oxidation of cyclohexane into cyclohexanone under sunlight irradiation was higher than that under dark condition. The photocatalytic activity of hybrid was enhanced than pure C QDs and Cu NPs. The recycling test indicated that there is no leaching of catalyst after oxidation reaction that showed the higher stability of composite. These results showed that the high catalytic activity of hybrid was due to the electron donor and acceptor nature of C QDs and also surface plasmon resonance of Cu NP that enhanced the visible light absorption. The active oxygen species $^{\cdot}$OH was involved in the oxidation of cyclohexane. Similarly, Chai et al. (2018) have prepared C QDs/Zn^{2+} ion-doped CdS nanowires through mild solution-phase route for reduction of 4-nitroaniline to p-phenylenediamine in the presence of ammonium formate under visible light irradiation ($\lambda > 420$ nm). Hydrothermal process was used for preparing C QDs using pyrene and nitric acid as starting precursors.

C QD-based photocatalyst was also used for the removal of NO present in air under visible light irradiation (Huang et al. 2017). C QDs were synthesized using ascorbic acid as carbon source. The photocatalytic activity of C QDs was enhanced by the formation of composite with $ZnFe_2O_4$. Electron spin resonance and radical trapping analyses showed that the reactive species $\cdot O^{2-}$ and ·OH radicals are involved in the removal of NO as NO^{3-}. Similar group has also used C

QD-modified FeOOH as photocatalyst for the removal of NO (Huang et al. 2018). In both cases, high selectivity was attained due to the inhibition in the generation of toxic nitrate intermediates.

Copper nanoparticles hybridized with C QDs were used as photocatalyst for the evolution of hydrogen under solar light irradiation (Zhang et al. 2017a, b). The hybrid was synthesized through in situ photoreduction. The enhanced photocatalytic activity toward H_2 evolution on hybrid materials was due to the broad-spectrum response and surface plasmon resonance (SPR) effect of Cu nanoparticles.

4.3.2 Graphene Quantum Dot-Based Photocatalyst

Graphene quantum dot (G OD), a new rising star material in carbon family, consists of very tiny pieces of graphene as layers with size in the range from 2 to 20 nm. G QDs exhibited fantastic properties such as stable photoluminescence, biocompatibility, chemically inert, excellent water solubility, excellent photostability, tunable bandgaps, and good electrical conductivity. Thus, they have been used as promising materials in several fields such as solar cells, sensing, photocatalysis, energy storage devices, and bioimaging. G QDs were synthesized through two processes as similar to C QDs synthesis: (a) bottom-up process and (b) top-down process. Pure G QDs is not suitable for photocatalytic application due to the lack of emission at long wavelength excitation and broad absorption in visible region. Therefore, G QDs was doped with heteroatoms such as S and N for enhancing the photocatalytic properties of G QDs. Moreover, the tunable bandgap offered more active sites and broaden the photoabsorption region (Bacon et al. 2014; Wang et al. 2015).

G QDs alone showed the photocatalytic activity for the degradation of organic pollutants. G QDs were synthesized by pyrolysis method using citric acid as a starting precursor (Roushani et al. 2015). The photocatalytic activity of G QDs was investigated from the decolorization of celestine blue (CB) dye and new fuchsin as a model under visible light irradiation. The G QDS was modified with semiconductor nanomaterials to improve the photocatalytic activity through the efficient utilization of sunlight.

Recently, G QDs was employed as green photocatalytic promoter to decorate titania nanosheet (TNSs) via simple electrostatic flocculation method (Bian et al. 2016). The composite was used for the degradation of RhB under visible light with enhanced photocatalytic performance compared with that of G QDs and titania nanosheets alone. G QDs is photochemically stable for long time due to the presence of strong sp^2 bonding. For instance, Pan et al. (2015) have synthesized amine functionalized G QDs through molecular fusion method followed by its deposition on the surface of TiO_2 nanoparticles using hydrothermal treatment. The incorporation of G QDs into TiO_2 NPs extended their light absorption range from UV to visible region. The composite can be used as a photocatalyst for degradation of methyl orange (MO) dye under visible light irradiation in which they absorbed more number of oxygen for generating active species to degrade MO. The complete

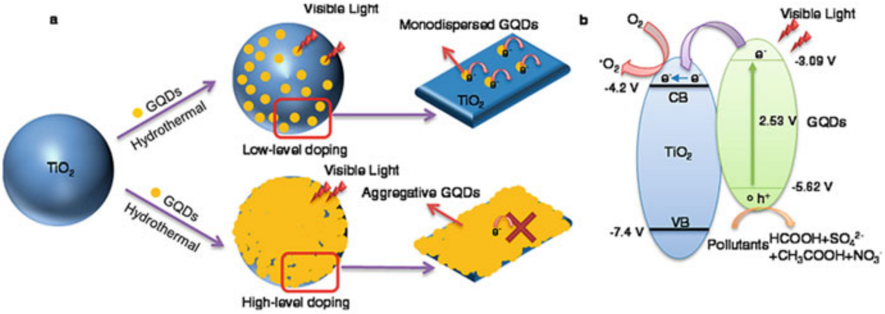

Scheme 4.3 (**a**) Schematic representation of photogenerated electron transfer between G QDs and surface of TiO_2; (**b**) mechanism for degradation of organic pollutants on G QDs/TiO_2

decolorization of MO has occurred after 120 min of irradiation with 1 wt % G QD doping content with the disappearance of MO characteristic peaks at 274 and 464 nm. The wide bandgap nature of TiO_2 NPs and large exciton binding energy of G QDs lower their degradation efficiency for MO compared to that of nanocomposite under same irradiation conditions. If the doping content of G QDs on TiO_2 NPs was increased further, the photocatalytic activity was reduced due to their agglomeration of TiO_2 NPs as shown in Scheme 4.3.

G QDs can also be used for hydrogen evolution along with TiO_2 nanotube array and CdS-modified TiO_2 nanotube array (Yu et al. 2013). Herein, the composite materials were prepared by using impregnation route. G QDs were synthesized by the reduction of GO QDs which was obtained from the solvothermal treatment of GO solution. G QDs were anchored inside the nanotube array without changing the tubelike structure of TiO_2. The evolution of H_2 was periodically monitored by using gas chromatography techniques. The hydrogen evolution rate during water splitting was higher than that of TiO_2 and CdS-TiO_2 nanotube arrays. Zou et al. (2016) have synthesized a cheap and environment-friendly metal-free catalyst N-G QDs/g-C_3N_4 for hydrogen evolution.

Graphene oxide quantum dots (GO QDs) can also be used to fabricate heterostructure with TiO_2 for degradation of organic matter present in water. GO QDs were prepared by refluxing Vulcan CX-72 carbon black in concentrated nitric acid (Zhang et al. 2017a, b). GO QDs were orderly arranged with quantum size and contained carboxyl, hydroxyl, and graphitic structure. The GO QDs were modified with TiO_2 microstructure for degradation of RhB under visible light irradiation. As compared with GO QDs and TiO_2 microsphere, the elimination of RhB using heterostructure was enhanced at same reaction conditions. This was due to the existence of large amount of interfaces in GO QD-sensitized porous TiO_2 microspheres. Some carbon and graphene QD-based photocatalysts are listed in Table 4.2.

Table 4.2 Photocatalytic applications of metal-free QDs

Photocatalyst	Method of synthesis	Starting precursor of QDs	Applications	References
C QDs@3D daisy like In_2S_3/SWCNT	Microwave	Citric acid	Ciprofloxacin, tetracycline, levofloxacin	Li et al. (2016)
Au NPs/C QDs	Electrochemical ablation	Graphite rod	Cyclohexane oxidation	Liu et al. (2013)
C QDs-TiO_2	Hydrothermal	Citric acid	Acetaldehyde oxidation	Hu et al. (2018)
N-C QDs/Ag_3PO_4	Hydrothermal	Glucose	MO and bisphenol degradation	Chen et al. (2016)
C QDs/Cu_2O	Hydrothermal	Glucose	Conversion of CO_2 to methanol	Li et al. (2015)
Fe (III) porphyrin supported S,N-G QDs	Hydrothermal	Citric acid	Oxidation of alcohol	Mahyari et al. (2016)
N-G QDs/$BiVO_4$	Ultrasonication	Graphene	MB	Yang et al. (2017)
G QDs/$AgVO_3$ nanoribbons	Hydrothermal	1,3,6-trinitropyrene	Ibuprofens	Lei et al. (2016)
G QDs/$LaCoO_3$/ attapulgite	Hydrothermal	Citric acid	Antibiotics	Zhu and Li (2017)

4.4 Conclusions

In summary, quantum dots were mainly used as photocatalyst for the degradation of waste organic matter from water, removal of toxic gases, and production of hydrogen from water and H_2S splitting. QDs-based photocatalyst has offered an effective way for solving environmental pollution and energy crises, providing a graceful environment for human life. The starting precursors for metal-free QDs were cheaper with low toxic than metal-based QDs. The photocatalytic activity of pure QDs was improved through doping, surface functionalization, and formation of nanocomposite. The modified QDs showed higher photocatalytic activity due to the inhibition of photogenerated electron and hole pair recombination and absorption of light in the whole spectrum of solar energy. All QD-based photocatalyst can be recycled and reused. Among various QDs, heteroatom-doped G QDs and C QDs have great potential for attaining environment-friendly photocatalyst to produce H_2 from water splitting with higher efficiency.

References

Aghamali A, Khosravi M, Hamishehkar H, Modirshahla N, Behnajady MA (2018) Synthesis and characterization of high efficient photoluminescent sun light driven photocatalyst of N-carbon quantum dots. J Lumin 201:265–274. https://doi.org/10.1016/j.jlumin.2018.04.061

Alqadami AA, Naushad M, Abdalla MA et al (2017) Efficient removal of toxic metal ions from wastewater using a recyclable nanocomposite: a study of adsorption parameters and interaction mechanism. J Clean Prod. https://doi.org/10.1016/j.jclepro.2017.04.085

Apte SK, Garaje SN, Valantb M, Kale BB (2012) Eco-friendly solar light driven hydrogen production from copious waste H_2S and organic dye degradation by stable and efficient orthorhombic CdS quantum dots–GeO_2 glass photocatalyst. Green Chem 14:1455–1462. https://doi.org/10.1039/c2gc16416g

Apte SK, Garaje SN, Naik SD, Waichal RP, Kale BB (2013) Environmentally benign enhanced H_2 production from abundant copious waste H_2S using size tuneable cubic bismuth (Bi0) quantum dots GeO_2 glass photocatalyst under solar light. Green Chem 15:3459–3467. https://doi.org/10.1039/c3gc41940a

Bacon M, Bradley SJ, Nann T (2014) Graphene quantum dots. Part Part Syst Charact 31 (4):415–428. https://doi.org/10.1002/ppsc.201300252

Bajorowicz B, Nadolna J, Lisowski W, Klimczuk T, Zaleska-Medynska A (2017) The effects of bifunctional linker and reflux time on the surface properties and photocatalytic activity of CdTe quantum dots decorated $KTaO_3$ composite photocatalysts. Appl Catal B Environ 203:452–464. https://doi.org/10.1016/j.apcatb.2016.10.027

Begum S, Devi B, Ahmaruzzaman M (2016) Surfactant mediated facile fabrication of SnO_2quantum dots and their degradation behavior of humic acid. Mater Lett 185:123–126. https://doi.org/10.1016/j.matlet.2016.07.028

Bhattacharjee A, Ahmaruzzaman M (2015) Facile synthesis of SnO_2quantum dots and its photocatalytic activity in the degradation of eosin Y dye: a green approach. Mater Lett 139:418–421. https://doi.org/10.1016/j.matlet.2014.10.121

Bi C, Cao J, Lin H, Wanga Y, Chenac S (2016) Enhanced photocatalytic activity of $Bi_{12}O_{17}Cl_2$ through loading Pt quantum dots as a highly efficient electron capturer. Appl Catal B 195:132–140. https://doi.org/10.1016/j.apcatb.2016.05.011

Bian S, Zhou C, Li P, Liu J, Dong X, Xi F (2016) Graphene quantum dots decorated titania nanosheets heterojunction: efficient charge separation and enhanced visible light photocatalytic performance. ChemCatChem 9(17):3349–3357. https://doi.org/10.1002/cctc.201601594

Cao J, Xu B, Luo B, Lin H, Chen S (2011) Novel BiOI/BiOBr heterojunction photocatalysts with enhanced visible light photocatalytic properties. Catal Commun 13(1):63–68. https://doi.org/10.1016/j.catcom.2011.06.019

Chai Y-Y, Qu D-P, Ma D-K, Chen W, Huang S (2018) Carbon quantum dots/Zn^{2+} ions doped CdS nanowires with enhanced photocatalytic activity for reduction of 4-nitroaniline to p-phenylenediamine. Appl Surf Sci 450:1–8. https://doi.org/10.1016/j.apsusc.2018.04.121

Chen XB, Mao SS (2007) Titanium dioxide nanomaterials: synthesis, properties, modifications, and applications. Chem Rev 107(7):2891–2959. https://doi.org/10.1021/cr0500535

Chen Q, Wang Y, Wang Y, Zhang X, Duan D, Fan C (2016) Nitrogen-doped carbon quantum dots/Ag_3PO_4 complex photocatalysts with enhanced visible light driven photocatalytic activity and stability. J Colloid Interface Sci 491:238–245. https://doi.org/10.1016/j.jcis.2016.12.013

Di U, Xia J, Ji M, Wang B, Yin S, Huang Y, Chen Z, Li H (2016) New insight of Ag quantum dots with the improved molecular oxygen activation ability for photocatalytic applications. Appl Catal B Environ 188:376–387. https://doi.org/10.1016/j.apcatb.2016.01.062

Fang S, Sun M, Zhou Y, Liang Q, Li Z, Xu S (2016) Solvothermal synthesis of CdS QDs/MWCNTs nanocomposites with high efficient photocatalytic activity under visible light irradiation. J Alloys Compd 656:771–776. https://doi.org/10.1016/j.jallcom.2015.09.229

Fu Y, Liang W, Guo J, Tang H, Liu S (2018) MoS_2 quantum dots decorated g-C_3N_4/Ag heterostructures for enhanced visible light photocatalytic activity. Appl Surf Sci 430:234–242. https://doi.org/10.1016/j.apsusc.2017.08.042

Fujishima A, Honda K (1972) Electrochemical photolysis of water at a semiconductor electrode. Nature 238:37–38. https://doi.org/10.1038/238037a0

Ge L, Zuo F, Liu J, Ma Q, Wang C, Sun D, Bartels L, Feng P (2012) Synthesis and efficient visible light photocatalytic hydrogen evolution of polymeric g-C_3N_4 coupled with CdS quantum dots. J Phys Chem C 116:13708–13714. https://doi.org/10.1021/jp3041692

Hemmateenejad B, Shadabipour P, Khosousi T, Shamsipur M (2015) Chemometrics investigation of the light-free degradation of methyl green and malachite green by starch-coated CdSe quantum dots. J Ind Eng Chem 27:384–390. https://doi.org/10.1016/j.jiec.2015.01.018

Hoffmann MR, Martin ST, Choi W, Bahneman DW (1995) Environmental applications of semiconductor photocatalysis. Chem Rev 95:69–96. https://doi.org/10.1021/cr00033a004

Hu N, Xie X, Wang X, Wang Y, Zeng Y, Pui DYH, Sun J (2018) Visible-light Upconversion carbon quantum dots decorated TiO_2 for the Photodegradation of flowing gaseous acetaldehyde. Appl Surf Sci 440:266–274. https://doi.org/10.1016/j.apsusc.2018.01.104

Huang Y, Gao Y, Zhang Q, Zhang Y, Cao J-J, Ho W, Lee SC (2018) Biocompatible FeOOH-carbon quantum dots nanocomposites for gaseous NO_x removal under visible light: improved charge separation and high selectivity. J Hazard Mater 354:54–62. https://doi.org/10.1016/j.jhazmat.2018.04.071

Huang Y, Liang Y, Rao Y, Zhu D, Cao J-J, Shen Z, Ho W, Lee SC (2017) Environment-friendly carbon quantum dots/$ZnFe_2O_4$ photocatalysts: characterization, biocompatibility, and mechanisms for NO removal. Environ Sci Technol 51:2924–2933. https://doi.org/10.1021/acs.est.6b04460

Janbandhu SY, Munishwar SR, Gedam RS (2018) Synthesis, characterization and photocatalytic degradation efficiency of CdS quantum dots embedded in sodium borosilicate glasses. Appl Surf Sci 449:221–227. https://doi.org/10.1016/j.apsusc.2018.02.065

Jiang Z, Qian K, Zhu C, Sun H, Wan W, Xie J, Li H, Wong PK, Yuan S (2017) Carbon nitride coupled with CdS-TiO_2 nanodots as 2D/0D ternary composite with enhanced photocatalytic H2 evolution: a novel efficient three-level electron transfer process. Appl Catal B 210:194–204. https://doi.org/10.1016/j.ap catb.2017.03.069

Kaur S, Sharma S, Umar A, Singh S, Mehta SK, Kansal SK (2017) Solar light driven enhanced photocatalytic degradation of brilliant green dye based on ZnS quantum dots. Superlattice Microst 103:365–375. https://doi.org/10.1016/j.spmi.2016.10.046

Kudo A, Miseki Y (2009) Heterogeneous photocatalyst materials for water splitting. Chem Soc Rev 38:253–278. https://doi.org/10.1039/B800489G

Kumar A, Kumar A, Sharma G et al (2017) Sustainable nano-hybrids of magnetic biochar supported g-C3N4/FeVO4for solar powered degradation of noxious pollutants- Synergism of adsorption, photocatalysis & photo-ozonation. J Clean Prod 165:431–451. https://doi.org/10.1016/j.jclepro.2017.07.117

Lei Z-D, Wang J-J, Wang L, Yang X-Y, Pan D-Y, Xu G, Tang L (2016) Efficient photocatalytic degradation of ibuprofen in aqueous solution using novel visible-light responsive graphene quantum dot/$AgVO_3$ nanoribbons. J Hazard Mater 312:298–306. https://doi.org/10.1016/j.jhazmat.2016.03.044

Li H, Zhang X, MacFarlane DR (2015) Carbon quantum dots/Cu_2O heterostructures for solar light-driven conversion of CO_2 to methanol. Adv Energy Mater 5(5):1401077. https://doi.org/10.1002/aenm.201401077

Li S, Ge Z-H, Zhang B-P, Yao Y, Wang H-C, Yang J, Li Y, Gao C, Lin Y-H (2016) Mechanochemically synthesized sub-5nm sized CuS quantum dots with high visible-light-driven photocatalytic activity. Appl Surf Sci 384:272–278. https://doi.org/10.1016/j.apsusc.2016.05.034

Liu R, Huang H, Li H, Liu Y, Zhong J, Li Y, Zhang S, Kang Z (2013) Metal nanoparticle/carbon quantum dot composite as photocatalyst for high efficiency cyclohexane oxidation. ACS Catal 4 (1):328–336. https://doi.org/10.1021/cs400913h

Liu J, Jing L, Gao G, Xu Y, Xie M, Huang L, Ji HY, Xie J, Li H (2017) Ag_2S quantum dots in situ coupled to hexagonal SnS_2 with enhanced photocatalytic activity for MO and Cr(VI) removal. RSC Adv 7:46823–46831. https://doi.org/10.1039/c7ra08369f

Lopes OF, Carvalho KTG, Nogueira AE, Avansi W, Ribeiro C (2016) Controlled synthesis of $BiVO_4$ photocatalysts: evidence of the role of heterojunctions in their catalytic performance driven by visible-light. Appl Catal B Environ 188:87–97. https://doi.org/10.1016/j.apcatb.2016.01.065

Lv Y-R, Huo R, Yang S-Y, Liu Y-Q, Li X-J, Xu Y-H (2018) Self-assembled synthesis of PbS quantum dots supported on polydopamine encapsulated $BiVO_4$ for enhanced visible-light-driven photocatalysis. Sep Purif Technol 197:281–288. https://doi.org/10.1016/j.seppur.2018.01.006

Mahyari M, Bide Y, Gavgani JN (2016) Iron(III) porphyrin supported on S and N co-doped graphene quantum dot as an efficient Photocatalyst for aerobic oxidation of alcohols under visible light irradiation. Appl Catal A Gen 517:100–109. https://doi.org/10.1016/j.apcata.2016.03.010

Moniz SJA, Shevlin SA, Martin DJ, Guo Z-X, Tang J (2015) Visible-light driven heterojunction photocatalysts for water splitting – a critical review. Energy Environ Sci 8:731–759. https://doi.org/10.1039/c4ee03271c

Naushad M, Sharma G, Kumar A et al (2018) Efficient removal of toxic phosphate anions from aqueous environment using pectin based quaternary amino anion exchanger. Int J Biol Macromol. https://doi.org/10.1016/j.ijbiomac.2017.07.169

Pan Y-X, Zhuang H, Hong J, Fang Z, Liu H, Liu B, Huang Y, Xu R (2014) Cadmium sulfide quantum dots supported on gallium and indium oxide for visible-light-driven hydrogen evolution from water. ChemSusChem 7(9):2537–2544. https://doi.org/10.1002/cssc.201402334

Pan D, Jiao J, Li Z, Guo Y, Feng C, Liu Y, Wang L, Wu M (2015) Efficient separation of electron−hole pairs in graphene quantum dots by TiO_2 heterojunctions for dye degradation. ACS Sustain Chem Eng 3(10):2405–2413. https://doi.org/10.1021/acssuschemeng.5b00771

Pan D, Han Z, Miao Y, Zhang D, Li G (2018) Thermally stable TiO_2 quantum dots embedded in SiO_2 foams: characterization and photocatalytic H_2 evolution activity. Appl Catal B 229:130–138. https://doi.org/10.1016/j.apcatb.2018.02.022

Ramar V, Moothattu S, Balasubramanian K (2018) Metal free, sunlight and white light based photocatalysis using carbon quantum dots from *Citrus grandis*: a green way to remove pollution. Sol Energy 169:120–127. https://doi.org/10.1016/j.solener.2018.04.040

Roushani M, Mavaei M, Rajabi HR (2015) Graphene quantum dots as novel and green nanomaterials for the visible-light driven photocatalytic degradation of cationic dye. J Mol Catal A Chem 409:102–109. https://doi.org/10.1016/j.molcata.2015.08.011

Samadi-Maybodi A, Farzinia H (2018) Application of CdS QDs incorporated in magnetized powder activated carbon for degradation of some dyes: photodegradation process and comprehensive catalytic and spectroscopic studies. J Photochem Photobiol A Chem 357:103–117. https://doi.org/10.1016/j.jphotochem.2018.01.019

Samadi-maybodi A, Abbasi F, Akhoondi R (2014) Aqueous synthesis and characterization of CdS quantum dots capped with some amino acids and investigations of their photocatalytic activities. Colloids Surf A Physicochem Eng Aspects 447:111–119. https://doi.org/10.1016/j.colsurfa.2014.01.036

Sawaguchi-Sato K, Kobayashi A, Yoshida M, Kato M (2017) Aggregation-enhanced photocatalytic H_2 evolution activity of photosensitizing cadmium selenide quantum dots and platinum colloidal catalysts. J Photochem Photobiol A Chem 335:182–189. https://doi.org/10.1016/j.jphotochem.2016.11.028

Sun S, Wang W, Jiang D, Zhang L, Li X, Zheng Y, An Q (2014) Bi_2WO_6 quantum dot-intercalated ultrathin montmorillonite nanostructure and its enhanced photocatalytic performance. Nano Res 7(10):1497–1506. https://doi.org/10.1007/s12274-014-0511-2

Tayyebi A, outokesh M, Tayebi M, Shafikhani A, Şengör SS (2016) ZnO quantum dots-graphene composites: formation mechanism and enhanced photocatalytic activity for degradation of Methyl Orange dye. J Alloys Compd 663:738–749. https://doi.org/10.1016/j.jallcom.2015.12.169

Thakur M, Sharma G, Ahamad T et al (2017) Efficient photocatalytic degradation of toxic dyes from aqueous environment using gelatin-Zr(IV) phosphate nanocomposite and its antimicrobial activity. Colloids Surf B Biointerfaces 157:456–463. https://doi.org/10.1016/j.colsurfb.2017.06.018

Thirugnanam N, Song H, Chinese YW (2017) Photocatalytic degradation of Brilliant Green dye using CdSe quantum dots hybridized with graphene oxide under sunlight irradiation. Chin J Catal 38:2150–2159. https://doi.org/10.1016/S18722067 (17) 62 9644

Wahab R, Tripathy SK, Shin H-S, Mohapatra M, Musarrat J, Al-Khedhairy AA, Kaushik NK (2013) Photocatalytic oxidation of acetaldehyde with ZnO-quantum dots. Chem Eng J 226:154–160. https://doi.org/10.1016/j.cej.2013.02.128

Wang J-J, Li Z-J, Li X-B, Fan X-B, Meng Q-Y, Yu S, Li C-B, Li J-X, Tung C-H, Wu L-Z (2014) Photocatalytic hydrogen evolution from glycerol and water over nickel-hybrid cadmium sulfide quantum dots under visible-light irradiation. ChemSusChem 7:1468–1475. https://doi.org/10.1002/cssc.201400028

Wang W, Chan DKL, Yu JC (2015) Graphene-based photocatalysts for energy applications: progress and future prospects. Chapter 9:277–294. https://doi.org/10.1002/9783527690312.ch9

Wang R, Lu K-Q, Tang Z-R, Xu Y-J (2017) Recent progress in carbon quantum dots: synthesis, properties and applications in photocatalysis. J Mater Chem A 5:3717–3734. https://doi.org/10.1039/c6ta08660h

Wang Q, Huang J, Sun H, Hau Y, Zhang K, Lai Y (2018a) MoS_2 quantum dots@TiO_2 nanotube arrays: an extended spectrum-driven photocatalyst for solar hydrogen evolution. ChemSusChem 11(10):1708–1721. https://doi.org/10.1002/cssc.201800379

Wang R, Kong X, Zhang W, Zhu W, Huang L, Wang J, Zhang X, Liu X, Hu N, Suo Y, Wang J (2018b) Mechanism insight into rapid photocatalytic disinfection of Salmonella based on vanadate QDs-interspersed g-C_3N_4 heterostructures. Appl Catal B 225:228–237. https://doi.org/10.1016/j.apcatb.2017.11.060

Wang T, Liu X, Ma C, Zhu Z, Liu Y, Liu Z, Wei M, Zhao X, Dong H, Huo P, Li C, Yan Y (2018c) Bamboo prepared carbon quantum dots (CQDs) for enhancing $Bi_3Ti_4O_{12}$ nanosheets photocatalytic activity. J Alloys Compd 752:106–104. https://doi.org/10.1016/j.jallcom.2018.04.085

Woan K, Pyrgiotakis G, Sigmund W (2009) Photocatalytic carbon-nanotube–TiO_2 composites. Adv Mater 21:2233–2239. https://doi.org/10.1002/adma.200802738

Wu G, Tian M, Chen A (2012) Synthesis of CdS quantum-dot sensitized TiO_2 nanowires with high photocatalytic activity for water splitting. J Photochem Photobiol A Chem 233:65–71. https://doi.org/10.1016/j.jphotochem.2012.02.021

Xiao J, Yang W, Li Q (2017) Bi quantum dots on rutile TiO_2 as hole trapping centers for efficient photocatalytic bromate reduction under visible light illumination. Appl Catal B 218:111–118. https://doi.org/10.1016/j.apcatb.2017.03.084

Yang H, Wang P, Wang D, Zhu Y, Xie K, Zhao X, Yang J, Wang X (2017) New understanding on photocatalytic mechanism of nitrogen doped graphene quantum dots-decorated $BiVO_4$ nanojunction photocatalysts. ACS Omega 2:3766–3773. https://doi.org/10.1021/acsomega.7b00603

Yang G, Miao W, Yuan Z, Jiang Z, Huang B, Wang P, Chen J (2018) Bi quantum dots obtained via in situ photodeposition method as a new photocatalytic CO_2 reduction cocatalyst instead of noble metals: borrowing redox conversion between $Bi_2O_3$and Bi. Appl Catal B Environ 237:302–308. https://doi.org/10.1016/j.apcatb.2018.06.018

Yousefi R, Azimi HR, Mahmoudianb MR, Basirun WJ (2018) The effect of defect emissions on enhancement photocatalytic performance of ZnSe QDs and ZnSe/rGO nanocomposites. Appl Surf Sci 435:886–893. https://doi.org/10.1016/j.apsusc.2017.11.183

Yu Y, Ren J, Meng M (2013) Photocatalytic hydrogen evolution on graphene quantum dots anchored TiO_2 nanotubes-array. Int J Hydrog Energy 38:12266–12272. https://doi.org/10.1016/j.ijhydene.2013.07.039

Yuan Y-J, Chen D-Q, Shi X-F, Tu J-R, Hu B, Yang N-X, Yu Z-T, Zou Z-G (2017) Facile fabrication of "green"SnS_2 quantum dots/reduced graphene oxide composites with enhanced photocatalytic performance. Chem Eng J 313:1438–1446. https://doi.org/10.1016/j.cej.2016.11.049

Yue D, Qian X, Zhang Z, Kan M, Ren M, Zhao Y (2016) CdTe/CdS Core/Shell quantum dots Cocatalyzed by sulfur tolerant $[Mo_3S_{13}]^{2-}$nanoclusters for efficient visible-light-driven hydrogen evolution. ACS Sustain Chem Eng 4(12):6653–6658. https://doi.org/10.1021/acssuschemeng.6b01520

Yue D, Qian X, Kan M, Ren M, Zhu Y, Jiang L, Zhao Y (2017) Sulfurated [NiFe]-based layered double hydroxides nanoparticles as efficient co-catalysts for photocatalytic hydrogen evolution using CdTe/CdS quantum dots. Appl Catal B 209:155–160. https://doi.org/10.1016/j.apcatb.2017.02.075

Zhang X, Zhang L, Xie T, Wang D (2009) Low-temperature synthesis and high visible-light induced photocatalytic activity of BiOI/TiO_2 heterostructures. J Phys Chem C 113(17):7371–7378. https://doi.org/10.1021/jp900812d

Zhang Y, Qi F, Li Y, Zhou X, Sun H, Zhang W, Liu D, Song X-M (2017a) Graphene oxide quantum dot-sensitized porous TiO_2 microsphere: visible-light-driven photocatalyst based on energy band engineering. J Colloid Interface Sci 498:105–111. https://doi.org/10.1016/j.jcis.2017.03.048

Zhang P, Song T, Wang T, Zeng H (2017b) In situ synthesis of Cu nanoparticles hybridized with carbon quantum dots as a broad spectrum photocatalyst for improvement of photocatalytic H_2 evolution. Appl Catal B 206:328–335. https://doi.org/10.1016/j.apcatb.2017.01.051

Zhang Q, Ye S, Song X, Luo S (2018) Photocatalyst based on TiO_2 nanotube arrays co-decorated with CdS quantum dots and reduced graphene oxide irradiated by γ rays for effective degradation of ethylene. Appl Surf Sci 442:245–255. https://doi.org/10.1016/j.apsusc.2018.02.139

Zhao H, Fang Q, Chen C, Chao Z, Tsang Y, Wu Y (2018) WO_3 quantum dots decorated GO/Mg-doped ZnO composites for enhanced photocatalytic activity under nature sunlight. Appl Organometal Chem 4449:1–10. https://doi.org/10.1002/aoc.4449

Zhou S, Liu N, Zhao J (2017) Phosphorus quantum dots as visible-light photocatalyst for water splitting. Comput Mater Sci 130:56–63. https://doi.org/10.1016/j.commatsci.2017.01.009

Zhu W, Li XS (2017) Graphene quantum dots/$LaCoO_3$/attapulgite heterojunction photocatalysts with improved photocatalytic activity. Appl Phys A Mater Sci Process 123:272. https://doi.org/10.1007/s00339-017-0907-4

Zhu Y, Wang Y, Chen Z, Qin L, Yang L, Zhu L, Tang P, Gao T, Huang Y, Sha Z, Tang G (2015) Visible light induced photocatalysis on CdS quantum dots decorated TiO_2 nanotube arrays. Appl Catal A Gen 498:159–166. https://doi.org/10.1016/j.apcata.2015.03.035

Zou J-P, Wang L-C, Luo J, Nie Y-C, Xing Q-J, Luo X-B, Du H-M, Luo S-L, Suib SL (2016) Synthesis and efficient visible light photocatalytic H_2 evolution of a Metalfree g-C_3N_4/graphene quantum dots hybrid Photocatalyst. Appl Catal B 193:103–109. https://doi.org/10.1016/j.apcatb.2016.04.017

Zou Y, Shi J-W, Ma D, Fan Z, Cheng L, Sun D, Wang Z, Niu C (2018) WS_2/graphitic carbon nitride heterojunction nanosheets decorated with CdS quantum dots for photocatalytic hydrogen production. ChemSusChem 11:1187–1197. https://doi.org/10.1002/cssc.201800053

Chapter 5
Evolution of ZnO-Based Photocatalyst for the Degradation of Pollutants

S. Kaviya

Contents

5.1 Introduction 110
  5.1.1 Water Contamination 110
  5.1.2 Why Photocatalytic Degradation of Pollutants 110
  5.1.3 Why a ZnO Photocatalyst? 112
5.2 ZnO Photocatalysis 113
  5.2.1 Synthesis of ZnO Nanoparticles 113
  5.2.2 Different Morphology of ZnO Nanoparticles 114
  5.2.3 Mechanism of Photocatalytic Degradation Under UV, Visible Light, and Sunlight 116
  5.2.4 Limitation of ZnO Photocatalyst 118
  5.2.5 Doped ZnO Photocatalyst 118
5.3 Conclusion 128
References 129

Abstract One exciting aspect of research is focused on the treatment of wastewater and complete mineralization of the pollutants by photocatalysis. The aromatic structure and complex nature of the pollutants cause difficulties in decomposition and complete mineralization. Progress in photocatalytic degradation would be very interesting if it were under moderate reaction conditions with a cost-effective catalyst with enhanced efficiency. Various nanocomposite materials have been used for this purpose. Here, we provide a detailed summary including the latest literature reports on the evolution of the zinc oxide (ZnO) photocatalyst used for the degradation of contaminants from wastewater.

Keywords ZnO nanoparticles · Transition metal · Rare earth metal · Doping · Photocatalyst · Degradation · Synthesis · Pollutants · Dye · Non-metals · Composite material · Charge carrier · Advanced oxidation process

---

S. Kaviya (✉)
Department of Chemical Engineering, Indian Institute of Science (IISC), Bangalore, India

S. Rajendran et al. (eds.), *Green Photocatalysts for Energy and Environmental Process*, Environmental Chemistry for a Sustainable World 36,
https://doi.org/10.1007/978-3-030-17638-9_5

5.1 Introduction

5.1.1 Water Contamination

Water quality as a resource is being poisoned by population growth, industrialization, and natural and domestic events (Nemerow and Dasgupta 1991; Ali and Aboul-Enein 2004; Daneshvar et al. 2017). The discharge of industrial effluent containing organic pollutants such as dyes, fertilizer, and surfactant molecules is setting serious concerns for society as these agents damage water resources, imperilling many living system (Ming-Twang et al. 2017). The bitter part is that 10% of the dyes used in industry have precipitated into water bodies (Bazin et al. 2012). Generally, dyes are categorized by their chromophores and auxochromic groups. They are considered toxic in themselves or from the toxicity of the raw constituents used for their preparation. Considering the adverse effects, the contaminant level of a particular dye is vital. Moreover, the dispersed dye in the contaminated water blocks sunlight irradiation, diminishes the dissolved oxygen level, and, therefore, causes biological oxygen demand (Ahmad et al. 2015). Hence, the contaminated water must be treated prudently before release into main watercourses to reduce the acute effect (Sharma et al. 2018). Such dye-filled wastewaters are discharged by the textile industry (Teh and Mohamed 2011), paper industry (Crini 2006), leather industry (Paschoal et al. 2009), the plastic, rubber, medicine, and food industries (Alves et al. 2008), and the hair-colouring industry (Nohynek et al. 2004). The most studied dyes are thiazine, xanthenes, azo dyes, anthraquinones, aryl-carbonium, triarylmethanes, phthalocyanines, polymethines, and natural dyes.

5.1.2 Why Photocatalytic Degradation of Pollutants

Photocatalysis is a reaction that uses light radiation to activate a substance which alters the rate of a chemical reaction without being involved itself. Significant efforts, such as filtration, coagulation-flocculation, electrochemical treatment, sorption processes, biological treatment, and combination treatments, are being made to remove pollutants (Ong et al. 2011) (Fig. 5.1). Each method has some merits and demerits. The absorption technique is the right choice for decolourization of dyes where activated carbon, nanoparticles, polymer (poly (amidoamine-*co*-acrylic acid) copolymer, poly(methacrylic acid)-based hydrogels, etc.), and low-cost absorbents (e.g., rice husks, castor bean press cake, coffee residue) can be used as absorbent (Ghasemi et al. 2014). Coagulation and flocculation methods destabilize the dispersed particles in the contaminated water and bring them together to form large particles. Then, the larger particles are removed by sedimentation. The coagulant could be a metal salt (calcium chloride, polymeric aluminium sulfate) or polymers and flocculants (e.g., epichlorohydrin-dimethylamine, sodium polymethacrylate). In the chemical precipitation method, carbonates, hydroxides, and sulfides react with

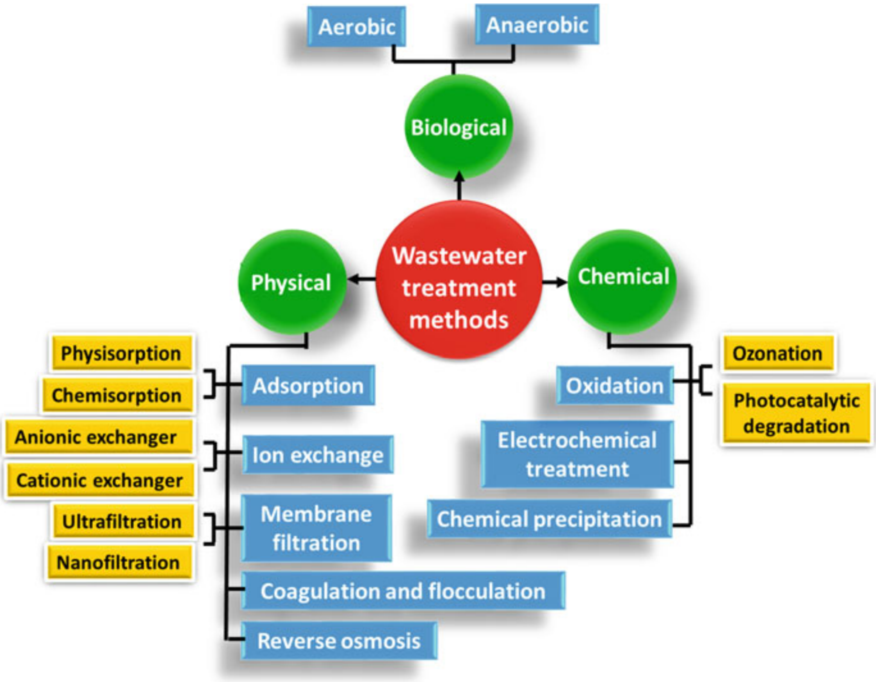

Fig. 5.1 Different methods of wastewater treatment

inorganic and organic pollutants in wastewater to form insoluble precipitates that are then discharged. In biological treatment, aerobic (presence of air) and anaerobic (absence of air) processes, which depend on the type of bacteria/microorganism, degrade the pollutants using a bioreactor. The microorganisms (aerobes) in the aerobic process convert the organic pollutant into water, carbon dioxide, and biomass, whereas anaerobes convert the pollutant into methane, carbon dioxide, and biomass during water treatment. However, these approaches merely transfer the pollutants from the liquid to the solid phase, demanding further treatment and causing secondary pollution (Tanaka et al. 2000). Among these advanced oxidation processes (AOP) by photocatalyst is an alternate treatment strategy that can be applied to dyes and many other organics in wastewater and industrial effluents. It can treat the dye solution without requiring high energy, and finally results in complete mineralization of the organic pollutants to water, carbon dioxide, and mineral acids. Hence, there is no waste disposal problem. The common degradation mechanism of dyes by photocatalysis is composed of photon absorption, charge separation, and the formation of active species on the exterior of the catalyst (Hustert and Zepp 1992). In this process, upon irradiation of the catalyst, the electron from the valence band (VB) is excited to the conduction band (CB) and leaves a hole (h^+) in the valence band. These electrons and holes are required for the formation of active species, which degrade the dye molecules. The mechanism for photocatalytic degradation is summarized next (Konstantinou and Albanis 2004b).

Homogeneous and heterogeneous photocatalysts are used in the AOP mechanism. Homogeneous photocatalysis contains Fenton's reagent, a mixture of hydrogen peroxide and Fe^{2+} salt, to produce hydroxyl radicals under irradiation (Malato et al. 2002). In contrast, heterogeneous photocatalysis employing a semiconductor as a photocatalyst has revealed pronounced potential as a low-cost, sustainable, and eco-friendly treatment technology to support the zero-waste criterion in wastewater management. Heterogeneous photocatalysis is observed as an effective way to degrade and remove hazardous compounds in the water (Konstantinou and Albanis 2004a) by stability and durability under the irradiation process. The photocatalytic degradation rate depends on the nature, concentration, and composition of the dye, surface properties, contact time and dosage of the photocatalyst (Kaviya and Prasad 2016), solution pH (Tian et al. 2013), nature (Neppolian et al. 2002), time of irradiation of light source (Poornaprakash et al. 2018), oxidants (Kaviya and Prasad 2015a), coexisting ions (Epling and Lin 2002), temperature, and impurities. Conversely, fast recombination of the photo-generated electrons and holes decreases photocatalytic efficacy, limiting the applications of semiconductors in photocatalysis (Dawson and Kamat 2001).

5.1.3 Why a ZnO Photocatalyst?

Semiconductor nanomaterials have gained more attention because their tunable optical and electrical properties are appropriate for various applications (Radzimska and Jesionowski 2014). Especially, semiconductor photocatalysts such as TiO_2 (Breault and Bartlett 2012), ZnO (Kaviya and Prasad 2016), SiO_2 (Guo et al. 2000), WO_3 (Hayat et al. 2011), CdS (Pan et al. 2012), ZnS (Sharma et al. 2012), CuO (Ejhieh and Shamsabadi 2013), ZrO_2 (Polisetti et al. 2011), MnO_2 (Ramesh et al. 2016), CeO_2 (Deng et al. 2015), PbO (Borhade et al. 2012), Fe_2O_3 (Dutta et al. 2014), Co_3O_4 (Warang et al. 2013), and MoO_3 (Kumar et al. 2016) have been used for treating various water pollutants (Khalil et al. 1998). In particular, ZnO has attracted much consideration with respect to the degradation of numerous pollutants because of its high photosensitivity, stability (thermal and mechanical), strong ferromagnetic property, larger excitonic binding energy (60 meV), electron affinity (4.2 eV), wide bandgap (3.37 eV), piezoelectric and pyroelectric properties, biocompatibility, low toxicity, biodegradability, and low cost (Kaviya and Prasad 2016;

Xiong et al. 2016). ZnO has a wurtzite crystalline structure with unbalanced charges dismissed in either Zn^{2+} or O^{2-}, respectively, to Zn-ZnO(0001) and O-ZnO(000-1) polar planes (Woll 2007). The basal polar planes of ZnO were described to be more dynamic in photocatalysis as related to the nonpolar facets, owing to a higher density of defects such as oxygen vacancies (Dai et al. 2012). Moreover, oxygen vacancies provoked a decrease in bandgap and improved visible light photocatalytic activity (Wang et al. 2012). ZnO nanomaterials of different sizes and shapes have attracted extensive interest because of their exclusive physical and chemical properties compared to the bulk materials (Jayaseelan et al. 2012). The photocatalytic performance of ZnO nanoparticles (NPs) is highly dependent on their morphology, size, surface area, and defects (Ali et al. 2010; Xu et al. 2009).

5.2 ZnO Photocatalysis

5.2.1 Synthesis of ZnO Nanoparticles

Researchers have established ZnO nanoparticles with various morphologies, chemical compositions, and surface structures for multiple photocatalytic applications. A number of approaches have been used to synthesize ZnO nanoparticles with uniform size and shape. These methods employ physical, chemical, and biological synthesis (Fig. 5.2) where various precursors (zinc chloride, zinc acetate, zinc nitrate) and reaction media (water, alcohol) are used. Diverse structures are produced, offering an extensive range of properties. In physical synthesis, the absence of solvent and uniformity of the nanoparticles are an advantage but this requires equipment and a large amount of energy and pressure (Iravani et al. 2014). Laser ablation (Ismail et al. 2001), arc plasma (Shoushtari et al. 2008), chemical vapour deposition (Guan and Pedraza 2008), spray pyrolysis (Wallace et al. 2013), and electro-spinning (Liu et al. 2008) are the most important physical methods used for the preparation of ZnO nanoparticles. In chemistry and biosynthesis, growth and self-assembly of the particles are achieved in solution under differing reaction conditions such as concentration of the precursor, capping, reducing, stabilizing agents, pH, temperature, time, and reaction medium. In the chemical method, reduction and stabilization of the particles take place in solution by organic, inorganic reducing, and capping agents that include sol-gel (Khan et al. 2016), hydrothermal (Bojesen et al. 2014), micro-emulsion (Wang et al. 2010a), electrochemical (Lu et al. 2009), and microwave methods (Tang et al. 2015). For example, Hong et al. (2009) synthesized ZnO nanoparticles from a precipitation method using zinc acetate as a precursor, with ammonia and polyethylene glycol as the capping and reducing agents, followed by calcination of the precipitate. The biosynthesis approach (Kaviya et al. 2017b; Kaviya 2018) is an eco-friendly, biocompatible, and cost-effective synthesis of nanoparticles using microorganism, bio-templates, and plant extracts. Moreover, the synthesis protocol does not contain toxic chemicals. The natural extracts and stains contain phytochemicals such as amino acids, flavonoids, polysaccharides, polyphenols, alkaloid, terpenes, and vitamins (Kaviya and Prasad 2015b; Kennedy and Wightman 2011; Kaviya

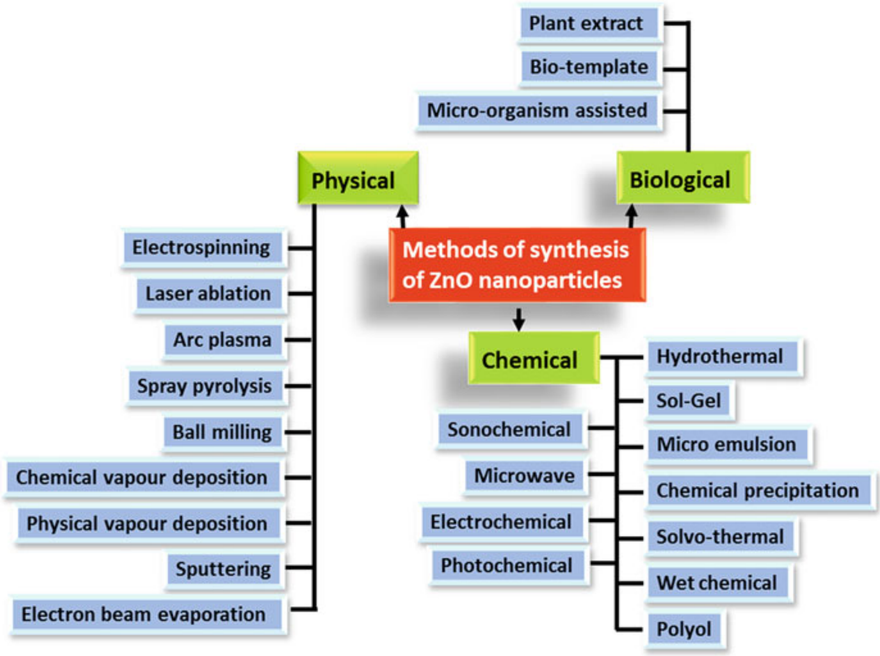

Fig. 5.2 Various methods for the synthesis of ZnO nanoparticles

2017) which act as reducing and stabilizing agents for the formation of nanoparticles. The synthesis relies on the type and nature of the source, phytochemicals, and reaction conditions. Using microorganisms [such as *Aeromonas hydrophila* (Jayaseelan et al. 2012) and *Lactobacillus plantarum* (Selvarajan and Mohanasrinivasan 2013)] for biosynthesis is a time-consuming process and also contaminating, with costs related to the media, careful surveillance of the culture broth, and lack of control on the size and shape of the particle, limitations in this process (Agarwal et al. 2017). Synthesis using bio-templates and plant extracts is simple, faster, and associated with mild reaction conditions. Bio-templates such as palm olein (Ramimoghada et al. 2013) and albumin (Shoeb et al. 2013) have been used for the synthesis of ZnO nanoparticles. Extracts from plant parts such as leaves (Senthilkumar et al. 2017), fruits (Rana et al. 2016), peels (Kaviya et al. 2017a), flowers (Sharma et al. 2016), seeds (Al-Shabib et al. 2016), stems (Lingaraju et al. 2016), and roots (Anand Raj and Jayalakshmy 2015) are preferred for the large-scale synthesis of nanoparticles with controlled size and shapes.

5.2.2 *Different Morphology of ZnO Nanoparticles*

The morphology and size of ZnO nanomaterials have gained attention because they show significance in determining physical, chemical, and optical properties. ZnO nanomaterials in zero (0D), one (1D), two (2D), and three (3D) dimensions, such as wire (Baxter and Schmuttenmaer 2006), spherical (Sangeetha et al. 2011), tube (Samadipakchin et al. 2017), flower (Xu et al. 2016), combs (Xu et al. 2012), nails (Dauda et al. 2016), rings (Peng and Bao 2008), cage (Snure and Tiwari 2007), swords and nano pills (Moulahi and Sediri 2014), helices (Zhou et al. 2017), bow (Hughes and Wang 2004), mulberry (Ma et al. 2013), belts (Hu et al. 2007), ribbon (Wang et al. 2010b), spindle (Lu et al. 2011), pencil (Kaviya and Prasad 2016), tetrapod (Lyapina et al. 2008), pyramid (Khan et al. 2014), sheets (Vempati et al. 2012), dumbbell (Hou et al. 2012), nano chain (Yubuta et al. 2007), dandelion (Liu and Zeng 2004), cone (Ren et al. 2007), and disk (Long et al. 2009), have been synthesized and found to have their own distinctive properties. Scanning electron microscopic images of diversely shaped ZnO nanoparticles are given in Fig. 5.3. Hierarchical structures of ZnO can be prepared by combining 0D, 1D, and 2D nanoparticles to form a wide range of architecture. Compared to other structures, 3D ZnO hierarchical structures usually display high surface-to-volume ratios, better

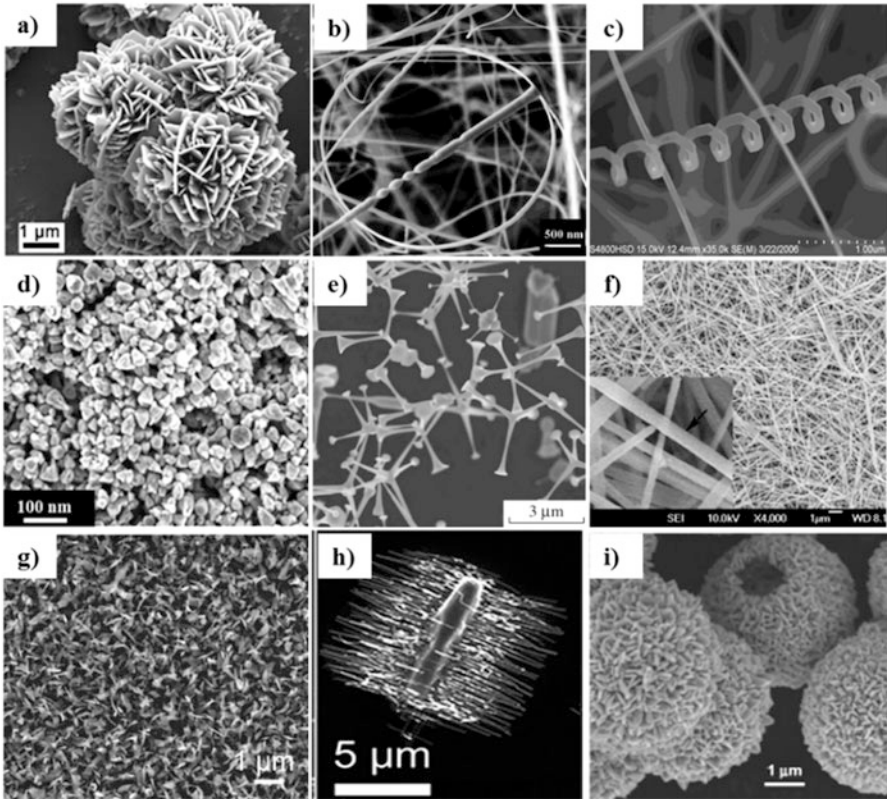

Fig. 5.3 Scanning electron microscopy (SEM) images of ZnO (**a**) flower, (**b**) bow, (**c**) helices, (**d**) pyramid, (**e**) tetrapod, (**f**) wire, (**g**) ribbon, (**h**) comb, and (**i**) dandelion (Xu et al. 2016; Hughes and Wang 2004; Zhou et al. 2017; Khan et al. 2014; Lyapina et al. 2008; Hu et al. 2007; Wang et al. 2010; Xu et al. 2012; Liu and Zeng 2004)

permeability, and higher light absorption by increasing the number of light travelling paths. The lesser crystallinity and huge defects in ZnO improve the photocatalytic process (Wang et al. 2017).

5.2.3 Mechanism of Photocatalytic Degradation Under UV, Visible Light, and Sunlight

For photocatalytic degradation, light energy should induce the ZnO photocatalyst. By the absorption of light energy that is higher than the bandgap of ZnO, the electrons are promoted from the valence band (VB) to the conduction band (CB) and leave a hole in the valence band, called the "charge separation phenomenon." The electron–hole pair created after the absorption of light energy is called an exciton. Further, the catalyst undergoes the light-prompted redox process. The photo-generated holes drift to the surface of ZnO nanoparticles and are then trapped by OH^-, generating hydroxyl radical ($OH^\cdot$) with high oxidative potential. The electrons could react with O_2 to produce the superoxide anion radical ($O_2{}^-$) (Wu et al. 2013). The consecutive formation of these radicals leads to the proficient photocatalytic degradation of organic pollutants. If the irradiation source contains both UV and visible light (e.g., sunlight) upon irradiation of ZnO NPs, there is a chance of both direct bandgap excitation and sensitization mechanisms (Kaviya and Prasad 2016). In the case of direct bandgap excitation, the sunlight (UV light) excites the electron in the valence band of ZnO NPs into the conduction band. The holes in the valence band react with water and produce $OH^\cdot$ radicals, and electrons in the conduction band generate superoxide anion radical ($O_2{}^{\cdot -}$). In the sensitization mechanism, sunlight (visible light) excites the dye molecule absorbed on the surface of ZnO, which inserts the electrons into the conduction band of ZnO nanoparticles. Further, these electrons are expended by the dissolved oxygen in the solution to create reactive oxidative species. Figure 5.4 illustrates the pictorial representation for the photocatalytic degradation of pollutants in the presence of ZnO nanoparticles under UV and visible light irradiation. However, a proficient photocatalyst process requires the suppression of electron–hole pair recombination, either by trapping charge carriers at the defect site or by surface orientation. The presence of oxygen vacancy (defect state) on ZnO nanoparticles acts as an electron acceptor and traps the photo-generated electrons, prohibiting the recombination of e^- and h^+. The defect state depends on the shape, size, and internally created defect within the bandgap via doping (Kanjwal et al. 2012). Photocatalytic degradation efficiency will vary by the difference in the surface properties (morphology, surface area) and defect-prompted properties of the ZnO catalyst. The mechanism for the photocatalytic degradation of organic pollutant in presence of ZnO under irradiation conditions is given in the figure (Fig. 5.4) (Kaviya and Prasad 2016; Kanjwal et al. 2012; Onga et al. 2018).

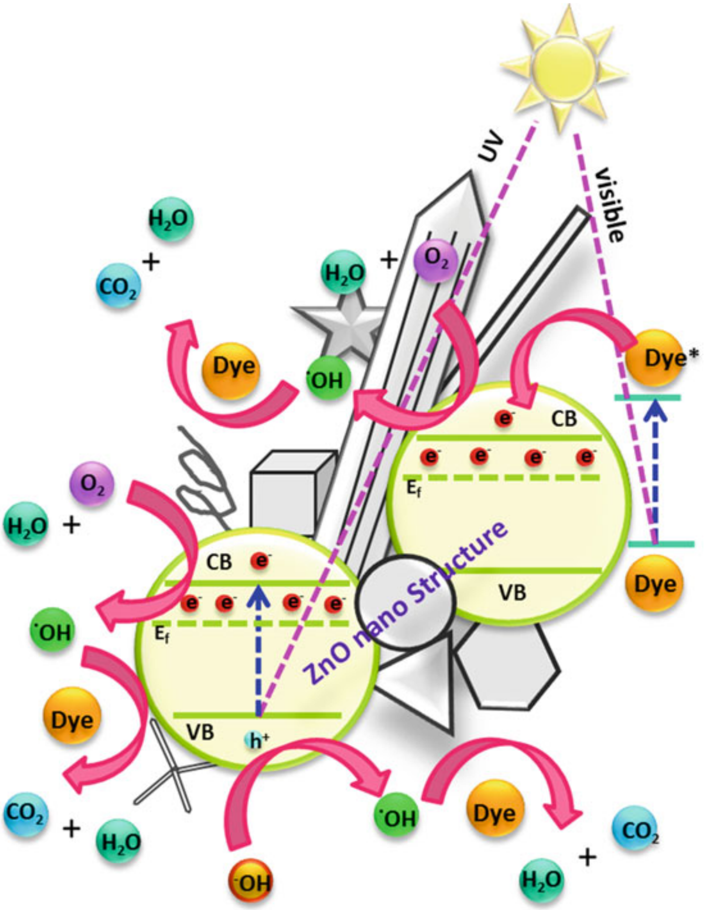

Fig. 5.4 Mechanism of electron transfer events occurring in various shapes of ZnO nanoparticles (NPs) during the degradation of pollutants in irradiation conditions

$$\mathrm{Dye}^{*} + \mathrm{ZnO\,NPs} \overset{\text{Visible light}}{\rightarrow} \mathrm{Dye}^{+\cdot} + \mathrm{ZnO\ NPs}\left(\mathrm{e}^{-}(\mathrm{CB}\right)$$

$$\mathrm{ZnO\,NPs}\left(\mathrm{e}^{-}(\mathrm{CB}\right) + \mathrm{O}_2 \rightarrow \mathrm{O}_2^{\cdot-}$$

$$\mathrm{Dye}^{+\cdot} + \mathrm{O}_2^{\cdot-}/\mathrm{O}_2 \rightarrow \mathrm{CO}_2 + \mathrm{H}_2\mathrm{O}$$

$$\mathrm{ZnO\ NPs} \overset{\text{UV light}}{\rightarrow} \mathrm{ZnO\,NPs}(\mathrm{e}^{-}(\mathrm{CB}) + \mathrm{h}^{+}(\mathrm{VB}))$$

$$\mathrm{ZnO\,NPs}(\mathrm{e}^{-}(\mathrm{CB})) + \mathrm{O}_2 \rightarrow \mathrm{ZnO\ NPs} + \mathrm{O}_2^{\cdot-}$$

$$\mathrm{O}_2^{\cdot-} + \mathrm{H}^{+} \rightarrow \mathrm{HO}_2^{\cdot}$$

$$HO_2^{\cdot} + H^+ + O_2 \rightarrow H_2O_2 + O_2$$

$$O_2^{\cdot-} + H_2O_2 \rightarrow {}^{\cdot}OH + {}^{-}OH + O_2$$

$$\text{ZnO NPs}(h^+(VB)) + {}^{-}OH \rightarrow \text{ZnO NPs} + {}^{\cdot}OH$$

$$^{\cdot}OH + \text{Dye} \rightarrow CO_2 + H_2O$$

5.2.4 Limitation of ZnO Photocatalyst

The efficiency of the ZnO photocatalyst is decreased by one or more limitations of light absorption, charge separation, charge migration, and charge recombination process. The foremost disadvantage of ZnO is the rapid recombination of photoexcited electrons and holes (Kaviya and Prasad 2015a). Moreover, ZnO is incapable of absorbing light in the visible region. To improve the photo response and photocatalytic activity in the visible region, attempts have been made such as doping (Kaviya and Prasad 2015a), surface modification (Hong et al. 2009), and formation of nanocomposites (Kumar et al. 2017). Surface modification would come on the synthesis part, and nanocomposite materials can be obtained from doping of ZnO NPs. Hence, we now focus on doping of ZnO NPs.

5.2.5 Doped ZnO Photocatalyst

The surface charge transfer process and electron–hole recombination process rely on the structural and optical properties of the photocatalyst. Hence, to increase photocatalytic performance, the surface charge transfer process should be increased and the recombination rate of electron and hole should be decreased. An interesting approach is to dope the ZnO photocatalyst with metal ions, which have been shown to enhance activity by varying the interfacial charge transfer effect and bandgap energy. Incorporation of metal ions increases solar light utilization and magnifies the light absorption wavelength to the visible light region (Wu et al. 2012). The introduction of dopant into ZnO nanoparticles would narrow the bandgap by insertion of a delocalized *d*-energy level between the conduction band and valence band, in which less energy is required to generate a hole (Qiu et al. 2008) (Fig. 5.5). The dopant may function as an electron or hole acceptor, which depends on the energy state and redox potential of the dopant. Doping with selective elements improves and controls the structural, electrical, and optical properties of ZnO. The strategy for synthesis of the doped ZnO nanostructure is addition of dopant ions into the ZnO precursor (Kaviya and Prasad 2015a). Chen et al. (2009) describes the doping mechanism in terms of surface adsorption and lattice incorporation. Moreover, surface adsorption of dopant can be followed by lattice incorporation, and lattice

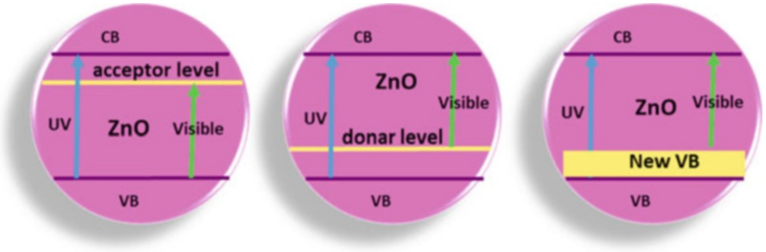

Fig. 5.5 Graphical illustration of the doped ZnO energy states

ejection also can occur upon thermal treatment. In many cases, the ejection happens only if the dopant exists within a few monolayers from the nanoparticle surface (Buonsanti and Milliron 2013). Generally, ZnO is an *n*-type semiconductor by the presence of zinc interstitials, zinc vacancy, and oxygen vacancies. The *n*-type doping of ZnO with a donor level is delivered by replacement of group I elements on the Zn site and group V on the O site. Subsequently, the exchange of group III elements on the Zn site and group VII elements on the O site leads to *n*-type ZnO (Samadi et al. 2016). Mostly, the efficacy of the dopant element relies on its electronegativity and variance between dopant ionic radius and zinc ionic radius. Reports have shown that doped ZnO exhibits better photocatalytic degradation efficiency than undoped ZnO. To attain stable and durable materials, the metal used in this method should be chemically inert, particularly towards photo-oxidation.

5.2.5.1 ZnO with Transition Metal Ions

The photocatalytic properties of ZnO have been studied with various transition metal ions. Modification of ZnO with noble metals such as platinum, silver, and gold would enhance photocatalytic degradation efficiency by localized surface plasmon resonance (LSPR), which is formed by the collective oscillation of the surface electrons showing pronounced potential for encompassing the light absorption range of wide bandgap semiconductors. Compared to other noble metals, Ag is more interesting because of its conductive and antibacterial properties. The synthesis of Ag–ZnO nanocomposite and Ag–ZnO core-shell nanoparticles has been reported.

Xiong et al. (2016) synthesized Ag–ZnO core-shell hetero-nanowires for the degradation of rhodamine 6G under solar light. They found that the photocatalytic activity and recycling stability of the hetero-nanowire is superior to that of the pure ZnO NPs. Dong and his research group studied the visible light response of ZnO/Ag photocatalyst towards xylenol orange dye degradation (Dong et al. 2014). They also examined the photocatalytic activity of Ag/ZnO with different Ag loading. The loading of Ag adjusts the band structure of ZnO/Ag to 2.85 eV, which leads to a better catalytic response. Gold is a significant noble metal that does not undergo corrosion during the process. The improved photocatalytic performance and enhanced plasmonic absorption of Au@ZnO core-shell NPs was studied by Shao et al. (2016) under stimulated sunlight and monochromatic LED light with three diverse wavelengths (365 nm, 520 nm, 660 nm) for degradation of rhodamine B. Platinum nanocrystals are widely used for their distinctive catalytic properties. Yu and his group observed a lower electron–hole recombination rate in the hollow Pt–ZnO nanocomposite and also showed high photocatalytic degradation towards acid orange II compared to pure ZnO and Pt-deposited ZnO NPs (Yu et al. 2013a). The ionic radii of iron (0.78 Å and 0.64 Å) and manganese are close to the ionic radius of zinc (0.74 Å). Hence, it can simply enter into Zn lattice sites either substitutionally or interstitially without altering the crystal structure of ZnO and can create extra charge carriers. The photocatalytic performance of Fe-doped ZnO for the degradation of methyl orange and methylene blue was studied by Saleh and Djaja (2014). The effect of Mg(II) doping on the optical, structural, and photocatalytic properties was also investigated: this increases surface area, shifts absorption to the visible region, and reduces the electron–hole recombination (Achouri et al. 2016). In Co doping, it can be easily substituted into ZnO lattices because the ionic radius is smaller compared to Zn^{2+}. Moreover, the third level of Co^{2+} located in the ZnO bandgap generates a new spectral band in the visible region that includes the ligand field (*d*–*d*) transaction focused at the dopant and charge transfer (CT) band. The improved charge separation and enhanced visible light absorption at Co sites in ZnO nano wires are observed towards the degradation of methyl orange under visible light irradiation (Sutka et al. 2016). Cu ion doping replaces Zn atoms in the ZnO lattice and induces *p*-type semi-conductivity in ZnO. Moreover, the addition of Cu increases the concentration of interstitial Zn, oxygen, and Zn vacancies, which leads to enhanced photoluminescence compared to pure ZnO NPs (Mittal et al. 2014). lIncorporation of Cu on ZnO leads a red shift towards the UV region in the absorption spectra, and extended absorption displays outstanding sunlight-driven photocatalytic degradation of methylene blue and rhodamine B dyes (Meshram et al. 2016). Vanadium-doped ZnO nano powders are also used for the removal of 2-chlorophenol under natural sunlight contact (Salah et al. 2016). The synthetic route varies the existence of V^{3+} along with V^{5+} state in vanadium-doped ZnO nanostructure. Absorption wavelength from UV-A to UV-B and UV-C regions can be extended by Mg ion doping. By changing the Mg^{2+} content, the bandgap can be altered from 3.3 to 7.8 eV for wurtzite and cubic structured $Mg_xZn_{1-x}O$ (Hullavarad et al. 2007). The superior photocatalytic activity of Mg-doped ZnO results from the increased bandgap, texture, and competent electron–hole separation (Etacheri et al. 2012). Ni-coupled ZnO nanoparticles quench the visible emission and increase the UV emission where the Ni NP performs as an electron trap and prolongs the charge separation period (Thein et al. 2016) (Fig. 5.6a–d). In the case of palladium (Pd), the ionic radius (0.080 nm) is close to the ionic radius of Zn^{2+} (0.074 nm). Hence, experiments were performed with different loadings of Pd into ZnO for the degradation of methyl orange (Zhong et al. 2012) and congo red (Guy et al. 2016). Similarly, other transition metal ions such as Ta (Kong et al. 2010) (Fig. 5.6e), Rh (Yu et al. 2013b), W (Changlin et al. 2011), and Yt (Sanoop et al. 2016) are also used as a dopant for ZnO NPs, and their influence on optical, electrical, and photocatalytic properties has been studied.

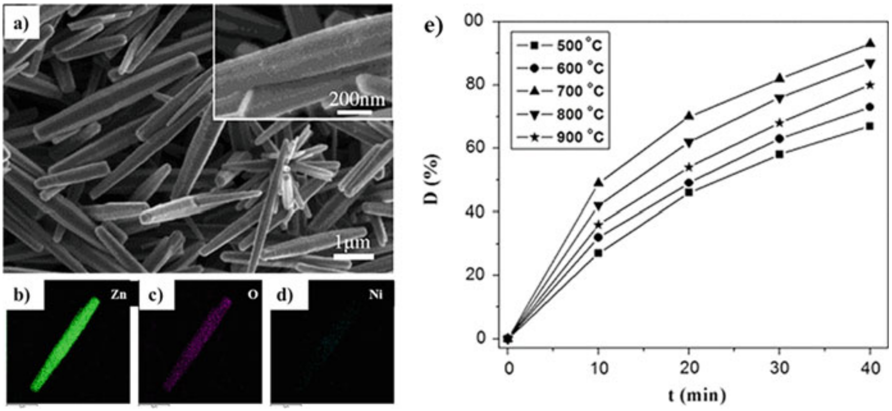

Fig. 5.6 (**a**) Field emission scanning electron microscopic image (FESEM) of Ni-doped ZnO NPs; (**b–d**) corresponding energy-dispersive spectroscopic (EDS) elemental mapping; (**e**) photo-degradation efficiency of methylene blue (MB) in presence of Ta-doped ZnO annealed at different temperatures (Thein et al. 2016; Kong at al. 2010)

5.2.5.2 ZnO with Rare Earth Metals

Rare earth (RE) metals are a substitute dopant of transition and other metals to alter the photocatalytic properties of ZnO. The insertion of rare earth metals into the semiconductor enhances the photocatalytic activity by concentrating the dye substrate onto the surface of the photocatalyst, retards the recombination of charge carriers upon excitation, and forms complexes with Lewis acid through the interaction of functional groups with the *f*-orbital (Myilsamy et al. 2016). Moreover, rare earth metal-doped ZnO serves as a diluted magnetic semiconductor by means of the higher magnetic moment of the RE ions, which are arbitrarily spread into the ZnO lattice and interact with other ions. The defect-induced optical absorption and photocatalytic degradation of Eu, Sm, Zr, Ce, Sm, and Ho have been studied with ZnO nanoparticles. Eu^{3+} is a promising dopant because of its great magnetic moment and optical property. It decreases the bandgap of ZnO upon doping and enhances the photocatalytic degradation of pollutants under visible light. Various doping concentrations of Eu^{3+} ions were studied with ZnO, revealing the room temperature ferromagnetism (RFM) property of the catalyst. Also, it displayed better degradation of RhB under UV light compared to pure ZnO NPs (Poornaprakash et al. 2018) (Fig. 5.7a, b). La-doped ZnO nanoparticles are used for the degradation of monocrotophos (MCP) (Anandan et al. 2007b) and 2,4,6-trichlorophenol (TCP) (Anandan et al. 2007a). X-ray powder diffraction (XRD) reports showed that addition of La to ZnO reduces the particle size compared to pure ZnO and also decreases with increasing La doping (Anandan et al. 2007a). Cerium (Ce) is a distinctive element with valence deviations in the rare earth group. The effect of Ce^{4+} doping on the structure and photocatalytic activity of ZnO has been studied (Wu et al. 2015; Liang et al. 2015). A porous 3D flower such as Ce^{4+}-doped ZnO

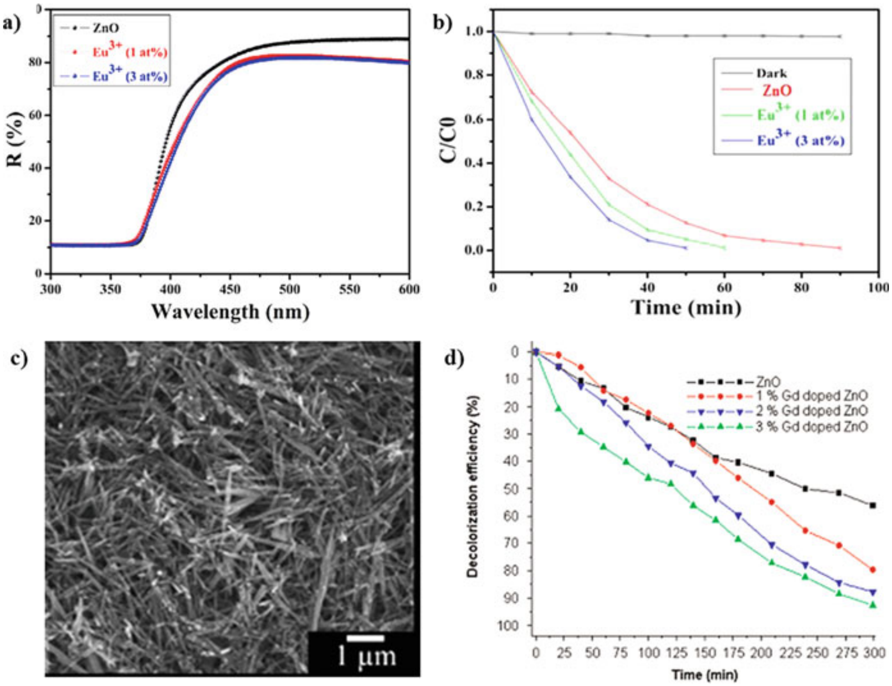

Fig. 5.7 (**a**) Diffused reflectance spectra (DRS) of Eu-doped ZnO NPs; (**b**) corresponding photocatalytic activity of the particles towards RhB; (**c**) SEM image of 3% Gd-doped ZnO NPs; (**d**) decolourization efficiency of Gd-doped ZnO NPs towards MB (Poornaprakasha et al. 2018; Yayapao et al. 2015)

nanoparticles and Ce^{3+}-doped ZnO superstructure were used for the photocatalytic degradation of RhB and methylene blue (MB), respectively (Liang et al. 2015; Wu et al. 2015). Bhatia et al. (2017) studied dysprosium-doped ZnO for the photocatalytic degradation of DR-31 dye. Y^{3+}-doping is expected to increase the photocatalytic proficiency of ZnO because the surface enhancement hampers the crystalline growth and also prompts oxygen vacancy (Atriabak et al. 2009). Sm doping increases the visible light absorption ability of Sm-doped ZnO NPs and creates an impurity energy level that enhances the degradation process. Photocatalytic degradation of malachite green (MG) was achieved using Sm-doped ZnO (Faraz et al. 2018). The average moment per Gd atom is more than 3278 µB. Hence, Gd-doped ZnO NPs can be controlled by temperature and external magnetic field. Moreover, oxygen vacancies and interstitial oxygen defects are rich in Gd-doped ZnO NPs (Franco and Pessoni 2017) and also show ferromagnetic properties at room temperature. The highest photocatalytic activity of Gd-doped ZnO NPs was observed in both UV and visible irradiation (Yayapao et al. 2015) (Fig. 5.7c, d). Nd incorporation increases the green emission of Nd-ZnO by increasing Nd concentration. Investigations of the effect of annealing on the properties of Nd-ZnO determined that it caused re-crystallization and assisted an extra photoluminescence band at 899 nm (Zhou et al. 2009). Photocatalytic degradation of MB was studied by Yayapao et al. (2013) using Nd-doped ZnO nano needles under UV light. Similarly, the photocatalytic activity of other RE metal ions such as Ho^{3+} (Phuruangrat et al. 2014), Pr^{3+} (Vaiano et al. 2017), and Er^{3+} (Bouhouche et al. 2018) has been studied towards the degradation of pollutants.

5.2.5.3 ZnO with Non-metals

Doping of non-metals with ZnO is a cost-effective method when compared to use of metal ions. Coupling of carbon materials with ZnO enhances photocatalytic performance in terms of photo-stability and photo-activity owing to its unique electronic and corrosion resistance properties. One of the drawbacks of ZnO NPs is photo-induced dissolution (Gerischer 1996). The overall photo-prompted dissolution of ZnO is described next.

$$\mathrm{ZnO} + 2\mathrm{h}^{+} \rightarrow \mathrm{Zn}^{2+} + 0.5\mathrm{O}_2$$

From the above equation, it can be understood that the dissolution occurred because of the reaction between the photo-generated hole and the surface oxygen. Moreover, the defect disorder also assists the photo-corrosion process. Hence, to boost stability, it is important to suppress both the defect disorder and the reaction. Incorporation of carbonaceous material with ZnO diminishes the activation of the surface oxygen atom by anchoring on the vacant site of ZnO NPs (Fu et al. 2008). Carbon materials such as carbon nano tube, C_{60}, graphene, and graphene oxide have been used to enhance the photocatalytic activity of ZnO NPs towards pollutant degradation (Han et al. 2014). Doping of nitrogen (N) results in bandgap narrowing of the ZnO process by mixing the *p*-state with the 2*p*-state of oxygen. Conversely, the replacing of O^{2-} with N is difficult compared to the metal ion because of variation in the charge state and ionic radii (Chen et al. 2005). The influence of N doping on the degradation of RhB was examined by Silva et al. (2016), who found that activity under UV and visible light varies with the loading of N on ZnO NPs. The photocatalytic performance of ZnO can be altered with doping of sulfur because of electro-negativity and large ionic radii. Research has shown controversy in bandgap narrowing (Bae et al. 2004) and broadening (Shen et al. 2005) with the addition of S into ZnO NPs, although the photocatalytic activity of S-ZnO NP has been studied for the degradation of congo red and azo dyes under visible light irradiation (Darzi et al. 2015).

5.2.5.4 ZnO–Metal Oxide System

The charge separation and photocatalytic performance of ZnO NPs (*n*-type) have been improved by coupled with other metal oxide (*p*/*n*-type) semiconductors. For

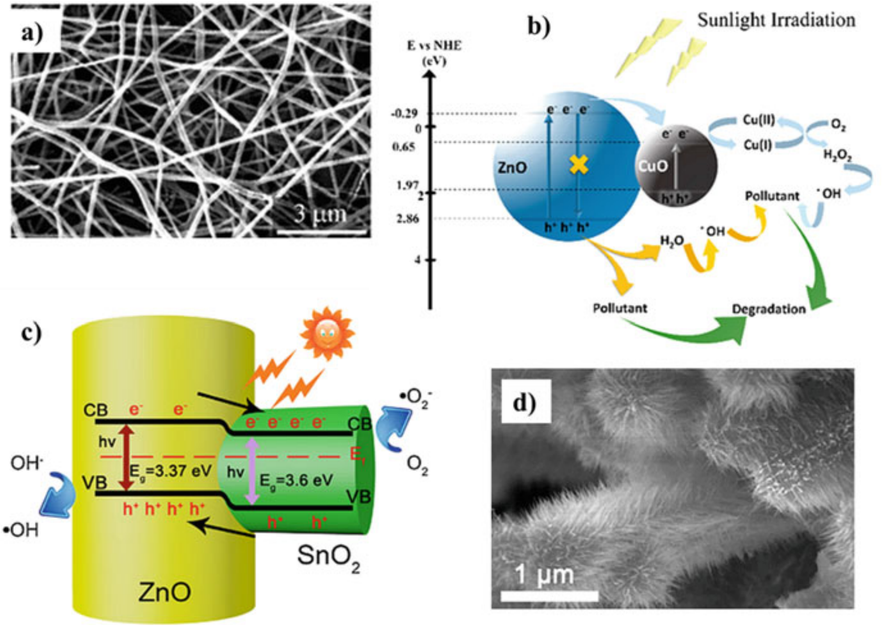

Fig. 5.8 (**a**) SEM image of ZnO/CuO (0.5 wt%); (**b**) graphic illustration of the band edge alignment and mechanism of charge transfer for degradation of pollutants by ZnO/CuO system; (**c**) SEM image of SnO_2@ZnO; (**d**) schematic diagram of the photocatalytic mechanism of SnO_2@ZnO (Naseri et al. 2017; Chen et al. 2008; Xu et al. 2018)

example, different loading of CuO added into the ZnO nanostructure improves the performance of ZnO towards the degradation of MB and bisphenol A under sunlight radiation (Naseri et al. 2017). Here, electro-spinning technique was used for fabrication of ZnO/CuO nanofibers (Fig. 5.8a). CuO is generally utilized as a co-catalyst with a huge bandgap catalyst and also a *p*-type semiconductor with a bandgap of 1.2–1.79 eV (Mageshwari et al. 2015). Incorporation of CuO into ZnO leads to reduction in the bandgap because of the existence of the Cu(3d) level, which is above the valence band, and also improves the charge separation. The results indicated that ZnO/CuO (0.5 wt%) samples showed better degradation activity than ZnO and CuO samples. Usually, these will produce *p*–*n* hetero-junctions and create an internal electric field at their interfaces. The inner electric field allows the photo-generated electrons to transfer to the conduction band (CB) of *n*-type semiconductors and the holes to the valence band (VB) of *p*-type semiconductors when irradiated with the light source (Chen et al. 2008) (Fig. 5.8b). Similarly, ZnO/CuO-coupled semiconductors were used for the degradation of MB, methyl orange (MO), congo red, and benzoic acid under visible light (Saravanan et al. 2013) and solar light illumination (Malwal and Gopinath 2017), respectively. The *p*–*n* hetero-junction was designed with cubic NiO and hexangular ZnO in NiO/ZnO nanofibers and utilized for the deprivation of rhodamine B (Zhang et al. 2010). The outcome revealed that

NiO/ZnO nanofibers have enhanced activity, more than NiO and ZnO nanofibers. Moreover, the catalyst can be simply recycled without decreasing photocatalytic activity with their 1D nanostructure. Higher photocatalytic degradation efficacy was observed towards rhodamine B and MO under UV light radiation from the ZnO@NiO core-shell hetero-nanostructure placed on a carbon fiber cloth substrate (Ding et al. 2018). Magnetically separable Fe_3O_4/ZnO material with graphene oxide was used for the deprivation of MO underneath visible light illumination (Feng et al. 2018). They observed a reduction in the bandgap of ZnO from 3.38 eV to 2.07 eV, which leads to enhanced recovery rate and efficiency. SnO_2 is the *n*-type extensive direct semiconductor (Eg = 3.6 eV) which is incorporated with ZnO. Xu et al. (2018) developed rutile SnO_2 nano wires on the surface of ZnO nano flowers and observed the photocatalytic performance of the material on MB degradation in visible light (Fig. 5.8c and d). The defect-related energy level, morphology, and hetero-junction are the factors responsible for the improved performance of the catalyst. In another study, Bi_2O_3 dots were sputtered on a ZnO thin film on a glass slide for deprivation of indigo carmine in UV and visible light (Medina et al. 2018). The catalyst showed excellent decolourization and mineralization under visible radiation by a synergetic effect when related to Bi_2O_3 and the ZnO thin film. Tubular In_2O_3/ZnO structures were synthesized by Wei and his research group (Wei et al. 2017) using carbon fiber as a template for deprivation of MO under visible light. They found that higher efficacy results from adsorption, diffusion, and charge separation. The effect of Eu_2O_3 on photocatalytic activity was examined with ZnO with different loading of Eu_2O_3 towards the degradation of MB under UV light, and a higher deprivation efficiency than ZnO was observed (Mohamed and Abu-Dief 2018). Similarly, other metal oxides such as Co_3O_4 (Reda et al. 2017), V_3O_4 (Harish et al. 2017), Al_2O_3 (Elhalil et al. 2018), and CeO_2 (Rajendran et al. 2016) were used with ZnO for photocatalytic degradation.

5.2.5.5 ZnO–Polymer System

The interaction between ZnO and polymer increases the photocatalytic performance of ZnO because (i) a large number of electrons are transported to the conduction band of ZnO; (ii) immobilization of the catalyst avoids recovery of the particles after treatment; and (iii) the elasticity of the polymer. Polyaniline (PANI), a conductive polymer used for the preparation of a polyaniline/ZnO composite material, was examined for the degradation of MB and MO in visible light illumination (Fig. 5.9a) (Saravanan et al. 2016). Various mole ratios of PANI were examined with ZnO, the better activity being found at a 1.5 M ratio. A decline has been observed in the crystallite size and crystallinity with increasing PANI concentration. The PANI/ZnO combination also used for the elimination of acid blue, AB25, from model wastewater (Gilja et al. 2018). Catalyst performance was monitored under solar irradiation. The studies indicate that dissolution of ZnO is prevented by the addition of PNI; morphology and surface area considerably affect catalytic performance. Pompon-like ZnO-PANI hetero-nanostructure (Fig. 5.9b) was used for

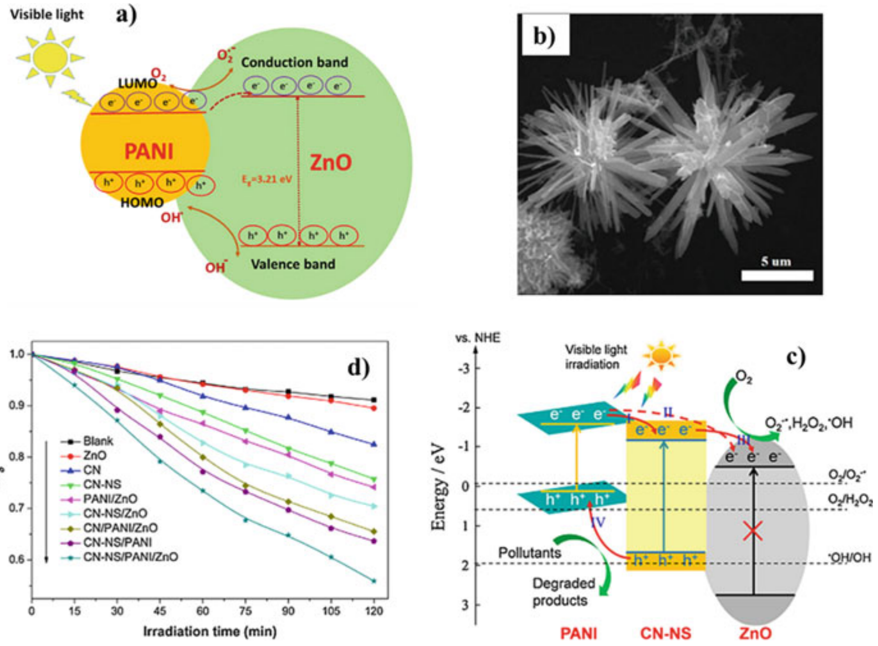

Fig. 5.9 (**a**) Photocatalytic mechanism of PANI/ZnO system. (**b**) SEM images of pompon-like ZnO-PANI. (**c**) Photocatalytic mechanism of carbon nitride/polyaniline/ZnO catalyst. (**d**) Photodegradation curve of 4-chlorophenol under visible light (Saravanan et al. 2016; Zou et al. 2017; Pandiselvi et al. 2016)

various water pollutant treatments such as photocatalytic degradation, photo-induced heavy metal adsorption, and deactivation of *Escherichia coli* and *Staphylococcus aureus* under visible light irradiation (Zou et al. 2017). Polyaniline@polyacrylonitrile@ZnO nanofiber is used for the derivation of MB under UV light irradiation (Zhu et al. 2018). The synthesis is done by the immobilization of polyaniline on electrospun polyacrylonitrile nanofiber. Then, ZnO NPs are placed on the polyaniline@polyacrylonitrile nanofiber. The catalyst has shown better activity than polyaniline@polyacrylonitrile and polyaniline@ZnO nanofiber owing to charge separation. Photocatalytic deprivation of congo red and crystal violet using cellulose/PVC/ZnO composites was studied by Linda and his research group (Linda et al. 2016). In the experiment, carried out under UV irradiation, 90% of dyes were degraded after a short period of illumination. Moreover, the composite showed better catalytic activity than the PVC/ZnO nanocomposite. Poly(amido amine) (PAMAM) dendrimer is used with ZnO through glycidoxypropyltrimethoxy silane as a binding material (Krishnakumar and Imae 2014). The nanocomposite was examined for photocatalytic degradation of naphthol blue black under UV radiation. A poly(methyl methacrylate) (PMMA)/ZnO nanocomposite was prepared by Mauro et al. (2017) using atomic layer deposition and used it for the photocatalytic deprivation of MB and phenol under UV light. The material is stable and reusable even after several runs of MB decolorization. Poly[2,20-(*m*-phenylen)-5,50-bisbenzimidazole/ZnO and poly(2,5-benzimidazole)/ZnO composites were prepared with different loading of ZnO (Penchev et al. 2018). Photocatalytic performance was examined using malachite green (MG), MB, and MO as model pollutants. Higher catalytic activity was found at 2.5 wt% of ZnO, and the highest deprivation rate was observed using poly[2,20-(*m*-phenylen)-5,50-bisbenzimidazole/ZnO (2.5 wt%). Carbon nitride/polyaniline/ZnO ternary composite material was utilized for the improved photocatalytic deprivation of MB and 4-chlorophenol under visible light (Fig. 5.9c, d) where exfoliated carbon nitride nanosheets were provisioned (Pandiselvi et al. 2016).

5.2.5.6 ZnO Hybrid/Composite System

The interesting part in the composite material is the semiconductor, which can be conjugated with either plasmonic/magnetic or plasmonic/magnetic/semiconductor. Hence, it can acquire the property of each component. The property of the hybrid material relies strongly on the crystal faces and morphology. Difficulties in the preparation of well-defined composite materials are (i) morphological control, (ii) lattice mismatching, and (iii) charge transfer. Metal–semiconductor hybrid nanomaterials show enhanced photocatalytic property when compared to a single dopant. Fernando et al. (2018) studied the photocatalytic degradation properties of Au-ZnO and Pt-Au-ZnO nanohybrids using thiazine dye. Moreover, they have examined the charge accumulation and discharging property of these materials. They discovered that Au-ZnO NPs are good for the photo-reduction process by the accumulation of electrons, whereas Pt-Au-ZnO showed superior photocatalytic activity and mineralization from the rapid electron discharge (Fig. 5.10a–c). Hence, it is important to choose the right metal for the desired application. Hybridization of transition and rare earth metal doping also studied with ZnO NPs. Vignesh et al. (2014) examined the photocatalytic activity of Ni-Th-ZnO NPs towards the degradation of MB under visible light. The result revealed the enhanced performance of the material from the cooperative activity of Ni and Th. The proficient charge separation and transmission to the reaction site were observed in ZnO NPs with other semiconductor materials such as Ag_2O, MoS_2, CuO, In_2S_3, and $FeWO_4$ because of the formation of hetero-junctions. The photocatalytic activity of $ZnWO_4$/ZnO and $FeWO_4$@$ZnWO_4$/ZnO hetero-junctions was examined towards the degradation of RhB, MB, and phenol by visible light (Wang et al. 2016). The interfacial carriage of photo-generated holes between $FeWO_4$ and $ZnWO_4$/ZnO, and enhanced charge separation and transfer of carriers in the hetero-junctions were observed, to which was attributed the superior performance of $FeWO_4$@$ZnWO_4$/ZnO NPs (Fig. 5.10d). Attempts have been made to incorporate carbonaceous material with ZnO as a support. The graphene oxide (GO)-based ternary GO–$CuFe_2O_4$–ZnO system was used for enhanced photocatalytic activity toward MO, MB, RhB, and phenol under sunlight irradiation (Kumar et al. 2017).

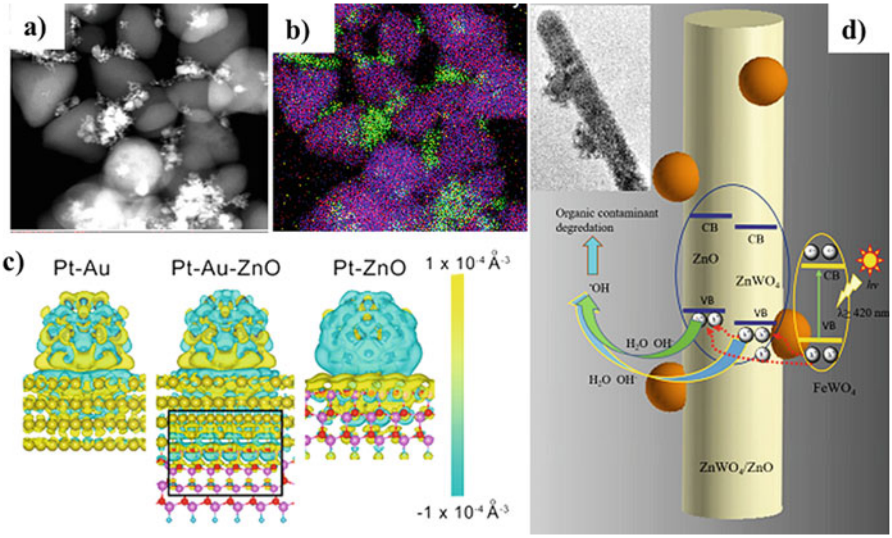

Fig. 5.10 (**a**) SEM image of Pt-Au-ZnO NPs. (**b**) EDS mapping of Pt-Au-ZnO NPs. (**c**) Charge difference between Pt-Au, Pt-Au-ZnO, and Pt-ZnO. (**d**) Schematic illustration for the mechanism of photocatalytic degradation over $FeWO_4@ZnWO_4/ZnO$ NPs [*inset* is the transmission electron microscopic (TEM) image of the corresponding particle] (Fernando et al. 2018; Wang et al. 2016)

5.3 Conclusion

Various synthetic methodologies have been developed to produce ZnO nanoparticles of amazing morphology and surface area. Size and shape are the main factors that influence the performance of ZnO NPs during the photocatalytic degradation process. The doped ZnO NPs exhibit better photocatalytic activitythan undoped ZnO NPs. Deposition of optimum loading of metal ions/non-metal ions/metal oxides/polymer on the surface of ZnO NPs enhances the degradation of pollutants by harvesting the light at higher wavelengths, lowering the bandgap of ZnO, extending the lifetime of charge carriers, enhancing the charge transfer process, and increasing the surface area and active site of the catalyst, although these improvements are not sufficient for real-life applications because the dopant leaches and charge carrier recombination centers in the catalyst increase during the recycling process. Hence, it is necessary to focus on the cost and lifetime of the catalyst and the operation. Under these conditions, the photocatalyst should be balanced between efficiency, energy, and economics.

Acknowledgments S.K. thanks SERB, Govt. of India, for SERB-National post-doctoral fellowship and Dr. S. Venugopal, Assistant Professor, Department of Chemical Engineering, Indian Institute of Science (IISc), for his constant support.

References

Achouri F, Corbel S, Balan L, Mozet K, Girot E, Medjahdi G, Said MB, Ghrabi A, Schneider R (2016) Porous Mn-doped ZnO nanoparticles for enhanced solar and visible light photocatalysis. Mater Des 101:309–316. https://doi.org/10.1016/j.matdes.2016.04.015

Agarwal H, Kumar SV, Rajeshkumar S (2017) A review on green synthesis of zinc oxide nanoparticles: an eco-friendly approach. Resour Effic Technol 3(4):406–413. https://doi.org/10.1016/j.reffit.2017.03.002

Ahmad A, Mohd-Setapar SH, Chuong CS, Khatoon A, Wani WA, Kumar R, Rafatullah M (2015) Recent advances in new generation dye removal technologies: novel search for approaches to reprocess wastewater. RSC Adv 5(39):30801–30818. https://doi.org/10.1039/C4RA16959J

Al-Shabib NA, Husain FM, Ahmed F, Khan RA, Ahmad I, Alsharaeh E, Khan MS, Hussain A, Rehman AT, Yusuf M, Hassan I, Khan JM, Ashraf GM, Alsalme A, Ajmi MFA, Tarasov VV, Aliev G (2016) Biogenic synthesis of zinc oxide nanostructures from *Nigella sativa* seed: prospective role as food packaging material inhibiting broad-spectrum quorum sensing and biofilm. Sci Rep 6(1):1–15. https://doi.org/10.1038/srep36761

Ali I, Aboul-Enein HY (2004) Chiral pollutants: distribution, toxicity and analysis by chromatography and capillary electrophoresis. Wiley, Chichester

Ali MA, Emanuelsson EAC, Patterson DA (2010) Photocatalysis with nanostructured zinc oxide thin films: the relationship between morphology and photocatalytic activity under oxygen limited and oxygen rich conditions and evidence for a Mars Van Krevelen mechanism. Appl Catal B 97(1-2):168–181. https://doi.org/10.1016/j.apcatb.2010.03.037

Alves SP, Brum DM, Branco de Andrade EC, Pereira Netto AD (2008) Determination of synthetic dyes in selected foodstuffs by high performance liquid chromatography with UV-DAD detection. Food Chem 107(1):489–496. https://doi.org/10.1016/j.foodchem.2007.07.054

Anand Raj LFA, Jayalakshmy E (2015) Biosynthesis and haracterization of zinc oxide nanoparticles using root extract of *Zingiber officinale*. Orient J Chem 3(1):51–56. https://doi.org/10.13005/ojc/310105

Anandan S, Vinu A, Mori T, Gokulakrishnan N, Srinivasu P, Murugesan V, Ariga K (2007a) Photocatalytic activity of La-doped ZnO for the degradation of monocrotophos in aqueous suspension. J Mol Catl A Chem 266(1):149–157. https://doi.org/10.1016/j.molcata.2006.11.008

Anandan S, Vinu A, Mori T, Gokulakrishnan N, Srinivasu P, Murugesan V, Ariga K (2007b) Photocatalytic degradation of 2,4,6-trichlorophenol using lanthanum doped ZnO in aqueous suspension. Catal Commun 8(9):1377–1382. https://doi.org/10.1016/j.catcom.2006.12.001

Atriabak I, Bueno-Lopez A, Garcia-Garcia A (2009) Role of yttrium loading in the physico-chemical properties and soot combustion activity of ceria and ceria-zirconia catalysts. J Mol Catal A Chem 300(1-2):103–110. https://doi.org/10.1016/j.molcata.2008.10.043

Bae SY, Seo HW, Park J (2004) Vertically aligned sulfur-doped ZnO nanowires synthesized via chemical vapor deposition. J Phys Chem B 108(17):5206–5210. https://doi.org/10.1021/jp036720k

Baxter JB, Schmuttenmaer CA (2006) Conductivity of ZnO nanowires, nanoparticles, and thin films using time-resolved terahertz spectroscopy. J Phys Chem B 110(50):25229–25239. https://doi.org/10.1021/jp064399a

Bazin I, Hassine AH, Hamouda YH, Mnif W, Bartegi A, Ferber ML, Waard MD, Gonzalez C (2012) Estrogenic and anti-estrogenic activity of 23 commercial textile dyes. Ecotoxicol Environ Saf 85:131–136. https://doi.org/10.1016/j.ecoenv.2012.08.003

Bhatia S, Verma N, Kumar R (2017) Morphologically-dependent photocatalytic and gas sensing application of Dy-doped ZnO nanoparticles. J Alloys Compd 726:1274–1285. https://doi.org/10.1016/j.jallcom.2017.08.048

Bojesen ED, Jensen KMO, Tyrsted C, Lock N, Christensen M, Iversen BB (2014) In situ powder diffraction study of the hydrothermal synthesis of ZnO nanoparticles. Cryst Growth Des 14 (6):2803–2810. https://doi.org/10.1021/cg5000606

Borhade AV, Tope DR, Uphade BK (2012) An efficient photocatalytic degradation of methyl blue dye by using synthesised PbO nanoparticles. E-J Chem 9(2):705–715. https://doi.org/10.1155/2012/362680

Bouhouche S, Bensouici F, Toubane M, Azizi A, Otmani A, Chebout K, Kezzoula F, Ighil RT, Bououdina M (2018) Effect of Er^{3+} doping on structural, morphological and photocatalytical properties of ZnO thin films. Mater Res Express 5:056407–056420. https://doi.org/10.1088/2053-1591/aac4e8

Breault TM, Bartlett BM (2012) Lowering the band gap of anatase-structured TiO_2 by coalloying with Nb and N: electronic structure and photocatalytic degradation of methylene blue dye. J Phys Chem C 116(10):5986–5994. https://doi.org/10.1021/jp2078456

Buonsanti R, Milliron DJ (2013) Chemistry of doped colloidal nanocrystals. Chem Mater 25 (8):1305–1317. https://doi.org/10.1021/cm304104m

Changlin Y, Kai Y, Qing S, Jimmy CY, Fangfang C, Xin L (2011) Preparation of WO_3/ZnO composite photocatalyst and its photocatalytic performance. Chin J Catal 32(3-4):555–565. https://doi.org/10.1016/S1872-2067(10)60212-4

Chen XB, Lou YB, Samia ACS, Burda C, Gole JL (2005) Formation of oxynitride as the photocatalytic enhancing site in nitrogen-doped titania nanocatalysts: Comparison to a commercial nanopowder. Adv Funct Mater 15(1):41–49. https://doi.org/10.1002/adfm.200400184

Chen S, Zhang S, Liu W, Zhao W (2008) Preparation and activity evaluation of *p*–*n* junction photocatalyst NiO/TiO_2. J Hazard Mater 155(1-2):320–326. https://doi.org/10.1016/j.jhazmat.2007.11.063

Chen D, Viswanatha R, Ong GL, Xie R, Balasubramaninan M, Peng X (2009) Temperature dependence of “elementary processes” in doping semiconductor nanocrystals. J Am Chem Soc 131(26):9333–9339. https://doi.org/10.1021/ja9018644

Crini G (2006) Non-conventional low-cost adsorbents for dye removal: a review. Bioresour Technol 97(9):1061–1085. https://doi.org/10.1016/j.biortech.2005.05.001

Dai K, Zhu G, Liu Z, Liu Q, Chen Z, Lu L (2012) Facile preparation and growth mechanism of zinc oxide nanopencils. Mater Lett 67(1):193–195. https://doi.org/10.1016/j.matlet.2011.09.079

Daneshvar E, Vazirzadeh A, Niazi A et al (2017) Desorption of methylene blue dye from brown macroalga: effects of operating parameters, isotherm study and kinetic modeling. J Clean Prod. https://doi.org/10.1016/j.jclepro.2017.03.119

Darzi SJ, Mahjoub AR, Bayat A (2015) Sulfur modified ZnO nanorod as a high performance photocatalyst for degradation of Congoredazo dye. Int J Nano Dimens 6(4):425–431

Dauda SNHM, Haw C, Chiu W, Aspanut Z, Chia M, Khanis NH, Khiew P, Hamid MAA (2016) ZnO nanonails: organometallic synthesis, self-assembly and enhanced hydrogen gas production. Mater Sci Semicond Process 56:228–237. https://doi.org/10.1016/j.mssp.2016.08.021

Dawson A, Kamat PV (2001) Semiconductor-metal nanocomposites. Photoinduced fusion and photocatalysis of gold-capped TiO_2 (TiO_2/gold) nanoparticles. J Phys Chem B 105(5):960–966. https://doi.org/10.1021/jp0033263

Deng W, Chen D, Chen L (2015) Synthesis of monodisperse CeO_2 hollow spheres with enhanced photocatalytic activity. Ceram Int 41(9):11570–11575. https://doi.org/10.1016/j.ceramint.2015.04.170

Ding M, Yang H, Yan T, Wang C, Deng X, Zhang S, Huang J, Shao M, Xu X (2018) Fabrication of hierarchical ZnO@NiO core-shell heterostructures for improved photocatalytic performance. Nanoscale Res Lett 13:260–269. https://doi.org/10.1186/s11671-018-2676-1

Dong Y, Feng C, Jiang P, Wang G, Li K, Miao H (2014) Simple one-pot synthesis of ZnO/Ag heterostructures and the application in visible light-responsive photocatalysis. RSC Adv 4 (14):7340–7346. https://doi.org/10.1039/C3RA46655H

Dutta AK, Maji SK, Adhikary B (2014) γ-Fe_2O_3 nanoparticles: an easily recoverable effective photo-catalyst for the degradation of rose bengal and methylene blue dyes in the waste-water treatment plant. Mater Res Bull 49:28–34. https://doi.org/10.1016/j.materresbull.2013.08.024

Ejhieh AN, Shamsabadi MK (2013) Decolorization of a binary azo dyes mixture using CuO incorporated nanozeolite-X as a heterogeneous catalyst and solar irradiation. Chem Eng J 228:631–641. https://doi.org/10.1016/j.cej.2013.05.035

Elhalil A, Elmoubarki R, Farnane M, Machrouhi A, Sadiq M, Mahjoubi FZ, Qourzal S, Barka N (2018) Photocatalytic degradation of caffeine as a model pharmaceutical pollutant on Mg doped ZnO-Al_2O_3 heterostructure. Environ Nanotechnol Monit Manag 10:63–72. https://doi.org/10.1016/j.enmm.2018.02.002

Epling GA, Lin C (2002) Investigation of retardation effects on the titanium dioxide photodegradation system. Chemosphere 46(6):937–944. https://doi.org/10.1016/S0045-6535(01)00172-2

Etacheri V, Roshan R, Kumar V (2012) Mg-doped ZnO nanoparticles for efficient sunlight-driven photocatalysis. ACS Appl Mater Interfaces 4(5):2717–2725. https://doi.org/10.1021/am300359h

Faraz M, Naqvi FK, Shakira M, Khare N (2018) Synthesis of samarium-doped zinc oxide nanoparticles with improved photocatalytic performance and recyclability under visible light irradiation. New J Chem 42(3):2295–2305. https://doi.org/10.1039/c7nj03927a

Feng Q, Li S, Ma W, Fan HJ, Wan X, Lei Y, Chen Z, Yang J, Qin B (2018) Synthesis and characterization of Fe_3O_4/ZnO-GO nanocomposites with improved photocatalytic degradation methyl orange under visible light irradiation. J Alloys Compd 737:197–206. https://doi.org/10.1016/j.jallcom.2017.12.070

Fernando JFS, Shortell MP, Firestein KL, Zhang C, Larionov KV, Popov ZI, Sorokin PB, Bourgeois L, Waclawik ER, Golberg DV (2018) Photocatalysis with Pt-Au-ZnO and Au-ZnO hybrids: effect of charge accumulation and discharge properties of metal nanoparticles. Langmuir 34(25):7334–7345. https://doi.org/10.1021/acs.langmuir.8b00401

Franco A Jr, Pessoni HVS (2017) Effect of Gd doping on the structural, optical band-gap, dielectric and magnetic properties of ZnO nanoparticles. Physica B 506:145–151. https://doi.org/10.1016/j.physb.2016.11.011

Fu H, Xu T, Zhu S, Zhu Y (2008) Photocorrosion inhibition and enhancement of photocatalytic activity for ZnO via hybridization with C_{60}. Environ Sci Technol 42(21):8064–8069. https://doi.org/10.1021/es801484x

Gerischer H (1996) Electrochemical behaviour of semiconductors under illumination. J Electrochem Soc 113:1174–1182

Ghasemi M, Naushad M, Ghasemi N, Khosravi-fard Y (2014) A novel agricultural waste based adsorbent for the removal of Pb(II) from aqueous solution: kinetics, equilibrium and thermodynamic studies. J Ind Eng Chem 20:454–461. https://doi.org/10.1016/j.jiec.2013.05.002

Gilja V, Vrban I, Mandic V, Žic M, Murgic ZH (2018) Preparation of a PANI/ZnO composite for efficient photocatalytic degradation of acid blue. Polymers 10:940–957. https://doi.org/10.3390/polym10090940

Guan YF, Pedraza AJ (2008) Synthesis and alignment of Zn and ZnO nanoparticles by laser-assisted chemical vapor deposition. Nanotechnology 19(4):045609–045616. https://doi.org/10.1088/0957-4484/19/04/045609

Guo Y, Wang Y, Hu C, Wang Y, Wang E (2000) Microporous polyoxometalates POMs/SiO_2: synthesis and photocatalytic degradation of aqueous organocholorine pesticides. Chem Mater 12(11):3501–3508. https://doi.org/10.1021/cm000074+

Guy N, Cakar S, Ozacar M (2016) Comparison of palladium/zinc oxide photocatalysts prepared by different palladium doping methods for congo red degradation. J Colloid Interface Sci 466:128–137. https://doi.org/10.1016/j.jcis.2015.12.009

Han C, Yang MQ, Weng B, Xu YJ (2014) Improving the photocatalytic activity and anti-photocorrosion of semiconductor ZnO by coupling with versatile carbon. Phys Chem Chem Phys 16(32):16891–16903. https://doi.org/10.1039/c4cp02189d

Harish S, Sabarinathan M, Archana J, Navaneethan M, Ponnusamy S, Muthamizhchelvan C, Ikeda H, Hayakawa Y (2017) Functional properties and enhanced visible light photocatalytic performance of V_3O_4 nanostructures decorated ZnO nanorods. Appl Surf Sci 418:171–178. https://doi.org/10.1016/j.apsusc.2017.02.261

Hayat K, Gondal MA, Khaled MM, Yamani ZH, Ahmed S (2011) Laser induced photocatalytic degradation of hazardous dye (Safranin-O) using self-synthesized nanocrystalline WO_3. J Hazard Mater 186(2-3):1226–1233. https://doi.org/10.1016/j.jhazmat.2010.11.133

Hong RY, Li JH, Chen LL, Liu DQ, Li HZ, Zheng Y, Ding J (2009) Synthesis, surface modification and photocatalytic property of ZnO nanoparticles. Powder Technol 189(3):426–432. https://doi.org/10.1016/j.powtec.2008.07.004

Hou Z, Wang Y, Shen L, Guo H, Wang G, Li Y, Zhou S, Zhang Q, Jiang Q (2012) Synthesis of dumbbell-like ZnO microcrystals via a simple solution route. Nanoscale Res Lett 7:507–514. https://doi.org/10.1186/1556-276X-7-507

Hu H, Huang X, Deng C, Chen X, Qian Y (2007) Hydrothermal synthesis of ZnO nanowires and nanobelts on a large scale. Mater Chem Phys 106(1):58–62. https://doi.org/10.1016/j.matchemphys.2007.05.016

Hughes WL, Wang ZL (2004) Formation of piezoelectric single-crystal nanorings and nanobows. J Am Chem Soc 126(21):6703–6709. https://doi.org/10.1021/ja049266m

Hullavarad SS, Hullavarad NV, Pugel DE, Dhar S, Venkatesan T, Takeuchi I, Vispute RD (2007) Homo- and hetero-epitaxial growth of hexagonal and cubic $Mg_xZn_{1-x}O$ alloy thin films by pulsed laser deposition technique. J Phys D Appl Phys 40(16):4887–4895. https://doi.org/10.1088/0022-3727/40/16/020

Hustert K, Zepp RG (1992) Photocatalytic degradation of selected azo dyes. Chemosphere 24 (3):335–342. https://doi.org/10.1016/0045-6535(92)90301-7

Iravani S, Korbekandi H, Mirmohammadi SV, Zolfaghari B (2014) Synthesis of silver nanoparticles: chemical, physical and biological methods. Res Pharm Sci 9(6):385–406. PMCID: PMC4326978

Ismail RA, Ali AK, Ismail MM, Hassoon KI (2001) Preparation and characterization of colloidal ZnO nanoparticles using nanosecond laser ablation in water. Appl Nanosci 1(1):45–49. https://doi.org/10.1007/s13204-011-0006-3

Jayaseelan C, Rahuman AA, Kirthi AV, Marimuthua S, Santhosh Kumar T, Bagavana A, Gaurav K, Karthik L, Bhaskara Rao KV (2012) Novel microbial route to synthesize ZnO nanoparticles using *Aeromonas hydrophila* and their activity against pathogenic bacteria and fungi. Spectrochim Acta A Mol Biomol Spectrosc 90:78–84. https://doi.org/10.1016/j.saa.2012.01.006

Kanjwal MA, Sheikh FA, Barakat NAM, Li X, Kim HY, Chronakis IS (2012) Zinc oxide's hierarchical nanostructure and its photocatalytic properties. Appl Surf Sci 258(8):3695–3702. https://doi.org/10.1016/j.apsusc.2011.12.008

Kaviya S (2017) Rapid naked eye detection of arginine by pomegranate peel extract stabilized gold nanoparticles. J King Saud Univ Sci. https://doi.org/10.1016/j.jksus.2017.12.001

Kaviya S (2018) Size dependent ratiometric detection of Pb (II) ions in aqueous solution by light emitting biogenic CdS NPs. J Lumin 195:209–215. https://doi.org/10.1016/j.jlumin.2017.11.031

Kaviya S, Prasad E (2015a) Biogenic synthesis of ZnO-Ag nano custard apple for efficent photocatalytic degradation of methylene blue by sunlight irradation. RSC Adv 5(22): 17179–17185. https://doi.org/10.1039/C4RA15293J

Kaviya S, Prasad E (2015b) Sequential detection of Fe^{3+} and As^{3+} ions by naked eye through aggregation and disaggregation of biogenic gold nanoparticles. Anal Methods 7(1):168–174. https://doi.org/10.1039/C4AY02342K

Kaviya S, Prasad E (2016) Eco-friendly synthesis of ZnO nano pencils in aqueous medium: a study of photocatalytic degradation of methylene blue under direct sunlight. RSC Adv 6 (40):33821–33827. https://doi.org/10.1039/C6RA04306B

Kaviya S, Kabila S, Jayasree KV (2017a) Hexagonal bottom-neck ZnO nano pencils: a study of structural, optical and antibacterial activity. Mater Lett 204:57–60. https://doi.org/10.1016/j.matlet.2017.06.018

Kaviya S, Kabila S, Jayasree KV (2017b) Room temperature biosynthesis of greatly stable fluorescent ZnO quantum dots for the selective detection of Cr^{3+} ions. Mater Res Bull 95:163–168. https://doi.org/10.1016/j.materresbull.2017.07.025

Kennedy DO, Wightman EL (2011) Herbal extracts and phytochemicals: plant secondary metabolites and the enhancement of human brain function. Adv Nutr 2(1):32–50. https://doi.org/10.3945/an.110.000117

Khalil LB, Mourad WE, Rophael MW (1998) Photocatalytic reduction of environmental pollutant Cr(VI) over some semiconductors under UV/visible light illumination. Appl Catal B 17 (3):267–273. https://doi.org/10.1016/S0926-3373(98)00020-4

Khan R, Hassan MS, Cho HS, Polyakov AY, Khil MS, Lee IH (2014) Facile low-temperature synthesis of ZnO nanopyramid and its application to photocatalytic degradation of methyl orange dye under UV irradiation. Mater Lett 133:224–227. https://doi.org/10.1016/j.matlet.2014.07.006

Khan MF, Ansari AH, Hameedullah M, Ahmad E, Husain FM, Zia Q, Baig U, Zaheer MR, Alam MM, Khan AM, Alothman ZA, Ahmad I, Ashraf GM, Aliev G (2016) Sol-gel synthesis of thorn-like ZnO nanoparticles endorsing mechanical stirring effect and their antimicrobial activities: potential role as nano-antibiotics. Sci Rep 6:27689–27691. https://doi.org/10.1038/srep27689

Kong JZ, Li AD, Li XY, Zhai HF, Zhang WQ, Gong YP, Li H, Wu D (2010) Photo-degradation of methylene blue using Ta-doped ZnO nanoparticle. J Solid State Chem 183(6):1359–1364. https://doi.org/10.1016/j.jssc.2010.04.005

Konstantinou IK, Albanis TA (2004a) DeNO$_x$ performance of Ag/Al$_2$O$_3$ catalyst using simulated diesel fuel-ethanol mixture as reductant. Appl Catal B 49(1–2):1–14. https://doi.org/10.1016/j.apcatb.2011.03.017

Konstantinou IK, Albanis TA (2004b) TiO$_2$ assisted photocatalytic degradation of azo dyes in aqueous solution: kinetic and mechanistic investigations: a review. Appl Catal B Environ 49 (1):1–14. https://doi.org/10.1016/j.apcatb.2003.11.010

Krishnakumar B, Imae T (2014) Chemically modified novel PAMAM-ZnO nanocomposite: synthesis, characterization and photocatalytic activity. Appl Catal A Gen 486:170–175. https://doi.org/10.1016/j.apcata.2014.08.010

Kumar VV, Gayathri K, Anthony SP (2016) Synthesis of α-MoO$_3$ nanoplates using organic aliphatic acids and investigation of sunlight enhanced photodegradation of organic dyes. Mater Res Bull 76:147–154. https://doi.org/10.1016/j.materresbull.2015.12.016

Kumar A, Rout L, Achary LSK, Mohanty SK, Dash P (2017) A combustion synthesis route for magnetically separable graphene oxide-CuFe$_2$O$_4$-ZnO nanocomposites with enhanced solar light mediated photocatalytic activity. New J Chem 41(19):10568–10583. https://doi.org/10.1039/C7NJ02070H

Liang Y, Guoa N, Lia L, Lia R, Jia G, Gan S (2015) Preparation of porous 3D Ce-doped ZnO microflowers with enhanced photocatalytic performance. RSC Adv 5(74):59887–59894. https://doi.org/10.1039/C5RA08519E

Linda T, Muthupoongodi S, Shajan XS, Balakumar S (2016) Photocatalytic degradation of congo red and crystal violet dyes on cellulose/PVC/ZnO composites under UV light irradiation. Mater Today Proc 3(6):2035–2041. https://doi.org/10.1016/j.matpr.2016.04.106

Lingaraju K, Naika HR, Manjunath K, Basavaraj RB, Nagabhushana H, Nagaraju G, Suresh D (2016) Biogenic synthesis of zinc oxide nanoparticles using *Ruta graveolens* (L.) and their antibacterial and antioxidant activities. Appl Nanosci 6(5):703–710. https://doi.org/10.1007/s13204-015-0487-6

Liu B, Zeng HC (2004) Fabrication of ZnO "dandelions" via a modified Kirkendall process. J Am Chem Soc 126(51):16744–16746. https://doi.org/10.1021/ja044825a

Liu H, Yang J, Liang J, Huang Y, Tang C (2008) ZnO nanofiber and nanoparticle synthesized through electrospinning and their photocatalytic activity under visible light. J Am Ceram Soc 91 (4):1287–1291. https://doi.org/10.1111/j.1551-2916.2008.02299.x

Long T, Yin S, Takabatake K, Zhnag P, Sato T (2009) Synthesis and characterization of ZnO nanorods and nanodisks from zinc chloride aqueous solution. Nanoscale Res Lett 4(3):247–253. https://doi.org/10.1007/s11671-008-9233-2

Lu XH, Wang D, Li GR, Su CY, Kuang DB, Tong YX (2009) Controllable electrochemical synthesis of hierarchical ZnO nanostructures on FTO glass. J Phys Chem C 113 (31):13574–13582. https://doi.org/10.1021/jp902834j

Lu HX, Zhao YL, Yu XJ, Chen DL, Zhang LW, Xu HL, Yang DY, Wang HL, Zhang R (2011) Controllable synthesis of spindle-like ZnO nanostructures by a simple low-temperature aqueous solution route. Appl Surf Sci 257(9):4519–4523. https://doi.org/10.1016/j.apsusc.2010.12.115

Lyapina OA, Baranov N, Panin GN, Knotko AV, Kononenko V (2008) Synthesis of ZnO nanotetrapods. Inorg Mater 44(8):846–852. https://doi.org/10.1134/S0020168508080116

Ma J, Liu J, Bao Y, Zhu Z, Wang X, Zhang J (2013) Synthesis of large-scale uniform mulberry-like ZnO particles with microwave hydrothermal method and its antibacterial property. Ceram Int 39 (3):2803–2810. https://doi.org/10.1016/j.ceramint.2012.09.049

Mageshwari K, Nataraj D, Pal T, Sathyamoorthy R, Park J (2015) Improved photocatalytic activity of ZnO coupled CuO nanocomposites synthesized by reflux condensation method. J Alloys Compd 625:362–370. https://doi.org/10.1016/j.jallcom.2014.11.109

Malato S, Blanco J, Vidal A, Richter C (2002) Photocatalysis with solar energy at a pilotplant scale: an overview. Appl Catal B Environ 37(1):1–15. https://doi.org/10.1016/S0926-3373(01)00315-0

Malwal D, Gopinath P (2017) CuO-ZnO nanosheets with p–n heterojunction for enhanced visible light mediated photocatalytic activity. Chem Sel 2(17):4866–4873. https://doi.org/10.1002/slct.201700837

Mauro AD, Cantarella M, Nicotra G, Pellegrino G, Gulino A, Brundo MV, Privitera V, Impellizzeri G (2017) Novel synthesis of ZnO/PMMA nanocomposites for photocatalytic applications. Sci Rep 7:40895–40907. https://doi.org/10.1038/srep40895

Medina JC, Vélez NSP, Bizarro M, Gordillo AH, Rodil SE (2018) Synergistic effect of supported ZnO/Bi^2O_3 heterojunctions for photocatalysis under visible light. Dyes Pigments 153:106–116. https://doi.org/10.1016/j.dyepig.2018.02.006

Meshram SP, Adhyapakn PV, Amalnerkar DP, Mulla IS (2016) Cu doped ZnO microballs as effective sunlight driven photocatalyst. Ceram Int 42(6):7482–7489. https://doi.org/10.1016/j.ceramint.2016.01.154

Ming-Twang S, Zaini MAA, Salleh LM et al (2017) Potassium hydroxide-treated palm kernel shell sorbents for the efficient removal of methyl violet dye. Desalin Water Treat 84:262–270. https://doi.org/10.5004/dwt.2017.21206

Mittal M, Sharma M, Pandey OP (2014) UV–visible light induced photocatalytic studies of Cu doped ZnO nanoparticles prepared by co-precipitation method. Sol Energy 110:386–397. https://doi.org/10.1016/j.solener.2014.09.026

Mohamed WS, Abu-Dief AM (2018) Synthesis, characterization and photocatalysis enhancement of Eu_2O_3-ZnO mixed oxide nanoparticles. J Phys Chem Solids 116:375–385. https://doi.org/10.1016/j.jpcs.2018.02.008

Moulahi A, Sediri F (2014) ZnO nanoswords and nanopills: hydrothermal synthesis, characterization and optical properties. Ceram Int 40(1):943–950. https://doi.org/10.1016/j.ceramint.2013.06.090

Myilsamy M, Mahalakshmi M, Subha N, Rajabhuvaneswari A, Murugesan V (2016) Visible light responsive mesoporous graphene–Eu_2O_3/TiO_2 nanocomposites for the efficient photocatalytic degradation of 4-chlorophenol. RSC Adv 6(41):35024–35035. https://doi.org/10.1039/C5RA27541E

Naseri A, Samadi M, Mahmoodi NM, Pourjavadi A, Mehdipour H, Moshfegh AZ (2017) Tuning composition of electrospun ZnO/CuO nanofibers: toward controllable and efficient solar photocatalytic degradation of organic pollutants. J Phys Chem C 121(6):3327–3338. https://doi.org/10.1021/acs.jpcc.6b10414

Nemerow N, Dasgupta A (1991) Industrial and hazardous waste treatment. Van Nostrand Reinhold, New York

Neppolian B, Choi HC, Sakthivel S, Arabindoo B, Murugesan V (2002) Solar/UV-induced photocatalytic degradation of three commercial textile dyes. J Hazard Mater 89 (1–2):303–317. https://doi.org/10.1016/S0304-3894(01)00329-6

Nohynek GJ, Fautz R, Kieffer FB, Toutain H (2004) Toxicity and human health risk of hair dyes. Food Chem Toxicol 42(4):517–543. https://doi.org/10.1016/j.fct.2003.11.003

Ong ST, Keng PS, Lee WN, Ha ST, Hung YT (2011) Dye waste treatment. Water 3:157–176. https://doi.org/10.3390/w3010157

Onga CB, Ngb LY, Mohammad AW (2018) A review of ZnO nanoparticles as solar photocatalysts: synthesis, mechanisms and applications. Renew Sust Energ Rev 81(1):536–551. https://doi.org/10.1016/j.rser.2017.08.020

Pan B, Xie Y, Zhang S, Lv L, Zhang W (2012) Visible light photocatalytic degradation of RhB by polymer-CdS nanocomposites: role of the host functional groups. ACS Appl Mater Interfaces 4 (8):3938–3943. https://doi.org/10.1021/am300769b

Pandiselvi K, Fang H, Huang X, Wang J, Xu X, Li T (2016) Constructing a novel carbon nitride/polyaniline/ZnO ternary heterostructure with enhanced photocatalytic performance using exfoliated carbon nitride nanosheets as supports. J Hazard Mater 314:67–77. https://doi.org/10.1016/j.jhazmat.2016.04.035

Paschoal FMM, Anderson MA, Zanoni MVB (2009) Simultaneous removal of chromium and leather dye from simulated tannery effluent by photoelectrochemistry. J Hazard Mater 166 (1):531–537. https://doi.org/10.1016/j.jhazmat.2008.11.058

Penchev H, Zaharieva K, Milenova K, Ublekov F, Dimova S, Budurova D, Staneva M, Stambolova I, Sinigersky V, Blaskov V (2018) Novel meta- and AB-polybenzimidazole/zinc oxide polymer hybrid nanomaterials for photocatalytic degradation of organic dyes. Mater Lett 230:187–190. https://doi.org/10.1016/j.matlet.2018.07.114

Peng Y, Bao L (2008) Controlled-synthesis of ZnO nanorings. Front Chem China 3(4):458–463. https://doi.org/10.1007/s11458-008-0081-5

Phuruangrat A, Yayapao O, Thongtem T, Thongtem S (2014) Preparation, characterization and photocatalytic properties of Ho doped ZnO nanostructures synthesized by sonochemical method. Superlattice Microstruct 67:118–126. https://doi.org/10.1016/j.spmi.2013.12.023

Polisetti S, Deshpande PA, Madras G (2011) Photocatalytic activity of combustion synthesized ZrO_2 and ZrO_2-TiO_2 mixed oxides. Ind Eng Chem Res 50(23):12915–12924. https://doi.org/10.1021/ie200350f

Poornaprakash B, Chalapathi U, Chandra Sekhar M, Rajendar V, Prabhakar Vattikuti SV, Siva Pratap Reddy M, Suh Y, Park SH (2018) Effect of Eu^{3+} on the morphology, structural, optical, magnetic, and photocatalytic properties of ZnO nanoparticles. Superlattice Microstruct 123:154–163. https://doi.org/10.1016/j.spmi.2018.07.010

Qiu X, Li L, Zheng J, Liu J, Sun X, Li G (2008) Origin of the enhanced photocatalytic activities of semiconductors: a case study of ZnO doped with Mg^{2+}. J Phys Chem C 112(32):12242–12248. https://doi.org/10.1021/jp803129e

Radzimska AK, Jesionowski T (2014) Zinc oxide from synthesis to application: a review. Materials 7(4):2833–2881. https://doi.org/10.3390/ma7042833

Rajendran S, Khan MM, Gracia F, Qin J, Gupta VK, Arumainathan S (2016) Ce^{3+}-ion-induced visible-light photocatalytic degradation and electrochemical activity of ZnO/CeO_2 nanocomposite. Sci Rep 6:31641–31652. https://doi.org/10.1038/srep31641

Ramesh M, Nagaraja HS, Rao MP, Anandan S, Huang NM (2016) Fabrication, characterization and catalytic activity of α-MnO_2 nanowires for dye degradation of reactive black 5. Mater Lett 172:85–89. https://doi.org/10.1016/j.matlet.2016.02.076

Ramimoghada D, Hussein MZB, Yap YHT (2013) Synthesis and characterization of ZnO nanostructures using palm olein as biotemplate. Chem Cent J 7:71–82. https://doi.org/10.1186/1752-153X-7-71

Rana N, Chand S, Gathania AK (2016) Green synthesis of zinc oxide nano-sized spherical particles using *Terminalia chebula* fruits extract for their photocatalytic applications. Int Nano Lett 6 (2):91–98. https://doi.org/10.1007/s40089-015-0171-6

Reda GM, Fan H, Tian H (2017) Room-temperature solid state synthesis of Co_3O_4/ZnO *p–n* heterostructure and its photocatalytic activity. Adv Powder Technol 28(3):953–963. https://doi.org/10.1016/j.apt.2016.12.025

Ren X, Han D, Chen D, Tang F (2007) Large-scale synthesis of hexagonal cone-shaped ZnO nanoparticles with a simple route and their application to photocatalytic degradation. Mater Res Bull 42(5):807–813. https://doi.org/10.1016/j.materresbull.2006.08.030

Salah N, Hameed A, Aslam M, Babkair SS, Bahabri FS (2016) Photocatalytic activity of V doped ZnO nanoparticles thin films for the removal of 2- chlorophenol from the aquatic environment under natural sunlight exposure. J Environ Manag 177:53–64. https://doi.org/10.1016/j.jenvman.2016.04.007

Saleh R, Djaja NF (2014) UV light photocatalytic degradation of organic dyes with Fe-doped ZnO nanoparticles. Superlattice Microst 74:217–233. https://doi.org/10.1016/j.spmi.2014.06.013

Samadi M, Zirak M, Naseri A, Khorashadizade E, Moshfegh AZ (2016) Recent progress on doped ZnO nanostructures for visible-light photocatalysis. Thin Solid Films 605:2–19. https://doi.org/10.1016/j.tsf.2015.12.064

Samadipakchin P, Mortaheb HR, Zolfaghari A (2017) ZnO nanotubes: preparation and photocatalytic performance evaluation. J Photochem Photobiol A Chem 337:91–99. https://doi.org/10.1016/j.jphotochem.2017.01.018

Sangeetha G, Rajeshwari S, Venckatesh R (2011) Green synthesis of zinc oxide nanoparticles by *Aloe barbadensis* miller leaf extract: structure and optical properties. Mater Res Bull 46 (12):2560–2566. https://doi.org/10.1016/j.materresbull.2011.07.046

Sanoop PK, Anas S, Ananthakumar S, Gunasekar V, Saravanan R, Ponnusami V (2016) Synthesis of yttrium doped nanocrystalline ZnO and its photocatalytic activity in methylene blue degradation. Arab J Chem 9:S1618–S1626. https://doi.org/10.1016/j.arabjc.2012.04.023

Saravanan R, Karthikeyan S, Gupta VK, Sekaran G, Narayanan V, Stephen A (2013) Enhanced photocatalytic activity of ZnO/CuO nanocomposite for the degradation of textile dye on visible light illumination. Mater Sci Eng C 33(1):91–98. https://doi.org/10.1016/j.msec.2012.08.011

Saravanan R, Sacari E, Gracia F, Khan MM, Mosquera E, Gupta VK (2016) Conducting PANI stimulated ZnO system for visible light photocatalytic degradation of coloured dyes. J Mol Liq 221:1029–1033. https://doi.org/10.1016/j.molliq.2016.06.074

Selvarajan E, Mohanasrinivasan V (2013) Biosynthesis and characterization of ZnO nanoparticles using *Lactobacillus plantarum* VITES07. Mater Lett 112:180–182. https://doi.org/10.1016/j.matlet.2013.09.020

Senthilkumar N, Nandhakumar E, Priya P, Soni D, Vimalane M, Potheher IV (2017) Synthesis of ZnO nanoparticles using leaf extract of *Tectona grandis* (L.) and their anti-bacterial, anti-arthritic, anti-oxidant and *in vitro* cytotoxicity activities. New J Chem 41(18):10347–10356. https://doi.org/10.1039/C7NJ02664A

Shao X, Li B, Zhang B, Shao L, Wu Y (2016) Au@ZnO core–shell nanostructures with plasmon-induced visible-light photocatalytic and photoelectrochemical properties. Inorg Chem Front 3 (7):934–943. https://doi.org/10.1039/C6QI00064A

Sharma M, Jainc T, Singhd S, Pandey OP (2012) Photocatalytic degradation of organic dyes under UV-visible light using capped ZnS nanoparticles. Sol Energy 86(1):626–633. https://doi.org/10.1016/j.solener.2011.11.006

Sharma D, Sabela MI, Kanchi S, Mdluli PS, Singh G, Stenstrom TA, Bisetty K (2016) Biosynthesis of ZnO nanoparticles using *Jacaranda mimosifolia* flowers extract: synergistic antibacterial activity and molecular simulated facet specific adsorption studies. J Photochem Photobiol B Biol 162:199–207. https://doi.org/10.1016/j.jphotobiol.2016.06.043

Sharma A, Sharma G, Naushad M et al (2018) Remediation of anionic dye from aqueous system using bio-adsorbent prepared by microwave activation. Environ Technol 39(7):917–930. https://doi.org/10.1080/09593330.2017.1317293

Shen G, Cho JH, Yoo JK, Yi GC, Lee CJ (2005) Synthesis and optical properties of S doped ZnO nanostructures: nanonails and nanowires. J Phys Chem B 109(12):5491–5496. https://doi.org/10.1021/jp045237m

Shoeb M, Singh BR, Khan JA, Khan W, Singh BN, Singh HB, Naqvi AH (2013) ROS-dependent anticandidal activity of zinc oxide nanoparticles synthesized by using egg albumen as a biotemplate. Adv Nat Sci Nanosci Nanotechnol 4:035015–035026. https://doi.org/10.1088/2043-6262/4/3/035015

Shoushtari MZ, Parhoodeh S, Farbod M (2008) Fabrication and characterization of zinc oxide nanoparticles by DC arc plasma. J Phys Conf Ser 100:052017–052021. https://doi.org/10.1088/1742-6596/100/5/052017

Silva IMP, Byzynski G, Ribeiro C, Longo E (2016) Different dye degradation mechanisms for ZnO and ZnO doped with N (ZnO:N). J Mol Catal A Chem 417:89–100. https://doi.org/10.1016/j.molcata.2016.02.027

Snure M, Tiwari A (2007) Synthesis, characterization, and green luminescence in ZnO nanocages. J Nanosci Nanotechnol 7(2):481–485. PMID:17450782

Sutka A, Kaambre T, Parna R, Juhnevica I, Maiorov M, Joost U, Kisand V (2016) Co doped ZnO nanowires as visible light photocatalysts. Solid State Sci 56:54–62. https://doi.org/10.1016/j.solidstatesciences.2016.04.008

Tanaka K, Padermpole K, Hisanaga T (2000) Photocatalytic degradation of commercial azo dyes. Water Res 34(1):327–333. https://doi.org/10.1016/S0043-1354(99)00093-7

Tang J, Chai J, Huang J, Deng L, Nguyen XS, Sun L, Venkatesan T, Shen Z, Tay CB, Chua SJ (2015) ZnO nanorods with low intrinsic defects and high optical performance grown by facile microwave-assisted solution method. ACS Appl Mater Interfaces 7(8):4737–4743. https://doi.org/10.1021/am508426z

Teh CM, Mohamed AR (2011) Roles of titanium dioxide and ion-doped titanium dioxide on photocatalytic degradation of organic pollutants (phenolic compounds and dyes) in aqueous solutions: a review. J Alloys Compd 509(5):1648–1660. https://doi.org/10.1016/j.jallcom.2010.10.181

Thein MT, Pung SY, Aziz A, Itoh M (2016) Effect of Ni coupling on the photoluminescence property and photocatalytic activity of ZnO nanorods. J Taiwan Inst Chem Eng 61:156–165. https://doi.org/10.1016/j.jtice.2015.11.024

Tian S, Zhang J, Chen J, Kong L, Lu J, Ding F, Xiong Y (2013) Fe_2 $(MoO_4)_3$ as an effective photon-Fenton-like catalyst for the degradation of anionic and cationic dyes in a wide pH range. Ind Eng Chem Res 52(37):13333–13341. https://doi.org/10.1021/ie401522a

Vaiano V, Matarangolo M, Sacco O, Sannino D (2017) Photocatalytic treatment of aqueous solutions at high dye concentration using praseodymium-doped ZnO catalysts. Appl Catal B Environ 209:621–630. https://doi.org/10.1016/j.apcatb.2017.03.015

Vempati S, Mitra J, Dawson P (2012) One-step synthesis of ZnO nanosheets: a blue-white fluorophore. Nanoscale Res Lett 7:470–480. https://doi.org/10.1186/1556-276X-7-470

Vignesh K, Rajarajan M, Suganthi A (2014) Visible light assisted photocatalytic performance of Ni and Th co-doped ZnO nanoparticles for the degradation of methylene blue dye. J Ind Eng Chem 20(5):3826–3833. https://doi.org/10.1016/j.jiec.2013.12.086

Wallace R, Brown AP, Brydson R, Wegner K, Milne SJ (2013) Synthesis of ZnO nanoparticles by flame spray pyrolysis and characterisation protocol. J Mater Sci 48(18):6393–6403. https://doi.org/10.1007/s10853-013-7439-x

Wang J, Tsuzuki T, Sun L, Wang X (2010a) Reverse microeulsion-mediated synthesis of SiO_2-coated ZnO composite nanoparticles: Multiple cores with tunable shell thickness

Wang L, Chen K, Dong L (2010b) Synthesis of exotic zigzag ZnO nanoribbons and their optical, electrical properties. J Phys Chem C114(41):17358–17361. https://doi.org/10.1021/jp104706q

Wang J, Wang Z, Huang B, Ma Y, Liu Y, Qin X, Zhang X, Dai Y (2012) Oxygen vacancy induced band-gap narrowing and enhanced visible light photocatalytic activity of ZnO. ACS Appl Mater Interfaces 4(8):4024–4030. https://doi.org/10.1021/am300835p

Wang F, Li W, Gu S, Li H, Liu X, Wang M (2016) Fabrication of $FeWO_4$@$ZnWO_4$/ZnO heterojunction photocatalyst: synergistic effect of $ZnWO_4$/ZnO and $FeWO_4$@$ZnWO_4$/ZnO heterojunction structure on the enhancement of visible-light photocatalytic activity. ACS Sustain Chem Eng 4(12):6288–6298. https://doi.org/10.1021/acssuschemeng.6b00660

Wang X, Ahmad M, Sun H (2017) Three-dimensional ZnO hierarchical nanostructures: solution phase synthesis and applications. Materials 10(11):1304–1328. https://doi.org/10.3390/ma10111304

Warang T, Patel N, Fernandes R, Bazzanella N, Miotello A (2013) Co_3O_4 nanoparticles assembled coatings synthesized by different techniques for photo-degradation of methylene blue dye. Appl Catal B Environ 132–133:204–211. https://doi.org/10.1016/j.apcatb.2012.11.040

Wei N, Cui H, Wang X, Xie X, Wang M, Zhang L, Tian J (2017) Hierarchical assembly of In_2O_3 nanoparticles on ZnO hollow nanotubes using carbon fibers as templates: enhanced photocatalytic and gas sensing properties. J Colloid Interface Sci 498:263–270. https://doi.org/10.1016/j.jcis.2017.03.072

Woll C (2007) The chemistry and physics of zinc oxide surfaces. Prog Surf Sci 82(2–3):55–120. https://doi.org/10.1016/j.progsurf.2006.12.002

Wu C, Shen L, Yu H, Zhang YC, Huang Q (2012) Solvothermal synthesis of Cu-doped ZnO nanowires with visible light-driven photocatalytic activity. Mater Lett 74:236–238. https://doi.org/10.1016/j.matlet.2012.01.125

Wu D, Wang W, Tan F, Sun F, Lu H, Qiao X (2013) Fabrication of pit-structured ZnO nanorods and their enhanced photocatalytic performance. RSC Adv 3(43):20054–20059. https://doi.org/10.1039/C3RA42874E

Wu C, Guo H, Cui S, Li H, Li F (2015) Influence of Ce doping on structure, morphology, and photocatalytic activity of three-dimensional ZnO superstructures synthesized via coprecipitation and roasting processes. J Nanoeng Nanosyst 229(2):66–73. https://doi.org/10.1177/1740349914526867

Xiong J, Sun Q, Chen J, Li Z, Dou S (2016) Ambient controlled synthesis of advanced core-shell plasmonic Ag@ZnO photocatalysts. CrystEngComm 18(10):1713–1722. https://doi.org/10.1039/C6CE00013D

Xu L, Hu YL, Pelligra C, Chen CH, Jin L, Huang H, Sithambaram S, Aindow M, Joesten R, Suib SL (2009) ZnO with different morphologies synthesized by solvothermal methods for enhanced photocatalytic activity. Chem Mater 21(13):2875–2885. https://doi.org/10.1021/cm900608d

Xu X, Wu M, Asoro M, Ferreira PJ, Fan DL (2012) One-step hydrothermal synthesis of comb-like ZnO nanostructures. Cryst Growth Des 12(10):4829–4833. https://doi.org/10.1021/cg3005773

Xu Y, Jin J, Li X, Han Y, Menga H, Wang T, Zhang X (2016) Simple synthesis of ZnO nanoflowers and its photocatalytic performances toward the photodegradation of metamitron. Mater Res Bull 76:235–239. https://doi.org/10.1016/j.materresbull.2015.11.062

Xu M, Jia S, Chen C, Zhang Z, Yan J, Guo Y, Zhang Y, Zhao W, Yun J, Wang Y (2018) Microwave-assistant hydrothermal synthesis of SnO_2@ZnO hierarchical nanostructures enhanced photocatalytic performance under visible light irradiation. Mater Res Bull 106:74–80. https://doi.org/10.1016/j.materresbull.2018.05.033

Yayapao O, Thongtem T, Phuruangrat A, Thongtem S (2013) Ultrasonic-assisted synthesis of Nd-doped ZnO for photocatalysis. Mater Lett 90:83–86. https://doi.org/10.1016/j.matlet.2012.09.027

Yayapao O, Thongtem T, Phuruangrat A, Thongtem S (2015) Synthesis and characterization of highly efficient Gd doped ZnO photocatalyst irradiated with ultraviolet and visible radiations. Mater Sci Semicond Process 39:786–792. https://doi.org/10.1016/j.mssp.2015.06.039

Yu C, Yang K, Xie Y, Fan Q, Yu JC, Shua Q, Wanga C (2013a) Novel hollow Pt-ZnO nanocomposite microspheres with hierarchical structure and enhanced photocatalytic activity and stability. Nanoscale 5(5):2142–2151. https://doi.org/10.1039/C2NR33595F

Yu C, Yang K, Zhou W, Fan Q, Wei L, Yu JC (2013b) Preparation, characterization and photocatalytic performance of noble metals (Ag, Pd, Pt, Rh) deposited on sponge-like ZnO microcuboids. J Phys Chem Solids 74(12):1714–1720 https://doi.org/10.1016/j.jpcs.2013.06.014

Yubuta K, Sato T, Nomura A, Haga K, Shishido T (2007) Structural characterization of ZnO nanochains studied by electron microscopy. J Alloys Compd 436(1–2):396–399. https://doi.org/10.1016/j.jallcom.2006.08.373

Zhang Z, Shao C, Li X, Wang C, Zhang M, Liu Y (2010) Electrospun nanofibers of *p*-type NiO/*n*-type ZnO heterojunctions with enhanced photocatalytic activity. ACS Appl Mater Interfaces 2(10):2915–2923. https://doi.org/10.1021/am100618h

Zhong JB, Li JZ, He XY, Zeng J, Lu Y, Hu W, Lin K (2012) Improved photocatalytic performance of Pd-doped ZnO. Curr Appl Phys 12(3):998–1001. https://doi.org/10.1016/j.cap.2012.01.003

Zhou Y, Lu SX, Xu WG (2009) Photocatalytic activity of Nd-doped ZnO for the degradation of CI reactive blue 4 in aqueous suspension. Environ Prog Sustain Energy 28(2):226–233. https://doi.org/10.1016/j.optlastec.2012.06.002

Zhou MY, Qu LS, Gao H (2017) Synthesis and photoluminescence properties of ZnO nanohelices. Conf Ser Mater Sci Eng 213:012009–012014. https://doi.org/10.1088/1757-899X/213/1/012009

Zhu J, Shao C, Li X, Han C, Yang S, Ma J, Li X, Liu Y (2018) Immobilization of ZnO/polyaniline heterojunction on electronspun polyacrylonitrile nanofibers and enhanced photoctalytic activity. Mater Chem Phys 214:507–515. https://doi.org/10.1016/j.matchemphys.2018.04.053

Zou T, Wang C, Tan R, Song W, Cheng Y (2017) Preparation of pompon-like ZnO-PANI heterostructure and its applications for the treatment of typical water pollutants under visible light. J Hazard Mater 338:276–286. https://doi.org/10.1016/j.jhazmat.2017.05.042

Chapter 6
Designing Metal-Organic Frameworks Based Photocatalyst for Specific Photocatalytic Reactions: A Crystal Engineering Approach

Partha Pratim Bag and Pathik Sahoo

Contents

6.1 Introduction 142
6.2 Basic Molecular Mechanism 144
  6.2.1 Light-Harvesting and Catalytic Centers in Photocatalysis 146
  6.2.2 Electrical Conductivity of MOFs 147
6.3 Engineering of MOFs 150
  6.3.1 Organic Linkers 151
  6.3.2 Secondary Building Unit 157
6.4 Designing Homogeneous Catalyst 158
6.5 Designing Asymmetric Catalyst 159
6.6 Developing Catalysts 162
  6.6.1 MOF-5 162
  6.6.2 UiO-66(Zr) 163
  6.6.3 MIL-101(Fe) 163
  6.6.4 MIL-125(Ti) 165
6.7 Designing for Special Purpose 167
  6.7.1 Water Oxidation 167
  6.7.2 CO_2 Reduction 169
6.8 Decorating MOFs with Nanomaterials 171
6.9 Conclusions 176
References 176

P. P. Bag (✉)
Department of Basic Science and Humanitics, Dumka Engineering College, Dumka, Jharkhand, India
e-mail: parthap.bag82@yahoo.com; parthap.bag82@hotmail.com

P. Sahoo
Soft Chemistry Group, International Center for Materials Nanoarchitectonics, National Institute for Materials Science (NIMS), Tsukuba, Ibaraki, Japan
e-mail: 2c.pathik@gmail.com; sahoo.pathik@nims.go.jp

S. Rajendran et al. (eds.), *Green Photocatalysts for Energy and Environmental Process*, Environmental Chemistry for a Sustainable World 36,
https://doi.org/10.1007/978-3-030-17638-9_6

Abstract The spatial arrangement of designed reaction centers with engineered porosity withdraws a special attention in exploring metal-organic frameworks (MOFs) for developing a wide range of photocatalyst in the last decade. This chapter targets to recapitulate the recent advancement of MOF-derived photocatalyst with their mechanism, types, structural engineering, and various practical uses.

Keywords Metal · Organic frameworks · Charge transfer mechanism · Semiconductor · Secondary building unit · Water oxidation · Asymmetric synthesis

6.1 Introduction

From addressing pollution-free global energy demand to carry out asymmetric synthesis, metal-organic frameworks (MOFs) (Zhou et al. 2012; Kang et al. 2017; Adarsh and Dastidar 2012; Adarsh et al. 2010; Bag et al. 2015) introduce an exceptional interest in environmentally friendly photocatalysis technology (Zhang and Lin 2014). MOFs form when organic ligands coordinate with two or more metal ions or metal clusters to form one-, two-, or three-dimensional supramolecular structures (Kumar et al. 2018). They can be designated as coordination polymer as well (Biradha et al. 2009). Solar energy is an unlimited but intermittent resource of the most attractive alternative energies for storing it in chemical bonds as solar fuels under two main solar-to-chemical energy conversion categories: (i) splitting water into H_2/O_2 and (ii) reducing CO_2 to hydrocarbons. Such novel inspiration was originated from the photosynthesis of green plants in converting carbon dioxide and water into carbohydrates and oxygen. Scientists from many fields are trying to develop the artificial photocatalyst by introducing various metal oxides, spinel nanoparticles, composite materials, inorganic complexes, or MOFs to minimize net energy uphill under photocatalytic reaction ($\Delta G > 0$) process. In short, this reaction is driven by absorbing photons to generate energetic electrons and holes in catalyst to promote reduction and oxidation reactions, respectively (Linsebigler et al. 1995; Schneider et al. 2014). Since the opening report of UV light-assisted water splitting (Fujishima and Honda 1972), a significant upsurge on photocatalysis is gaining interest for improving the cost-effectiveness, efficiency, and stability of photocatalyst to utilize full solar spectrum in energy storage. Besides energy storage, the last decade is witnessing the use of MOFs in photochemical synthesis of organic compounds (Yu et al. 2017; Wang et al. 2015) or degrading some specific ingredients in purification process (de Koning et al. 2017; Andrew Lin et al. 2015, Bagheri et al. 2017). When multidentate organic linkers coordinate to transition metal cations forming one-, two- or three-dimensional crystalline architecture, it forms MOF. Though there is a long-standing debate to define MOF sharply, generally people consider MOFs only after having the feature of porosity in the crystalline structures. MOFs are generally used for several applications like gas storage (Furukawa et al. 2010), purification and separation (Vlasova et al. 2016, Evans et al. 2018), catalysis (Jiao et al. 2017), drug delivery (Bag et al. 2016, Wu and Yang 2017), or sensing (Kreno et al. 2012; Sharma and Ghosh 2018). In case of developing the MOFs as photocatalysts, there are completely distinct principles for preparing homogeneous and heterogeneous photocatalysts. Homogeneous MOF photocatalysts are generally prepared by introducing solvophilic functionalities in organic ligands and larger supramolecular channels to allow solvents passing through it. The periodic arrangement of catalytic centers inside MOF lattices behaves as an individual reaction sites and makes reactions happen throughout the entire lattice. Only very few articles are reported so far on homogeneous photocatalysts. In contrary, heterogeneous MOF photocatalysts are abundant and normally developed by introducing semiconducting behavior in crystal lattice. Additionally, their surface activity can be promoted by exploring site engineering at lattice surface. As in the case of heterogeneous MOF catalysts, reaction sites are located only on the lattice surface; it is therefore highly desirable to increase the surface area by reducing the MOF size into a nanodimensional crystal (Fang et al. 2017).

For constructing inorganic semiconductors, charge separation should take place to separate electrons and holes by irradiating with light. These electrons moving in wide conducting bands are subjected to very limited scattering and, hence, feature relatively high mobility and behave as a reducing agent. In case of organic semiconductors, conjugate π-bonds are delocalized for allowing charge carrier mobility. While two transition metals are bonded via π-conjugated bridging ligand in MOF formation, the valence electrons from metal atoms get delocalized easily through the bridging ligands, and nonbonding nature of valence electron does not influence much at the coordination sphere of metal atoms in a one-electron oxidation process (Hendon et al. 2012). Though semiconductivity is measured by optical transitions and electrochemical and photochemical activity (Llabres i Xamena et al. 2007; Lopez et al. 2011; Silva et al. 2010a, b), the measurement of electrical conductivity through the material or the charge carrier mobility directly confirms a material as a semiconductor.

Thus, a smart designing of MOFs is highly essential to construct the cost-effective, durable, target-specific homogeneous or heterogeneous catalysts. Herein, a crystal engineering (Desiraju 1989; Desiraju 2007) approach plays a pivotal role in designing MOFs by employing supramolecular synthon concept. Supramolecular synthons (Desiraju 1995) play the same fundamental role in building supramolecular materials as molecular synthons (Corey 1967) do for covalent syntheses. Such synthons are defined as the spatial arrangements of intermolecular non-covalent interactions appear in supramolecular architecture with high precession of predictability. This concept has been widely exploited in developing supramolecular materials, including MOFs with maintaining the structural robustness. A MOF-based semiconductor was first reported almost a decade ago (Alvaro et al. 2007). They had estimated a bandgap of 3.4 eV, and the charge-separated state was found to decay the energy within a microsecond timescale. Herein, the simple organic ligand, terephthalate, is used in light harvesting and promoted photoinduced electron transport from terephthalate anion to Zn in ZnO_4 cluster (Fig. 6.1).

Finally, microporous semiconductor was capable to degrade organic pollutants like phenol in aqueous medium (Kumar et al. 2016). This work encouraged on developing MOF-based semiconductors (Silva et al. 2010a, b) for further use, and the last decade witnessed a series of successful application in solar energy storage in

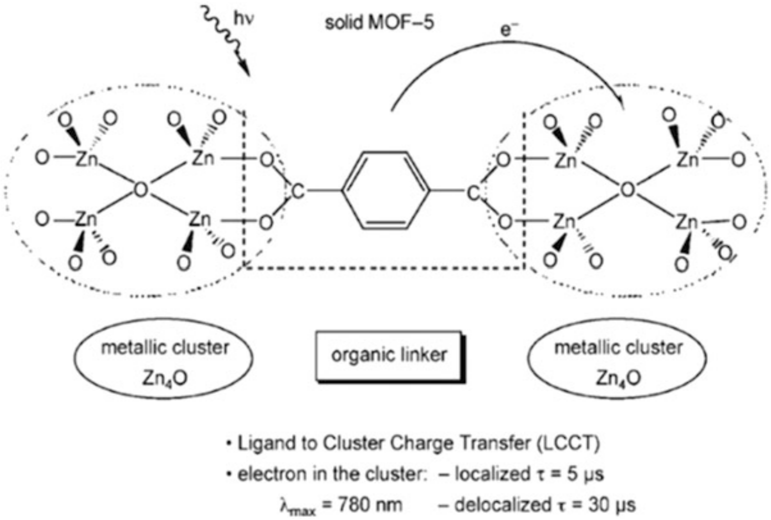

Fig. 6.1 Electron transfer from ligand to catalytic site in MOF-5 (Alvaro et al. 2007)

chemical bond, degradation of organic pollutants (Alqadami et al. 2018). Moreover, several MOFs are reported to be more efficient than real semiconductors (Hendon et al. 2012; Silva et al. 2010a, b; Foster et al. 2014; Zeng et al. 2016).

6.2 Basic Molecular Mechanism

The organic ligands used in bridging between metal ions can also be exploited as light-harvesting antenna under photochemical process to activate metal nodes under metal cluster charge transition (LCCT) in generating MOF-based semiconductor (Silva et al. 2010a, b; Alvaro et al. 2007; Feng et al. 2010; Llabrés i Xamena et al. 2007; Tachikawa et al. 2008; Nasalevich et al. 2014; Wang and Wang 2015) (Fig. 6.2).

This property withdraws a special interest in developing a numerous type of photocatalysts for artificial photosynthetic reactions. To design a photocatalyst with a specific goal, a clear understanding behind photosynthetic molecular mechanism is required. Fujishima and Honda (1972) discovered the photocatalytic property first in the n-type TiO_2. They employed the catalyst in electrochemical photolysis of water which inspired the people to design MOFs with titanium cation later (Chambers et al. 2017). Dan Hardi et al. modified the first semiconductor reported by Alvaro et al. (2007) and employed in MOF [MIL-125, $Ti_8O_8(OH)_4(bdc)_6$]-based photocatalyst under UV irradiation (Dan–Hardi et al. 2009). They introduced an amine group in terephthalate backbone and substituted ZnO_4 cluster by $Ti_8O_8(OH)_4$ to develop a photocatalyst with higher efficiency (Fig. 6.3).

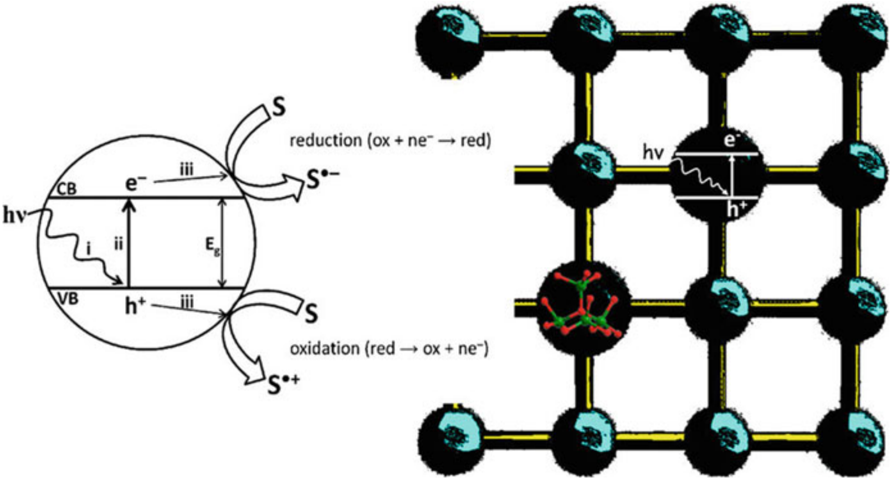

Fig. 6.2 Photocatalytic mechanism, (*i*) light absorption, (*ii*) promotion of electron from VB to CB, (*iii*) migration of electron from CB for reduction (S → $S^{\cdot -}$) and migration of h^+ from VB for reduction (S → $S^{\cdot +}$) (Zeng et al. 2016)

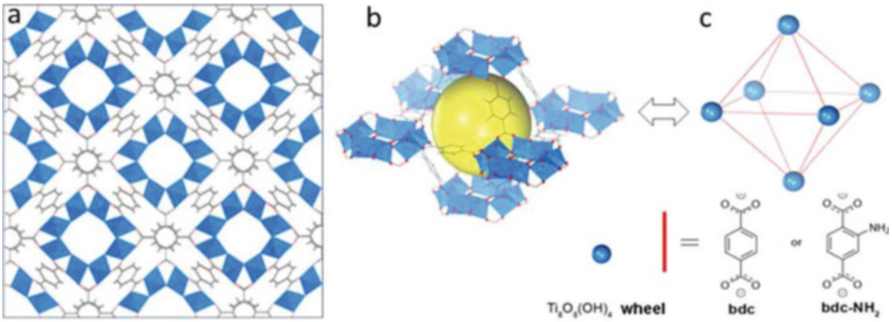

Fig. 6.3 (**a**) (001) view of MIL-125 with Ti (blue), O (red), and C (and H, gray). (**b**) A yellow void inside octahedral cage at MIL-125. (**c**) Octahedral arrangement of Ti8O8 octahedra connected by terephthalate linkers (Chambers et al. 2017)

Thereafter, keeping the anion the same, Wang et al. just substituted Ti_8O_8 cluster with Fe-O cluster for CO_2 photoreduction reaction (Wang et al. 2014; Portillo et al. 2017; Li et al. 2016) (Fig. 6.4).

Such smart modification on designing MOF for developing a new photocatalyst with certain purpose is a continuous process, but scrutinization molecular mechanism on available catalyst helps crystal engineering society to design a MOF-based photocatalyst with a certain mechanistic accurateness with significant structural requirement. To envisage the mechanism, the detail working principles of light-harvesting centers and catalytic sites, charge transport mechanism should be analyzed in detail.

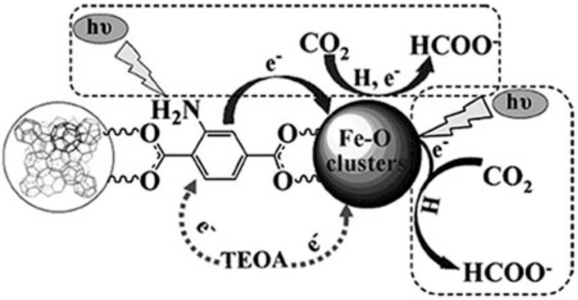

Fig. 6.4 Dual excitation of at antenna and catalytic site in NH_2-MIL-101(Fe) (Wang et al. 2014)

6.2.1 Light-Harvesting and Catalytic Centers in Photocatalysis

There are a considerable number of MOFs reported in literature, which shows an intriguing semiconducting property in presence of light. Irradiating an inorganic material by light with energy (hυ) equal to or greater than the bandgap will eject a negatively charged electron (e^-) to the conduction band (CB), leaving a positive hole (h^+) on the valence band (VB), which reacts with the adsorbed reactant separately (Li et al. 2016; Chen et al. 2010; Serpone and Emeline 2012). These both charged species behave as the reaction centers and get drifted toward catalytic sites for performing photochemical reaction on adsorbed chemical species. In consequence, electrons and holes reduce and oxidize the reaction species under such photochemical reactions. While light irradiation on organic semiconducting materials keeps the working principle the same, electrons are mainly localized with the same molecules where these two energy levels can be described as the highest occupied molecular orbital (HOMO) and the lowest unoccupied molecular orbital (LUMO) (Pasveer et al. 2005; Coropceanu et al. 2007; Kaake et al. 2010). Usually, the energy difference between HOMO and LUMO in organic ligands is more than 3 eV. This makes the metal-organic hybrid system less likely in matching energy between a metal center and its associated ligands. Besides energy level, symmetry mismatch in metal and organic orbital also plays a crucial role to generate localized electronic states. As a result, these energy difference and symmetry mismatch between metal and its associated ligands prevent efficient charge transport through metal-organic framework (MOF). Despite the general insulating behavior endorsed by high bandgap energy, various simulation techniques have been applied to minimize their resultant bandgap energy for transforming the ordinary MOF into a semiconductor. Herein, density functional theory (DFT) calculation can play a significant role while calculating energy difference between HOMO-LUMO for the reported MOFs.

While designing a photocatalyst, the light-harvesting centers and reaction sites should be designed independently but need to integrate them carefully for developing an efficient photocatalytic system. When we focus on designing light-harvesting centers, generally absorption of visible or infrared light is concerned to maximize the utilization of sunlight as sunlight consists only 5% ultraviolet (UV, 300–400 nm) light but 43% visible (400–700 nm) and 52% infrared (IR, 700–2500 nm) light (Chen and Burda 2008; Gao et al. 2017). Mainly for harvesting light, various π-conjugate organic backbones with different organic functionalities are introduced in designing organic ligands.

And in designing catalytic reaction centers, we need to introduce metal driven reaction centers inside MOF. Single metal or metal oxide centers not only promote photocatalytic reactions, but these also play a crucial role in determining geometry of supramolecular spatial geometry to generate supramolecular cavity for hosting reactant molecules. In building supramolecular architecture with proper ligands, the metal centers also play very fundamental role in creating octahedral or tetrahedral voids. In addition, the length and functionalities of organic ligands play the crucial role in determining perfect pore sizes and comfortable supramolecular bonding to promote the reactant guest undergoing such photochemical reaction smoothly. Hence organic ligands should be selected in such a careful way that those can efficiently transport the charge and can create the supramolecular voids in front of photochemical reaction sites very well.

6.2.2 Electrical Conductivity of MOFs

Once light is harvested, the energy should be transported as negatively charged electron and positively charged holes to the reaction site for reduction and oxidation, respectively. However, this charge kinetics may also follow a complicated pathway. Besides, after photo harvested charge generation, these positively charged holes and negatively charged electrons are often consumed through unwanted charge recombination process while reaching to reaction site in the transportation period. This self-destructive recombination process should be eliminated very carefully while designing an organic ligand for MOF-based photocatalyst preparation. Finally, after reaching to the reaction site, charged species need to activate the reactant molecules by matching their orbital symmetry (Bai et al. 2015). The complete energy and orbital symmetry match from light-harvesting center to catalytic site make the charge kinetics fast to enhance the reaction rate. In most of the cases, MOFs become poor electrical conductor as metal node bridging ligands are mostly insulators with their limited π-orbital conjugation. To enhance the electrical conductivity in MOFs, Allendorf et al. established a beautiful roadmap in preparing MOF-based microelectronic devices (Allendorf et al. 2011; Stavila et al. 2014; Kobayashi et al. 2010). In addition, proton conduction MOFs are also reported recently for battery and fuel cell (Sen et al. 2014; Maity et al. 2015; Okawa et al. 2009, 2013; Horike et al. 2013; Hurd et al. 2009). To the best of our knowledge, the highest proton conduction observed in MOF is 10^{-2} S cm^{-1} at 90% relative humidity and 85 °C (Shimizu et al. 2013). For practical uses of electrical materials, electrical conductivity range categorized them

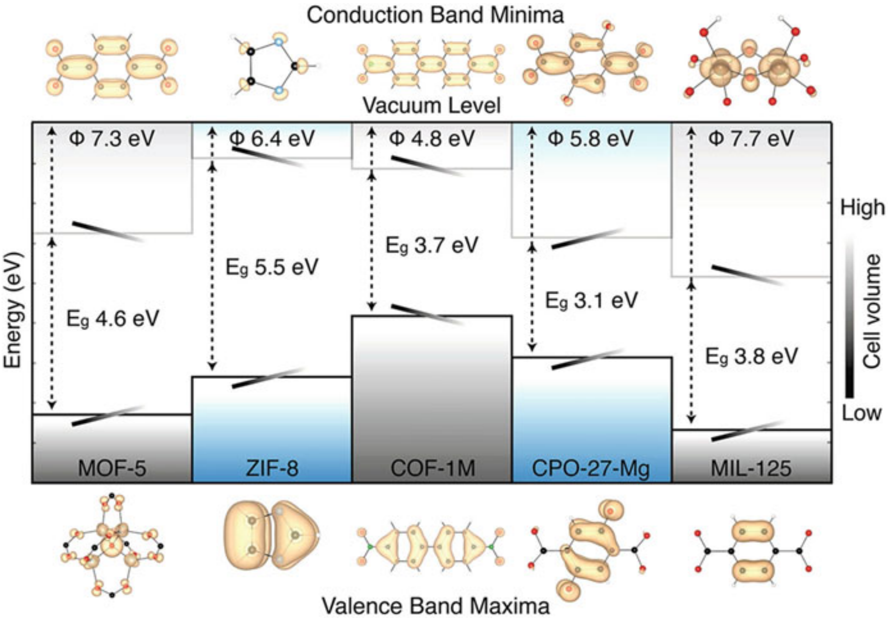

Fig. 6.5 A DFT-HSE06 study of energy level differences among five materials between CB and VB changes against the volume change (external pressure). They are aligned through the hartree potential keeping at their centers of their pores (Butler et al. 2014a, b)

as conductor (10^5–10^1 S cm^{-1}), semiconductor (10^1–10^{-10} S cm^{-1}), and insulator (>10^{-10} S cm^{-1}) (Li et al. 2016; Givaja et al. 2012) (Fig. 6.5).

In 2010 Kobayashi et al. enhanced the electrical conductivity from 1×10^{-8} S cm^{-1} with an optical bandgap of 2 eV to 1×10^{-4} S cm^{-1} by simple partial oxidation technique with a stream of iodine vapor at 50 °C to transform it into a p-type semiconductor (Kobayashi et al. 2010). Measurement of electrical conductivity of MOF inside the Ohmic regime always depends upon the experimental temperature, and hence monitoring thermal variation only makes the measurement reliable (Givaja et al. 2012). For example, charge mobility of ~ 10^{-5} cm2 V^{-1} s^{-1} decreased drastically in MIL-125(Ti) by simply reducing the temperature at 153 K, in a 340 nm light illumination (Nasalevich et al. 2013; Marcus 1956; Savenije et al. 2013). This implies that electrical conductivity in MOFs is deeply influenced by the thermal variation inside crystal lattice (Fig. 6.6). Unlike the classical band model associated with crystalline semiconductor, MOFs show phonon-assisted quantum tunnelling of charges (Bellitto et al. 1985). This tunnelling model obeys a modified Arrhenius equation: $\sigma = \sigma_0 \exp[-(T_0/T)^a]$, where σ_0 and T_0 are expressed as electronic density of the states at the Fermi level and the temperature. The electronic dimensionality a equals to $1/(1 + d)$, where d represents dimensionality. This equation can explain the higher electrical conductivity of 1D MOFs over 2D- and 3D-MOFs very well (Givaja et al. 2012).

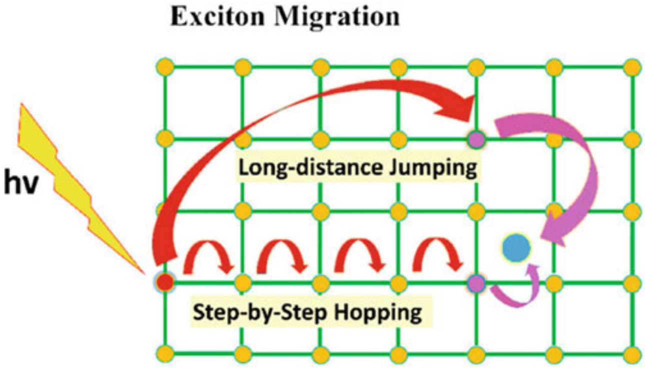

Fig. 6.6 Exciton migration through step-by-step migration and hopping process (Zhang et al. 2016)

Electron transfer is a very common phenomenon that is observed in chemical, biological, photosynthesis, photovoltaics, and homogeneous or heterogeneous catalytic processes (Bolton et al. 1991; Marcus and Sutin 1985; Weinberg et al. 2012; Wasielewski 1992). The rates of electron transfer in inter- or intramolecular system can be explained by semiclassical Marcus equation

$$k_{\mathrm{ET}} \sim k_0 \exp(-\beta(d - R_0))\exp\left(-\left(\Delta G^0 + \lambda\right)2/4\,\lambda RT\right.$$

where k_0 is the rate constant related to barrier-less electron transfer, R_0 stands for van der Waals contact distance between a donor and acceptor, β is electronic coupling factor, d is the distance between donor and acceptor, λ is the entire reorganizational energy (inner sphere plus outer sphere), and ΔG^0 is the reaction driving force (Marcus and Sutin 1985). In solution phase reaction, both intra- and intermolecular electron transfer may occur with considerable reaction rates (ns to ms) over comparatively long distances (tens of Å), promoted by electronic coupling between the donor and acceptor functionalities (Larsen and Wojtas 2013, 2015; Van Wyk et al. 2018; Hua et al. 2018; Tachikawa et al. 2008). There are some reports, where intercavity photoinduced electron transfer occurred between co-encapsulated photoactive electron donor to catalytic electron acceptor inside the HKUST-1(Zn) MOF (the HKUST is named after Hong Kong University of Science and Technology, where from this MOF was developed first) (Larsen and Wojtas 2015). However, it might fail in longer distance (Larsen and Wojtas 2015). To best of our knowledge, the first evidence of intercavity photoinduced electron transfer occurred between co-encapsulated complexes within a polyhedral Zn(II)-trimesic acid-based MOF. That electron transfer occurred from exited state of Ru(II)tris(2,2′-bipyridine) to the ground state of the ground state Co(II)tris(2, 2′- 10 bipyridine) with $k_{\mathrm{ET}} = 3.7 \times 106\ \mathrm{S}^{-1}$ (Larsen and Wojtas 2013).

Intervalence charge transfer (IVCT) was known in some metal to metal (e.g., in prussian blue; Allendorf and Stavila 2015; Rosseinsky et al. 1987) and among 2,5-

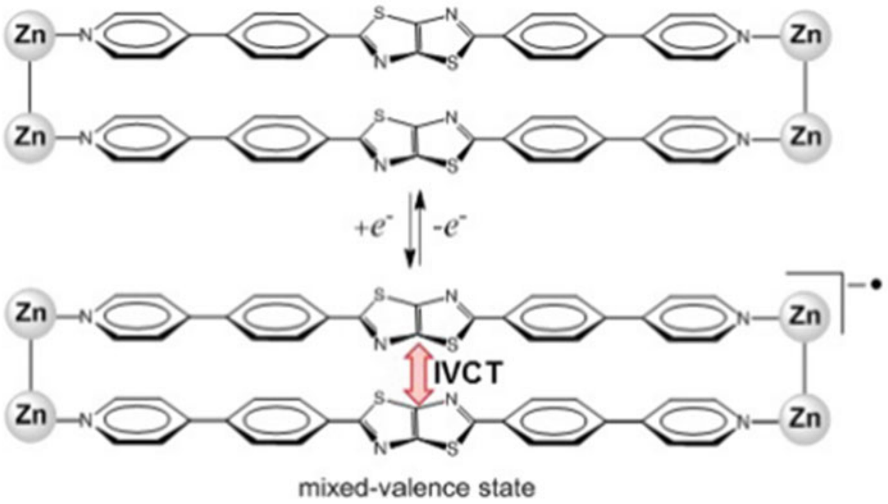

Fig. 6.7 Reduction to mixed-valence state through IVCT interaction in cofacial ligand pair (Hua et al. 2018)

dihydroxybenzoquinone redox centers through ligand (Abrahams et al. 2011; Darago et al. 2015), but for the first time, D'Alessandro et al. showed that IVCT can also take place through space (Hua et al. 2018) (Fig. 6.7). This Zn-based MOF contains two mixed-valence cofacial thiazolo[5,4-d]thiazole units in 2,5-bis(4-(pyridine-4-yl)phenyl)thiazolo[5,4-d]thiazole) ligand to promote IVCT, which can be elucidated further by density functional theory (DFT). The extinction coefficients of IVCT transition were determined by Kubelka-Munk analysis method to calculate the extent of delocalization quantitatively by Marcus-Hush theory.

6.3 Engineering of MOFs

Designing a MOF for developing a photocatalyst (Diercks et al. 2018) always needs to incorporate at least one light-harvesting center and transport of electron from light-harvesting site to reaction center and a reaction site. The reaction sites must be equipped with desired catalytic center protruding toward supramolecular cavity for hosting reactant molecules. In some cases, some metal cluster-based reaction sites also can absorb light to promote desired reaction. Basically, light-harvesting organic group increases the conjugation of electrons in the delocalized π-cloud of organic ligands. This functional group introduction does not change the crystalline packing pattern but just promote a red shift in absorption spectrum as per requirement. In most of the cases, this ligand modification enhances the photochemical reaction rate as sunlight spectrum consists of only 5% UV (300–400 nm) against 43% visible light (400–700 nm). However, after preparing a MOF, it can be modified further by exchanging the ligands or by thermal elimination of guest molecules followed by some specific reaction under post-synthetic modification technique (Sun et al. 2013). A smart selection of functional group for receiving light can be also useful in forming supramolecular bond to promote the reaction rate. By introducing the extended conjugation in ligand and designing electron rich metal cluster, the bandgap can be decreased to fasten the photochemical reaction. In addition, the organic ligand should have a good charge transport ability, so that electron and holes will not fuse massively.

For designing the photocatalyst MOF, the energy level of light-harvesting sites and reaction center should be matched to promote smooth electron transfer. In addition, a smaller particle size of the photocatalyst also suppresses the possibility of electron-hole pair recombination, which eventually promotes the catalytic performance (Takanabe 2017). In case of nanomaterials, a very high surface-to-volume ratio makes photogenerated charges available to the interface without recombination, as they travel shorter (Habisreutinger et al. 2013). Finally, nano-dimension-driven higher surface area decorated with reaction site and reactant adsorbing supramolecular cavity enhances the reaction rate (Kubacka et al. 2012).

6.3.1 Organic Linkers

Designing a single organic linker in constructing photocatalytic MOFs is very crucial as it serves several roles like harvesting light, transferring electrons and holes to reaction centers, and finally constructing a framework by coordinating at least two reaction centers. All these antenna, anchor, lengths, and conjugation extents greatly influence on the charge transfer kinetics.

6.3.1.1 Antenna

An antenna in organic ligand can help in harvesting the photon by lowering the bandgap energy for a targeted MOF. These groups can donate the electrons to the π-cloud of organic linkers to suppress the bandgap energy and act as an antenna for MOF system. The methyl group with +I effect is the weakest electron-donating group and can decrease the band group from 3.57 eV [25] to 3.5 eV which is almost similar to –Cl (3P electron) (Hendon et al. 2013). However, the 2p electron-donating functional groups like –OH (2.8 eV) and $-NH_2$ (2.6 eV) can extend the π electron cloud conjugation of aromatic ligands to decrease the bandgap in for the 10% MIL-125 (functional group) model (Fig. 6.8). Interestingly, diaminated benzenedicarboxylic acid ligand can decrease the band group utmost (1.3 eV). In contrary, $-CF_3$ group can withdraw the electron from the π-cloud of benzenedicarboxylate and reduce the CB + n band in the bandgap and destabilization of the Ti-O bond to result an unstable MOF. Similar to Ti-based MIL-125, the Zn-bdc-based IRMOF also has a similar electronic structure comparable (Gascon et al. 2008; Tranchemontagne et al. 2008).

Fig. 6.8 HSE06-predicted bandgap energy of bdc and its analogues bdc linkers with 10% substitution in MIL-125 (Hendon et al. 2013)

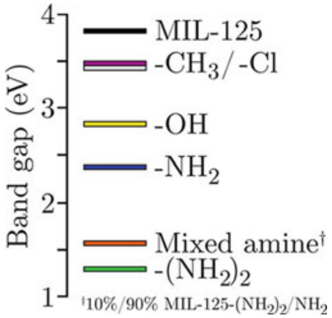

6.3.1.2 Anchors

Binding functionality of an organic linker may play a very crucial role in transferring electron and toward the stability of the frame work. These linkers also determine the charge transfer rate during photocatalysis reaction (Akimov et al. 2015). They showed that electron transfer with COOH anchors is much faster than PO_3H_2 anchors in complexes by nonadiabatic molecular dynamics simulation techniques for broader nonadiabatic coupling. Herein, -COOH group can sustain the higher electron density than –PO_3H_2 as revealed in theoretical calculation. The lighter atomic weight of C against P and strong double over single bond promotes electron transfer significantly faster. While computational study showed the electron transfer in 7.50 and 56.7 ps for COOH and PO_3H_2, respectively, experimentally electron transfer time for COOH took 12 ± 1 ps. However, –COOH group decomposes in some cases and makes the turnover number smaller in photocatalytic reactions. They proposed that the experimentally observed turnover numbers do not imply the electron transfer rate for semiconductors or in Ru-complex and COOH anchor is basically more competent than PO_3H_2 in photocatalysis.

6.3.1.3 Charge Transportation

Electron can travel through ligand or space depending on supramolecular architecture and ligand quality in MOF. For long-distance charge transport, consumption of charge carriers increases with charge recombination and relaxation processes. Recombination of photoexcited electrons and holes becomes unavoidable when ligands are employed in transporting these charges from antenna to catalytic centers. By reducing the lengths of bridge ligands, the probability of charge recombination can be reduced, but simultaneously for shortening the conjugation, the absorption energy spectrum will be shifted to the UV region to slower the charge transfer kinetics (Johansson et al. 2013; Abrahamsson et al. 2010). Besides the length of ligand, geometric torsion in bridging ligand may also influence the charge transfer kinetics by changing the degree of conjugation (Hu et al. 2016; Ding et al. 2014). Introducing an antenna or electron-donating group for capturing light also increases the conjugation in organic linker, which promotes charge transfer kinetics. In

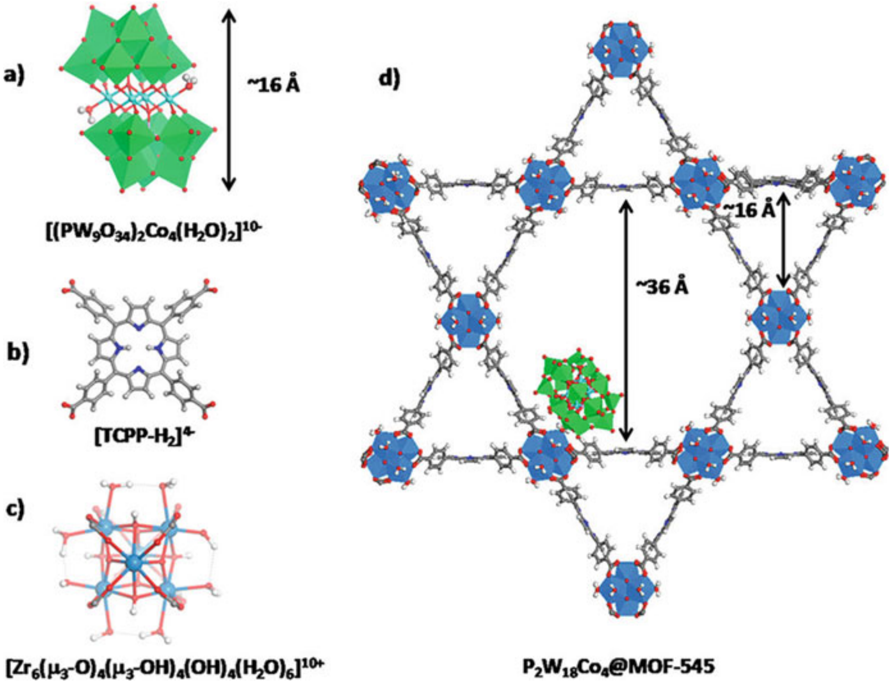

Fig. 6.9 (**a**) $P_2W_{18}Co_4$ (POM), (**b**) TCPP-H_2 ligand, (**c**) Zr-based SBU, and (**d**) $P_2W_{18}Co_4$@MOF-545. Presented WO6 in green polyhedral, ZrO8 in blue polyhedra or spheres, Co in cyan spheres, O in red spheres, C plus H in gray, and N in dark blue (Paille et al. 2018)

contrary, a lethargic charge transfer kinetics can be found by the introduction of electron-withdrawing functional group at the organic linker (Karnahl et al. 2011; Lau et al. 2016). Organic linkers basically provide a better electron transfer pathway than nonbridging frameworks. Electrons are expected to be localized on organic linkers for a while before reaching to the catalytic sites, which makes the catalytic reaction feasible (Gao et al. 2017). Such effect can be observed, when porphyrin system is introduced in Zr(IV)-based MOF (PCN-222) for visible light-induced photoreduction reaction in converting CO_2 to formate (Xu et al. 2015). They carried out ultrafast transient absorption and photoluminescence spectroscopy and demonstrated that extremely long-lived electron basically suppresses the detrimental electron-hole recombination to improve the efficiency in CO_2 photoreduction. Herein, the presence of such deep electron trap state in PCN-222 affords this improved catalytic performance, which revealed a new designing strategy for heterogeneous MOF-based photocatalyst. This beautiful strategy was adopted by Paille et al. 2018. They immobilized sandwich-like cobalt-polyoxometalate (POM), $[(PW_9O_{34})_2Co_4(H_2O)2]_{10}$ in the porphyrinic MOF, PCN-222 to develop a noble metal-free supramolecular heterogeneous photocatalytic system for the visible light-driven water oxidation (Fig. 6.9). Notably, the use of Co ions as an efficient catalytic centers for water oxidation is a common practice (Sahoo et al. 2018; Wang et al. 2016). The introduction of both catalyst and photosensitizer inside this framework with an efficient electron trap makes this heterogeneous photocatalyst highly efficient in oxidizing water.

6.3.1.4 Complex Formation

In some cases, organic linkers are employed for complex formation inside the targeted supramolecular channel to promote catalytic efficiency. These ligands are designed in such a way that these can form the photoactive complexes with Ru or Ir ions for constructing some excellent photosensitizers inside the MOFs. Most of the times, such technique is used for reducing CO_2. Besides this photosensitization, they also play the major role in stabilizing photogenerated electrons and holes for the longer time. Precisely, organic ligands are highly efficient in localizing electrons, while ionized metal centers can sustain holes in the metal complexes to promote MOFs as an efficient photocatalyst.

Wang et al. (2011) replaced 4,4′-biphenyl dicarboxylic acid with 2,2′-bipyridine-5,5′-dicarboxylic acid backbone to form several Ru-, Re-, and Ir-based derivatives. In this way, they basically modified the UiO-67 with introducing such photosensitizing complexes and employed them for water oxidation, carbon dioxide reduction, and organic reactions (Fig. 6.10).

In 2015, Li and his co-workers introduced the 2,2′-bipyridine moiety in this same way and formed Ru complex in MOF-253 (MOF-253–$Ru(CO)_2Cl_2$) for visible light-driven photocatalytic CO_2 reduction (Sun et al. 2015a, b). The MOF UiO-67 $[Zr_6(OH)_4(O)_4(O_2C\text{-}C_6H_4\text{-}C_6H_4\text{-}CO_2)_6]$ has been improved by Fontecave and his co-workers by introducing 2,2′-bipyridine-5,5′-dicarboxylic acid backbone to replace 4,4′-biphenyl dicarboxylic acid to prepare Rh-based complex (Chambers et al. 2015). For preparing this complex-based MOF (Cp*Rh@UiO-67), they have introduced post-synthetic linker exchange technique, which is shown schematically in Fig. 6.11. The catalytic activity of Cp*Rh@UiO-67 may be comparable to the homogeneous and heterogeneous systems, but it is highly advantageous over others regarding stability. This MOF reduces CO_2 to formate under visible light-driven photochemical reduction. However, with increasing the photosensitizing Ru $(bpy)_3Cl_2$ in MOF, it generally favors thermal decomposition of formate to H_2.

Fei et al. (2015) also used the same MOF (UiO-67) and introduced Mn(bpydc) $(CO)_3Br$ a manganese at 2,2′-bipyridine 5,5′-dicarboxylate linker. They tried to replace the expensive rare earth metal by Mn and employed for CO_2 reduction successively (Fig. 6.12).

Kitagawa and his co-workers also used UiO-67 and introduced a Ru^{II}-CO complex, $[Ru^{II}(bpy)(terpy)(CO)](PF_6)_2$, for reducing CO_2 to Co and HCOOH with high turnover number (TON) (Kajiwara et al. 2016). Choi et al. (2017) modified this UiO-67 by including $Re^{I}(CO)_3$(BPYDC)Cl complex inside the MOF and fabricated over Ag nanocubes (Fig. 6.13). They found that photosensitizers require a fine balance on close residing for cooperatively enhancing photocatalytic activity, which can be maximized at by optimization of Re complexes per unit cell (Re3-MOF). A structure-activity correlation revealed that Ag nanocube impregnated

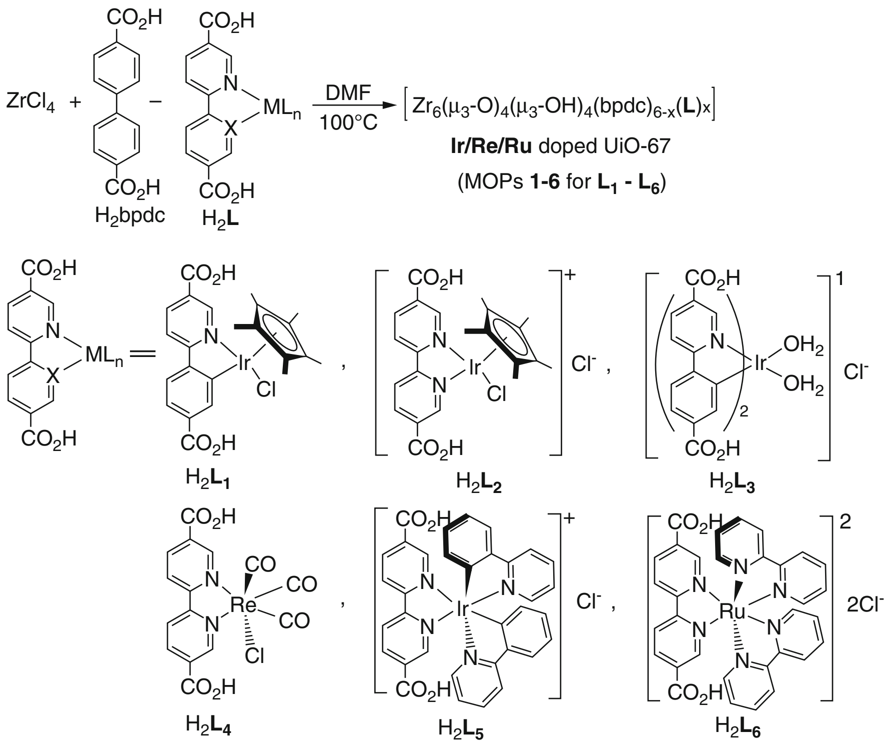

Fig. 6.10 Schematic presentation of Doped UiO-67 synthesis (Wang et al. 2011)

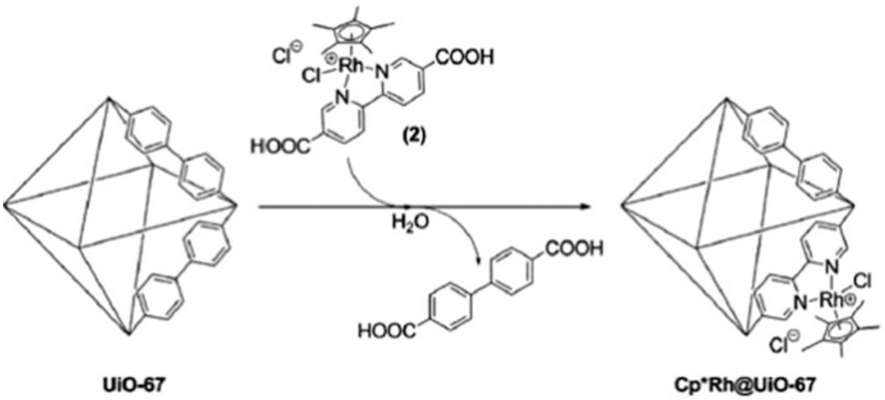

Fig. 6.11 Post-synthetic linker exchange for Rh complex formation in UiO-67 (Chambers et al. 2015)

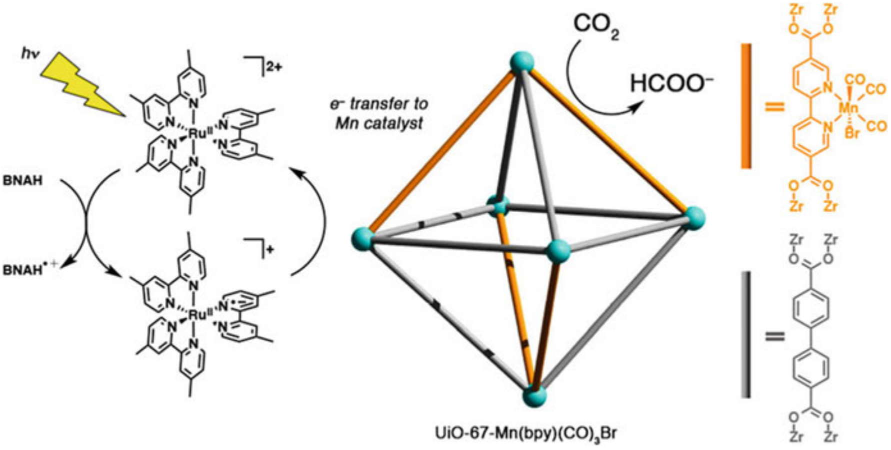

Fig. 6.12 Mn carbonyl complex formation at ligand backbone for CO_2 reduction (Fei et al. 2015)

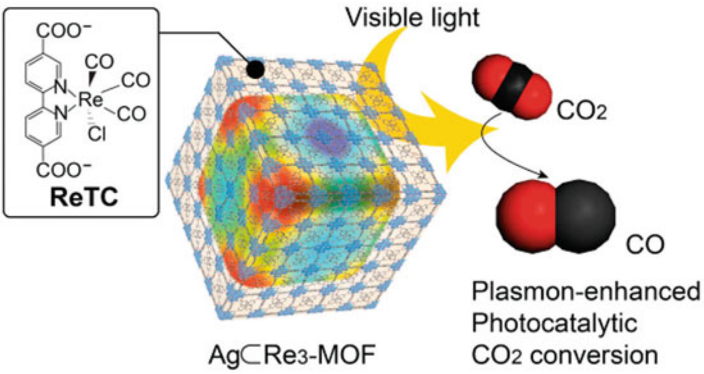

Fig. 6.13 Ag impregnated Re_n-MOF for CO_2 reduction (Choi et al. 2017)

Re_3-MOF spatially restricted photoactive Re sites near Ag surface against increased near-surface electric fields. This effect increases CO_2-to-CO conversion by sevenfold under visible light with a long 48-h stability.

By using a secondary building unit (SBU, $Cd_2(CO_2)_6$), Zhang et al. (2015a) employed 2,2′-bipyridine-4,4′-dicarboxylic acid as an organic linker to form MOF-based heterogeneous photocatalyst for reducing CO_2. This linker simultaneously can form Ru complex to develop the photosensitizer and plays the same typical role of generating electrons and hole for photoreaction. These Ru centers generate electrons and can be localized over pyridine rings of dicarboxylate linkers, whereas holes can be located over Ru centers. These highly stable MOF forms nanoflower-like architecture and reduce CO_2 efficiently.

The secondary building units (SBU, $Zr_6O_4(OH)_4$) are linked with 1,4-benzene-dicarboxylate to form UiO-66. Lee et al. (2015) modified this structure further by post-synthetic exchanging of 1,4-benzene-dicarboxylate with 2,3-

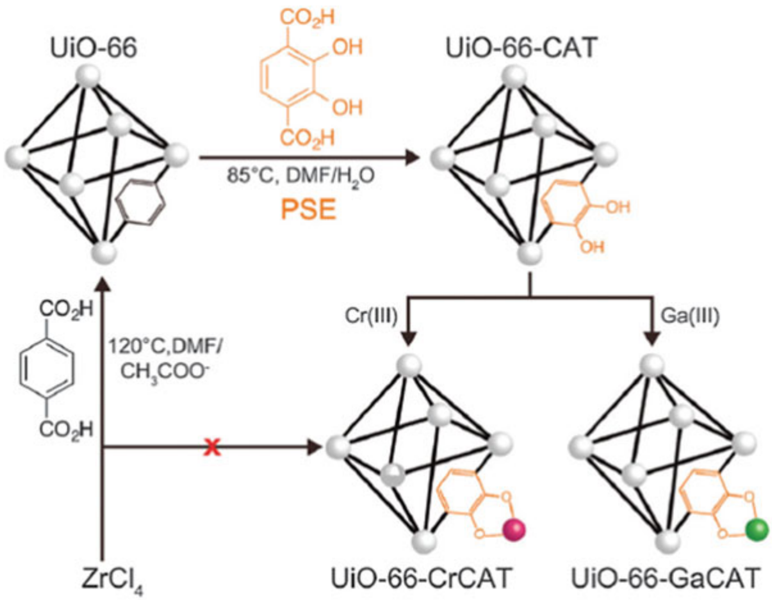

Fig. 6.14 Modification of UiO-66 by post-synthetic exchange and metalation (Lee et al. 2015)

dihydroxyterephthalate (catbdc) and formed unprecedented Cr- or Ga-monocatecholato in robust UiO-66 (Fig. 6.14). However, the Cr-modified MOF exhibited a better CO_2-reducing efficiency over Ga derivatives for its open shell electronic arrangement.

6.3.2 Secondary Building Unit

Besides playing crucial role in developing geometry of the lattice structure, the secondary building unit (SBU) acts as a catalytic center for photocatalytic reactions. SBU should be selected according to the targeted reaction while designing a MOF. For example, Fe, Zr, and Ti oxide-base MOFs are used for CO_2 reduction. For developing the exact role of SBU, a detailed experimental investigation on previous report, coupled with theoretical insight, is important in designing MOFs. Yang et al. (2014) showed the theoretical way of controlling the bandgap while designing MOF-5. MOF-5 is comprised of a tetrahedral SBU, Zn_4O, linked with 1,4-benzenedicarboxylate linker to form face-centered cubic (FCC) crystal with $Fm\bar{3}m$ symmetry. They systematically tuned the bandgap by designing SBU in computer simulations employing DFT. Therein, they substituted the atoms in SBU and changed Zn (by Cd, Be, Mg, Ca, Sr, Ba) and O (by S, Se, Te) in engineering bandgap from 1.7 to 3.6 eV. While moving from O → S → Se → Te, the bandgap decreases with increasing minimum absorption wavelength. However, while in preparation, the formation energy increases continuously moving from Te to O.

6.3.2.1 Adding Functional Group at Catalytic Sites

Van Wyk et al. (2018) modified the MOF NU-1000 by anchoring a ferrocene moiety at Zr node to build Fc@NU-1000. They explore the previously reported MOF NU-1000 and made off deprotonated 1,3,6,8-tetrakis(pbenzoicacid)pyrene (H_4TBAPy) anchored at $[Zr_6(\mu3 - O)_4(\mu3 - OH)_4{}^- (-OH)_4(-OH_2)_4]^{8+}$ nodes (Mondloch et al. 2013), and charge transfer (CT) process was facilitated in a unique way. To retrospect the decay pattern, they showed that while excited-state absorption (ESA) band of NU-1000 appeared at 730 nm ($\tau \sim 15$ ps), the modified Fc@NU-1000 exhibited ESA peak at 600 nm($\tau delay = 56$ ps). To envisage the mechanism, they found that a charged transferred product ([NU-1000]•−/Fc+) was fixed at the mesopores, allowing the dielectric variation in a wide range of $\epsilon s = 1–37$ without involving any electrolyte-based counterions. Such dielectrics bound in CT kinetic data clearly demonstrates that the involvement of ferrocene necessitates a large reorganization energy. This energy polarizes the hydroxyl/aqua ligands, attached at the nodes by photoinduced charged products. This experiment might open a new avenue in designing new useful electrocatalytic or photocatalytic MOFs in near future (Fig. 6.15). Despite of efficient electron tunnelling efficiency exhibited by some anchoring functionalities like –COOH, reaction process gets sluggish for paying a reorganization energy as penalty at reaction nodes. Such additional anchoring technique at reaction center for eliminating node bound hydroxyl/aqua ligands may be useful in designing some efficient MOF-based photocatalyst or electrocatalyst in future.

6.4 Designing Homogeneous Catalyst

Designing a homogeneous MOF for catalytic use is a daunting tusk. MOFs, soluble in organic or aqueous medium, are not unavailable, but designing a MOF with light-harvesting center and reaction site in a common strategy makes it insoluble basically. Nonetheless, a new insight can be useful in designing homogeneous photocatalytic MOF as designed by Tian et al. (2016). They prepared a water-soluble MOF in a novel strategy and explored it for homogeneous photocatalytic purpose for the first time (Fig. 6.16). Interestingly, it can also work as a heterogeneous catalyst. Zhang et al. (2015b) prepared the MOF (supramolecular metal-organic framework SMOF-1) by reacting hexaarmed $[Ru(bpy)_3]2þ$-based precursor with cucurbit[8]uril (CB[8]), where estimated void volume was ~80%. This SMOF-1 can host the anionic Wells-Dawson-type polyoxometalate (WD-POM) clusters effectively, without leaving any cavity free. This WD-POM-encapsulated SMOF-1 (WD-POM@ SMOF-1) can be excited by visible light (500 nm) to promote multielectron ejection from Ru centers to WD-POM anions and produce hydrogen efficiently from both organic and aqueous medium. They did the hydrogen production in an acidic aqueous medium at pH = 1.8 in presence of methanol, as a sacrificial electron donor. UV-visible experiments exhibited that WD-POM was not released from both the homogeneous

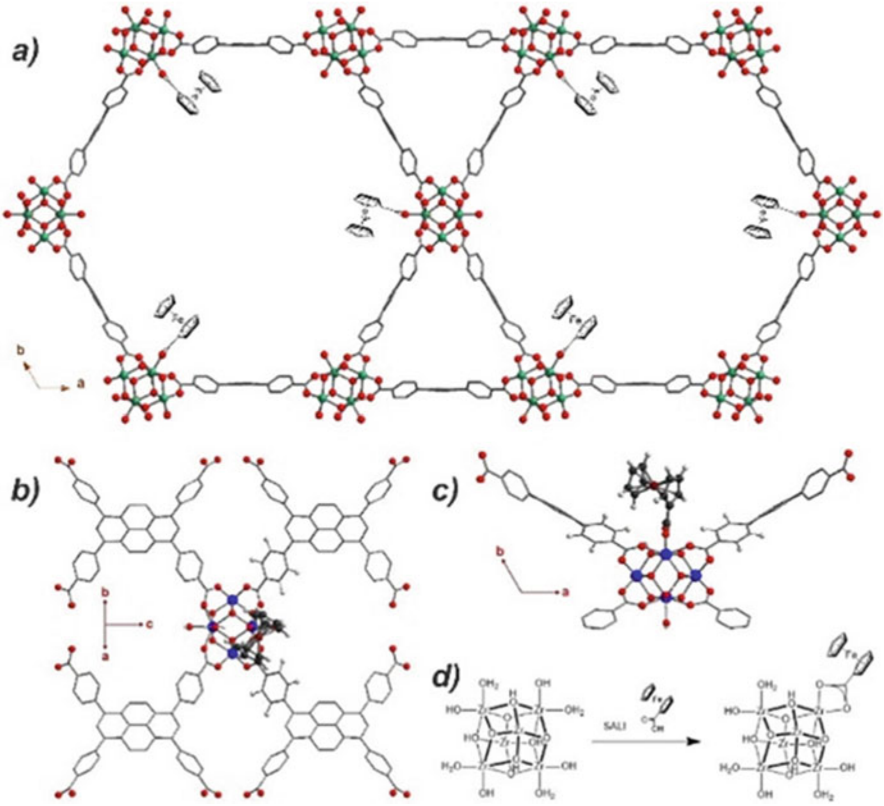

Fig. 6.15 (**a**) Fc moieties protrude inside the mesopores of Fc@NU-1000 ($d \sim 30$ Å), (**b** and **c**) DFT optimized partial structures at ferrocene attached Zr^{IV}-oxo node, (**d**) SALI functionalization technique (Van Wyk et al. 2018)

and heterogeneous reaction condition even after irradiating for 50 h. Such beautiful strategy can open a new path in developing homogeneous catalyst for photocatalytic process. For designing a homogeneous MOF, several hydrophilic functionalities can also be introduced (Banerjee et al. 2016) [113] along with required photocatalytic functionality.

6.5 Designing Asymmetric Catalyst

There are some reports based on MOF-catalyzed asymmetric synthesis in literature, but MOF-based asymmetric photocatalysts are very rare because of their present designing challenge (Bhattacharjee et al. 2018; Zhu et al. 2016; Mo et al. 2014; Song et al. 2011). Nonetheless, a couple of reports came on MOF-based asymmetric photocatalyst so far. The first report came by Wu et al. (2012), where they prepared Zn based two enantiomeric heterogeneous photocatalyst MOFs for alpha alkylation

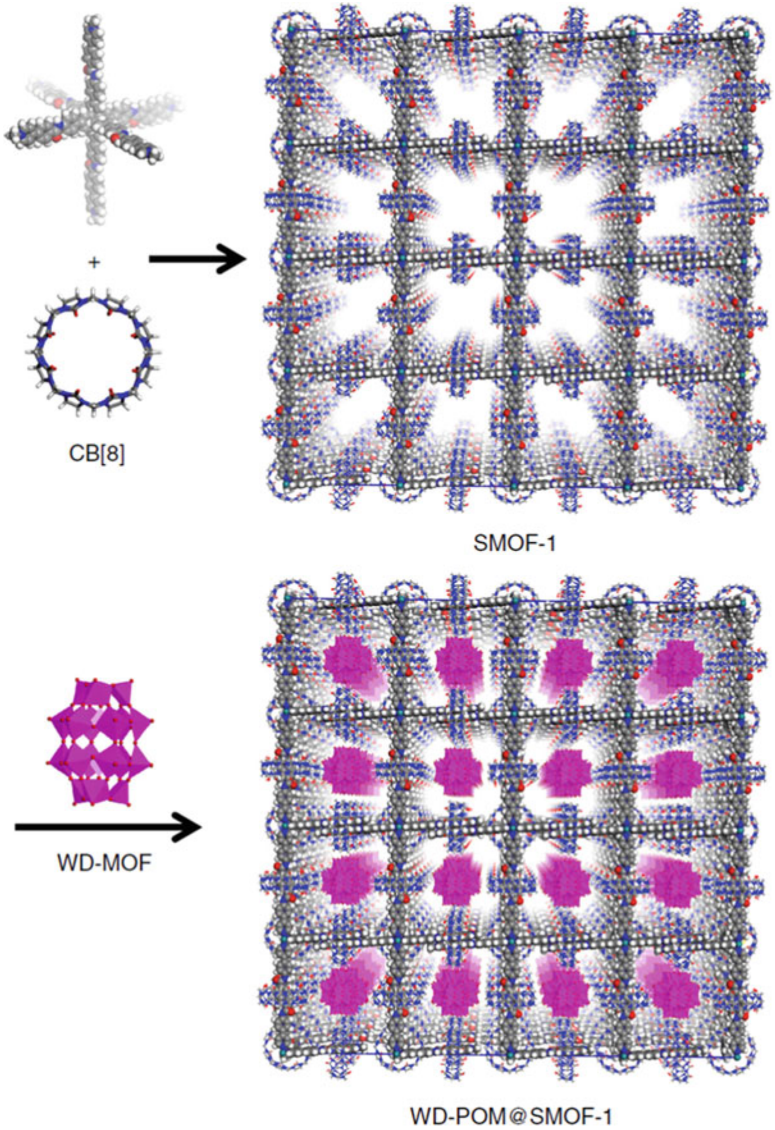

Fig. 6.16 SMOF-1 preparation by reacting hexa-armed $[\mathrm{Ru(bpy)_3}]$2þ-based precursor and cucurbit [8]uril (CB[8]) followed by adsorption of WD-POM. Presentation mode: H in white, C in light gray, N in blue, O in red, Ru in cyan, and WD-POM ($[P_2W_{18}O_{62}]^{6-}$) in purple polyhedron (Tian et al. 2016)

of aliphatic aldehydes. They prepared these two MOFs by introducing a photosensitizer ligand (4,4′,4″-nitrilotribenzoic acid), a photoredox functionality (triphenylamine), and a stereoselective organocatalyst (D- or L-pyrrolidin-2-ylimidazole, PY) for preparing the MOFs, Zn−PYI1, and Zn−PYI2 (Fig. 6.17). UV-vis absorption spectrum of exhibited a $\pi-\pi^*$ transition of triphenylamine group

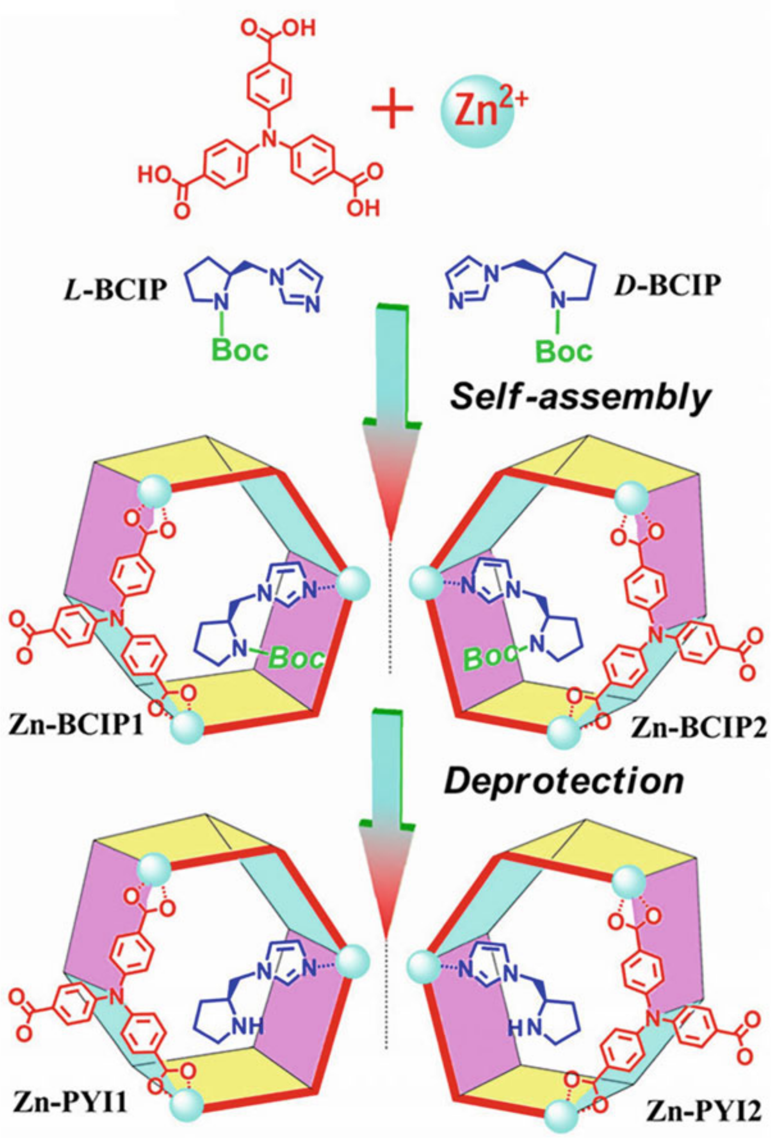

Fig. 6.17 Preparation of Zn−PYI1 and Zn−PYI2 schematically (Wu et al. 2012)

at 350 nm. An intense luminescence spectrum appeared at 450 nm while exciting the Zn−PYI1 by light with 350 nm. This excitation produces the photoelectron from triphenylamine, and it takes part to produce the active intermediate for stereoselective reaction. The chiral catalytic environment inside the supramolecular void and the presence of photocatalyst make the MOFs superior for carrying out enantioselective reaction effectively rather than keeping the MOF forming ingredients individual for asymmetric photosynthesis. This designing principle will provide a smart guideline to the crystal engineers for designing MOF-based asymmetric photocatalyst.

This concept later improvised by Zhang et al. (2017) and prepared Zn^{2+}-, Zr^{4+}-, and Ti^{4+}-based MOFs carrying out visible light-driven asymmetric α-alkylation on 3-phenylpropionaldehyde. They have introduced Zr^{4+} and Ti^{4+} which are more prone to undergo photoreactions in those MOFs and selected the 2-amino terephthalic acid as the ligand precursor, which is considered as a good ligand in constructing photocatalyst. They adopted the same principle of protruding a pyrrolidine functionality inside the supramolecular cavity with an asymmetric linkage to the terephthalic moiety. Such improvisation of organic linkers will be revolutionary in developing MOF-based heterogeneous asymmetric catalyst as 2-amino terephthalate is a very popular backbone in MOF-based heterogeneous catalytic system. By simply changing the pyrrolidine functionality with some other catalytic centers, one can change the reacting substrate accordingly. Lastly, by changing metal ions or by introducing metal cluster-based reaction site, one can easily engineer the MOF for some specific asymmetric organic synthesis.

6.6 Developing Catalysts

Before going to discuss the designing aspects of organic linkers, metal cluster, some modification of MOF will be presented here for clearing their fundamental roles.

6.6.1 MOF-5

Li et al. (1999) reported a Zn-based super tetrahedron cluster, bridged by terephthalate anions to form a highly stable and porous MOF (MOF-5). In 2007, Garcia at al. showed that it has 3.4 eV bandgap value, where photo-driven charge separation promotes electron in conduction band, leaving holes in valence band to establish it as a semiconductor (Alvaro et al. 2007). They use this material for degradation of phenol under photochemical reaction. Realizing the importance of MOF-5, Hausdorf et al. (2008) tried to modify the synthetic procedure to make the MOF-5 cheaper in 2008. To envisage the clear mechanism, in a parallel but separate study, Majima et al. investigated the luminescence transitions in MOF-5 and the interfacial charge transfer from photoexcited MOF-5 to the adsorbed reactant molecules. The prepared nanodimensional MOF-5 observed a temperature-dependent spectroscopic study over MOF-5 emission, which has a very similar transition pattern with ZnO nanoparticles. However, they deviate from temperature-dependent PL intensity change and shift of activation energies under thermal quenching or activation courses.

The time-resolved and steady-state PL measurements were carried out to determine the reaction rates between MOF-5 and aromatic sulfides and amines (S). TDR spectroscopy was also carried out in acetonitrile medium under laser flash photolysis procedure at 355 nm wavelength. It was observed that $S^{\bullet+}$ produced in the MOF-5 has over 50 μs long lifetime, which is very significant to enhance the quantum yield for degradation. They also employed Marcus theory in this electron transfer reactions to establish a relatively low HT rate and a long lifetime of intermediate $S^{\bullet+}$ which attribute higher λ value ($\lambda_{V,D}$, 1.2) in contrary to other semiconductor nanoparticles, like ZnO and TiO_2. Interestingly, they showed photoexcited triplet state of terephthalate gets separated from MOF-5 structure to undergo in redox processes.

6.6.2 UiO-66(Zr)

This **UiO** is named after *Universitetet i Oslo* (University of Oslo). Cavka et al. (2008) developed a zirconium-based extremely stable MOF, which consisted an inner $Zr_6O_4(OH)_4$ core, bridged by 1,4-benzene-dicarboxylate (UiO-66), 4,4′ biphenyl-dicarboxylate (UiO-67), or terphenyl dicarboxylate (UiO-68) linkers. They incorporated previously reported the same inner Zr6-cluster inside the MOF (Puchberger et al. 2006). Herein, Langmuir surface area like 1187 m^2/g and high structural resistance toward mechanical pressure 10.000 kg/cm^2 established UiO-66 as an exceptionally stable MOF for practical uses. Silva et al. (2010a, b) modified UiO-66 by introducing light receiving $-NH_2$ functionality to enhance photocatalytic H_2 generation. The attached NH_2 group in 1,4-benzene-dicarboxylate is expected to enhance the light absorption capability to enhance the quantum yield for hydrogen generation in water/methanol (3:1) mixtures from >0.1% (UiO-66) to 3.5% UiO-66 (NH_2) (Fig. 6.18). XRD pattern revealed that NH_2 group does not influence the structure formation but just was protruding inside supramolecular according to the single crystal X-ray structure analysis. Nonetheless, it just shifted the absorption band in a desirable range to promote catalytic activity (Fig. 6.18).

While studying mechanism it was observed that the presence of O_2 completely quenches the transient spectra, revealing O_2 plays a crucial role both as electron quencher and photogenerated transient triplet excited states (Fig. 6.19). This excited triplet state acts as a precursor in charge-separated state, like MOF-5, which is discussed here earlier. Photolysis by 355 nm laser excitation revealed that long-lived triplet state, which quenches positive holes and electrons, established the MOF as true semiconductor.

6.6.3 MIL-101(Fe)

The term **MIL** is named after the Materials Institute Lavoisier. In 2005 Férey et al. (2005) prepared a chromium-based MOF with a large surface area to construct a high pore volume (~30–34 Å) by a smart computational designing. In 2013, Roeffaers et al.

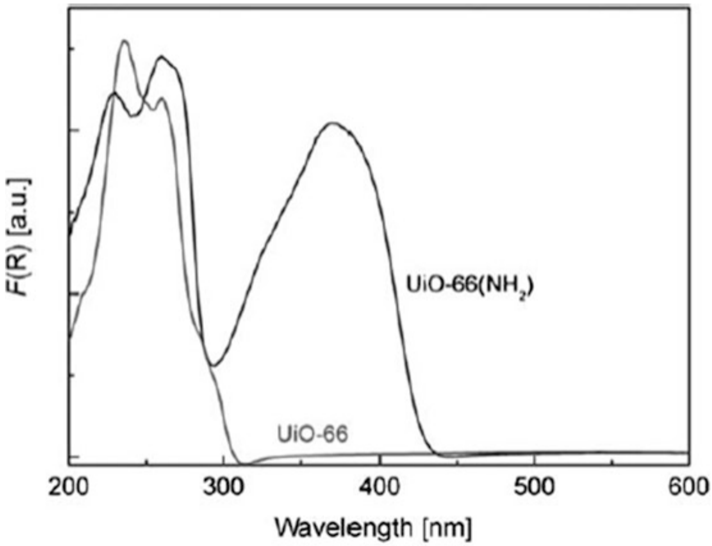

Fig. 6.18 UV/Vis spectra from UiO-66 and UiO-66(NH_2) (Silva et al. 2010a, b)

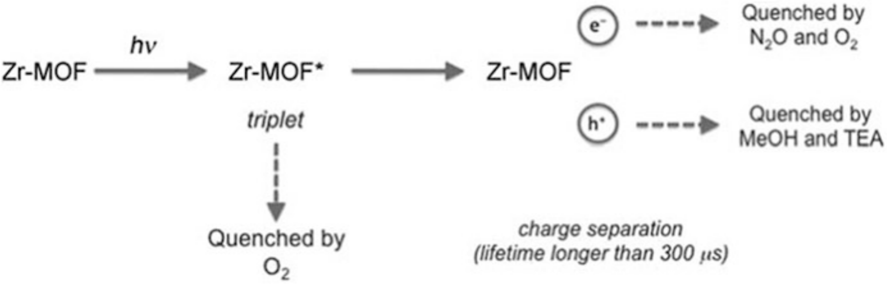

Fig. 6.19 Expected mechanism of photocatalytic transformation of two Zr-MOFs; TEA, triethylamine (Silva et al. 2010a, b)

replaced the chromium oxide by Fe_3-μ_3-oxo clusters to shift the absorption band in visible light range by reducing the bandgap to degrade rhodamine 6G successfully in contrast to similar experiment carried out by inactive Fe_2O_3. To scrutinize the mechanism, it was found that a high electron-hole consumption rate suppresses the rhodamine 6G oxidative degradation. However, it can be nullified by reducing the particle size of MOF. Later Wang et al. (2014) showed by introducing –NH_2 functionality in terephthalic acid backbone, MIL-101 NH_2(Fe) become more efficient in absorbing light at visible range. And finally, MIL-101NH_2(Fe) can reduce CO_2 to $HCOO^-$ under visible light selectively about 3.0-fold higher than MIL-101(Fe). While scrutinizing the efficiency, it was revealed that in MIL-101NH_2(Fe), the dual excitation from 2-amino terephthalate and Fe–O clusters helps to generate Fe^{2+} from Fe^{3+} for reducing CO_2. In case of MIL-101(Fe), the only Fe–O clusters directly absorb visible light and reduce CO_2, while in MIL-101NH$_2$(Fe), the 2-aminoterepthalate linker also excites Fe–O cluster to drive the CO_2 reduction fast. In 2015, by keeping the catalyst same, Shi et al. (2015) showed that MIL-101NH$_2$(Fe) can also reduce Cr (IV) to Cr (III) under the same electron transfer mechanism. In this same year, Liang et al. (2015) found that a similar type of MOF, namely, MIL-53(Fe), can also be used for Cr (IV) reduction and oxidative photocatalytic degradation of some organic dyes (MG or RhB) and reduction of Cr (VI), which can be explained by the synergetic effect of photogenerated electrons and holes.

6.6.4 MIL-125(Ti)

Another highly porous MOF has been reported in 2009 by Dan-Hardi et al. (2009). They prepared this new photoactive MOF, MIL-125(Ti) [$Ti_8O_8(OH)_4$-(O_2C-C_6H_4-CO_2)$_6$], by using the terephthalic acid linker to the Ti cluster. It showed an interesting reversible photochromic effect after adsorbing alcohol inside the pores (Fig. 6.20).

Under UV-visible irradiation, the Ti(IV) in MIL-125 undergoes white to purple-gray-blue transformation to form Ti(III)-Ti(IV) mixed-valence state. Here the presence of Ti(III) was confirmed by ESR spectroscopy. The Ti(IV) reduction and adsorbed alcohol oxidation occur simultaneously. However, the presence of O_2 re-oxidizes titanium-oxo-hydroxo nodes. Under inert atmosphere, these mixed-valence states show long stability for exhibiting stable coloration. Fu et al. (2012) introduced a-NH_2 functionality in terephthalic acid backbone and showed that CO_2 adsorption capability was increased (Fig. 6.21).

The MIL-125NH$_2$(Ti), for the first time, exhibited the visible light-driven photocatalytic reduction of CO_2 to form $HCOO^-$ (Fig. 6.22). They used triethanolamine (TEOA) with acetonitrile in this reduction process. This TEOA acts as electron donor, and they also observed a bright yellow to green color change in nitrogen atmosphere under UV radiation. The change in Ti electronic state from Ti (IV) to Ti(III) was further established by ESR spectroscopy.

In this same year, Horiuchi et al. (2012) used the same MIL-125NH$_2$(Ti) to show the visible light-driven photocatalytic hydrogen production. This group also used TEOA as a sacrificial reagent for donating electron under visible light irradiation. Under UV irradiation, they showed that Ti^{3+} can be generated by direct exciting Ti-O cluster and hence they showed, under simultaneous irradiation of both UV and visible, the photocatalytic hydrogen production which is faster in rate.

By exploring same MIL-125NH$_2$(Ti), Sun et al. (2015a, b) did a series of organic amines to imines transformation reaction under visible light.

They showed that the presence of oxygen molecules oxidizes Ti^{3+} into Ti^{4+}, which causes color changes from green to yellow and proposed a mechanism as well (Fig. 6.23). The oxidation state change was further confirmed by ESR experiment, and they showed the same mechanism as previous workers (Fu et al. 2012). In a very recent study, Li et al. (2018) showed the effect of ligand functionalization on

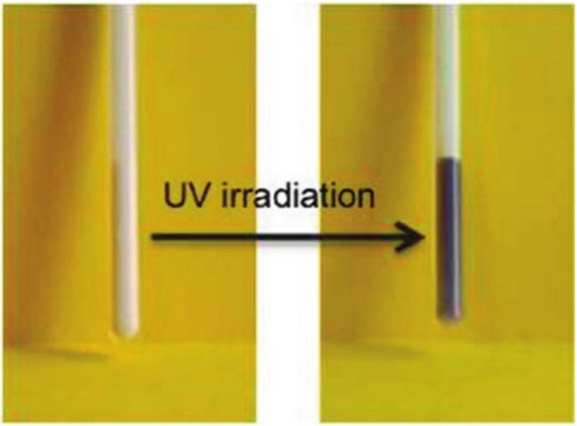

Fig. 6.20 UV irradiation effect over a capillary filled with MIL-125 and benzyl alcohol (Dan-Hardi et al. 2009)

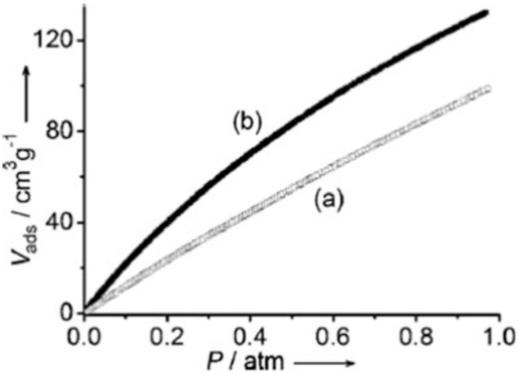

Fig. 6.21 CO_2 adsorption isotherms of (*a*) MIL-125 (Ti) and (*b*) NH2-MIL-125 (Ti) at 1 atm, 273 K (Fu et al. 2012)

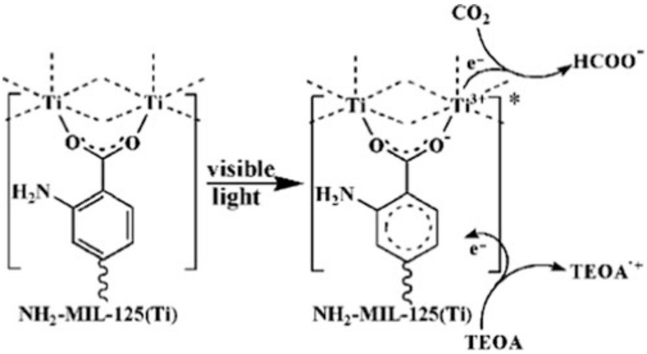

Fig. 6.22 Expected mechanism for visible light-driven CO_2 reduction by NH_2-MIL-125(Ti) (Fu et al. 2012)

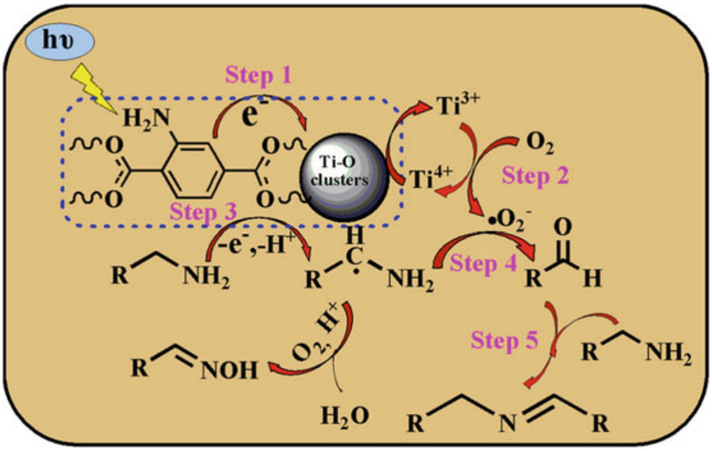

Fig. 6.23 Proposed mechanism for photocatalytic amines oxidation over NH_2-MIL-125(Ti) (Sun et al. 2015a, b)

electronic structures, optical absorptions, and photocatalytic properties by DFT calculation.

6.7 Designing for Special Purpose

In pursuit of designing a catalyst for a specific purpose, we must pay attention over every contributing factor like ligands, catalytic sites, bandgaps, and activation energies. After the discovery of Honda-Fujishima effect (Fujishima and Honda 1972), a considerable amount of research is reported on photocatalytic water oxidation. However, MOF-based photocatalytic water oxidation is relatively new, and much theoretical insights are yet to discover. Nonetheless, reported literatures will be attributed by for developing a designing principle here.

6.7.1 Water Oxidation

While photogenerated electrons reduce water molecules to produce hydrogen, holes oxidize the water to produce oxygen in an energetically uphill reaction. The associated Gibbs-free energy change (ΔG) for water splitting is 237 kJ mol^{-1} or 1.23 eV, implying the bandgap between the CB and VB must be greater than 1.23 eV, which basically rules out the use of conductor as photocatalyst. A wavelength associated to 1100 nm might be equivalent to this ΔG value, but due to energy loss during photo physical process, energy associated to bigger bandgap like 1.6–2.0 eV is required (Bak et al. 2002; Holladay et al. 2009; Wang et al. 2017). In addition, the bottom

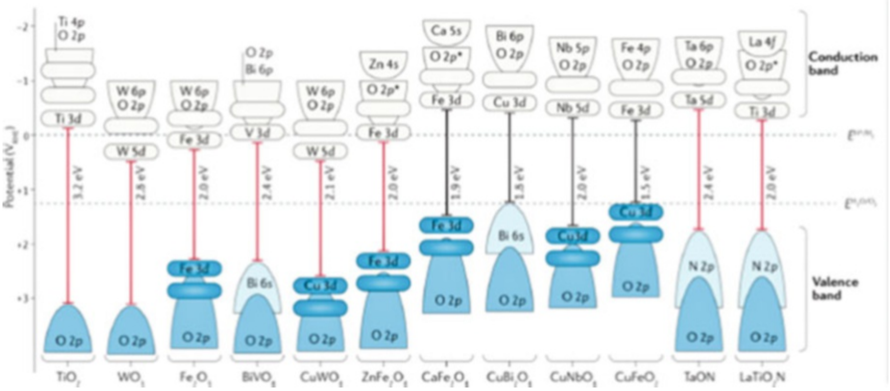

Fig. 6.24 Bandgap energy of various metal oxides and oxynitride-based semiconductors (red for n-type, black for p-type) (Takanabe 2017)

level of CB is required to be more negative than H^+/H_2 potential (0.0 V vs normal hydrogen electrode, NHE), whereas the top level of VB should be more positive than the redox potential of O_2/H_2O (1.23 V vs NHE) (Fig. 6.24) (Maeda and Domen 2007).

Electronic states of metal oxide-base semiconductors are well studied and found that VB is comprised of O 2P orbital (Takanabe 2017; Sivula and van de Krol 2016). The uppermost level of VB is considerably higher than O_2/H_2O redox potential. When energy of photon possesses the energy higher than the bandgap energy, electron from VB gets excited and transferred into the CB and generates a positive hole in VB in consequence. In pursuit of photochemical reaction, this band structure is only the thermodynamic requirement. As described earlier, there are several other factors like separation, transportation, and lifetime of charges that also influence the reaction (Fig. 6.5). However, the electronic states of organic ligands generally define the band edges in MOF, whereas the energy level splitting can be attributed by an overlap integral (β), between adjacent centers (Butler et al. 2014a, b). Though both Hückel theory (Hückel 1931) and extended Hückel theory (Hoffmann 1963) explain that the β parameter does not play any role on interatomic separation by formal analytical dependence, the extended approach results in an analogous d^{-2} dependence of the energy levels (Harrison 1983). Butler et al. (2014a, b) explored some available MOFs and metal oxides for studying electronic chemical potentials and showed that the binding energy of an electron develops the inherent chemical and physical properties in a material. They proposed that the valence band alignment cannot only explain the electrochemical activities; it can also help understanding optical and electrical properties.

Besides the band structure, reaction centers also play a crucial role in designing catalyst. Silva et al. (2010a, b) showed that $Zr_6O_4(OH)_4$ can be used for HER for the first time. The SBU used here was $Zr_6O_4(OH)_4$ core and replaced terephthalate with 2-aminoterephthalate ligands to increase the HER from 248 to 372 μmol h^{-1} g^{-1}. Later, people used co-catalyst to improve the reaction rate intensely (Toyao et al.

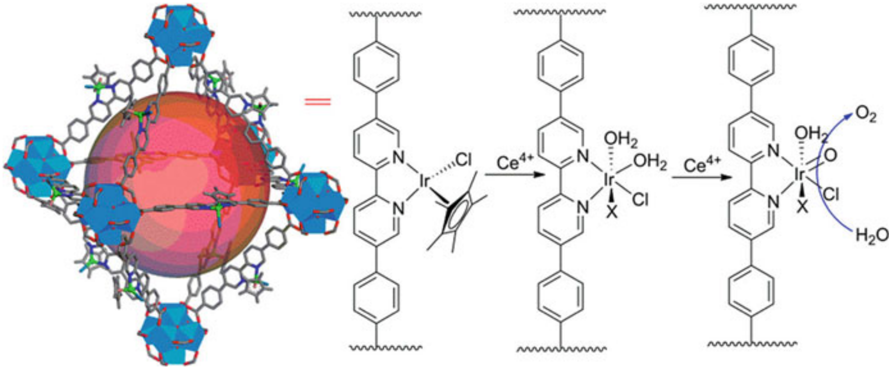

Fig. 6.25 By employing DFT, Wang et al. found that water molecule can be activated by bonding to the Co center, while exiting proton gets accepted by the adjacent benzimidazolate in Co-ZIF-9 (Wang et al. 2012)

2013). In case when MoS_2/UiO66-CdS was used, it went up to 32,500 μmol h^{-1} g^{-1} (Shen et al. 2015). deKrafft et al. (2012) employed MIL-101 (Fe_2O_3 is used as SBU) and coated by amorphous TiO_2 for the HER. They found a poor catalytic property (600 μmol h^{-1} g^{-1}) there.

Zr-based $Zr_6O_4(OH)_4(carboxylate)_{12}$ SBUs coordinated with dibenzoate-substituted 2,2′-bipyridine were also employed for water oxidation (Fig. 6.25). This bipyridine functionality coordinated to Cp*Ir moiety to form the excellent photosensitizers inside this MOF (Wang et al. 2012).

Li et al. (2018) showed theoretically that an introduction of NH_2 group in MIL-125 does not influence much on photocatalytic oxygen evolution even after absorbing the light efficiently. Instead, it increases the hydrogen production significantly. Introduction of NH_2 group promotes absorbing reaction, which eventually helps water splitting. Significantly, they introduced a smart insight in designing MOF, where balancing optical response and energy level at band edge is crucial to optimize the catalytic efficiency. At present, computational designing with DFT analysis becomes essential as higher-order electronic interaction and conjugative catalytic effort restrict crystal engineers to start designing a new MOF for a very specific catalytic purpose. With a considerable amount of theoretically established strategy, crystal engineers will make this path wider to reach the goal.

6.7.2 CO_2 Reduction

Like water oxidation, CO_2 reduction (Wang and Wang 2015; Diercks et al. 2018; Chen et al. 2017a; Lingampalli et al. 2017; Meng et al. 2017) not only faces the challenge to excite electrons by using visible light, it also competes with hydrogen evolution reaction additionally. A substantial amount of energy is required to break a

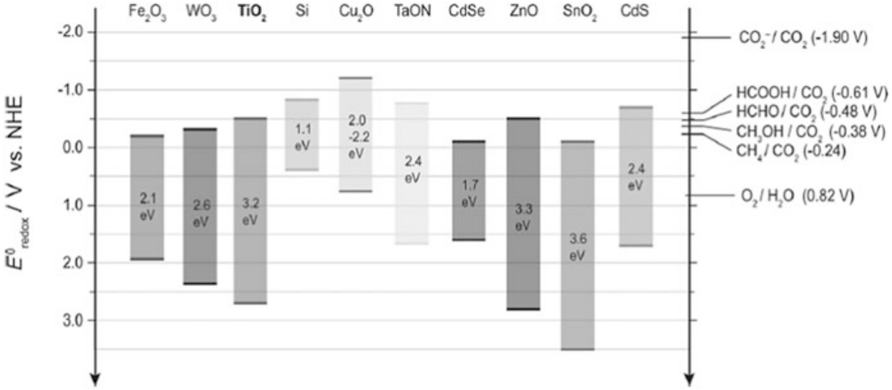

Fig. 6.26 Bandgap structures of several semiconductors at pH 7 involved in CO_2 reduction. Conduction band, valence band potentials, and bandgap energies of various semiconductor photocatalysts relative to the redox potentials at pH 7 of compounds involved in CO_2 reduction (Habisreutinger et al. 2013)

highly stable CO_2 (bond enthalpy is +805 kJ/mol). This reduction reaction is an uphill process, where it requires a significant energy input ($\Delta G^0 > 0$) unlike some other catalytic process ($\Delta G^0 < 0$) for lowering the kinetic barrier of the reaction (Habisreutinger et al. 2013). The energy required for such reaction is supplied by photons always (Fig. 6.26). Under photocatalytic process, exited electron moves from valence band to higher energy conduction band. The energy level of photogenerated holes located at the top of the VB determines oxidation potential of the photoreaction, whereas reduction potential is associated with the energy level of electrons, residing at the bottom of conduction band. The bandgap of MOF and catalytic futility determines the possibility and nature of photo reaction. In designing a MOF for CO_2 reduction, VB should be placed near to the water oxidation potential (0.81 eV, at pH 7) to make the bandgap smaller and increase the light absorbing capability (Fig. 6.27). However, the reduction potential values change according to the following product formation (Table 6.1).

Ren et al. (2015) employed DFT for the three mechanisms listed above on Ni (111) surface and concluded that rate-determining steps involving CO are most energetically plausible than the direct participation of $HCOO^-$ species.

We have described the effect of complex formation on CO_2 reduction previously. We have described several MOFs like MIL-125NH$_2$(Ti) and MIL-101NH$_2$(Fe) also (vide supra). Wang et al. (2014) recently developed several iron-based MOFs like (MIL-101, MIL-53, MIL-88B) for visible light-driven CO_2 reduction to produce $HCOO^-$ efficiently. Ideally, CO_2 reduction should be coupled with water oxidation or organic hazard oxidation process to make the process cost-effective. However, the role of Fe-, Ti-, and Zr-based SBU for CO_2 reduction is not clear so far and needs a detailed theoretical insight to explain the mechanism. Recently, ZIF-67 is used as a co-catalyst for reducing CO_2 effectively (Wang et al. 2018a).

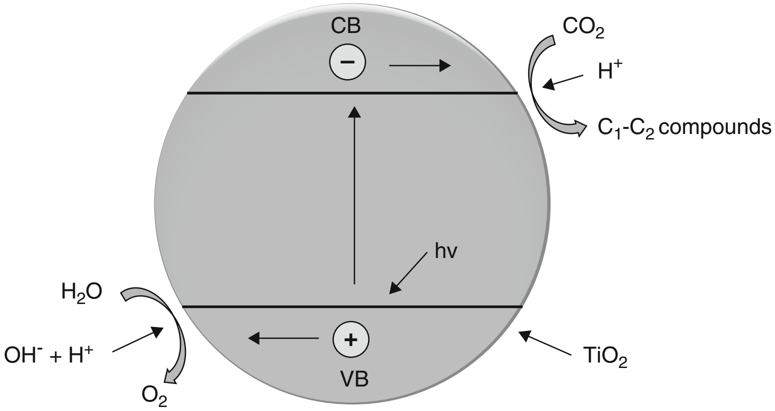

Fig. 6.27 CB derived CO_2 reduction and VB derived water oxidation under photocatalytic CO_2 reduction process (Ola and Maroto-Valer 2015)

Table 6.1 Electrochemical CO_2 reduction and water oxidation potentials versus the NHE at pH 7 (Habisreutinger et al. 2013)

Reaction	E^0 (V vs NHE)
$CO_2 + 2e^- \rightarrow {}^{\bullet}CO_2^-$ (1)	−1.90
$CO_2 + 2H^+ + 2e^- \rightarrow HCOOH$ (2)	−0.61
$CO_2 + 2H^+ + 2e^- \rightarrow CO + H_2O$ (3)	−0.53
$CO_2 + 4H^+ + 4e^- \rightarrow HCHO + H_2O$ (4)	−0.48
$CO_2 + 6H^+ + 6e^- \rightarrow CH_3OH + H_2O$ (5)	−0.38
$CO_2 + 8H^+ + 8e^- \rightarrow CH_4 + 2H_2O$ (6)	−0.24
$2H_2O + 4\ h^+ \rightarrow O_2 + 4H^+$ (7)	+0.81
$2H^+ + 2e^- \rightarrow H_2$(8)	−0.41

6.8 Decorating MOFs with Nanomaterials

In many cases, MOFs are not suitable to perform themselves as photocatalysts due to low efficiency in exciton generation and charge separation. Such restriction bottlenecks the photochemical catalytic applications. Therefore, combining guest like nanomaterials in MOFs might be one effective solution for an improved photocatalytic efficiency.

The decoration of nanoparticles that is on/into MOF was observed in several ways. Wang et al. (2011) reported that incorporation of Ir, Re, or Ru complexes H_2L_1–H_2L_6 with dicarboxylic acid functionalities into a highly stable porous-structured UiO-67(Zr), developing the highly efficient heterogeneous catalysts for solar energy utilization. Among them, Cp*Ir^{III}(dcppy)Cl] (H_2L_1) shows excellent performance to oxidize water (cerium ammonium nitrate as an oxidant) with the turnover frequencies of up to 4.8 h^{-1}. Even L_1-UiO-67(Zr) shows superior activity to CO_2 photoreduction using trimethylamine as a sacrificial agent with a total turnover number of 10.9 over $H_2[Re^I(CO)_3(dcbpy)Cl](H_2L_4)$ and $H_2[Ru^{II}(bpy)_2(dcbpy)]$

$Cl_2)(H_2L_6)$. Also, L_1-UiO-67(Zr) may work on various photocatalytic organic transformations (e.g., Aza-Henry reaction, aerobic amine coupling, etc.). Another catalyst, MoS_2/UiO-66/CdS, fabricated with MoS_2 and duel modification of UiO-66/CdS shows excellent hydrogen evolution under visible light (Shen et al. 2015). MoS_2/UiO-66/CdS produces 650 μmol g^{-1} h^{-1} containing 50 wt% UiO-66 and 1.5 wt% MoS_2. The amount of hydrogen production is 60 times higher than pure CdS and even better than Pt/UiO-66/CdS. This exceptional performance is due to the formation of heterojunction between UiO-66 and CdS which enhanced the separation of photogenerated electron-hole pairs. The composite material AgI/UiO-66, conjugation of AgI and UiO-66, was formed by a simple solution method (Sha et al. 2015). It shows exhibited remarkable activity for the degradation of rhodamine B (RhB) under visible light irradiation. When the Ag/Zr ratio was increased from 0.1:1 to 1:1, the photocatalytic activity of the composite increased 29.5%, i.e., from 0.0545 to 0.0706 min^{-1}. This increased activity is due to increased amount of Ag and the specific surface area (Fig. 6.28).

Pt and dye loaded UiO-66-NH_2, Pt@UiO-66-NH_2 shows excellent photocatalytic hydrogen production under visible light (Chen et al. 2017b). Calix-3-sensitized Pt@UiO-66-NH_2 catalysts, loading amount of Pt is 0.65 wt% and Calix-3 dye is 15.7 μmol/g, exhibit much higher hydrogen production activity (1528 μmol $g^{-1}h^{-1}$based on the mass of MOF or 236 mmol $g^{-1}{}_{[Pt]}h^{-1}$ based on Pt mass) than that sensitized by single dyes (516 μmol g^{-1} h^{-1} or 24 mmol $g^{-1}{}_{[Pt]}h^{-1}$) under the similar conditions. The enhanced performance and stability might be due to lower tendency for aggregation, higher molar absorption coefficients, more efficient electron transfer, and better stability.

Now the decoration of nanoparticles was applied on another well-known MOF, MIL series. Among them, a ternary component was fabricated using MIL-125(Ti) with reduced graphene oxide (rGO) and dispersed silver nanoparticles (Ag NPs) in an efficient one-pot self-assembly and photoreduction strategy (Yuan et al. 2016). The ternary component performs over binary and the second one over single component under visible light. The order of photocatalytic degradation performance for rhodamine B (RhB) is Ag/rGO/MIL-125(Ti) (0.0644 min^{-1}) > rGO/MIL-125 (Ti) (0.0595 min^{-1}) > Ag/MIL-125(Ti) (0.0520 min^{-1}) > pure MIL-125(Ti) (0.0396 min^{-1}), which is 1.62 times higher than that of the pure MIL-125(Ti). The improved photocatalytic performance is due to localized surface plasmon resonance of Ag NP (electron reservoir), inter conversion of Ti^{3+}–Ti^{4+} in MOF. Moreover, the synergistic effects among MIL-125(Ti), Ag NPs, and rGO (electron transporter and collector) contributed significantly to improve the performance. Another composite material Ni@MIL-125NH_2(Ti) synthesized by simple solution method by using NH_2- MIL-125(Ti) with $[Ni(dmobpy)(2\text{-}mpy)_2]$ generates appreciable quantities of hydrogen under UV light with a TOF of 28 mol H_2 $g(Ni)^{-1}$ h^{-1} and keeps active over 50 h (Meyer et al. 2016). The composite material COM50 made by potassium poly(heptazine imide) (PHIK) and MIL-125-NH_2 (Ti) shows photocatalytic degradation of rhodamine B under blue light irradiation (Rodríguez et al. 2017). The electron paramagnetic resonance (EPR) investigations and electronic structures of

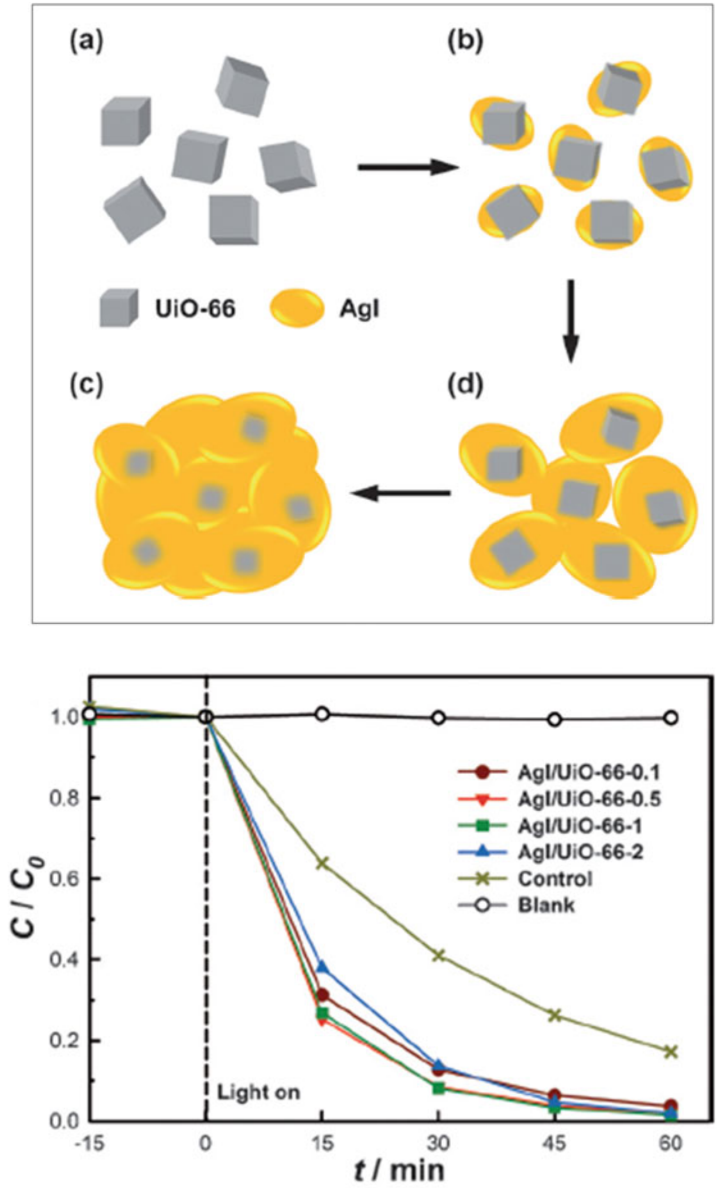

Fig. 6.28 (Top) schematic presentation of synthesis of an AgI-conjugated UiO-66 composite with increasing AgI content from (**a**) to (**d**) and (the graph) photocatalytic degradation of RhB in the presence and absence (blank) of different catalysts (AgI/UiO-66-0.1, AgI/UiO-66-0.5, AgI/UiO-66-1, and AgI/UiO-66-2). (Bottom) Absorption spectra under visible light irradiation (Sha et al. 2015)

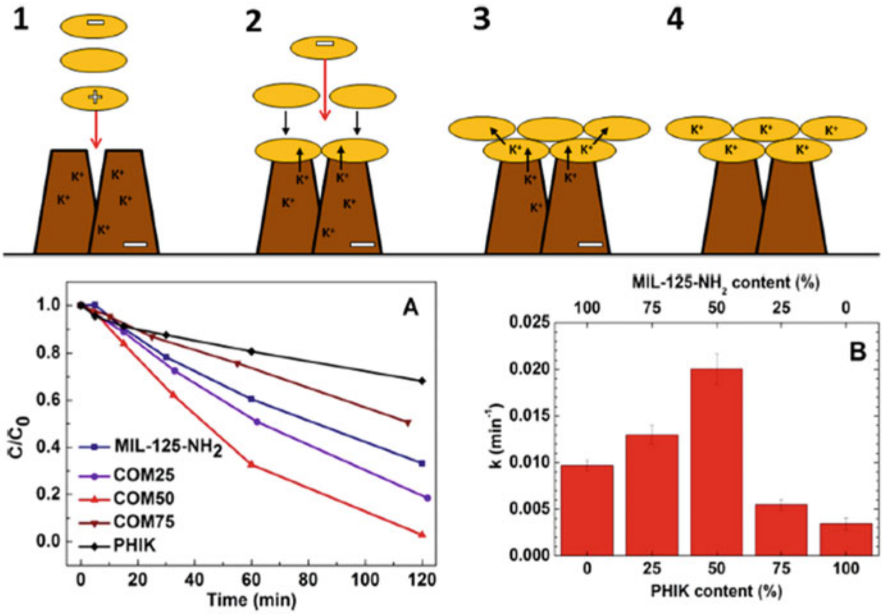

Fig. 6.29 (Top) Step 1, approach of MIL-125-NH_2 (yellow disks) to PHIK (brown tetrahedron) by electrostatic forces (red arrow); Step 2, diffusion (black arrow) of K^+ ions to MIL-125-NH_2; Step 3, diffusion of additional K^+ ions to MIL-125-NH_2; Step 4, final composite with K^+ ions inside the micropores of MIL-125-NH_2. (Bottom) (**a**) degradation of RhB by different materials and (**b**) calculated rate constants of RhB degradation using PHIK/MIL-125-NH_2 photocatalyst as a function of its composition (Rodríguez et al. 2017)

the solids suggest the electron transfer from MIL-125-NH_2 to PHIK in the composite, which is responsible for enhance photocatalytic activity (Fig. 6.29).

The degradation of dye was performed by using charge separation concept. A composite material combines with MIL-53(Fe) with cationic (Amberlite IRA 200) or anionic (Amberlite IRA 900) resin results DMIL-53(Fe) and AMIL-53 (Fe), respectively (Araya et al. 2017). These composites can degrade 96%, whereas only MIL-53 (Fe) can do 24%. Interestingly, DMIL-53(Fe) and AMIL-53 (Fe) degrade negative and positive, respectively.

In this case of nanoparticle decoration on MOF, carbon nanotube (CNT) plays an important role. The composite of multiwalled carbon nanotube (MWCNT) and NH_2-MIL-68(In) shows dominant photocatalytic reduction of heavy toxic metal (Pi et al. 2017). In this composite, MWCNTs act as efficient carriers of photogenerated electrons and provide more mesopores for Cr (VI) diffusion to enhance the visible light adsorption without lowering the conduction band position. To prepare the nanocomposite materials, graphene is an excellent candidate. Vu et al. (2017) prepared a composite by solvothermal reaction between reduced graphene oxide (RGO) and Fe-MIL-88B, which shows excellent photocatalytic degradation capability of reactive dye (reactive red-RR195) after 25 min under simulated sunlight. Han et al. (2018) prepared composite material by simple grinding of AgI and MIL-53(Fe) to produce g-AgI/MIL-53(Fe) and show excellent performance of photodegradation of rhodamine B (RhB) completely within 45 min under visible light. Also, it degrades 39% and 65% of acid blue (AB) and methyl orange (MO) within 45 min at the same condition, respectively. AgI effectively hinders the recombination of photogenerated electron-hole pairs, which enhance the activity. Wang et al. (2018b) prepared a bimetallic MOF containing Fe and Ti (Fe/Ti-MOF-NH2(3,1)) which can degrade 100% orange II within 10 min in presence of persulfate (PS)-assisted visible light. The enhanced photocatalytic activity appeared mainly due to the efficient electrons transfer by Fe^{3+}/Fe^{2+} and Ti^{4+}/Ti^{3+} redox couples, and activation of PS by photogenerated electrons to produce sulfate radicals ($SO4^{*-}$), which also enhance the degradation. MOF can also be used as upconversion photocatalyst by combining with suitable nanomaterials. Li et al. (2017) synthesized such materials by combining MIL-53(Fe) and $NaYF_4$:Yb,Tm in solution method, which exhibits tunable photocatalytic degradation of RhB under NIR irradiation. The activity depends on the thickness of layer of MOF on $NaYF_4$:Yb,Tm and shows maximum when it becomes 30 nm. This is due to after achieving optimal thickness, the light scattering decreases with increasing thickness. Also after introducing –NH_2 group to MIL-53 (Fe), activity increases due to serve as an antenna to absorb additional light and transfer energy to the Fe(III)−O clusters (Chi et al. 2016).

Nanomaterials decorated MOF may also serve as a platform to simultaneously production of H_2 fuel and a valuable organic chemical. Liu et al. proposed excellent composite materials formed by PCN-777 and Pt nanoparticles, i.e., Pt/PCN-177, which shows the photocatalytic performance without using sacrificial agent (Liu et al. 2018). Mott-Schottky plots indicate that PCN-177 is an n-type semiconductor. Pt loading amount in the MOF is 2.3 wt%. In presence of TEOA as a sacrificial agent, Pt/PCN-777 exhibits excellent H_2 production rate of 586 $mmolg^{-1}\ h^{-1}$, whereas with the same amount of benzylamine as TEOA, H_2 evolution rate decreases to 332 $mmolg^{-1}\ h^{-1}$, due to weaker electron-donating ability of benzylamine than TEOA. Interestingly, the benzylamine can be converted to N-benzylbenzaldimine at a rate of 486 $mmolg^{-1}\ h^{-1}$ with >99% selectivity. The enhanced rate of efficiency of benzylamine oxidative coupling reaction with electron scavenger indicates holes on the HOMO of PCN-777 that plays a critical role. The improvement of charge separation might be due to elongated conjugated ligand in PCN-777 which extends the light absorption (Fig. 6.30).

MOFs can also be decorated with oxide-based QD@MOF (Feng et al. 2010; Ameloot et al. 2011; Gascon et al. 2008; Wee et al. 2014; Li et al. 2014), S/Se/Te-based QD@MOF (Lu et al. 2012; Imaz et al. 2009; Wakaoka et al. 2014; Bag et al. 2017), nitride-based QD@MOF (Esken et al. 2011), and carbon-based QD@MOF (Li et al. 2015; Biswal et al. 2013) quantum dots (QD)

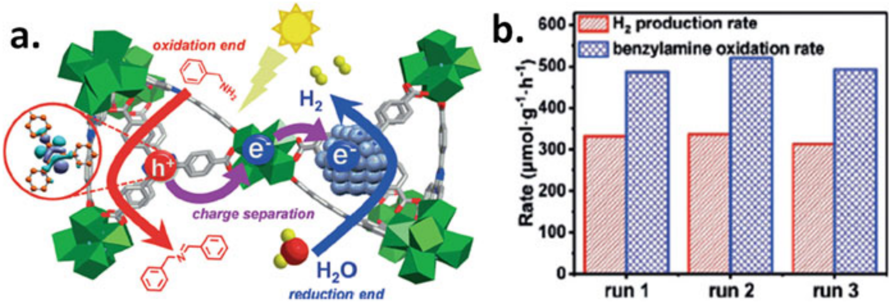

Fig. 6.30 (**a**) Illustration of simultaneous proton reduction and selective benzylamine oxidation over Pt/PCN-777 by photocatalysis; (**b**) recycling performance of Pt/PCN-777 toward coupling photocatalytic H_2 production with selective benzylamine oxidation (Liu et al. 2018)

6.9 Conclusions

Crystal engineering makes supramolecular synthon a handy tool for designing a functional supramolecular material with a certain predictability and robustness. In this chapter we have analyzed the present role of crystal engineering in designing different MOF-derived photocatalysts systematically. Designing a MOF may be an established procedure at present, where topology, geometry, void spaces, or functionality can be tuned, but an exact designing for certain photocatalytic goal needs the complete functional behavior knowledge of each constructing units. In this regard, the detailed mechanisms are described here to envisage the role of individual ingredients before employing them in designing a MOF for a specific purpose. With a clear insight on photocatalytic mechanism, various roles of ligands and SBUs are described elaborately, so that one can easily tune catalytic centers, porosity (long and rigid ligand), bandgap, or supramolecular functionality while designing a MOF. We also have described the designing principle and homogeneous or asymmetric photocatalysts. A DFT-based computational designing on higher-order electronic interaction and conjugative catalytic effort could be coupled with the power of crystal engineering to design any specific catalysts. An interdisciplinary approach can make reaching goal comfortable.

References

Abrahams BF, Hudson TA, McCormick LJ, Robson R (2011) Coordination polymers of 2,5-dihydroxybenzoquinone and chloranilic acid with the (10,3)-*a* topology. Cryst Growth Des 11:2717–2720. https://doi.org/10.1021/cg2005908@proofing

Abrahamsson M, Johansson PG, Ardo S, Kopecky A, Galoppini E, Meyer GJ (2010) Decreased interfacial charge recombination rate constants with N3-type sensitizers. J Phys Chem Lett 1:1725–1728. https://doi.org/10.1021/jz100546y

Adarsh NN, Dastidar P (2012) Coordination polymers: what has been achieved in going from innocent 4,4′-bipyridine to bis-pyridyl ligands having a non-innocent backbone? Chem Soc Rev 41:3039–3060. https://doi.org/10.1039/C2CS15251G

Adarsh NN, Sahoo P, Dastidar P (2010) Is a crystal engineering approach useful in designing metallogels? A case study. Cryst Growth Des 10:4976–4986. https://doi.org/10.1021/cg101078f

Akimov AV, Asahi R, Jinnouchi R, Prezhdo OV (2015) What makes the photocatalytic CO_2 reduction on N-doped Ta2O5 efficient: insights from nonadiabatic molecular dynamics. J Am Chem Soc 137:11517–11525. https://doi.org/10.1021/jacs.5b07454

Allendorf MD, Stavila V (2015) Crystal engineering, structure–function relationships, and the future of metal–organic frameworks. CrystEngComm 17:229–246. https://doi.org/10.1039/C4CE01693A

Allendorf MD, Schwartzberg A, Stavila V, Talin AA (2011) A roadmap to implementing metal-organic frameworks in electronic devices: challenges and critical directions. Chem Eur J 17:11372–11388. https://doi.org/10.1002/chem.201101595

Alqadami AA, Naushad M, Alothman ZA, Ahamad T (2018) Adsorptive performance of MOF nanocomposite for methylene blue and malachite green dyes: kinetics, isotherm and mechanism. J Environ Manag 223:29–36. https://doi.org/10.1016/j.jenvman.2018.05.090

Alvaro M, Carbonell E, Ferrer B, Llabrés i Xamena FX, Garcia H (2007) Semiconductor behavior of a Metal-Organic Framework (MOF). Chem Eur J 13:5106–5112. https://doi.org/10.1002/chem.200601003

Ameloot R, Roeffaers MBJ, De Cremer G, Vermoortele F, Hofkens J, Sels BF, De Vos DE (2011) Metal–organic framework single crystals as photoactive matrices for the generation of metallic microstructures. Adv Mater 23:1788–1791. https://doi.org/10.1002/adma.201100063

Andrew Lin K-Y, Chang H-A, Hsu C-J (2015) Iron-based metal organic framework, MIL-88A, as a heterogeneous persulfate catalyst for decolorization of Rhodamine B in water. RSC Adv 5:32520–32530. https://doi.org/10.1039/C5RA01447F

Araya T, Jia MK, Yang J, Zhao P, Cai K, Ma WH, Huang YP (2017) Resin modified MIL-53 (Fe) MOF for improvement of photocatalytic performance. Appl Catal B Environ 203:768–777. https://doi.org/10.1016/j.apcatb.2016.10.072

Bag PP, Wang X-S, Cao R (2015) Microwave-assisted large scale synthesis of lanthanide metal–organic frameworks (Ln-MOFs), having a preferred conformation and photoluminescence properties. Dalton Trans 44:11954–11962. https://doi.org/10.1039/C5DT01598G

Bag PP, Wang D, Chen Z, Cao R (2016) Outstanding drug loading capacity by water stable microporous MOF: a potential drug carrier. Chem Commun 52:3669–3672. https://doi.org/10.1039/C5CC09925K

Bag PP, Wang X-S, Sahoo P, Xiong J, Cao R (2017) Efficient photocatalytic hydrogen evolution under visible light by ternary composite CdS@NU-1000/RGO. Catal Sci Technol 7:5113–5119. https://doi.org/10.1039/C7CY01254C

Bagheri M, Masoomi MY, Morsali A (2017) A MoO_3–metal–organic framework composite as a simultaneous photocatalyst and catalyst in the PODS process of light oil. ACS Catal **7**:6949–6956. https://doi.org/10.1021/acscatal.7b02581

Bai S, Jiang J, Zhang Q, Xiong Y (2015) Steering charge kinetics in photocatalysis: intersection of materials syntheses, characterization techniques and theoretical simulations. Chem Soc Rev 44:2893–2939. https://doi.org/10.1039/C5CS00064E

Bak T, Nowotny J, Rekas M, Sorrell CC (2002) Photo-electrochemical hydrogen generation from water using solar energy. Materials-related aspects. Int J Hydrog Energy 27:991–1022. https://doi.org/10.1016/S0360-3199(02)00022-8

Banerjee R, Sahoo SC, Kundu T (2016) Water soluble Metal-Organic Frameworks (MOFs). U.S. Patent US 9290518 B2, filed October 3, 2012, and issued March 22, 2016

Bellitto C, Dessy G, Fares V (1985) Synthesis, x-ray crystal structure, and chemical and physical properties of the new linear-chain mixed-valence complex (.mu.- iodo)tetrakis(dithioacetato) dinickel, $Ni_2(CH_3CS_2)_4I$, and x-ray crystal structure of the precursor tetrakis(dithioacetato) dinickel(II), $Ni_2(CH_3CS_2)_4$. Inorg Chem 24:2815–2820. https://doi.org/10.1021/ic00212a023

Bhattacharjee S, Khan MI, Li X, Zhu Q-L, Wu X-T (2018) Recent progress in asymmetric catalysis and chromatographic separation by chiral metal–organic frameworks. Catalysts 8:120. https://doi.org/10.3390/catal8030120

Biradha K, Ramanan A, Vittal JJ (2009) Coordination polymers versus metal−organic frameworks. Cryst Growth Des 9:2969–2970. https://doi.org/10.1021/cg801381p

Biswal BP, Shinde DB, Pillai VK, Banerjee R (2013) Stabilization of graphene quantum dots (GQDs) by encapsulation inside zeolitic imidazolate framework nanocrystals for photoluminescence tuning. Nanoscale 5:10556–10561. https://doi.org/10.1039/C3NR03511E

Bolton JR, Mataga N, McLendon G (eds) (1991) Electron transfer in inorganic, organic and biological systems, Advances in chemistry series. American Chemical Society, Washington, DC

Butler KT, Hendon CH, Walsh A (2014a) Electronic structure modulation of metal–organic frameworks for hybrid devices. ACS Appl Mater Interfaces 6:22044–22050. https://doi.org/10.1021/am507016r

Butler KT, Hendon CH, Walsh A (2014b) Electronic chemical potentials of porous metal–organic frameworks. J Am Chem Soc 136:2703–2706. https://doi.org/10.1021/ja4110073

Cavka JH, Jakobsen S, Olsbye U, Guillou N, Lamberti C, Bordiga S, Lillerud KP (2008) A new zirconium inorganic building brick forming metal organic frameworks with exceptional stability. J Am Chem Soc 130:13850–13851. https://doi.org/10.1021/ja8057953

Chambers MB, Wang X, Elgrishi N, Hendon CH, Walsh A, Bonnefoy J, Canivet J, Quadrelli EA, Farrusseng D, Mellot-Draznieks C, Fontecave M (2015) Photocatalytic carbon dioxide reduction with rhodium-based catalysts in solution and heterogenized within metal–organic frameworks. ChemSusChem 8:603–608. https://doi.org/10.1002/cssc.201403345

Chambers MB, Wang X, Ellezam L, Ersen O, Fontecave M, Sanchez C, Rozes L, Mellot-Draznieks C (2017) Maximizing the photocatalytic activity of metal–organic frameworks with aminated-functionalized linkers: substoichiometric effects in MIL-125-NH_2. J Am Chem Soc 139: 8222–8228 and the reference there in. https://doi.org/10.1021/jacs.7b02186

Chen X, Burda C (2008) The electronic origin of the visible-light absorption properties of C-, N- and S-doped TiO_2 nanomaterials. J Am Chem Soc 130:5018–5019. https://doi.org/10.1021/ja711023z

Chen X, Shen S, Guo L, Mao SS (2010) Semiconductor-based photocatalytic hydrogen generation. Chem Rev 110:6503–6570. https://doi.org/10.1021/cr1001645

Chen Y, Wang D, Deng X, Li Z (2017a) Metal–organic frameworks (MOFs) for photocatalytic CO_2 reduction. Cat Sci Technol **7**:4893–4490. https://doi.org/10.1039/C7CY01653K

Chen Y-F, Tan L-L, Liu J-M, Qin S, Xie Z-Q, Huang J-F, Xu Y-W, Xiao L-M, Su C-Y (2017b) Calix[4]arene based dye-sensitized Pt@UiO-66-NH_2 metal-organic framework for efficient visible-light photocatalytic hydrogen production. Appl Catal B 206:426–433. https://doi.org/10.1016/j.apcatb.2017.01.040

Chi L, Xu Q, Liang XY, Wang JD, Su XT (2016) Iron-based metal–organic frameworks as catalysts for visible light-driven water oxidation. Small 12:1351–1135. https://doi.org/10.1002/smll.201503526

Choi KM, Kim D, Rungtaweevoranit B, Trickett CA, Barmanbek JTD, Alshammari AS, Yang P, Yaghi OM (2017) Plasmon-enhanced photocatalytic CO_2 conversion within metal–organic frameworks under visible light. J Am Chem Soc 139:356–362. https://doi.org/10.1021/jacs.6b11027

Corey EJ (1967) General methods for the construction of complex molecules. Pure Appl Chem 14:19–38. https://doi.org/10.1351/pac196714010019

Coropceanu V, Cornil J, da Silva FDA, Olivier Y, Silbey R, Brédas J-L (2007) Charge transport in organic semiconductors. Chem Rev 107:926–952. https://doi.org/10.1021/cr050140x

Dan-Hardi M, Serre C, Frot T, Rozes L, Maurin G, Sanchez C, Férey G (2009) A new photoactive crystalline highly porous titanium (IV) dicarboxylate. J Am Chem Soc 131:10857–10859. https://doi.org/10.1021/ja903726m

Darago LE, Aubrey ML, Yu CJ, Gonzalez MI, Long JR (2015) Electronic conductivity, ferrimagnetic ordering, and reductive insertion mediated by organic mixed-valence in a ferric semiquinoid metal–organic framework. J Am Chem Soc 137:15703–15711. https://doi.org/10.1021/jacs.5b10385

de Koning MC, van Grol M, Breijaert T (2017) Degradation of paraoxon and the chemical warfare agents VX, tabun, and soman by the metal–organic frameworks UiO-66-NH2, MOF-808, NU-1000, and PCN-777. Inorg Chem 56:11804–11809. https://doi.org/10.1021/acs.inorgchem.7b01809

deKrafft KE, Wang C, Lin W (2012) Metal-organic framework templated synthesis of Fe_2O_3/TiO_2 nanocomposite for hydrogen production. Adv Mater 24:2014–2018. https://doi.org/10.1002/adma.201200330

Desiraju GR (ed) (1989) Crystal engineering: the design of organic solids. Elsevier Scientific Publishers, Amsterdam/New York

Desiraju GR (1995) Supramolecular synthons in crystal engineering—a new organic synthesis. Angew Chem Int Ed 34:2311–2327. https://doi.org/10.1002/anie.199523111

Desiraju GR (2007) Crystal engineering: a holistic view. Angew Chem Int Ed 46:8342–8356. https://doi.org/10.1002/anie.200700534

Diercks CS, Liu Y, Cordova KE, Yaghi OM (2018) The role of reticular chemistry in the design of CO2 reduction catalysts. Nat Mater 17:301–307. https://doi.org/10.1038/s41563-018-0033-5

Ding W, Negre CFA, Palma JL, Durrell AC, Allen LJ, Young KJ, Milot RL, Schmuttenmaer CA, Brudvig GW, Crabtree RH, Batista VS (2014) Linker rectifiers for covalent attachment of transition-metal catalysts to metal-oxide surfaces. ChemPhysChem 15:1138–1147. https://doi.org/10.1002/cphc.201400063

Esken D, Turner S, Wiktor C, Kalidindi SB, Van Tendeloo G, Fischer RA (2011) GaN@ZIF-8: selective formation of gallium nitride quantum dots inside a zinc methylimidazolate framework. J Am Chem Soc 133:16370–16373. https://doi.org/10.1021/ja207077u

Evans A, Luebke R, Petit C (2018) The use of metal–organic frameworks for CO purification. J Mater Chem A 6:10570–10594. https://doi.org/10.1039/C8TA02059K

Fang Y, Ma Y, Zheng M, Yang P, Asiri AM, Wang X (2017) Metal–organic frameworks for solar energy conversion by photoredox catalysis. Coord Chem Rev 373:83–115. https://doi.org/10.1016/j.ccr.2017.09.013

Fei H, Sampson MD, Lee Y, Kubiak CP, Cohen SM (2015) Photocatalytic CO_2 reduction to formate using a Mn(I) molecular catalyst in a robust metal–organic framework. Inorg Chem 54:6821–6828. https://doi.org/10.1021/acs.inorgchem.5b00752

Feng PL, Perry JJ IV, Nikodemski S, Jacobs BW, Meek ST, Allendorf MD (2010) Assessing the purity of metal−organic frameworks using photoluminescence: MOF-5, ZnO quantum dots, and framework decomposition. J Am Chem Soc 132:15487–15489. https://doi.org/10.1021/ja1065625

Férey G, Mellot-Draznieks C, Serre C, Millange F, Dutour J, Surble S, Margiolaki I (2005) A chromium terephthalate-based solid with unusually large pore volumes and surface area. Science 309:2040–2042. https://doi.org/10.1126/science.1116275

Foster ME, Azoulay JD, Wong BM, Allendorf MD (2014) Novel metal–organic framework linkers for light harvesting applications. Chem Sci 5:2081–2090. https://doi.org/10.1039/C4SC00333K

Fu Y, Sun D, Chen Y, Huang R, Ding Z, Fu X, Li Z (2012) An amine-functionalized titanium metal-organic framework photocatalyst with visible-light-induced activity for CO_2 reduction. Angew Chem Int Ed 51:3364–3367. https://doi.org/10.1002/anie.201108357

Fujishima A, Honda K (1972) Electrochemical photolysis of water at a semiconductor electrode. Nature 238:37–38

Furukawa H, Ko N, Go YB, Aratani N, Choi SB, Choi E, Yazaydin AÖ, Snurr RQ, O'Keeffe M, Kim J, Yaghi OM (2010) Ultrahigh porosity in metal-organic frameworks. Science 329:424–428. https://doi.org/10.1126/science.1192160

Gao C, Wang J, Xu H, Xiong Y (2017) Coordination chemistry in the design of heterogeneous photocatalysts. Chem Soc Rev 46:2799–2823. https://doi.org/10.1039/C6CS00727A

Gascon J, Hernández-Alonso MD, Almeida AR, van Klink GPM, Kapteijn F, Mul G (2008) Isoreticular MOFs as efficient photocatalysts with tunable band gap: an operando FTIR study of the photoinduced oxidation of propylene. ChemSusChem 1:981–983. https://doi.org/10.1002/cssc.200800203

Givaja G, Amo-Ochoa P, Gómez-Garcíab CJ, Zamora F (2012) Electrical conductive coordination polymers. Chem Soc Rev 41:115–147. https://doi.org/10.1039/C1CS15092H

Habisreutinger SN, Schmidt-Mende L, Stolarczyk JK (2013) Photocatalytic reduction of CO_2 on TiO_2 and other semiconductors. Angew Chem Int Ed 52:7372–7408. https://doi.org/10.1002/anie.201207199

Han Y, Bai C, Zhang L, Wu J, Meng H, Xu J, Xu Y, Liang Z, Zhang X (2018) A facile strategy for fabricating AgI–MIL-53(Fe) composites: superior interfacial contact and enhanced visible light photocatalytic performance. New J Chem 42:3799–3807. https://doi.org/10.1039/C8NJ00417J

Harrison WA (1983) Theory of the two-center bond. Phys Rev B 27:3592. https://doi.org/10.1103/PhysRevB.27.3592

Hausdorf S, Wagler J, Mossig R, Mertens FORL (2008) Proton and water activity-controlled structure formation in zinc carboxylate-based metal organic frameworks. J Phys Chem A 112:7567–7576. https://doi.org/10.1021/jp7110633

Hendon CH, Tiana D, Walsh A (2012) Conductive metal–organic frameworks and networks: fact or fantasy? Phys Chem Chem Phys 14:13120–13132. https://doi.org/10.1039/C2CP41099K

Hendon CH, Tiana D, Fontecave M, Sanchez C, D'arras L, Sassoye C, Rozes L, Mellot-Draznieks C, Walsh A (2013) Engineering the optical response of the titanium-MIL-125 metal–organic framework through ligand functionalization. J Am Chem Soc 135:10942–10945. https://doi.org/10.1021/ja405350u

Hoffmann R (1963) An extended Hückel theory. I Hydrocarbons. J Chem Phys 39:1397. https://doi.org/10.1063/1.1734456

Holladay JD, Hu J, King DL, Wang Y (2009) An overview of hydrogen production technologies. Catal Today 139:244–260. https://doi.org/10.1016/j.cattod.2008.08.039

Horike S, Umeyama D, Kitagawa S (2013) Ion conductivity and transport by porous coordination polymers and metal–organic frameworks. Acc Chem Res 46:2376–2384. https://doi.org/10.1021/ar300291s

Horiuchi Y, Toyao T, Saito M, Mochizuki K, Iwata M, Higashimura H, Anpo M, Matsuoka M (2012) Visible-light-promoted photocatalytic hydrogen production by using an amino-functionalized Ti(IV) metal–organic framework. J Phys Chem C 116:20848–20853. https://doi.org/10.1021/jp3046005

Hu K, Blair AD, Piechota EJ, Schauer PA, Sampaio RN, Parlane FGL, Meyer GJ, Berlinguette CP (2016) Kinetic pathway for interfacial electron transfer from a semiconductor to a molecule. Nat Chem 8:853–859. https://doi.org/10.1038/NCHEM.2549

Hua C, Doheny P, Ding B, Chan B, Yu M, Kepert CJ, D'Alessandro DM (2018) Through-space intervalence charge transfer as a mechanism for charge delocalization in metal–organic frameworks. J Am Chem Soc 140:6622–6630. https://doi.org/10.1021/jacs.8b02638

Hückel E (1931) Perspective on "Quantentheoretische Beiträge zum Benzolproblem. I. Die Elektronenkonfiguration des Benzols und verwandter Beziehungen". Z Phys 70:204–286

Hurd JA, Vaidhyanathan R, Thangadurai V, Ratcliffe CI, Moudrakovski IL, Shimizu GKH (2009) Anhydrous proton conduction at 150°C in a crystalline metal-organic framework. Nat Chem 1:705–710. https://doi.org/10.1038/NCHEM.402

Imaz I, Hernando J, Ruiz-Molina D, Maspoch D (2009) Metal-organic spheres as functional systems for guest encapsulation. Angew Chem Int Ed 48:2325–2329. https://doi.org/10.1002/anie.200804255

Jiao L, Wang Y, Jiang HL, Xu Q (2017) Metal–organic frameworks as platforms for catalytic applications. Adv Mater 30:e1703663. https://doi.org/10.1002/adma.201703663

Johansson PG, Kopecky A, Galoppini E, Meyer GJ (2013) Distance dependent electron transfer at TiO_2 interfaces sensitized with phenylene ethynylene bridged Ru^{II}–isothiocyanate compounds. J Am Chem Soc 135:8331–8341. https://doi.org/10.1021/ja402193f

Kaake L, Barbara PF, Zhu X-Y (2010) Intrinsic charge trapping in organic and polymeric semiconductors: a physical chemistry perspective. J Phys Chem Lett 1:628–635. https://doi.org/10.1021/jz9002857

Kajiwara T, Fujii M, Tsujimoto M, Kobayashi K, Higuchi M, Tanaka K, Kitagawa S (2016) Photochemical reduction of low concentrations of CO_2 in a porous coordination polymer with a ruthenium(II)-CO complex. Angew Chem Int Ed 55:2697–2700. https://doi.org/10.1002/anie.201508941

Kang Z, Fana L, Sun D (2017) Recent advances and challenges of metal–organic framework membranes for gas separation. J Mater Chem A 5:10073–10091. https://doi.org/10.1039/C7TA01142C

Karnahl M, Kuhnt C, Ma F, Yartsev A, Schmitt M, Dietzek B, Rau S, Popp J (2011) Tuning of photocatalytic hydrogen production and photoinduced intramolecular electron transfer rates by regioselective bridging ligand substitution. ChemPhysChem 12:2101–2109. https://doi.org/10.1002/cphc.201100245

Kobayashi Y, Jacobs B, Allendorf MD, Long JR (2010) Conductivity, doping, and redox chemistry of a microporous dithiolene-based metal−organic framework. Chem Mater 22:4120–4122. https://doi.org/10.1021/cm101238m

Kreno LE, Leong K, Farha OK, Allendorf M, Van Duyne RP, Hupp JT (2012) Metal–organic framework materials as chemical sensors. Chem Rev 112:1105–1125. https://doi.org/10.1021/cr200324t

Kubacka A, Fernández-García M, Colón G (2012) Advanced nanoarchitectures for solar photocatalytic applications. Chem Rev 112:1555–1614. https://doi.org/10.1021/cr100454n

Kumar A, Guo C, Sharma G et al (2016) Magnetically recoverable ZrO2/Fe3O4/chitosan nanomaterials for enhanced sunlight driven photoreduction of carcinogenic Cr(VI) and dechlorination & mineralization of 4-chlorophenol from simulated waste water. RSC Adv 6:13251–13263. https://doi.org/10.1039/C5RA23372K

Kumar A, Rana A, Sharma G et al (2018) Aerogels and metal–organic frameworks for environmental remediation and energy production. Environ Chem Lett 16:797–820. https://doi.org/10.1007/s10311-018-0723-x

Larsen RW, Wojtas L (2013) Photoinduced inter-cavity electron transfer between Ru(II)tris(2,2′-bipyridne) and Co(II)tris(2,2′-bipyridine) Co-encapsulated within a Zn(II)-trimesic acid metal organic framework. J Mater Chem A 1:14133–14139. https://doi.org/10.1039/C3TA13422A

Larsen RW, Wojtas L (2015) Fixed distance photoinduced electron transfer between Fe and Zn porphyrins encapsulated within the Zn HKUST-1 metal organic framework. Dalton Trans 44:2959–2963. https://doi.org/10.1039/c4dt02685c

Lau VW-H, Moudrakovski I, Botari T, Weinberger S, Mesch MB, Duppel V, Senker J, Blum V, Lotsch BV (2016) Rational design of carbon nitride photocatalysts by identification of cyanamide defects as catalytically relevant sites. Nat Commun 7:12165. https://doi.org/10.1038/ncomms12165

Lee Y, Kim S, Fei H, Kang JK, Cohen SM (2015) Photocatalytic CO_2 reduction using visible light by metal-monocatecholato species in a metal–organic framework. Chem Commun 51:16549–16552. https://doi.org/10.1039/C5CC04506A

Li H, Eddaoudi M, O’Keeffe M, Yaghi OM (1999) Design and synthesis of an exceptionally stable and highly porous metal-organic framework. Nature 402:276–279. https://doi.org/10.1038/46248

Li R, Hu J, Deng M, Wang H, Wang X, Hu Y, Jiang H-L, Jiang J, Zhang Q, Xie Y, Xiong Y (2014) Integration of an inorganic semiconductor with a metal–organic framework: a platform for enhanced gaseous photocatalytic reactions. Adv Mater 26:4783–4788. https://doi.org/10.1002/adma.201400428

Li J-S, Tang Y-J, Li S-L, Zhang S-R, Dai Z-H, Si L, Lan Y-Q (2015) Carbon nanodots functional MOFs composites by a stepwise synthetic approach: enhanced H_2 storage and fluorescent sensing. CrystEngComm 17:1080–1085. https://doi.org/10.1039/C4CE02020K

Li Y, Xu H, Ouyangab S, Ye J (2016) Metal-organic frameworks for photocatalysis. Phys Chem Chem Phys 18:7563–7572. https://doi.org/10.1039/C5CP05885F

Li M, Zheng Z, Zheng Y, Cui C, Li C, Li Z (2017) Controlled growth of metal–organic framework on upconversion nanocrystals for NIR-enhanced photocatalysis. ACS Appl Mater Interfaces 9:2899–2905. https://doi.org/10.1021/acsami.6b15792

Li Y, Fu Y, Ni B, Ding K, Chen W, Wu K, Huang X, Zhang Y (2018) Effects of ligand functionalization on the photocatalytic properties of titanium-based MOF: a density functional theory study. AIP Adv 8:035012. https://doi.org/10.1063/1.5021098

Liang R, Jing F, Shen L, Qin N, Wu L (2015) MIL-53(Fe) as a highly efficient bifunctional photocatalyst for the simultaneous reduction of Cr (VI) and oxidation of dyes. J Hazard Mater 287:364–372. https://doi.org/10.1016/j.jhazmat.2015.01.048

Lingampalli SR, Ayyub MM, Rao CNR (2017) Recent progress in the photocatalytic reduction of carbon dioxide. ACS Omega 2:2740–2748. https://doi.org/10.1021/acsomega.7b00721

Linsebigler AL, Lu G, Yates JT (1995) Photocatalysis on TiO2 surfaces: principles, mechanisms, and selected results. Chem Rev 95:735–758. https://doi.org/10.1021/cr00035a013

Liu H, Xu C, Li D, Jiang H-L (2018) Photocatalytic hydrogen production coupled with selective benzylamine oxidation over MOF composites. Angew Chem Int Ed 57:5379–5383. https://doi.org/10.1002/anie.201800320

Llabres i Xamena FX, Abad A, Corma A, Garcia H (2007) MOFs as catalysts: activity, reusability and shape-selectivity of a Pd-containing MOF. J Catal 250:294–298. https://doi.org/10.1016/j.jcat.2007.06.004

Llabrés i Xamena FX, Corma A, Garcia H (2007) Applications for Metal−Organic Frameworks (MOFs) as quantum dot semiconductors. J Phys Chem C 111:80–85. https://doi.org/10.1021/jp063600e

Lopez HA, Dhakshinamoorthy A, Ferrer B, Atienzar P, Alvaro M, Garcia H (2011) Photochemical response of commercial MOFs: $Al_2(BDC)_3$ and its use as active material in photovoltaic devices. J Phys Chem C 115:22200–22206. https://doi.org/10.1021/jp206919m

Lu G, Li S, Guo Z, Farha OK, Hauser BG, Qi X, Wang Y, Wang X, Han S, Liu X, DuChene JS, Zhang H, Zhang Q, Chen X, Ma J, Loo SCJ, Wei WD, Yang Y, Hupp JT, Huo F (2012) Imparting functionality to a metal–organic framework material by controlled nanoparticle encapsulation. Nat Chem 4:310–316. https://doi.org/10.1038/nchem.1272

Maeda K, Domen K (2007) New non-oxide photocatalysts designed for overall water splitting under visible light. J Phys Chem C 111:7851–7861. https://doi.org/10.1021/jp070911w

Maity K, Kundu T, Banerjee R, Biradha K (2015) One-dimensional water cages with repeat units of (H2O)24 resembling pagodane trapped in a 3D coordination polymer: proton conduction and tunable luminescence emission by adsorption of anionic dyes. CrystEngComm 17:4439–4443. https://doi.org/10.1039/C5CE00969C

Marcus RA (1956) On the theory of oxidation-reduction reactions involving electron transfer. I. J Chem Phys 24:966. https://doi.org/10.1063/1.1742723

Marcus RA, Sutin N (1985) Electron transfers in chemistry and biology. Biochim Biophys Acta 811:265–322. https://doi.org/10.1016/0304-4173(85)90014-X

Meng X, Yu Q, Liu G, Li S, Zhao G, Liu H, Li P, Chang K, Kako T, Ye J (2017) Efficient photocatalytic CO_2 reduction in all-inorganic aqueous environment: cooperation between reaction medium and Cd (II) modified colloidal ZnS. Nano Energy 34:524–532. https://doi.org/10.1016/j.nanoen.2017.03.021

Meyer K, Bashir S, Llorca J, Idriss H, Ranocchiari M, van Bokhoven JA (2016) Photocatalyzed hydrogen evolution from water by a composite catalyst of NH_2-MIL-125(Ti) and surface nickel (II) species. Chem Eur J 22:13894–13899. https://doi.org/10.1002/chem.201601988

Mo K, Yang Y, Cui Y (2014) A homochiral metal–organic framework as an effective asymmetric catalyst for cyanohydrin synthesis. J Am Chem Soc 136:1746–1749. https://doi.org/10.1021/ja411887c

Mondloch JE, Bury W, FairenJimenez D, Kwon S, DeMarco EJ, Weston MH, Sarjeant AA, Nguyen ST, Stair PC, Snurr RQ, Farha OK, Hupp JT (2013) Vapor-phase metalation by atomic layer deposition in a metal–organic framework. J Am Chem Soc 135:10294–10297. https://doi.org/10.1021/ja4050828

Nasalevich MA, Goesten MG, Savenije TJ, Kapteijn F, Gascon J (2013) Enhancing optical absorption of metal–organic frameworks for improved visible light photocatalysis. Chem Commun 49:10575–10577. https://doi.org/10.1039/C3CC46398B

Nasalevich MA, van der Veen M, Kapteijn F, Gascon J (2014) Metal–organic frameworks as heterogeneous photocatalysts: advantages and challenges. CrystEngComm 16:4919–4926. https://doi.org/10.1039/C4CE00032C

Okawa H, Shigematsu A, Sadakiyo M, Miyagawa T, Yoneda K, Ohba M, Kitagawa H (2009) Oxalate-bridged bimetallic complexes {NH(prol)$_3$}[MCr(ox)$_3$] (M = Mn^{II}, Fe^{II}, Co^{II}; NH(prol)$_3^+$ = Tri(3-hydroxypropyl)ammonium) exhibiting coexistent ferromagnetism and proton conduction. J Am Chem Soc 131:13516–13522. https://doi.org/10.1021/ja905368d

Okawa H, Sadakiyo M, Yamada T, Maesato M, Ohba M, Kitagawa H (2013) Proton-conductive magnetic metal–organic frameworks, {NR$_3$(CH$_2$COOH)}[M$_a^{II}$M$_b^{III}$(ox)$_3$]: effect of carboxyl residue upon proton conduction. J Am Chem Soc 135:2256–2262. https://doi.org/10.1021/ja309968u

Ola O, Maroto-Valer MM (2015) Review of material design and reactor engineering on TiO$_2$ photocatalysis for CO$_2$ reduction. J Photochem Photobiol C Photochem Rev 24:16–42. https://doi.org/10.1016/j.jphotochemrev.2015.06.001

Paille G, Gomez-Mingot M, Roch-Marchal C, Lassalle-Kaiser B, Mialane P, Fontecave M, Mellot-Draznieks C, Dolbecq A (2018) A fully noble metal-free photosystem based on cobalt-polyoxometalates immobilized in a porphyrinic metal–organic framework for water oxidation. J Am Chem Soc 140:3613–3618. https://doi.org/10.1021/jacs.7b11788

Pasveer W, Cottaar J, Tanase C, Coehoorn R, Bobbert P, Blom P, De Leeuw D, Michels M (2005) Unified description of charge-carrier mobilities in disordered semiconducting polymers. Phys Rev Lett 94:206601. https://doi.org/10.1103/PhysRevLett.94.206601

Pi Y, Li X, Xia Q, Wu J, Li Z, Li Y, Xiao J (2017) Formation of willow leaf-like structures composed of NH2-MIL68(In) on a multifunctional multiwalled carbon nanotube backbone for enhanced photocatalytic reduction of Cr (VI). Nano Res 10:3543–3556. https://doi.org/10.1007/s12274-017-1565-8

Portillo AS, Baldoví HG, Fernandez MTG, Navalón S, Atienzar P, Ferrer B, Alvaro M, Garcia H, Li Z (2017) Ti as mediator in the photoinduced electron transfer of mixed-metal NH$_2$–UiO-66(Zr/Ti): transient absorption spectroscopy study and application in photovoltaic cell. J Phys Chem C 121:7015–7024. https://doi.org/10.1021/acs.jpcc.6b13068

Puchberger M, Kogler FR, Jupa M, Gross S, Fric H, Kickelbick G, Schubert U (2006) Can the clusters Zr$_6$O$_4$(OH)$_4$(OOCR)$_{12}$ and [Zr$_6$O$_4$(OH)$_4$(OOCR)$_{12}$]$_2$ be converted into each other? Eur J Inorg Chem 6:3283–3293. https://doi.org/10.1002/ejic.200600348

Ren J, Guo H, Yang J, Qin Z, Lin J, Li Z (2015) Insights into the mechanisms of CO$_2$ methanation on Ni(111) surfaces by density functional theory. Appl Surf Sci 351:504–516. https://doi.org/10.1016/j.apsusc.2015.05.173

Rodríguez NA, Savateev A, Grela MA, Dontsova D (2017) Facile synthesis of potassium poly(heptazine imide) (PHIK)/Ti-based metal–organic framework (MIL-125-NH$_2$) composites for photocatalytic applications. ACS Appl Mater Interfaces 9:22941–22294. https://doi.org/10.1021/acsami.7b04745

Rosseinsky DR, Tonge JS, Berthelot J, Cassidy JF (1987) Site-transfer conductivity in solid iron hexacyanoferrates by dielectric relaxometry, voltammetry and spectroscopy. Prussian Blue, congeners and mixtures. J Chem Soc Faraday Trans 83:231–243. https://doi.org/10.1039/F19878300231

Sahoo P, Tan JB, Zhang Z-M, Singh SK, Lu TB (2018) Engineering the surface structure of binary/ternary ferrite nanoparticles as high-performance electrocatalysts for the oxygen evolution reaction. ChemCatChem 10:1075–1083. https://doi.org/10.1002/cctc.201701790

Savenije TJ, Ferguson AJ, Kopidakis N, Rumbles G (2013) Revealing the dynamics of charge carriers in polymer: fullerene blends using photoinduced time-resolved microwave conductivity. J Phys Chem C 117:24085–24103. https://doi.org/10.1021/jp406706u

Schneider J, Matsuoka M, Takeuchi M, Zhang J, Horiuchi Y, Anpo M, Bahnemann DW (2014) Understanding TiO2 photocatalysis: mechanisms and materials. Chem Rev 114:9919–9986. https://doi.org/10.1021/cr5001892

Sen S, Yamada T, Kitagawa H, Bharadwaj PK (2014) 3D coordination polymer of Cd(II) with an imidazolium-based linker showing parallel polycatenation forming channels with aligned imidazolium groups. Cryst Growth Des 14:1240–1244. https://doi.org/10.1021/cg401760m

Serpone N, Emeline A (2012) Semiconductor photocatalysis — past, present, and future outlook. J Phys Chem Lett 3:673–677. https://doi.org/10.1021/jz300071j

Sha Z, Sun J, Chan HSO, Jaenicke S, Wu J (2015) Enhanced photocatalytic activity of the AgI/UiO-66(Zr) composite for rhodamine B degradation under visible-light irradiation. ChemPlusChem 80:1321–1328. https://doi.org/10.1002/cplu.201402430

Sharma S, Ghosh SK (2018) Metal−organic framework-based selective sensing of biothiols via chemidosimetric approach in water. ACS Omega 3:254–258. https://doi.org/10.1021/acsomega.7b01891

Shen L, Luo M, Liu Y, Liang R, Jing F, Wu L (2015) Noble-metal-free MoS2 co-catalyst decorated UiO-66/CdS hybrids for efficient photocatalytic H_2 production. Appl Catal B 166–167:445–452. https://doi.org/10.1016/j.apcatb.2014.11.056

Shi L, Wang T, Zhang H, Chang K, Meng X, Liu H, Ye J (2015) An amine-functionalized iron (III) metal–organic framework as efficient visible-light photocatalyst for Cr (VI) reduction. Adv Sci 2:1500006. https://doi.org/10.1002/advs.201500006

Shimizu GKH, Taylor JM, Kim S (2013) Proton conduction with metal-organic frameworks. Science 341:354–355. https://doi.org/10.1126/science.1239872

Silva CG, Luz I, LlabrésiXamena FX, Corma A, García H (2010a) Water stable Zr–benzenedicarboxylate metal–organic frameworks as photocatalysts for hydrogen generation. Chem Eur J 16:11133–11138. https://doi.org/10.1002/chem.200903526

Silva CG, Corma A, Garcia H (2010b) Metal–organic frameworks as semiconductors. J Mater Chem 20:3141–3156. https://doi.org/10.1039/B924937K

Sivula K, van de Krol R (2016) Semiconducting materials for photoelectrochemical energy conversion. Nat Rev Mater 1:15010. https://doi.org/10.1038/natrevmats.2015.10

Song F, Wang C, Lin W (2011) A chiral metal–organic framework for sequential asymmetric catalysis. Chem Commun 47:8256–8258. https://doi.org/10.1039/C1CC12701B

Stavila V, Talin AA, Allendorf MD (2014) MOF-based electronic and opto-electronic devices. Chem Soc Rev 43:5994–6010. https://doi.org/10.1039/C4CS00096J

Sun F, Yin Z, Wang Q-Q, Sun D, Zeng M-H, Kurmoo M (2013) Tandem postsynthetic modification of a metal–organic framework by thermal elimination and subsequent bromination: effects on absorption properties and photoluminescence. Angew Chem Int Ed 52:1–6. https://doi.org/10.1002/ange.201300821

Sun D, Gao Y, Fu J, Zeng X, Chenb Z, Li Z (2015a) Construction of a supported Ru complex on bifunctional MOF-253 for photocatalytic CO_2 reduction under visible light. Chem Commun 51:2645–2648. https://doi.org/10.1039/C4CC09797A

Sun D, Ye L, Li Z (2015b) Visible-light-assisted aerobic photocatalytic oxidation of amines to imines over NH_2-MIL-125(Ti). Appl Catal B Environ 164:428–432. https://doi.org/10.1016/j.apcatb.2014.09.054

Tachikawa T, Choi JR, Fujitsuka M, Majima T (2008) Photoinduced charge-transfer processes on MOF-5 nanoparticles: elucidating differences between metal-organic frameworks and semiconductor metal oxides. J Phys Chem C 112:14090–14101. https://doi.org/10.1021/jp803620v

Takanabe K (2017) Photocatalytic water splitting: quantitative approaches toward photocatalyst by design. ACS Catal 7:8006–8022. https://doi.org/10.1021/acscatal.7b02662

Tian J, Xu Z-Y, Zhang D-W, Wang H, Xie S-H, Xu D-W, Ren Y-H, Wang H, Liu Y, Li Z-T (2016) Supramolecular metal-organic frameworks that display high homogeneous and heterogeneous photocatalytic activity for H_2 production. Nat Commun 7:11580. https://doi.org/10.1038/ncomms11580

Toyao T, Saito M, Horiuchi Y, Mochizuki K, Iwata M, Higashimura H, Matsuoka M (2013) Efficient hydrogen production and photocatalytic reduction of nitrobenzene over a visiblelight-responsive metal–organic framework photocatalyst. Cat Sci Technol 3:2092–2097

Tranchemontagne DJ, Hunt JR, Yaghi OM (2008) Room temperature synthesis of metal-organic frameworks: MOF-5, MOF-74, MOF-177, MOF-199, and IRMOF-0. Tetrahedron 64:8553–8557

Van Wyk A, Smith T, Park J, Deria P (2018) Charge-transfer within Zr-based metal–organic framework: the role of polar node. J Am Chem Soc 140:2756–2760. https://doi.org/10.1021/jacs.7b13211

Vlasova EA, Yakimov SA, Naidenko EV, Kudrik EV, Makarov SV (2016) Application of metal–organic frameworks for purification of vegetable oils. Food Chem 190:103–109. https://doi.org/10.1016/j.foodchem.2015.05.078

Vu TA, Le GH, Vu HT, Nguyen KT, Quan TTT, Nguyen QK, Tran HTK, Dang PT, Vu LD, Lee GD (2017) Highly photocatalytic activity of novel Fe-MIL-88B/GO nanocomposite in the degradation of reactive dye from aqueous solution. Mater Res Express 4:035038. https://doi.org/10.1088/2053-1591/aa6079

Wakaoka T, Hirai K, Murayama K, Takano Y, Takagi H, Furukawa S, Kitagawa S (2014) Confined synthesis of CdSe quantum dots in the pores of metal–organic frameworks. J Mater Chem C 2:7173–7175. https://doi.org/10.1039/C4TC01136H

Wang S, Wang X (2015) Multifunctional metal-organic frameworks for photocatalysis. Small 11:30973112. https://doi.org/10.1002/smll.201500084

Wang C, Xie Z, deKrafft KE, Lin W (2011) Doping metal–organic frameworks for water oxidation, carbon dioxide reduction, and organic photocatalysis. J Am Chem Soc 133:13445–13454. https://doi.org/10.1021/ja203564w

Wang C, Wang J-L, Lin W (2012) Elucidating molecular iridium water oxidation catalysts using metal–organic frameworks: a comprehensive structural, catalytic, spectroscopic, and kinetic study. J Am Chem Soc 134:19895–11990. https://doi.org/10.1021/ja310074j

Wang D, Huang R, Liu W, Sun D, Li Z (2014) Fe-based MOFs for photocatalytic CO_2 reduction: role of coordination unsaturated sites and dual excitation pathways. ACS Catal 4:4254–4260. https://doi.org/10.1021/cs501169t

Wang D, Wang M, Li Z (2015) Fe-based metal–organic frameworks for highly selective photocatalytic benzene hydroxylation to phenol. ACS Catal 5:6852–6857. https://doi.org/10.1021/acscatal.5b01949

Wang J-W, Sahoo P, Lu T-B (2016) Reinvestigation of water oxidation catalyzed by a dinuclear cobalt polypyridine complex: identification of CoO_x as a real heterogeneous catalyst. ACS Catal 6:5062–5068. https://doi.org/10.1021/acscatal.6b00798

Wang W, Xu X, Zhou W, Shao Z (2017) Recent progress in metal-organic frameworks for applications in electrocatalytic and photocatalytic water splitting. Adv Sci 4:1600371. https://doi.org/10.1002/advs.201600371

Wang M, Liu J, Guo C, Gao X, Gong C, Wang Y, Liu B, Li X, Gurzadyana GG, Sun L (2018a) Metal–organic frameworks (ZIF-67) as efficient cocatalysts for photocatalytic reduction of CO_2: the role of the morphology effect. J Mater Chem A 6:4768–4775. https://doi.org/10.1039/C8TA00154E

Wang M, Yang L, Guo C, Liu X, He L, Song Y, Zhang Q, Qu X, Zhang H, Zhang Z, Fang S (2018b) Bimetallic Fe/Ti-based metal–organic framework for persulfate-assisted visible light photocatalytic degradation of orange II. Chem Sel 3:3664–3674. https://doi.org/10.1002/slct.201703134

Wasielewski MR (1992) Photoinduced electron transfer in supramolecular systems for artificial photosynthesis. Chem Rev 92:435–461. https://doi.org/10.1021/cr00011a005

Wee LH, Janssens N, Sree SP, Wiktor C, Gobechiya E, Fischer RA, Kirschhock CEA, Martens JA (2014) Local transformation of ZIF-8 powders and coatings into ZnO nanorods for photocatalytic application. Nanoscale 6:2056–2060. https://doi.org/10.1039/C3NR05289C

Weinberg DR, Gagliard CJ, Hull JF, Murphy CF, Kent CA, Westlake BC, Paul A, Ess DH, McCafferty DG, Meyer TJ (2012) Proton-coupled electron transfer. Chem Rev 112:4016–4093. https://doi.org/10.1021/cr200177j

Wu MX, Yang YW (2017) Metal–Organic Framework (MOF)-based drug/cargo delivery and cancer therapy. Adv Mater 29:1606134. https://doi.org/10.1002/adma.201606134

Wu P, He C, Wang J, Peng X, Li X, An Y, Duan C (2012) Photoactive chiral metal–organic frameworks for light-driven asymmetric α-alkylation of aldehydes. J Am Chem Soc 134:14991–14999. https://doi.org/10.1021/ja305367j

Xu H-Q, Hu J, Wang D, Li Z, Zhang Q, Luo Y, Yu S-H, Jiang H-L (2015) Visible-light photoreduction of CO_2 in a metal–organic framework: boosting electron–hole separation via electron trap states. J Am Chem Soc 137:13440–13443. https://doi.org/10.1021/jacs.5b08773

Yang L-M, Fang G-Y, Ma J, Ganz E, Han SS (2014) Band gap engineering of paradigm MOF-5. Cryst Growth Des 14:2532–2541. https://doi.org/10.1021/cg500243s

Yu X, Wang L, Cohen SM (2017) Photocatalytic metal–organic frameworks for organic transformations. CrystEngComm 19:4126–4136. https://doi.org/10.1039/C7CE00398F

Yuan X, Wang H, Wu Y, Zeng G, Chen X, Leng L, Wu Z, Li H (2016) One-pot self-assembly and photoreduction synthesis of silver nanoparticle-decorated reduced graphene oxide/MIL-125(Ti) photocatalyst with improved visible light photocatalytic activity. Appl Organomet Chem 30:289–296. https://doi.org/10.1002/aoc.3430

Zeng L, Guo X, He C, Duan C (2016) Metal–organic frameworks: versatile materials for heterogeneous photocatalysis. ACS Catal 6:7935–7945. https://doi.org/10.1021/acscatal.6b02228

Zhang T, Lin W (2014) Struct Bond 157: 89. https://doi.org/10.1007/430_2013_131 # Springer, Berlin/Heidelberg 2013, Published online: 7 September (2013)

Zhang S, Li L, Zhao S, Sun Z, Hongab M, Luo J (2015a) Hierarchical metal–organic framework nanoflowers for effective CO_2 transformation driven by visible light. J Mater Chem A 3:15764–15768. https://doi.org/10.1039/C5TA03322E

Zhang Z-M, Zhang T, Wang C, Lin Z, Long L-S, Lin W (2015b) Photosensitizing metal–organic framework enabling visible-light-driven proton reduction by a Wells–Dawson-type polyoxometalate. J Am Chem Soc 137:3197–3200. https://doi.org/10.1021/jacs.5b00075

Zhang Q, Zhang C, Cao L, Wang Z, An B, Lin Z, Huang R, Zhang Z, Wang C, Lin W (2016) Förster energy transport in metal–organic frameworks is beyond step-by-step hopping. J Am Chem Soc 138:5308–5315. https://doi.org/10.1021/jacs.6b01345

Zhang Y, Guo J, Shi L, Zhu Y, Hou K, Zheng Y, Tang Z (2017) Tunable chiral metal organic frameworks toward visible light–driven asymmetric catalysis. Sci Adv 3:e1701162. https://doi.org/10.1126/sciadv.1701162

Zhou H-C, Long JR, Yaghi OM (2012) Introduction to metal–organic frameworks. Chem Rev 112:673–674. https://doi.org/10.1021/cr300014x

Zhu C, Xia Q, Chen X, Liu Y, Du X, Cui Y (2016) Chiral metal–organic framework as a platform for cooperative catalysis in asymmetric cyanosilylation of aldehydes. ACS Catal 6:7590–7596. https://doi.org/10.1021/acscatal.6b02359

Chapter 7
Photobiocatalysis: At the Interface of Photocatalysis and Biocatalysts

Madan L. Verma, Sarita Devi, and Motilal Mathesh

Contents

7.1 Introduction 188
7.2 Photocatalyst 189
  7.2.1 Working Principle 189
  7.2.2 Current Photocatalytic Systems 190
  7.2.3 Current Applications 192
  7.2.4 Limitations of Photocatalysts 194
7.3 Photobiocatalysis 195
  7.3.1 Reaction Mechanism in Photobiocatalysis 195
  7.3.2 The Control of Photobiocatalysis 195
  7.3.3 Effect of Mutation with Deletion of Dehydrogenase Gene 197
  7.3.4 Effect of Organic Dyes as Photosensitizers 197
  7.3.5 Key Enzymes Deciphering the Reaction Mechanism of Photobiocatalysis 198
  7.3.6 Role of Mediators in Photobiocatalytic System 201
7.4 Conclusion 203
References 203

Abstract Photobiocatalysis is a novel concept that aims at merging the features from photocatalysis and enzymatic catalysis. The process of photocatalysis involves the degradation of contaminants in water and air. It has also shown promising application in solar energy. However, many photocatalytic processes have low efficiency as compared to other enzymatic processes. Therefore, to improve the performance of such photocatalytic processes, a promising photobiocatalysis

---

M. L. Verma (✉)
Center for Chemistry and Biotechnology, Deakin University, Geelong, VIC, Australia

Department of Biotechnology, Dr. YS Parmar University of Horticulture and Forestry, Hamirpur, Himachal Pradesh, India

S. Devi
Department of Patents and Designs, BoudhikSampada Bhawan, Dwarka, New Delhi, India

M. Mathesh
Institute of Molecules and Materials, Radboud University, Nijmegen, The Netherlands

S. Rajendran et al. (eds.), *Green Photocatalysts for Energy and Environmental Process*, Environmental Chemistry for a Sustainable World 36,
https://doi.org/10.1007/978-3-030-17638-9_7

approach shows a great promise to enhance the effectiveness of the photocatalytic system. The combination of photocatalysis and biocatalysis technologies is an alternative to develop environmentally benign process for the synthesis of renewable chemicals. In photobiocatalysis, the semiconductor coupled with the enzyme which regularly needs a natural compound and a relay transferring charge carriers from the semiconductor. The enzyme diminution mediated by NAD^+/NADH along with an electron relay utilized the conductivity band electrons of excited semiconductors for photobiocatalysis. The photosynthetic organisms are the natural source for photobiocatalysis.

The present write-up discusses the working mechanism and applications of the current photocatalytic system such as metal oxide photocatalyst and graphene-based photocatalyst. Advances in enzyme-mediated photocatalysis are particularly discussed. The critical factors to control the photobiocatalytic process and key enzymes involved in deciphering the reaction mechanism of photobiocatalysis are critically discussed. Cofactor vs mediator medicated photobiocatalysis is also discussed.

Keywords Photobiocatalysis · Biocatalysis · Photocatalysis · Redox reaction · Photosensitizer · Photosynthesis · Cyanobacteria

7.1 Introduction

The most important challenges that humanity must solve in the twenty-first century include the environmental problems like pollution, energy crisis, and global warming (Naushad and ALOthman 2015; Sharma et al. 2017). Many recent investigations are focused to improve the availability of renewable, sustainable, and eco-friendly energy sources. The different sources of renewable energy like solar, wind, rain, waves, and geothermal heat which are present in the environment could contribute approximately 16% of the energy used. Among all these different energy sources, the sunlight is the most accessible and consistent energy source (Sekar and Ramasamy 2015). The Sun delivers energy to Earth's surface at an average of 4.3×10^{20} J h^{-1} which is approximately equivalent to the world's total annual energy consumption in all other forms (Zhu et al. 2008). However, the humans have used the solar energy with limited efficiency. The photosynthetic process involves the combination of light harvesting, photoinduced charge separation, and catalysis that is required to carry out the oxidation of water and reduction of carbon dioxide (Bryson 2004).

The plants and organisms (algae) that are involved in the photosynthesis have a specialized mechanism for the conversion of solar energy into biochemical energy in the form of glucose biomolecules from CO_2 and reducing agents such as NADH and $FADH_2$. There is the requirement of the thylakoid scaffold to arrange the total components of the photosynthetic machinery in the space by this complex biochemical system (Antonio et al. 2015). In the natural photosynthetic system, there are two light-absorbing systems, photosystem I (PSI) and photosystem II (PSII). These photosystems function simultaneously by transferring electrons from PSII to PSI system with the aid of cytochrome complex (Kim et al. 2014). But this photosynthetic production accounts for only 0.03% of the solar energy reaching the Earth (Gratzel 2012).

The present write-up discusses the working mechanism and applications of the current photocatalytic system such as metal oxide photocatalyst and graphene-based photocatalyst. Advances in enzyme-mediated photocatalysis are particularly discussed. The critical factors to control the photobiocatalytic process and key enzymes involved in deciphering the reaction mechanism of photobiocatalysis are discussed. Cofactor as well as mediator-dependent photobiocatalysis is comparatively discussed.

7.2 Photocatalyst

The branch of chemistry that deals with the use of photons to trigger chemical reactions in the presence of light-sensitive catalyst is known as photocatalysis. This phenomenon was first discovered in 1972 for carrying out artificial photosynthesis (Fujishima and Honda 1972). With growing environmental issues, there has been an increased research interest in this field for applications such as hydrogen production, air purifying systems, wastewater treatment, etc. (Ameta et al. 2018; Kumar et al. 2017). For any photocatalyst to perform well, it should have certain features such as a significant bandgap, stability, reusability, surface structure, and large surface area (Hisatomi et al. 2014; Kumar et al. 2019). Photocatalysis is broadly categorized into two main groups, namely, homogeneous and heterogeneous catalyzes (Khan et al. 2015). Till date, most of the photocatalysts are semiconductors, based on heterogeneous catalysis (e.g., Fe_2O_3, CdS, TiO_2, ZnO), which undergo light-reduced redox reactions due to the electronic structure, comprising of an empty conduction band (CB) and filled valence band (VB). According to web of science in the last 5 years, around 18,000 research articles have been published (date of search: 17 August 2017), showcasing the importance of this work for future applications (Fig. 7.1; Zhou et al. 2016). In this section, the main focus will be on its working principle, different types of photocatalyst and applications, and future perspective.

7.2.1 Working Principle

Different photocatalysts behave in a different way in terms of their mechanisms and the reactions carried out, but it can be broadly classified into four major steps (Shasha and Dunwei 2017) (Fig. 7.2): (I) absorbing light (photons) to generate a pair of electron (e^-) and hole (h^+), (II) excited charge separation, (III) transfer of charges to the surface of the photocatalyst, and (IV) use of this excited charges to perform redox reactions. The major challenge in these systems is to keep e^-–h^+ pair

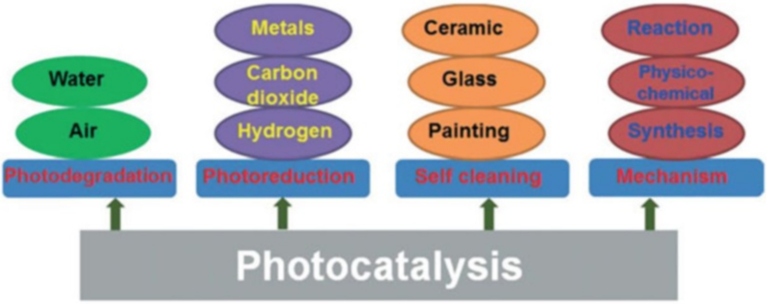

Fig. 7.1 Main applications of photocatalysis. (Reproduced with permission from Zhou et al. 2016)

Fig. 7.2 Steps in photocatalytic reaction process. R, chemicals in reductive reactions; O, chemicals in oxidative reactions. Steps I–IV in the above figure are explained in the text above. (Reproduced with permission from Shasha and Dunwei 2017)

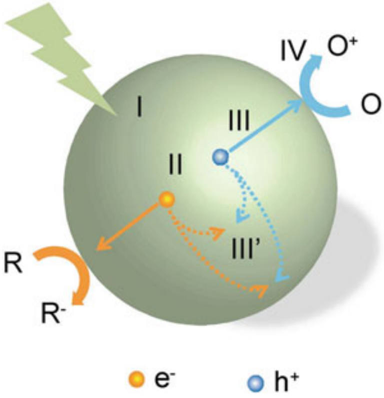

separated as they tend to recombine before reaching to the photocatalyst surface, thus inhibiting the redox reactions, thereby decreasing its efficiency (Zhang et al. 2014). To overcome these issues, a variety of photocatalyst has been discovered such as metal oxide photocatalysts and graphene-based photocatalysts.

7.2.2 Current Photocatalytic Systems

7.2.2.1 Metal Oxide Photocatalysts (MOPs)

MOPs undergo light-catalyzed redox reactions depending on their electronic state and their efficiency in generating e^{-}–h^{+} pairs, which in turn is dependent on the bandgap that differs from each semiconductor. Hence, different MOPs have their own corresponding light wavelengths for producing e^{-}–h^{+} pairs by photoactivation. Table 7.1 gives an account of the common MOPs used in photocatalysis, with their excitation wavelengths and corresponding pros and cons (Yemmireddy and Hung 2017).

Table 7.1 Common MOPs with their corresponding bandgaps

Photocatalyst	Bandgap (eV)	Spectral region	Pros and cons
SnO_2	3.8	UV (326 nm)	Large bandgap
TiO_2 (anatase)	3.24	UV (383 nm)	Stable, corrosion resistant, large bandgap
$SrTiO_2$	3.2	UV (387 nm)	Large bandgap
ZnO	3.2	UV (387 nm)	Large bandgap
TiO_2 (rutile)	3.02	Visible (411 nm)	Stable, less photoactive
WO_3	2.8	Visible (443 nm)	Photo corrode
Fe_2O_3	2.3	Visible (539 nm)	Photo corrode
Cu_2O	2.2	Visible (564 nm)	Unstable
MoS_2	1.8	Visible (689 nm)	Unstable

Adapted with permission from Yemmireddy and Hung (2017)

Among the MOPs, TiO_2 is the most widely studied due to its higher photoactivity, economic viability, and stability, its environmental friendliness, and its safety toward humans (Lan et al. 2013). The UV light exposure of wavelength between 280 and 400 nm to TiO_2 (depending on it structural configuration), an e^- is elevated from VB to the CB, creating a h^+ in VB as in below equation:

$$TiO_2 + hv \rightarrow e^- + h^+$$

This e^-–h^+ pair acts as strong redox systems. The h^+ can oxidize hydroxyl and water molecules into hydroxyl radicals, and the e^- can reduce electron acceptors in the presence of adsorbed air on the surface, according to the following equations:

$$h^+ + OH^- \rightarrow {}^{\cdot}OH$$

$$h^+ + H_2O \rightarrow {}^{\cdot}OH + H^+$$

$$e^- + O_2 \rightarrow {}^{\cdot}O^-$$

Even though TiO_2 is the most widely studied, there are some drawbacks in terms of using wavelength in the UV region and limited activity. To overcome these issues, scientists have been studying various MOPs like zinc oxide for higher photocatalytic effect in neutral pH (Muruganandham et al. 2009), molybdenum oxide for the use of visible light (Xu and Ni 2010), and cerium oxide for higher stability in both UV and visible lights (Hernández-Alonso et al. 2009).

7.2.2.2 Graphene-Based Photocatalysts

The majority of the photocatalyst used till date has limitations in terms of low quantum yield, stability, and the use of visible light (Xin et al. 2016). To overcome these drawbacks, there is a need for fabrication of alternative photocatalyst that provoked researchers to combine graphene with semiconductor materials described

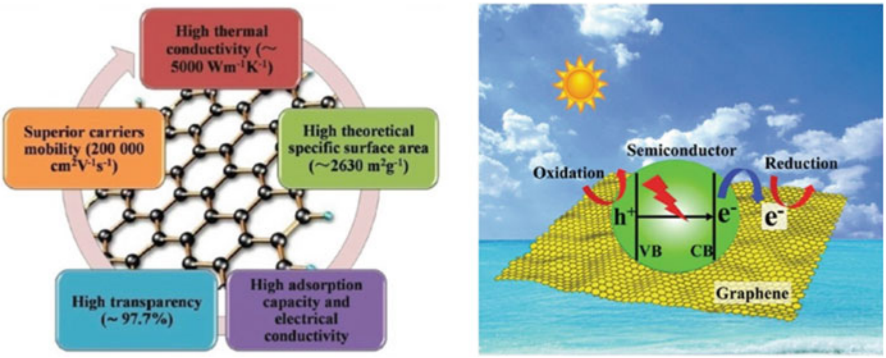

Fig. 7.3 Graphene as photocatalyst, (**a**) unique properties of graphene, and (**b**) working principle behind graphene combined with semiconductor nanocomposites. (Reproduced with permission from Xin et al. 2016)

Table 7.2 Graphene properties and its advantages to serve as photocatalyst

Properties	Advantages
Crystal structure	Electrical properties due to its high-quality 2D crystal lattice (Neto et al. 2009)
Semimetal	Strongly accepts electrons (Lang and Kohn 1970)
Semiconductor	Functionalization of graphene can facilitate in fabrication of n-type or p-type semiconductor (Sreeprasad and Berry 2013)
Surface chemistry	Its high adsorption power of targeted molecules increases the photoredox reactions (Kemp et al. 2013)
Charge transport	The presence of impurity is beneficial for enhancing electronic conductivities and carrier mobility (Wang et al. 2010)
Electrochemistry	Graphene as co-catalyst in the presence of photoexcited electrons can be used for photocatalytic H_2 evolution (Wang et al. 2014)

above. Graphene, a 2D nanosheet, has received considerable attention in the research field owing to its unique properties and is also termed as the “dream material” (Xin et al. 2016). This material can be combined with semiconductor to increase their stability and activity. Fig. 7.3 shows the unique properties (a) and the working principle (b) behind graphene to be used as a photocatalyst.

The main characteristics of graphene that renders them suitable for photocatalysts are listed in Table 7.2.

7.2.3 Current Applications

7.2.3.1 Water Splitting

Researchers have always been in search for a way to split water into hydrogen and oxygen as it has immense potential for energy generation and overcomes the use of fossil fuels to produce energy. They are clean and environmentally friendly power source from a renewable source of energy. The first water-splitting reaction was carried out using TiO_2 as anode and platinum as cathode (Fujishima and Honda 1972). The setup was irradiated with wavelength shorter than 415 nm, and water was observed to be decomposed on TiO_2 surfaces. But the use of UV light and lower efficiency rate provoked researchers to look for new photocatalysts. Recent studies based on Cu_2O photocatalyst have shown to carry out water-splitting reaction using visible light source without any decrease in activity for 1900 h (Hara et al. 1998). On the other hand, N-doped graphene oxide quantum dots showed water-splitting capabilities under visible light conditions (Te-Fu et al. 2014). Graphene has also been studied for its electron-mediating capabilities for water-splitting reactions and high electrical conductivity. The water-splitting capability of Ru/$SrTiO_3$:Rh and $BiVO_4$ was observed to increase in the presence of graphene as electron mediator (Iwase et al. 2011).

7.2.3.2 Environmental Decontamination

TiO_2 has been extensively studied for degrading environmental contaminations such as CO_2, H_2O, and other organic and inorganic materials. Its capability to degrade is based on the generation of ·OH and h^+ that can act as oxidizing agents (Lan et al. 2013). Cyanide ions (Frank and Bard 1977) and organochlorides (Hsiao et al. 1983) have been successfully decontaminated using TiO_2 as catalysts. CO_2, one of the widely present pollutant in air, has also been photoreduced to methanol, formaldehyde, and methane in the presence of water with the help of TiO_2 (Inoue et al. 1979). The use of graphene/semiconductor combination has boosted the photocatalytic ability in reducing CO_2 and making it more economically viable (Wenguang et al. 2013). One such example is the use of reduced graphene oxide (0.5 wt%) together with cadmium-sulfur (CdS) nanorods, which helped in boosting the photocatalytic ability of CdS nanorods up to ten times for degradation of CO_2 into methane in the presence of visible light (Yu et al. 2014).

7.2.3.3 Antibacterial and Sterilization

Apart from the above applications, TiO_2 has also found its way in the field of antibacterial and sterilization process. Many microorganisms such as *E.coli* (Mitoraj et al. 2007), *Streptococcus sobrinus* (Saito et al. 1992), and even HeLa cells (Blake et al. 1999) have been tested to be killed by TiO_2 when they are irradiated with UV light. The photocatalytic activity of TiO_2 destroys the cell wall of microorganisms and then progressively damages the cell membranes, thereby causing cell death with continuous irradiation reactions that was also confirmed with electron microscopy (Fig. 7.4; Saito et al. 1992). Composites made of TiO_2 on graphene sheets have also been studied for antibacterial activity. It was observed that upon visible light illumination on the composites, only 9.5% of *E. coli* survived when compared to 91.2% when only TiO_2 was present (nine times more active) (Cao et al. 2013).

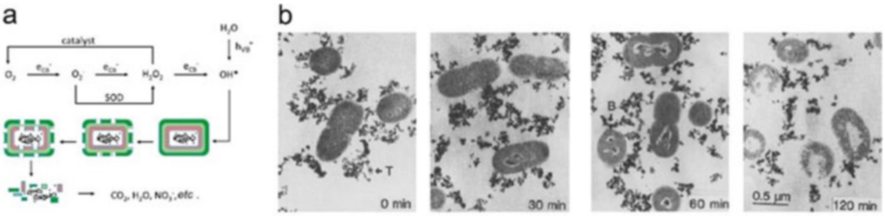

Fig. 7.4 Photo-biocidal processes of *E. coli* in the presence of photocatalytic TiO_2. *E. coli* cell wall composed of three layers: outer layer, peptidoglycan layer, and cytoplasmic layer. (**b**) TEM images of *S. sobrinus* with catalytic TiO_2 after light irradiation. T, TiO_2 catalysts; B, broken cells. (Reproduced with permission from Mitoraj et al. 2007 and Saito et al. 1992)

7.2.4 Limitations of Photocatalysts

Even though TiO_2 and other metal oxide photocatalysts have been widely studied, the most important drawback is it utilizes UV light that forms only 3% of the solar radiation as the remaining 97% is comprised of visible light radiations. Hence, first and foremost efforts need to be made for broadening the wavelength that can be utilized by metal oxides for photocatalysis. Even though some advancements have been made in this field, there is still a need to tune the efficiency of visible light-sensitive photocatalysts. Another important limitation is its lower efficiency due to higher recombination efficiency of the e^-–h^+ generated on their surfaces. One possible solution to reduce this is surface modification of the photocatalyst or doping them with transition metal ions that can reduce the recombination efficiency and make the system more stable. The surface morphology controls the efficiency of photocatalysts; hence it is mandatory to have complete control over their shape and size that can further enhance the efficiency. In terms of using graphene as efficient photocatalyst, more research is required to improve the stability and understand the working principle, as it is still in its infancy. As in the case of metal oxide photocatalyst, there is a need for synthesizing high-quality graphene and study the effect of impurities on their photocatalytic ability. Graphene on itself doesn't possess photocatalytic activity; they have to be combined with semiconductors to make composites for high efficiency. There has been some research supporting the above statement, but still there is a lot of scope for improvement. Each material of the composite should be studied systematically and combined together in a fashion that effects are synergistic to achieve the highest performance. Both theoretical and experimental approaches would be required to achieve the best performing photocatalyst.

Low efficiency of these photocatalytic processes is improved by enzyme-mediated photocatalysis. Therefore, to increase these low yields, a promising photobiocatalysis approach has considerably improved the efficiency of the photocatalytic system and make the "green process" greener by the use of the solar energy in chemical synthesis.

7.3 Photobiocatalysis

7.3.1 Reaction Mechanism in Photobiocatalysis

The process of photosynthesis acts as the key regulator in photobiocatalytic reactions (Gratzel 2012). The chlorophylls are the pigment molecules present in chloroplasts which use the light energy produced by the Sun to produce high-energy electrons with immense reducing potential (Darnell et al. 1990). All the photosynthetic organisms harvest light energy for the production of NADPH from $NADP^+$ by photosynthetic electron transfer reactions and the generation of ATP. The CO_2 is converted into sugar by using NADPH and ATP (Darnell et al. 1990).

The NADPH produced during the photosynthesis can also be utilized for exogenous substrate reduction (Patel 2016). Therefore, the biomolecules which are essential for photobiocatalysis provide the cofactor recycling system for the reduction of biocatalytic (Patel 2016). The cyanobacterium *Synechococcus* PCC 7942 ketone reduction is extremely enantioselective and outstandingly increased in the presence of the light. The reduction mechanism of exogenously supplied ketone with *Synechococcus* PCC7942 was studied in details using different inhibitors (e.g., 3-(3,4-dichlorophenyl)-1, 1-dimethylurea (DCMU), and D, L-glyceraldehyde) for enzymes and photosynthetic electron transport system in the Calvin cycle. Moreover, the reduction of ketone in *Synechococcus* species particularly depends upon NADPH and not upon NADH. Hence, the cyanobacteria provide the biocatalytic systems for using light energy in synthesis of valuable compounds and remediation of environmental contaminants (Yamanaka et al. 2011). The different inhibitors of photosynthetic electron transport system and light intensity significantly affected the ketones reduction, which shows the dependence of reduction on photosynthetic activity. The major cofactor involved in the exogenous ketone reduction is achieved by photosynthetically produced NADPH (Nakamura and Yamanaka 2002). The ketoreductase (3-ketoacyl-acyl carrier protein reductase) carries out the artificial ketone reduction by whole cell of *Synechococcus* PCC7942 with the aid of NADPH coenzyme (Yamanaka et al. 2011; Patel 2016).

7.3.2 The Control of Photobiocatalysis

The photobiocatalysis reaction is differed from the microbial reactions. It may require novel processes to control chemical and stereochemical yields. The significant photosynthetic factors like light and CO_2 can be of great importance for photobiocatalysis.

7.3.2.1 Effect of Light Intensity (Light Quantity)

The stereochemical route of the asymmetric reduction of ketones by a photosynthetic microorganism is mainly regulated by light (Nakamura et al. 2003). Thus, the very low enantioselectivities of the reduction of α, α-difluoroacetophenone by a cyanobacterium in the dark were enhanced by illumination (Nakamura et al. 2003; Patel 2016).

The light energy used by cyanobacterium is transformed into NADPH (chemical energy) through an electron transfer system. Consequently, the chemical energy is further used to produce the chiral alcohol via substrate reduction (Nakamura et al. 2003). The DCMU (a photosynthetic inhibitor) was utilized to monitor the reduction of enantioselectivity under illumination and confirm the effect of photosynthesis on enantioselectivities (Yee and Bartholomew 1989; Patel 2016). Hence, the addition of a photosensitizer is necessary in the absence of a photosynthetic organism. The process uses the light energy to help electron transfer from a photosensitizer to NAD $(P)^+$ through an electron transport reagent.

7.3.2.2 Effect of Light Wavelength (Light Quality)

The light wavelength directly relates with the performance of photosynthesis process. Thus, it plays an important role on the photobiocatalysis (Rauch et al. 2017). The simple LEDs are more compatible than conventional light sources in flavin-based NAD^+ regeneration systems to enhance the dehydrogenase-mediated oxidation reactions. More specifically, the expressively low energy demand of LED systems makes it versatile and a eco-friendly synthesis (Rauch et al. 2017). The substrate, 2′-3′-4′-5′-6′-pentafluoroacetophenone, is used for the production of S-pentafluoro(phenyl-)ethanol with an enantiomeric excess >99% (a measurement of purity used for chiral substances), and the sugar (e.g., glucose) is used as co-substrate if no light is available for regeneration of the cofactor nicotinamide adenine dinucleotide phosphate (reduced form, NADPH; Havel and Weuster-Botz 2007). Asymmetric reduction of 2′, 3′, 4′, 5′, 6′-pentafluoroacetophenone by whole-cell *Synechocystis* PCC6803 to the corresponding (S)-alcohol in an outstanding optical yield of >99% ee with the help of selected illuminated light (orange and red LED lights) that were twofold efficient as compared to other selected LEDs (blue and green lights) in the renewable chemical yields (Havel and Weuster-Botz 2007; Patel 2016).

7.3.2.3 Effect of CO_2 Concentrations

The enantioselectivity in asymmetric ketone reduction was controlled by carbon dioxide concentrations of the atmosphere under illumination of fluorescent light; the reaction in high carbon dioxide concentrations results in the production of the corresponding L-alcohol, while that under dark conditions in low carbon dioxide concentrations and in the presence of glucose, there is production of D-alcohol (Kojima et al. 2009). To check the effect of CO_2, the asymmetric ketone reduction is performed with the help of whole-cell *Nicotiana tabacum* biocatalysts. The various reaction conditions were optimized by changing the concentrations of CO_2 ("normal air" vs "high CO_2" conditions) or the states of light ("dark" vs "light" conditions). *N. tabacum* var. Samsun NN cells by acting as a photosynthetic biocatalyst reduced t-butyl acetoacetate to the corresponding (S)-alcohol with very low chemical yield and optical yield in the absence of light. However, the reaction in the presence of light (illuminating light) gave the corresponding (S)-alcohol with high chemical yield and optical yield in the natural atmospheric CO_2 concentration. Furthermore, the atmospheric CO_2 concentration (high) enhanced both the chemical yield (up to 98%) and the optical yield (up to 98%) in the reaction (Kojima et al. 2009; Patel 2016).

In contrast, the antipode, ®-alcohol, gave 82% ee when glucose was provided to the reaction in the absence of light with 0.04% atmospheric CO_2 concentrations. ®-alcohol is different from the reduction system that produces the (S)-alcohol that is directly connected with photosynthesis (Kojima et al. 2009; Patel 2016).

7.3.3 Effect of Mutation with Deletion of Dehydrogenase Gene

The t-butyl acetoacetate reduction by the whole-cell *Synechocystis* PCC6803 mutant (Δslr0942) with the deletion of slr0942 gene which is a short chain ($NADP^+$)-dependent alcohol dehydrogenase afforded (R)-alcohol with high optical yield of 53% ee as compared to the reaction with wild type of *Synechocystis* PCC6803 under illumination. In contrast, deletion of slr0315 gene [3-oxyacyl-(acyl carrier protein) reductase] converts to the corresponding (S)-alcohol (Takemura et al. 2009).

7.3.4 Effect of Organic Dyes as Photosensitizers

The ultraviolet and visible regions of electromagnetic waves are absorbed by the photosensitizers, and they further trigger the changes in the redox sites of adjacent molecules. The electrons which are delocalized in photosensitizers assist the photons' absorption, and the photoexcited electrons occupy the conduction bands or the lowest unoccupied molecular orbitals (LUMO) of photosensitizers (De Silva et al. 1997; Imahori et al. 2009; Pal and Hanan 2014). The photochemical reduction of enzyme cofactors is enhanced by the use of an organic dye in the presence of appropriate electron donors (quenchers) that induced electron transfer (Lee et al. 2018). Sometimes, a mediator molecule is also required to transfer electrons from the dye in its excited state to the cofactor (Lee et al. 2018). Photobiocatalysts are comprised of a semiconductor with or without a light harvester that triggers an enzyme (Antonio et al. 2015). The use of light harvesters (dyes) to trigger the cofactor reduction is normal. The electronically excited states are, concurrently, easiest reduced by electron donation to the semi-occupied highest occupied molecular orbital during the excited state (Antonio et al. 2015).

The excited states of photosensitizers are triplets with few longer microsecond lifetimes that make electron transfer quenching more proficient as compared to singlets with a few nanosecond lifetime (Antonio et al. 2015). The organic dyes such as porphyrins, xanthenes, Ru complexes, flavins, and colloidal dispersions of nanomaterials such as quantum dots, carbon nitrides, and carbon dots have been employed for photosensitizer development to carry out the transfer of photoexcited electrons to enzymes for redox biocatalysis. Some of the examples of the natural dyes as photosensitizers are the extractions from black rice, capsicum, *Rosa xanthina*, kelp, and *Erythrina variegata* flower (Hao et al. 2006). The organic dyes, photosensitizers for the photochemical production of NADH, are Zn porphyrins and proflavine (Kim et al. 2011; Nam and Park 2012).

7.3.5 Key Enzymes Deciphering the Reaction Mechanism of Photobiocatalysis

The photobiocatalytic enzymes can be utilized to understand the reaction mechanism of photocatalytic reactions. Amalric et al. (1994) studied two enzymes, catalase and superoxide dismutase, to deal with the nature of the reactive oxygen species (ROS) employed for the degradation of the organic pollutants. The enzyme-catalyzed conversions of hydrogen peroxide and superoxide ion by catalase and superoxide dismutase in the presence of two TiO_2/ZnO photocatalytic annihilation of dimethoxybenzene in water are feasible following the addition of the corresponding enzyme (Amalric et al. 1994). A relatively moderate decrease in rate of disappearance is caused by catalase with TiO_2 photocatalyst that catalyzes the overall reaction from $2H_2O_2 \rightarrow 2H_2O + O_2$, showing that hydrogen peroxide formed in situ is not needed for the pollutant removal (Amalric et al. 1994). The photocatalyst ZnO exhibited the negative effect in the presence of H_2O_2. TiO_2 was either good or adverse depending on the initial ratio of $[H_2O_2]/[1,2\text{-DMB}]$ due to the competition for the adsorption sites, holes, OH' radicals, and the harmful modification of the TiO_2 surface. The positive and adverse effects of H_2O_2 were controlled by catalase (Okamoto et al. 1985; Amalric et al. 1994).

Mifsud et al. (2014) developed catalytic water oxidation mediated by robust TiO_2 semiconductors. TiO_2 in conjunction with oxidoreductases enzymes makes photobiocatalytic redox reactions. The water acted as a sacrificial electron donor that has facilitated the biocatalytic redox reactions. TiO_2 photocatalyst facilitated thermodynamic driving force for water oxidation in the presence of ultraviolet and visible light. The oxidoreductases used electrons released in the water oxidation process with the aid of flavin redox mediators (Mifsud et al. 2014). The oxidoreductases catalyze various synthetically valuable conversions ranging from enantioselective reduction and oxidations to specific oxy-functionalization or halogenations (Drauz et al. 2012; Churakova 2014). Oxy-functionalization of carbon-hydrogen bonds represents a very selective reaction that requires a deeper insight of selectivity and reactivity (Zhang et al. 2018) and, therefore, still represents a key hurdle in organic synthesis (Monti et al. 2011). The cytochrome P450 monooxygenases (P450s) are widely considered as the preference biocatalyst for enzymatic reactions (Churakova 2014).

The reactive oxo-ferryl species occupied a defined three-dimensional protein structure allowing regio-, chemo-, and enantioselective oxy-functionalization reactions (Urlacher and Schmid 2002; Schulz et al. 2012; Urlacher and Girhard 2012). However, the application is restricted to whole-cell biotransformation due to their dependency on cofactor and complex molecules (Hollmann et al. 2010; Hollmann et al. 2011). Apart from this, the relevance of peroxygenases for selective oxy-functionalization reactions in preparative organic synthesis is growing fast (Wang et al. 2017). Especially the "novel" peroxygenases from *Agrocybe aegerita* (Ullrich et al. 2004), *Marasmius rotula* (Grobe et al. 2011), or *Coprinopsis cinerea* (Babot et al. 2013) stand out in terms of substrate scope and specific activity over the well-recognized chloroperoxidase from *Caldariomyces fumago* P450 monooxygenases and chemical counterparts (van Rantwijk and Sheldon 2000). High turnover numbers provide basis to expect truly preparative-scale use of these very promising biocatalysts. In addition, the crystal structures of AaeUPO (Piontek et al. 2013) and directed evolution protocols (Molina-Espeja et al. 2014) along with suitable recombinant expression systems have been documented. The peroxygenases do not use complex and vulnerable electron transport chains delivering reducing equivalents to the heme active site needed for the reductive activation of molecular oxygen as compared to P450 monooxygenases and therefore are not subjected to the oxygen puzzle (Holtmann and Hollmann 2016). The peroxygenases use H_2O_2 directly for the production of the catalytically active oxyferryl heme species. Simultaneously, the peroxygenases suffer from a marked instability against H_2O_2 making controlled in situ provision with H_2O_2 inevitable. The well-recognized glucose/glucose oxidase system to produce H_2O_2 from O_2 exists at lab scale but shows diminutive potential for larger, preparative applications due to its reduced atom efficiency (Trost 1991). The small alcohols or electrochemical sources have recently been proposed to function as more efficient electron (Krieg et al. 2011; Ni et al. 2016).

The water molecule could preferably serve as co-substrate and electron donor for in situ production of H_2O_2. Peroxygenase reactions are normally carried out in aqueous media that provides molecular oxygen as the sole by-product of the water oxidation reaction (Zhang et al. 2018). A large number of catalysts for heterogeneous water oxidation have been studied in recent years that could be used for the partial oxidation of water to hydrogen peroxide (Kofuji et al. 2016). The reaction of water and molecular oxygen (O_2) in the presence of sunlight ends in the production of photocatalytic hydrogen peroxide (H_2O_2). This is an exciting route for sustainable production of H_2O_2 (Kofuji et al. 2016; Hirakawa et al. 2016). The thermodynamic driving force to reaction completion is derived from visible light. Mostly, this approach is assessed in terms of catalytic water splitting into H_2 and O_2. However, the electrons released from water can also be moved to O_2 yielding H_2O_2, and the incomplete oxidation of water to H_2O_2 can be considered (Zhang et al. 2018). The oxidoreductases, more specifically cofactor-dependent dehydrogenase enzymes, show a major limitation in practical applications. Normally, the reductants needed for either substrate reduction or reductive activation of molecular oxygen to perform oxy-functionalization reaction are transported through natural electron transport chains (Mifsud et al. 2014). The electron transport chains frequently comprise many enzymes and cofactors to unite the oxidoreductases. The nicotinamide coenzymes NAD(P)H/NAD(P)$^+$ are commonly employed that undergo reactions with substrates in biocatalytic processes. It changes into the reductive or oxidative forms (Wu et al. 2013). Nowadays, a large number of regeneration or production systems are available to solve this cofactor puzzle (Van der Donk and Zhao 2003; Weckbecker et al. 2010; Rodriguez et al. 2012). The resulting multienzyme cascades include up to two more enzymes and cofactors in addition to the original enzyme.

So, these kinds of complex electron transport chains are tricky to optimize and lack robustness required for a chemical transformation at large scale. This also provides a justification on why cofactor-dependent oxidoreductases (dehydrogenases or monooxygenases) are lagging behind “simple” cofactor-independent enzymes (hydrolases, oxidases, and peroxidases) with regard to functioning in preparative organic chemistry (Mifsud et al. 2014).

Unquestionably, the water molecule would be the outstanding sacrificial electron donor, but its high stability and very low oxidation potential require additional energy input to trigger water as electron donor. This problem can be resolved in natural photosynthesis where visible light is used as thermodynamic driving force to enhance water oxidation leading to the production of molecular oxygen and biogenic reducing equivalents in the form of reduced nicotinamide cofactors (NAD(P)H). However, the photosynthesis which is present naturally is challenging to apply in vitro, mainly due to concerns related to stability as it lacks the chemical stability necessary for long-term in vivo operation and its oxide is susceptible to in-diffusion of ions, which can result in major electronic performance drift and high levels of electronic noise (Schoell et al. 2012). Photosynthesis has always encouraged the researchers to search for robust photocatalysts capable of mimicking the native process (Qu and Duan 2013).

An enormous array of potentially useful photocatalysts has produced from the ongoing research on the conversion of solar energy into chemical energy (Tuller 2017). To meet rising energy requirements, the photoelectrochemical/photocatalytic systems could be designed wherein electrochemical decomposition reactions are driven directly in light, without individually producing electricity (Tuller 2017). The light-driven water splitting resulted in many excellent biomimetic photocatalytic systems where titanium dioxide is the mostly used photocatalyst (Cargnello and Fornasiero 2010). Although there are many significant reactions, one significant reaction is to split water into H_2 and O_2 using a visible light-responsive photocatalyst with an adequate potential to attain water splitting. The photocatalyst system needs appropriate thermodynamic potential for water splitting by using narrow bandgap and stability against corrosion. Such stringent requirements, very few available number of reliable-cum-reproducible photocatalysts is suitable for water splitting (Maeda and Domen 2010). The extensive study was also done for TiO_2 doped with noble metals and nonmetal elements. However, the reports are not found for the consumption of these reducing equivalents to promote biocatalytic redox reactions. It is however extensively investigated that the TiO_2-generated H_2O_2 has been used to facilitate peroxidase-catalysis activity in potential biosensing area (Zhang et al. 2004; Liu and Chen 2005; Chen et al. 2010).

7.3.6 Role of Mediators in Photobiocatalytic System

The main setback in the design of a photobiocatalyst is the requirement of a mediator that should be capable to lessen the cofactor that subsequently will trigger the prosthetic group of the enzyme. The effectiveness of the photobiocatalytic system is strongly dependent on the type of mediator. Recent study has demonstrated the role of mediator on the biocatalytic potential of laccase enzyme (Könst et al. 2013). The laccase-mediator system is well recognized and has also been explored to promote alcohol dehydrogenase-mediated oxidation reactions (Aksu et al. 2009; Ferrandi et al. 2012). Laccase is proficient to oxidize NADPH to $NADP^+$ and acts as a cofactor for alcohol dehydrogenase to oxidize alcohols. An appropriate mediator plays a vital role in exchange electrons from the laccase center to oxidize NADPH.

It demonstrates that the laccase coupled with alcohol dehydrogenase facilitates the conversion of aerobic oxidation of alcohol. In this study, 18 mediators were monitored for the significant reduction of laccase. Out of these, three mediators including acetosyringone, syringaldehyde, and caffeic acid were the hyperproducer for the synthesis of NAD^+ (Könst et al. 2013). Other structurally closely related molecules are less inefficient for NAD^+ production. Thus, it is a major hurdle in predicting the potential mediator for every enzyme. In general, laccase signify an attractive approach for the aerobic production of oxidized nicotinamide cofactors ($NAD(P)^+$) to promote catalysis of alcohol dehydrogenase oxidation (Könst et al. 2013). Additionally, source of the biocatalyst and working conditions also regulate the performance of photobiocatalysis process. Apart from this, titanium dioxide, in the anatase crystal form, become known as an exceptional photocatalyst material for environmental decontamination (Fujishima and Zhang 2006). Titanium dioxide with anatase phase is a promising substrate for degradation of contaminants in air and water; its photocatalytic activities show only under ultraviolet light (Asahi et al. 2001; Ohno et al. 2004; Gole et al. 2004). To study the effect of p-doped TiO_2 for NAD^+ reduction, it was observed that visible light illumination facilitates the NADH production by using water as a sacrificial electron donor (Shi et al. 2006; Jagadale et al. 2008).

Rhodium cyclopentadiene organometallic complex is required as a mediator to transfer electrons from p-doped TiO_2 conduction band to NAD^+ (Esswein and Nocera 2007; Oppelt et al. 2014). This organometallic complex is coated on a redox-active electrode for the conversion of NAD^+ to NADH (Portenkirchner et al. 2013; Oppelt et al. 2014). It is well documented that organometallic rhodium complexes of the type $[RhCp^*(1,2\text{-diimine})H_2O]^{2+}$ (with 1,2-diimine being derivatives of 2,2′-bipyridine (bpy) or 1,10-phenanthroline; Cp* = pentamethylcyclopentadienyl) speed up the NADH production in the pH range from 7 to slightly basic solutions (Oppelt et al. 2014). In addition, p-doped TiO_2 nanomaterial also exhibits stronger visible light absorption as compared to the pristine sample due to an impurity energy level formation within the bandgap of TiO_2. Correspondingly, p-doped TiO_2 nanomaterials show higher ability of NADH photogeneration in the visible light irradiation than pure TiO_2 (Shi et al. 2006). It was reported that the effect of doping regulates the NADH production. Percentage of p-doping up to 6% on TiO_2 renders maximum NADH yield. Researchers attributed the higher photobiocatalytic performance in the visible light due to the higher surface area and narrowing down of the bandgap (Antonio et al. 2015).

Asahi et al. (2001) reported that N-doped TiO_2 shows photoabsorption at longer wavelengths and improved photocatalytic activity such as degradations of the methylene blue dye. Ohno et al. (2004) have synthesized chemically modified titanium dioxide photocatalysts with a substitution of some of the lattice titanium atoms with S^{4+} or S^{2-}. The modified photobiocatalyst exhibited a strong absorption for visible light and high photobiocatalytic activities for degradation of methylene blue, 2-propanol, and adamantane under irradiation at a longer wavelength of 440 nm. Hence, the sulfur-coated titanium dioxide shows a strong antibacterial effect in the visible light. X-ray photoelectron spectra studies of sulfur-doped TiO_2 particles confirmed the oxidation state of S^{4+} (Ohno et al. 2004). Khan et al. (2002) performed the controlled combustion of titanium metal in a natural gas flame in order to develop a modified C-coated TiO_2. C-doped TiO_2 exhibited high visible light absorption. Theoretical calculations using full-potential linearized augmented plane wave formalism method further endorsed the experimental findings (Ohno et al. 2004). Recently many studies were carried out in the discovery of organic mediator. It led to a search of suitable bipyridinium ions analogous to NAD^+ structure that act as noble mediator and accept hydride ions (Antonio et al. 2015).

Glutathione reductase plays an important role in the regulation of glutathione (Antonio et al. 2015). Glutathione, an oligopeptide of three amino acids, has antioxidant properties that regulate the oxidative stress in the cell. Glutathione reductase regulates the redox pair governed by glutathione and its oxidized derivative. The study reported the activation mechanism of glutathione reductase with the aid of an organic mediator. Bipyridinium compound, the $[Ru(bpy)^3]^{2+}$, works in collaboration with this enzyme in the presence of visible light (Willner et al. 1994). The triplet excited state of the photosensitizer is quenched by the bipyridinium ion that renders electron transfer from the electron donor photosensitizer to the electron acceptor bipyridinium. Thus, covalently bound bipyridinium to the enzyme behaved as electron transporter without the aid of natural cofactor.

It is obvious from the above-cited few studies that enzyme-mediated photocatalysis, a greener process, has improved significantly the yield of many photocatalysis processes.

7.4 Conclusion

One of the foremost details in photobiocatalysis is to handle the likelihood to avoid the utilization of mediators and even cofactors by transferring directly electrons from the semiconductor surface to the active site of the biocatalyst (Antonio et al. 2015). As the field of photobiocatalysis is still nascent and also the current systems far away from achieving optimum performance, the future work ought to deal the issue to resolve in a proficient way that are the simplest mediators to transfer electrons from the photocatalyst to the natural cofactor. The possibility to straightway inject the electrons from the semiconductor to the active center of some enzymes ought to be determined. Understanding of the interaction between intermediator and natural cofactor and therefore possibility to activate directly the biocatalyst by the semiconductor may also be vital to expand the kind of enzymes and processes which will be promoted by photobiocatalysis (Antonio et al. 2015). Currently, noble metals, either coordination complexes or organometallic complexes, are directly involved in electron transfer from the semiconductor surface to the biocatalyst active site (Shaikh 2014), but the exploration for improved efficiencies, enantioselectivities, or recycling continues to be a matter of intense researches. The organic mediators with quinine or its derivative structure or alternative organic redox pairs ought to be explored to design new processes. The possibility of the biocatalyst activation without cofactor(s) will improve significantly the operation of photobiocatalytic systems by using conduction band electrons of excited semiconductors. Thus, it is opined with discussion that photobiocatalysis has improved considerably the efficiency of many processes.

References

Aksu S, Arends IW, Hollmann F (2009) A new regeneration system for oxidized nicotinamide cofactors. Adv Synth Catal 351(9):1211–1216. https://doi.org/10.1002/adsc.200900033

Amalric L, Guillard C, Pichat P (1994) Use of catalase and superoxide dismutase to assess the roles of hydrogen peroxide and superoxide in the TiO_2 or ZnO photocatalytic destruction of 1, 2-dimethoxybenzene in water. Res Chem Intermed 20(6):579–594. https://doi.org/10.1163/156856794X00234

Ameta R, Solanki MS, Benjamin S, Ameta SC (2018) Photocatalysis. In: Ameta SC, Ameta R (eds) Advanced oxidation processes for waste water treatment. Academic, London, pp 135–175. https://doi.org/10.1016/B978-0-12-810499-6.00006-1

Antonio JMA, Corma A, Garcia H (2015) Photobiocatalysis: the power of combining photocatalysis and enzymes. Chem Eur J 21(31):10940–10959. https://doi.org/10.1002/chem.201406437

Asahi RY, Morikawa TA, Ohwaki T, Aoki K, Taga Y (2001) Visible-light photocatalysis in nitrogen-doped titanium oxides. Science 293(5528):269–271. https://doi.org/10.1126/science.1061051

Babot ED, del Río JC, Kalum L, Martínez AT, Gutiérrez A (2013) Oxyfunctionalization of aliphatic compounds by a recombinant peroxygenase from *Coprinopsiscinerea*. Biotechnol Bioeng 110 (9):2323–2332. https://doi.org/10.1002/bit.24904

Blake DM, Maness PC, Huang Z, Wolfrum EJ, Huang J, Jacoby WA (1999) Application of the photocatalytic chemistry of titanium dioxide to disinfection and the killing of cancer cells. Sep Purif Methods 28:1–50. https://doi.org/10.1080/03602549909351643

Bryson (2004) A short history of nearly everything. Black Swan, p 362. https://www.penguin.co.uk/books/1004856/a-short-history-of-nearly-everything/9781409095484.html

Cao B, Cao S, Dong P, Gao J, Wang J (2013) High antibacterial activity of ultrafine TiO_2/graphene sheets nanocomposites under visible light irradiation. Mater Lett 93:349–352. https://doi.org/10.1016/j.matlet.2012.11.136

Cargnello M, Fornasiero P (2010) Photocatalysis by nanostructured TiO_2 based semiconductors. In: Selva M, Perosa A (eds) Handbook of green chemistry, green nanoscience. Wiley-VCH, Weinheim. https://doi.org/10.1002/9783527628698.hgc088

Chen D, Zhang H, Li X, Li J (2010) Biofunctional titania nanotubes for visible-light-activated photoelectrochemical biosensing. Anal Chem 82(6):2253–2261. https://doi.org/10.1021/ac9021055

Churakova E (2014) Novel approaches for biocatalytic oxyfunctionalization reactions. TU Delft, Delft University of Technology. https://doi.org/10.4233/uuid:421f5969-82bb-4978-94f7-b393ed455d3f

Darnell JE, Lodish H, Baltimore D (1990) Molecular cell biology. Scientific American Books, New York. https://www.ncbi.nlm.nih.gov/books/NBK21475/

De Silva AP, Gunaratne HN, Gunnlaugsson T, Huxley AJ, McCoy CP, Rademacher JT, Rice TE (1997) Signaling recognition events with fluorescent sensors and switches. Chem Rev 97 (5):1515–1566. https://doi.org/10.1021/cr960386p

Drauz K, Gröger H, May O (eds) (2012) Enzyme catalysis in organic synthesis. Wiley-VCH, Weinheim. https://doi.org/10.1002/anie.201304466

Esswein AJ, Nocera DG (2007) Hydrogen production by molecular photocatalysis. Chem Rev 107 (10):4022–4047. https://doi.org/10.1021/cr050193e

Ferrandi EE, Monti D, Patel I, Kittl R, Haltrich D, Riva S, Ludwig R (2012) Exploitation of a laccase/meldola's blue system for NAD^+ regeneration in preparative scale hydroxysteroid dehydrogenase-catalyzed oxidations. Adv Synth Catal 354(14–15):2821–2828. https://doi.org/10.1002/adsc.201200429

Frank SN, Bard AJ (1977) Heterogeneous photocatalytic oxidation of cyanide ion in aqueous solutions at titanium dioxide powder. J Am Chem Soc 99:303–304. https://doi.org/10.1021/ja00443a081

Fujishima A, Honda K (1972) Electrochemical photolysis of water at a semiconductor electrode. Nature 238:37–38. https://doi.org/10.1038/238037a0

Fujishima A, Zhang X (2006) Titanium dioxide photocatalysis: present situation and future approaches. C R Chim 9(5-6):750–760. https://doi.org/10.1016/j.crci.2005.02.055

Gole JL, Stout JD, Burda C, Lou Y, Chen X (2004) Highly efficient formation of visible light tunable TiO2-x N x photocatalysts and their transformation at the nanoscale. J Phys Chem B108 (4):1230–1240. https://doi.org/10.1021/jp030843n

Gratzel M (2012) Editor. Energy resources through photochemistry and catalysis. Elsevier. https://www.sciencedirect.com/book/9780122957208

Grobe G, Ullrich R, Pecyna MJ, Kapturska D, Friedrich S, Hofrichter M, Scheibner K (2011) High-yield production of aromatic peroxygenase by the agaric fungus *Marasmius rotula*. AMB Express 1(1):31. https://doi.org/10.1186/2191-0855-1-31

Hao S, Wu J, Huang Y, Lin J (2006) Natural dyes as photosensitizers for dye-sensitized solar cell. Sol Energy 80(2):209–214. https://doi.org/10.1016/j.solener.2005.05.009

Hara M, Kondo T, Komoda M, Ikeda S, Kondo JN, Domen K, Hara M, Shinohara K, Tanaka A (1998) Cu_2O as a photocatalyst for overall water splitting under visible light irradiation. Chem Commun:357–358. https://doi.org/10.1039/A707440I

Havel J, Weuster-Botz D (2007) Cofactor regeneration in phototrophic cyanobacteria applied for asymmetric reduction of ketones. Appl Microbiol Biotechnol 75(5):1031–1037. https://doi.org/10.1007/s00253-007-0910-3

Hernández-Alonso MD, Fresno F, Suárez S, Coronado JM (2009) Development of alternative photocatalysts to TiO_2: challenges and opportunities. Energy Environ Sci 2:1231–1257. https://doi.org/10.1039/B907933E

Hirakawa H, Shiota S, Shiraishi Y, Sakamoto H, Ichikawa S, Hirai T (2016) Au nanoparticles supported on $BiVO_4$: effective inorganic photocatalysts for H_2O_2 production from water and O_2 under visible light. ACS Catal 6(8):4976–4982. https://doi.org/10.1021/acscatal.6b01187

Hisatomi T, Kubota J, Domen K (2014) Recent advances in semiconductors for photocatalytic and photoelectrochemical water splitting. Chem Soc Rev 43:7520–7535. https://doi.org/10.1039/C3CS60378D

Hollmann F, Arends IW, Buehler K (2010) Biocatalytic redox reactions for organic synthesis: nonconventional regeneration methods. Chem Cat Chem 2(7):762–782. https://doi.org/10.1002/cctc.201000069

Hollmann F, Arends IW, Buehler K, Schallmey A, Bühler B (2011) Enzyme-mediated oxidations for the chemist. Green Chem 13(2):226–265. https://doi.org/10.1039/C0GC00595A

Holtmann D, Hollmann F (2016) The oxygen dilemma: a severe challenge for the application of monooxygenases? Chembio Chem 17(15):1391–1398. https://doi.org/10.1002/cbic.201600176

Hsiao CY, Lee CL, Ollis DF (1983) Heterogeneous photocatalysis: degradation of dilute solutions of dichloromethane (CH_2Cl_2), chloroform ($CHCl_3$), and carbon tetrachloride (CCl_4) with illuminated TiO_2 photocatalyst. J Catal 82:418–423. https://doi.org/10.1016/0021-9517(83)90208-7

Imahori H, Umeyama T, Ito S (2009) Large π-aromatic molecules as potential sensitizers for highly efficient dye-sensitized solar cells. Acc Chem Res 42(11):1809–1818. https://doi.org/10.1021/ar900034t

Inoue T, Fujishima A, Konishi S, Honda K (1979) Photoelectrocatalytic reduction of carbon dioxide in aqueous suspensions of semiconductor powders. Nature 277:637–638. https://doi.org/10.1038/277637a0

Iwase A, Ng YH, Ishiguro Y, Kudo A, Amal R (2011) Reduced graphene oxide as a solid-state electron mediator in z-scheme photocatalytic water splitting under visible light. J Am Chem Soc 133:11054–11057. https://doi.org/10.1021/ja203296z

Jagadale TC, Takale SP, Sonawane RS, Joshi HM, Patil SI, Kale BB, Ogale SB (2008) N-doped TiO_2 nanoparticle based visible light photocatalyst by modified peroxide sol-gel method. J Phys Chem C 112(37):14595–14602. https://doi.org/10.1021/jp803567f

Kemp KC, Seema H, Saleh M, Le NH, Mahesh K, Chandra V, Kim KS (2013) Environmental applications using graphene composites: water remediation and gas adsorption. Nanoscale 5:3149–3171. https://doi.org/10.1039/C3NR33708A

Khan SU, Al-Shahry M, Ingler WB (2002) Efficient photochemical water splitting by a chemically modified n-TiO_2. Science 297(5590):2243–2245. https://doi.org/10.1126/science.1075035

Khan MM, Adil SF, Al-Mayouf A (2015) Metal oxides as photocatalysts. J Saudi Chem Soc 19:462–464. https://doi.org/10.1016/j.jscs.2015.04.003

Kim JH, Lee SH, Lee JS, Lee M, Park CB (2011) Zn-containing porphyrin as a biomimetic light-harvesting molecule for biocatalyzed artificial photosynthesis. Chem Commun 47(37):10227–10229. https://doi.org/10.1039/C1CC12222C

Kim JH, Nam DH, Park CB (2014) Nanobiocatalytic assemblies for artificial photosynthesis. Curr Opin Biotechnol 28:1–9. https://doi.org/10.1016/j.copbio.2013.10.008

Kofuji Y, Ohkita S, Shiraishi Y, Sakamoto H, Tanaka S, Ichikawa S, Hirai T (2016) Graphitic carbon nitride doped with biphenyl diimide: efficient photocatalyst for hydrogen peroxide production from water and molecular oxygen by sunlight. ACS Catal 6(10):7021–7029. https://doi.org/10.1021/acscatal.6b02367

Kojima H, Okada A, Takeda S, Nakamura K (2009) Effect of carbon dioxide concentrations on asymmetric reduction of ketones with plant-cultured cells. Tetrahedron Lett 50(50):7079–7081. https://doi.org/10.1016/j.tetlet.2009.10.002

Könst P, Kara S, Kochius S, Holtmann D, Arends IW, Ludwig R, Hollmann F (2013) Expanding the scope of laccase-mediator systems. ChemCatChem 5(10):3027–3032. https://doi.org/10.1002/cctc.201300205

Krieg T, Hüttmann S, Mangold KM, Schrader J, Holtmann D (2011) Gas diffusion electrode as novel reaction system for an electro-enzymatic process with chloroperoxidase. Green Chem 13 (10):2686–2689. https://doi.org/10.1039/C1GC15391A

Kumar A, Kumar A, Sharma G et al (2017) Solar-driven photodegradation of 17-β-estradiol and ciprofloxacin from waste water and CO2 conversion using sustainable coal-char/polymeric-g-C3N4/RGO metal-free nano-hybrids. New J Chem 41:10208–10224. https://doi.org/10.1039/c7nj01580a

Kumar A, Sharma SK, Sharma G et al (2019) Wide spectral degradation of Norfloxacin by Ag@BiPO4/BiOBr/BiFeO3 nano-assembly: elucidating the photocatalytic mechanism under different light sources. J Hazard Mater 364:429–440. https://doi.org/10.1016/j.jhazmat.2018.10.060

Lan Y, Lu Y, Ren Z (2013) Mini review on photocatalysis of titanium dioxide nanoparticles and their solar applications. Nano Energy 2:1031–1045. https://doi.org/10.1016/j.nanoen.2013.04.002

Lang ND, Kohn W (1970) Theory of metal surfaces: charge density and surface energy. Phys Rev B 1:4555–4568. https://doi.org/10.1103/PhysRevB.1.4555

Lee SH, Choi DS, Kuk SK, Park CB (2018) Photobiocatalysis: activating redox enzymes by direct or indirect transfer of photoinduced electrons. Angew Chem Int EdEng l57(27):7958–7985. https://doi.org/10.1002/anie.201710070

Liu S, Chen A (2005) Coadsorption of horseradish peroxidase with thionine on TiO_2 nanotubes for biosensing. Langmuir 21(18):8409–8413. https://doi.org/10.1021/la050875x

Maeda K, Domen K (2010) Photocatalytic water splitting: recent progress and future challenges. J Phys Chem Lett 1(18):2655–2661. https://doi.org/10.1021/jz1007966

Mifsud M, Gargiulo S, Iborra S, Arends IW, Hollmann F, Corma A (2014) Photobiocatalytic chemistry of oxidoreductases using water as the electron donor. Nat Commun 5:3145. https://doi.org/10.1038/ncomms4145

Mitoraj D, Janczyk A, Strus M, Kisch H, Stochel G, Heczko PB, Macyk W (2007) Visible light inactivation of bacteria and fungi by modified titanium dioxide. Photochem Photobiol Sci 6:642–648. https://doi.org/10.1039/B617043A

Molina-Espeja P, Garcia-Ruiz E, Gonzalez-Perez D, Ullrich R, Hofrichter M, Alcalde M (2014) Directed evolution of unspecific peroxygenase from *Agrocybe aegerita*. Appl Environ Microbiol 80:3496–3507. https://doi.org/10.1128/AEM.00490-14

Monti D, Ottolina G, Carrea G, Riva S (2011) Redox reactions catalyzed by isolated enzymes. Chem Rev 111(7):4111–4140. https://doi.org/10.1021/cr100334x

Muruganandham M, Chen IS, Wu JJ (2009) Effect of temperature on the formation of macroporous ZnO bundles and its application in photocatalysis. J Hazard Mater 172:700–706. https://doi.org/10.1016/j.jhazmat.2009.07.053

Nakamura K, Yamanaka R (2002) Light mediated cofactor recycling system in biocatalytic asymmetric reduction of ketone. Chem Commun (16):1782–1783. https://doi.org/10.1039/B203844G

Nakamura K, Yamanaka R, Matsuda T, Harada T (2003) Recent developments in asymmetric reduction of ketones with biocatalysts. Tetrahedron Asymm 14(18):2659–2681. https://doi.org/10.1016/S0957-4166(03)00526-3

Nam DH, Park CB (2012) Visible light-driven NADH regeneration sensitized by proflavine for biocatalysis. Chembiochem 13(9):1278–1282. https://doi.org/10.1002/cbic.201200115

Naushad M, ALOthman ZA (2015) Separation of toxic Pb2+ metal from aqueous solution using strongly acidic cation-exchange resin: analytical applications for the removal of metal ions from pharmaceutical formulation. Desalin Water Treat 53:2158–2166. https://doi.org/10.1080/19443994.2013.862744

Neto AC, Guinea F, Peres NM, Novoselov KS, Geim AK (2009) The electronic properties of graphene. Rev Mod Phys 81:109–162. https://doi.org/10.1103/RevModPhys.81.109

Ni Y, Fernández-Fueyo E, Baraibar AG, Ullrich R, Hofrichter M, Yanase H, Alcalde M, van Berkel WJ, Hollmann F (2016) Peroxygenase-catalyzed oxyfunctionalization reactions promoted by the complete oxidation of methanol. Angew Chem Int Ed 55(2):798–801. https://doi.org/10.1002/anie.201507881

Ohno T, Akiyoshi M, Umebayashi T, Asai K, Mitsui T, Matsumura M (2004) Preparation of S-doped TiO_2 photocatalysts and their photocatalytic activities under visible light. Appl Catal A Gen 265(1):115–121. https://doi.org/10.1016/j.apcata.2004.01.007

Okamoto KI, Yamamoto Y, Tanaka H, Tanaka M, Itaya A (1985) Heterogeneous photocatalytic decomposition of phenol over TiO_2 powder. B Chem Soc Jpn 58(7):2015–2022. https://doi.org/10.1246/bcsj.58.2015

Oppelt KT, Gasiorowski J, Egbe DA, Kollender JP, Himmelsbach M, Hassel AW, Sariciftci NS, Knör G (2014) Rhodium-coordinated poly (arylene-ethynylene)-alt-poly (arylene-vinylene) copolymer acting as photocatalyst for visible-light-powered NAD^+/NADH reduction. J Am Chem Soc 136(36):12721–12729. https://doi.org/10.1021/ja506060u

Pal AK, Hanan GS (2014) Design, synthesis and excited-state properties of mononuclear Ru (II) complexes of tridentate heterocyclic ligands. Chem Soc Rev 43(17):6184–6197. https://doi.org/10.1039/C4CS00123K

Patel RN (2016) Editor. Green biocatalysis. Wiley. https://doi.org/10.1002/9781118828083

Piontek K, Strittmatter E, Ullrich R, Gröbe G, Pecyna MJ, Kluge M, Scheibner K, Hofrichter M, Plattner DA (2013) Structural basis of substrate conversion in a new aromatic peroxygenase: P450 functionality with benefits. J Biol Chem 288:34767–34776. https://doi.org/10.1074/jbc.M113.514521

Portenkirchner E, Oppelt K, Egbe DA, Knör G, Sariçiftçi NS (2013) Electro-and photo-chemistry of rhenium and rhodium complexes for carbon dioxide and proton reduction: a mini review. Nanomater Energy 2(3):134–147. https://doi.org/10.1680/nme.13.00004

Qu Y, Duan X (2013) Progress, challenge and perspective of heterogeneous photocatalysts. Chem Soc Rev 42(7):2568–2580. https://doi.org/10.1039/C2CS35355E

Rauch M, Schmidt S, Arends IW, Oppelt K, Kara S, Hollmann F (2017) Photobiocatalytic alcohol oxidation using LED light sources. Green Chem 19(2):376–379. https://doi.org/10.1039/C6GC02008A

Rodriguez C, Lavandera I, Gotor V (2012) Recent advances in cofactor regeneration systems applied to biocatalyzed oxidative processes. Curr Org Chem 16(21):2525–2541. https://doi.org/10.2174/138527212804004643

Saito T, Iwase T, Horie J, Morioka T (1992) Mode of photocatalytic bactericidal action of powdered semiconductor TiO_2 on mutans streptococci. J Photochem Photobiol B Biol 14:369–379. https://doi.org/10.1016/1011-1344(92)85115-B

Schoell SJ, Oliveros A, Steenackers M, Saddow SE, Sharp ID (2012) Multifunctional SiC surfaces: from passivation to biofunctionalization. Silicon Carbide Biotechnol:63–117. https://doi.org/10.1016/B978-0-12-385906-8.00003-9

Schulz S, Girhard M, Urlacher VB (2012) Biocatalysis: key to selective oxidations. ChemCatChem 4(12):1889–1895. https://doi.org/10.1002/cctc.201200533

Sekar N, Ramasamy RP (2015) Recent advances in photosynthetic energy conversion. J Photochem Photobiol Photochem Rev 22:19–33. https://doi.org/10.1016/j.jphotochemrev.2014.09.004

Shaikh IR (2014) Organocatalysis: key trends in green synthetic chemistry, challenges, scope towards heterogenization, and importance from research and industrial point of view. J Catal. https://doi.org/10.1155/2014/402860

Sharma G, Naushad M, Al-Muhtaseb AH et al (2017) Fabrication and characterization of chitosan-crosslinked-poly(alginic acid) nanohydrogel for adsorptive removal of Cr(VI) metal ion from aqueous medium. Int J Biol Macromol 95:484–493. https://doi.org/10.1016/j.ijbiomac.2016.11.072

Shasha Z, Dunwei W (2017) Photocatalysis: basic principles, diverse forms of implementations and emerging scientific opportunities. Adv Energy Mater 7:1700841. https://doi.org/10.1002/aenm.201700841

Shi Q, Yang D, Jiang Z, Li J (2006) Visible-light photocatalytic regeneration of NADH using P-doped TiO_2 nanoparticles. J Mol Catal B Enzym 43(1–4):44–48. https://doi.org/10.1016/j.molcatb.2006.06.005

Sreeprasad TS, Berry V (2013) How do the electrical properties of graphene change with its functionalization? Small 9:341–350. https://doi.org/10.1002/smll.201202196

Takemura T, Akiyama K, Umeno N, Tamai Y, Ohta H, Nakamura K (2009) Asymmetric reduction of a ketone by knockout mutants of a cyanobacterium. J Mol Catal B Enzym 60(1-2):93–95. https://doi.org/10.1016/j.molcatb.2009.03.017

Te-Fu Y, Chiao-Yi T, Shean-Jen C, Hsisheng T (2014) Nitrogen-doped graphene oxide quantum dots as photocatalysts for overall water-splitting under visible light illumination. Adv Mater 26:3297–3303. https://doi.org/10.1002/adma.201305299

Trost BM (1991) The atom economy – a search for synthetic efficiency. Science 254:1471–1477. https://doi.org/10.1126/science.1962206

Tuller HL (2017) Solar to fuels conversion technologies: a perspective. Mater Renew Sustain Energy 6(1):3. https://doi.org/10.1007/s40243-017-0088-2

Ullrich R, Nüske J, Scheibner K, Spantzel J, Hofrichter M (2004) Novel haloperoxidase from the agaric basidiomycete *Agrocybe aegerita* oxidizes aryl alcohols and aldehydes. Appl Environ Microbiol 70(8):4575–4581. https://doi.org/10.1128/AEM.70.8.4575-4581.2004

Urlacher VB, Girhard M (2012) Cytochrome P450 monooxygenases: an update on perspectives for synthetic application. Trends Biotechnol 30(1):26–36. https://doi.org/10.1016/j.tibtech.2011.06.012

Urlacher V, Schmid RD (2002) Biotransformations using prokaryotic P450 monooxygenases. Curr Opin Biotechnol 13(6):557–564. https://doi.org/10.1016/S0958-1669(02)00357-9

Van der Donk WA, Zhao H (2003) Recent developments in pyridine nucleotide regeneration. Curr Opin Biotechnol 14(4):421–426. https://doi.org/10.1016/S0958-1669(03)00094-6

van Rantwijk F, Sheldon RA (2000) Selective oxygen transfer catalysed by heme peroxidases: synthetic and mechanistic aspects. Curr Opin Biotechnol 11(6):554–564. https://doi.org/10.1016/S0958-1669(00)00143-9

Wang S, Ang PK, Wang Z, Tang ALL, Thong JTL, Loh KP (2010) High mobility, printable, and solution-processed graphene electronics. Nano Lett 10:92–98. https://doi.org/10.1021/nl9028736

Wang Y, Yu J, Xiao W, Li Q (2014) Microwave-assisted hydrothermal synthesis of graphene based Au-TiO_2 photocatalysts for efficient visible-light hydrogen production. J Mater Chem A 2:3847–3855. https://doi.org/10.1039/C3TA14908K

Wang Y, Lan D, Durrani R, Hollmann F (2017) Peroxygenases en route to becoming dream catalysts. What are the opportunities and challenges? Curr Opin Chem Biol 37:1–9. https://doi.org/10.1016/j.cbpa.2016.10.007

Weckbecker A, Gröger H, Hummel W (2010) Regeneration of nicotinamide coenzymes: principles and applications for the synthesis of chiral compounds. In: Biosystems engineering I: creating superior biocatalysts. Springer, Berlin, pp 195–242. https://doi.org/10.1007/10_2009_55

Wenguang T, Young Z, Qi L, Shicheng Y, Shanshan B, Xiaoyong W, Min X, Zhigang Z (2013) An *in situ* simultaneous reduction-hydrolysis technique for fabrication of TiO_2-graphene 2D sandwich-like hybrid nanosheets: graphene-promoted selectivity of photocatalytic-driven hydrogenation and coupling of CO_2 into methane and ethane. Adv Funct Mater 23:1743–1749. https://doi.org/10.1002/adfm.201202349

Willner I, Lapidot N, Riklin A, Kasher R, Zahavy E, Katz E (1994) Electron-transfer communication in glutathione reductase assemblies: electrocatalytic, photocatalytic, and catalytic systems for the reduction of oxidized glutathione. J Am Chem Soc 116(4):1428–1441. https://doi.org/10.1021/ja00083a031

Wu H, Tian C, Song X, Liu C, Yang D, Jiang Z (2013) Methods for the regeneration of nicotinamide coenzymes. Green Chem 15(7):1773–1789. https://doi.org/10.1039/C3GC37129H

Xin L, Yu J, Wageh S, Al-Ghamdi A, Xie J (2016) Graphene in photocatalysis: a review. Small 12:6640–6696. https://doi.org/10.1002/smll.201600382

Xu X, Ni Q (2010) Synthesis and characterization of novel Bi_2MoO_6/NaY materials and photocatalytic activities under visible light irradiation. Catal Commun 11:359–363. https://doi.org/10.1016/j.catcom.2009.11.001

Yamanaka R, Nakamura K, Murakami A (2011) Reduction of exogenous ketones depends upon NADPH generated photosynthetically in cells of the cyanobacterium *Synechococcus* PCC 7942. AMB Express 1(1):24. https://doi.org/10.1186/2191-0855-1-24

Yee MC, Bartholomew JC (1989) Effects of 3-(3, 4-dichlorophenyl)-1, 1-dimethylurea on the cell cycle in *Euglena gracilis*. Plant Physiol 91(3):1025–1029. https://doi.org/10.1104/pp.91.3.1025

Yemmireddy VK, Hung YC (2017) Using photocatalyst metal oxides as antimicrobial surface coatings to ensure food safety-opportunities and challenges. Compr Rev Food Sci F 16:617–631. https://doi.org/10.1111/1541-4337.12267

Yu J, Jin J, Cheng B, Jaroniec M (2014) A noble metal-free reduced graphene oxide-CdS nanorod composite for the enhanced visible-light photocatalytic reduction of CO_2 to solar fuel. J Mater Chem A 2:3407–3416. https://doi.org/10.1039/C3TA14493C

Zhang Y, He P, Hu N (2004) Horseradish peroxidase immobilized in TiO_2 nanoparticle films on pyrolytic graphite electrodes: direct electrochemistry and bioelectrocatalysis. Electrochim Acta 49(12):1981–1998. https://doi.org/10.1016/j.electacta.2003.12.028

Zhang P, Zhang J, Gong J (2014) Tantalum-based semiconductors for solar water splitting. Chem Soc Rev 43:4395–4422. https://doi.org/10.1039/C3CS60438A

Zhang W, Fernández-Fueyo E, Ni Y, van Schie M, Gacs J, Renirie R, Wever R, Mutti FG, Rother D, Alcalde M, Hollmann F (2018) Selective aerobic oxidation reactions using a combination of photocatalytic water oxidation and enzymatic oxyfunctionalizations. Nat Catal 1(1):55. https://doi.org/10.1038/s41929-017-0001-5

Zhou L, Zhang H, Sun H, Liu S, Tade MO, Wang S, Jin W (2016) Recent advances in non-metal modification of graphitic carbon nitride for photocatalysis: a historic review. Cat Sci Technol 6:7002–7023. https://doi.org/10.1039/C6CY01195K

Zhu XG, Long SP, Ort DR (2008) What is the maximum efficiency with which photosynthesis can convert solar energy into biomass? Curr Opin Biotechnol 19(2):153–159. https://doi.org/10.1016/j.copbio.2008.02.004

Chapter 8
Photo-/Electro-catalytic Applications of Visible Light-Responsive Porous Graphitic Carbon Nitride Toward Environmental Remediation and Solar Energy Conversion

Sulagna Patnaik, Gayatri Swain, and K. M. Parida

Contents

8.1 Introduction 212
  8.1.1 Shortcomings of g-C_3N_4 as a Photocatalyst 214
  8.1.2 Potential Solutions to Overcome the Disadvantages 214
8.2 An Insight into Porous g-C_3N_4 215
  8.2.1 Soft-Templating Methods for the Fabrication of Mesoporous g-C_3N_4 217
  8.2.2 Hard-Templating Methods for the Fabrication of Mesoporous g-C_3N_4 218
8.3 Photocatalytic Applications of Porous g-C_3N_4 220
  8.3.1 Applications of Porous g-C_3N_4 in Dye Degradation 221
  8.3.2 Applications of Porous g-C_3N_4 in Cr(VI) Reduction 227
  8.3.3 Applications of Porous g-C_3N_4 in CO_2 Reduction 229
  8.3.4 Applications of Porous g-C_3N_4 in Water Reduction Reactions for Solar Energy Conversion 234
8.4 Conclusion 240
References 243

Abstract Among various renewable energy projects, harvestation of clean solar energy through semiconductor-based photocatalysis is now emerging as a feasible technology and has gained considerable interdisciplinary attention for its diversified potential in energy and environmental applications. Until now, although a good number of photocatalytic materials were reported, g-C_3N_4 is found to be a promising material in a variety of applications. To introduce desirable electronic properties and more number of surface active sites, designing of nanoporous g-C_3N_4 has been recognized as one of the most agreeable avenues to extend its potential applications. In nanoporous g-C_3N_4 network, the highly interconnected pores render the material with high surface area, offer numerous pathways for mass transport and multiple

---

S. Patnaik · G. Swain · K. M. Parida (✉)
Centre for Nano Science and Nanotechnology, Siksha O Anusandhan
(Deemed to be University), Bhubaneswar, Odisha, India

S. Rajendran et al. (eds.), *Green Photocatalysts for Energy and Environmental Process*, Environmental Chemistry for a Sustainable World 36,
https://doi.org/10.1007/978-3-030-17638-9_8

reflection of incident light, and favor strong adsorption at the active sites. Here, we have highlighted how further control over porosity and morphology can be achieved by using different templates during formation. Large available surface not only absorbs the organic/inorganic pollutants effectively by offering more number of active sites but also prevents aggregation of particles by accelerating diffusion kinetics. This chapter mainly focused on various types of templates used for the preparation of porous g-C_3N_4 and its applications in detail with special reference to dye degradation, reduction of hexavalent Cr, and reduction of CO_2 and for the evolution of H_2 photocatalytically.

Keywords Nanoporous g-C_3N_4 · Dye degradation · Reduction of hexavalent Cr · Reduction of CO_2 and water reduction

8.1 Introduction

With rapid industrialization and population growth in the past few decades, the energy demand in globe is projected to be two times of the current requirement by 2050. This increases the challenges of sustainable energy development and environmental concerns in the present scenario (Elliot and Turner 1972; Root and Attanasi 1978). Due to the abundant availability, sunlight is considered as a resource, which enriches the scope of green chemistry (Naushad et al. 2019). In this context photochemical reactions possess advantages over other methods as they reduce formation of secondary pollutants and excess use of chemicals. Owing to which, photocatalysis has attracted intensive interest and potential for wide application in the field of clean energy development and pollution abatement (Kumar et al. 2019). In this context, search for a good photocatalyst has been a worldwide continuing endeavor (Zhu et al. 2014; Veziroglu and Basar 1974).

In the present era, making use of solar energy effectively, designing of photocatalytic materials is vastly studied by the scientists. In this regard, metal-free polymeric graphitic carbon nitride (g-C_3N_4) has elicited ripples of excitement in the field of research due to its robust nature and wealth of attractive properties. This polymeric metal-free organic semiconducting material (g-C_3N_4) is now emerging as a good photocatalyst with attractive properties like super hardness, reliable thermal and chemical stability, low density, easy preparation from earth's abundant materials, wear resistance, biocompatibility, and bandgap energy (2.7 eV) to harness visible light and tunable electronic properties (Zhu et al. 2014). It was first synthesized in the laboratory by Jöns Jakob Berzelius, father of modern chemistry, by heating mercuric thiocyanate [$Hg(SCN)_2$] and was named by Justus von Liebig in 1834 (Liebig 1834; Franklin 1922) (Fig. 8.1).

Actually, C_3N_4 exists in seven different phases, which are represented by the corresponding bandgap energies as α-C_3N_4 (5.49 eV), β-C_3N_4 (4.85 eV), cubic C_3N_4 (4.30 eV), pseudocubic C_3N_4 (4.13 eV), g-h-triazine (2.97 eV), g-o-triazine (0.93 eV), and g-h-heptazine (2.88 eV) (Wang et al. 2017a, b; Kumar et al. 2018). Different allotropic forms differ from each other due to diverse electronic

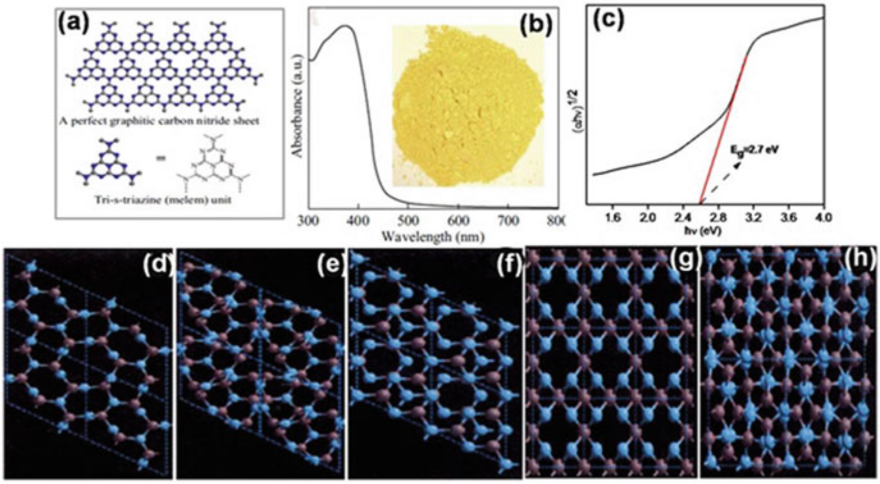

Fig. 8.1 Crystal structure and optical nature of g-C_3N_4. (**a**) Schematic illustration of sheet of graphitic carbon nitride made from melamine units, (**b**) UV-Vis DRS absorbance spectra and image (inset figure) of g-C_3N_4, (**c**) bandgap energy plot of g-C_3N_4, crystal representation of (**d**) β-C_3N_4, (**e**) α-C_3N_4, (**f**) g-C_3N_4, (**g**) pseudocubic-C_3N_4 and (**h**) cubic-C_3N_4. The carbon and nitrogen atoms are indicated as gray and blue spheres, respectively (Wang et al. 2017a, b)

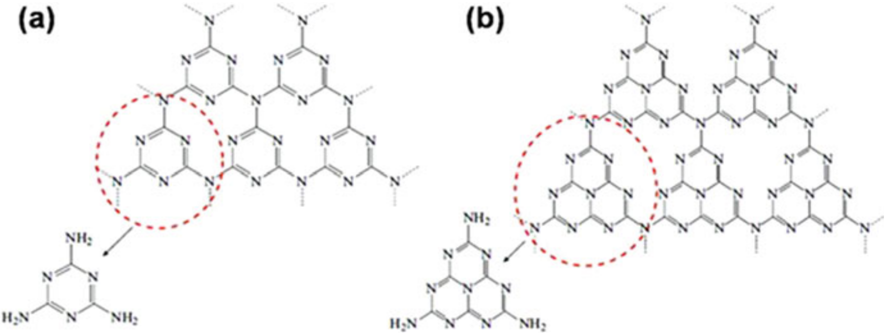

Fig. 8.2 Structural representation of (**a**) triazine (C_3N_3) and (**b**) tri-s-triazine/heptazine (C_6N_7) rings (Wang et al. 2017a, b)

environments around the N-atom. Among different analogs, graphitic C_3N_4 having triazine (C_3N_3) and tri-s-triazine (C_6N_7) rings are most stable due to minimum repulsive interaction between lone pairs of electrons present on the N-atom, and suitable size of the nitride pores (Fig. 8.2). Based on the contribution from various factors, tri-s-triazine is energetically favored with maximum bond distance at ambient conditions.

This novel nanostructured semiconducting material by harvesting solar energy was found to have significant impacts in the areas such as mineralization of pollutants from contaminated water, as a catalyst for NO decomposition, ability in the degradation of dyes, reduction of CO_2 into useful fuels, as a functional material to design various nano-sized metal particles, in solar energy conversion and also achieved functionality as a stable photocatalyst for organic transformations and finally in fuel cells (Patnaik et al. 2018a, b; OmoIbhadon and Fitzpatrick 2013; Hoffmann et al. 1995).

8.1.1 Shortcomings of g-C_3N_4 as a Photocatalyst

Although g-C_3N_4 has a good number of potential applications, the photocatalytic performance of g-C_3N_4 is not satisfactory due to (Zhang et al. 2012a, b; Zou et al. 2011; Guo et al. 2010):

1. The bulk layered structure hinders the migration of photogenerated charge carriers and thus increases the mass transfer resistance.
2. Fast recombination of charge carriers.
3. Neat g-C_3N_4 confines the utilization of the whole range of solar spectrum by only absorbing blue light up to 450 nm.
4. High degree of condensation during synthesis results in low surface area (~10 m^2/g) in the material without forming textured pores.
5. Grain boundary effect also hinders the delocalization of photogenerated electrons from the surface of the photocatalyst through the interface.

8.1.2 Potential Solutions to Overcome the Disadvantages

As a visible light active polymeric semiconducting material, g-C_3N_4 not only provides flexible channel to achieve controllable band edges but also makes the modification process simpler mainly by cationic/anionic doping or in the designing of heterojunction by coupling with other semiconducting materials, to broaden its applications (Kumar et al. 2017). Moreover, the interaction between the guest molecules through functional groups (–NH, N, NH_2) available on g-C_3N_4 results high optical sensitivity to make available large internal surface, for charge delocalization.

Designing of efficient g-C_3N_4-based photocatalytic material is mainly dependent on the surface area, particle size, morphology, availability of sufficient surface active sites, and improved light-absorbing capacity. Several imperative strategies to optimize the photocatalytic activity are summarized as (Patnaik et al. 2015, 2016):

1. Designing of texturally and morphologically controlled g-C_3N_4
2. Preparing mesoporous and ordered mesoporous g-C_3N_4
3. Doping with cationic/anionic species
4. Loading noble metal nanoparticles as co-catalysts
5. Constructing heterojunction/composite with transition metal/metal oxides
6. Incorporating conducting polymers to improve charge delocalization

In order to harvest solar radiation effectively in the whole spectrum, a semiconductor must have a suitable bandgap energy which corresponds well with the wavelength of the irradiated light. Various research groups reported modifications in g-C_3N_4 giving special emphasis on improving surface active sites by increasing surface area, by surface functionalization, loading noble metal nanoparticles as co-catalyst, designing composites/heterojunctions with transitional metal oxides/sulfides, etc. which can effectively change the electronic properties as well as the band edge potential of g-C_3N_4 to extend the absorption of light radiation. Although semiconductor hybridization and designing heterojunctions/composites with a proper semiconductor are effective strategies to extend the potential applications, a number of active sites, tunable pore diameter, and specific surface area also act an important role to achieve better efficiency in photo-catalytic activity by providing more number of reaction sites (Yang et al. 2015).

8.2 An Insight into Porous g-C_3N_4

Porous materials due to their accessible porosity and enhanced surface areas are especially attractive as heterogeneous catalysts for solar energy conversion and related photocatalytic reactions for environmental remediation. Based on the reported studies, it can be said that one major focus to enhance the photocatalytic performance of g-C_3N_4 is controlling particle size and specific surface area (Dong and Zhang 2012). Introducing porosity into the structure of bulk g-C_3N_4 results in more number of surface active sites, with superior photocatalytic performance. For surface modification, template modeling has been used long before to prepare mesoporous g-C_3N_4 materials with large internal surface area to extend its photocatalytic applications. By designing porous materials, the enhanced surface area plays an important role not only by improving mass transfer during the photocatalytic reaction but also providing more number of surface active sites. Moreover, the diffusion path of charge carriers from the bulk to the surface becomes shorter in case of porous materials and the recombination process during the photocatalytic reaction is also greatly suppressed (Patnaik et al. 2015; Zheng et al. 2012).

The most often used pathways for the designing of mesoporous g-C_3N_4 are mostly dependent on the use of templating methods, soft-templating method involving self-assembly (Fig. 8.3a), and hard-templating method involving nanocasting (Fig. 8.3b).

In these methods, a continuous porous framework with cylindrical or spherical mesopores and their inverse replicas can be obtained. In many cases also porous g-C_3N_4 can be obtained by simple calcination process from urea, thiourea, etc. Among which, urea results more porous structure due to lesser degree of condensation (Zhang et al. 2012a, b). Presence of more electronegative O-atom in urea is unfavorable for high degree of polycondensation due to presence of stronger hydrogen bond, which lowers the heat of polymerization in comparison to thiourea where

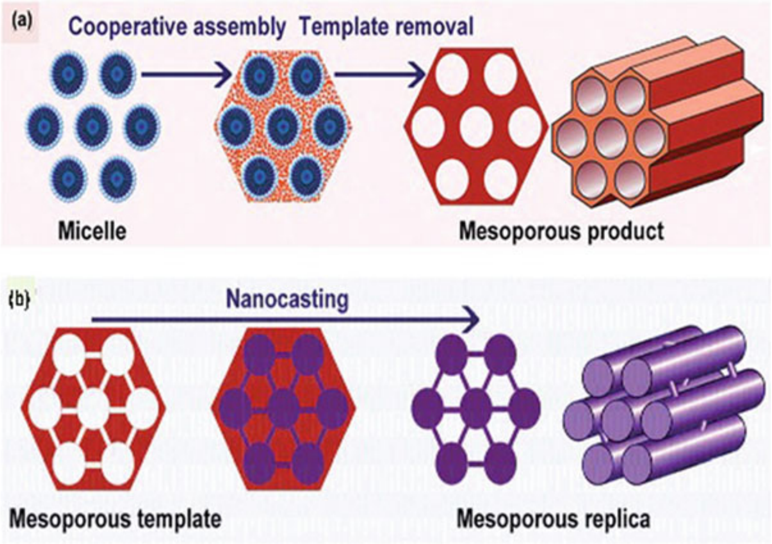

Fig. 8.3 Schematic representation of (**a**) soft-templating and (**b**) hard-templating technique for the synthesis of mesoporous-g-C_3N_4 (Zheng et al. 2012)

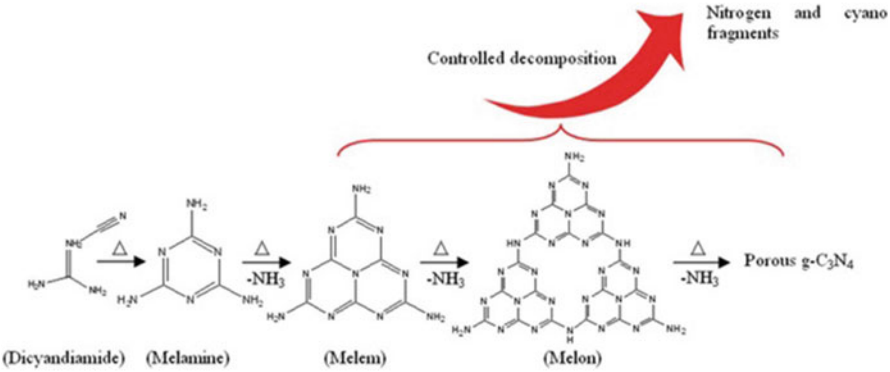

Fig. 8.4 Schematic representation of mechanism of polymerization of g-C_3N_4 (Zhang et al. 2012a, b)

the strength of hydrogen bond is comparatively less. In urea, stronger C–O with bond energy 385 kJ/mol decreases the rate of release of gases than in thiourea having bond energy 272 kJ/mol. Although self-generated NH_3 gas was liberated, pyrolysis with urea results less condensed and more porous structure. The formation of polymeric of g-C_3N_4 from different precursors is shown in Fig. 8.4.

8.2.1 Soft-Templating Methods for the Fabrication of Mesoporous g-C_3N_4

Designing of porous nanostructures of g-C_3N_4, soft-templating methods have witnessed great success. During the formation process, although the exact mechanism of templating is challenging, the constituent and properties of the templates play a decisive role in introducing porosity. Most commonly organic templates are used as surfactants and block copolymers to synthesize porous materials. To introduce various types of morphologies in crystal growth, the use of different templates is remarkable. One major challenge in the synthesis of porous carbon nitrides by using these molecular soft templates is their low stability.

In soft-templating method, cooperative assembly is often carried out under hydrothermal conditions to incorporate porosity in the network of g-C_3N_4. To obtain different pore diameters and specific surface area, the most frequently used soft templates are P123, Triton-X-100, F127, Brij30, Brij58, and Brij76 (Kumar et al. 2014). However, the designing of self-porous materials by soft templates is very difficult. In the process of designing of porous g-C_3N_4, the practical problem is the condensation temperature for the formation of polymeric C_3N_4-structures, which is nearly equal to the decomposition temperature of most of the soft templates. The general designing procedure involves dissolution of the soft template, and the g-C_3N_4 precursor, in water, dried at 100 °C in air and subjected to calcinations, results in the formation of porous g-C_3N_4 polymer along with simultaneous removal of the soft template during calcination. However, to get ordered porous g-C_3N_4, using soft templates is comparatively complicated for thermodynamic and physicochemical point of view. For example, preparation of porous g-C_3N_4 from bulk g-C_3N_4 obtained in the traditional approach is essentially inapplicable by using soft templates, since the use of surfactants usually promotes the generation of volatile intermediates and reduces the yield of the product. This problem can be overcome by introducing sequences of program at moderate temperatures to modulate the process of template decomposition and thermal condensation steps to suppress volatilization. Structural changes are expected owing to controlled condensation and rearrangements at moderate temperatures. Moreover, these soft templates are prone to hydrolysis due to relatively weak interactions with the starting materials, likely to cause various redox reactions, and undergo thermal breakdown during synthesis. The condensation temperature, nature of soft template, surface area, and pore volume are summarized in Table 8.1.

Along with the use of surfactants and block copolymers, some ionic liquids (ILs) are also reported to design porous g-C_3N_4 and behave as soft template (Yang et al. 2015; Han et al. 2013). The advantages of using ionic liquids are as follows: such liquids contain heteroatoms containing cations, which can easily be incorporated

Table 8.1 Represent the condensation temperature, surface area, and pore diameter of porous g-C_3N_4 synthesized by using various soft template

Template	Condensation temperature	Surface area in m^2 g^{-1}	Pore volume cm^3 g^{-1}	C/N ratio	References
Melamine/P123in 5:1 ratio	500 °C for 2 h	90 m^2 g^{-1}	–	–	Yan (2012)
Cyanuric acid, melamine, Pluronic F-127	500 °C for 4 h	200	0.6	1.6	Peer et al. (2017)
Cyanuric acid, melamine, Pluronic P123	500 °C for 4 h	158	0.54	0.70	Peer et al. (2017)
Triton X-100 and dicyanamide	500 °C for 4 h	92	–	0.82	Wang et al. (2010)
Dicyanamide $K_2Cr_2O_7$/ H_2SO_4	500 °C for 4 h	235.2	–	0.66	Fan et al. (2014)
Triton X-100-modified dicyanamide	550 °C for 4 h	116	0.89	0.284	Fan et al. (2014)
Dicyanamide and Bmim PF_6	550 °C for 4 h	81	0.179	0.81	Li et al. (2015)
Freeze-drying thiourea and NaCl	550 °C for 0.5 h	37	–	–	Chen et al. (2018)

into the porous template as well as into the crystal lattice. The higher thermal stability and lower vapor pressure of ILs also provide a valuable alternative to solvents through solid-state synthesis that is hybrid between sol-gel method and solid-state chemistry. Some commonly used ILs are 1-ethyl-3-methylimidazolium (EMIM) or 3-methyl-1-butylpyridine (3-MPB), *N*, *N*-dialkylimidazolium, etc. Using ILs as soft template has benefit of introducing dopants during the synthesis. Some studies also reported for the designing of porous g-C_3N_4 through gas bubbles as soft templates. In comparison to other templating methods use of gas bubbles as template is relatively simple, convenient and involves one-step process. Addition of $CaCO_3$, H_2SO_4, urea, sulfur, etc. during calcination simultaneously introduces porosity, removes impurity, and results in exfoliated sheetlike structures in majority. The condensation temperature, nature of gas bubble template, surface area, pore volume, and C/N ratio are summarized in Table 8.2.

8.2.2 *Hard-Templating Methods for the Fabrication of Mesoporous g-C_3N_4*

Hard-templating method, commonly known as nano-casting, has been extensively used to design porous g-C_3N_4-based composite materials. It involves filling/coating of a hard template with a precursor of g-C_3N_4, and finally the template is to be removed to get a duplicate model. The hard templates possess superiority over soft templates as these templates are easy to remove and able to form an exact replica. On

Table 8.2 Represent the condensation temperature, surface area, and pore diameter of porous g-C_3N_4 synthesized by using various gas bubble templates

Template	Condensation temperature	Surface area in $m^2\ g^{-1}$	Pore volume $cm^3\ g^{-1}$	C/N ratio	References
Adjustable window during calcination	550 °C for 5 h	201–209	0.5–0.52	0.659	Wang et al. (2012)
Bulk-g-CN in ethanol-water	Sonicated for 5 h	112.8	0.39		Kumar et al. (2014)
Urea and water	Calcined at 550 °C 2 h	106	0.68		Wang et al. (2015a, b)
Urea	Calcined at 550 °C 3 h	69.6	0.32	0.72	Zhang et al. (2012a, b)
Thiourea	Calcined at 550 °C 3 h	11.3	0.085	0.78	Zhang et al. (2012a, b)
Dicyanamide	Calcined at 550 °C 3 h	12.3	0.086	0.79	Zhang et al. (2012a, b)
Urea and HNO_3	Calcined at 550 °C 3 h	83.5	0.47	–	Xue et al. (2015)
Dicyanamide, $CaCO_3$, and water	Calcined at 400 °C 2 h	38.6	–	–	Wang et al. (2015a, b)
Bulk g-C_3N_4 and HCl	Calcined at 550 °C 2 h	15.95	–	0.99	Pawar et al. (2016)
Bulk g-C_3N_4 and HNO_3	Calcined at 550 °C 2 h	58.92	–	1.01	Pawar et al. (2016)
Bulk g-C_3N_4 and H_2SO_4	Calcined at 550 °C 2 h	32.05	–	1.97	Pawar et al. (2016)
Freeze-drying assembled dicyandiamide	600 °C 2 h	331	–	–	Han et al. (2016)
Melamine	550 °C for 4 h	190.1	0.61	–	Xu et al. (2017)
Freeze-drying assembled of GO and g-C_3N_4	Hydrothermally at 180 °C for 6 h	289.2	–	–	Tong et al. (2015)
Melamine hydrochloride	500 ° C for 2 h followed by 520 ° C for 2 h	69.0	–	–	Dong et al. (2016)
Melamine and urea	Hydrothermal treatment followed calcined at 520 ° C for 3 h	44.2	0.211	–	Huang et al. (2017)

Table 8.3 Represent the condensation temperature, surface area, and pore diameter of porous g-C_3N_4 synthesized by using various hard templates

Template	Condensation temperature	Surface area in $m^2\ g^{-1}$	Pore diameter $cm^3\ g^{-1}$	C/N ratio	References
Melamine and SBA-15	550 °C for 4 h	239	0.34	0.73	Chen et al. (2009)
Melamine and Ludox HS40	550 °C for 2 h	135	0.5	–	Lin et al. (2014)
Melamine and SiO_2	600 °C for 4 h	107.4	0.58	–	Zhao et al. (2017)
g-C_3N_4 and SBA-15	600 °C for 5 h	505	0.55	85.27	Xu et al. (2013)
Cyanamide and SBA-15	Hydrothermal treatment followed by calcination at 550 °C for 4 h	239.17	0.59	0.72	Jun et al. (2009)
Spherical mesostructured cellular silica foams and g-C_3N_4	400 °C for 2 h	183	0.18	–	Li et al. (2010)

the other hand, soft templates involve only a cooperative assembly between the inorganic phase and the surfactant (Kumar et al. 2014). Silica is the most commonly used material in hard-templating methods to obtain porous g-C_3N_4, due to its advantageous properties like tunable pore size, robustness, thermal stability, and easily controlled morphologies. By using silica as the template, the primary nanopores in silica result in formation of stable replica arrays to design nanoporous g-C_3N_4. Most commonly silica nanoparticles, 2D hexagonal SBA-15, IBN-4, 3D cubic KIT-6, etc. are used as hard templates (Zhao et al. 2017). When mesoporous-C_3N_4 was synthesized by means of silica nanoparticles, although there is an increase in specific surface area, the crystallinity decreases. Therefore, simultaneous increase in surface area and crystallinity is still a challenge. Moreover, the removal of most of the hard templates involves hazardous chemicals, and it is not environment friendly. Recently various template-free methods are explored to design porous g-C_3N_4 materials with better photocatalytic performance to overcome the difficulties in templating methods. The condensation temperature, nature of hard template, surface area, and pore volume are summarized in Table 8.3.

8.3 Photocatalytic Applications of Porous g-C_3N_4

Although fabrication of porous g-C_3N_4 in single-step calcination process is most agreeable, g-C_3N_4 nanosheets result during calcination are prone to aggregation due to high surface energy, during application process and makes the process unfavorable for photocatalytic reactions. Due to this severe disadvantage, generally designing of hierarchical nanoporous networks with more exposed surface area is beneficial to enhance light-harvesting capacity and facilitate diffusion kinetics for improved photocatalytic performance. In this regard some important visible light-induced photocatalytic applications are discussed with special reference to dye degradation, hexavalent chromium reduction, phenol oxidation, CO_2 reduction, NO oxidation, etc. (Jing et al. 2017)

8.3.1 Applications of Porous g-C_3N_4 in Dye Degradation

Organic dyes are now considered as most common pollutant in large-scale processes involving synthesis of printing, textiles, food industries, photography, etc. (Alqadami et al. 2016; Sharma et al. 2018). Even in low concentrations, these dyes possess serious threat to living organisms and are associated with great challenges in degradation, for which semiconductor-based photocatalysis involving advanced oxidation processes (AOP) offers an effective and economic solution. Photogenerated electrons and holes upon reacting with water and dissolved oxygen result in various powerful oxidants and attack the adsorbed pollutants to cause mineralization into CO_2 and H_2O. The brief mechanism of photocatalytic oxidation is as follows (Eqs. 8.1, 8.2, 8.3, 8.4, 8.5, 8.6, 8.7, 8.8, 8.9, 8.10, 8.11, and 8.12):

$$p-g-\mathrm{C_3N_4} \rightarrow p-g-\mathrm{C_3N_4}(\mathrm{e}^-) + p-g-\mathrm{C_3N_4}(\mathrm{h}^+) \tag{8.1}$$

$$p-g-\mathrm{C_3N_4}(\mathrm{e}^-) + \mathrm{O_2} \rightarrow \mathrm{O_2^{\cdot -}} \tag{8.2}$$

$$p-g-\mathrm{C_3N_4}(\mathrm{h}^+) + \mathrm{H_2O} \rightarrow \mathrm{OH^{\cdot}} + \mathrm{H^+} \tag{8.3}$$

$$\mathrm{O_2^{\cdot -}} + \mathrm{H^+} \rightarrow \mathrm{HO_2^{\cdot}} \tag{8.4}$$

$$\mathrm{O_2^{\cdot -}} + \mathrm{H_2O} \rightarrow \mathrm{OH^{\cdot}} + \mathrm{HO_2^{\cdot}} \tag{8.5}$$

$$\mathrm{HO_2^{\cdot}} + \mathrm{HO_2^{\cdot}} \rightarrow \mathrm{H_2O_2} + \mathrm{O_2} \tag{8.6}$$

$$\mathrm{H_2O_2} + \mathrm{O_2^{\cdot -}} \rightarrow \mathrm{OH^{\cdot}} + \mathrm{OH^-} + \mathrm{O_2} \tag{8.7}$$

$$\mathrm{H_2O_2} + p-g-\mathrm{C_3N_4} \rightarrow \mathrm{OH^{\cdot}} + \mathrm{OH^-} \tag{8.8}$$

$$p-g-\mathrm{C_3N_4}(\mathrm{h}^+) + \mathrm{OH^-} \rightarrow p-g-\mathrm{C_3N_4} + \mathrm{OH^{\cdot}} \tag{8.9}$$

$$\text{Organic Pollutant} + \mathrm{OH^{\cdot}} \rightarrow \text{Degradation products} \tag{8.10}$$

$$\text{Organic Pollutant} + p-g-\mathrm{C_3N_4}(\mathrm{h}^+) \rightarrow \text{Degradation products} \tag{8.11}$$

$$\text{Organic Pollutant} + p-g-\mathrm{C_3N_4}(\mathrm{h}^+) + \mathrm{O_2^{\cdot -}} \rightarrow \text{Degradation products} \tag{8.12}$$

Graphitic C_3N_4 having suitable VB and CB potential for the formation of $HO^{\bullet}$ $(E^0_{\mathrm{H_2O/HO^{\bullet}}} = 2.8\ \ \mathrm{eV})$ and $\mathrm{O_2^{\bullet -}}\left(E^0_{\mathrm{O_2}}/\mathrm{O_2^{\bullet -}} = -0.3\ \ \mathrm{eV}\right)$ is capable of producing hydroxyl radicals and superoxide radicals efficiently and carrying out pollutant

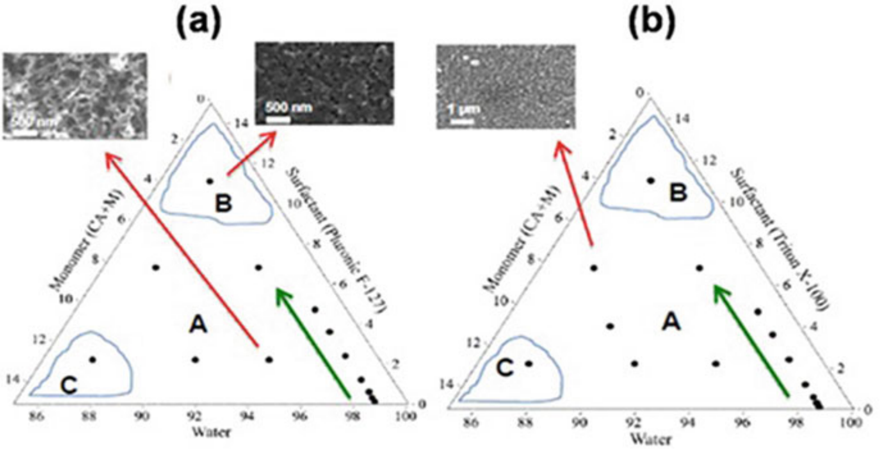

Fig. 8.5 Pseudo-ternary phase diagrams of the materials synthesized by various nonionic surfactants such as (**a**) Pluronic F-127 and (**b**) Triton X-100. Here green arrow represents the transition from sheetlike to globular and curved in region "A" followed by irregular structures in region "B." In region "C" samples are synthesized having a sheetlike structure (Peer et al. 2017)

degradation. However, as it is a surface phenomena, surface area plays a deciding role. In this regard, porous g-C_3N_4 materials were reported to show good visible light-induced dye degradation activity due to existence of structural defects, enhanced light absorption, and large BET surface area. Increased light absorption in case of porous g-C_3N_4 is also attributed to low C/N ratios. Further, porosity, particle size, and morphology can be controlled by using different templates during composite formation. Large available surface not only absorbs the organic/inorganic pollutants effectively by offering more number of active sites but also prevents aggregation of particles by accelerating diffusion kinetics. A tubular porous structure can provide internal and external surface for adsorption of pollutants and favors mass transfer by decreasing the resistance and thereby improves separation of photogenerated charges.

Degradation of RhB was studied by Peer et al. using mesoporous g-C_3N_4 prepared by using a hydrogen-bonded melamine cyanurate complex and various nonionic surfactants (Pluronic P-123, Triton X-100, and Pluronic F-127) as the starting material (Peer et al. 2017). Pseudo-ternary phase diagrams for the 3D assembled nanostructures synthesized by using different nonionic surfactants are as shown in Fig. 8.5, which represents the composition of the reaction solution to the resultant morphology of g-C_3N_4. The HRTEM images of 3D assembled nanostructures result in low-dimensional highly porous g-C_3N_4 sheets, depending upon the template and acquired sheetlike, hollow spherical and tubular morphology as shown in Fig. 8.6.

The normalized absorption in UV-Vis plot gives an indication about therate of degradation of RhB. Shift of the peaks clearly confirms higher degradation rate as a function of the surface area of porous g-C_3N_4 materials as shown in Fig. 8.7. Simultaneous de-ethylation of the dye and its intermediate products shift in the

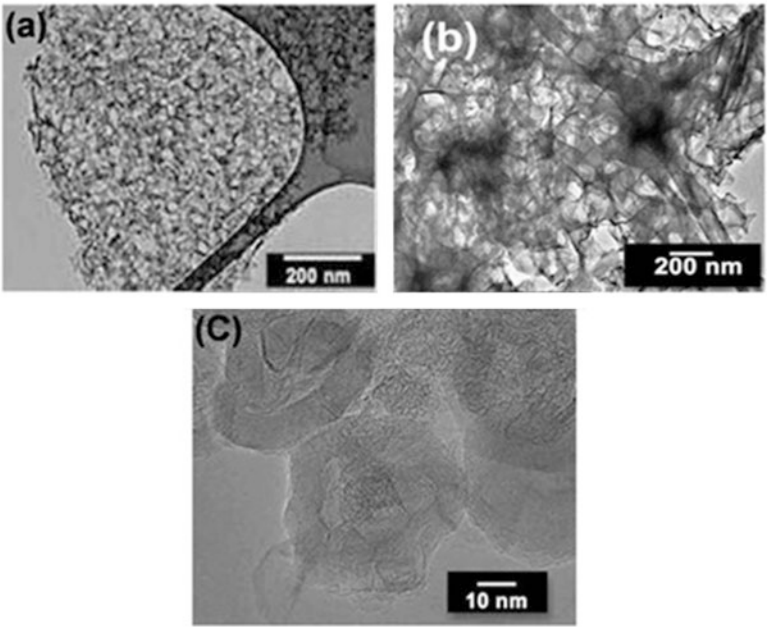

Fig. 8.6 HRTEM images of porous g-C_3N_4 formed by using (**a**) Pluronic P-123, (**b**) Pluronic F-127, and (**c**) Triton X-100 as surfactants (Peer et al. 2017)

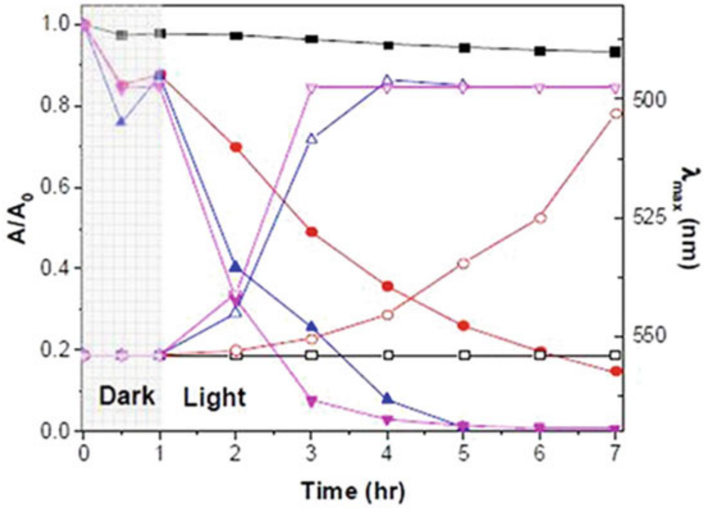

Fig. 8.7 Normalized UV-Vis absorption spectra of RhB solution (closed symbols) and wavelength of maximum absorption i.e. λ_{max} (open symbol) under visible light illumination without catalyst (□) and with the presence of M-CN (○), Tri-S-0.2 (Δ) and F_{127}-T-0.5 (∇) (Peer et al. 2017)

main absorbance peak (Zhao et al. 1998). When the control experiment was carried out without any catalyst, insignificant degradation was observed via photolysis even after irradiating visible light for over 6 h. The degradation involves de-ethylation reaction occurred by photosensitization of the adsorbed dye (Li and Jinhua 2007; Watanabe et al. 1977).

In another study, Tong et al. studied the degradation of MO over porous 3D g-C_3N_4/graphene oxide aerogel with superior activity (Tong et al. 2015). The highly interconnected porous network of the photocatalyst offers several pathways for strong adsorption, efficient mass transport, and multiple reflection of the incident light. It has been observed that only neat g-C_3N_4 is capable of degrading MO only 12% under 4 h, while neat GO shows no degradation under the same conditions although it possesses a strong adsorption potential for the pollutant owing to high available specific surface area. However, upon integration between neat g-C_3N_4 and GO, 92% of MO get degraded within the same time (6.0 times more than neat g-C_3N_4).

Xu et al. designed 2.0-nm-thick porous g-C_3N_4 nanosheets, having a surface area of 190.1 m^2 g^{-1} through a simple template-free method involving two steps (hydrothermal treatment followed by thermal etching) (Xu et al. 2017). In the hydrothermal condition, partial dissociation of tri-s-triazine units occurred via hydrolysis followed by oxidation and introduces a number of oxygen-containing groups on the surface of g-C_3N_4. After the formation of porous g-C_3N_4, successful delamination occurred upon thermal etching. The photodegradation rates of MB, bisphenol A, and Acid Red 27 studied over porous g-C_3N_4 were found to be almost 6.4, 1.9, and 4.0 times than that of bulk g-C_3N_4, respectively. The enhanced activity (about 3.7 times) in case of porous g-C_3N_4 nanosheets was also supported by the photocurrent density. The photocatalytic degradation performance was further supported by the reduced resistance shown in electrochemical impedance spectroscopy and transient photocurrent response of the photocatalysts. The photocurrent response of PGCNS (porous g-C_3N_4 nanosheets) in comparison to PGCN (porous g-C_3N_4) and BCN (bulk g-C_3N_4) was found to be much more in good agreement with the activity (Fig. 8.8).

Porous g-C_3N_4 has been synthesized in an easy and nontoxic bubble-templating method, by mixing dicyandiamide and thiourea, where thiourea acts as an effective bubble template (Xu et al. 2013). During calcination, thiourea undergoes decomposition to liberate huge amount of gas bubbles and plays an important role in the formation of porous g-C_3N_4. Xu et al. investigated the photodegradation of MB over porous-C_3N_4, found to be about 80%, having highest apparent rate constant ($k = 0.146\ h^{-1}$), which is about 3.4 times more than that of bulk g-C_3N_4 ($k = 0.0430\ h^{-1}$) (Fig. 8.9). In the case of nanoporous structure, the charge separation is more effective and favors transfer through solid-liquid interface. Moreover the bandgap energy in case of porous-C_3N_4 is found to enlarge owing to quantum confinement effect and leads to strengthen the redox ability.

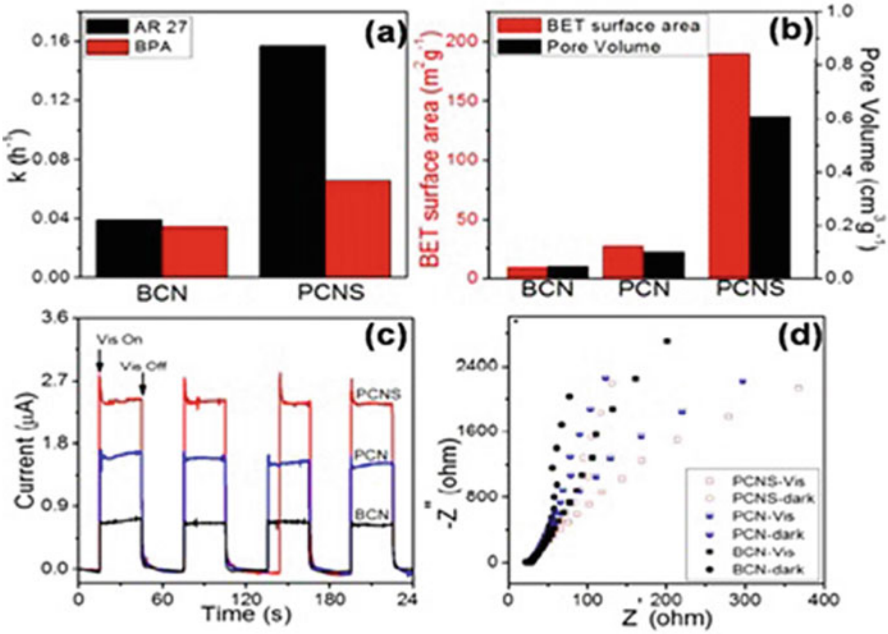

Fig. 8.8 (**a**) Apparent rate constant for the photodegradation of AR 27 and BPA under visible light illumination over BCN and PCNS; (**b**) BET surface area and pore volume data of BCN, PCN, and PCNS; (**c**) photocurrent response of BCN, PCN, and PCNS under visible light; and (**d**) electrochemical impedance graph of BCN, PCN, and PCNS in dark as well as light condition (Xu et al. 2017)

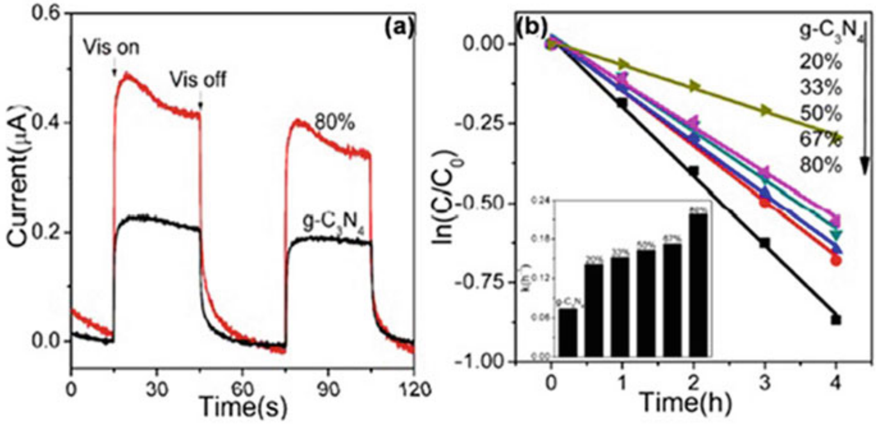

Fig. 8.9 (**a**) Photocurrent response of bulk g-C_3N_4 and porous g-C_3N_4 in presence of visible light, (**b**) rate of photocatalytic degradation of MB under visible light irradadiation (Xu et al. 2013)

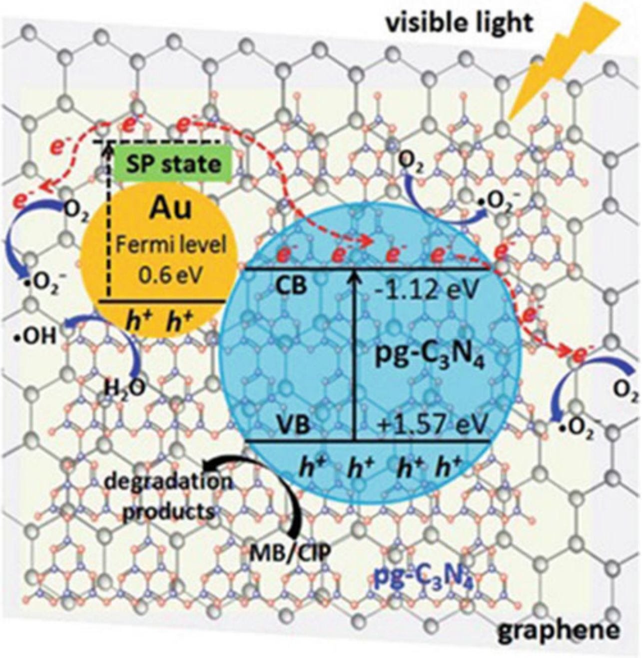

Scheme 8.1 Schematic representation of MB/CIP over porous g-C_3N_4 in presence of Au in Au/pg-C_3N_4/graphene composite (Xue et al. 2015)

Furthermore, by introducing noble metal nanoprticles, plasmonic photocatalyst by efficient light absorption shows very high performance in photocatalysis. As reported by Xue et al., both g-C_3N_4 and graphene act as ideal supports for noble metals and facilitate photocatalytic MB degradation reactions induced by a strong localized electric field (Xue et al. 2015). Au/pg-C_3N_4/graphene displayed 100% photodegradation of MB in 180 min, whereas only 47.4% MB get degraded by neat g-C_3N_4 in the same time. The degradation rate of CIP is found to be in the order of Au/pg-C_3N_4/GR (96.7%) > Au/pg-C_3N_4 (88.3%) > pg-C_3N_4/GR (81.0%) > pg-C_3N_4 (72.6%) > g-C_3N_4 (44.5%) in 240 min, which follows the same order as that for MB degradation. The light absorption capacity of Au nanoparticles was not only improved by the SPR effect but also helps to create intense local electromagnetic field to speed up the photocatalytic reaction. As the Fermi level of Au (0.6 eV) is at more negative potential than the CB position of both porous g-C_3N_4, the photogenerated hot electrons get easily transferred to the CB of both g-C_3N_4 and help to produce active species. Moreover, the photogenerated electrons react with dissolved O_2 present in the reaction medium to generate superoxide radicals. These active species readily react with the adsorbed pollutants to achieve degradation as shown in Scheme 8.1.

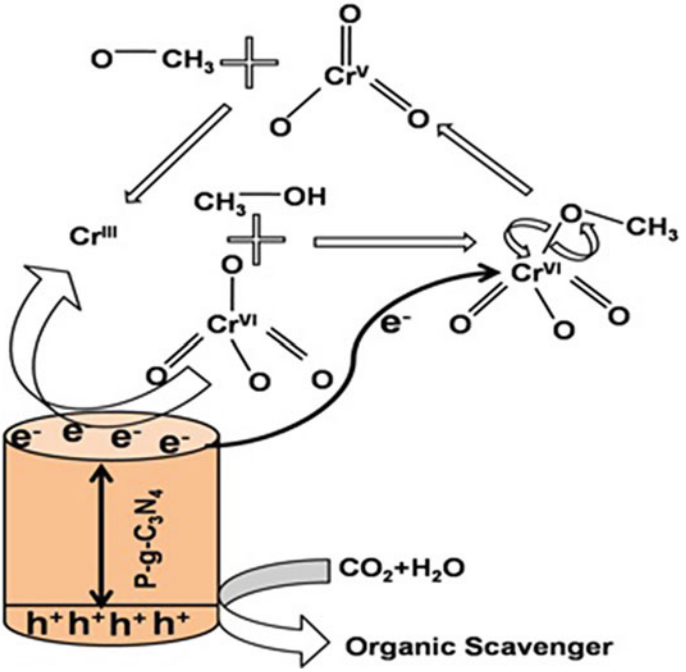

Scheme 8.2 Schematic representation of reduction of Cr (VI) photocatalytically in presence of organic compounds as hole scavengers

8.3.2 *Applications of Porous g-C_3N_4 in Cr(VI) Reduction*

Chromium is mainly found naturally in rocks, soil, volcanic dust, gases, etc. and exists mainly as Cr(VI) and Cr(III). Among which, Cr (VI) is found to be highly mutagenic and carcinogenic, whereas Cr(III) is less harmful and also an essential component in the human body. Cr (VI) is approximately 10–100 times more noxious than Cr(III). The permissible limit of Cr(VI) according to USEPA (United States Environmental Protection Agency) is only 50 ppb in drinking water (Xu et al. 2017). Therefore, reduction of Cr(VI) to Cr(III) is a main challenge before research community. Cr (VI) is a major pollutant mainly available as $Cr_2O_7^{2-}$, CrO_4^{2-}, and $HCrO_4^-$ ions in aqueous solution depending on the pH of the solution, redox potential, and concentration. The reduction of Cr(VI) to Cr(III) photocatalytically using semiconducting materials under UV/Visible light illumination was reported since 1979 and found effective in comparison to various conventional methods (Yoneyama et al. 1979). Among various semiconducting materials, g-C_3N_4 utilizes solar light more effectively for the reduction of Cr(VI) and was investigated extensively in the recent decades. Photoreduction of Cr(VI) over g-C_3N_4 both in absence and presence of hole scavenger has also been studied. Schematically, Cr (VI) reduction is shown in Scheme 8.2.

The overall reaction of Cr (VI) reduction is proposed as:

$$2Cr_2O_7^{2-} + 16H^+ \rightarrow 4Cr^{3+} + 8H_2O + 3O_2 \tag{8.13}$$

Being a surface phenomena, Cr (VI) reduction was found to increase in case of g-C_3N_4 by introducing porosity. The well-defined crystalline structure and pores on the surface of porous g-C_3N_4 can offer adequate number of active sites for adsorption and help in mass transportation. Wang et al. reported a Mn-doped porous g-C_3N_4 composite by calcination-refluxing method, which shows much improved Cr (VI) reduction, i.e., up to 76.5%. The efficiencies Cr (VI) reduction in case of all modified g-C_3N_4 samples were found superior in comparison to pristine g-C_3N_4, which was basically dependent on their surface area (Wang et al. 2017a, b). Owing to the presence of carboxylic groups on the surface, the thermodynamic driving force increases by 79 mV for Cr(VI) reduction with unit decrease in pH of the photocatalytic system. The result of photocatalytic activities of Cr (VI) reduction explains the presence of acidic group ion of photogenerated charge carriers and transfer of electron at interface.

Fabrication highly efficient porous ultra nanosheets P-doped g-C_3N_4 by Deng et al. through thermal exfoliation strategy was reported using 2-aminoethylphosphonic acid (AEP) as the source for phosphorous and also acts as gas bubble template (Deng et al. 2017). Photocatalytic tandem reaction for simultaneous removal of the Cr (VI) and 2,4-DCP over P-doped porous g-C_3N_4 was investigated (Scheme 8.4). It is well known that reduction of single species Cr (VI) through photogenerated electrons and oxidation of single species 2,4-DCP in presence of light is not significant in comparison to tandem reaction. However, in presence of 2,4-DCP as hole scavengers (organic compounds), efficient reduction of Cr (VI) was achieved than in the absence of a hole scavengers. The reason for increase in photocatalytic redox reaction was due to the combined effect of broadened visible light response of P doping, large specific surface areas. In this tandem reaction, Cr(VI) acts as an electron trapper, and at the same time 2,4-DCP serves as an electron donor, which get oxidized in presence of photogenerated holes. Presence of electron/hole scavengers simultaneously promotes the separation rate of electron-hole pairs, to carry out reduction/oxidation reaction (Scheme 8.3). In our group also we have investigated the extent of reduction of Cr(VI) over Cu-loaded MoO_3/g-C_3N_4 heterostructure (Patnaik et al. 2018a, b). The formation of MoO_3/g-C_3N_4 from a mixture of thiourea and ammonium molybdate, in a one-step in situ calcination process, involves evolution of significant amount of gases to introduce porosity in the material as well as to create oxygen vacancy. The Cu-loaded MoO_3/g-C_3N_4 composite, through double Z-scheme mechanism, shows efficient electron-hole separation and is able to reduce 95% of Cr(VI) photocatalytically in presence of citric acid as a hole scavenger.

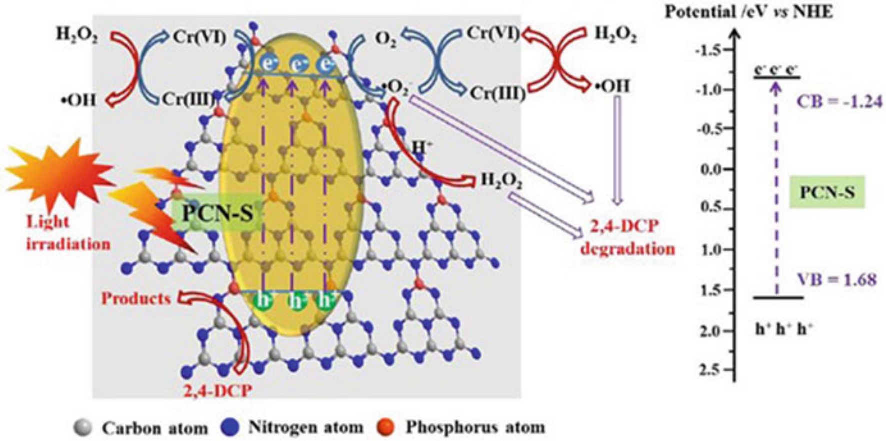

Scheme 8.3 Schematic representation of photocatalytic tandem reaction for the reduction of Cr (VI) in and oxidation of 2,4-DCP over porous g-C_3N_4 (Deng et al. 2017)

8.3.3 Applications of Porous g-C_3N_4 in CO_2 Reduction

Global warming caused due to the emission of CO_2 into the atmosphere has aroused significant environmental issues. For which conversion of CO_2 into chemical feedstocks is now a main challenge before research community. After the discovery of photoelectrocatalytic reduction of CO_2 into hydrocarbon fuels by Inoue et al. (1979) in aqueous media, semiconductor-based photoreduction of CO_2 by is a compelling approach to circumvent global warming and has been studied extensively. Among various semiconducting materials, metal-free porous g-C_3N_4 has a significant role in light-induced conversion of solar to fuel.

As the most stable compound, it involves considerable amount of energy [CO_2 ($\Delta G = -394.39$ kJ/mol)]. Compared to conventional methods, photocatalytic reduction of CO_2 is associated with lower energy input (Sun et al. 2018). Photoreduction of CO_2 mainly involves five steps: (1) efficient adsorption of CO_2 on the surface of the photocatalyst, (2) generation of electrons (e^-) in the CB and holes (h^+) in the VB upon light irradiation, (3) transport of photogenerated e^- and h^+ onto the catalyst surface, (4) reaction of the charge carriers with CO_2 species adsorbed on the surface, and (5) desorption of the by-products. Most of the transformation reactions in CO_2 reduction occurred between the potential range of -0.24 V to -0.6 V, whereas the single electron reduction that occurs at -1.9 V is not favorable and associated with high overvoltage. Moreover, the conversion into hydrocarbon fuel

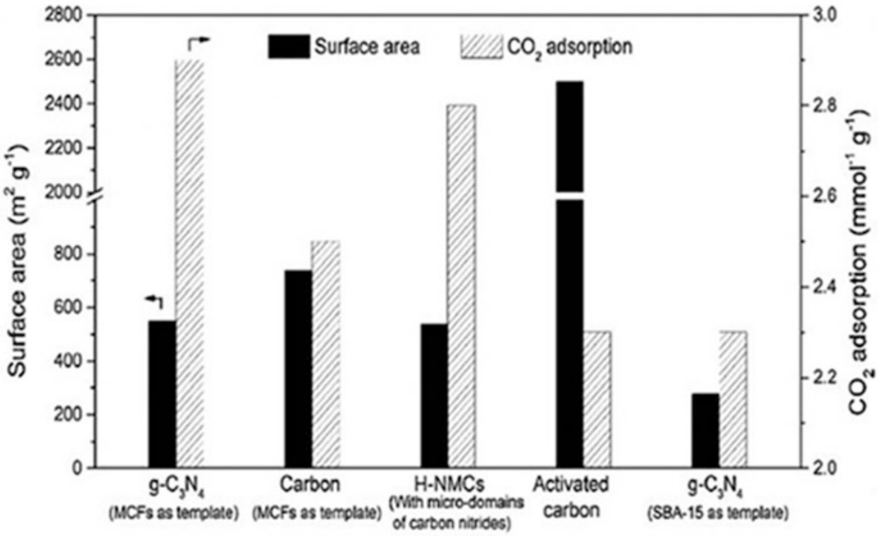

Fig. 8.10 Effect of porosity and surface area on CO_2 reduction using various templates (Sun et al. 2018)

through reduction involves two to eight electrons according to the following (Eqs. 8.14, 8.15, 8.16, 8.17, 8.18, and 8.19):

Equations

$$CO_2 + e^- \rightarrow CO_2^{-} \qquad -1.90\ V \tag{8.14}$$

$$CO_2 + 2H^+ + 2e^- \rightarrow HCOOH \qquad -0.61\ V \tag{8.15}$$

$$CO_2 + 2H^+ + 2e^- \rightarrow CO + H_2O \qquad -0.53\ V \tag{8.16}$$

$$CO_2 + 4H^+ + 4e^- \rightarrow HCHO + H_2O \qquad -0.48\ V \tag{8.17}$$

$$CO_2 + 6H^+ + 6e^- \rightarrow CH_3OH + H_2O \qquad -0.38\ V \tag{8.18}$$

$$CO_2 + 8H^+ + 8e^- \rightarrow CH_4 + H_2O \qquad -0.24\ V \tag{8.19}$$

Bulk g-C_3N_4 directly obtained by thermal polymerization of melamine possess hardly ever used in CO_2 adsorption due to its low specific surface area (Sun et al. 2018). Although various strategies were reported to enrich the surface of g-C_3N_4 with CO_2 adsorption sites, introduction porosity is most adoptable. The effect of porosity along with surface area on CO_2 adsorption using various templates in the formation of mesoporous g-C_3N_4 is shown in Fig. 8.10.

In another study, Sun et al. prepared porous g-C_3N_4 with hierarchical 3D structure from ethylenediamine and CCl_4 using spherical mesoporous cellular silica foams (MCFs) as hard template for excellent CO_2 adsorption. g-C_3N_4 having Lewis and

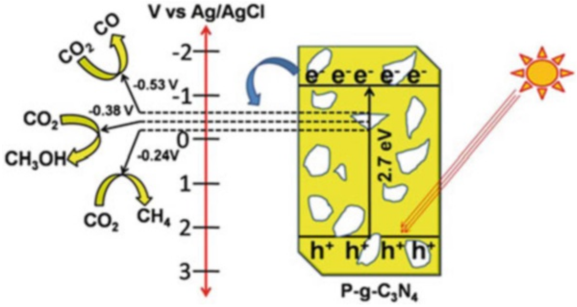

Scheme 8.4 Schematic representation of photocatalytic CO_2 reduction over porous g-C_3N_4

Brönsted basic sites is found suitable for CO_2 fixation and activation (Li et al. 2010). The porous g-C_3N_4 obtained by using MCF provides extraordinarily increased surface area (~550 m^2/g) and makes available plentiful nitrogen-containing basic groups. Moreover, a large number of micro-pores are also available for CO_2 adsorption through capillary condensation effect (Scheme 8.4). Porous g-C_3N_4 material formed by using different templates offers variable C/N ratio for the formation of stable microdomains in the matrix and provides different surface areas. When SBA-15 is used as the template, the surface area increases to 278 $m^2\ g^{-1}$ and adsorbs 2.35 mmol g^{-1} of CO_2 at 25 °C and found inferior than bulk g-C_3N_4. Zhang et al. studied the reduction of CO_2 over porous g-C_3N_4 prepared from melamine hydrochloride, which shows 4.9 times enhanced CO_2 reduction due to enhanced surface area compared to bulk g-C_3N_4 synthesized from melamine only (Sun et al. 2018).

To trigger CO_2 reduction reaction, the CB potential should be more negative than the required potential. The potential required for the conversion of molecular CO_2 to CO_2^- via excitation of one electron is −1.90 V vs NHE (Sun et al. 2018; Li et al. 2010). As it is difficult to have a semiconductor photocatalyst with more negative potential than −1.90 V, the process is supposed to be unfavorable. Usually, when CO_2 molecules get adsorbed on the surface of the metallic photocatalyst, it would lower the energy barrier significantly required for the reduction process, as its structure changes from linear to bent (Li et al. 2016; Karamian and Sharifnia 2016) to favor CO_2 adsorption. However, in the case of g-C_3N_4, CO_2 adsorption modes are different than on metal compounds. Rather it shows physisorption, involving binding of CO_2 to the available abundant nitrogen-containing basic groups of tris-triazine-based covalent framework (Xu et al. 2012).

Lin et al. reported a Co-modified porous g-C_3N_4 photocatalytic system for deoxygenative reduction of CO_2 to CO under light irradiation, where porous g-C_3N_4 has been used as a substrate to capture or activation of CO_2 (Lin et al. 2014). The incorporated Co species act as promoters to accelerate separation and transfer of charge carrier. This Co-modified porous g-C_3N_4 hybrid photosystem synergetically catalyzes reduction of CO_2 under mild conditions with high reusability. Imparting SiO_2 nanoparticles, the surface area of hybrid photocatalytic system

Scheme 8.5 Cooperative effect of Cobalt on CO_2 reduction (Lin et al. 2014)

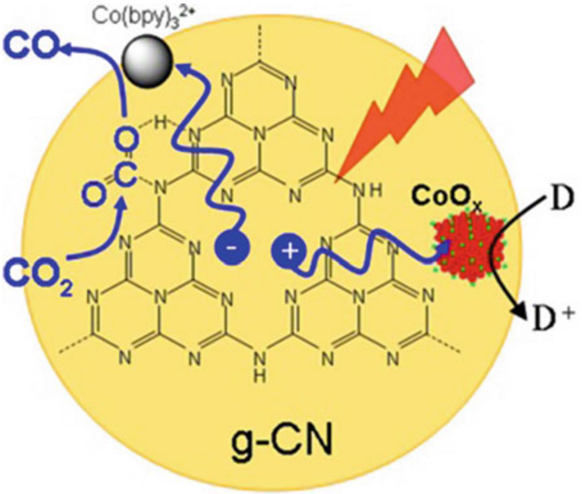

Fig. 8.11 CO_2 reduction as a function of $CoCl_2$ in presence of bipy (1 and 2) and in the absence of bpy (3 and 4) (Lin et al. 2014)

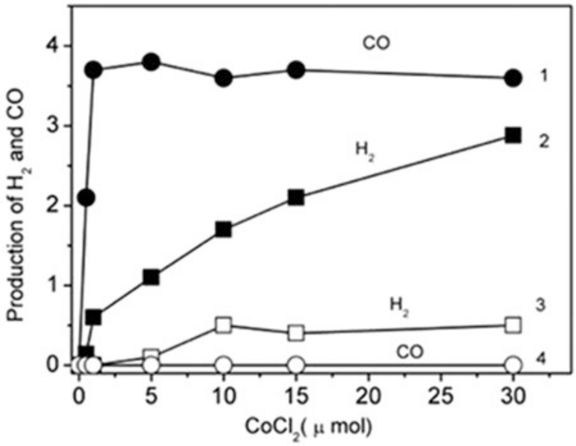

enlarged to 135 m^2/g, with efficient CO_2 reduction in presence of CO^{2+} and bpy as electron mediator and CO^{2+} as oxidative catalyst, was shown in Scheme 8.5.

Upon visible light irradiation, the electron mediator and CO^{2+} as an oxidative cocatalyst induces generation and transfer of charge carriers through the interface. High-energy electrons and holes are capable of converting CO_2 into CO and [O], along with the liberation of some amount of H_2 from the oxidative hydrogenation of TEOA as shown in Fig. 8.11 and Eq. (8.20)

$$CO_2 + 2H^+ + 2e^- \rightarrow CO + H_2O \qquad (8.20)$$

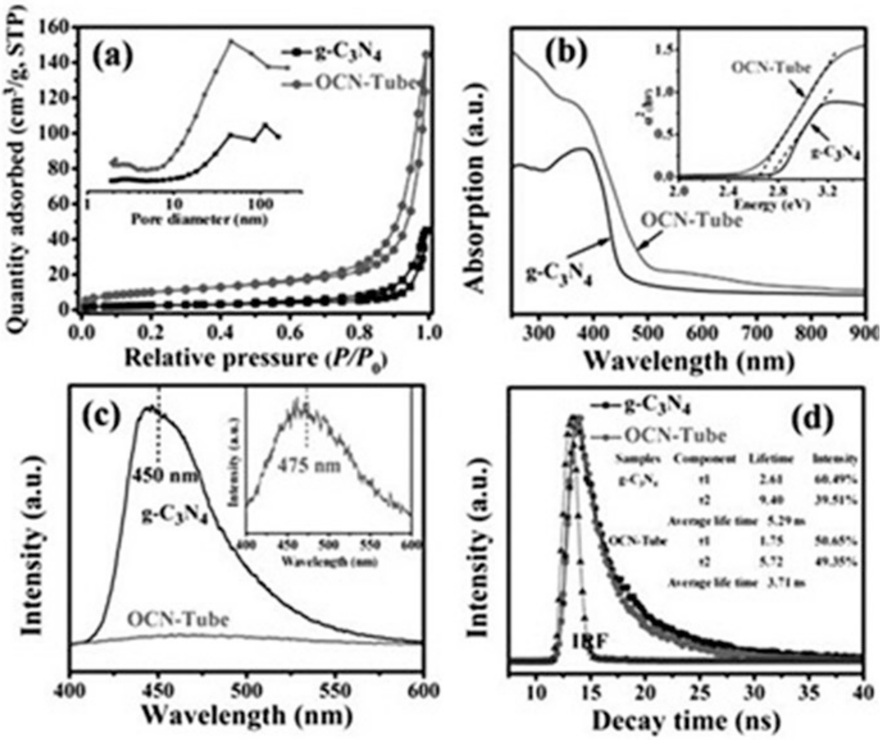

Samples	Component	Lifetime	Intensity
g-C3N4	τ1	2.61	60.49%
	τ2	9.40	39.51%
	Average life time	5.29 ns	
OCN-Tube	τ1	1.75	50.65%
	τ2	5.72	49.35%
	Average life time	3.71 ns	

Fig. 8.12 (**a**) N_2 adsorption-desorption isotherms curve and pore-size distribution graph (inset figure), (**b**) UV-Vis DRS plot and corresponding bandgap energy graph (inset image), (**c**) PL spectra, and (**d**) TRPL spectra of the bulk g-C_3N_4 and OCN tube (Fu et al. 2018)

Tong et al. designed a highly efficient 3D porous g-C_3N_4/GO aerogel photocatalyst with highly interconnected framework having numerous macropores. When investigated for CO_2 photoreduction, the optimized porous g-C_3N_4/GO sample reduces CO_2 into CO with a yield of 23 mmol g^{-1} in 6 h, exhibiting 2.3-fold enhanced activity compared to bulk g-C_3N_4 (Tong et al. 2015). A porous O-doped g-C_3N_4 nanotubes were designed through condensation of bulk g-C_3N_4 followed by thermal exfoliation, which shows good results for photocatalytic CO_2 reduction (Fu et al. 2017). The interconnected multiwalled nanotubes of O-doped g-C_3N_4 with uniform diameter (20–30 nm) evolve methanol at the rate of 0.88 μmol·g^{-1} h^{-1}, about five times more compared to bulk g-C_3N_4 (0.17 μmol g^{-1} h^{-1}). Specifically, the higher pore-size distribution in case of O-doped g-C_3N_4 nanotubes, the more pore volume (0.128 cm^3 g^{-1}) and enhanced surface area (36 m^2 g^{-1}) indicating a more porous structure (Fig. 8.12).

8.3.4 Applications of Porous g-C_3N_4 in Water Reduction Reactions for Solar Energy Conversion

Hydrogen is now emerging as one of the important alternative sources of energy to fossil fuels, and semiconductor-based photocatalysis is the most emerging method to produce hydrogen energy in a sustainable manner. Upon light irradiation, when electron-hole pairs are generated, they diffuse to the surface of the photocatalyst to initiate water reduction/oxidation reactions. The major challenge in semiconductor-based photocatalysis is to restrain the recombination of charge carriers. In majority of cases, defect levels present on the surface act as recombination centers and decrease the photocatalytic activity. However, nano-sized, highly crystalline stoichiometric materials with fewer defects are beneficial to carry out redox reactions. Highly crystalline nano-sized materials with small particle size and high surface area endow the photocatalyst with shorter diffusion distances for photogenerated electrons to go to the active sites and decrease the probability of recombination. When the migrated electrons properly interact with the surface active sites, they undergo water-splitting reactions (reduction/oxidation) to produce hydrogen and oxygen. Hence, the number of active sites and intrinsic activity are very crucial for photocatalytic activity of a semiconductor. In this context, designing of porous g-C_3N_4 materials is important to investigate photocatalytic water reduction reactions for the generation of hydrogen energy. The appropriate CB and VB potentials of g-C_3N_4 make it suitable for water reduction reaction. However, the large energy barrier associated with photocatalytic water splitting reactions is still a challenge for practical applications.

A number of studies were carried out to show the efficiency of porous g-C_3N_4 materials prepared by using various templates toward H_2 evolution. Yan et al. synthesized wormlike porous g-C_3N_4 using Pluronic P123 as soft template, which not only offers highly specific surface area but also extends the absorbance edge up to 800 nm (Yan 2012). The prepared porous g-C_3N_4 showed significant H_2 evolution rate under light illumination. It was observed that by increasing the ratio of P123 to melamine, the H_2 evolution rate also increases as shown in Fig. 8.13. With an optimum amount of P123, the H_2 evolution was 148.2 μmole h^{-1}, whereas it decreases to 60.5 μmole h^{-1} in case of bulk g-C_3N_4 prepared without using P123.

Fabrication of porous g-C_3N_4 was reported by Wang et al. using low-cost $CaCO_3$ as the hard template, which can be easily removed by using dilute HCl (Wang et al. 2015a, b). It was observed that, upon engineering the weight ratio of the template to the precursor, resulting porous g-C_3N_4 shows an increase in the cathodic photocurrent by an amount of 4 and 7.5 times in presence of light when biased at 0.2 V and 0 V (vs. Ag/AgCl electrode), respectively. Huang et al. reported the development of a precendented template-free precursor (melamine) for the designing of porous g-C_3N_4 nanosheets by hydrothermal treatment (Huang et al. 2017). This process involves adjustment of porosity of g-C_3N_4 nanosheets by controlling the addition of thiourea, which etches the surface of g-C_3N_4 to yield porous material. That shows profoundly strengthened photocatalytic H_2 evolution (3.3-times more than the neat

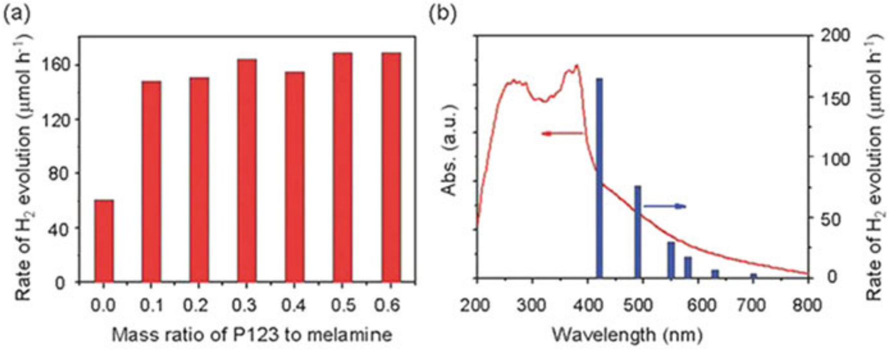

Fig. 8.13 (**a**) Rate of H_2 evolution with varying P123 to melamine mass ratio and (**b**) wavelength dependence of H_2 evolution over porous g-C_3N_4 (Yan 2012)

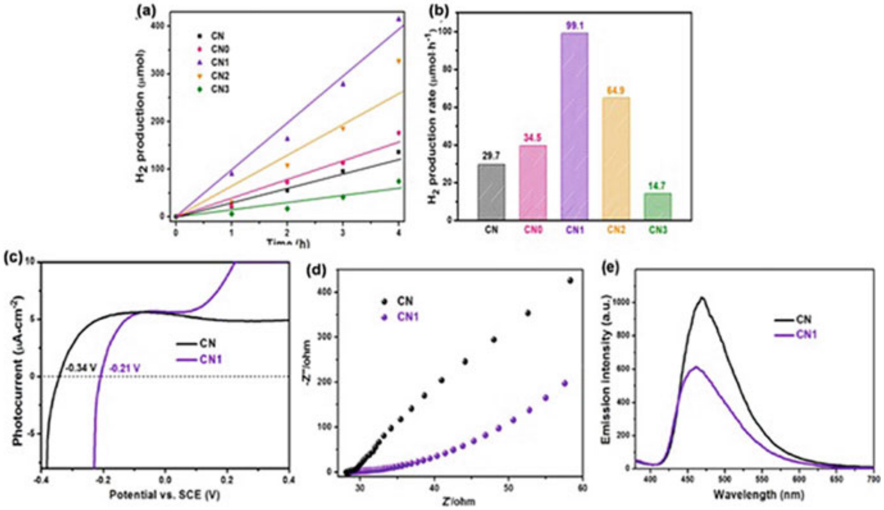

Fig. 8.14 Photocatalytic rate (**a**) and (**b**) H_2 evolution curves of porous CNX samples ($X = 0,1,2,3$), (**c**) linear sweep voltammetry (LSV) curves, (**d**) EIS analysis, and (**e**) PL spectral analysis of porous g-C_3N_4 (Huang et al. 2017)

counterpart) which is in good agreement with the cathodic photocurrent observed in linear sweep voltammetry (LSV) curves, EIS analysis, and PL spectral analysis as shown in Fig. 8.14.

In our group also the visible light-induced photocatalytic H_2 evolution was studied over Cu-promoted porous MoO_3/g-C_3N_4 heterostructure. H_2 evolution rate of MoO_3/g-C_3N_4 hybrid heterostructure activated by Cu NPs as cocatalyst was observed to be 652 μmol/h, with 13.46% apparent conversion efficiency. The remarkably improved H_2 evolution activity was attributed to synergistic effect of

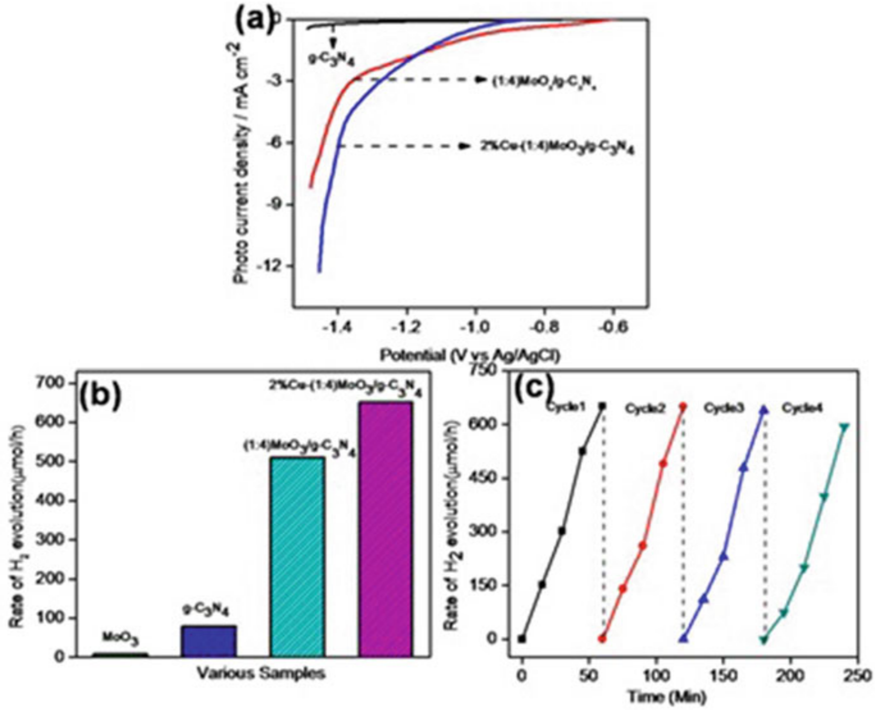

Fig. 8.15 (**a**) Linear sweep voltammeter study of neat MoO_3, neat g-C_3N_4, and 2% copper-loaded (1:4) MoO_3/g-C_3N_4 (sweeping potential from −1.5 V to 0.5 V, V vs Ag/AgCl by using 0.5 M Na_2SO_4 electrolyte solution), (**b**) H_2 evolution data of various samples, and (**c**) reusability test for 2%Cu-(1:4) MoO_3/g-C_3N_4 (Patnaik et al. 2018a, b)

defective MoO_3 and double Z-scheme mechanism. In situ preparation method of MoO_3/g-C_3N_4 hybrid results in the generation of defected sites at the interface and improves charge separation through a direct Z-scheme mechanism, whereas loading Cu NPs results in deposition of Cu as CuO as well as Cu^0. Presence of p-type CuO and n-type g-C_3N_4 builds up a p-n heterojunction to establish double (direct/indirect) Z-scheme charge transfer mechanism. The photocatalytic performance and stability of the hybrid material was also supported by an enhanced photocurrent density of 12.1 mA cm^{-2} (Fig. 8.15) in case of 2%Cu-MoO_3/g-C_3N_4 in comparison to MoO_3/g-C_3N_4 and neat g-C_3N_4 (Patnaik et al. 2018a, b).

Chen et al. established designing of a functionalized 3D open porous g-C_3N_4 with cyano groups (3D OPG-C_3N_4-CN) by a facile NaCl-assisted freeze-drying two-step process (Han et al. 2013). NaCl in the synthesis procedure not only works as a template to induce porosity in the structure but also induces decomposition of g-C_3N_4 to generate moderate amount of cyano groups upon calcination at 500 °C. The cyano groups introduced at the edge of the 3D open porous g-C_3N_4 structure act as electron trapping centers and make available more active sites for enhanced H_2 production. Compared to bulk g-C_3N_4, the 3D OPG- C_3N_4-CN exhibits superior

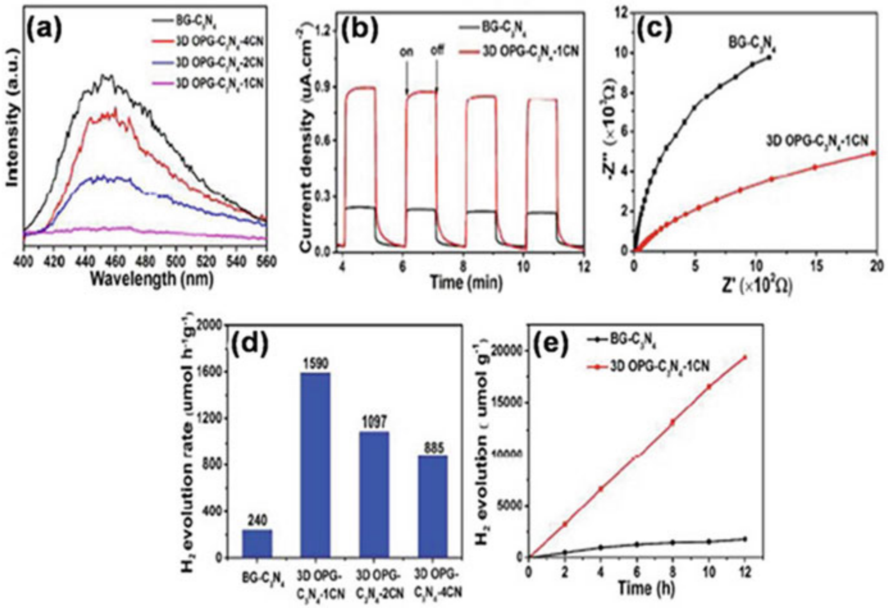

Fig. 8.16 (**a**) Photoluminescence spectra (excitation wavelength = 315 nm), (**b**) photocurrent response under visible light illumination, (**c**) EIS Nyquist spectra, (**d**) photocatalytic H_2 evolution, and (**e**) hydrogen evolution graph with the time course over 12 h of BG-C_3N_4 and OPG-C_3N_4-CN (Han et al. 2013)

light absorption and generates 1590 μmol/h/g of H_2 using Pt as cocatalyst. The reason for the formation of ultrathin walls of 3D OPG-C_3N_4-1CN is the cleavage of the g-C_3N_4 sheets into many small pores in presence of NaCl and O_2 in air at 500 °C. The TEM and SEM image also confirms the decomposition of g-C_3N_4 at 500 °C. It is observed that with increase in the amount of CS $(NH_2)_2$ during preparation, the wall of 3D OPG-C_3N_4-CN becomes thicker due to the presence of cyano groups. The 3D open porous structure and ultrathin wall contributes to improve the surface area (Fig. 8.16). The BET surface area of 3D OPG-C_3N_4-1CN is found to be 37 m^2/g, which is almost six times more than that of neat g-C_3N_4 (5.7 m^2/g). The enhanced H_2 evolution was further in accordance with the photocurrent data, PL spectral analysis, and low resistance offered by the photocatalyst as in Nyquist plot.

Fabrication of an atomically thin nanomesh of mesoporous g-C_3N_4 was reported by Han et al. using freeze-drying dicyanamide through thermal polycondensation followed by solvothermal exfoliation (Han et al. 2016). Which possess unique structural advantages of fast electron transfer due to properly aligned band edges, efficient light harvesting capacity and plentily available active reaction sites. Mesoporous g-C_3N_4 nanomesh shows better H_2 evolution rate of 8510 μmol h^{-1} g^{-1} with an apparent quantum efficiency of 5.1%. The efficient H_2 generation by mesoporous g-C_3N_4 nanomesh in comparison to neat g-C_3N_4 was also supported by the widened bandgap, more negative shift in CB potential, decreased PL

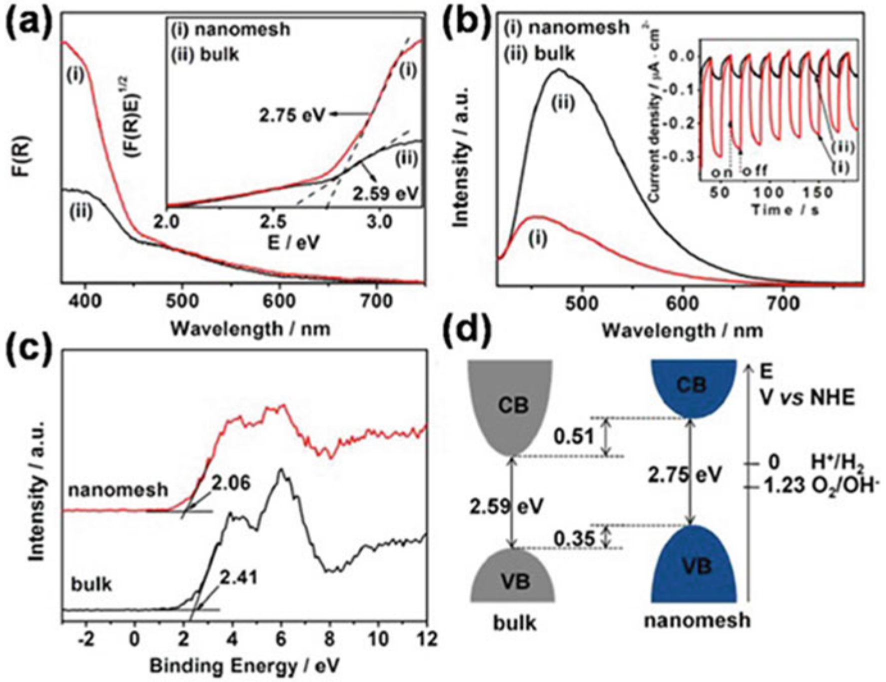

Fig. 8.17 (**a**) Absorbance spectra and corresponding bandgap energy (tauc) plot (inset image), (**b**) photoluminescence spectra and photocurrent response in light (inset figure), (**c**) and (**d**) XPS valence band spectra and electronic band structure of the monolayer mesoporous g-C_3N_4 nanomesh and the bulk counterpart (Han et al. 2016)

intensity, XPS valence band spectra, and improved photocurrent data as shown in Fig. 8.17. The blueshifts in fluorescence emission peak further support the enlarged bandgap by 0.16 eV in case of mesoporous g-C_3N_4 nanomesh owing to quantum confinement effect. In addition, the light-harvesting ability also remarkably increased due to multiple scattering effects and presence of defect sites in the mesoporous surface. The strong photoluminescence quenching further confirms the energy-wasteful charge recombination, with improved charge separation that was also supported by the transient photocurrent measurements.

In another study, She et al. reported designing of 2D ultrathin O-doped porous g-C_3N_4 through template-free thermal exfoliation method followed by chemical oxidation method (She et al. 2016). 2D porous ultrathin structure and incorporated oxygen is favorable for the improvement of the photocatalytic hydrogen evolution rate. The average rate of H_2 evolution is found to be ~189.3 μmol h^{-1}, which is about ~5.2 times more than that of neat g-C_3N_4. The increased H_2 evolution is due to the availability of more number of active adsorption sites with enhanced redox ability and improved charge transfer ability. The efficiency of charge transfer and separation was evaluated by electrochemical studies like transient photocurrent measurement and Nyquist plot as shown in Fig. 8.18. Upon light irradiation, the transient photocurrent response of O-doped porous g-C_3N_4 show remarkably enhanced data with respect to bulk g-C_3N_4.

This can be attributed to the presence of electrophilic groups (C–O, C=O and COOH) on 2D porous ultrathin g-C_3N_4, which is favorable for the transfer of photogenerated electrons in CB through the electrophilic groups inhibiting direct recombination of charge carriers. The reduced radius in Nyquist plot in case of O-doped porous g-C_3N_4 in comparison to neat g-C_3N_4 is consistent with photoluminescence spectral analysis. These results indicate that 2D porous g-C_3N_4 ultrathin structure by introduction of O-containing functional groups is advantageous for improved photocatalytic performance. The photocatalytic mechanism is schematically represented in Scheme 8.6.

Pawar et al. designed a 1D microrod of g-C_3N_4 with porous network showing exceptional photocatalytic H_2 generation through a facile and template-free method (Pawar et al. 2016). Use of conc. acids not only results in exfoliation through protonation but also lifts off strong oxidation and protonation. Upon protonation in presence of various acids (HCl, HNO_3 and H_2SO_4), the acid ions intercalate and result in nonuniform bonding inside the g-C_3N_4 network to form interconnected nanopores in 1D microrod morphology. The resulted porous morphology in case of H_2SO_4 treatment forms more prominent interconnected nanopores in comparison to other acids. The FESEM images of bulk g-C_3N_4 (BCN), hydrochloric acid-treated g-C_3N_4 (HCN), nitric acid-treated g-C_3N_4 (NCN), and sulfuric acid-treated g-C_3N_4 (SCN) are shown in Fig. 8.19.

The rate of H_2 evolution by 1D porous microrod of g-C_3N_4 (34 μmol g^{-1}) was found to be 26 times more than that of the neat g-C_3N_4 (1.26 μmol g^{-1}) under visible light irradiation. Additionally, the photocatalyst shows remarkably high photocurrent stability over 24 h indicating effective resistance toward photocorrosion. The reason for improved photocatalytic H_2 evolution was mainly attributed to prolonged lifetime of charge carriers due to quantum confinement effect, increased number of active sites from interconnected nanopores in 1D microrod morphology, and effective separation of charge carriers. The enhanced H_2 evolution by BCN, HCN, NCN,

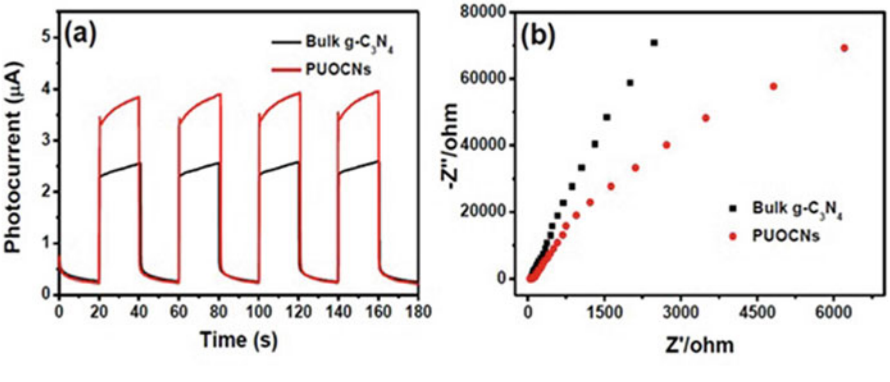

Fig. 8.18 (**a**) Time-dependent photocurrent response (**b**) EIS plot of bulk g-C_3N_4 and porous O-doped g-C_3N_4 (PUOCN) (She et al. 2016)

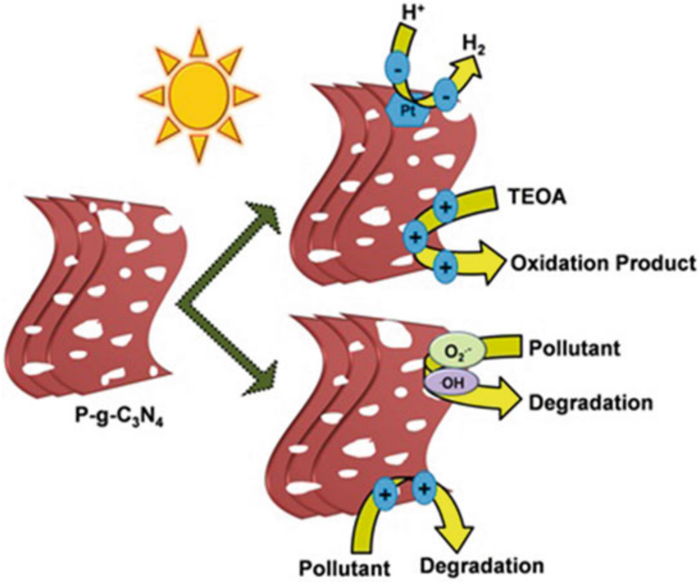

Scheme 8.6 Scheme for proposed mechanism for the photocatalytic H_2 evolution and the pollutant degradation

and SCN nanostructures was further confirmed by the transient photocurrent response supporting efficient separation and charge carrier transport. The transient photocurrent measured as a function of time is shown in Fig. 8.20 and represented in Table 8.4, which is in agreement with the increased surface area. 1D g-C_3N_4 microrod during the facile, template-free synthesis generates nanopores through the 1D microrod and creates number of active sites to show good photocatalytic and electrochemical response. Compared to bulk counterpart, the porous microrod morphology records high photocorrosion stability (more than 24 h).

From the results of photocatalytic H_2 evolution, it was observed that porous SCN having unique interconnected porous network and large contact surface makes available more number of active sites and thus provides superior charge separation, in agreement with the transient photocurrent response.

8.4 Conclusion

In summary, the designing of nanoporous g-C_3N_4 with tunable pore diameter, small particle size, and high surface area is of particular interest because photocatalytic reactions are favorable by the availability of more surface active sites. Although various soft and hard templates are used to introduce porosity, template-free methods

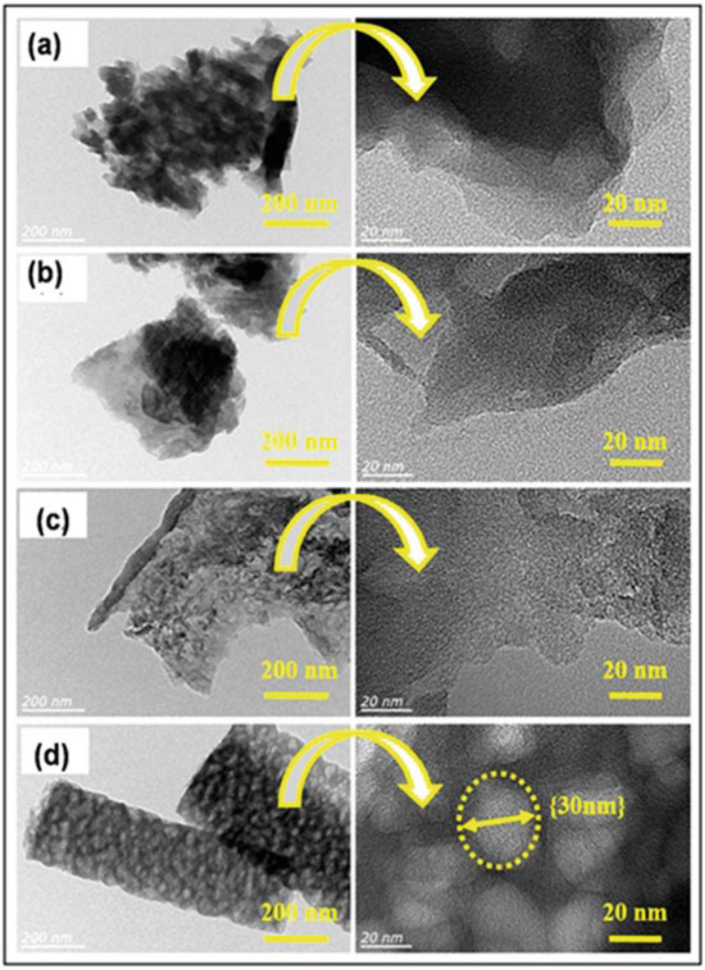

Fig. 8.19 TEM images of bulk g-C_3N_4 (BCN), hydrochloric acid-treated g-C_3N_4 (HCN), nitric acid treated g-C_3N_4 (NCN), and sulfuric acid-treated g-C_3N_4 (SCN); right-hand side represents the images at higher magnification (Pawar et al. 2016)

through self-polymerization of the precursors in presence of some greener chemicals are more acceptable. By using some solvents like water, ethanol-water, etc., also different degrees of porosity can be developed by changing the window size during calcination. By controlling the window size during calcination in a semi-closed system, the release of gases can be controlled, which introduce lots of pores into the material to reduce electron-hole recombination. Moreover, in presence of some volatile materials, gas bubbles are evolved during calcination to introduce useful pore system. Recently many template-free methods are adopted as they provide simplest one-step synthesis and exclude the use of hazardous chemicals. Use of various hard and soft templates also lowers the photocatalytic performance of porous

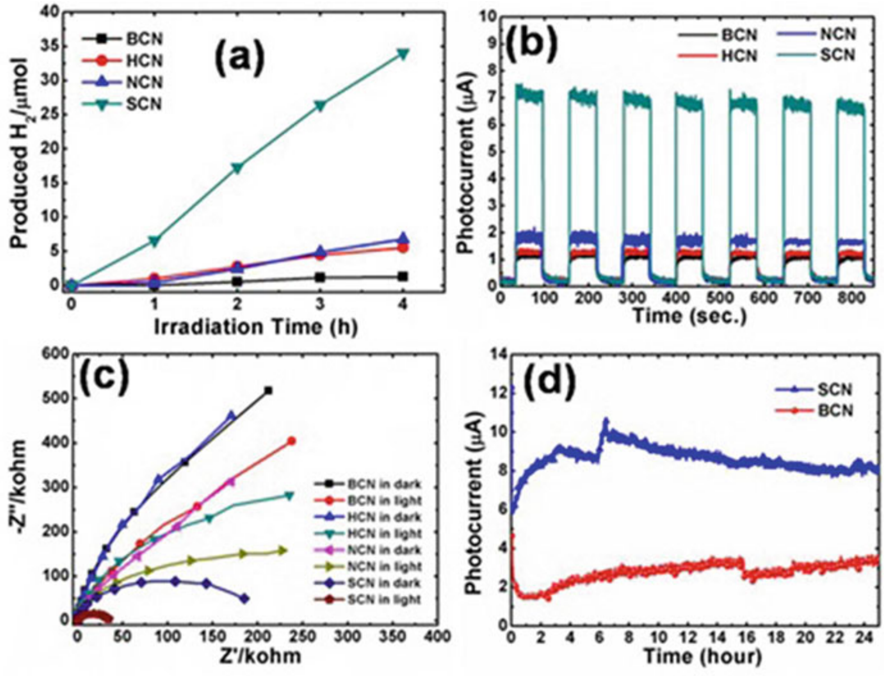

Fig 8.20 (**a**) Photocatalytic hydrogen evolution data and (**b**) transient photocurrent response of bulk g-C_3N_4 (BCN), hydrochloric acid-treated g-C_3N_4 (HCN), nitric acid-treated g-C_3N_4 (NCN), and sulfuric acid-treated g-C_3N_4 (SCN), (**c**) electrochemical impedance spectra (EIS) of BCN, HCN, NCN, and SCN under dark as well as light irradiation and (**d**) photocurrent stability test in visible light illumination of BCN and SCN (Pawar et al. 2016)

Table 8.4 Representing H_2 evolution rate, surface area, and photocurrent response of bulk g-C_3N_4 (BCN), hydrochloric-treated g-C_3N_4 (HCN), nitric acid-treated g-C_3N_4 (NCN), and sulfuric acid-treated g-C_3N_4 (SCN)

Photocatalyst	Photocurrent in μA	Surface area in $m^2\ g^{-1}$	H_2 evolution in μmolg^{-1}	References
BCN	1.12	7.46	1.26	Pawar et al. (2016)
HCN	1.33	15.95	5.54	Pawar et al. (2016)
NCN	1.87	58.82	6.80	Pawar et al. (2016)
SCN	7.09	30.05	34.00	Pawar et al. (2016)

g-C_3N_4 significantly by lowering the final nitrogen content due to the presence of carbon residue in porous g-C_3N_4 after calcination. Porous g-C_3N_4 owing to the interfacial mesoporous structure favors light absorption, much higher high surface area possesses efficient adsorption ability and show high photocatalytic performance. Although use of template-free methods with prolonged calcination time is more adoptable, detrimentally excess surface area also increases the number of surface defects. As a result these defected sites capture the photogenerated electrons and hinder their participation in photocatalytic reaction. Thus, due to thermodynamic and physicochemical point of view, use of various strategies for the designing of porous g-C_3N_4 is still challenging, and more research is required in this field to pave the way for better photocatalytic applications in a sustainable manner.

References

Alqadami AA, Naushad M, Abdalla MA et al (2016) Adsorptive removal of toxic dye using Fe3O4−TSC nanocomposite: equilibrium, kinetic, and thermodynamic studies. J Chem Eng Data 61(11):3806–3813. https://doi.org/10.1021/acs.jced.6b00446

Chen X, Jun YS, Takanabe K, Maeda K, Domen K, Fu X, Antonietti M, Wang X (2009) Ordered mesoporous SBA-15 type graphitic carbon nitride: a semiconductor host structure for photocatalytic hydrogen evolution with visible light. Chem Mater 21(18):4093–4095. https://doi.org/10.1021/cm902130z

Chen Z, Lu S, Wu Q, He F, Zhao N, He C, Shi C (2018) Salt-assisted synthesis of 3D open porous g-C_3N_4 decorated with cyano groups for photocatalytic hydrogen evolution. Nanoscale 10 (6):3008–3013. https://doi.org/10.1039/C7NR05927B

Deng Y, Tang L, Zeng G, Zhu Z, Yan M, Zhou Y, Wang J, Liu Y, Wang J (2017) Insight into highly efficient simultaneous photo catalytic removal of Cr(VI) and 2,4-diclorophenol under visible light irradiation by phosphorus doped porous ultrathin g-C_3N_4 nanosheets from aqueous media: performance and reaction mechanism. Appl Catal B 203:343–354. https://doi.org/10.1016/j.apcatb.2016.10.046

Dong G, Zhang L (2012) Porous structure dependent photoreactivity of graphitic carbon nitride under visible light. J Mater Chem 22(3):1160. https://doi.org/10.1039/C1JM14312C

Elliot MA, Turner NC (1972) Estimating the future rate of production of the World' s fossil fuels. Presented at the American Chemical Society's 163rd national meeting, division of fuel chemistry symposium on "Non-fossil chemical fuels", Boston

Fan Q, Liu J, Yu Y, Zuo S (2014) A template induced method to synthesize nanoporous graphitic carbon nitride with enhanced photocatalytic activity under visible light. RSC Adv 4 (106):61877–61883. https://doi.org/10.1039/C4RA12033G

Franklin EC (1922) The ammono carbonic acid. J Am Chem Soc 44(3):486–509. https://doi.org/10.1021/ja01424a007

Fu J, Zhu B, Jiang C, Cheng B, You W, Yu J (2017) Hierarchical porous O-doped g-C_3N_4 with enhanced photocatalytic CO_2 reduction activity. Small 13(15):1603938. https://doi.org/10.1002/smll.201603938

Guo Y, Chu S, Yan S, Wang Y, Zou Z (2010) Developing a polymeric semiconductor photocatalyst with visible light response. Chem Commun 46(39):7325–7327. https://doi.org/10.1039/C0CC02355H

Han KK, Wang CC, Li YY, Wan MM, Wang Y, Zhu JH (2013) Facile template-free synthesis of porous g-C_3N_4 with high photocatalytic performance under visible light. RSC Adv 3 (24):9465–9469. https://doi.org/10.1039/C3RA40765A

Han Q, Wang B, Gao J, Cheng Z, Zhao Y, Zhang Z, Qu L (2016) Atomically thin mesoporous nanomesh of graphitic C_3N_4 for high-efficiency photocatalytic hydrogen evolution. ACS Nano 10(2):2745–2751. https://doi.org/10.1021/acsnano.5b07831

Hoffmann MR, Martin ST, Choi W, Bahnemann DW (1995) Environmental applications of semiconductor photocatalysis. Chem Rev 95(1):69–96. https://doi.org/10.1021/cr00033a004

Huang H, Xiao K, Tian N, Dong F, Zhang T, Du X, Zhang Y (2017) Template-free precursor-surface-etching route to porous g-C_3N_4 thin nanosheets for enhancing photocatalytic reduction and oxidation activity. J Mater Chem A 5(33):17452–17463. https://doi.org/10.1039/C7TA04639A

Inoue T, Fujishima A, Konishi S, Honda K (1979) Photoelectrocatalytic reduction of carbon dioxide in aqueous suspensions of semiconductor powders. Nature 277(5698):637–638. https://doi.org/10.1038/277637a0

Jing X, Wang Z, Zhu Y (2017) Enhanced visible-light-driven photocatalytic disinfection performance and organic pollutants degradation activity of porous g-C_3N_4 nanosheets. ACS Appl Mater Interfaces 33(9):27727–27735. https://doi.org/10.1021/acsami.7b07657

Jun YS, Hong WH, Antonietti M, Thomas A (2009) Mesoporous, 2D hexagonal carbon nitride and titanium nitride/carbon composites. Adv Mater 21(42):4270–4274. https://doi.org/10.1002/adma.200803500

Karamian E, Sharifnia S (2016) On the general mechanism of photocatalytic reduction of CO_2. J CO2 Util 16:194–203. https://doi.org/10.1016/j.jcou.2016.07.004

Kumar S, Surendar T, Kumar B, Baruah A, Shanker V (2014) Synthesis of highly efficient and recyclable visible-light responsive mesoporous gC_3N_4 photocatalyst via facile template-free sonochemical route. RSC Adv 4(16):8132–8137. https://doi.org/10.1039/C3RA43942A

Kumar A, Kumar A, Sharma G et al (2017) Solar-driven photodegradation of 17-β-estradiol and ciprofloxacin from waste water and CO2 conversion using sustainable coal-char/polymeric-g-C3N4/RGO metal-free nano-hybrids. New J Chem 41:10208–10224. https://doi.org/10.1039/c7nj01580a

Kumar S, Karthikeyan S, Lee AF (2018) g-C3N4-based nanomaterials for visible light-driven photocatalysis. Catalysts 8(2):74. https://doi.org/10.3390/catal8020074

Kumar A, Sharma G, Naushad M et al (2019) Visible photodegradation of ibuprofen and 2,4-D in simulated waste water using sustainable metal free-hybrids based on carbon nitride and biochar. J Environ Manag 231:1164–1175. https://doi.org/10.1016/j.jenvman.2018.11.015

Li X, Jinhua Y (2007) Photocatalytic degradation of Rhodamine B over $Pb_3Nb_4O_{13}$/fumed SiO_2 composite under visible light irradiation. J Phys Chem C 111(35):13109–13116. https://doi.org/10.1021/jp072752m

Li Q, Yang J, Feng D, Wu Z, Wu Q, Park SS, Ha CS, Zhao D (2010) Facile synthesis of porous carbon nitride spheres with hierarchical three-dimensional mesostructures for CO_2 capture. Nano Res 3(9):632–642. https://doi.org/10.1007/s12274-010-0023-7

Li HJ, Sun BW, Sui L, Qian DJ, Chen M (2015) Preparation of water-dispersible porous g-C_3N_4 with improved photocatalytic activity by chemical oxidation. Phys Chem Chem Phys 17 (5):3309–3315. https://doi.org/10.1039/C4CP05020G

Li K, Peng B, Peng T (2016) Recent advances in heterogeneous photocatalytic CO_2 conversion to solar fuels. ACS Catal 6(11):7485–7527. https://doi.org/10.1021/acscatal.6b02089

Liebig JV (1834) About some nitrogen compounds. Ann Pharmacother 10:10

Lin J, Pan Z, Wang X (2014) Photochemical reduction of CO_2 by graphitic carbon nitride polymers. ACS Sustain Chem Eng 2(3):353–358. https://doi.org/10.1021/sc4004295

Naushad M, Ahamad T, AlOthman ZA, Al-Muhtaseb AH (2019) Green and eco-friendly nanocomposite for the removal of toxic Hg(II) metal ion from aqueous environment: adsorption kinetics & isotherm modelling. J Mol Liq 279:1. https://doi.org/10.1016/j.molliq.2019.01.090

OmoIbhadon A, Fitzpatrick P (2013) Heterogeneous photocatalysis: recent advances and applications. Catalysts 3(1):189–218. https://doi.org/10.3390/catal3010189

Patnaik S, Martha S, Acharya S, Parida KM (2015) An overview on modification of g-C_3N_4 by high carbon containing materials for photocatalytic applications. Inorg Chem Front 3(3):336–347. https://doi.org/10.1039/C5QI00255A

Patnaik S, Martha S, Parida KM (2016) An overview on structural, textural and morphological modulations of g-C_3N_4 towards photocatalytic hydrogen production. RSC Adv 6 (52):46929–46951. https://doi.org/10.1039/C5RA26702A

Patnaik S, Sahoo DP, Parida KM (2018a) An overview on Ag modified g-C_3N_4 based nanostructured materials for energy and environmental applications. Renew Sust Energ Rev 82:1297–1312. https://doi.org/10.1016/j.rser.2017.09.026

Patnaik S, Swain G, Parida KM (2018b) Highly efficient charge transfer through double Z-scheme mechanism by Cu promoted MoO_3/g-C_3N_4 hybrid nanocomposite with superior electrochemical and photo catalytic performance. Nanoscale 10(13):5950–5964

Pawar RC, Kang S, Park JH, Kim J, Ahn S, Lee CS (2016) Room-temperature synthesis of nanoporous 1D microrods of graphitic carbon nitride (g-C_3N_4) with highly enhanced photo catalytic activity and stability. Sci Rep 6:31147. https://doi.org/10.1038/srep31147

Peer M, Lusardi M, Jensen KF (2017) A facile soft-templated synthesis of high surface area and highly porous carbon nitrides. Chem Mater 29(4):1496–1506. https://doi.org/10.1021/acs.chemmater.6b03570

Root D, Attanasi E (1978) The American Association of Petroleum Geologists Bulletin

Sharma A, Sharma G, Naushad M et al (2018) Remediation of anionic dye from aqueous system using bio-adsorbent prepared by microwave activation. Environ Technol 39(7):917–930. https://doi.org/10.1080/09593330.2017.1317293

She X, Liu L, Ji ZH, Yeping M, Liying L, Daolin H, Hui D, Li XH (2016) Template-free synthesis of 2D porous ultrathin nonmetal-doped g-C_3N_4 nanosheets with highly efficient photocatalytic H_2 evolution from water under visible light. Appl Catal B 187:144–153. https://doi.org/10.1016/j.apcatb.2015.12.046

Sun Z, Wang H, Wu Z, Wang L (2018) g-C_3N_4 based composite photocatalysts for photocatalytic CO_2 reduction. Catal Today 300:160–172. https://doi.org/10.1016/j.cattod.2017.05.033

Tong Z, Yang D, Shi J, Nan Y, Sun Y, Jiang Z (2015) Three-dimensional porous aerogel constructed by g-C_3N_4 and graphene oxide nanosheets with excellent visible-light photocatalytic performance. ACS Appl Mater Interfaces 7(46):25693–25701. https://doi.org/10.1021/acsami.5b09503

Veziroglu TN, Basar O (1974) Dynamics of a universal hydrogen fuel system. In: Hydrogen energy. Part B. Plenum Press, Heidelberg, pp 1309–1326

Wang Y, Wang X, Antonietti M, Zhang Y (2010) Facile one-pot synthesis of nanoporous carbon nitride solids by using soft templates. ChemSusChem 3(4):435–439. https://doi.org/10.1002/cssc.200900284

Wang Y, Wang X, Antonietti M (2012) Polymeric graphitic carbon nitride as a heterogeneous organocatalyst: from photochemistry to multipurpose catalysis to sustainable chemistry. Angew Chem Int Ed Engl 51(1):68–89. https://doi.org/10.1002/anie.201101182

Wang Z, Guan W, Sun Y, Dong F, Zhou Y, Ho W-K (2015a) Water-assisted production of honeycomb-like g-C_3N_4 with ultralong carrier lifetime and outstanding photocatalytic activity. Nanoscale 7(6):2471. https://doi.org/10.1039/C4NR05732E

Wang J, Zhang C, Shen Y, Zhou Z, Yu J, Li Y, Wei W, Liu S, Zhang Y (2015b) Environment-friendly preparation of porous graphite-phase polymeric carbon nitride using calcium carbonate as templates, and enhanced photoelectrochemical activity. J Mater Chem A 3(9):5126. https://doi.org/10.1039/C4TA06778A

Wang JC, Cui CX, Li Y, Liu L, Zhang YP, Shi W (2017a) Porous Mn doped g-C_3N_4 photocatalysts for enhanced synergetic degradation under visible-light illumination. J Hazard Mater 3894:30432–30436. https://doi.org/10.1016/j.jhazmat.2017.06.011

Wang A, Wang C, Fu L, Wong-Ng W, Lan Y (2017b) Recent advances of graphitic carbon nitride-based structures and applications in catalyst, sensing, imaging, and LEDs. Nanomicro Lett 9 (4):47. https://doi.org/10.1007/s40820-017-0148-2

Watanabe T, Takizawa T, Honda K, Takirawa T, Honda K, Takizawa T, Honda K (1977) Photocatalysis through excitation of adsorbates. 1. Highly efficient N-deethylation of rhodamine B adsorbed to cadmium sulfide. J Phys Chem 81(19):1845–1851. https://doi.org/10.1021/j100534a012

Xu F, Chen J, Guo L, Lei S, Ni Y (2012) In situ electrochemically etching-derived ZnO nanotube arrays for highly efficient and facilely recyclable photocatalyst. Appl Surf Sci 258 (20):8160–8165. https://doi.org/10.1016/j.apsusc.2012.05.014

Xu J, Wang Y, Zhu Y (2013) Nanoporous graphitic carbon nitride with enhanced photocatalytic performance. Langmuir 29(33):10566–10572. https://doi.org/10.1021/la402268u

Xu F, Webster RD, Chen J, Tan TTY, Sit PHL, Teoh WY (2017) Revisiting the mechanism of hexavalent chromium ion reduction: the parallel photodecomposition and photocatalytic reduction of chromate (VI) ester. Appl Catal B 210:444–453. https://doi.org/10.1016/j.apcatb.2017.04.024

Xue J, Ma S, Zhou Y, Wang Q (2015) Au-loaded porous graphitic C_3N_4/graphene layered composite as a ternary plasmonic photocatalyst and its visible-light photocatalytic performance. RSC Adv 5(107):88249–88257. https://doi.org/10.1039/C5RA17719G

Yan H (2012) Soft-templating synthesis of mesoporous graphitic carbon nitride with enhanced photocatalytic H_2 evolution under visible light. Chem Commun 48(28):3430–3432. https://doi.org/10.1039/C2CC00001F

Yang Z, Zhang Y, Schnepp Z (2015) Soft and hard templating of graphitic carbon nitride. J Mater Chem A 3(27):14081. https://doi.org/10.1039/C5TA02156A

Yoneyama H, Yamashita Y, Tamura H (1979) Heterogeneous photocatalytic reduction of dichromate on n-type semiconductor catalysts. Nature 282:817–818. https://doi.org/10.1038/282817a0

Zhang Y, Liu J, Wu G, Chen W (2012a) Porous graphitic carbon nitride synthesized via directly polymerization of urea for efficient sunlight-driven photocatalytic hydrogen production. Nanoscale 4(17):5300–5305. https://doi.org/10.1039/C2NR30948C10.1039/C7NR09049H

Zhang G, Zhang J, Zhang M, Wang X (2012b) Polycondensation of thiourea into carbon nitride semiconductors as visible light photocatalysts. J Mater Chem 22(16):8083. https://doi.org/10.1039/C2JM00097K

Zhao J, Wu T, Wu K, Oikawa K, Hidaka H, Serpone N (1998) Photoassisted degradation of dye pollutants. V. Self-photosensitized oxidative transformation of Rhodamine B under visible light irradiation in aqueous TiO_2 dispersions. J Phys Chem B 102(30):5845–5851. https://doi.org/10.1021/jp980922c

Zhao R, Gao J, Mei S, Wu Y, Wang X, Zhai X, Yang J, Hao C, Yan J (2017) Facile synthesis of graphitic C_3N_4 nanoporous-tube with highly enhancement of visible-light photocatalytic activity. Nanotechnology 28:49. https://doi.org/10.1088/1361-6528-aa929a

Zheng Y, Liu J, Liang J, Jaroniecc M, Qiao SZ (2012) Graphitic carbon nitride materials: controllable synthesis and applications in fuel cells and photocatalysis. Energy Environ Sci 5 (5):6717. https://doi.org/10.1039/C2EE03479D

Zhu J, Xiao P, Li H, Carabineiro SAC (2014) Graphitic carbon nitride: synthesis, properties, and applications in catalysis. ACS Appl Mater Interfaces 6(19):16449–16465. https://doi.org/10.1021/am502925j

Zou XX, Li GD, Wang YN, Zhao J, Yan C, Guo MY, Li L, Chen JS (2011) Direct conversion of urea into graphitic carbon nitride over mesoporous TiO_2 spheres under mild condition. Chem Commun 47(3):1066. https://doi.org/10.1039/C0CC03530K

Chapter 9
Photocatalysts for Indoor Air Pollution: A Brief Review

Shanmuga Sundar Dhanabalan, Sivanantha Raja Avaninathan, Saravanan Rajendran, and Marcos Flores Carrasco

Contents

9.1 Introduction 248
9.2 Ideal Catalyst 249
9.3 Photocatalytic Materials for Air Pollution 249
9.4 Biological and Chemical Contaminants 252
  9.4.1 Biological Contaminants 252
  9.4.2 Chemical Contaminants 253
9.5 Methods to Control the Mobilization of TiO_2 256
9.6 Purification Techniques for Indoor Air Pollution 257
  9.6.1 Indoor Source Control 257
  9.6.2 Ventilation 258
  9.6.3 Filtration 258
  9.6.4 Adsorption 259
  9.6.5 Ultraviolet Germicidal Irradiation 260
  9.6.6 Ozonation 260
9.7 Photocatalytic Oxidation 261
  9.7.1 Photocatalyst Oxidation Removal of Volatile Organic Compounds 261
  9.7.2 Removal of Inorganic Gas Pollutants Using PCO 264
  9.7.3 Non-Titanium-Based Photocatalyst for Air Purification 266
  9.7.4 Photocatalysis with Ozone 266
9.8 Summary 267
References 267

Abstract Photocatalysis is one of the fastest growing technologies for the treatment of pollutants, utilizing the mechanism of reaction with the help of light (photo

---

S. S. Dhanabalan (✉) · M. F. Carrasco
Department of Physics, Universidad de Chile, Santiago, Chile
e-mail: mflorescarra@ing.uchile.cl

S. R. Avaninathan
Department of ECE, Alagappa Chettiar Government College of Engineering & Technology, Karaikudi, Tamil Nadu, India

S. Rajendran
Faculty of Engineering, Mechanical Department, University of Tarapacá, Arica, Chile

S. Rajendran et al. (eds.), *Green Photocatalysts for Energy and Environmental Process*, Environmental Chemistry for a Sustainable World 36,
https://doi.org/10.1007/978-3-030-17638-9_9

emissions). Photocatalysis has captured broad academic and research interest during the past three decades for its potential of controlling pollution in air and water. Its qualities, such as low cost and high efficiency, have caused researchers all over the world to focus on it and also promoted many industrial applications and much research. Photocatalysis has been used to remove major air pollutants, disinfect water, and oxidize various organic chemicals. In this connection, this chapter considers the properties of the ideal photocatalyst, available photocatalytic materials for air pollution control, common indoor air pollutants and their severe health effects, and purification techniques for indoor air pollution. Furthermore, photocatalytic oxidation techniques for the removal of volatile organic compounds are discussed in detail.

Keywords Photocatalyst · Indoor air pollution · Titanium dioxide · Photocatalytic oxidation

9.1 Introduction

Today the entire world is struggling with the severe effects of environmental pollution and researchers all over the world are looking to provide solutions for this problem (Anpo 2000; Naushad 2014). In 2012, one in eight of all deaths, around 7 million people, died because of bad air quality, which has a vast negative impact around the worldwide (Naushad 2014; Lelieveld et al. 2015). To have more yield and more profits, chemical industries provide products with more favourable usage although they have hazardous impacts on the human health and environment. Compounds such as phenol, pesticides from wastewater sewage, polymeric surfactants, and herbicides release dangerous chemical substances that are not easily biodegradable (Hoffmann et al. 1995; Alshehri et al. 2014; Al-Othman et al. 2011; Al-Kahtani et al. 2018).

People think that pollutants occur more in the outdoor environment compared to indoors because of heavy traffic pollutes the air. But, although this may be shocking, an urban area with average traffic might be cleaner than indoor air. Some of the studies reported that the concentration of air pollution indoors is five times higher than in the outdoor environment (Zhang and Smith 2003; Bernstein et al. 2008; Kolarik et al. 2010). Factors such as smoke, electronic equipment, inadequate ventilation, mould damage, and furniture increase air pollution in schools, homes, and public places. Sick building syndrome is a disorder found to occur in a group of people who spent time in a certain building with indoor air pollution (Wolkoff and Nielsen 2001; Crook and Burton 2010; Norhidayah et al. 2013). Some pollutants may cause diseases such as respiratory infections or cancer that are diagnosed later (Zhang and Smith 2003). From the foregoing facts and the literature, it is evident that the people spend 90% of their time in an indoor environment, which is a key factor to be considered for human health and comfort (Li 2016). Also, some of the studies state that compared to the outdoor environment there is a lag in public health awareness in indoor air pollution (Challoner and Gill 2014; Rohra and Taneja 2016).

The quality of the indoor air can be improved by eliminating or reducing contaminants by ventilation, by controlling indoor source pollutant emission, and by using low emission materials. Adequate ventilation and effective infiltration are the traditional methods to improve indoor air quality (IAQ) in which indoor air pollution can be reduced by introducing outside air into the building. As ventilation is inadequate (Bennett 2009) in modernized buildings, the only way to achieve air quality is to purify the air.

Photocatalysis is one of the fastest growing technologies for the treatment of air pollutants, utilizing the mechanism of reaction with the help of light (photo emissions). Fujishima and Honda 1972, while working on the photolysis of water, initially recognized this as a heterogeneous photocatalyst. Much research was put forward in their work towards the development and growth of photocatalysis techniques, and in recent years researchers have explored and reported the use of semiconductor materials as photocatalysts for elimination of organic and inorganic species. It has been considered an effective tool for the protection of the environment because of its large oxidation capacity (Robert and Malato 2002). Still, applications towards the improvement of indoor air by reducing the contaminants are open to wide usages. Hence, this chapter discusses photocatalysis for efficient indoor air pollution remediation, techniques and methods available for the elimination of pollutants, and the perspectives.

9.2 Ideal Catalyst

Fujishima et al. have reported that a photocatalyst to be considered as an ideal candidate should possess such characteristics as these (Fujishima et al. 2000):

1. Photo-activity, nontoxic nature, low cost
2. Inert to chemical and biological activity
3. Photo-corrosion stability
4. Active towards visible light

The various steps involved in photocatalysis activities (Shan et al. 2010) are diffusion, adsorption, reaction, desorption, and diffusion of the final products from the surface of the catalyst (Serpone and Emeline 2012). Figure 9.1 represents the steps involved in photocatalytic activities.

9.3 Photocatalytic Materials for Air Pollution

Semiconductors such as TiO_2, Fe_2O_3, ZnO, CdS, WO_3, and SnO_2 (Vinu and Madras 2010) have major roles in photocatalytic activity. Compared to TiO_2, all the other candidates have some limitations: for example, ZnO is unstable at low pH values, CdS, iron oxides, and ZnS suffer from corrosion, and WO_3 is less active. Among these, TiO_2 is considered to be a potential candidate for photocatalytic activities

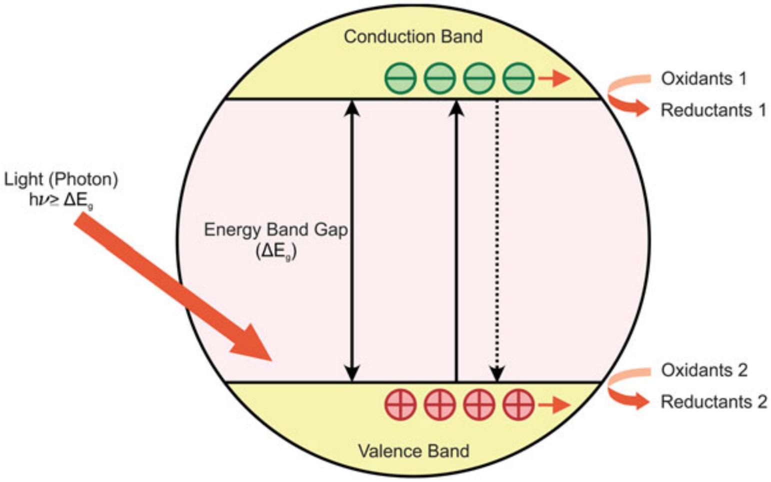

Fig. 9.1 Schematic representation of photocatalysis scheme (Demeestere et al. 2007)

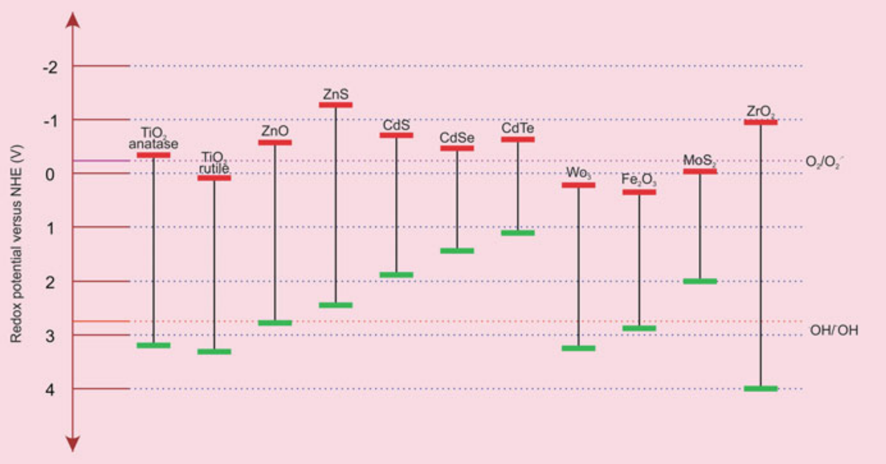

Fig. 9.2 Energy bandgap diagram of various semiconductor oxides (Demeestere et al. 2007)

because of its numerous advantages: chemical stability, low cost, expected electronic and optical properties, and nontoxicity (Litter 1999). Figure 9.2 represents the energy bandgap diagram of various semiconductor oxides.

Generally, TiO_2 is available in three forms: anatase, rutile, and brookite. Of these the third is an uncommon form and stable only at high temperatures. Figure 9.3 represents the structures of TiO_2 in three different forms. Although TiO_2 has several merits towards photocatalytic activities, it is also restricted because of the wide bandgap (3.2 eV), which requires an excitation source of ultraviolet (UV) wavelength

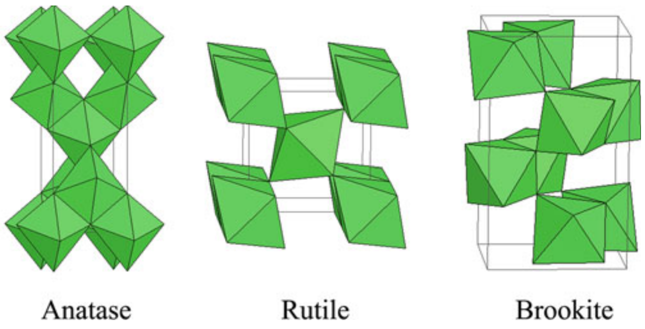

Fig. 9.3 Various TiO_2 phases (Smyth 2010)

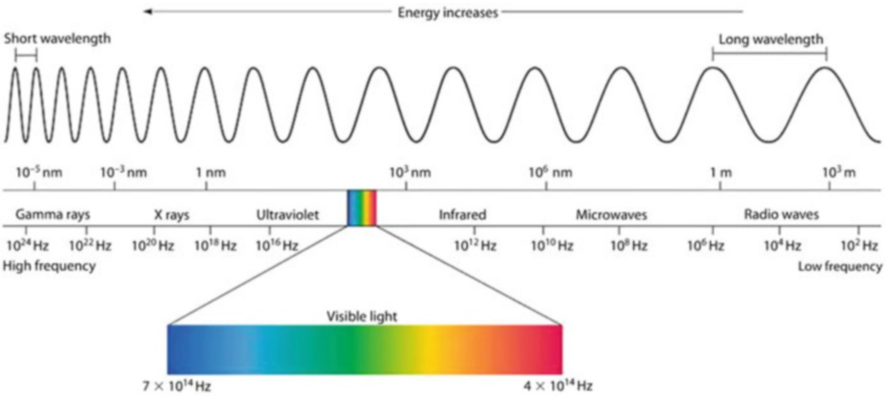

Fig. 9.4 Electromagnetic spectrum representing the entire wavelength region (www.miniphysics.com)

at 387 nm. The availability of this excitation energy is only 5% (Fig. 9.4). The photocatalytic oxidation (PCO) of volatile organic compounds (VOC) and inorganic pollutants are mostly treated by using wide bandgap semiconductor materials. The surface reactants on the semiconductors are the main reason for the foundation of the PCO air purification process (Bickley and Stone 1973; Spanhel et al. 1987; Cant and Cole 1992; Linsebigler et al. 1996; Khan and Ghoshal 2000; Shen and Ku 2002). The properties such as catalyzing, adsorbing, deodorizing, and disinfection of TiO_2 project it as a potential candidate for air pollution treatments.

Serious studies were put forward by researchers all over the world to improve the photocatalytic activity of existing materials or to find an alternate to enhance photocatalytic activity. Li et al. (2005) stated that shifting the optical absorption point of TiO_2 near to the lower energy can improve photocatalytic activities in the visible wavelength. It is a renewable energy source and can be used for large-scale operations. Photocatalysis can be achieved by doping anions (such as sulfur, fluorine, nitrogen, boron, and carbon) in TiO_2 to achieve high efficiency. Several modification techniques are used for producing highly active TiO_2 for photocatalytic activities, such as doped TiO_2 (e.g., self-doping, non-metal doping, co-doping, metal doping), mesoporous TiO_2, shape-controlled TiO_2, supported TiO_2, surface-modified TiO_2, and dye-sensitized TiO_2 (Sun et al. 2010).

Nitrides, metal sulfides, and oxynitrides are also proposed as candidates for photocatalytic activity using visible light (Inoue 2009). Researchers have proposed a surface plasmonic effect-based plasmonic photocatalyst (Kale et al. 2014). Very recently, graphitic carbon nitride-based metal-free photocatalysts have also been used as a photocatalyst using visible light (Sun et al. 2014; Cao et al. 2015). Although the technique and the enactment of PCO for purification of air pollutants are customized, the difficult aspect is the advances in photocatalytic material and reactors for this application.

Machado et al. 2006 reported that photocatalytic activities can be enhanced by increasing the surface area of the catalyst. A high interaction of reactant with catalyst takes place when the surface area is large. Doping of materials helps reduce the energy bandgap between the valence and conduction bands, which in turn requires low energy (visible light source) for the excitation of electrons from the lower to the higher band (Juanru et al. 2007).

9.4 Biological and Chemical Contaminants

People spend most of their time in an indoor air environment, which determines the health and well-being of a person. Perilous substances emanating from construction materials and indoor tools cause a wide range of health problems and even may be fatal. Around 4.3 million people died in 2012 because of illnesses produced by household air pollution (WHO 2014). Indoor contaminants can be classified into two major categories: chemical and biological.

9.4.1 Biological Contaminants

Biological contaminants are living entities that can be transported via air and are often invisible. Bacteria, viruses, animal dander, moulds, and pollen are some of the common biological impurities which can cause dangerous effects in humans (Nelson et al. 1988). Nutrients and poor moisture content are the two important reasons for the growth of these pollutants (US Department of Health and Human Services 2006). The amount of contaminant that is needed to cause infection in the human being is unknown but will vary from one person to other.

Among the contaminants, airborne bacteria and fungi are considered to be major pollutants that cause challenging health issues. These pollutants will grow under high humidity conditions in materials such as grease, soap scum, dirt, textiles, and paper. Once the mould colony has been formed, it will start floating on the air

(Dallongeville et al. 2015) and fall on land or surfaces, which leads to symptoms such as eye and skin irritation, nasal stuffiness, and wheezing (Taskinen et al. 1997). Madureira et al. (2015) proposed a brief investigation of biological pollutants by accumulating air samples from homes, primary schools, childcare centres, and elderly care centres in the area of North Portugal, and reported that the pollutants are high in childcare centres and schools because of lack of ventilation and different density of occupants. Dust mines are another source causing biological pollutants (Calderón et al. 2015).

9.4.2 Chemical Contaminants

Among chemical contaminants, gases such as nitrogen dioxide (NO_2), carbon monoxide (CO), sulfur dioxide (SO_2), particulate matter ($PM_{2.5}$ and PM_{10}), and chemical and microbial volatile organic compounds (VOCs) are the most serious candidates causing air pollution (Bernstein et al. 2008). One second-most candidate is radon, a colourless radioactive gas that causes lung cancer in most countries (Environmental Protection Agency 2017).

Possible health problems caused by some of the most significant indoor air pollutants, their effects, and the indoor sources are listed in Table 9.1. The first step to reduce or avoid problems from these materials is to know their impact.

Stranger et al. (2009) reported a brief investigation on particulate matter in which the collected samples revealed that 90% of indoor and 85% of outdoor particles are smaller than 2.5 μg. The approximate indoor mass density of $PM_{2.5}$ was found to be 46.6 $\mu g/m^3$ and 29.5 $\mu g/m^3$ in a smoker's and non-smoker's house, respectively, which are above the normal $PM_{2.5}$ EU norm of 25 $\mu g/m^3$. The indoor $PM_{2.5}$ concentrations of ten various buildings in Dublin, Ireland, were analyzed and reported by Challoner and Gill 2014. The concentration of $PM_{2.5}$ was found to be greater during working hours when compared to non-working hours, of which five locations exceeded the EU norm.

The concentration of PM_{10} is approximately equal to 49.4 $\mu g/m^3$ in a smoker's house and 33.8 $\mu g/m^3$ in a non-smoker's house (Stranger et al. 2009). The obtained PM_{10} concentration is found to be more or less equal with the WHO indoor air guidelines value and in good agreement with the mass concentration ranges published by the US Environmental Protection Agency (USEPA 2004a, b).

Concentrations of NO_2 for personal exposure, indoor and outdoor, were 41.4, 32.6, and 38.9 $\mu g/m^3$, respectively. The concentrations of NO_2 were in the range 25–43 $\mu g/m^3$ for personal exposure, 13–62 $\mu g/m^3$ indoors, 24–61 $\mu g/m^3$ outdoors, and 27–36 $\mu g/m^3$ in the workplace, as reported in the INDEX report by the European Commission (EC). In European homes, the maximum associated levels for the use of gas appliances are in the range 180–2500 $\mu g/m^3$ (Koistinen et al. 2008). Rivas et al. (2014) recently examined the concentrations of NO_2 in Barcelona schools and reported that the mean concentration of NO_2 (30 $\mu g/m^3$) is below the guideline level. The concentration of SO_2 both indoors and outdoors was investigated by

Table 9.1 Common chemical indoor air pollutants: their health effects and sources

References	Potential health effects	Compound	Source
Environmental Protection Agency (2017), European Commission. Air Quality Standards (2015), National Ambient Air Quality Standards (NAAQS) (2014), WHO. Technical report (2005), Leung (2015), WHO (2000)	Respiratory and cardiovascular effects	Fine particles (PM2.5)	Furnaces, cleaning and cooking sprays, heaters, fireplaces, and outdoor air
European Commission. Air Quality Standards (2015), National Ambient Air Quality Standards (NAAQS) (2014), WHO. Technical report, World Health Organization (2005), Leung (2015), WHO (2000)	Respiratory and cardiovascular effects	Particulate matter (PM10)	Outdoor air and combustion sources
European Commission. Air Quality Standards (2015), WHO (2005), WHO. Technical report (2010), Leung (2015), WHO (2000)	Asthma, inflammation, reduced resistance to respiratory contagions, broncho-constriction	Nitrogen dioxide (NO_2)	Tobacco, outdoor air, smoke, heating equipment, coal or wood stoves
Leung (2015), WHO. Technical report (2010), WHO (2000)	Highly toxic and fatal	Carbon monoxide (CO)	Tobacco, outdoor air, smoke, heating equipment, coal or wood stoves
European Commission. Air Quality Standards (2015), WHO. Technical report, (2005)	Asthma and respiratory symptoms	Sulfur dioxide (SO_2)	Tobacco, outdoor air, smoke, heating equipment, coal or wood stoves
Bahri and Haghighat (2014), European Commission, Air Quality Standards (2015), WHO Regional Office for Europe. Technical report (2010), WHO (2000)	Leukemia, bone marrow damage, cancer, genotoxic, respiratory problems	Benzene (C_6H_6)	Paints, tobacco, lubricants, stored fuel, detergents, and pesticides
Bahri and Haghighat (2014), WHO Regional Office for	Eye irritation, throat and nose infections,	Formaldehyde (CH_2O)	Combustion sources, detergents, wood products, solvents,

(continued)

Table 9.1 (continued)

References	Potential health effects	Compound	Source
Europe, Technical report (2010), WHO (2000)	headaches, asthma, cancer symptoms		waxes, nail polish removers, tobacco smoke and glues
Bahri and Haghighat (2014), WHO (2000), WHO, Regional Office for Europe, Technical report (2010)	Risk of cancer, reproductive risks, central nervous system (CNS) damage	Trichloroethylene (TCE, C_2HCl_3)	Paint removers, printing ink, solvents, etc.
WHO, Regional Office for Europe, Technical report (2010)	Airway tumours, respiratory tract lesions	Naphthalene ($C_{10}H_8$)	Biomass combustion, mothballs
Bahri and Haghighat (2014), WHO (2000), WHO, Regional Office for Europe, Technical report (2010)	Narcosis, cumulative liver, menstrual disorders, altered sperm structure and reduced fertility, CNS damage	Tetrachloroethylene (C_2Cl_4)	Solvents, printing ink, paint removers, etc.
The US Environmental Protection Agency website (2016), WHO, Regional Office for Europe, Technical report (2010), WHO (2000)	Leukemia, lung cancer and cancers of extra-thoracic airways	Radon (Rn)	Groundwater, some earth-derived building materials, earth and rock under buildings and tobacco smoke
European Commission. Air Quality Standards (2015), WHO (2000)	Brain damage, problems in kidney and nervous system, death, and anemia	Lead (Pb)	Soil near highway, water from lead pipes, and dust from lead paints
EPA. Ground Level Ozone – Health effects (2014a), European Commission. Air Quality Standards (2015), WHO, Technical report, (2005), WHO (2000)	Lung infections and respiratory symptoms	Ozone (O_3)	From photochemical reactions in the presence of sunlight and pollutants
European Commission. Air Quality Standards (2015), United States Environmental Protection Agency. Benzo(*a*)pyrene (BaP). TEACH Chemical Summary (2007), WHO Regional Office for Europe. Technical report (2010)	Lung cancer	Benzo[*a*]pyrene (C20H12)	Fireplaces, stoves, tobacco smoke and wood

Stranger et al. (2009), who reported that the levels found were much lower than the guidelines level.

The indoor air quality in ten energy-efficient French schools was examined for 4.5 days (Verriele et al. 2016), and about 150 VOC species were characterized. Measured VOC level varied from 100 μg/m^3 to 680 μg/m^3, depending on occupancy level. At most, 40–85% of ketones and aldehydes are detected from the overall VOC. Acetone, formaldehyde, pentanal, acetaldehyde, 2-butanone, heptane, hexaldehyde, and toluene are present in major concentrations. Aromatic compounds and formaldehyde have concentrations of 8–50 μg/m^3 and 14.8 μg/m^3, respectively, and terpenes are always a minor compound (Verriele et al. 2016). VOC concentration varies sharply in various indoor environments.

9.5 Methods to Control the Mobilization of TiO_2

For the development of photo-reactors for the purification of air contaminants, the controlling of TiO_2 is a tedious process. To control the mobilization of TiO_2, techniques such as fabrication of TiO_2 as a film and depositing TiO_2 on the supported materials are followed. Thevenet et al. (2014) reported that the mobilization of TiO_2 can be controlled by depositing P25-loaded TiO_2 in glass fibers and using these for PCO removal of acetylene. Colloidal silica at 50% and 50% TiO_2 by weight are suspended in water for coating on silica glass fibers. Materials such as PVC sheets (Tejasvi et al. 2015), monoliths (Monteiro et al. 2015), optical fibers (Hou and Ku 2013), and graphene oxides (Andryushina and Stroyuk 2014) were also used for controlling the mobilization of photocatalytic materials.

Compared to the deposition of TiO_2 on supported materials, the synthesis of TiO_2 film is the most powerful method for controlling the mobilization of the photocatalyst materials. Antonello et al. (2014) proposed a novel method for the fabrication of transparent TiO_2 with high mechanical strength using an electrochemical technique. The fabricated film was then used for the PCO removal of volatile oxidation compounds as well as a self-cleaning material. TiO_2 thin films for application to glass windows were suggested by Xie et al. (2016), using a polyvinylpyrrolidone (PVP) modified sol-gel route.

Chemical vapour deposition (CVD), electrophoretic deposition, sol-gel, layer-by-layer method, and thermal methods are important methods proposed for controlling TiO_2 mobilization. In CVD techniques, at high temperature the supporting material is exposed to the gaseous form of the catalyst, which decomposes at the support surface (Shan et al. 2010; Robert et al. 2013). These methods can be used for the synthesis of N-doped TiO_2 from various mixtures (Dunnill et al. 2009), in situ crystallization of TiO_2 (Nizard et al. 2008; Sun et al. 2008), and for controlling film thickness (Nolan et al. 2006).

The sol-gel is a very simple method, in which the support materials are dipped into a solution of TiO_2 mixture heated at high temperature above 450 °C at a controlled rate. Flexibility, simplicity, and low cost make this method the one most used (Shan et al. 2010; Lopez et al. 2013; Sampaio et al. 2013). For substrates such as stainless steel, Al_2O_3 monoliths, and aluminum and glass fibers, a low-temperature sol-gel method is proposed to fabricate thick, robust, and stable photocatalytic layers for various commercial applications (Kete et al. 2014).

In thermal techniques, the catalyst mixture is directly interspersed on the supporting substrate and then thermally treated to form desired characteristics (Tennakone et al. 1995; Shan et al. 2010). However, performance and characteristics of the deposited catalyst hinge on the calcination temperature (Yu et al. 2000). In the layer-by-layer method, the support material that is to be coated is dipped or sprayed using a catalyst solution for the required thickness. The thickness of the catalyst can be easily controlled and hence a large surface area can be obtained (Yu et al. 2000; Nolan et al. 2006; Krogman et al. 2008; Nizard et al. 2008; Sun et al. 2008; Nakajima et al. 2009; Priya et al. 2009). In the electrophoretic deposition method, under the influence of an electric field, the charge particles are moved in a stable support material. This method is found to be most environmentally safe for the complex shapes and provides uniform film thickness. It can be used to deposit TiO_2 composites on the metal (Raddaha et al. 2014) or plastic (Chen et al. 2011) substrates, TiO_2 nanotube arrays (Bavykin et al. 2013), and perhaps used for coating biological molecules in future (Chávez-Valdez et al. 2012).

9.6 Purification Techniques for Indoor Air Pollution

Various measures should be taken to provide a healthy and comfortable indoor environment by limiting the concentration levels of pollutants and improving indoor air quality (IAQ). Various methods for prevention of air pollution are indoor source control, ventilation, and indoor air purification. Both destructive and nondestructive methods are explained briefly in the following sections.

9.6.1 Indoor Source Control

As said by the modern hygiene and preventive medicine pioneer Max Von Pettenkoffer (1958), "*If there is a pile of manure in a space, do not try to remove the odor by ventilation. Remove the pile of manure.*" (Paunović et al. 2005). This quote explains the significance of controlling the source in an indoor environment as a primary approach. To improve IAQ, the most inexpensive operative method is to eradicate or decrease the indoor air pollution sources (Guo et al. 2003).

Source control includes different principles and applications based on the properties of the particular contaminants, preventing contaminants from entering the buildings, and exchanging emitting sources with low-emitting or non-emitting sources (Nazaroff 2013). Also, indoor environment factors such as climate and humidity can be controlled to decrease the emission rate or to avoid conditions that can lead to the generation of contaminants (Clements-Croome et al. 2008).

Several combinations are proposed to improve IAQ. Hult et al. (2015) have carried out examinations of new US residences to determine the extent to which formaldehyde exposure can be reduced by controlling indoor sources (building materials). Homes built with low-VOC materials were compared for formaldehyde concentration with buildings with conventional materials. At an air exchange rate of 0.35 per hour, the formaldehyde concentration in conventionally built homes (46 μg/m^3) was found to be higher than in homes with low-emitting materials (34 μg/m^3), that is, 27% reduction was found in buildings with low-emitting materials. This investigation proves the merits and importance of source control.

9.6.2 Ventilation

The second most useful approach for maintaining good IAQ is by providing ventilation by either natural or mechanical methods (Technical 2008). By ventilation, indoor pollutants can be reduced by mixing with conditioned outdoor air, dispensing this conditioned air throughout the building, and exhausting indoor air to the outside environment.

The difference in air pressure of indoor and outdoor environments provides ventilation by passing the air through leaks in the building shell. However, this is not possible in recently built new buildings, which are constructed to be more airtight and use insulation to reduce loss of energy. Fresh air is reduced in mechanical ventilation systems to exchange indoor air with a supply of relatively clean outdoor air (Yu et al. 2009).

Lyng et al. (2015) has studied the effect of concentrations of polychlorinated biphenyl (PCB) in air by employing mechanically balanced ventilation units. Air exchange rates were increased from 0.2 to 5.5 per hour with mechanical ventilation, and PCB concentrations were decreased to 30%. Hence, it is evident that indoor air pollution can be significantly reduced by installing ventilation in buildings.

9.6.3 Filtration

Filtering is one of the most important techniques in which contaminants responsible for air pollution can be removed and contaminants in the environment can be reduced significantly. Mechanical and electronic air filters are the two basic types of filters employed to remove pollutants and airborne microbes. Mechanical filters simply capture the pollutant particles passing through them. High-efficiency particulate air (HEPA) filters are examples of such mechanical filters, with the filtering efficiency of 99.97% for larger particles (0.3 μm airborne particles). In spite of its advantages, HEPA has disadvantages such as low filtering efficiency for smaller particles: these may be a source of infection from microorganisms harmful to human health and act as a source of pollution when they have not been used properly. Deposition of organic and inorganic matter on the filter leads to microbial growth that decreases filter efficiency and finally causes filter deterioration (Yu et al. 2009). Also, and at the same time, the reaction of deposited particles in the filter with ozone results in formation of by-products such as formic acid, formaldehyde, ultra-fine particles, and carbonyls (Hyttinen et al. 2006; Waring et al. 2008; Yu et al. 2009). Hence, use of mechanical filters for prevention of air pollution requires constant monitoring, cleaning, and replacing of filters (Zhang et al. 2011).

Electronic air filters such as electrostatic precipitators (ESP), which follow the principle of electrostatic attraction to catch air particles, can be used to remove contaminants from the air. The air is passed through an ionization section of the filter where the particles are charged. The ionized particles then pass through the collector plates of opposite charge where they are attracted and trapped by the plates. For the efficient use of filters, the particles must be cleaned frequently from the collector plates. In wet ESP, water is used to clean off the particles whereas in dry ESP rappers are used. A demerit of the ESP is the rapping re-entrainment. While cleaning the dust from the filters, some dust must remain in the filter itself, which causes filter efficiency to decrease. In another method to remove particles from the air, a large quantity of charged particles is passed through a room using an ionizer. Instead of collecting the charged particles as in ESP, here the airborne particles mingle with the ions and seem to be become charged particles. These particles in turn become attached to the nearby surface or attract each other and go out of the air (Environmental Protection Agency 2014b).

Compared to the filters (HEPA or ESP), ionizers seem to have less efficiency in filtering particles such as pollen, tobacco, fungal spores, smoke, and dust (Shaughnessy et al. 1994; Pierce et al. 1996). Regrettably, a few of the electronic filters emit ozone as a secondary product of their operation (Poppendieck et al. 2014). In a comparative study of different ionizers the ozone generation rates range from 56 μg/h to 2757 μg/h (Niu et al. 2001). Berry et al. (2007) examined the consequences of indoor ozone level with a commercially available ionic air cleaner. The measured ozone level was found to be very high in front of the ionic cleaner (77 ppb) when compared to the same room without an ionic cleaner (13–19 ppb). The obtained ozone level was found to be close to EC guidelines.

9.6.4 Adsorption

Electronic and mechanical air filters remove only particulate matter, whereas adsorption units can remove VOC. In the adsorption process, the gasses are attracted towards the surface of a solid such as zeolite, activated carbon, or activated alumina and subsequently removed from the air stream (Yu et al. 2009). Adsorption can occur as physical adsorption or chemical adsorption. If adsorption is induced by Van der Waals forces (intermolecular attractive force), it is then called physical adsorption in which there is no modification in the properties of either the adsorbent or the gas. Chemical adsorption, also called chemisorption, includes the formation of new chemical bonds (Zhong and Haghighat 2015; WHO 2000). It is a vital reaction in which electron or ion exchange occurs among gas and adsorbent. Particles that have a greater attraction towards the adsorbent will be adsorbed and the remaining molecules will be retained in air. Hence, this method is only efficient for a limited quantity of pollutants. It is also reported that the accretion of pollutants will provide a path for the growth of bacteria and moulds (Van Durme et al. 2008). Schleibinger and Rüden 1999 reported growth of VOC before and after the use of filter pieces. They also proved the presence of VOCs such as esters, alcohols, aldehydes, and ketones in the used filter. Another major demerit is that adsorption will be easily carried out at humidity and lower temperatures, which has a negative impact on targeted indoor pollutants. Similar to filters, absorbents also have limited capacity in reducing air pollution. Hence, these should be frequently maintained for better results (Ge et al. 2015).

9.6.5 Ultraviolet Germicidal Irradiation

The aforementioned techniques will change the phase of the molecules from one form to another instead of destroying them. To destroy pollutants in the air, numerous innovative methods have been proposed, named advanced oxidation processes (AOP). These methods eliminate a broad range of VOCs by producing such agents as atomic oxygen and ozone. Ozone generators, photocatalytic oxidation, plasma reactors, and UV lamps are some examples of AOP. Ultraviolet germicidal irradiation (UVGI) kills biological pollutants by flouting the molecular bonds in their DNA using ultraviolet radiation (Zhang et al. 2015). The replication of the pollutants can be completely limited by breaking their DNA, which in turn causes cell death (Bennett 2009). The UVGI cleaners can be used for the timely purpose but not as an effective replacement technique for filtration systems (Zhang et al. 2011). The efficiency of the UVGI has been limited because of the devastation of moulds and bacteria requires high radiation, which in turn became harmful (Environmental Protection Agency 2009; Wang et al. 2009).

9.6.6 Ozonation

Ozonisers as mostly used for indoor air purification purposefully emit ozone by utilizing electrical discharge or UV lamps to clean the environment. The ozone generators are considered to be an effective purification tool that is highly oxidative and destroys most of the unsaturated VOCs in the indoor air environment. The ozone vendors generally state that ozone generators are effective and safe devices for reducing indoor air pollution. They also claim that the ozone, also called energized oxygen, activated oxygen, or super oxygen, can kill all the contaminants and provide a pollutant-free indoor air environment by destroying all airborne particles, viruses, moulds, chemicals, odors, and bacteria and produce secondary products such as water, carbon dioxide, and oxygen. In spite of all the advantages just mentioned, the ozone purifiers have many demerits (Environmental Protection Agency 2009, 2014b).

In principle, ozone generators are not an efficient method for destroying pollutants at low ozone levels, being an effective approach only at unsafe, high ozone levels. The emitted levels of ozone generators are approximately 500 ppb (Hubbard et al. 2005), which is five times higher than the maximum ozone exposure reported by the World Health Organization (WHO). Boeniger 1995 also reported that the reaction time for ozone with air pollutants is very high and may last for several months or even years. Contrary to claims by ozone vendors, ozone generators are not efficient in removing formaldehyde (Esswein and Boeniger 1994) or carbon monoxide (Shaughnessy et al. 1994) from the air. Some researchers also report that the reaction of ozone with pollutants may result in harmful secondary products (Weschler et al. 1992a, b; Weschler and Shields 1996).

9.7 Photocatalytic Oxidation

Photocatalytic oxidation (PCO) is an inventive and encouraging technique for removing contaminants from indoor air. With the help of light energy, enactment of the semiconductor is improved and thus can eradicate a wide range of indoor pollutants into CO_2 and H_2O (Demeestere et al. 2007; Nakata and Fujishima 2012; Chen et al. 2015a). Based on band structure, the semiconductors are characterized and the energy bandgap is defined as the bandgap (Eg) between the valence band and conduction band. The semiconductor material is activated by UV light that has energy equal to or greater than the bandgap. The electron in the valence band absorbs the energy from a photon and shifts to the higher valence band (conduction band), creating a hole in the conduction band. This pair is called an electron–hole pair.

9.7.1 Photocatalyst Oxidation Removal of Volatile Organic Compounds

Compared to outdoor air quality, indoor air quality is a cause of major anxiety and many problems to humans. VOCs, important contaminants in indoor air pollution, have become the most widespread PCO targets (Zhao and Yang 2003; Wang et al. 2007). Some studies related to TiO_2-based PCO for VOCs are tabulated in Table 9.2. The PCO confiscation of VOCs together with toluene, acetone, benzene, acetaldehyde, etc. are removed using continuous reactors rather than aqueous degradation. The reproducibility of pure TiO_2 depends on parameters such as shape control (Le Bechec et al. 2015), size dependence (Bianchi et al. 2014), preferentially

Table 9.2 Photocatalytic oxidation of VOCs using TiO_2-based photocatalyst

Authors	Photocatalyst	Source	Pollutant	Performance
Bianchi et al. (2014)	Nano- and micro-sized TiO_2	UVA at 30 W/m^2	Acetone, acetaldehyde, toluene	PC105 (Cristal) > P25 (Evonik) > 1077 (Kronos) > AT-1 (Cristal)
Le Bechec et al. (2015)	TiO_2 microfibers	UV-365 from LEDs	Acetone, heptane, toluene	For acetone, toluene, and heptane on TiO_2 fibers the quantum efficiencies of 0.0106, 0.0024, and 0.0027 is obtained
He et al. (2014)	Mesoporous TiO_2	UVA of 0.19 mW/cm^2	Benzene	Conversion efficiency of 80% is achieved on TS-400 (the best prepared sample)
Ren et al. (2016)	Anatase (F-doped) TiO_2 nano sheets with exposed 0 0 1 facets	UV-A of 4.97 mW/cm^2 and visible light (400–1000 nm) 15.04 mW/cm^2	Acetone, benzene, toluene	High efficiency is obtained using UV and visible light
Liu et al. (2013)	TiO_2/SiO_2 nano composites	160 W high-pressure mercury lamp	Benzene	When Ti/Si = 30: 1, 92.3% conversion in 120 min, 6.8 times higher than P25
Huang et al. (2015)	Transition metal modified TiO_2	Vacuum ultraviolet (VUV)	Benzene	Highest conversion of about 58% is obtained for Mn/TiO_2
Murcia et al. (2013)	Pt/TiO_2	UV-365 from LEDs (90 mW/cm^2)	Cyclohexane	Conversion efficiency of 100% is obtained and the $C0_2$ is promoted by platinum
Chen et al. (2013)	N-doped and O-deficient TiO_2	Visible light (>400 nm)	Benzene	72% conversion of benzene and CO_2 yield is obtained
Thevenet et al. (2014)	Silica glass fibers supported P25-Degussa TiO_2	UV-365 (8–10 mW/ cm^2)	Acetylene	Intermediates such as formaldehyde, formic acid and glyoxal are obtained with mineralization rate of 85%
Monteiro et al. (2015)	A monolithic catalytic bed coated with P25 and PC500	A solar simulator	Perchloroethylene (PCE) and *n*-decane	69% mineralization rate for PCE and 100% for *n*-decane
Andryushina and Stroyuk (2014)	Graphene oxide supported P25	UV at 25 mW/cm^2	Ethanol and benzene	95% conversion is achieved

(continued)

Table 9.2 (continued)

Authors	Photocatalyst	Source	Pollutant	Performance
Hou and Ku (2013)	TiO_2-coated on optical fiber	UV-LED of 126.1 mW/cm^2	Isopropanol	22% IPA removal
Xie et al. (2016)	TiO_2 thin film on window glass	UV with 11.02 mW/cm^2	Acetone and benzene	100% acetone conversion in 25 min and 100% benzene conversion in 110 min
Antonello et al. (2014)	Transparent, mechanically robust TiO_2 films	23 mW/cm^2 UV (280–400 nm) and simulated sunlight	Ethanol and acetaldehyde	Conversion rate of 100% is achieved under UV with 125 and 70 min for acetaldehyde and ethanol respectively
Banisharif et al. (2015)	Fe_2O_3-doped TiO_2	UV and visible light irradiation	Trichloroethylene (TCE)	Conversion rate of 95% is achieved for TCE
Martínez Vargas et al. (2015)	Cu-doped TiO_2	UV365 at 1.0 mW/cm^2	TCE	0.2 wt % Cu content favored the mobility of both TCE and water
Zhuang et al. (2014)	Sn_{2+}-doped TiO_2	Visible light >420 nm	Benzene	TS-40 (Ti/Sn = 40: 1) provided 27% benzene conversion
Han et al. 2013	Spray-coated polyester fiber supported non- metal doped TiO_2	30 W fluorescent lamp at 400–700 nm	Formaldehyde	Highest conversion rate of 38% at C-TiO_2

exposed facets (Ren et al. 2016), and tailored porous structures (He et al. 2014). The larger Brunauer–Emmett–Teller (BET) surface, a more active surface, and pre-adsorption would provide good PCO performance. Figures 9.5 and 9.6 represent the mechanism proposed for the photocatalytic oxidation degradation of benzene and trichloroethylene, respectively.

In PCO air purification, better stability and higher activity can be achieved by the modification of TiO_2 methods of transition metal doping (Park et al. 2004; Huang et al. 2015), non-metal doping (Chen et al. 2013), semiconductor coupling (Liu et al. 2013), and noble metal doping (Murcia et al. 2013). The immobilization technique and material development can be assimilated in practical applications to obtain better outcomes.

Pham and Lee 2015 reported that the V-doped TiO improved photocatalytic activity. The prepared V-doped TiO was then loaded onto polyurethane and then allowed to remove the toluene in a continuous reactor. It is evident from Table 9.2 that the TiO-based photocatalysts are efficient candidates to decompose a vast range of organic contaminants.

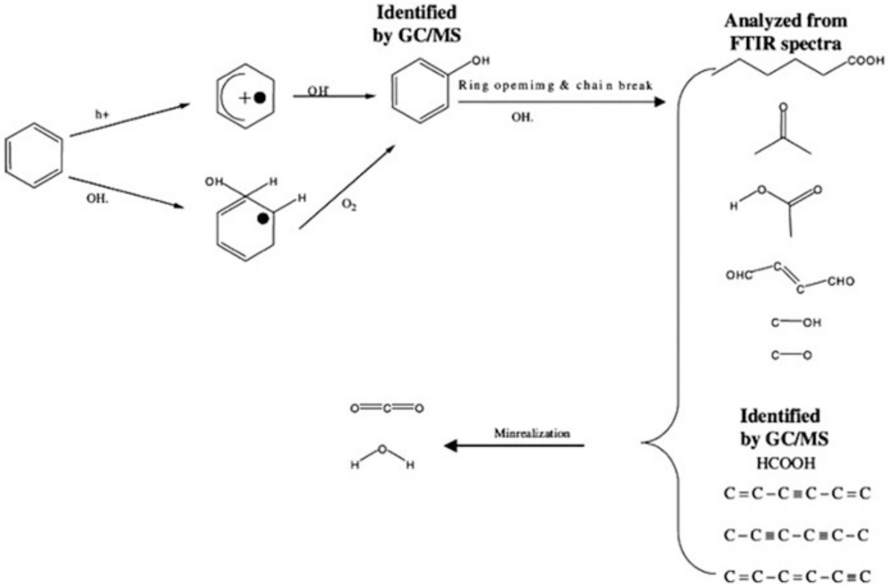

Fig. 9.5 Photocatalytic oxidation of benzene (Ma et al. 2007)

9.7.2 *Removal of Inorganic Gas Pollutants Using PCO*

Inorganic gas pollutants such as NO_x, CO, H_2S, and SO_x are very hazardous in both the outdoor and indoor environment. In contrast to VOC removal, research on the removal of inorganic gas pollutants is very minor. Continuous reactors are considered to be a best choice for the removal of organic compounds in practice. High mechanical strength can be provided by the TiO_2 film rather than powders. It is also reported that the functionalized polystyrene or polyamide six fibers can be used for the conversion of NO to NO_2 and HNO_3 (Szatmáry et al. 2014). Hence, the TiO_2 (anatase) are coated on the electron-spun polymeric nanofibers. The TiO_2 (pristine) are found to be active only to UV; to make that active in the visible region, oxygen-deficient TiO_2 was prepared for the oxidation of NO in the visible region (Wang et al. 2015). The reduction in the bandgap, increased absorption threshold to visible region, and improved electron–hole pair separation rates are studied and confirmed by the first principle density functional theory calculations.

Metal doping can be used in designing enhanced TiO_2 for photocatalyst oxidation of inorganic gas contaminants. Hu et al. (2015) reported the removal of NO_x can be improved by the synergistic effect of two Pt species together in the catalyst by doping the Pt^{4+} ions in TiO_2 as Pt/TiO_2. Ma et al. (2015) has reported that the UV-visible absorption spectra and TiO_2 photoluminescence activity can be improved by doping the Fe ions. They have used this method in the visible light photocatalytic oxidation of NO_x.

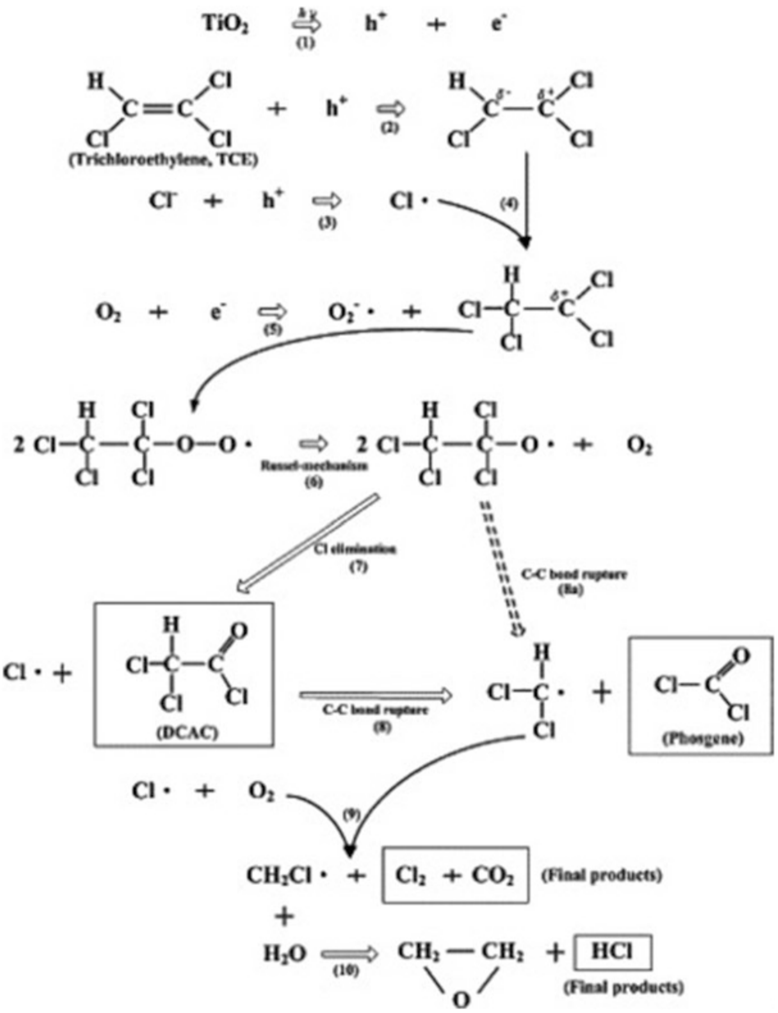

Fig. 9.6 Mechanism for the degradation of trichloroethylene (TCE) (Ou and Lo 2007)

Light absorbance and improved photocatalysis can also be achieved by coupling the TiO_2 to another semiconductor. Alonso-Tellez et al. (2014) reported the new method of coupling in the photocatalytic oxidation of H_2S. The photocatalyst can also be obtained by applying the surface modification method. Jiao et al. reported the preparation of $RuO_2/TiO_2/Pt$ (ternary photocatalyst) with the precise particle size of RuO_2 at about 2 nm, which can be used to remove CO under UV. They have also reported that the finest RuO_2 altered TiO_2 has 20 times greater improved activity than P25, 15 times more than anatase, and 8 times than rutile TiO_2, correspondingly. For the improvement in PCO removal of CO, the noteworthy exposure of RuO_2 (1 1 0) facets are supposed to be the key factor.

9.7.3 Non-Titanium-Based Photocatalyst for Air Purification

Researchers are focusing towards the development of photocatalysts based on TiO_2 rather than other novel photocatalytic materials. Great amounts of other novel photocatalysts are also available for the photocatalytic activities of air purification. Zinc oxide is the next best semiconductor photocatalytic candidate. The photocatalytic activity of ZnO is much higher when compared to TiO_2 in aqueous phase, but the stability of ZnO might be a problem. It has poor stability, but the stability of ZnO can be improved only at high temperatures. Liao et al. (2013) has examined the characteristics of the modified morphology (six prisms of both short and long pyramid shape) and defect-induced ZnO. The modified ZnO has much higher degradation efficiency than the P25 for formaldehyde removal because the modified ZnO polar planes possess higher surface energy, which will result in increased photocatalytic activity.

Y.C. Chen et al. proposed a ZnO/graphene composite by a green one-pot hydrothermal method for the removal of gaseous acetaldehyde (Liao et al. 2013). The photocatalytic activity can be improved by increasing the transfer rate of electrons by introducing rGO (reduced graphene oxide). The degradation rate and CO_2 generation can be drastically improved by controlling the proper rGO content. Sugranez et al. reported that the Fe_2O_3 can be a perfect candidate for the PCO removal of NO_x by retaining HNO_2/NO_3. The Fe_2O_3 is a very stable iron oxide that holds *n*-type semiconductor properties and an energy bandgap of 1.9–2.2 eV.

Bimetal oxides rather than a single metal oxide also can be used as photocatalyst. Huang et al. reported a $ZrxTi1xO_2$ photocatalyst material which can be used for the decomposition of gaseous HCHO (Chen et al. 2015b). For the removal of formaldehyde using PCO compared to the single Bi_2SiO_5, improved results were observed by using coupled Bi_2SiO_4 and AgI prepared by an in situ preparation method (Wan and Zhang 2015).

Graphitic carbon nitride has considered as a much desired metal-free photocatalyst candidate for air pollution (Sun and Wang 2014; Sun et al. 2014). Sun et al. (2015) reported that the Ag nanoparticle-deposited g-C_3N_4 nano sheets could be used for the PCO removal of NO_x under visible light radiation. Ag nanoparticles not only improve photocatalytic activity but also lead to the selectivity of final products. Katsumata et al. (2013) proposed g-C_3N_4/WO_3 composites for the photo-degradation of acetaldehyde pollution.

9.7.4 Photocatalysis with Ozone

Photocatalysis in combination with ozone (O_3-PCO) has been found to have better efficiency in the destruction of pollutants such as toluene and formaldehyde. To make this method marketable, the stability and efficiency of the same were analyzed and reported by researchers. Haibao Huang in 2010 investigated and reported the mechanism to improve the stability and performance of the O_3-PCO process under various operating circumstances. The outcome of the process shows that it has admirable stability during the change of initial O_3 concentration and humidity. Compared to the PCO, the O_3-PCO has excellent characteristics for eliminating pollutants. Efficiency in removing toluene and formaldehyde in the ozone-PCO process seemed to be increased from 12% to 96% and from 64% to 97.5%, respectively, when compared to that of PCO. Secondary products for this toluene oxidation were also significantly reduced. It is evident from the foregoing discussion that O_3-PCO is an effective method to reduce the air pollutants compared to the PCO method.

9.8 Summary

In this chapter, we concluded that the basic properties of a photocatalyst, the photocatalyst materials, and their application for the removal of indoor air pollutants clearly indicate that the photocatalyst is an effective method for environmental cleanliness. It is a potential tool for numerous industrial applications such as wastewater treatment, air pollution, and hydrogen generation to maintain a hygienic environment. Although photocatalysts are considered to be suitable for environment pollution remediation, many improvements are still needed to provide a cheap, highly efficient, stable, nontoxic, and highly active photocatalyst in visible regions.

Acknowledgments The authors (D. Shanmuga Sundar and Marcos Flores Carrasco) wish to thank the Conicyt FONDECYT (Fondo Nacional de Desarrollo Científico y Tecnológico) Project No. 3180089 and Millennium Nucleus MULTIMAT for funding and support.

References

Al-Kahtani AA, Almuqati T, Alhokbany N, Ahamad T, Naushad M, Alshehri SM (2018) A clean approach for the reduction of hazardous 4-nitrophenol using gold nanoparticles decorated multiwalled carbon nanotubes. J Clean Prod 191:429–435

Alonso-Tellez A, Robert D, Keller V, Keller N (2014) H_2S photocatalytic oxidation over WO_3/TiO_2 Hombikat UV100. Environ Sci Pollut Res. https://doi.org/10.1007/s11356-013-2329-y

Al-Othman ZA, Inamuddin, Naushad M (2011) Adsorption thermodynamics of trichloroacetic acid herbicide on polypyrrole Th(IV) phosphate composite cation-exchanger. Chem Eng J 169:38–42. https://doi.org/10.1016/j.cej.2011.02.046

Alshehri SM, Naushad M, Ahamad T et al (2014) Synthesis, characterization of curcumin based ecofriendly antimicrobial bio-adsorbent for the removal of phenol from aqueous medium. Chem Eng J 254:181–189. https://doi.org/10.1016/j.cej.2014.05.100

Andryushina NS, Stroyuk OL (2014) Influence of colloidal graphene oxide on photocatalytic activity of nanocrystalline TiO_2 in gas-phase ethanol and benzene oxidation. Appl Catal B Environ. https://doi.org/10.1016/j.apcatb.2013.11.044

Anpo M (2000) Applications of titanium oxide photocatalysts and unique second-generation TiO_2 photocatalysts able to operate under visible light irradiation for the reduction of environmental toxins on a global scale. Stud Surf Sci Catal. https://doi.org/10.1016/S0167-2991(00)80952-0

Antonello A, Soliveri G, Meroni D et al (2014) Photocatalytic remediation of indoor pollution by transparent TiO_2 films. Catal Today. https://doi.org/10.1016/j.cattod.2013.12.033

Bahri M, Haghighat F (2014) Plasma-based indoor air cleaning technologies: the state of the art-review. Clean (Weinh) 42(12):1667–1680

Banisharif A, Khodadadi AA, Mortazavi Y et al (2015) Highly active Fe_2O_3-doped TiO_2 photocatalyst for degradation of trichloroethylene in air under UV and visible light irradiation: experimental and computational studies. Appl Catal B Environ. https://doi.org/10.1016/j.apcatb.2014.10.023

Bavykin DV, Passoni L, Walsh FC (2013) Hierarchical tube-in-tube structures prepared by electrophoretic deposition of nanostructured titanates into a TiO_2 nanotube array. Chem Commun. https://doi.org/10.1039/c3cc43264e

Bennett A (2009) Strategies and technologies: controlling indoor air quality. Filtr Sep. https://doi.org/10.1016/S0015-1882(09)70155-7

Bernstein JA, Alexis N, Bacchus H et al (2008) The health effects of non-industrial indoor air pollution. J Allergy Clin Immunol. https://doi.org/10.1016/j.jaci.2007.10.045

Berry D, Mainelis G, Fennell D (2007) Effect of an ionic air cleaner on indoor/outdoor particle ratios in a residential environment. Aerosol Sci Technol 41:315–328

Bianchi CL, Gatto S, Pirola C et al (2014) Photocatalytic degradation of acetone, acetaldehyde and toluene in gas-phase: comparison between nano and micro-sized TiO_2. Appl Catal B Environ. https://doi.org/10.1016/j.apcatb.2013.02.047

Bickley RI, Stone FS (1973) Photoadsorption and photocatalysis at rutile surfaces. I. Photoadsorption of oxygen. J Catal. https://doi.org/10.1016/0021-9517(73)90310-2

Boeniger MF (1995) Use of ozone generating devices to improve indoor air quality. Am Ind Hyg Assoc J. https://doi.org/10.1080/15428119591016827

Calderón MA, Linneberg A, Kleine-Tebbe J et al (2015) Respiratory allergy caused by house dust mites: what do we really know? J Allergy Clin Immunol 136(1):38–48

Cant NW, Cole JR (1992) Photocatalysis of the reaction between ammonia and nitric oxide on TiO_2 surfaces. J Catal. https://doi.org/10.1016/0021-9517(92)90231-6

Cao S, Low J, Yu J, Jaroniec M (2015) Polymeric photocatalysts based on graphitic carbon nitride. Adv Mater. https://doi.org/10.1002/adma.201500033

Challoner A, Gill L (2014) Indoor/outdoor air pollution relationships in ten commercial buildings: PM 2.5 and NO_2. Build Environ. https://doi.org/10.1016/j.buildenv.2014.05.032

Chávez-Valdez A, Herrmann M, Boccaccini AR (2012) Alternating current electrophoretic deposition (EPD) of TiO_2 nanoparticles in aqueous suspensions. J Colloid Interface Sci. https://doi.org/10.1016/j.jcis.2012.02.054

Chen HW, Liang CP, Huang HS et al (2011) Electrophoretic deposition of mesoporous TiO_2 nanoparticles consisting of primary anatase nanocrystallites on a plastic substrate for flexible dye-sensitized solar cells. Chem Commun. https://doi.org/10.1039/c1cc12514a

Chen Y, Cao X, Gao B, Lin B (2013) A facile approach to synthesize N-doped and oxygen-deficient TiO_2 with high visible-light activity for benzene decomposition. Mater Lett. https://doi.org/10.1016/j.matlet.2012.12.010

Chen K, Zhu L, Yang K (2015a) Tricrystalline TiO_2 with enhanced photocatalytic activity and durability for removing volatile organic compounds from indoor air. J Environ Sci (China). https://doi.org/10.1016/j.jes.2014.10.023

Chen YC, Katsumata KI, Chiu YH et al (2015b) ZnO-graphene composites as practical photocatalysts for gaseous acetaldehyde degradation and electrolytic water oxidation. Appl Catal A Gen. https://doi.org/10.1016/j.apcata.2014.10.055

Clements-Croome DJ, Awbi HB, Bakó-Biró Z et al (2008) Ventilation rates in schools. Build Environ. https://doi.org/10.1016/j.buildenv.2006.03.018

Crook B, Burton NC (2010) Indoor moulds, sick building syndrome and building related illness. Fungal Biol Rev 24(3-4):106–113

Dallongeville A, Le Cann P, Zmirou-Navier D et al (2015) Concentration and determinants of molds and allergens in indoor air and house dust of French dwellings. Sci Total Environ. https://doi.org/10.1016/j.scitotenv.2015.06.039

Demeestere K, Dewulf J, Van Langenhove H (2007) Heterogeneous photocatalysis as an advanced oxidation process for the abatement of chlorinated, monocyclic aromatic and sulfurous volatile organic compounds in air: state of the art. Crit Rev Environ Sci Technol 37(6):489–538

Dunnill CWH, Aiken ZA, Pratten J et al (2009) Enhanced photocatalytic activity under visible light in N-doped TiO_2 thin films produced by APCVD preparations using *t*-butylamine as a nitrogen source and their potential for antibacterial films. J Photochem Photobiol A Chem. https://doi.org/10.1016/j.jphotochem.2009.07.024

Environmental Protection Agency (2009) Residential air cleaners. A summary of available information, 2nd edn. United States Environmental Protection Agency, Washington, DC. doi:EPA 402-F-09-002

Environmental Protection Agency (2014a) Ground level ozone – health effects. EPA, Washington, DC

Environmental Protection Agency (2014b) Ozone generators that are sold as air cleaners. www.epa.gov

Environmental Protection Agency (2017) Health risk of radon. US EPA, Washington, DC

Esswein EJ, Boeniger MF (1994) Effect of an ozone-generating air-purifying device on reducing concentrations of formaldehyde in air. Appl Occup Environ Hyg. https://doi.org/10.1080/1047322X.1994.10388285

Fujishima A, Honda K (1972) Electrochemical photolysis of water at a semiconductor electrode. Nature (Lond) doi: https://doi.org/10.1038/238037a0

Fujishima A, Rao TN, Tryk DA (2000) TiO_2 photocatalysts and diamond electrodes. Electrochim Acta. https://doi.org/10.1016/S0013-4686(00)00620-4

Ge H, Hu D, Li X et al (2015) Removal of low-concentration benzene in indoor air with plasma-MnO_2 catalysis system. J Electrost. https://doi.org/10.1016/j.elstat.2015.06.003

Guo H, Murray F, Lee SC (2003) The development of low volatile organic compound emission house: a case study. Build Environ. https://doi.org/10.1016/S0360-1323(03)00156-2

Han Z, Chang VW, Wang X et al (2013) Experimental study on visible-light induced photocatalytic oxidation of gaseous formaldehyde by polyester fiber supported photocatalysts. Chem Eng J. https://doi.org/10.1016/j.cej.2012.12.025

He F, Li J, Li T, Li G (2014) Solvothermal synthesis of mesoporous TiO_2: the effect of morphology, size and calcination progress on photocatalytic activity in the degradation of gaseous benzene. Chem Eng J. https://doi.org/10.1016/j.cej.2013.10.028

Hoffmann MR, Martin ST, Choi W, Bahnemann DW (1995) Environmental applications of semiconductor photocatalysis. Chem Rev. https://doi.org/10.1021/cr00033a004

Hou WM, Ku Y (2013) Photocatalytic decomposition of gaseous isopropanol in a tubular optical fiber reactor under periodic UV-LED illumination. J Mol Catal A Chem. https://doi.org/10.1016/j.molcata.2013.03.016

Hu Y, Song X, Jiang S, Wei C (2015) Enhanced photocatalytic activity of Pt-doped TiO_2 for NO_x oxidation both under UV and visible light irradiation: a synergistic effect of lattice Pt^{4+} and surface PtO. Chem Eng J. https://doi.org/10.1016/j.cej.2015.03.135

Huang H, Huang H, Zhang L et al (2015) Enhanced degradation of gaseous benzene under vacuum ultraviolet (VUV) irradiation over TiO_2 modified by transition metals. Chem Eng J. https://doi.org/10.1016/j.cej.2014.08.057

Hubbard HF, Coleman BK, Sarwar G, Corsi RL (2005) Effects of an ozone-generating air purifier on indoor secondary particles in three residential dwellings. Indoor Air. https://doi.org/10.1111/j.1600-0668.2005.00388.x

Hult EL, Willem H, Price PN et al (2015) Formaldehyde and acetaldehyde exposure mitigation in US residences: in-home measurements of ventilation control and source control. Indoor Air. https://doi.org/10.1111/ina.12160

Hyttinen M, Pasanen P, Kalliokoski P (2006) Removal of ozone on clean, dusty and sooty supply air filters. Atmos Environ. https://doi.org/10.1016/j.atmosenv.2005.09.040

Inoue Y (2009) Photocatalytic water splitting by RuO_2-loaded metal oxides and nitrides with d0- and d10-related electronic configurations. Energy Environ Sci. https://doi.org/10.1039/b816677n

Juanru H, Mingwei L, Zhong C (2007) Advances in doping of titania photocatalytic catalysts. Ind Catal 15:1–4

Kale MJ, Avanesian T, Christopher P (2014) Direct photocatalysis by plasmonic nanostructures. ACS Catal 4(1):116–128

Katsumata KI, Motoyoshi R, Matsushita N, Okada K (2013) Preparation of graphitic carbon nitride (g-C_3N_4)/WO_3 composites and enhanced visible-light-driven photodegradation of acetaldehyde gas. J Hazard Mater. https://doi.org/10.1016/j.jhazmat.2013.05.058

Kete M, Pavlica E, Fresno F et al (2014) Highly active photocatalytic coatings prepared by a low-temperature method. Environ Sci Pollut Res. https://doi.org/10.1007/s11356-014-3077-3

Khan FI, Ghoshal AK (2000) Removal of volatile organic compounds from polluted air. J Loss Prev Process Ind. https://doi.org/10.1016/S0950-4230(00)00007-3

Koistinen K, Kotzias D, Kephalopoulos S et al (2008) The INDEX project: executive summary of a European Union project on indoor air pollutants. Allergy 63(7):810–819

Kolarik B, Wargocki P, Skorek-Osikowska A, Wisthaler A (2010) The effect of a photocatalytic air purifier on indoor air quality quantified using different measuring methods. Build Environ. https://doi.org/10.1016/j.buildenv.2009.12.006

Krogman KC, Zacharia NS, Grillo DM, Hammond PT (2008) Photocatalytic layer-by-layer coatings for degradation of acutely toxic agents. Chem Mater. https://doi.org/10.1021/cm703096w

Le Bechec M, Kinadjian N, Ollis D et al (2015) Comparison of kinetics of acetone, heptane and toluene photocatalytic mineralization over TiO_2 microfibers and Quartzel® mats. Appl Catal B Environ. https://doi.org/10.1016/j.apcatb.2015.05.015

Lelieveld J, Evans JS, Fnais M et al (2015) The contribution of outdoor air pollution sources to premature mortality on a global scale. Nature. https://doi.org/10.1038/nature15371

Leung DYC (2015) Outdoor-indoor air pollution in urban environment: challenges and opportunity. Front Environ Sci. https://doi.org/10.3389/fenvs.2014.00069

Li Y (2016) The "impurity" of indoor air. Indoor Air 26(1):3–5

Li Y, Hwang DS, Lee NH, Kim SJ (2005) Synthesis and characterization of carbon-doped titania as an artificial solar light sensitive photocatalyst. Chem Phys Lett. https://doi.org/10.1016/j.cplett.2005.01.062

Liao Y, Xie C, Liu Y, Huang Q (2013) Enhancement of photocatalytic property of ZnO for gaseous formaldehyde degradation by modifying morphology and crystal defect. J Alloys Compd. https://doi.org/10.1016/j.jallcom.2012.09.109

Linsebigler AL, Lu GQ, Yates JT (1996) CO photooxidation on TiO_2. J Phys Chem. https://doi.org/10.1021/jp952018f

Litter MI (1999) Heterogeneous photocatalysis: transition metal ions in photocatalytic systems. Appl Catal B Environ 23(2-3):89–114

Liu Z, Chen F, Fang P et al (2013) Study of adsorption-assisted photocatalytic oxidation of benzene with TiO_2/SiO_2 nanocomposites. Appl Catal A Gen. https://doi.org/10.1016/j.apcata.2012.11.020

Lopez L, Daoud WA, Dutta D et al (2013) Effect of substrate on surface morphology and photocatalysis of large-scale TiO_2 films. Appl Surf Sci. https://doi.org/10.1016/j.apsusc.2012.10.156

Lyng NL, Gunnarsen L, Andersen HV (2015) The effect of ventilation on the indoor air concentration of PCB: an intervention study. Build Environ. https://doi.org/10.1016/j.buildenv.2015.08.019

Ma CM, Wang W, Ku Y, Jeng FT (2007) Photocatalytic degradation of benzene in air streams in an optical fiber photoreactor. Chem Eng Technol. https://doi.org/10.1002/ceat.200700138

Ma J, He H, Liu F (2015) Effect of Fe on the photocatalytic removal of NO_x over visible light responsive Fe/TiO_2 catalysts. Appl Catal B Environ. https://doi.org/10.1016/j.apcatb.2015.05.003

Machado LCR, Torchia CB, Lago RM (2006) Floating photocatalysts based on TiO_2 supported on high surface area exfoliated vermiculite for water decontamination. Catal Commun. https://doi.org/10.1016/j.catcom.2005.10.020

Madureira J, Paciência I, Rufo JC et al (2015) Assessment and determinants of airborne bacterial and fungal concentrations in different indoor environments: homes, child day-care centres, primary schools and elderly care centres. Atmos Environ. https://doi.org/10.1016/j.atmosenv.2015.03.026

Martínez Vargas DX, Rivera De la Rosa J, Lucio-Ortiz CJ et al (2015) Photocatalytic degradation of trichloroethylene in a continuous annular reactor using Cu-doped TiO_2 catalysts by sol-gel synthesis. Appl Catal B Environ. https://doi.org/10.1016/j.apcatb.2015.05.019

Monteiro RAR, Miranda SM, Rodrigues-Silva C et al (2015) Gas phase oxidation of *n*-decane and PCE by photocatalysis using an annular photoreactor packed with a monolithic catalytic bed coated with P25 and PC500. Appl Catal B Environ. https://doi.org/10.1016/j.apcatb.2014.10.026

Murcia JJ, Hidalgo MC, Navío JA et al (2013) Cyclohexane photocatalytic oxidation on Pt/TiO_2 catalysts. Catal Today. https://doi.org/10.1016/j.cattod.2012.11.018

Nakajima A, Akiyama Y, Yanagida S et al (2009) Preparation and properties of Cu-grafted transparent TiO_2-nanosheet thin films. Mater Lett. https://doi.org/10.1016/j.matlet.2009.05.016

Nakata K, Fujishima A (2012) TiO_2 photocatalysis: design and applications. J Photochem Photobiol C Photochem Rev. https://doi.org/10.1016/j.jphotochemrev.2012.06.001

Naushad M (2014) Surfactant assisted nano-composite cation exchanger: development, characterization and applications for the removal of toxic Pb^{2+} from aqueous medium. Chem Eng J 235:100–108. https://doi.org/10.1016/j.cej.2013.09.013

Nazaroff WW (2013) Four principles for achieving good indoor air quality. Indoor Air 23 (5):353–356

Nelson HS, Hirsch SR, Ohman JL et al (1988) Recommendations for the use of residential air-cleaning devices in the treatment of allergic respiratory diseases. J Allergy Clin Immunol. https://doi.org/10.1016/0091-6749(88)90980-3

Niu JL, Tung TCW, Burnett J (2001) Quantification of dust removal and ozone emission of ionizer air-cleaners by chamber testing. J Electrost. https://doi.org/10.1016/S0304-3886(01)00118-8

Nizard H, Kosinova ML, Fainer NI et al (2008) Deposition of titanium dioxide from TTIP by plasma enhanced and remote plasma enhanced chemical vapor deposition. Surf Coat Technol. https://doi.org/10.1016/j.surfcoat.2008.02.023

Nolan MG, Pemble ME, Sheel DW, Yates HM (2006) One step process for chemical vapour deposition of titanium dioxide thin films incorporating controlled structure nanoparticles. Thin Solid Films. https://doi.org/10.1016/j.tsf.2006.07.182

Norhidayah A, Chia-Kuang L, Azhar MK, Nurulwahida S (2013) Indoor air quality and sick building syndrome in three selected buildings. Procedia Eng. https://doi.org/10.1016/j.proeng.2013.02.014

Ou HH, Lo SL (2007) Photocatalysis of gaseous trichloroethylene (TCE) over TiO_2: the effect of oxygen and relative humidity on the generation of dichloroacetyl chloride (DCAC) and phosgene. J Hazard Mater. https://doi.org/10.1016/j.jhazmat.2006.12.039

Park SE, Joo H, Kang JW (2004) Effect of impurities in TiO_2 thin films on trichloroethylene conversion. Sol Energy Mater Sol Cells. https://doi.org/10.1016/j.solmat.2004.02.012

Paunović K, Maksimović M, Davidović D et al (2005) Max Josef von Pettenkofer – founder of modern hygiene (1818–1901). Srp Arh Celok Lek 133(9-10):450–453

Pham TD, Lee BK (2015) Novel adsorption and photocatalytic oxidation for removal of gaseous toluene by V-doped TiO_2/PU under visible light. J Hazard Mater. https://doi.org/10.1016/j.jhazmat.2015.07.048

Pierce WM, Janczewski JN, Roethlisberger B et al (1996) Effectiveness of auxiliary air cleaners in reducing ETS components in offices. ASHRAE J 38:51–57

Poppendieck DG, Rim D, Persily AK (2014) Ultrafine particle removal and ozone generation by in-duct electrostatic precipitators. Environ Sci Technol. https://doi.org/10.1021/es404884p

Priya DN, Modak JM, Raichur AM (2009) LbL fabricated poly(styrene sulfonate)/TiO_2 multilayer thin films for environmental applications. ACS Appl Mater Interfaces. https://doi.org/10.1021/am900566n

Raddaha NS, Cordero-Arias L, Cabanas-Polo S et al (2014) Electrophoretic deposition of chitosan/h-BN and chitosan/h-BN/TiO_2 composite coatings on stainless steel (316L) substrates. Materials (Basel). https://doi.org/10.3390/ma7031814

Ren L, Li Y, Hou J et al (2016) The pivotal effect of the interaction between reactant and anatase TiO_2 nanosheets with exposed {001} facets on photocatalysis for the photocatalytic purification of VOCs. Appl Catal B Environ. https://doi.org/10.1016/j.apcatb.2015.08.034

Rivas I, Viana M, Moreno T et al (2014) Child exposure to indoor and outdoor air pollutants in schools in Barcelona. Spain Environ Int. https://doi.org/10.1016/j.envint.2014.04.009

Robert D, Malato S (2002) Solar photocatalysis: a clean process for water detoxification. Sci Total Environ. https://doi.org/10.1016/S0048-9697(01)01094-4

Robert D, Keller V, Keller N (2013) Immobilization of a semiconductor photocatalyst on solid supports: methods, materials, and applications. In: Photocatalysis and water purification: from fundamentals to recent applications. Wiley-VCH, Weinheim

Rohra H, Taneja A (2016) Indoor air quality scenario in India—an outline of household fuel combustion. Atmos Environ 129:243–255

Sampaio MJ, Silva CG, Silva AMT et al (2013) Photocatalytic activity of TiO_2-coated glass raschig rings on the degradation of phenolic derivatives under simulated solar light irradiation. Chem Eng J. https://doi.org/10.1016/j.cej.2012.11.027

Schleibinger H, Rüden H (1999) Air filters from HVAC systems as possible source of volatile organic compounds (VOC): laboratory and field assays. Atmos Environ. https://doi.org/10.1016/S1352-2310(99)00274-5

Serpone N, Emeline AV (2012) Semiconductor photocatalysis – past, present, and future outlook. J Phys Chem Lett 3(5):673–677

Shan AY, Ghazi TIM, Rashid SA (2010) Immobilisation of titanium dioxide onto supporting materials in heterogeneous photocatalysis: a review. Appl Catal A Gen. https://doi.org/10.1016/j.apcata.2010.08.053

Shaughnessy RJ, Levetin E, Blocker J, Sublette KL (1994) Effectiveness of portable indoor air cleaners: sensory testing results. Indoor Air. https://doi.org/10.1111/j.1600-0668.1994.t01-1-00006.x

Shen YS, Ku Y (2002) Decomposition of gas-phase trichloroethene by the UV/TiO_2 process in the presence of ozone. Chemosphere. https://doi.org/10.1016/S0045-6535(00)00585-3

Smyth J (2010) The TiO_2 Group. University of Colorado. USA

Spanhel L, Weller H, Henglein A (1987) Photochemistry of semiconductor colloids. 22. Electron ejection from illuminated cadmium sulfide into attached titanium and zinc oxide particles. J Am Chem Soc. https://doi.org/10.1021/ja00256a012

Stranger M, Potgieter-Vermaak SS, Van Grieken R (2009) Particulate matter and gaseous pollutants in residences in Antwerp, Belgium. Sci Total Environ. https://doi.org/10.1016/j.scitotenv.2008.10.019

Sun H, Wang S (2014) Research advances in the synthesis of nanocarbon-based photocatalysts and their applications for photocatalytic conversion of carbon dioxide to hydrocarbon fuels. Energy Fuel 28(1):22–36

Sun H, Wang C, Pang S et al (2008) Photocatalytic TiO_2 films prepared by chemical vapor deposition at atmosphere pressure. J Non-Cryst Solids. https://doi.org/10.1016/j.jnoncrysol.2007.01.108

Sun H, Wang S, Ang HM et al (2010) Halogen element modified titanium dioxide for visible light photocatalysis. Chem Eng J 162(2):437–447

Sun H, Zhou G, Wang Y et al (2014) A new metal-free carbon hybrid for enhanced photocatalysis. ACS Appl Mater Interfaces 6:16745–16754. https://doi.org/10.1021/am503820h

Sun Y, Xiong T, Ni Z et al (2015) Improving g-C_3N_4 photocatalysis for NO_x removal by Ag nanoparticles decoration. Appl Surf Sci. https://doi.org/10.1016/j.apsusc.2015.07.071

Szatmáry L, Šubrt J, Kalousek V et al (2014) Low-temperature deposition of anatase on nanofiber materials for photocatalytic NO_x removal. Catal Today. https://doi.org/10.1016/j.cattod.2013.09.023

Taskinen T, Meklin T, Nousiainen M et al (1997) Moisture and mould problems in schools and respiratory manifestations in schoolchildren: clinical and skin test findings. Acta Paediatr. https://doi.org/10.1111/j.1651-2227.1997.tb14841.x

Technical, Report Efficiency and REC House (EREC) (2008) Spot ventilation: Source control to improve indoor air quality

Tejasvi R, Sharma M, Upadhyay K (2015) Passive photo-catalytic destruction of air-borne VOCs in high traffic areas using TiO2-coated flexible PVC sheet. Chem Eng J. https://doi.org/10.1016/j.cej.2014.10.040

Tennakone K, Tilakaratne CTK, Kottegoda IRM (1995) Photocatalytic degradation of organic contaminants in water with TiO2 supported on polythene films. J Photochem Photobiol A Chem. https://doi.org/10.1016/1010-6030(94)03980-9

Thevenet F, Guillard C, Rousseau A (2014) Acetylene photocatalytic oxidation using continuous flow reactor: gas phase and adsorbed phase investigation, assessment of the photocatalyst deactivation. Chem Eng J. https://doi.org/10.1016/j.cej.2014.01.038

US Department of Health and Human Services (2006) Centers for Disease Control and Prevention. In: Healthy housing reference manual. US Department of Health and Human Services, Washington, DC

USEPA (2004a) Air quality criteria for particulate matter October 2004, volume 1. EPA, Washington, DC

USEPA (2004b) Air quality criteria for particulate matter October 2004, volume 2. EPA, Washington, DC

Van Durme J, Dewulf J, Leys C (2008) Development of heterogeneous plasma catalysis for the abatement of health damaging organic micropollutants in indoor environments, UGent. Faculty of Bioscience Engineering

Verriele M, Schoemaecker C, Hanoune B et al (2016) The MERMAID study: indoor and outdoor average pollutant concentrations in 10 low-energy school buildings in France. Indoor Air. https://doi.org/10.1111/ina.12258

Vinu R, Madras G (2010) Environmental remediation by photocatalysis. J Indian Inst Sci 90 (2):189–230

Wan Z, Zhang G (2015) Synthesis and facet-dependent enhanced photocatalytic activity of Bi_2SiO_5/AgI nanoplate photocatalysts. J Mater Chem A. https://doi.org/10.1039/C5TA03465E

Wang S, Ang HM, Tade MO (2007) Volatile organic compounds in indoor environment and photocatalytic oxidation: state of the art. Environ Int 33(5):694–705

Wang B, Mortazavi R, Haghighat F (2009) Evaluation of modeling and measurement techniques of ultraviolet germicidal irradiation effectiveness – towards the design of immune buildings. Indoor Built Environ. https://doi.org/10.1177/1420326X09103024

Wang C, Ma J, Liu F et al (2015) The effects of Mn^{2+} precursors on the structure and ozone decomposition activity of cryptomelane-type manganese oxide (OMS-2) catalysts. J Phys Chem C. https://doi.org/10.1021/acs.jpcc.5b08095

Waring MS, Siegel JA, Corsi RL (2008) Ultrafine particle removal and generation by portable air cleaners. Atmos Environ. https://doi.org/10.1016/j.atmosenv.2008.02.011

Weschler CJ, Shields HC (1996) Production of the hydroxyl radical in indoor air. Environ Sci Technol. https://doi.org/10.1021/es960032f

Weschler CJ, Hodgson AT, Wooley JD (1992a) Indoor chemistry: ozone, volatile organic compounds, and carpets. Environ Sci Technol. https://doi.org/10.1021/es00036a006

Weschler CJ, Michael B, Petros K (1992b) Indoor ozone and nitrogen dioxide: a potential pathway to the generation of nitrate radicals, dinitrogen pentoxide, and nitric acid indoors. Environ Sci Technol. https://doi.org/10.1021/es00025a022

WHO (2000) Air quality guidelines for Europe. Environ Sci Pollut Res. https://doi.org/10.1007/BF02986808

WHO (2014) Indoor air quality guidelines: household fuel combustion. World Health Organization. isbn:9789241548878

Wolkoff P, Nielsen GD (2001) Organic compounds in indoor air—their relevance for perceived indoor air quality? Atmos Environ 35(26):4407–4417

Xie H, Liu B, Zhao X (2016) Facile process to greatly improve the photocatalytic activity of the TiO_2 thin film on window glass for the photodegradation of acetone and benzene. Chem Eng J. https://doi.org/10.1016/j.cej.2015.09.049

Yu JC, Lin J, Lo D, Lam SK (2000) Influence of thermal treatment on the adsorption of oxygen and photocatalytic activity of TiO_2. Langmuir. https://doi.org/10.1021/la000309w

Yu BF, Hu ZB, Liu M et al (2009) Review of research on air-conditioning systems and indoor air quality control for human health. Int J Refrig 32(1):3–20

Zhang J, Smith KR (2003) Indoor air pollution: a global health concern. Br Med Bull 68:209–225

Zhang Y, Mo J, Li Y et al (2011) Can commonly-used fan-driven air cleaning technologies improve indoor air quality? A literature review. Atmos Environ 45(26):4329–4343

Zhang P, Liu L, He Y et al (2015) One-dimensional angular surface plasmon resonance imaging based array thermometer. Sens Actuators B Chem. https://doi.org/10.1016/j.snb.2014.10.055

Zhao J, Yang X (2003) Photocatalytic oxidation for indoor air purification: a literature review. Build Environ. https://doi.org/10.1016/S0360-1323(02)00212-3

Zhong L, Haghighat F (2015) Photocatalytic air cleaners and materials technologies – abilities and limitations. Build Environ. https://doi.org/10.1016/j.buildenv.2015.01.033

Zhuang H, Gu Q, Long J et al (2014) Visible light-driven decomposition of gaseous benzene on robust Sn^{2+}-doped anatase TiO_2 nanoparticles. RSC Adv. https://doi.org/10.1039/c4ra05904b

(2014) 7 million deaths annually linked to air pollution. Cent Eur J Public Health

(2005) WHO. Air quality guidelines for particulate matter, ozone, nitrogen dioxide and sulfur dioxide. Technical report, World Health Organization

(2014) US Environmental Protection Agency. National ambient air quality standards (NAAQS)

(2015) European Commission. Air quality standards

(2010) WHO Regional Office for Europe. Guidelines for indoor air quality. Technical report

(2016) The US Environmental Protection Agency Website. Exposure to radon causes lung cancer in non-smokers and smokers alike

(2007) United States Environmental Protection Agency. Benzo(a)pyrene (BaP). TEACH Chemical Summary 1:1–14

Chapter 10
Two Dimensional-Based Materials for Photocatalysis Applications

Gnanaseelan Natarajan, Felipe Caballero-Briones, and Sathish-Kumar Kamaraj

Contents

10.1 Introduction 276
10.2 Generalized Mechanism of a Photocatalyst for Various Applications 277
10.3 Artificial Photosynthesis 278
  10.3.1 Generation of Hydrogen by Artificial Photosynthesis 279
  10.3.2 g-C_3N_4-Based Materials 281
  10.3.3 Graphene-Based Materials 281
  10.3.4 Generation of Solar Fuels by Artificial Photosynthesis 283
10.4 Photodegradation 286
10.5 Self-Cleaning Photocatalysis 287
10.6 Cancer Therapy 289
10.7 Summary and Future Orientation 289
References 290

Abstract Energy and environmental crisis are two major challenges in present-day life. The advent usage of fossil fuels for electricity and transportation had resulted in global warming with deadly repercussions. Photocatalysis could be a good alternative to solve the present-day problems. Engineering the material for maximum solar irradiation harvesting, efficient charge generation, its transport to reaction centers, and high catalytic properties are the main priorities; in this sense, two-dimensional materials could be suitable for photocatalysis because of its physical, electrical, and chemical properties and the possibility to chemically tailor them. Photoinduced charge carriers could catalyze various chemical reactions for crucial applications.

G. Natarajan · F. Caballero-Briones
Instituto Politécnico Nacional, Materiales para Energía, Salud y Medio Ambiente (GESMAT), CICATA Altamira, Altamira, México
e-mail: fcaballero@ipn.mx

S.-K. Kamaraj (✉)
Instituto Tecnológico El Llano (ITEL)/Tecnológico Nacional de México (TecNM), Laboratorio de Cultivo de Tejidos Vegetales, Aguascalientes, México
e-mail: sathish.kamaraj@tecnmitel.edu.mx

S. Rajendran et al. (eds.), *Green Photocatalysts for Energy and Environmental Process*, Environmental Chemistry for a Sustainable World 36,
https://doi.org/10.1007/978-3-030-17638-9_10

Hydrogen fuel could be used for hydrogen fuel cell to generate the electricity and power the electric vehicles. Major greenhouse gas, such as CO_2 emitted by various industries and conventional automobiles, could be reduced to high-energy fuel such as methanol, ethanol, or formate. Photodegradation could decompose toxic organic substances from water-polluted sources. Human effort and expenditures could be saved by self-cleaning photocatalysis in offices, hospitals, or photovoltaic panels. Photocatalytic materials may play a critical role in effective cancer therapy for its sensitizing property and ability to produce reactive oxygen species which kills cancer.

Keywords Photocatalysis · Artificial photosynthesis · Photodegradation · Self-cleaning · Cancer therapy

10.1 Introduction

Nowadays, solar energy conversion technologies gained wider attention in all arena from the scientific community to government policy-makers around the world. Although the most known applications are solar photovoltaic and solar thermal conversion for heating and electricity generation, photocatalysis is a family of technologies with the potential of solving current mankind problems associated with transportation, cancer therapy, water purification, and greenhouse effect in Earth. Photocatalysis is defined as the process where photons drive a chemical reaction, lowering the required activation energy, using an engineered material for efficient light harvesting and exciton generation, fast charge carrier transfer, and chemical stability (Masao and Okuru 2002). Its plethora of potential applications is listed below (Table 10.1).

In the present work, an analysis of the fundamentals of photocatalysis will be done, followed by the application of photocatalysis to the production of hydrogen and solar fuels by artificial photosynthesis using several material systems. Afterward, applications of photocatalysis in environment and health will be discussed.

Table 10.1 Applications of photocatalysis

Energy	Artificial photosynthesis	Converts greenhouse gases into fuel
	Hydrogen photogeneration	Hydrogen fuel for electricity generation and transportation
Environment	Photodegradation	Pollutant degradation in water
	Indoor air cleaners	Photocatalyst-equipped air conditioners for domestic and industrial applications
	Outdoor air purifiers	Concrete for roads and footpaths and tunnel walls for pollutant degradation
Health	Self-sterilization	In hospital surfaces and operating rooms
	Cancer therapy	Induces programmed death of cell cancers

The chapter closes with a summary of the applications and future orientations for scaling up photocatalysis systems.

10.2 Generalized Mechanism of a Photocatalyst for Various Applications

Figure 10.1 presents a scheme of the general process of photocatalysis using a semiconductor as the photocatalytic material. The scheme presents the possible applications, taking advantage of the photogenerated carriers.

When a photon from the Sun or other excitation source impinges on the PhotocatalystsSemiconductor, semiconductor electron (e^-) gains enough of energy for photoexcitation from the valence band (VB) to conduction band (CB) which leads to the generation of an electron-hole (h^+) pair. The charge carriers can undergo recombination by the following equations through nonradiative mechanisms:

$$\text{Semiconductor} + h\upsilon \rightarrow h^{+}{}_{VB} + e^{-}{}_{CB} \tag{10.1}$$

$$e^{-}{}_{CB} + h^{+}{}_{VB} \rightarrow \text{Energy} \tag{10.2}$$

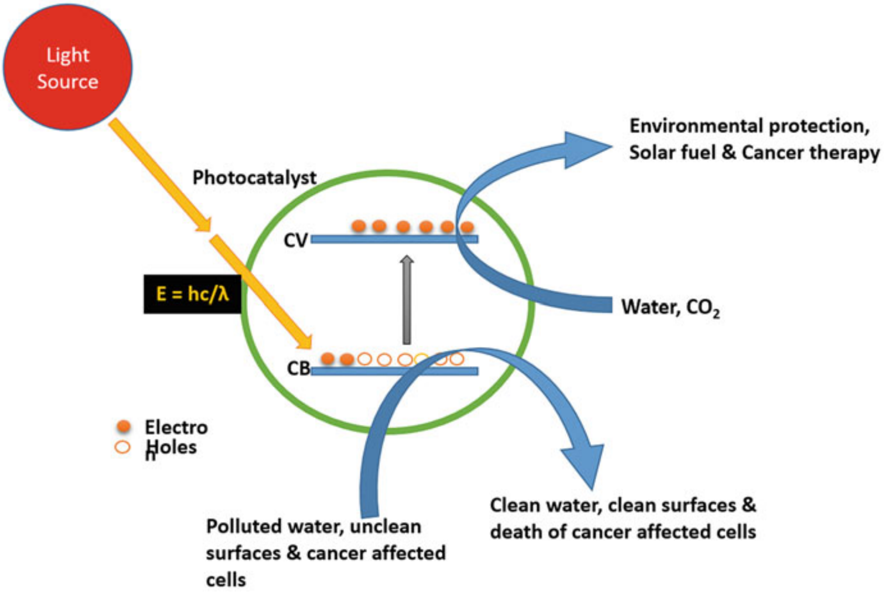

Fig. 10.1 Generalized mechanism of a photocatalyst for various applications. A photon with suitable energy induces the generation of electrons and holes in the photocatalyst. The carriers diffuse to the interface to catalyze chemical reactions

The charges which do not undergo charge recombination migrate to the catalyst surface and react with the environment either in the liquid/solid or gas/liquid interface. In the liquid/solid interface, photogenerated electrons could split the water and generate hydrogen, which is broadly considered as a future fuel. Otherwise, the electron could generate superoxide or hydroxide radicals which would degrade pollutants in either gas/solid or liquid/solid interface, transform pollutants into solar fuel, or kill cancer cells, for example. On the other hand, photogenerated holes can produce highly reactive ions like ·OH– or radicals such as ·OH, which lead to oxidation of organically polluted water or applicability in cancer therapy (Banerjee et al. 2014).

Photocatalyst must satisfy some principles for efficient operation:

Firstly, the light harvesting that includes a high absorption coefficient and a bandgap as close as possible to the maximum of Sun emission for the highest quantum efficiency, i.e., the highest creation of holes and electrons. For example, TiO_2, one of the most efficient photocatalysts, absorbs in the UV region; thus several approaches have been proposed to tune its bandgap to the visible range or to have secondary absorbers to inject carriers in its conduction band.

Secondly, an effective separation of holes and electrons without recombination that depends on the electronic structure and the presence of external or internal electric fields, crystal structure, morphology, etc.; the carrier diffusion length is also a factor to be considered at this point.

Thirdly, the band alignment of the photocatalyst material with the redox levels of the substrate to be attacked or the fast diffusion of reactive species within the heterogeneous phase.

Fourth, chemical stability against the media, to avoid photocorrosion or photodegradation; in some cases, a hole scavenger or a co-catalyst is employed to keep the material unaltered (Kumar and Devi 2011).

Two-dimensional (2D) materials such as graphene, Mo and W chalcogenides, have been proposed as highly suitable for photocatalysis applications because the chances of improving photon-matter interaction at semiconductor/electrolyte interface, taking advantage of size effects in the nanoscale, such as increased active area, enhanced reactivity, reduction of carrier diffusion length, increase of charge mobility, and bandgap/band position tuning, to mention some (Zhou et al. 2013).

10.3 Artificial Photosynthesis

Artificial photosynthesis (APS) is a chemical process that replicates the natural process of photosynthesis that converts sunlight, water, and carbon dioxide into more complex hydrocarbon substances. During APS occur photoinduced charge generation and separation that leads to photocatalytically generated hydrogen by water splitting. Other catalytic centers can be added to reduce CO_2 to produce CO. The process could be extended to generate more complex solar fuels by absorbing

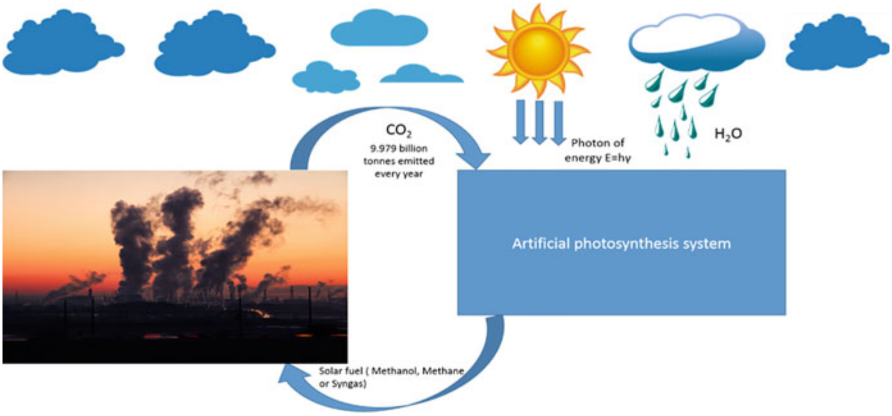

Fig. 10.2 Artificial photosynthesis processes, a technology that converts harmful greenhouse gas, CO_2, and returns to the source of emission by using sunlight and water from the environment, which is safeguarded in return

CO_2 and converting it as a useful fuel such as methanol, syngas ($CO + H_2$), and methane. Adaptation of this technology could ensure alleviation of the adverse effect of burning of fossil fuel for various needs from generating electricity to transport which leads to CO_2 emission and global warming as shown in Fig. 10.2.

Many authors consider APS as a suitable way to produce hydrogen as fuel, while others consider APS as the generation of hydrocarbons from the reaction of CO from CO_2 reduction and photogenerated H_2. Both approaches and some materials are discussed in the following sections.

10.3.1 Generation of Hydrogen by Artificial Photosynthesis

The free energy change required for the reaction of water splitting and H_2 generation is $\Delta G^{o} = 237.2$ kJ/mol or 2.46 eV/molecule of H_2O. One or more light-absorbing species are required to convert solar radiation into electrons and holes to drive the oxidation and reduction reactions (Tran et al. 2012).

$$2H_2O \rightarrow O_2 + 4H^+ + 4e, \ +0.81V \tag{10.3}$$

$$2H^+ + 2e \rightarrow H_2, 0.42\ V \tag{10.4}$$

As shown in Fig. 10.3a, light is harvested in semiconductor from the light source. It results in electron excitation from valence band to conduction band. Reduction potential is created at CB due to photoexcited electron, and oxidation potential is created at the VB due to creation of hole. At this point, water splitting reactions take

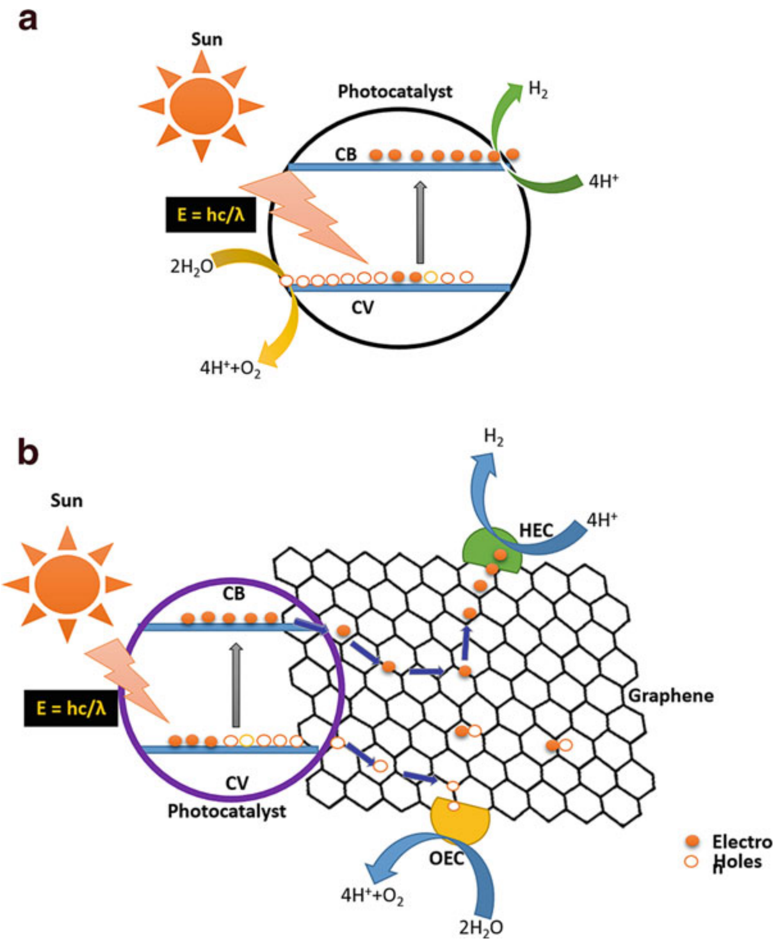

Fig. 10.3 Photocatalytic mechanism for hydrogen generation. (**a**) One-step water splitting process at single semiconductor. (**b**) Two-step reactions of the photocatalyst, charge mobility decide the overall quantum efficiency of the process

place according to Eqs. 10.3 and 10.4 Light-harvesting wavelength of the photocatalyst could be engineered by tuning the bandgap structure of the semiconductor. Co-catalyst may further accelerate the water splitting reactions. As shown in Fig. 10.3b, process of artificial photosynthesis similar to natural photosynthesis opens up a plethora of choices for choosing suitable semiconductor. It is easier to collect the product in the two-step process than the single-step process. After the photoinduced generation of electrons and holes, oxidation occurs at the oxygen-evolution catalytic site, while reduction takes place at the hydrogen-evolution one. Usage of two-dimensional materials like graphene could reduce charge recombination and enhance catalytic activity. Charge recombination is majorly reducing quantum efficiency of the photocatalytic process. Nevertheless, photocatalytic process which mimics natural photosynthesis could suffer over-control of kinetic balance, and ineffective co-catalysis might end up in an increased rate of charge recombination (Montoya et al. 2016; Tachibana et al. 2012).

10.3.2 g-C_3N_4-Based Materials

Qing Han et al. synthesized mesoporous nanomesh of graphitic C_3N_4 by solvothermal exfoliation of mesoporous g-C_3N_4. The hydrogen evolution rate was 8510 μmolh^{-1}g^{-1} under the wavelength greater than 420 nm and had a quantum efficiency of 5.1%. Aligned energy levels, electron transfer, light harvesting, and presences of more reaction sites were attributed to the increased performance (Han et al. 2016). CdS-C_3N_4 nanocomposite had a higher photocatalytic generation of hydrogen due to efficient charge transfer between g-C_3N_4 and CdS. The corresponding hydrogen evolution rate of 4.494 mmol–1h–1g–1 was more than 115 times greater than that of pure g-C3N4 at an optimized weight of 12% CdS in the nanocomposite. The photocatalytic performance was evaluated under visible light irradiation by L-ascorbic acid as a hole scavenger (Cao et al. 2012). Yuewei Zhang et al. compared the photocatalytic activity of g-C_3N_4 derived from urea, thiourea, and dicyanamide. Urea-derived g-C_3N_4 had a higher rate of hydrogen production rate. It was believed that porous structure with the increased surface area and pore value played a significant role in photoactivity than electronic property (Zhang et al. 2010). Xiaoxiang Xu et al. coated g-C3N4 on SrTiO3 to decompose urea in the presence of oxalic acid as hole scavenger, and demonstrated high H2 production rate at 440 μmolh–1g–1. Higher activity was attributed by the interfacial interaction between $SrTiO_3$ crystalline and g-C_3N_4. Photogenerated electrons in the conduction band of g-C_3N_4 under visible light irradiation either are involved in the photocatalytic activity on its surface or get injected in the conduction band of $SrTiO_3$ (Xu et al. 2011). Lei Ge et al. synthesized MoS_2-decorated g-C_3N_4 by a facile impregnation method. At the optimal weight 0.5 Wt%, MoS_2-g-C_3N_4 exhibited the highest hydrogen evolution rate of 23.10 μmol^{-1}h^{-1}. Photogenerated electrons from g-C_3N_4 were mobilized to MoS_2, and it acted as active sites for hydrogen production. It reduced charge recombination and enhanced photocatalytic activity (Ge et al. 2013) (Table 10.2).

10.3.3 Graphene-Based Materials

Graphene is regarded as a wonder material with exciting physical properties, such as theoretical surface area of (2630 m^{2}g^{-1}), an intrinsic mobility of (200,000 cm^{2}v^{-1}s^{-1}), a Young modulus of 1.0 TPa, thermal conductivity of (5000 Wm^{-1}K^{-1}), and optical transmittance ~97.7% (Lee et al. 2008). Strain and deformation could modify the electronic, optical, and phonon properties. Its band

Table 10.2 Materials based on g-C_3N_4 for hydrogen production

Material	Reason for enhanced activity	Hydrogen evaluation rate at $\mu mol^{-1}h^{-1}$	References
MWCNTs/g-C_3N_4	Less rate of recombination and efficient separation of the electron-hole pair	7.58	Ge and Han (2012)
CdS QDs/g-C_3N_4	Migration of electron from CdS to g-C_3N_4 and holes from g-C_3N_4 to CdS were ensured effective charge separation and increase in CdS bandgap due to the quantum size effect	17.27	Ge et al. (2012)
CdS/g-C_3N_4 core/shell nanowires	Suitable overlapping band structures between CdS and g-C_3N_4 and effective mobility of corrosive holes from CdS to g-C_3N_4	4152	Zhang et al. (2013)
g-C_3N_4/$Ni_xCo_{1-x}S_2$	The synergetic effect of Co and Ni restrained charge recombination	400.81	Fan et al. (2017)
Ni@NiO/CdS/g-C_3N_4	The superior catalytic activity of Ni/CdS	1258.7	Yue et al. (2016)
CdS-C_3N_4	Effective charge separation is attributed by interfacial transfer of charges between g-C_3N_4 and CdS	4494	Cao et al. (2012)
$Sr_{0.4}H_{1.2}Nb_2O_6H_2O$/g-$C_3N_4$	Heterojunction structure reduced charge recombination	469.4	Ma et al. (2018)
SnS_2/g-C_3N_4	Heterojunction structure formed by two photocatalysts, namely, g-C_3N_4 and SnS_2, leads mobility of charges to the respective bands. This reduced the charge recombination	972.6	Liu et al. (2018)
$MoSe_2$/g-C_3N	Interfacial charge transfer and higher active sites at $MoSe_2$	114.5	Zeng et al. (2018)
g-C_3N_4/$LaxCo_3$-xO_4	Active interfaces and cascading band structures between the photocatalyst	63.12	Xu et al. (2018)

structure could be altered. Graphene is the thinnest and strongest material ever quantified. Its charge carriers exhibit enormous intrinsic mobility and have zero effective mass, and mobility could happen for micrometer without scattering at room temperature (Pereira et al. 2009). Graphene could absorb a wide range of radiation of spectrum from ultraviolet to the infrared spectrum. Charge carriers are extracted at the ultrafast rate due to the high mobility of carriers (Singh et al. 2011).

Young Juan Yuan et al. hydrothermally synthesized MoS_2-graphene/$ZnIn_2S_4$ photocatalyst. Na_2SO_3 and Na_2S were used as the sacrificial agent. Under visible light, electrons are excited from the valence band (VB) to the conduction band (CB) of $ZnIn_2S_4$. CB of $ZnIn_2S_4$ is more negative than graphene/graphene reduction potential which paves the way for the thermodynamic driving force for charge mobility to graphene. Again CB of graphene is more negative than that of MoS_2 which leads to electron transfer to more active sites of MoS_2 for hydrogen evolution

(Yuan et al. 2016). The photocatalytic activity of CdS/Nb_2O_5/N-doped graphene was evaluated at the visible light range light source. The highest amount of hydrogen was evolved with 2% weight of nitrogen-doped graphene-containing composite. The evolution rate was about 800 $\mu mol^{-1} g^{-1}$. After absorption of light, it was believed that electron mobility occurred from CdS to Nb_2O_5 in respective bands and hydrogen evolution reactions happened at the active sites of nitrogen-doped graphene (Yue et al. 2017). Jian Ping Zou et al. synthesized metal-free g-C_3N_4/graphene quantum dots hybrid photocatalyst. Fifteen percent loading of nitrogen-doped graphene quantum dots showed hydrogen evolution rate around 2.18 $mmol^{-1} g^{-1}$ under long wavelength ($\lambda > 590$ nm) (Zou et al. 2016). Fujun Niu et al. reported an artificial photosynthesis system which contains fluorescein as a photosensitizer, single-layer ultrasmall MoS_2 nanoplates embedded in carbon nanofibers as electron relay and redox catalyst, and triethanolamine as a sacrificial electron donor. This system shows excellent H_2 generation rate and evolution performance. This system has high-density reactive S sites which leads to excellent photoactivity (Niu et al. 2017).

10.3.4 Generation of Solar Fuels by Artificial Photosynthesis

Direct conversion of solar energy into fuel with the presence of carbon dioxide and water is termed as solar fuel. It involves converting the solar fuels into energy stored chemical bonds with the aid of artificial photocatalyst. It can be stored in high density and long-lived (Tran PD et al. 2012). Solar fuels can be produced in the form of hydrogen derived from photo-assisted water splitting (as discussed in the previous topic), or as high-energy carbon compounds (Eqs. 10.3, 10.4, 10.5, 10.6 and 10.7) by the following reactions and respective fuel forms at redox potentials mentioned below at pH 7 vs standard hydrogen electrode (SHE) (Morris et al. 2009):

$$CO_2 + 2H^+ + 2e \rightarrow HCOOH, 0.61V \tag{10.5}$$

$$CO_2 + 2H^+ + 2e \rightarrow CO + H_2O, 0.53V \tag{10.6}$$

$$CO_2 + 4H^+ + 4e \rightarrow HCHO + H_2O, 0.48V \tag{10.7}$$

$$CO_2 + 6H^+ + 6e \rightarrow CH3OH + H_2O, 0.38V \tag{10.8}$$

$$CO_3 + 8H^+ + 8e \rightarrow CH_4 + 2H_2O, 0.24 \tag{10.9}$$

Different potentials are favoring the photoreduction of different solar fuels such as methane, methanol, ethanol, carbon monoxide, formic acid, or formaldehyde. Still, it has not been explained well about how different potentials favor various products by reducing CO_2.

The solar radiation spectrum available on the Earth consists of 4.6% of ultraviolet radiation ($\lambda < 400$ nm), 54.3% of visible light (400 nm $< \lambda <$ 800 nm), and 41.1% of

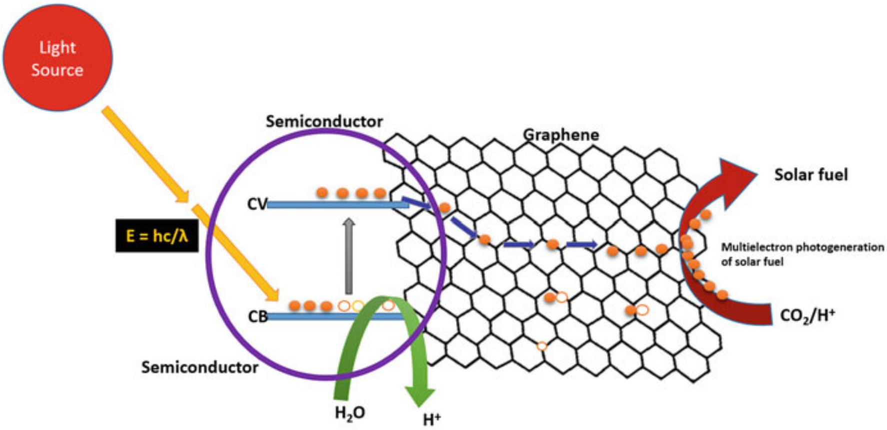

Fig. 10.4 Mechanism of artificial photosynthesis which involves the multi-electron process. This process demands higher energy for the conversion of notorious greenhouse gas, carbon dioxide, into high-energy fuel. As mentioned before, graphene has excellent physical and electrical properties, that allow to reduce charge recombination. This property fulfils the requirement of multi-electron photogeneration of solar fuel process

infrared radiation (λ < 800 nm). The energy and wavelength are related as E (eV) = 1240/λ. Therefore, it is mandatory to have a smaller bandgap in order to maximize the utilization of sunlight. Bandgap could be engineered by various processes such as doping, solid solution, elemental substitution, and surface sensitization (Rozhkova and Ariga 2015). Transformation of CO_2 into high energy involves the multi-electron process. It is of paramount importance to have a material which is efficient in charge mobility without recombination. Graphene decorated with suitable semiconductor could be suitable photocatalyst for CO_2 reduction as shown in Fig. 10.4.

Cristina Lavorato et al. used an alginate, a natural polysaccharide from algae, simultaneously graphene precursors, and template agent for ceria nanoparticle. They demonstrated three times higher photocatalytic activity for water oxidation by varying percentage of ceria/alginate and that pyrolysis enables the temperature of a ceria/graphene (Lavorato et al. 2014).

The review paper by Sakineh Chabi et al. discussed the recent advances of membranes for artificial photosynthesis system. Membrane plays a critical role in managing the charge carrier and separation of the same. This paper emphasizes on the membrane-based architecture for efficient charge transportation over small distances and improved kinetics (Chabi et al. 2017).

Xian-fu Zang et al. attached the graphene with tetrasulfonated zinc phthalocyanine (Pc) molecule. They had observed excellent electron transport and multi-electron-accepting ability, multichromophore binding, and concurrent multiphoton-absorbing ability. Graphene here accepts the excited electron; in addition, it transported the captured to the unexcited Pcs. Graphene sheets quenched the excited Pcs at the rate constant as high as 10^{16} $M^{-1}s^{-1}$ (Najafpour et al. 2014).

Rajesh K Yadav and co-workers coupled chemically converted (CCG) graphene with multi-anthraquinone-substituted porphyrin (MAQSP). This system reduces CO_2 into formic acid. The material also demonstrated good selectivity Fermi level of graphene is calculated 4.14 eV. The calculated bandgap of MAQSP is ~0.6. Triethanolamine is a hole scavenger. The photogenerated electrons in MAQSP are transported to CCG irreversibly. Graphene also acted as a reservoir for multi-electron transport. It favors the multiple addition or removal of an electron because of delocalized nature of wave function on its surface. This photocatalyst coupled enzyme system is highly active in visible light (Yadav et al. 2012). Akhide Iwase et al. demonstrated the photoreduced graphene oxide (PRGO) using $BiVO_4$ as a solid-state electron mediator. It effectively transported the photogenerated electrons from the O_2 photocatalyst (PRGO/$BiVO_4$) to H_2 photocatalyst (Ru/$SrTiO_3$: Rh). PRGO prepared $BIVO_4$ showed higher conductivity and a low degree of hydrophobicity (Iwase et al. 2011).

Xinjuan Liu et al. synthesized Cds-RGO composite by microwave-assisted reduction of GO in Cds precursor solution. CdS-RGO showed better photocatalytic activity than pure CdS. Composite’s photocatalytic activity depends upon proportion content of RGO. RGO introduction of the CdS increased the light absorption intensity lead to enhanced photocatalytic performance and reduced electron-hole pair recombination (Liu et al. 2011). Mohammad Mahdi Najafpour and co-workers synthesized nano-sized Mn oxide/CNT, graphene, and GO as water oxidizing agents by a simple method and showed that simple Van der Waals interactions are sufficient to provide strong adhesion between Mn oxides and CNT. Water oxidation activities of Mn oxide/CNT, G, or GO depend on Mn oxide, and nanocarbon structure had no effect on the activity of Mn oxides toward water oxidation. MnOx material’s lower conductivity was improved nanocarbons. The temperature of calcination also affects the water oxidation (Najafpour et al. 2014).

Wee-Jun Ong and co-workers reported a facile one-pot impregnation thermal reduction approach to synthesis sandwich-like metal-free graphene-g-C_3N_4(CGN) nanocomposite. CO_2 was photocatalytically reduced to methane with water as hole scavenger and it was demonstrated that graphene played a substantial role in the photocatalytic activity of g–C_3N_4 for CO_2 conversion. In above all cases, no significant CH_4 gas was detected. Graphene played a substantial role in the photocatalytic activity of g-C_3N_4 for CO_2 conversion. In the absence of graphene, least amount of CH_4 was detected due to rapid recombination of electrons and holes. The yield was 2.55 μmol $g_{catalyst}{}^{-1}$. But yield jumped to 5.87 μmol $g_{catalyst}{}^{-1}$ with 15% loading of graphene (Ong et al. 2015). Xiaqiang An et al. showed the photocatalytic reduction of CO_2 to CO sixfold increases in Cu_2O/RGO when compared to Cu_2O. Also, the absorption ability of Cu_2O was enhanced in both UV and visible range by loading 0.5% of RGO. The yield of CO was 46 PPM g-1 with Cu_2O/0.5% RGO. Stability was a serious problem with Cu_2O photocatalyst. This was improved introduction of RGO. The protective function of RGO reduced charge recombination, and efficient electron transfer was attributed to the greater performance (An et al. 2014). Enhanced electron transportation from the CeO_2 semiconductor and reduced recombination of the photogenerated electron-hole pair are backing N-doped graphene as suitable candidate for artificial photosynthesis. Lone pairs of an electron on N atoms can coordinate with metal ions to form Cu (II) metal complex which can well work as metalloenzyme to reduce CO_2 into methanol (Liu et al. 2016).

10.4 Photodegradation

Water bodies have been polluted by residues coming from several industries such as dyes, heavy metals, pesticides, farmaceuticals, eutrophicating substances, sewage waters, to mention some. Photodegradation could be the solution for sustainable degradation of organic pollutants (Pathania et al. 2016; Sharma et al. 2015) (Fig. 10.5).

The quintessential requisites of photodegradation materials are optimum bandgap which absorbs the visible light, strong oxidative ability, and being stable in water. g-C_3N_4 is stable from acidic (pH = 0, HCl) to basic (pH = 14, NaOH) because of strong bond attachments with carbon and nitride atoms (Yan et al. 2009).

Rapid charge recombination and long mobility distance influence the photocatalytic activity. Changun Han et al. used a facile mixing and heating method to synthesize Co_3O_4-g-C_3N_4. Organic pollutants could be degraded by the photocatalytic degradation process.

Species such as h^+, hydroxyl (OH^+), and superoxide (O_2^-) are believed to be involved in photocatalytic degradation. The heterojunction was formed between two

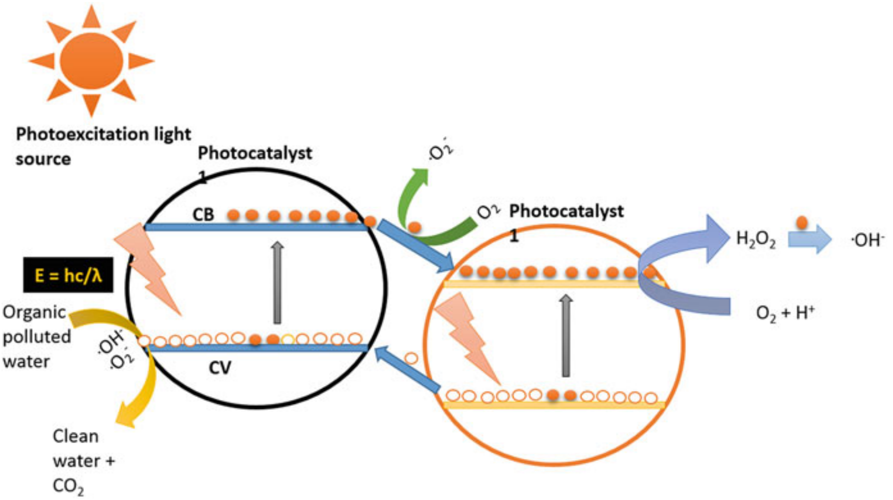

Fig. 10.5 Mechanism of photocatalytic degradation in heterojunction composite material. Enhanced activity of photodegradation could be attributed to the formation of heterojunction with different semiconductors because of charge mobility between respective bands. After induced charge generation and mobility, they are possibilities formation superoxide and radicals. These radicals are involved in the photodegradation

semiconductors. It was believed that holes were transported to from CV of g-C_3N_4 to Co_3O_4 after electrons in g-C_3N_4 to CB under light illumination. Thereby charge recombination had been hindered. Electrons in CB tend to produce superoxide $\cdot O_2^-$ radicals (Han et al. 2014).

2,4,6-Trichlorophenol possesses high toxicity and carcinogenic properties which had been degraded under visible light irradiation over g-C_3N_4 by Huan Huan Ji et al. Oxygen scavenges electrons and forms $\cdot O_2^-$. Then superoxide radical reacts with proton and forms ·OOH by the following reactions.

$$O_2 + e^- \rightarrow {}^{\cdot}O_2$$
$$O_2{}^- + H^+ \rightarrow {}^{\cdot}OOH$$

Hydroxyl radical, another important species, is responsible for the degradation.

$$O_2{}^- + e^- + 2H^+ \rightarrow H_2O_2$$
$${}^{\cdot}OOH + e^- + H^+ \rightarrow H_2O_2$$
$$H_2O_2 + e^- \rightarrow {}^{\cdot}OH + OH^-$$

Actually these species contribute for photodegradation of 2,4,6-TCP (Ji et al. 2013).

Shanomang Wang et al. anchored Ag_3VO_4 on g-C_3N_4. The higher photocatalytic rate was exhibited at 40% wt g-C_3N_4/Ag_3VO_4 with removal rate constant of 0.92 h^{-1}. This photocatalyst could remove malachite green and crystal violet (Wang et al. 2014). Tingtig Li et al. synthesized g-C_3N_4 using mixing calcination method. They demonstrated an increase in calcination temperature which leads to the formation of a chemical bond between $SmVO_4$ and g-C_3N_4 which reduced the interface energy barrier and enhanced electron-hole mobility. Here rhodamine B was the target pollutant (Li et al. 2013).

10.5 Self-Cleaning Photocatalysis

The butterfly wing and leaves of plants are natural examples of self-cleaning technology. This technology has numerous applications from domestic cleaner of window glasses to the labor-saving device in textiles and cement industries. It categorized into hydrophilic (carries away the dirt by sheeting of water) and hydrophobic (cleans by sliding and rolling of water droplets on the surface) (Fig. 10.6, Ganesh et al. 2011). The additional hydrophilic self-cleaning coating could break down the absorbed dirt chemically in the presence of sunlight (Parkin et al. 2005).

The process of self-cleaning does not rely only on water wash of dirty elements. These self-cleaning coated materials chemically break down dirt which is catalyzed by photocatalytic reaction. Here few interesting 2D materials, which are suitable for self-cleaning, are discussed.

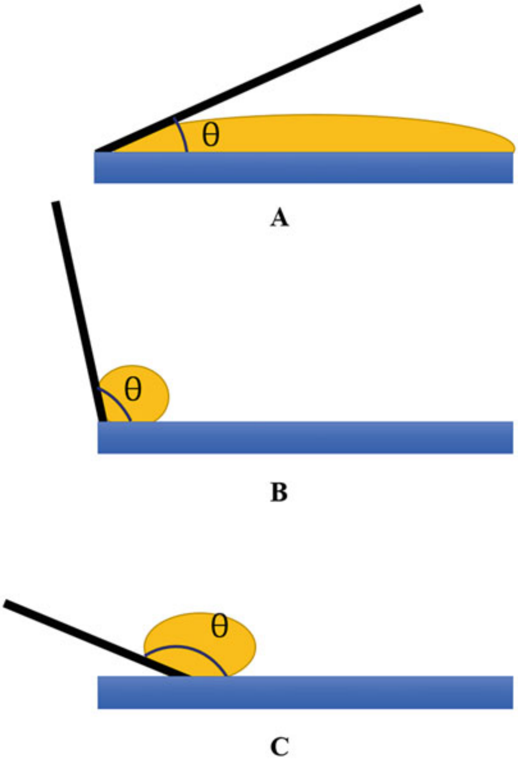

Fig. 10.6 Angle between liquid drop and surface contact at three-phase boundary determines nature of self-cleaning. (**a**) Hydrophilic, when contact angle is less than 90° ($\theta < 90°$). (**b**) Hydrophobic, when contact angle is greater than 90° ($\theta > 90°$). (**c**) Ultra (super) hydrophilic, when contact angle is greater than 150° ($\theta > 150°$)

Srinivasan Ananadan et al. coated graphene-loaded TiO_2 thin films on a glass substrate by the spin-coating method. Graphene/TiO_2 had shown superhydrophilicity under white fluorescent light bulb as compared to pure TiO_2 film. Electrons are effectively transported to the graphene due to conduction band gradient (graphene = −0.08 V vs SHE, pH = 7, TiO_2 = −0.4 V vs SHE, pH = 7). Photogenerated holes oxidize the methyl blue followed by the dissociative adsorption of H_2O molecule. Finally, it paves the way to the superhydrophilic surface (Anandan et al. 2012). H-Y et al. stress the important materialistic characteristic requirements for a self-cleaning catalyst such as high photocatalytic activity, induced superhydrophilicity, and optical transparency. ZnO-rGo had been deposited on the glass substrate by the sol-gel technique. The author observed photocatalytic activity increases with increasing the amount of rGO and temperature of calcination (350–450 °C) (He 2015). Siqi Liu et al. combined one-dimensional (1D) structure with two-dimensional (2D) structure which is CdS nanowire-reduced graphene oxide nanocomposite. The author stated the addition of RGO improved the lifetime and mobility of charge. It also increased the adsorption capacity of aromatic organics. The catalyst was used the selective reduction of nitro organics (4 nitroamines) to the corresponding amino organics (4-phenylenediamine) under the visible light illumination (Liu et al. 2013).

10.6 Cancer Therapy

Photocatalysis has some interesting application in cancer therapy, and few works are highlighted here. Di Wei et al. reported the continuous exposure of carbon monoxide which could sensitize cancer cells to chemotherapy and increased the cytotoxicity of anticancer drug (doxorubicin DOX) by 70%. The photocatalyst named as HisAgCCN, was used to catalyze CO_2 reduction to CO under 600 nm irradiation. Ag_3PO_4 was doped with carbon-dot-decorated C_3N_4 nanoparticles. Then it was functionalized with histidine-rich peptide to synthesize HisAgCCN. It was proved that this photocatalyst underwent mitochondria biogenesis and aggravates oxidative stress in cancer cells (Zheng et al. 2017). Elena A. Rozhkova et al. and co-workers used a 5 nm TiO_2 nanoparticle covalently tethered through DOPAC (3,4-dihydroxyphenylacetic acid) linker to antihuman IL13α3R to form a nanocomposite. The photocatalyst under illumination initiates the generation of reactive oxygen species which kills the notorious form of brain cancer glioblastoma multiforme (GBM) (Rozhkova et al. 2009).

10.7 Summary and Future Orientation

Photocatalysis has been extensively researched for various applications. The major process will be photoinduced charge generation, charge mobility, and catalytic reaction at active sites. The literature revision indicates that there is still lack of understanding of some of the fundamental mechanisms of photocatalysis, particularly on 2D materials. This will restrict the scale up for practical applications, which leads to the need of more theoretical studies with experimental validation to unveal the basic mechanisms. The major environmental concern is global warming. It could be mitigated by scaling up the artificial photosynthesis in the following ways. Highways, traffic signals, municipal roads, and CO_2-emitting industries will have to be equipped with the AP system. It will benefit thrice:

1. Producing fuels without greenhouse gas emission.
2. Treating already emitted greenhouse gas.
3. Maintenance of roads or others can be done by the selling the fuel.

We should concentrate how to channelize the fuels generated at the highways and roads to the gasoline stations. Photocatalytic applications in cancer therapy could be open to new avenues in terms of patient recovery rate and cost of treatment.

Acknowledgments Financial support from Projects SIP-IPN 20181187 and 20181196 is granted for undergoing this work.

References

An X, Li K, Tang J (2014) Cu_2O/reduced graphene oxide composites for the photocatalytic conversion of CO_2. ChemSusChem 7(4):1086–1093. https://doi.org/10.1002/cssc.201301194

Anandan S, Rao TN, Sathish M, Rangappa D, Honma I, Miyauchi M (2012) Superhydrophilic graphene-loaded TiO 2 thin film for self-cleaning applications. ACS Appl Mater Interfaces 5 (1):207–212. https://doi.org/10.1021/am302557z

Banerjee S, Pillai SC, Falaras P, O'shea KE, Byrne JA, Dionysiou DD (2014) New insights into the mechanism of visible light photocatalysis. J Phys Chem Lett 5(15):2543–2554. https://doi.org/10.1021/jz501030x

Cao S, Yuan Y, Fang J, Mehdi M, Boey FYC, Barber J, Xue C (2012) In-situ growth of CdS quantum dots on g-C $_3$ N $_4$ nanosheets for highly efficient photocatalytic hydrogen generation under visible light irradiation. Int J Hydrog Energy 38(3):1258–1266. https://doi.org/10.1016/j.ijhydene.2012.10.116

Chabi S, Papadantonakis KM, Lewis NS, Freund MS (2017) Membranes for artificial photosynthesis. Energy Environ Sci 10(6):1320–1338. https://doi.org/10.1039/C7EE00294G

Fan K, Jin Z, Yang H, Liu D, Hu H, Bi Y (2017) Promotion of the excited electron transfer over Ni- and Co -sulfide (g-C $_3$ N $_4$/Ni $_x$ Co $_{1-x}$ S $_2$) for hydrogen production under visible light irradiation. Sci Rep 7(7710):1–10. https://doi.org/10.1038/s41598-017-08163-y

Ganesh VA, Raut HK, Nair AS, Ramakrishna S (2011) A review on self-cleaning coatings. J Mater Chem 21(41):16304–16322. https://doi.org/10.1039/c1jm12523k

Ge L, Han C (2012) Environmental synthesis of MWNTs/g-C_3N_4 composite photocatalysts with efficient visible light photocatalytic hydrogen evolution activity. App Catal B 118:268–274. https://doi.org/10.1016/j.apcatb.2012.01.021

Ge L, Zuo F, Liu J, Ma Q, Wang C, Sun D, Bartels L, Feng P (2012) Synthesis and efficient visible light Photocatalytic hydrogen evolution of polymeric g-C_3N_4 coupled with CdS quantum dots. J Phys Chem C 116(25):13708–13714. https://doi.org/10.1021/jp3041692

Ge L, Han C, Xiao X, Guo L (2013) Synthesis and characterization of composite visible light active photocatalysts MoS_2-g-$C_3N_4$with enhanced hydrogen evolution activity. Int J Hydrog Energy 38(17):6960–6969. https://doi.org/10.1016/j.ijhydene.2013.04.006

Global Carbon Emission Data (2014). https://www.co2.earth/global-co2-emissions

Global Greenhouse gas emissions data by US Environmental Protection Agency. https://www.epa.gov/ghgemissions/global-greenhouse-gas-emissions-data

Han C, Ge L, Chen C, Li Y, Xiao X, Zhang Y, Guo L (2014) Novel visible light induced Co_3O_4-g-C_3N_4 heterojunction photocatalysts for efficient degradation of methyl orange. Appl Catal B Environ 147:546–553. https://doi.org/10.1016/j.apcatb.2013.09.038

Han Q, Wang B, Gao J, Cheng Z, Zhao Y, Zhang Z, Qu L (2016) Atomically thin Mesoporous Nanomesh of graphitic $C_3N_4$for high-efficiency Photocatalytic hydrogen evolution. ACS Nano 10(2):2745–2751. https://doi.org/10.1021/acsnano.5b07831

He HY (2015) Photoinduced superhydrophilicity and high photocatalytic activity of ZnO-reduced graphene oxide nanocomposite films for self-cleaning applications. Mater Sci Semicond Process 31:200–208. https://doi.org/10.1016/j.mssp.2014.11.029

Iwase A, Ng YH, Ishiguro Y, Kudo A, Amal R (2011) Reduced graphene oxide as a solid-state electron mediator in Z-scheme photocatalytic water splitting under visible light. Am Chem Soc 133(29):11054–11057. https://doi.org/10.1021/ja203296z

Ji H, Chang F, Hu X, Qin W, Shen J (2013) Photocatalytic degradation of 2,4,6-trichlorophenol over g-C_3N_4 under visible light irradiation. Chem Eng J 218:183–190. https://doi.org/10.1016/j.cej.2012.12.033

Kumar SG, Devi LG (2011) Review on modified TiO_2 photocatalysis under UV/visible light: selected results and related mechanisms on interfacial charge carrier transfer dynamics. J Phys Chem A 115(46):13211–13241. https://doi.org/10.1021/jp204364a

Lavorato C, Primo A, Molinari R, García H (2014) Natural alginate as a graphene precursor and template in the synthesis of nanoparticulate ceria/graphene water oxidation photocatalysts. ACS Catal 4(2):497–504. https://doi.org/10.1021/cs401068m

Lee C, Wei X, Kysar JW, Hone J (2008) Measurement of the elastic properties and intrinsic strength of monolayer graphene. Science 321(5887):385–388. https://doi.org/10.1126/science.1157996

Liu X, Pan L, Lv T, Zhu G, Sun Z, Sun C (2011) Microwave-assisted synthesis of CdS-reduced graphene oxide composites for photocatalytic reduction of Cr(vi). Chem Commun 47 (43):11984–11986. https://doi.org/10.1039/C1CC14875C

Li T, Zhao L, He Y, Cai J, Luo M, Lin J (2013) Synthesis of g-C_3N_4/$SmVO_4$composite photocatalyst with improved visible light photocatalytic activities in RhB degradation. Appl Catal B Environ 129:255–263. https://doi.org/10.1016/j.apcatb.2012.09.031

Liu S, Chen Z, Zhang N, Tang Z, Xu Y (2013) An efficient self-assembly of CdS nanowires – reduced graphene oxide nanocomposites for selective reduction of nitro organics under visible light irradiation. J Phys Chem 117(16):8251–8261. https://doi.org/10.1021/jp400550t

Liu SQ, Zhou SS, Chen ZG, Liu CB, Chen F, Wu ZY (2016) An artificial photosynthesis system based on CeO_2 as a light harvester and N-doped graphene Cu(II) complex as artificial metalloenzyme for CO_2 reduction to methanol fuel. Catal Commun 73:7–11. https://doi.org/10.1016/j.catcom.2015.10.004

Liu C, Chai B, Wang C, Yan J, Ren Z (2018a) Solvothermal fabrication of MoS_2 anchored on $ZnIn_2S_4$ microspheres with boosted photocatalytic hydrogen evolution activity. Int J Hydrog Energy 43(14):6977–6986. https://doi.org/10.1016/j.ijhydene.2018.02.116

Liu E, Chen J, Ma Y, Feng J, Jia J, Fan J, Hu X (2018b) Journal of colloid and Interface science fabrication of 2D SnS_2/g-C_3 N $_4$ heterojunction with enhanced H $_2$ evolution during photocatalytic water splitting. J Colloid Interface Sci 524(229):313–324. https://doi.org/10.1016/j.jcis.2018.04.038

Ma W, Li D, Wen B, Ma X, Jiang D, Chen M (2018) Construction of novel $Sr_{0.4}H_{1.2}Nb_2O_6$.H2O/g-C_3N_4 enhanced visible light photocatalytic activity for hydrogen evolution. J Colloid Interface Sci 526:451–458. https://doi.org/10.1016/j.jcis.2018.05.019

Masao K, Okura I (2002) Photocatalysis science and technology. Springer, Berlin/Heidelberg/New York

Morris AJ, Meyer GJ, Fujita E (2009) Molecular approaches to the photocatalytic reduction of carbon dioxide for solar fuels. Acc Chem Res 42(12):1983–1994. https://doi.org/10.1021/ar9001679

Montoya JH, Seitz LC, Chakthranont P, Vojvodic A, Jaramillo TF, Nørskov JK (2016) Materials for solar fuels and chemicals. Nat Mater 16(1):70–81. https://doi.org/10.1038/nmat4778

Najafpour MM, Rahimi F, Fathollahzadeh M, Haghighi B, HoŁyŃska M, Tomo T, Allakhverdiev SI (2014) Nanostructured manganese oxide/carbon nanotubes, graphene and graphene oxide as water-oxidizing composites in artificial photosynthesis. J Chem Soc Dalton Trans 43 (28):10866–10876. https://doi.org/10.1039/c4dt01295j

Niu F, Dong CL, Zhu C, Huang YC, Wang M, Maier J, Yu Y, Shen S (2017) A novel hybrid artificial photosynthesis system using MoS_2embedded in carbon nanofibers as electron relay and hydrogen evolution catalyst. J Catal 352:35–41. https://doi.org/10.1016/j.jcat.2017.04.027

Ong WJ, Tan LL, Chai SP, Yong ST (2015) Graphene oxide as a structure-directing agent for the two-dimensional interface engineering of sandwich-like graphene-g-C_3N_4 hybrid nanostructures with enhanced visible-light photoreduction of CO_2 to methane. Chem Commun 51(5):858–861. https://doi.org/10.1039/C4CC08996K

Pathania D, Katwal R, Sharma G et al (2016) Novel guar gum/Al2O3 nanocomposite as an effective photocatalyst for the degradation of malachite green dye. Int J Biol Macromol 87:366–374. https://doi.org/10.1016/j.ijbiomac.2016.02.073

Parkin IP, Palgrave RG (2005) Self-cleaning coatings. J Mater Chem 15:1689–1695. https://doi.org/10.1039/b412803f

Pereira VM, Castro Neto AH, Peres NMR (2009) Tight-binding approach uniaxial strain in graphene. Phys Rev B Condens Matter Mater Phys 80(4):1–9. https://doi.org/10.1103/PhysRevB.80.045401

Rozhkova EA, Ariga K (2015) From molecules to materials. Springer, Cham

Rozhkova EA, Ulasov I, Lai B, Dimitrijevic NM, Lesniak MS, Rajh T (2009) A high-performance nano-bio photocatalyst for targeted brain cancer therapy. Nano Lett 9(9):2005–2008. https://doi.org/10.1021/nl901610f

Sharma G, Naushad M, Pathania D et al (2015) Modification of *Hibiscus cannabinus* fiber by graft copolymerization: application for dye removal. Desalin Water Treat 54:3114–3121. https://doi.org/10.1080/19443994.2014.904822

Singh V, Joung D, Zhai L, Das S, Khondaker SI, Seal S (2011) Graphene-based materials: past, present and future. Prog Mater Sci 56(8):1178–1271. https://doi.org/10.1016/j.pmatsci.2011.03.003

Tachibana Y, Vayssieres L, Durrant JR (2012) Artificial photosynthesis for solar water-splitting. Nat Photonics 6(8):511–518. https://doi.org/10.1038/nphoton.2012.175

Tran PD, Wong LH, Barber J, Loo JSC (2012) Recent advances in hybrid photocatalysts for solar fuel production. Energy Environ Sci 5(3):5902–5918. https://doi.org/10.1039/c2ee02849b

Wang S, Li D, Sun C, Yang S, Guan Y, He H (2014) Synthesis and characterization of g-C_3N_4/Ag_3VO_4composites with significantly enhanced visible-light photocatalytic activity for triphenylmethane dye degradation. Appl Catal B Environ 144:885–892. https://doi.org/10.1016/j.apcatb.2013.08.008

Xu X, Liu G, Randorn C, Irvine JTS (2011) G-C_3N_4 coated $SrTiO_3$ as an efficient photocatalyst for H_2 production in aqueous solution under visible light irradiation. Int J Hydrog Energy 36(21):13501–13507. https://doi.org/10.1016/j.ijhydene.2011.08.052

Xu J, Yu H, Guo H (2018) Synthesis and behaviours of g-C_3 N $_4$ coupled with La $_x$ Co $_{3\text{-}x}$ O $_4$ nanocomposite for improved photocatalytic activity and stability under visible light. Mater Res Bull 105(April):342–348. https://doi.org/10.1016/j.materresbull.2018.04.006

Yadav RK, Baeg JO, Oh GH, Park NJ, Kong KJ, Kim J, Biswas SK (2012) A photocatalyst-enzyme coupled artificial photosynthesis system for solar energy in the production of formic acid from CO_2. J Am Chem Soc 134(28):11455–11461. https://doi.org/10.1021/ja3009902

Yan SC, Li ZS, Zou ZG (2009) Photodegradation performance of g-C_3N_4 fabricated by directly heating melamine. Langmuir 25(17):10397–10401. https://doi.org/10.1021/la900923z

Yuan YJ, Tu JR, Ye ZJ, Chen DQ, Hu B, Huang YW et al (2016) MoS_2-graphene/$ZnIn_2S_4$hierarchical microarchitectures with an electron transport bridge between light-harvesting semiconductor and cocatalyst: a highly efficient photocatalyst for solar hydrogen generation. Appl Catal B Environ 188:13–22. https://doi.org/10.1016/j.apcatb.2016.01.061

Yue X, Yi S, Wang R, Zhang Z, Qiu S (2016) Cadmium sulfide and nickel synergetic co-catalysts supported on graphitic carbon nitride for visible-light-driven photocatalytic hydrogen evolution. Nature Publishing Group (November 2015), pp 1–9. https://doi.org/10.1038/srep22268

Yue Z, Liu A, Zhang C, Huang J, Zhu M, Du Y, Yang P (2017) Noble-metal-free hetero-structural CdS/Nb_2O_5/N-doped-graphene ternary photocatalytic system as a visible-light-driven photocatalyst for hydrogen evolution. Appl Catal B Environ 201:202–210. https://doi.org/10.1016/j.apcatb.2016.08.028

Zeng D, Wu P, Ong W, Tang B, Wu M, Zheng H, Peng D (2018) Applied catalysis B: environmental construction of network-like and flower-like 2H-$MoSe_2$ nanostructures coupled with porous g-C_3N $_4$ for noble-metal-free photocatalytic H 2 evolution under visible light. Appl Catal B Environ 233(March):26–34. https://doi.org/10.1016/j.apcatb.2018.03.102

Zhang Y, Liu J, Wu G, Chen W (2010) Porous graphitic carbon nitride synthesized via directly polymerization of urea for efficient sunlight-driven photocatalytic hydrogen production. Nanoscale 4(8):1166–1169. https://doi.org/10.1039/b000000x

Zhang J, Wang Y, Jin J, Zhang J, Lin Z, Huang F, Yu J (2013) Efficient visible-light photocatalytic hydrogen evolution and enhanced photostability of core/shell CdS/g – C $_3$ N $_4$ nanowires. ACS Appl Mater Interfaces 5(20):10317–10324. https://doi.org/10.1021/am403327g

Zheng D-W, Li B, Li C-X, Xu L, Fan J-X, Lei Q, Zhang X-Z (2017) Photocatalyzing CO $_2$ to CO for enhanced cancer therapy. Adv Mater 29(44):1703822–1703822. https://doi.org/10.1002/adma.201703822

Zhou M, Lou XW, Xie Y (2013) Two-dimensional nanosheets for photoelectrochemical water splitting: possibilities and opportunities. Nano Today 8(6):598–618. https://doi.org/10.1016/j.nantod.2013.12.002

Zou JP, Wang LC, Luo JM, Nie YC, Xing QJ, Luo XB, Du HM, Suib SL (2016) Synthesis and efficient visible light photocatalytic H_2 evolution of a metal-free g-C_3N_4/graphene quantum dots hybrid photocatalyst. Appl Catal B Environ 193:103–109. https://doi.org/10.1016/j.apcatb.2016.04.017

Chapter 11

Synthesis and Characterization of Single-Phased $BiFeO_3$ Nanostructures for Photocatalytic Applications: Hydrothermal Approach

Muniyandi Muneeswaran, Radhalayam Dhanalakshmi, and Ali Akbari-Fakhrabadi

Contents

11.1 Introduction 296
11.2 Properties of $BiFeO_3$ 298
  11.2.1 Hydrothermal Approach of $BiFeO_3$ 298
  11.2.2 Effect of $BiFeO_3$ Nanoparticles on Different Textile Dyes 302
11.3 Conclusion and Perspectives 310
References 310

Abstract The multiferroic material bismuth ferrite ($BiFeO_3$, BFO) is a newly emerging photocatalytic material reported to be comparable with other oxide semiconductor materials. BFO photocatalysis encounters challenges based on its practical use. As it has a narrow energy bandgap (about 1.8–2.8 eV), the photocatalysis of visible and UV light such as hydrogen (H_2) generation by water splitting becomes possible. This chapter discusses the synthesis of single-phase BFO nanostructures approached by the hydrothermal method, and optimization of single-phase BFO nanostructures by tuning the particle size and morphology with assistance of sodium hydroxide (NaOH) and potassium hydroxide (KOH) as precipitating agents. Outlooks on the expansion of advanced BFO photocatalysts with possible improvement for the remediation of environmental pollution are discussed.

M. Muneeswaran (✉) · A. Akbari-Fakhrabadi (✉)
Advanced Materials Laboratory, Department of Mechanical Engineering, University of Chile, Santiago, Chile
e-mail: aliakbarif@uchile.cl

R. Dhanalakshmi
Department of Chemical Engineering, Indian Institute of Technology Madras, Chennai, Tamil Nadu, India

S. Rajendran et al. (eds.), *Green Photocatalysts for Energy and Environmental Process*, Environmental Chemistry for a Sustainable World 36,
https://doi.org/10.1007/978-3-030-17638-9_11

Keywords Nanostructured photocatalysts · Bismuth ferrite ($BiFeO_3$) · Hydrothermal method · Photocatalytic activity · Particle size · Morphology

11.1 Introduction

Wastewater discharges from many industries around the world such as textile, chemical, and pharma sources are hazardous to the environment (Borker and Salker 2006; Pathania et al. 2015; Javadian et al. 2014). For wastewater treatment to eliminate toxic elements and decolourisation, researchers have reported many environmentally friendly techniques using different dyes for water splitting and photocatalytic degradation (Humayun et al. 2016; Wu et al. 2008; Wang et al. 2016a, b; Dhanalakshmi et al. 2015). Also, alternative water treatment techniques such as the advanced oxidation process (AOP), which is very flexible on a small scale, have been reported recently. AOP techniques are follows: (1) photo-Fenton process, (2) ozonation process, (3) UV-photolytic technique, (4) Fenton process, (5) photocatalysis, (6) bio-degradation, and (7) sonolysis (Baruah et al. 2012; Chong et al. 2010; Ni et al. 2007). Among these techniques, photocatalysis is a very desirable process that uses solar energy to treat effects in wastewater (Al-Kahtani et al. 2019). Researchers have focused on semiconductor photocatalyst materials because these materials exhibit a smaller and narrow bandgap energy. These materials have high photocatalytic efficiency, accomplish the photocatalytic degradation of different organic pollutants, and also the generation of hydrogen (H_2) from wastewater treatment (Veeramani et al. 2019; Ponraj et al. 2017). However, well-known materials are used, such as bismuth ferrite, one of the semiconductor oxide materials observed as a noble photocatalyst material with response in the UV and visible light regions (Fig. 11.1).

The following steps are involved in photocatalysis. The e^-–hole pair is generated when the light energy is equal to or higher than the bandgap energy of the

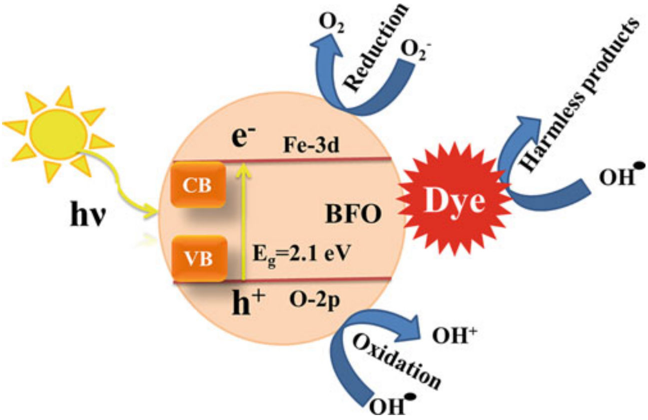

Fig. 11.1 Photocatalysis mechanism of bismuth ferrite (BFO) nanoparticles with dye degradation

semiconductor. The $OH^{\bullet}$ radicals are produced by the oxidization of water (H_2O) molecules, and the superoxide ions O_2^{-} are produced by the reduction of electrons in the dissolved oxygen.

$$\text{Photocatalyst} + h\upsilon \rightarrow e^{-} + h^{+} \tag{11.1}$$

$$H_2O + h^{+} \rightarrow OH^{\bullet} + h^{+} \tag{11.2}$$

$$O_2 + e^{-} \rightarrow O_2^{-} \tag{11.3}$$

The produced ($OH^{\bullet}$) hydroxyl radicals and ($O_2^{-)}$ superoxide ions, which are highly reactive electrons, are consequently important to decolourisation of the dye.

The H^{+} ions react with superoxide radical anions and form more $OH^{\bullet}$ radicals, which assist dye oxidation.

$$OH + \text{dye} \rightarrow \text{dye (oxidation)} \tag{11.4}$$

$$e - +\text{dye} \rightarrow \text{dye (reduction)} \tag{11.5}$$

The formation of $OH^{\bullet}$ radicals is reduced because of the deficiency of dissolved water molecules and oxygen, which results in no photodegradation of the molecules of dye over the photocatalysis (Rauf et al. 2011).

For the past decades, some semiconductors with high photodegradation efficiency, such as TiO_2, ZnO, and CdS, are materials generally used in numerous photocatalytic applications with response to UV irradiation. They have nontoxicity, low cost, high stability, and high oxidation potential properties (Chen and Mao 2007; Zhang et al. 2009), but only 4% of wide bandgap semiconducting materials absorb under the UV region, and these materials are used for the solar spectrum. Thus, to utilize the energy of sunlight in the photocatalysis field, growth of innovative semiconductors with strong absorbing properties in the wide-range visible region is indicated as the current development in the field of photocatalysis. Perovskite materials with the general formula of ABX_3 and wide bandgap energy exhibit good photocatalytic qualities and give high degradation efficiency. However, the B cation is smaller than the A cations. The anion X bonds to the cations. Specific ABO_3 perovskite materials are only used for several photocatalysis applications such as $ATiO_3$ (A = Sr, Ba, Ca, Co, Ni, Fe, Cd), $BTaO_3$ (B = Na, Ag, K), $CFeO_3$ (C = Bi and Gd), and $LaCaO_3$ and $LaNiO_3$ (Maeda 2014; Konta et al. 2004; Qu et al. 2014; Kim et al. 2009; Zheng et al. 2011; Parida et al. 2010; Tang et al. 2011a, b; Sun et al. 2010; Qu et al. 2011). Among these perovskite materials, the BFO material is one of the best examples of room temperature multiferroics, which exhibit (i) high chemical stability and (ii) efficient charge carrier separation (Yu and An 2009; Wang et al. 2008; Han et al. 2016; Wang et al. 2014; Huang et al. 2014; Wang et al. 2015).

The photocatalytic activity of BFO nanostructures towards effective degradation of different dyes under visible and UV light irradiation on the hydrothermal approach has been studied.

11.2 Properties of $BiFeO_3$

In recent years, perovskite-type bismuth ferrite ($BiFeO_3$) has been widely studied as a multiferroic material. At room temperature (RT), it exhibits both ferroelectric and ferromagnetic behaviors, which makes it attractive as a noble material for its prospective application in data storage, multifunctional devices, sensors, photocatalysis, water-splitting applications, and photovoltaics because of the narrow (2.1 eV) bandgap energy (Chen et al. 2007; Li et al. 2015; Papadas et al. 2015; Kudo and Miseki 2009; Chen et al. 2010). Thus, many synthesis methods have been implemented to fabricate BFO nanostructures. The photocatalytic knack to degrade with various waste products such as methylene blue, rhodamine B (Rh B), Congo red, methyl orange, reactive black-5, and phenol has been studied under UV and visible light irradiation. To augment the ability of photocatalytics on pollutant degradation, BFO has been synthesized by varying parameters such as temperature, surfactant, reaction time, and molarity of the precipitating agent: these are the parameters that mainly affect the crystal structure, size, and morphology.

Many techniques can achieve the uniform and highly homogeneous structure of nano-crystalline powders such as co-precipitation (Ghosh et al. 2005), hydrothermal (Wang et al. 2009; Cho et al. 2008; Du et al. 2010), solvothermal (Chaudhuri et al. 2010; Huo et al. 2010), sonochemical, microemulsion (Das et al. 2007), polyacrylamide gel (Xian et al. 2009), ferrioxalate (Wei and Xue 2008), sol–gel (Xu et al. 2009), combustion synthesis (Farhadi and Zaidi 2009), molten salt (He and Gao 2009), tartaric acid-assisted gel strategy (Wang et al. 2010), and polymeric precursor (Popa et al. 2007). However, there are a few methods which have some drawbacks, for example, the solid-state reaction method requires high-temperature treatment (above 800 °C) for formation of the single-phase BFO crystal, and also there are some difficulties in achieving uniform nano-sized BFO particles by other chemical methods. However, it could be attained by a microwave or hydrothermal synthesis, which gives a most significant method to achieve a single-phase crystal structure with nano-sized and uniform particles at temperature less than 250 °C (Xua et al. 2018).

Here, we have tabulated the hydrothermal approach characterization and synthesis of single-phase BFO nanostructures for photocatalytic applications.

11.2.1 Hydrothermal Approach of $BiFeO_3$ (Table 11.1)

However, synthesis of BFO microcubes with help of polyethylene glycol (PEG) used as a surfactant is favourable to reduce the size of the microcube into a nanocube and the arranged uniform surface of cubic-shaped BFO. We adjusted the molarity of the PEG and KOH concentration during the BFO synthesis, resulting in microcubes, microspheres, and submicrocubes. The detailed progress of BFO microcrystals is demonstrated in Scheme 11.1 (Table 11.2).

Table 11.1 Impacts on the formation of $BiFeO_3$ powder prepared by hydrothermal approach using KOH

KOH (M)	Source	Time, (h)	Temperature (°C)	Formed crystal phase	Size and shape	References
2	$Bi(NO_3)_3$. $5H_2O$ Fe $(NO_3)_3$. $9H_2O$	6	200	$Bi_{25}FeO_{40}$, $BiFeO_3$	–	Marzoukia et al. (2016)
12	Bi $(NO_3)_3.5H_2O$ $Fe(NO_3)_3$. $9H_2O$	24	200	$BiFeO_3$	1.5 μm cubes	Li et al. (2017)
4	Bi $(NO_3)_3.5H_2O$ Fe $(NO_3)_3.9H_2O$ PEG	6	200	$BiFeO_3$	Wafer	Jiang et al. (2011)
8.98 g	Bi $(NO_3)_3.5H_2O$ Fe $(NO_3)_3.9H_2O$	6	200	$BiFeO_3$	Plates	Tsai et al. (2012)
5	Bi $(NO_3)_3.5H_2O$ Fe $(NO_3)_3.9H_2O$	6	200	$Bi_{25}FeO_{40}$, $BiFeO_3$	–	Marzoukia et al. (2016)
10	Bi $(NO_3)_3.5H_2O$ $Fe(NO_3)_3$. $9H_2O$	13.3	120	$Bi_{25}FeO_{40}$, $BiFeO_3$	–	Wei et al. (2012)
10	Bi $(NO_3)_3.5H_2O$ Fe $(NO_3)_3.9H_2O$ 0.05 M urea	13.3	120	$Bi_{25}FeO_{40}$, $BiFeO_3$	–	Wei et al. (2012)
10	Bi $(NO_3)_3.5H_2O$ Fe $(NO_3)_3.9H_2O$ 0.1 M urea	13.3	120	$BiFeO_3$	Spherical 100–150 nm	Wei et al. (2012)
1.403 g	Bi $(NO_3)_3.5H_2O$ Fe $(NO_3)_3.9H_2O$	6	200	$BiFeO_3$	Nano rods	Arazas et al. (2018)
12	Bi $(NO_3)_3.5H_2O$ Fe $(NO_3)_3.9H_2O$	24	180	$BiFeO_3$	Nano sheets	Yun-hui Si et al. (2018)
8	Bi $(NO_3)_3.5H_2O$	6	180		–	Li et al. (2013)

(continued)

Table 11.1 (continued)

KOH (M)	Source	Time, (h)	Temperature (°C)	Formed crystal phase	Size and shape	References
	Fe $(NO_3)_3.9H_2O$					
8	Bi $(NO_3)_3.5H_2O$ Fe $(NO_3)_3.9H_2O$	6	200	$BiFeO_3$	–	Marzoukia et al. (2016)
0.5	Bi $(NO_3)_3.5H_2O$ Fe $(NO_3)_3.9H_2O$	0.30	180	$BiFeO_3$	Spherical 18 nm	Guo et al. (2017)
10	Bi $(NO_3)_3.5H_2O$ Fe $(NO_3)_3.9H_2O$	6	200	$Bi_{25}FeO_{40}$, $BiFeO_3$	–	Marzoukia et al. (2016)
14	Bi $(NO_3)_3.5H_2O$ Fe $(NO_3)_3.9H_2O$	6	220	$BiFeO_3$	Cubic 40 μm	Xu et al. (2009)
14	Bi $(NO_3)_3.5H_2O$ Fe $(NO_3)_3.9H_2O$	6	120	$Bi_{25}FeO_{40}$, $BiFeO_3$	Cubic grains	Xu et al. (2009)
8	Bi $(NO_3)_3.5H_2O$ Fe $(NO_3)_3.9H_2O$	10	200	$BiFeO_3$	5–68 μm	Kim et al. (2012)
1	Bi $(NO_3)_3.5H_2O$ Fe $(NO_3)_3.9H_2O$	1	250	$BiFeO_3$	1–10 μm	Chen et al. (2013)
14	Bi $(NO_3)_3.5H_2O$ Fe $(NO_3)_3.9H_2O$	12	200	$BiFeO_3$	Grains 30 μm	Du et al. (2010)
4	Bi $(NO_3)_3.5H_2O$ Fe $(NO_3)_3.9H_2O$	24	200	$BiFeO_3$	Hexa 2 μm	Gonjal et al. (2009)
	Bi $(NO_3)_3.5H_2O$ Fe $(NO_3)_3.9H_2O$	3	220	$BiFeO_3$	55 nm	Basu et al. (2011)
10	Bi $(NO_3)_3.5H_2O$ Fe $(NO_3)_3.9H_2O$	9	180	$BiFeO_3$	Spherical 7–13 μm	Li et al. (2010)

(continued)

Table 11.1 (continued)

KOH (M)	Source	Time, (h)	Temperature (°C)	Formed crystal phase	Size and shape	References
0.9	Bi $(NO_3)_3.5H_2O$ Fe $(NO_3)_3.9H_2O$	6	200	$BiFeO_3$	–	Lee et al. (2015)
9	Bi $(NO_3)_3.5H_2O$ Fe $(NO_3)_3.9H_2O$ CTAB	1.30	180	$BiFeO_3$	Sphere 50–500 nm	Sun et al. (2018)
12	Bi $(NO_3)_3.5H_2O$ Fe $(NO_3)_3.9H_2O$	6	200	$Bi_{25}FeO_{40}$, $BiFeO_3$		Marzoukia et al. (2016)
4	Bi $(NO_3)_3.5H_2O$ Fe $(NO_3)_3.9H_2O$	6	200	$BiFeO_3$	Cuboid 100–200 nm	Di et al. (2014)
4.5	Bi $(NO_3)_3.5H_2O$ Fe $(NO_3)_3.9H_2O$	6	200	$BiFeO_3$	30 μm	Gholam et al. (2017)
1.5	Bi $(NO_3)_3.5H_2O$ Fe $(NO_3)_3.9H_2O$ PVP	6	200	$BiFeO_3$	Particles 10 μm	Wang et al. (2016b)
0.5–1.25	Bi $(NO_3)_3.5H_2O$ Fe $(NO_3)_3.9H_2O$	6	220	$BiFeO_3$	50 nm	Xu et al. (2009)
8	Bi $(NO_3)_3.5H_2O$ Fe $(NO_3)_3.9H_2O$	4	200	$Bi_{25}FeO_{40}$, $BiFeO_3$	–	Marzoukia et al. (2016)
8	Bi $(NO_3)_3.5H_2O$ Fe $(NO_3)_3.9H_2O$	6	200	$BiFeO_3$	–	Marzoukia et al. (2016)
8	Bi $(NO_3)_3.5H_2O$ Fe $(NO_3)_3.9H_2O$	8	200	$Bi_{25}FeO_{40}$, $BiFeO_3$	–	Marzoukia et al. (2016)
8	Bi $(NO_3)_3.5H_2O$ Fe $(NO_3)_3.9H_2O$	10	200	$Bi_{25}FeO_{40}$, $BiFeO_3$	–	Marzoukia et al. (2016)

(continued)

Table 11.1 (continued)

KOH (M)	Source	Time, (h)	Temperature (°C)	Formed crystal phase	Size and shape	References
6	Bi $(NO_3)_3.5H_2O$ Fe $(NO_3)_3.9H_2O$	8	160	$Bi_{25}FeO_{40}$, $BiFeO_3$	–	Marzoukia et al. (2016)
6	Bi $(NO_3)_3.5H_2O$ Fe $(NO_3)_3.9H_2O$	8	180	$Bi_{25}FeO_{40}$, $BiFeO_3$	–	Marzoukia et al. (2016)
6	Bi $(NO_3)_3.5H_2O$ Fe $(NO_3)_3.9H_2O$	8	200	$BiFeO_3$	–	Marzoukia et al. (2016)
6	Bi $(NO_3)_3.5H_2O$ Fe $(NO_3)_3.9H_2O$	8	220	$Bi_{25}FeO_{40}$, $BiFeO_3$	–	Marzoukia et al. (2016)
1	Bi $(NO_3)_3.5H_2O$ Fe $(NO_3)_3.9H_2O$	0.15	160	$Bi_{25}FeO_{40}$, $BiFeO_3$	–	Tan et al. (2012)
1	Bi $(NO_3)_3.5H_2O$ Fe $(NO_3)_3.9H_2O$	0.15	180	$Bi_{25}FeO_{40}$, $BiFeO_3$	–	Tan et al. (2012)
1	Bi $(NO_3)_3.5H_2O$ Fe $(NO_3)_3.9H_2O$	0.15	190	$Bi_{25}FeO_{40}$, $BiFeO_3$	–	Tan et al. (2012)
1	Bi $(NO_3)_3.5H_2O$ Fe $(NO_3)_3.9H_2O$	0.15	200	$BiFeO_3$	–	Tan et al. (2012)

11.2.2 Effect of $BiFeO_3$ Nanoparticles on Different Textile Dyes

In the visible solar spectrum, $BiFeO_3$ nanoparticles are found to possess good catalytic properties. The effect of $BiFeO_3$ nanoparticles on different dyes such as methyl orange (MO), methylene blue (MB), reactive black-5 (RB-5), rhodamine B (RhB), and Congo red (CR) are summarized here.

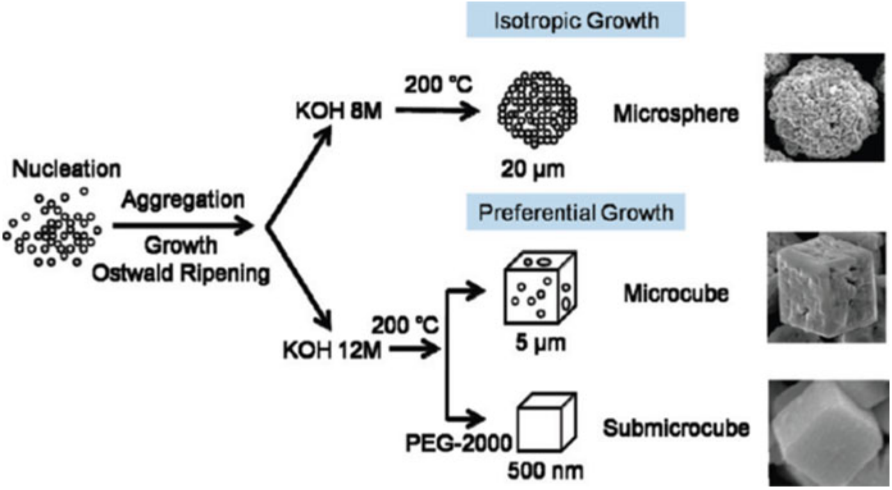

Scheme 11.1 Formation and growth of bismuth ferrite (BFO) crystals (Li et al. 2010)

11.2.2.1 Rhodamine B (RhB)

Guo et al. (2017) reported that the BFO nanoparticles prepared by the hydrothermal method achieved 72.0% of photocatalytic degradation efficiency and discussed the variation of photocatalytic degradation efficiency with different nano-sized BFO nanoparticles under UV and visible light irradiation. According to synthesis conditions such as concentration of citric acid, the different particle sizes and morphology of spherical BFO nanoparticles have been observed. This work recommended that the narrow bandgap and smallest size of particles lead to high photocatalytic activity for RhB degradation under UV and visible light irradiation.

Mushtaq et al. (2018) reported that two different BFO nanostructures, BFO nano sheets (NS) and nano wires (NW), were successfully prepared by the tunable hydrothermal method. The growth of BFO NS and NW controls the important experimental parameters such as stoichiometry of the starting materials, reaction temperatures, and duration of reaction time. Experimental procedures follow the starting materials used, bismuth nitrate and iron nitrate, and NaOH was used as the precipitating agent for the synthesis. After preparation of solution and transfer to the Teflon, the structures were kept in a autoclave sealed furnace for hydrothermal heat treatment. For BFO NSs, the reaction temperature and the reaction time were 140 °C and 72 h, and for preparing BFO NWs, reaction temperature and reaction time were 180 °C and 72 h. In this method, the main effect of the surfactant is changing the morphology; PEG directs the growth of BFO crystals to form BFO NWs. The BFO NSs are 2–3 mm long with a thickness of about 150 nm; BFO NWs are about 30 mm long, and the diameter ranges from about 200 to 700 nm.

Photocatalytic efficiency was obtained for both BFO NSs and NWs for RhB dye under UV–visible light irradiation, about 66% for BFO NSs and about 60% for NWs

Table 11.2 Impacts on the formation of $BiFeO_3$ powder prepared by the hydrothermal approach using NaOH

NaOH (M)	Source	Time, (h)	Temperature (°C)	Formed crystal phase	Size and shape	References
0.01	Bi $(NO_3)_3.5H_2O$ Fe $(NO_3)_3.9H_2O$	16	170	$Bi_2Fe_4O_9$, $BiFeO_3$	–	Peng et al. (2011)
5	Bi $(NO_3)_3.5H_2O$ Fe $(NO_3)_3.9H_2O$	72	140	$BiFeO_3$	Nano sheet 2–3 mm and 150 nm	Mushtaq et al. (2018)
5	Bi $(NO_3)_3.5H_2O$ Fe $(NO_3)_3.9H_2O$ 5 mL of polyethylene glycol	72	180	$BiFeO_3$	Nano wire 30 mm and 200–700 nm	Mushtaq et al. (2018)
0.03	Bi $(NO_3)_3.5H_2O$ Fe $(NO_3)_3.9H_2O$ 5 mL of polyethylene glycol	16	170	$BiFeO_3$	–	Peng et al. (2011)
0.5	Bi $(NO_3)_3.5H_2O$ Fe $(NO_3)_3.9H_2O$ PVP	72	180	$BiFeO_3$	Spindle 50 nm	Wang et al. (2016b)
15 g	Bi $(NO_3)_3.5H_2O$ Fe $(NO_3)_3.9H_2O$ Acetone, NaOH, ammonia	72	180	$BiFeO_3$	Nano cubes 50–250 nm	Wang et al. (2016a)
4	Bi $(NO_3)_3.5H_2O$ Fe $(NO_3)_3.9H_2O$	0.07	170	$Bi_2Fe_4O_9$, $BiFeO_3$	–	Peng et al. (2011)
5	Bi $(NO_3)_3.5H_2O$ Fe $(NO_3)_3.9H_2O$ Bi^{3+}/Fe^{3} (1:2)	24	200	$BiFeO_3$	Disks like 2 μm	Tang et al. (2011a)

(continued)

Table 11.2 (continued)

NaOH (M)	Source	Time, (h)	Temperature (°C)	Formed crystal phase	Size and shape	References
5	Bi $(NO_3)_3.5H_2O$ Fe $(NO_3)_3.9H_2O$ Bi^{3+}/Fe^{3+} (1:1)	24	200	$BiFeO_3$	Cubes 15 μm	Tang et al. (2011b)
6	Bi $(NO_3)_3.5H_2O$ Fe $(NO_3)_3.9H_2O$	0.07	170	$BiFeO_3$	–	Peng et al. (2011)
10	Bi $(NO_3)_3.5H_2O$ Fe $(NO_3)_3.9H_2O$	0.07	170	$BiFeO_3$	–	Peng et al. (2011)
16	Bi $(NO_3)_3.5H_2O$ Fe $(NO_3)_3.9H_2O$	0.07	140	$Bi_{25}FeO_{40}$, $BiFeO_3$	–	Peng et al. (2011)
16	Bi $(NO_3)_3.5H_2O$ Fe $(NO_3)_3.9H_2O$	0.07	150	$BiFeO_3$	–	Peng et al. (2011)
16	Bi $(NO_3)_3.5H_2O$ Fe $(NO_3)_3.9H_2O$	0.07	170	$BiFeO_3$	–	Peng et al. (2011)
16	Bi $(NO_3)_3.5H_2O$ Fe $(NO_3)_3.9H_2O$	0.07	190	$BiFeO_3$	–	Peng et al. (2011)
16	Bi $(NO_3)_3.5H_2O$ Fe $(NO_3)_3.9H_2O$	0.07	200	$Bi_2Fe_4O_9$, $BiFeO_3$	–	Peng et al. (2011)
20	Bi $(NO_3)_3.5H_2O$ Fe $(NO_3)_3.9H_2O$	0.07	170	$BiFeO_3$	–	Peng et al. (2011)
16	Bi $(NO_3)_3.5H_2O$ Fe $(NO_3)_3.9H_2O$	0.10	170	$BiFeO_3$	–	Peng et al. (2011)
16	Bi $(NO_3)_3.5H_2O$ Fe $(NO_3)_3.9H_2O$	0.12	170	$BiFeO_3$		Peng et al. (2011)

(continued)

Table 11.2 (continued)

NaOH (M)	Source	Time, (h)	Temperature (°C)	Formed crystal phase	Size and shape	References
72	Bi $(NO_3)_3.5H_2O$ Fe $(NO_3)_3.9H_2O$	5	180	$BiFeO_3$	Spindle 0.6 μm	Han et al. (2006)
16	Bi $(NO_3)_3.5H_2O$ Fe $(NO_3)_3.9H_2O$	0.15	170	$Bi_2Fe_4O_9$, $BiFeO_3$		Peng et al. (2011)
16	Bi $(NO_3)_3.5H_2O$ Fe $(NO_3)_3.9H_2O$	0.20	170	$Bi_2Fe_4O_9$, $BiFeO_3$, $Bi_{25}FeO_{40}$		Peng et al. (2011)

under UV–visible light over 3 h. Comparison of the results shows BFO NSs photocatalytic efficiency is higher than with the photocatalyst of BFO NWs, possibly the result of bandgap energy. The bandgap energy value of BFO NSs is about Eg~2.075 eV and Eg~2.1 eV for the BFO NWs. Hence, the photocatalyst BFO NSs bandgap energy is lower than that of photocatalyst BFO NWs. Photocatalytic degradation of RhB with the stimulation of light and also applied mechanical vibrations used simultaneously has been observed, with results showing photocatalytic degradation efficiency for NSs is about 71% and about 97% for NWs. However, the photocatalyst of BFO NWs for RhB photocatalytic efficiency is increased under piezoelectric stimulation, which may be attributed to the internal piezoelectric field-induced bias and other reasons such as influence on suppressing the electron–hole recombination. These samples give higher photocatalytic efficiency, and these results allow for the design of better catalysts that could be used for environmental applications (Table 11.3).

11.2.2.2 Methyl Orange (MO) (Table 11.4)

Wang et al. (2016b) successfully synthesized BFO nanostructures by the polyvinylpyrrolidone (PVP)-assisted hydrothermal method and tuned the morphology by using sodium hydroxide. PVP is used as a surfactant and also has a main role in controlling the growth and direction of the BFO nanostructures. Different shapes of BFO nanoparticles such as cubes, spindles, and plates have been observed. BFO (104) plates are employed as a photocatalytic activity, and the observed higher photo-degradation efficiency is about 69.1% for methyl orange (MO) under visible light irradiation, compared to other samples such as cubes and spindle nanostructures.

Table 11.3 BFO nanoparticles as photocatalyst on rhodamine B

Number	Synthesis route	Size and shape	Bandgap (eV)	Experimental conditions	Percent (%) of dye degradation	References
1	Hydrothermal	100–150 nm spherical	2.1	0.15 g PC; 4.8 mg/l dye; 500 W Xe lamp	40% after 4 h	Wei et al. (2012)
2	Hydrothermal	20–200 nm spherical	1.88	50 mg PC; 5 mg/l dye 500 W Xe lamp	72.0% after 180 min	Guo et al. (2017)
3	Hydrothermal	100–500 nm wafer-like	2.05	50 g PC; 10 mg/l dye 450 W mercury fluorescent lamp	90.5% after 3 h	Jiang et al. (2011)
4	Hydrothermal	NSs length 2–3 μm and thickness 150 nm; NWs of 30 mm long, diameter 200–700 nm	2.07 for BFO NSs and 2.1 for BFO NWs,	30 mg PC; 4 mg/l dye 300 W Xenon lamp	NSs for 59% and NWs for 91% after 1 h	Mushtaq et al. (2018)
5	Hydrothermal	100 nm spherical	2.12	0.3 g PC; 4 mg/l dye 100 W two halogen lamps	30% after 3 h	Cho et al. (2008)

Gao et al. (2015) suggested that BFO morphology is important in changing the efficiency of photo-degradation in the experimental parameters. Tuning the morphology by using different concentrations of KOH with molarity 2–7 M and photodegradation were rarely affected by impurity phases and particle sizes. The absorption and photocatalytic activity of BFO nanoparticles are affected by the observed microstructures, and these microstructures can be controlled by adjusting the experimental parameters during sample preparation. Higher photocatalytic degradation efficiency has been obtained, about 44.7% for methylene orange (MO) under visible light, with PVP-assisted BFO photocatalyst. However, variation in photodegradation efficiency has been related to BFO morphology rather than particle size. The BFO nanoparticle may have more potential applications in UV and visible regions such as treatment of wastewater from industries, water splitting, and so on. In addition, the BFO photocatalyst can be explored for other applications such as biological studies and H_2 production using advanced technique (AOP).

Niu et al. (2015) reported that successfully grown Pt/BFO obtained good photocatalytic stability in acidic experimental conditions. These results indicate

Table 11.4 BFO nanoparticles as photocatalyst on methyl orange (MO)

Number	Synthesis route	Size and shape	Band gap (eV)	Experimental Conditions	Percent (%) of dye degradation	References
1	Hydrothermal	510–550 nm BFO cubes, spindles and plates	–	50 mg of PC; 5 mg/l of dye; 500W Xe lamp.	Cubes for 38.7% spindles for 49.8% and plates 69.1% after 180 min	Wang et al. (2016b)
2	Hydrothermal	2.6–2.7 μm	1.96–2.05	0.30 g PC; 5 mg/l of dye 300 W Xe lamp.	44.7% after 330 min	Gao et al. (2015)
3	Hydrothermal	1–2 μm	2.14	0.25 g PC; 5 mg/l of dye 300 W Xe lamp	70% after 210 min	Niu et al. (2015)

that the BFO photocatalyst works well in photocatalytic degradation of different organic pollutants or in wastewater treatment. In addition, Pt is used as a co-catalyst with BFO nanoparticles, and these co-catalysts efficiently enhanced the photocatalytic activity of BFO under visible light irradiation. The efficiency of methyl orange (MO) photodegradation activity of the Pt/BFO sample concentration of 1.0 wt% Pt was five times higher than that of the pure BFO sample.

11.2.2.3 Methylene Blue, Reactive Black-5, and Congo Red (Table 11.5)

Arazas et al. (2018) reported that BFO nano rods grown on indium tin oxide (ITO)/glass substrates were successfully prepared by the hydrothermal method. These samples are characteristic of current–voltage measurement for piezotronic and piezophototronic properties. In addition, photocatalytic and piezo-photocatalytic activity for photo-degradation of methylene blue (MB) was demonstrated under visible light irradiation. A high efficiency of 30% at 30 min has been observed for both O_2^- and OH radicals.

Lam et al. (2018) reported that BFO spindly nanoparticles were successfully prepared by the urea-assisted hydrothermal route. The BFO nano spindles were employed for the photocatalytic degradation of MG under visible light irradiation, with a high efficiency observed, about 72.6% for 240 min. Li et al. (2015) reported that three different BFO microcrystals, such as microspheres and micro/submicrocubes, were successfully prepared by the one-step hydrothermal process with assistance of added template-directing agent PEG. It has been observed that BFO submicrocubes had a high photo-degradation efficiency against CR, about 95%

Table 11.5 $BiFeO_3$ nanoparticles as photocatalyst (PC) on dyes: methylene blue, reactive black-5, Congo red, and methyl violet 2B (MV)

NumberNo	Dye	Size and shape	Bandgap (eV)	Experimental conditions	Percent of dye degradation	Reference
1	Methylene blue	Nano rods	2.3	3 g PC; 5 mg/l dye;	70% after 90 min	Arazas et al. (2018)
2	Malachite green	Length 120 nm Width 50 nm Spindles	2.5	100 mg PC; 10 mg/l dye 105 W fluorescent lamp	72.6% after 240 min	Lam et al. (2018)
3	Congo red	5 and 50 nm	2.19 and 2.1	10 mg/l dye; 2 g/l PC; 500 W Xe lamp	95% after 120 min	Li et al. (2009)
4	Congo red	500 nm	2.27	20 mg/l dye; 2 g/l PC; 500 W Xe lamp	40% after 3 h	Li et al. (2010)
5	Methyl violet 2B (MV)	15 and 20 nm and diameter of about 2–3 nm	2.1	3.9 mg/l dye 100 mg PC –	97.6% after 120 min	Dhanalakshmi et al. (2016)

after 120 min under visible light irradiation. However, the optical properties can be related to the microstructure of the BFO nanoparticles.

11.3 Conclusion and Perspectives

This work has discussed and summarized the synthesis of BFO nanostructures prepared by the hydrothermal method. This method tunes size and morphology with the use of NaOH and KOH as the precipitating agent. The effect of the size of the particles and the morphology that affected photocatalytic activities in using different dyes under UV and visible light are also discussed. For higher photocatalytic efficiency, it is important that the particles be nano-sized BFO and with higher surface area with lower bandgap energy.

To increase the photocatalytic efficiency in the BFO materials, the following techniques are used.

(i) BFO is a perovskite material similar to the ABO_3 system with rare earth doping in A-site- and B-site-doped transition metals.
(ii) Different synthesis methods are hydrothermal in microwave, sol-gel, and electro-spinning.
(iii) BFO nanoparticle size and shape of the morphology are tuned using different surfactants.
(iv) Hetero-structures such as the binary system, core-shell nanoparticles, co-catalysis, and nano composites.
(v) 1-D and 2-D nanostructures.

These techniques appear to enhance the photocatalytic behavior of BFO nanostructures. However, it has been studied and reviewed that photocatalytic degradation is strongly related to lower bandgap energies, shape of the morphology, and higher surface area of the BFO nanoparticles. Further, BFO photocatalysts are greatly needed for research studies of the photocatalytic behavior of BFO in different research areas such as biological, pesticides, and H_2 production.

Acknowledgments The authors acknowledge FONDECYT Postdoctoral Research Project No. 3180055, Government of Chile, for the financial support.

References

Al-Kahtani AA, Alshehri SM, Naushad M et al (2019) Fabrication of highly porous N/S doped carbon embedded with ZnS as highly efficient photocatalyst for degradation of bisphenol. Int J Biol Macromol 121:415–423. https://doi.org/10.1016/j.ijbiomac.2018.09.199

Arazas, Wu CC, Chang KS (2018) Hydrothermal fabrication and analysis of piezotronic-related properties of $BiFeO_3$ nanorods. Ceram Inter 44:14158–14162. https://doi.org/10.1016/j.ceramint.2018.05.017

Baruah S, Pal SK, Dutta J (2012) Nanostructured zinc oxide for water treatment. Nanosci Nanotechnol Asia 2:90–102. https://doi.org/10.2174/2210681211202020090

Basu S, Hossain M, Chakravorty D, Pal M (2011) Enhanced magnetic properties in hydrothermally synthesized Mn-doped $BiFeO_3$ nanoparticles. Curr Appl Phys 11:976–980. https://doi.org/10.1016/j.cap.2010.12.034

Borker P, Salker AV (2006) Photocatalytic degradation of textile azo dye over $Ce_{1-x}Sn_xO_2$ series. Mater Sci Eng B 133:55–60. https://doi.org/10.1016/j.mseb.2006.05.007

Chaudhuri A, Mitra S, Mandal M, Mandal K (2010) Nanostructured bismuth ferrites synthesized by solvothermal process. J Alloys Compd 491:703. https://doi.org/10.1016/j.jallcom.2009.11.049

Chen XB, Mao SS (2007) Titanium dioxide nanomaterials: synthesis, properties, modifications, and applications. Chem Rev 107:2891. https://doi.org/10.1021/cr0500535

Chen XY, Yu T, Gao F, Zhang HT, Liu LF, Wang YM, Li ZS, Zou ZG, Liu JM (2007) Application of weak ferromagnetic $BiFeO_3$ films as the photoelectrode material under visible-light irradiation. Appl Phys Lett 91:022114. https://doi.org/10.1063/1.2757132

Chen X, Shen S, Guo L, Mao SS (2010) Semiconductor-based photocatalytic hydrogen generation. Chem Rev 110:6503. https://doi.org/10.1021/cr1001645

Chen XZ, Yang RL, Zhou JP, Chen XM, Jiang Q, Liu P (2013) Dielectric and magnetic properties of multiferroic BiFeO3 ceramics sintered with the powders prepared by hydrothermal method. Solid State Sci 19:117–121. https://doi.org/10.1016/j.solidstatesciences.2013.02.012

Cho CM, Noh JH, Cho IS, An JS, Hong KS, Kim JY (2008) Low-temperature hydrothermal synthesis of pure $BiFeO_3$ nanopowders using triethanolamine and their applications as visible-light. Photocatalysts J Am Ceram Soc 91:3753. https://doi.org/10.1111/j.1551-2916.2008.02689.x

Chong MN, Jin B, Chow CWK, Saint C (2010) Recent developments in photocatalytic water treatment technology: a review. Water Res 44:2997–3027. https://doi.org/10.1016/j.watres.2010.02.039

Das N, Majumdar R, Sen A, Maiti HS (2007) Nanosized bismuth ferrite powder prepared through sonochemical and microemulsion techniques. Mater Lett 61:2100. https://doi.org/10.1016/j.matlet.2006.08.026

Dhanalakshmi R, Muneeswaran M, Pradeep RV, Ashok M, Giridharan NV (2015) Photocatalytic activity of $BiFeO_3$ nanoparticles synthesized through hydrothermal method. AIP Conf Proc 1665:130014. https://doi.org/10.1063/1.4918162

Dhanalakshmi R, Muneeswaran M, Shalini K, Giridharan NV (2016) Enhanced hotocatalytic activity of La-substituted $BiFeO_3$ nanostructures on the degradation of phenol red. Mater Lett 165:205–209. https://doi.org/10.1007/s00339-015-9527-z

Di LJ, Yanga H, Xiana T, Lib RS, Feng YC, Feng WJ (2014) Influence of precursor Bi^{3+}/Fe^{3+} ion concentration on hydrothermal synthesis of $BiFeO_3$ crystallites. Ceram Int 40:4575–4578. https://doi.org/10.1016/j.ceramint.2013.08.134

Du Y, Cheng ZX, Shahbazi M, Collings EW, Dou SX, Wang XL (2010) Enhancement of ferromagnetic and dielectric properties in lanthanum doped $BiFeO_3$ by hydrothermal synthesis. J Alloys Compd 490:637–641. https://doi.org/10.1016/j.jallcom.2009.10.124

Farhadi S, Zaidi M (2009) Bismuth ferrite $BiFeO_3$ nanopowder prepared by sucrose-assisted combustion method: a novel and reusable heterogeneous catalyst for acetylation of amines, alcohols and phenols under solvent-free conditions. J Mol Catal A Chem 299:18. https://doi.org/10.1016/j.molcata.2008.10.013

Gao T, Chen Z, Niu Huang O, Zhu Y, Qin, Sun X, Huang Y (2015) Shape-controlled preparation of bismuth ferrite by hydrothermal method and their visible-light degradation properties. J Alloys Compd 648:564–570. https://doi.org/10.1016/j.jallcom.2015.07.059

Gholam T, Ablat A, Mamat M, Wu R, Aimidula A, Bake MA, Zheng L, Wang J, Qian H, Wu R, Ibrahim K (2017) Local electronic structure analysis of Zn-doped $BiFeO_3$ powders by X-ray absorption fine structure spectroscopy. J Alloys Compd 710:843–849. https://doi.org/10.1016/j.jallcom.2017.03.242

Ghosh S, Dasgupta S, Sen A, Maiti HS (2005) Low temperature synthesis of bismuth ferrite nanoparticles by a ferrioxalate precursor method. Mater Res Bull 40:2073. https://doi.org/10.1016/j.materresbull.2005.07.017

Gonjal JP, Villafuerte-Castrejo ME, Fuentes L, Mora E (2009) Microwave–hydrothermal synthesis of the multiferroic $BiFeO_3$. Mater Res Bull 44:1734–1737. https://doi.org/10.1016/j.materresbull.2009.03.015

Guo Y, Pu Y, Cui Y, Hui C, Wan J, Cui C (2017) A simple method using citric acid as the template agent to improve photocatalytic performance of $BiFeO_3$ nanoparticles. Mater Lett 196:57–60. https://doi.org/10.1016/j.matlet.2017.03.023

Han JT, Huang YH, Wu XJ, Wu CL, Wei W, Peng B, Huang W, Goodenough JB (2006) Tunable synthesis of bismuth ferrites with various morphologies. Adv Mater 18:2145–2148. https://doi.org/10.1002/adma.200600072

Han YL, Liu WF, Wu P, Xu XL, Guo MC, Rao GH, Wang SY (2016) Effect of aliovalent Pd substitution on multiferroic properties in $BiFeO_3$ nanoparticles. J Alloys Compd 661:115–121. https://doi.org/10.1016/j.jallcom.2015.11.157

He X, Gao L (2009) Synthesis of pure phase $BiFeO_3$ powders in molten alkali metal nitrates. Ceram Int 35:975. https://doi.org/10.1016/j.ceramint.2008.04.013

Huang J, Tan G, Yang W, Zhang L, Ren H, Xia A (2014) Microwave hydrothermal synthesis of $BiFeO_3$: impact of different surfactants on the morphology and photocatalytic properties. Mater Sci Semicond Process 25:2584–2588. https://doi.org/10.1016/j.mssp.2013.08.012

Humayun M, Zada A, Li Z, Xie M, Zhang X, Qu Y, Raziq F, Jing L (2016) Enhanced visible-light activities of porous $BiFeO_3$ by coupling with nanocrystalline TiO_2 and mechanism. Appl Catal B 180:219–226. https://doi.org/10.1016/j.apcatb.2015.06.035

Huo Y, Jin Y, Zhang Y (2010) Citric acid assisted solvothermal synthesis of BiFeO3 microspheres with high visible-light photocatalytic activity. J Mol Catal A Chem 331:15–20. https://doi.org/10.1016/j.molcata.2010.08.009

Javadian H, Angaji MT, Naushad M (2014) Synthesis and characterization of polyaniline/γ-alumina nanocomposite: a comparative study for the adsorption of three different anionic dyes. J Ind Eng Chem 20:3890–3900. https://doi.org/10.1016/j.jiec.2013.12.095

Jiang J, Zou J, Anjum MN, Yan J, Huang L, Zhang Y, Chen J (2011) Synthesis and characterization of wafer-like $BiFeO_3$ with efficient catalytic activity. Solid State Sci 13:1779–1785. https://doi.org/10.1016/j.solidstatesciences.2011.07.008

Kim YJ, Gao B, Han SY, Jung MH, Chakraborty AK, Ko T, Lee C, Lee WI (2009) Heterojunction of $FeTiO_3$ nanodisc and TiO_2 nanoparticle for a novel visible light photocatalyst. J Phys Chem C 113:19179–19184. https://doi.org/10.1021/jp908874k

Kim AY, Han SH, Kang HW, Lee HG, Kim JS, Cheon CI (2012) Dielectric and magnetic properties of $BiFeO_3$ ceramics prepared by hydrothermal synthesis. Ceram Int 38S:S397–S401

Konta R, Ishii T, Kato H, Kudo A (2004) Photocatalytic activities of noble metal ion doped $SrTiO_3$ under visible light irradiation. J Phys Chem B 108:8992–8995. https://doi.org/10.1021/jp049556p

Kudo A, Miseki Y (2009) Heterogeneous photocatalyst materials for water splitting. Chem Soc Rev 38:253. https://doi.org/10.1039/B800489G

Lam SM, Jaffari ZH, Sin JC, Mohamed AR (2018) Spindly $BiFeO_3$ nanoparticles for photodegradation of organic pollutants under a compact fluorescent lamp. IOP Conf Ser Earth Environ Sci 151:012021

Lee TK, Sung DK, Hoon JJ (2015) Electric polarization and diode-like conduction in hydrothermally grown $BiFeO_3$ thin films. J Alloys Compd 622:734–737. https://doi.org/10.1016/j.jallcom.2014.10.196

Li S, Lin HY, Zhang PB, Nan WC, Wang Y (2009) Photocatalytic and magnetic behaviors observed in nanostructured $BiFeO_3$ particles. J Appl Phys 105:056105. https://doi.org/10.1063/1.3080131

Li, Lin YH, Zhang BP, Wang Y, Nan CW (2010) Controlled fabrication of $BiFeO_3$ uniform microcrystals and their magnetic and photocatalytic behaviors. J Phys Chem C 114:2903–2908. https://doi.org/10.1021/jp910401u

Li T, Shen J, Li N, Ye M (2013) Hydrothermal preparation, characterization and enhanced properties of reduced graphene-$BiFeO_3$ nanocomposite. Mater Lett 91:42–44. https://doi.org/10.1016/j.matlet.2012.09.045

Li X, Yu J, Low J, Fang Y, Xiao J, Chen X (2015) Engineering heterogeneous semiconductors for solar water splitting. J Mater Chem A 3:2485. https://doi.org/10.1039/C4TA04461D

Li P, Li L, Xu M, Chen Q, He Y (2017) Enhanced photocatalytic property of $BiFeO_3$/N-doped graphene composites and mechanism insight. Appl Surf Sci 396:879–887. https://doi.org/10.1016/j.apsusc.2016.11.052

Maeda K (2014) Rhodium-doped barium titanate perovskite as a stable *p*-type semiconductor photocatalyst for hydrogen evolution under visible light. ACS Appl Mater Interfaces 6:2167–2173. https://doi.org/10.1021/am405293e

Marzoukia A, Harzalia H, Saida F, Megriche A, Zehani K, Bessais L (2016) Optimization of the synthesis of multiferroic bismuth ferrite $BiFeO_3$ nanopowders by hydrothermal method. J Tunis Chem Soc 18:38–42

Mushtaq F, Chen X, Hoop M, Gattinoni C, Bradley JN, Pane S (2018) Piezoelectrically enhanced photocatalysis with $BiFeO_3$ nanostructures for efficient water remediation synthesis and characterization of wafer-like $BiFeO_3$ with efficient catalytic activity. iScience 4:236–246. https://doi.org/10.1016/j.isci.2018.06.003

Ni M, Leung MKH, Leung DYC, Sumathy K (2007) A review and recent developments in photocatalytic water-splitting using TiO_2 for hydrogen production. Renew Sust Energ Rev 11:401–425. https://doi.org/10.1016/j.rser.2005.01.009

Niu F, Chen D, Qin L, Gao T, Zhang Z, Wang S, Chen Z, Wang J, Sun X, Huang Y (2015) Synthesis of Pt/$BiFeO_3$ heterostructured photocatalysts for highly efficient visible-light photocatalytic performances. Sol Energy Mater Sol Cells 143:386–396. https://doi.org/10.1016/j.solmat.2015.07.008

Papadas I, Christodoulides JA, Kioseoglou G, Armatas GS (2015) A high surface area ordered mesoporous $BiFeO_3$ semiconductor with efficient water oxidation activity. J Mater Chem A 3:1587. https://doi.org/10.1039/C4TA05272B

Parida KM, Reddy KH, Martha S, Das DP, Biswal N (2010) Fabrication of nanocrystalline $LaFeO_3$: an efficient sol–gel auto-combustion assisted visible light responsive photocatalyst for water decomposition. Int J Hydrog Energy 35:12161–12168. https://doi.org/10.1016/j.ijhydene.2010.08.029

Pathania D, Sharma G, Kumar A et al (2015) Combined sorptional–photocatalytic remediation of dyes by polyaniline Zr(IV) selenotungstophosphate nanocomposite. Toxicol Environ Chem 97:526–537. https://doi.org/10.1080/02772248.2015.1050024

Peng JH, Hojamberdiev M, Cao BW, Wang JA, Xu YH (2011) Surfactant-free hydrothermal synthesis of submicron $BiFeO_3$ powders. Appl Phys A 103:511. https://doi.org/10.1007/s00339-010-6024-2

Ponraj C, Vinitha G, Daniel J (2017) A review on the visible light active $BiFeO_3$ nanostructures as suitable photocatalyst in the degradation of different textile dyes. Environ Nanotechnol Monit Manag 7:110–120. https://doi.org/10.1016/j.enmm.2017.02.001

Popa M, Crespo D, Moreno JMC (2007) Synthesis and structural characterization of single-phase $BiFeO_3$ powders from a polymeric precursor. J Am Ceram Soc 90:2723. https://doi.org/10.1111/j.1551-2916.2007.01779.x

Qu Y, Zhou W, Ren Z, Du S, Meng X, Tian G, Pan K, Wang G, Fu HJ (2011) Facile preparation of porous $NiTiO_3$ nanorods with enhanced visible-light-driven photocatalytic performance. Mater Chem 22:16471–16476. https://doi.org/10.1039/C2JM32044D

Qu Y, Zhou W, Fu H (2014) Porous cobalt titanate nanorod: a new candidate for visible light-driven photocatalytic water oxidation. ChemCatChem 6:265–270. https://doi.org/10.1002/cctc.201300718

Rauf MA, Meetani MA, Hisaindee S (2011) An overview on the photocatalytic degradation of azo dyes in the presence of TiO_2 doped with selective transition metals. Desalination 276:13–27. https://doi.org/10.1016/j.desal.2011.03.071

Sun M, Jiang Y, Li F, Xia M, Xue B, Liu D (2010) Dye degradation activity and stability of perovskite-type $LaCoO_3-x$ (x=0–0.075). Mater Trans 51:2208–2214. https://doi.org/10.2320/matertrans.M2010200

Sun X, Liu Z, Yu H, Zheng Z, Zeng D (2018) Facile synthesis of $BiFeO_3$ nanoparticles by modified microwave-assisted hydrothermal method as visible light driven photocatalysts. Mater Lett 219:225–228. https://doi.org/10.1016/j.matlet.2018.02.052

Tan GQ, Zheng YQ, Miao HY, Xia A, Ren HJ (2012) Controllable microwave hydrothermal synthesis of bismuth ferrites and photocatalytic characterization. J Am Ceram Soc 95:280–289

Tang P, Chen H, Cao F, Pan G (2011a) Magnetically recoverable and visible-light-driven nanocrystalline $YFeO_3$ photocatalysts. Catal Sci Technol 1:1145–1148. https://doi.org/10.1039/C1CY00199J

Tang P, Sun H, Cao F, Yang J, Ni S, Chen H (2011b) Visible-light driven $LaNiO_3$ nanosized photocatalysts prepared by a sol-gel process. Adv Mater Res 279:83–87. https://doi.org/10.4028/www.scientific.net/AMR.279.83

Tsai CJ, Yang CY, Liao YC, Chueh YL (2012) Hydrothermally grown bismuth ferrites: controllable phases and morphologies in a mixed KOH/NaOH mineralizer. J Mater Chem 22:17432. https://doi.org/10.1039/c2jm33859a

Veeramani V, Matsagar BM, Yamauchi Y et al (2019) Metal organic framework derived nickel phosphide/graphitic carbon hybrid for electrochemical hydrogen generation reaction. J Taiwan Inst Chem Eng 96:634–638. https://doi.org/10.1016/j.jtice.2018.12.019

Wang Y, Xu G, Ren Z, Wei X, Weng W, Du P, Shen G, Han G (2008) Low temperature polymer assisted hydrothermal synthesis of bismuth ferrite nanoparticles. Ceram Int 34:1569–1571. https://doi.org/10.1155/2011/797639

Wang Y, Xu G, Yang L, Ren Z, Wei X, Weng W, Du P, Shen G, Han G (2009) Hydrothermal synthesis of single-crystal bismuth ferrite nanoflakes assisted by potassium nitrate. Ceram Int 35:1285. https://doi.org/10.1016/j.ceramint.2008.04.016

Wang X, Zhang Y, Wu Z (2010) Magnetic and optical properties of multiferroic bismuth ferrite nanoparticles by tartaric acid-assisted sol–gel strategy. Mater Lett 64:486–488. https://doi.org/10.1016/j.matlet.2009.11.059

Wang J, Wei Y, Zhang J, Ji L, Huang Y, Chen Z (2014) Synthesis of pure-phase $BiFeO_3$ nanopowder by nitric acid-assisted gel. Mater Lett 124:242–244. https://doi.org/10.1016/j.matlet.2014.03.105

Wang XF, Mao WW, Zhang J, Han YM, Quan CY, Zhang QX, Yang T, Yang JP, Li XA, Huang W (2015) Facile fabrication of highly efficient $y\text{-}C_3N_4/BiFeO_3$ nanocomposites with enhanced visible light photocatalytic activities. Colloid Interf Sci 448:17–23. https://doi.org/10.1016/j.jcis.2015.01.090

Wang S, Chen D, Niu F, Zhang N, Qin L, Huang Y (2016a) Hydrogenation-induced surface oxygen vacancies in $BiFeO_3$ nanoparticles for enhanced visible light photocatalytic performance. J Alloys Compd 688:399–406. https://doi.org/10.1016/j.jallcom.2016.07.076

Wang X, Mao W, Zhang Q, Wang Q, Zhu Y, Zhang J, Yang T, Yang J, Li XA, Huang W (2016b) PVP assisted hydrothermal fabrication and morphology-controllable fabrication of $BiFeO_3$ uniform nanostructures with enhanced photocatalytic activities. J Alloys Compd 677:288–293. https://doi.org/10.1111/j.1551-2916.2008.02689.x

Wei J, Xue DS (2008) Low-temperature synthesis of $BiFeO_3$ nanoparticles by ethylenediaminetetraacetic acid complexing sol–gel process. Mater Res Bull 43:3368–3373. https://doi.org/10.1016/j.materresbull.2008.02.009

Wei J, Zhang C, Xu Z (2012) Low-temperature hydrothermal synthesis of $BiFeO_3$ microcrystals and their visible-light photocatalytic activity. Mater Res Bull 47:3513–3517. https://doi.org/10.1016/j.materresbull.2012.06.068

Wu Y, Han W, Zhou SX, Lototsky MV, Solberg JK, Yartys VA (2008) Microstructure and hydrogenation behavior of ball-milled and melt-spun Mg–10Ni–2Mm alloys. J Alloys Compd 466:176. https://doi.org/10.1016/j.jallcom.2007.11.128

Xian T, Yang H, Shen X, Jiang JL, Wei ZQ, Feng WJ (2009) Preparation of high-quality $BiFeO_3$ nanopowders via a polyacrylamide gel route. J Alloys Compd 480:889–892. https://doi.org/10.1016/j.jallcom.2009.02.068

Xu JH, Ke H, De C, Jia WW, Zhou Y (2009) Low-temperature synthesis of $BiFeO_3$ nanopowders via a sol–gel method. J Alloys Compd 472:473–477. https://doi.org/10.1016/j.jallcom.2008.04.090

Xua Y, Gao Y, Xing H, Zhang J (2018) Room temperature spontaneous exchange bias in $BiFeO_3$ micro/nano powders synthesized by hydrothermal method. Ceram Int 44:17459–17463. https://doi.org/10.1016/j.ceramint.2018.06.214

Yu X, An X (2009) Enhanced magnetic and optical properties of pure and (Mn, Sr) doped $BiFeO_3$ nanocrystals. Solid State Commun 149:711–714. https://doi.org/10.1016/j.ssc.2009.02.010

Yun-hui Si, Xia Y, Shang SK, Xiong XB, Zeng XR, Zhou J, Li YY (2018) Enhanced visible light driven photocatalytic behavior of $BiFeO_3$/reduced graphene oxide composites. Nanomaterials 8:526. https://doi.org/10.3390/nano8070526

Zhang HJ, Chen GH, Bahnemann DW (2009) Photoelectrocatalytic materials for environmental applications. J Mater Chem 19:5089. https://doi.org/10.1039/B821991E

Zheng PD, Chen J, Kanhere Z (2011) Site, specific optical and photocatalytic properties of Bi-doped $NaTaO_3$. J Phys Chem C 115:11846–11853. https://doi.org/10.1021/jp2003936

Index

A
Activated carbon, 12, 110, 259
Advanced oxidation process (AOPs), 111, 112, 221, 260, 296, 307
Aghamali, A., 99
Ahmaruzzaman, M., 98
Akbari-Fakhrabadi, A., 296–310
Allendorf, M.D., 147
Alonso-Tellez, A., 265
Alrousan, D., 9
Alvaro, M., 144
Amalric, L., 198
An, X., 285
Ananadan, S., 288
Andryushina, N.S., 262
Antonello, A., 256, 263
Artificial photosynthesis (APS), 189, 276, 278, 283, 284, 286, 289
Asahi, R.Y., 202
Asymmetric synthesis, 142, 159, 162

B
Bag, P.P., 142–176
Banisharif, A., 263
Bard, A.J., 36
Bashiri, R., 43
Basu, S., 300
Berry, D., 259
Berzelius, J.J., 212
Bhattacharjee, A., 98
Bhunia, P., 20–45
Bi, C., 94
Bianchi, C.L., 262
Biocatalysis, 188–203
Bismuth ferrite ($BiFeO_3$), 296–310
Boeniger, M.F., 261
Boppella, R., 70, 80
Butler, K.T., 168

C
Caballero-Briones, F., 276
Cancer therapy, 276, 278, 289
Cao, S., 282
Carbon quantum dots (C QDs), 98–101
Carrasco, M.F., 248–267
Cavka, J.K., 163
Chabi, S., 284
Chai, Y.-Y., 100
Challoner, A., 253
Charge carriers, 8, 21–23, 25, 33, 39, 40, 59–61, 65, 73, 76–83, 89, 92, 95, 99, 116, 120, 121, 128, 143, 152, 214, 215, 228, 229, 231, 232, 234, 239, 240, 276, 277, 282, 284, 297
Charge transfer dynamics, 73, 78
Charge transfer mechanism, 236
Chen, D., 118
Chen, X., 220
Chen, Y., 262
Chen, Y.C., 266
Chen, Z., 218, 236
Cheng, P., 64
Cho, C.M., 307
Choi, K.M., 154
Clasen, T., 9
Clean energy, 21, 212

S. Rajendran et al. (eds.), *Green Photocatalysts for Energy and Environmental Process*, Environmental Chemistry for a Sustainable World 36,
https://doi.org/10.1007/978-3-030-17638-9

Composite materials, 102, 125, 127, 142, 172, 174, 175, 218, 286
Cyanobacteria, 195

D
D'Alessandro, D.M., 150
Dan-Hardi, M., 165
Degradation, v, 6, 21, 88, 111, 144, 193, 213, 261, 276, 296
deKrafft, K.E., 169
Deng, Y., 228
Devi, S., 88–103, 188–203
Dhanalakshmi, R., 296–310
Di, U., 94
Djaja, N.F., 120
Dong, G., 219
Dong, J., 65
Dong, S., 4
Dong, Y., 119
Doping, 4, 7, 10, 41, 59, 66, 89, 99, 102, 103, 116, 118, 120–123, 127, 194, 202, 214, 228, 251, 252, 263, 264, 284
Du, Y., 300
Durgalakshmi, D., 2–13
Dutta, K., 38–41
Dye degradation, v, 96, 99, 119, 221–226, 296, 307–309
Dyes, v, 2, 24, 59, 88, 110, 165, 197, 213, 252, 296

E
Elbanna, O., 64, 78
Electrochemical impedance spectroscopy (EIS), 76, 80, 235, 237, 239, 242
Environmental pollutants, 21, 88–103
Esposito, D.V., 43

F
Fan, Q., 218
Fang, S., 98
Faulkner, L.R., 36
Fei, H., 154
Férey, G., 163
Fernando, J.F.S., 127
Fu, Y., 165
Fuel cells, v, 8, 9, 20–44, 147, 214
Fujishima, A., v, 6, 21, 58, 249

G
Ganesh, V.A., 287
Gao, H., 68
Gao, T., 307, 308
Gao, Y., 78
Ge, L., 281, 282
Gholam, T., 301
Gillan, E.G., 66
Gonjal, J.P., 300
Graphene quantum dots (G QDs), 101–103, 283
Green materials, 5, 8, 9
Green photocatalyst, 2–13, 88–103, 194, 266
Guo, Y., 300, 303, 307

H
Han, C., 282, 286
Han, Q., 219, 237, 281
Han, Y., 175
Han, Z., 263
Hao, C., 67
Hardi, D., 144
Hausdorf, S., 162
He, F., 262
He, H., 65
Hemmateenejad, B., 95
Heterojunctions, 58–83, 88, 124, 125, 127, 172, 214, 236, 282, 286
Honda, K., v, 6, 21, 58
Hong, R.Y., 113
Horiuchi, Y., 165
Hou, W.M., 263
Hu, N., 103
Hu, Y., 264
Huang, H., 219, 234, 262, 266
Hult, E.L., 258
Hung, Y.C., 191
Hydrogen generation, 42, 58–83, 163, 267, 280
Hydrothermal method, 217, 224, 298, 303, 306, 308, 310

I
Indoor air pollution, 248–267, 276
Inoue, T., 229
Iwase, A., 285
Iwu, K.O., 43

J
Janbandhu, S.Y., 91
Jang, J.S., 78
Ji, H.H., 287
Jia, Q., 40
Jiang, J., 299
Jiao, L., 265
Jun, Y.S., 220

K
Kafizas, A., 76
Kalamaras, E., 43
Kalanur, S.S., 64
Kamaraj, S.-K., 276
Kaneko, M., 21
Kang, J., 82
Karthik, S., 66
Katsumata, K.I., 266
Kaur, S., 93
Kaviya, S., 110–128
Kelvin probe spectroscopy, 76, 78–79
Khan, S.U., 202
Kobayashi, Y., 148
Ku, Y., 263
Kumar, S., 219

L
Lam, S.M., 308, 309
Lavorato, C., 284
Le Bechec, M., 262
Lee, B.K., 263
Lee, T.K., 301
Lee, Y., 156
Lei, Z.-D., 103
Li, G.-S., 90
Li, H., 103, 162
Li, H.J., 218
Li, M., 175
Li, Q., 220
Li, S., 98, 103, 309
Li, T., 287
Li, X., 308
Li, Y., 165, 169, 251
Lian, Z., 65, 80
Liang, X., 43
Lianos, p., 43
Liao, Y., 266
Liebig, J.V., 212
Light matter interaction, 73, 82, 83
Lin, J., 220, 231
Linda, T., 126
Linsebigler, A.L., 23, 33, 34
Liu, C., 282
Liu, H., 175
Liu, J., 98
Liu, L., 63, 67, 80
Liu, S., 288
Liu, X., 285
Liu, Z., 262
Lyng, N.L., 258

M
Ma, J., 264
Ma, W., 282
Madureira, J., 253
Mahyari, M., 103
Mandatory, 194
Mansur, A.A.P., 93
Martínez Vargas, D.X., 263
Marzoukia, A., 299, 301, 302
Mathesh, M., 188–203
Mauro, A.D., 126
Metal-organic frameworks (MOFs), 142–176
Metal oxides, v, 4, 6, 7, 26, 27, 88, 90, 93–95, 98, 123, 125, 128, 142, 147, 168, 189–191, 194, 214, 266
Mifsud, M., 198
Monteiro, R.A.R., 262
Montoya, A.T., 66
Morphology, 40, 59, 83, 89, 113, 114, 116, 125, 127, 128, 214, 217, 220, 222, 239, 240, 266, 278, 298, 303, 306, 307, 310
Muneeswaran, M., 296–310
Murcia, J.J., 262
Mushtaq, F., 303, 304, 307

N
Nanoporous g-C_3N_4, 220, 224
Nanostructured photocatalysts, 22, 93
Natarajan, G., 276
Naushad, M., 2–13, 88, 188, 212, 248
Niu, F., 283, 307, 308
Non-metals, 4, 97, 123, 128, 201, 252, 263

O
Ohno, T., 202
Ong, S.-T., 110
Ong, W.-J., 285

P
Pan, D., 93, 101
Particle size, 99, 121, 151, 164, 214, 215, 222, 234, 240, 265, 303, 307, 310
Pawar, R.C., 219, 239, 242
Peer, M., 218, 222
Peng, J.H., 304–306
Pereira, V.M., 282
Pham, T.D., 263
Photoanodes, 25–27, 29, 30, 36–42, 44, 63, 67, 68

Photobiocatalysis, 188–203
Photocatalysis (PC), v, 4, 6–7, 9, 21–31, 39, 68, 72, 76, 89, 92, 93, 97–99, 101, 110, 112–127, 142, 146–147, 152, 176, 188–203, 212, 221, 226, 234, 249–251, 265, 266, 276, 296–298, 307
Photocatalysts, v, 2–13, 20–45, 59–61, 68, 69, 71, 73, 74, 81–83, 88, 89, 92–95, 97–103, 110–128, 142–176, 189–194, 198, 200–203, 212, 214–216, 224, 226, 229, 231, 234, 237, 239, 242, 248–267, 276–278, 280, 282–285, 287, 289, 296, 306–310
Photocatalytic activity, 4, 21, 59, 89, 113, 154, 193, 214, 249, 281, 297
Photocatalytic oxidation (PCO), 25, 37, 251, 252, 256, 260, 261, 263–267
Photocathodes, 35, 37, 41, 42, 44
Photodegradation, 28, 44, 121, 126, 175, 224–226, 266, 276, 278, 297, 306, 308
Photoelectrocatalysts, 20–45
Photoelectrochemical (PEC) cells, 21, 73
Photofuel cells, 20–44
Photosensitizers, 154, 156, 160, 169, 196–198, 202, 283
Photosynthesis, 60, 142, 149, 188, 189, 195–197, 200, 276, 278, 283, 284, 286, 289
p-n heterojunction, 61, 67–68, 124, 236
Pollutants, v, 2, 4, 6, 7, 12, 13, 21, 25, 30, 37, 88–103, 110–128, 143, 193, 198, 212, 213, 221, 222, 224, 226, 227, 240, 248, 249, 251–255, 257, 258, 260, 261, 263–267, 276, 278, 286, 287, 296, 298, 308
Preethi, L.K., 58–83

Q
Quantum dots (QDs), v, 30, 39, 44, 65, 76, 77, 82, 88–103, 175, 193, 198, 283

R
Raja, A.S., 248–267
Rajendran, S., 2–13, 248–267
Rakkesh, R.A., 2–13
Rare earth metal, 121–123, 127, 154, 310
Redox reactions, 21, 72, 92, 189, 190, 198, 201, 217, 228, 234
Reduction of CO_2, v, 165, 213, 229, 231, 285
Reduction of hexavalent Cr, v, 221
Ren, J., 170
Ren, L., 262
Renewable energy, 8, 12, 13, 20, 25, 37, 88, 188, 193, 251
Rivas, I., 253
Roeffaers, M.B.J., 163
Rozhkova, E.A., 289

S
Sahoo, P., 142–176
Saleh, R., 120
Sawaguchi-Sato, K., 98
Sayama, K., 40
Scanlon, D.O., 59, 81
Schleibinger, H., 260
Schottky heterojunction, 61, 65–67
Secondary building unit (SBU), 153, 156–158, 168, 170
Seger, B., 43
Self-cleaning, 256, 287–288
Semiconductors, 5, 21, 59, 88, 93–95, 112, 143, 189, 215, 249, 277, 296, 297
Sfaelou, S., 26–31, 42, 43
Shao, X., 120
She, X., 238
Shi, L., 165
Si, Y.-H., 299
Silva, C.G., 163, 168
Silva, I.M.P., 123
Solar disinfectants, 9, 10
Solar energy, v, 20, 21, 33, 34, 36, 88, 97, 103, 142, 143, 171, 188, 194, 200, 212–243, 276, 283, 296
Stranger, M., 253
Stroyuk, O.L., 262
Sun, D., 165
Sun, S., 98
Sun, Y., 266
Sun, Z., 230
Sundar, D.S., 248–267
Synthesis, 4, 5, 58, 59, 62–71, 73, 76, 79, 81, 82, 93, 97–99, 103, 113, 114, 118, 119, 126, 142, 155, 159, 162, 173, 194–196, 199, 201, 214, 216–218, 221, 236, 240, 241, 256, 285, 295–310

T
Tan, G.Q., 302
Tan, Y., 64
Tharmaraj, V., 88–103
Thevenet, F., 256, 262
Thirugnanam, N., 95

Tian, J., 158
Time resolved spectroscopy, 76–78
Titania, 29, 30, 37–39, 44, 58–83, 101
Titanium dioxide (TiO_2), 4, 21, 58, 88, 112, 144, 189, 249, 278, 297
Tong, Z., 219, 224, 233, 304
Transition metal, 66, 119–121, 127, 142, 143, 194, 214, 262, 263, 310
Tsai, C.J., 299
Type 2 heterojunction, 60, 62–63

V
Van Wyk, A., 158
Verma, M.L., 188–203
Vignesh, K., 127
Vu, T.A., 174

W
Wahab, R., 93
Wang, C., 154, 169, 171
Wang, D., 145, 164, 170
Wang, J.C., 228
Wang, J.-J., 91
Wang, M., 175
Wang, S., 287
Wang, X., 77, 304, 306
Wang, Y., 218, 219
Wang, Z., 219, 234
Water oxidation, 27, 64, 66, 73, 154, 167–171, 198–200, 284
Water reduction, 234–240
Wei, D., 289
Wei, J., 299, 307
Wei, N., 125
Wu, P., 159

X
Xiao, J., 95
Xie, H., 256, 263
Xie, M., 78
Xiong, J., 119
Xu, F., 219, 224
Xu, J., 220, 224, 282
Xu, J.H., 300, 301
Xu, M., 125
Xue, J., 219, 226

Y
Yadav, R.K., 285
Yan, H., 218, 234
Yan, J., 69
Yang, H., 103
Yang, J.-S., 67
Yang, L.-M., 157
Yayapao, O., 123
Yemmireddy, V.K., 191
Yousefi, R., 98
Yuan, Y.J., 282
Yue, D., 97
Yue, X., 282

Z
Zang, X.-F., 284
Zeng, D., 282
Zhang, D., 90
Zhang, G., 219
Zhang, J., 282
Zhang, M., 219
Zhang, P., 77
Zhang, S., 156
Zhang, Y., 43, 162, 219, 281
Zhang, Z.-M., 158
Zhao, H., 94
Zhao, R., 220
Zhong, R., 65
Zhou, L., 190
Zhou, S., 97
Zhu, W., 103
Zhuang, H., 263
ZnO nanoparticles, 113–118, 120, 121, 128, 162
Zou, J.-P., 102, 283
Zou, Y., 91
Z-scheme, 60, 61, 68–70, 228, 236